H_2 MAGIE

H_2 as a Major Agent to Galaxy Interaction and Evolution

PhD THESIS

by

Pierre Guillard

Shock Wave in Stephan's Quintet — Spitzer Space Telescope • IRAC — Visible: Calar Alto Observatory — NASA / JPL-Caltech / Max-Planck Institute / P. Appleton (SSC/Caltech) — ssc2006-08a

Institut d'Astrophysique Spatiale, Universit Paris-Sud 11
UMR 8617, Bt. 121, 91405 Orsay Cedex, France

Front page : The Universe is smiling! This spectacular picture shows the Stephan's Quintet, a compact group of interacting galaxies. A violent galaxy collision is occurring, which creates a giant shock wave highlighted in green (Hα) on the image. This is a composite image made up of optical, Hα and infrared observations.

Institut d'Astrophysique Spatiale   Interstellar Matter and Cosmology Group

University of Paris-Sud 11   École doctorale d'Astrophysique d'Île de France

"H$_2$ MAGIE"
H$_2$ as a Major Agent to Galaxy Interaction and Evolution

THESIS

submitted and publicly defended on November, the 12th, 2009

in fulfilment of the requirements for the

Doctorat de l'Université de Paris-Sud XI
Spécialité Astrophysique et Intrumentation Associées

by

Pierre Guillard

Composition of the jury

President :	Alain Abergel	IAS, University of Paris-Sud XI, Orsay
Referees:	Cristina Popescu	University of Central Lancashire
	Amiel Sternberg	University of Tel-Aviv
Examiners:	François Boulanger	IAS, Orsay, thesis supervisor
	Guillaume Pineau des Forêts	IAS, Orsay, co-supervisor
	Matthew Lehnert	GEPI, Obs. Paris-Meudon
	Ronald J. Allen	STScI, Baltimore, USA
	Philip N. Appleton	Herschel Science Center, IPAC, USA

CENTRE NATIONAL
DE LA RECHERCHE
SCIENTIFIQUE

UNIVERSITÉ
PARIS-SUD 11

"H$_2$ MAGIE"
L'Hydrogène moléculaire dans l'évolution des galaxies

THÈSE

présentée et soutenue publiquement le 12 Novembre 2009

pour l'obtention du grade de

Docteur de l'Université de Paris-Sud XI
Spécialité Astrophysique et Intrumentation Associées

par

Pierre Guillard

Composition du jury

Président :	Alain Abergel	IAS, Université Paris-Sud XI, Orsay
Rapporteurs:	Cristina Popescu	University of Central Lancashire
	Amiel Sternberg	Université de Tel-Aviv
Examinateurs:	François Boulanger	IAS, Orsay, Directeur de thèse
	Guillaume Pineau des Forêts	IAS, Orsay, co-directeur
	Matthew Lehnert	GEPI, Obs. Paris-Meudon
	Ronald J. Allen	STScI, Baltimore, USA
	Philip N. Appleton	Herschel Science Center, IPAC, USA

CENTRE NATIONAL DE LA RECHERCHE SCIENTIFIQUE   UNIVERSITÉ PARIS-SUD 11

Contents

Contents

---

[1]Photon-Dominated Region

Acknowledgments

Art is I, science is we.

Claude Bernard

During these three years my work was extremely diversified and I had the opportunity to do widely different things such as (take a deep breath!) preparing proposals for observing time, getting married with you Carole, observing at the telescope, reducing data, going out with people I've met during schools or meetings, building empirical and analytical models, or use numerical codes to interpret the data, doubting, working on the JWST/MIRI instrument and being part of such a huge project as MIRI, running, traveling and giving talks, teaching at the University, etc! I am aware of having been lucky and privileged, and obviously all of this would not have been possible without all the people I've been working or interacting with. So, a big big thank you…

. . . to Franois Boulanger for his enthusiastic supervision of this thesis. Franois, it has been a pleasure to work with you during these three years. I've learned so much science at your side. I greatly benefited from your experience, your general vision of physical processes in the interstellar medium, from your rigour and work methods. You always pushed me to the first line, "at the shock front", to do things by myself, to be responsible. After three years, I'm always impressed by your long-term vision of astrophysics and astropolitics, by your ability to raise new ideas and to question what we thought to understand. I greatly appreciated your humility, your optimism, and your breezy, zestful character. It is thus difficult to ask more from a supervisor!

2009, Publication of the Marina del Rey, L.A., Vol. 2

. . . to Guillaume Pineau des Forts, my co-supervisor. Despite your incredibly busy schedule, you were always available. I'm proud to had such an expert in shocks and chemistry on my side! I greatly appreciated the clarity of your explanations, both during your masters courses and discussions about gas physics we had together.

. . . to the californians Phil Appleton, Patrick Ogle, and Michelle Cluver. Thanks for having invited me at Caltech and allowed me to join you for an observing run at Palomar to observe our favorite
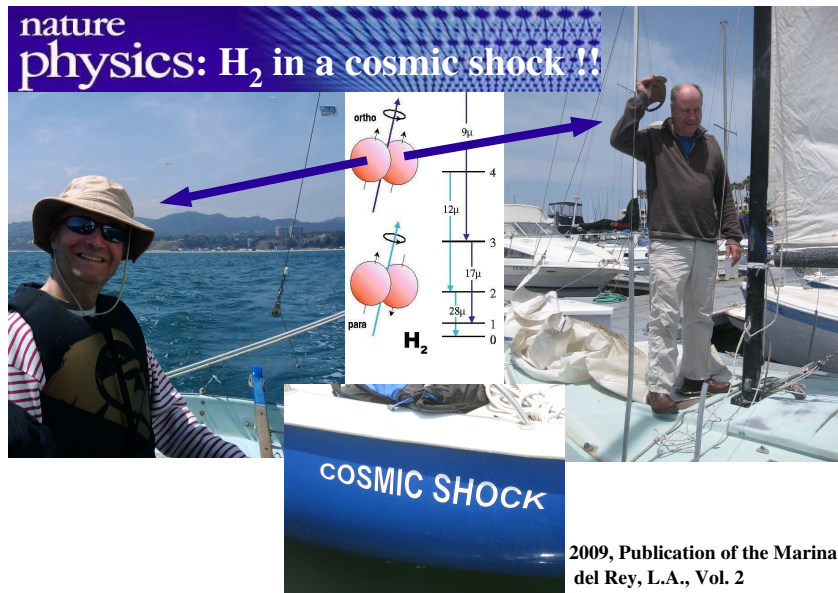
object, Stephan's Quintet. I'm grateful to Patrick and Phil for the postdoc position they offered me, and I'm particularly glad to continue our fruitful collaboration. Your team has opened a new "H_2 route", so let's explore it together... Now, I'm looking forward to see your "cosmic boat" Phil! It looks really great! Thanks Michelle for the energy you put in reducing all these new data! I'm looking forward to meet you!

... to Alain Abergel for pushing me into the MIRI project. You have been always enthusiastic and giving value to the work I was doing. I do not forget the CEA team at Saclay, in particular Samuel Ronayette, Jrme Amiaux, Vincent Moreau, Pierre-Olivier Lagage and Jean-Louis Augures. I am particularly grateful to Thomas Rodet from the LSS for his skills in signal processing and deconvolution algorithms.

... to Vincent Guillet and Nicole Nesvadba. You were postdoc at the beginning of my PhD, and now both of you have permanent positions! Congratulations! Thanks a lot Vincent for all the nice discussions we had together about shocks and dust processing. I am also indebted to you for your help with the shock code. I also thanks Nicole for her dynamism, the efficient help she provided me to write my postdoc applications, and her careful reading of the chapters 1 and 9 of this manuscript.

... to Anthony Jones, for having supervised my Masters Thesis. I greatly appreciated his kindness, and of course his hindsight view at dust evolution in the interstellar medium. I particularly thank Anthony for having put me in contact with his colleagues Xander Tielens and Hugues Leroux, with whom we collaborated for my masters prohect.

... to all the people who invited me for giving talks in prestigious places, in particular Tom Abel in Standford University, Bruce Draine in Princeton, or David Neufeld at Johns Hopkins University/STScI. You listened to me with attention, and I greatly benefited from your questions and suggestions.

... to the IAS staff, and particularly to the members of the "Matire Interstellaire et Cosmologie" group. I enjoyed all the many seminars organized by the group. Relaxing coffee and lunch breaks also contributed to this friendly work atmosphere. Thanks Mathieu and Alexandre for the good time in Prag. Thanks to the IAS computer scientists, for your efficiency solving problems and good humor. I would like to thank Ghislaine Renoux for the hard-to-find articles she managed to get for me. Thanks also to the administration, and especially Alain Belvindrah for his efficient handling of all my late mission requests!

... to my teacher colleagues with whom I worked during these years. Thanks Alain Abergel, Laurent Verstrate, Herv Dole for the courses at the University. I also thank Michel Dennefeld and Herv Dole for the OHP trainings and nice flying over Provence! Thanks a lot Michel for your invitation to an observing school in India.

... to my jury. I sincerely thank my referees, Amiel Sternberg and Cristina Popescu for examining my work and reading this manuscript with attention. They form a ideal combination, since Cristina is an expert in dust observations and modeling in extragalactic environments, and Amiel is an expert in gas physics and modeling of gas cooling processes. I am very honoured to have such a team of scientists at my side!

... A glimpse to my BSc and MSc project supervisors, Karl-Ludwig Klein and Gilles Theureau. You were both models for me, and you contributed to shape my interest for astrophysics.

... to all the PhD students and postdocs at IAS, especially Benjamin B.[1] (for nice relaxing mo-

ments playing tennis), Nicolas F. (thanks for your welcome in Pasadena!), Nicolas T.[1], Doug, Mathieu, Eleonore[1] (I really enjoy your laughs!), Aurlie[1], Nathalie, John[1], Sophie[1] Pierre[1], Alexandre, Delphine, Benjamin S.[1] , etc. I am also indebted to Manuel Gonzalez for his help with the DUSTEM and PDR codes. Thanks Mathieu and Doug for being so cheerful, and for the good time spent in Les Houches! I also thank all the students I've met during schools or conferences with whom we had good times together. Leo, Ccile, the Benjamins, Hans, Verena, thanks so much for the great time in Evora!

. . . to my family and friends. I will always be gratefull to my parents and in-laws. Thanks to Damien, Nicolas, Benjamin G. (remember that sleepless night we spent writing our manuscripts. . .). Last but not least, a big kiss to my wife Carole, for her love, her smile, and unfailing support. I can't help thinking I was so lucky to meet you!

<div align="right">
Pierre Guillard

Orsay

January 20, 2010
</div>

---

[1]I'd like to thanks these actors for the delirium-kind-of-little-lipdub we made together. You can watch it here.

Abstract

My main thesis work is to understand the origin of molecular Hydrogen (H_2) emission in active phases of galaxy evolution. Spitzer space telescope observations reveal a new class of H_2-luminous galaxies with enhanced H_2 line emission but where star formation is strongly suppressed. This is in sharp contrast with what is observed in standard star forming galaxies.

The Stephan's Quintet (SQ) galaxy collision is a striking example I initially focus on. We present a scenario and a detailed model to account for the presence of H_2 in the SQ giant shock, to characterize its physical state, and to describe its role as a cooling agent of a violent phase of galaxy interactions. In this scenario, the dissipation of the mechanical energy of the collision produces a multiphase medium where molecular gas fragments coexist with a hot ($\sim 5 \times 10^6$ K), X-ray emitting plasma. Our model quantifies the gas cooling, dust destruction, H_2 formation and emission in the postshock multiphase gas. The dynamical interaction between the ISM phases drives a cycle where H_2 is formed out of atomic gas that cools, and is excited repeatedly before being destroyed. A cascade of energy is associated with this cycle, in which the mechanical energy powers supersonic turbulence within the molecular gas. The H_2 emission is associated with the dissipation of this turbulent energy.

New results of mid-infrared and radio observations in the SQ shock are presented. These observations reveal that dust and CO emission gas is associated with the warm ($\gtrsim 100$ K) H_2 seen by Spitzer, and that this gas is in an unusual physical state where star formation is suppressed. In addition, to test the scenario proposed for the formation of H_2 in the SQ shock, I carry on a detailed observational study and modeling of the dust emission from the H_2 gas. Observational perspectives with the Herschel satellite are discussed.

These observations suggest that H_2 contributes significantly to the energy bugdet of galaxies which are in key phases of their evolution (galaxy interaction, gas accretion in galaxy clusters, starburst or AGN feedback). My thesis work is a first step to understand the role that molecular gas plays in galaxy evolution. Our model developped for SQ is extended to the context of radio galaxies, which allow for the first time to peer at the impact of the AGN-driven jet on the multiphase ISM of the host galaxy. A natural extension of this work is the characterization of the energetics of galactic winds (in the M82 starburst galaxy for instance) and in AGN-driven winds recently discovered in high-redshift radio-galaxies. This thesis includes the tools to perform a detailed modeling of Spitzer and upcoming Herschel data.

Besides this work, as a member of the JWST/MIRI consortium, I also report my contribution to the optical performance tests of the MIRI instrument, which will extend the study of H_2-luminous galaxies to high redshifts. The observational and theoretical work presented in this manuscript may help to develop a phenomenological "recipe" of the impact of H_2 on the energetics of galaxy evolution. This work will certainly be helpful for the preparation of future observing programs aiming at testing this phenomenology directly, thanks to spectroscopy of high-redshift galaxies with the JWST and SPICA missions.

Abstract

Ce travail est dédié à la compréhension de l'émission du dihydrogène (H_2) dans les phases actives de l'évolution des galaxies. La découverte d'une nouvelle population de sources extragalactiques avec un spectre dans l'infrarouge moyen dominé par les raies d'émission de H_2 est un résultat inattendu des observations spectroscopiques du satellite Spitzer. La faiblesse des bandes d'émission des poussières et des raies du gaz ionisé par rapport à celles de H_2 indique la présence de grandes quantités de gaz H_2 (jusqu'à $10^{10} M_\odot$ au centre des amas de galaxies) avec peu de formation d'étoiles, contrairement à ce qui est observée dans les galaxies standard.

Une interprétation physique de l'émission H_2 associée à une collision à grande vitesse (1000 km/s) entre galaxies dans le Stephan's Quintet (SQ) est d'abord présentée. La dissipation de l'énergie cinétique de la collision crée un milieu multi phases où des fragments de gaz moléculaire coexistent avec un plasma de gaz chaud ($\sim 5 \times 10^6$ K) émetteur en rayons X. Notre interprétation relie la structure multi phases du gaz post-choc à la structure en densité du gaz pré-choc. L'interaction dynamique entre les phases entretient un cycle où H_2 se forme à partir de gaz atomique chaud qui se refroidit puis est excité de manière répétée avant d'être détruit. A ce cycle est associée une cascade énergétique où l'énergie cinétique du gaz alimente une turbulence supersonique dans le gaz moléculaire. Le rayonnement H_2 est associé à la dissipation de l'énergie turbulente.

Les résultats de nouvelles observations moyen-infrarouge et radio dans le choc de SQ sont présentés. L'émission de la poussière et du gaz CO associé au gaz H_2 est détectée. Le gaz CO est extrêmement turbulent, ce qui pourrait expliquer pourquoi la formation stellaire est si peu efficace dans cet environnement. Pour tester notre interprétation de l'émission de H_2, les résultats de la modélisation de l'émission de la poussière associée au gaz H_2, ainsi que les perspectives observationelles apportées par le satellite Herschel, sont discutés.

Ces observations et ce travail théorique inscrivent l'étude du gaz moléculaire dans le cadre de la formation et de l'évolution des galaxies. Les mêmes caractéristiques d'émission H_2 sont observées dans les interactions entre galaxies, la rétroaction de la formation stellaire et celle des noyaux actifs de galaxies sur le milieu interstellaire, ainsi que l'accrétion de gaz dans les amas. Un dénominateur commun de ces phases violentes de l'évolution des galaxies est la libération d'énergie mécanique en quantité suffisante pour affecter globalement le milieu interstellaire. Cette interprétation est étendue à l'émission H_2 des radio-galaxies où le jet relativiste est la source d'énergie mécanique. Dans les deux cas, le gaz moléculaire apparaît comme un acteur de l'évolution dynamique des galaxies en amont de la formation stellaire.

Cette thèse présente également un travail d'analyse des tests de qualité optique réalisés au CEA sur l'instrument MIRI, une caméra moyen-infrarouge qui sera intégrée sur le futur télescope spatial JWST. Cet instrument permettra d'étendre ce travail de thèse à haut redshift, pour comprendre l'impact du gaz moléculaire sur l'évolution des galaxies lorsque l'Univers était plus jeune. Cette étude servira de base pour de futurs programmes d'observations avec le JWST.

Introduction

À ces belles nuits claires passées la tête en l'air
A ma famille et ma belle-famille pour m'avoir transmis l'amour
de la nature, de la science, et la passion du vin
A ces joyeux gosiers qui me servent d'amis
A l'appellation d'origine contrôlée "L'étoile"
A Carole, pour son sourire

L'Univers, c'est un peu comme un grand vin...

Levez les yeux au ciel lors d'une belle nuit. Vous voyez d'abord sa belle robe scintillante. Quelques milliers d'étoiles, sur les cent milliards que contient notre galaxie. Regardez plus attentivement. Un nuage laiteux traverse le ciel, il s'agit d'un des bras spiraux de notre "Voie Lactée", où la concentration des étoiles est telle que notre œil ne peut les distinguer. Arrêtez-y vous un instant. Des reflets, des zones plus sombres se dévoilent. C'est le milieu interstellaire, "entre les étoiles", qui n'est pas vide, comme on l'a longtemps cru. Ce milieu est constitué d'un mélange de gaz (atomes, molécules) et de poussières, représentant environ $5 - 10\%$ de la masse d'une galaxie.

Tout apparait si tranquille, si calme. Vous commencez juste à sentir les parfums enivrants de votre nectar. Mais maintenant goutez-y. Pour cela, imaginez que vos yeux soient équipés des plus puissants instruments capables d'explorer tout le domaine du spectre électromagnétique. Vous découvrez une explosion de saveurs, un Univers bouillonnant, violent, explosif !

Les galaxies sont loin d'être des objets "statiques", immuables. Elles évoluent d'un point de vue dynamique et chimique. La matière interstellaire joue précisément un rôle très important dans cette évolution, à petite échelle (celle d'une étoile), mais aussi à l'échelle de la galaxie toute entière. La gaz moléculaire, la phase la plus froide du milieu interstellaire (MIS), est le matériau de base pour la formation des étoiles. Celles-ci se forment dans les régions les plus denses des nuages moléculaires. Au cours de leur vie, les étoiles émettent du rayonnement UV, façonnent des "bulles" dans leur nuage parent, et lorsque ces bulles crèvent, le gaz chaud éjecté peut nourrir la phase ionisée du MIS. La chimie de ce vin évolue lentement avec le temps, développant des arômes de plus en plus complexes. Certaines étoiles massives explosent en supernovae, et participent à l'évolution chimique du gaz en enrichissant la phase chaude du MIS en éléments plus lourds que l'Hélium. Lorsque

cette source d'ionization s'éteint, le gas chaud peut se recombiner, pour reformer du gaz neutre, et éventuellement du gaz moléculaire. Une galaxie est donc une machine "écologique" à recycler la matière interstellaire! Ce vin, si tranquille et si simple au premier coup d'œil, se révèle d'une extraordinaire richesse, d'une incroyable complexité! L'Univers, c'est comme un grand vin, plus on l'étudie, plus on l'apprécie!

L'évolution des galaxies, qui forme le cadre général de cette thèse, met en jeu des phases extrêmement énergétiques, comme par exemple la collision entre deux galaxies. Une quantité phénoménale d'énergie mécanique est libérée. Comment le MIS réagit-il à ces phénomènes énergétiques? Que devient ce cycle de la matière interstellaire, et comment la formation stellaire est-elle affectée? Ces questions sont au cœur de ce travail, et sont clés pour comprendre comment les galaxies, telles que nous les voyons aujourd'hui, se sont formées.

Mais mon petit, qu'as-tu cherché?

Le sujet de cette thèse a pour point de départ la découverte observationnelle d'une émission extraordinairement puissante de H_2, la molécule la plus simple et la plus abondante de l'Univers, dans un groupe compact de galaxies en interaction, appelé le Quintette de Stephan. Cette découverte observationnelle a été suivi par la détection d'autres objets, comme des radio-galaxies, ou des flots de gaz dans les amas de galaxies, présentant les mêmes caractéristiques spectroscopiques dans le domaine moyen-infrarouge. Le spectre de ces objets est dominé par les raies rotationelles de H_2, avec de faibles signatures de formation stellaire (émission de la poussière ou du gaz ionisé), contrairement à ce qui est observé dans les galaxies classiques (par exemple les spirales), formant des étoiles. De grandes quantités de gaz moléculaire sont détectés, mais avec étonnamment peu de formation stellaire. Une partie de mon travail a été de donner une interprétation physique de cette émission.

et donc, qu'as-tu fait exactement?

J'ai cherché à comprendre la formation et l'émission du H_2 dans ces phases actives de l'évolution des galaxies, en me focalisant d'abord sur le Quintette de Stephan. Ce travail a été très varié. J'ai développé et utilisé des outils théoriques pour calculer le refroidissement du gaz dans ces environnements astrophysiques, la formation et l'émission de H_2. Les observations existantes et ce travail de modélisation ont conduit à de nouvelles propositions d'observations. J'ai conduit plusieurs campagnes d'observations au radiotélescope de 30m de l'IRAM[2] pour chercher le gaz CO (monoxyde de Carbone, gaz moléculaire "froid", i.e. $\sim 10 - 20$ K) associé au gaz H_2 "chaud" ($\sim 100 - 1000$ K) détecté dans le Quintette en infrarouge. Mon travail inclue la réduction de ces données radio et leur interprétation.

En parallèle, j'ai eu la chance de participer au projet spatial JWST, le James Webb Space Telescope, qui succèdera au télescope spatial Hubble. Une partie de mon travail est dédié aux tests de performance optique d'une caméra infrarouge, MIRI, qui sera un des 5 instruments embarqués à bord du JWST. Cette instrument sera sans nul doute le futur proche des observations du gaz moléculaire,

---

[2]Institut de Radio Astronomie Millimétrique

notamment de H_2, dans le domaine moyen-infrarouge. Il permettra de tester si les galaxies lumineuses en H_2 sont présentes à haut décalage vers le rouge, c'est-à-dire lorsque l'Univers était plus jeune.

Cette thèse a aussi été une aventure humaine internationale, faite de rencontres, lors d'écoles, de conférences, ou de séminaires. J'ai eu la chance de voyager et d'interagir avec de nombreuses personnes. Vous l'aurez compris, j'ai pris beaucoup de plaisir pendant ces trois années de thèse. De manière plus générale, comme tout travail de recherche, la thèse est parsemée de moments de doute, mais aussi d'euphorie où l'on croit avoir compris ou découvert quelque chose, pour finalement le remettre en question et douter à nouveau !

Tu as cherché, soit... et as-tu "trouvé" au moins?

La notion de "découverte", de "trouvaille", est très subjective en astrophysique! Les "grandes" découvertes sont rarement le fruit d'un programme préétabli, elles apparaissent très souvent de manière inattendue. Les percées théoriques sont aussi, bien souvent, le fruit d'un long travail et d'une grande expérience. Guidé par mon directeur de thèse, François Boulanger, j'ai essayé de produire un travail théorique qui ne soit jamais trop éloigné des observations, c'est-à-dire qui puisse interpréter des données existantes, ou bien être vérifié par de futures observations. Je vous invite maintenant à lire cette aventure dans les "quelques" pages qui suivent...

Part I

Molecules, dust, and galaxy evolution

Chapter 1

The discovery of a new population of H$_2$-luminous objects

The most exciting phrase to hear in science, the one that heralds new discoveries, is not "Eureka!" but "That's funny..."

Isaac Asimov

Abstract

One of the surprising results obtained with the Spitzer space telescope is the discovery of a significant and diverse population of low-redshift objects where the mid-infrared rotational line emission of molecular hydrogen is strongly enhanced, while star formation is suppressed. This is in sharp contrast with previous observations, where H$_2$ was solely associated with star formation. These "H$_2$-luminous sources" include galaxies that are in key-phases of their evolution, dominated by gas accretion, galaxy interactions, or galactic winds driven by star formation and active galactic nuclei. These observations open a new perspective on ISM physics, and on the role that molecular gas plays in active phases of galaxy evolution. Why is H$_2$ present in these violent environments? How is the H$_2$ emission powered? Why is the H$_2$ gas unefficient at forming stars? These questions are the core issues addressed in my thesis work.

1.1   Introduction

The molecular gas plays a central role in galaxy evolution. In most galaxies, it carries the bulk of the mass of the interstellar matter and it is the fuel for star formation. Stars are indeed made from gravitationally unstable cores within molecular clouds. Therefore, the mass of molecular gas is generally associated with the star formation rate by defining a star formation efficiency[1] (see Schmidt, 1959). The bulk of the molecular gas in most galaxies is known from molecular line spectroscopy to be cold ($\approx 10 - 20$ K, Fixsen et al., 1999). Most of the present studies primarily rely on tracing molecular gas through the observation of low rotational emission of carbon monoxyde (CO) in the radio domain.

The H$_2$ molecule, being the most abundant molecule in the Universe, is the main constituent of the molecular gas. To be seen in emission, the H$_2$ gas temperature must be warmer than ≈ 100 K. Mid-infrared (Mid-IR) rotational line H$_2$ emission traces what I will call "warm H$_2$" throughout my manuscript, at temperatures $T \approx 10^{2-3}$ K (see chapter 3). Warm H$_2$ was first observed within galactic star-forming regions, and associated with the illumination of the surface of molecular clouds by UV light from massive stars, creating Photo-Dissociation Regions (PDRs, see e.g. Habart et al., 2003). In the Galaxy, H$_2$ is also observed in proto-stellar outflows (e.g. Neufeld et al., 2006; Maret et al., 2009) or supernovae remnants (e.g. Hewitt et al., 2009), where it is shock-heated.

---

[1] star formation rate per unit gas mass.
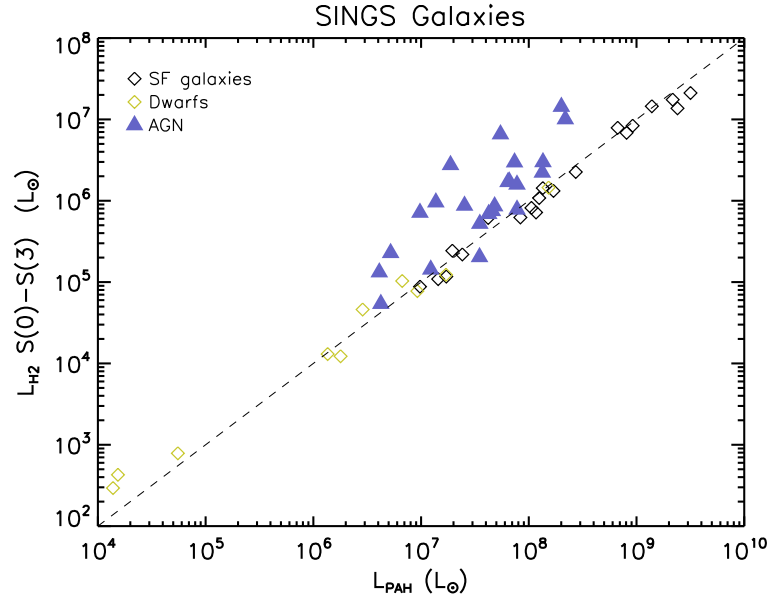
Figure 1.1: Relationship between H$_2$ and IR emission from PAHs in nearby (spatially resolved) star-forming (SF) galaxies, dwarf galaxies, and Active Galactic Nuclei (AGN). The data is from Roussel et al. (2007). These galaxies belong to the SINGS[a] sample of galaxies observed with the *Spitzer* space telescope. The H$_2$ luminosity is summed over the S(0) to S(3) rotational lines of H$_2$.

---

[a]Spitzer Infrared Nearby Galaxies Survey, http://sings.stsci.edu/.

The *ISO*[2] and *Spitzer*[3] IR satellites have started to peer at H$_2$ emission from external galaxies. In star forming galaxies, rotational H$_2$ line emission is thought to come from PDRs (Rigopoulou et al., 2002; Higdon et al., 2006; Roussel et al., 2007). A general relationship between the H$_2$ and IR luminosity is inferred from these data. This correlation is shown for nearby galaxies observed with the *Spitzer* space telescope on Fig. 1.1. Note that the Active Galactic Nuclei (AGN) galaxies stand above the tight correlation found for dwarf and star-forming (SF) galaxies. Roussel et al. (2007) indicate that the H$_2$ to PAH luminosity ratio in star forming galaxies is within the range of values that are expected from PDR emission. For the AGN sample, Roussel et al. (2007) suggest that the radiation from the AGN is not sufficient to power the H$_2$ emission.

Recent mid-IR spectroscopy performed with the *IRS*[4] onboard the *Spitzer* space telescope suggests that our census of warm molecular gas in galaxies may be severely incomplete, revealing a new class of galaxies with strongly enhanced H$_2$ rotational emission lines, while classical star formation indicators (far-infrared continuum emission, ionized gas lines, polycyclic aromatic hydrocarbons, PAHs) are strongly suppressed. These galaxies are called in this manuscript *H$_2$-luminous galaxies*.

In this chapter we paint the global observational framework of this PhD work. Section 1.2 presents the observational discovery of H$_2$-luminous objects. We point out the key astrophysical questions that we address in this manuscript in sect. 1.3. The main goal of my thesis work is to interpret these

---

[2]Infrared Space Observatory, http://iso.esac.esa.int/

[3]http://www.spitzer.caltech.edu/

[4]InfraRed Spectrograph, http://ssc.spitzer.caltech.edu/irs/

surprising observations.

1.2 H$_2$-luminous galaxies

1.2.1 Global observational characteristics

The first extragalactic mid-IR spectrum dominated by H$_2$ rotational lines has been detected in the Stephan's Quintet (hereafter SQ) compact group of galaxies (Appleton et al., 2006). Strikingly, the H$_2$ emission is detected outside the galactic disks of the group, and is more powerful that the X-ray emission from the hot gas lying in the group halo. I started my PhD shortly after the publication of that paper. My research quickly focused on this object, with the aim of explaining the origin of the H$_2$ gas and its power compared to that of the hot, X-ray emitting gas. To determine and model the excitation mechanisms that can power the observed H$_2$ emission was a driver to tackle the latter problem. This observational discovery and my interpretation and modeling work are detailed in chapters 5 and 6.

The detection of H$_2$ emission from SQ was the first of a series of discoveries of powerful H$_2$ emission in extragalactic sources that we present here. Fig. 1.2 gathers a sample of this new class of extremely luminous H$_2$ emission galaxies, up to 10^{10} L$_\odot$ in pure rotational molecular hydrogen emission lines and relatively weak total IR emission. This plot shows how H$_2$ galaxies stand out above star forming galaxies from the SINGS[5] survey when plotting the ratio of H$_2$ rotational lines to the PAH 7.7 μm luminosities vs. continuum luminosity at 24 μm. These H$_2$-luminous galaxies are therefore out of the correlation presented in Fig. 1.1. Some of the sources have undetected 7.7 μm emission, so lower limits for $\mathcal{L}_{H_2}/\mathcal{L}_{PAH7.7}$ are indicated.

The global characteristics of H$_2$-luminous galaxies are the following. Ogle et al. (2009) use empirical criteria to define H$_2$-luminous galaxies[6]. H$_2$-luminous galaxies have a large total H$_2$ to IR luminosity ratio:

$$\frac{\mathcal{L}(H_2)}{\nu \mathcal{L}_\nu(24\,\mu\text{m})} \approx 10^{-3} - 10^{-1} \tag{1.1}$$

and more specifically a large H$_2$ to 7.7 μm PAH luminosity:

$$\frac{\mathcal{L}(H_2)}{\mathcal{L}_{PAH7.7}} \approx 0.04 - 10 \tag{1.2}$$

The lower limit of 0.04 is an empirical value and also depends on the depth of the *Spitzer* observations. These ratios are up to two orders of magnitude greater than the median values for the normal star-forming galaxies. This is why they stand out of normal star-forming galaxies and luminous infrared galaxies in the plot of Fig. 1.2.

H$_2$-luminous galaxies point at a generic source of H$_2$ emission not powered by star formation. The most contrasted examples show bright H$_2$ emission lines with almost no spectroscopic signature (IR continuum of thermal dust emission, or ionized gas lines) of star formation. For instance, this is the case in Stephan's Quintet (see chapter 6) and in the 3C326 radio-galaxy (Ogle et al., 2007). The spectrum of 3C326 is shown in Fig. 1.2, on top of the standard spectrum of a starburst galaxy.

---

[5] Spitzer Infrared Nearby Galaxies Survey, http://sings.stsci.edu/

[6] In Ogle et al. (2009), H$_2$-luminous galaxies are named MOHEGs, for MOlecular Hydrogen Emission Galaxies
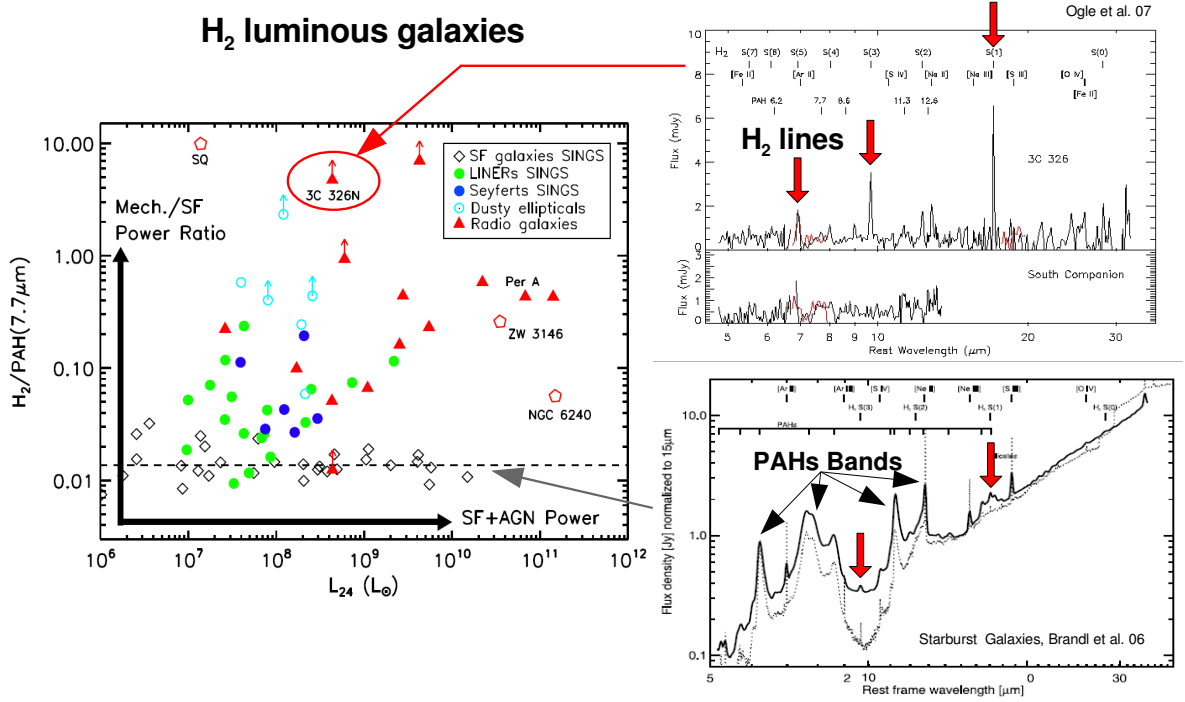
Figure 1.2: H$_2$-luminous galaxies in one plot. *Left:* Ratio of H$_2$ rotational emission summed over the 0-0 S(0)−S(3) lines to 7.7μm PAH luminosity, as a function of the 24μm continuum luminosity. The ratio indicates the relative importance of mechanical heating and power by star formation. At all IR luminosities, the observations reveal galaxies with excess H$_2$ emission beyond that expected from Star Formation (SF). The empty diamonds and the dashed line show the range spanned by SF-dominated galaxies. The H$_2$-luminous galaxies include active galactic nuclei galaxies (Seyferts, LINERs and radio galaxies), cooling flows (Perseus A, ZW3146) and interacting galaxies/mergers (Stephan's Quintet –SQ– and NGC 6240). The H$_2$-luminous radio-galaxies are from the Ogle et al. (2009) sample. The excess H$_2$ emission reveals large (up to 10^{10} M$_\odot$) quantities of warm ($T >$ 150 K) molecular gas. On the *right* side we compare the spectrum of the 3C326 H$_2$-luminous radio-galaxy (Ogle et al., 2007) with that of starburst galaxies (Brandl et al., 2006).

Note the absence of dust continuum and features in the H$_2$-luminous 3C326 radio-galaxy spectrum as compared to a star-forming galaxy.

In many of these galaxies, molecular gas has been detected through the mid-IR H$_2$ rotational lines prior to any CO observation. This sample of H$_2$-luminous objects comprises different types of astrophysical sources. We briefly describe below some of the most important examples in each category of sources.

1.2.2   Examples among different types of H$_2$-luminous astrophysical sources

Among the sample of H$_2$-luminous objects, Stephan's Quintet is certainly the object where the astrophysical context is clear enough to identify the dominant source of energy that powers the H$_2$ emission (chapter 6) and to associate this H$_2$ emission with the mechanical energy released in a galaxy colli-
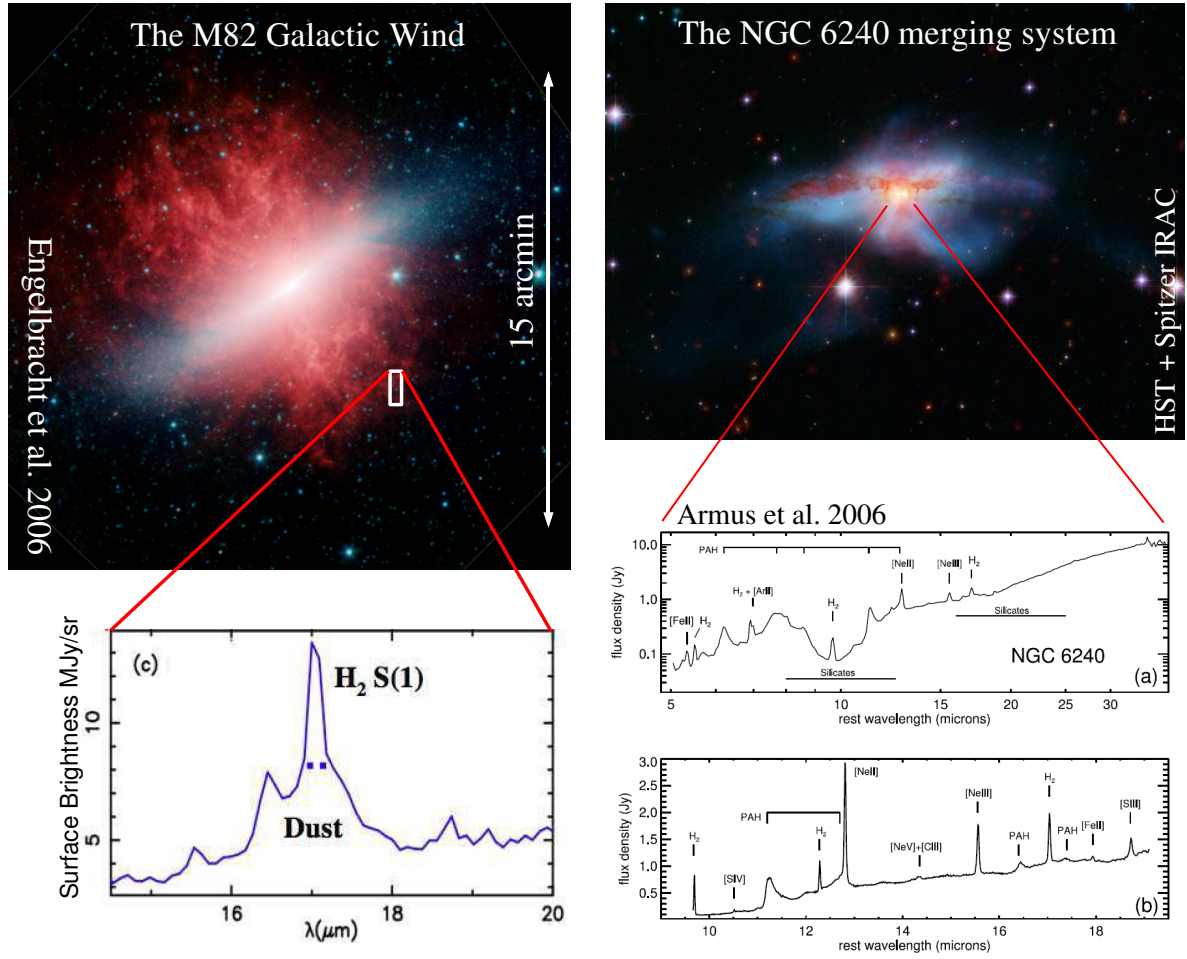
Figure 1.3: H$_2$ emission in the starburst-driven galactic wind of M82 and in the NGC 6240 merger. *Left:* In the M82 starburst galaxy, the wind is observed to be loaded with dusty molecular gas entrained and/or formed in the interaction of the hot wind with galactic halo gas. A *Spitzer* low spectral resolution ($\mathcal{R} = 80$) spectrum is shown, with the H$_2$ 0-0S(1) line on top of the $17\,\mu$m PAH feature. Taken from Engelbracht et al. (2006). *Right:* Composite image (*Spitzer IRAC* at 3.6 and 8 μm –red– and visible light from *HST* –green and blue–) of the NGC 6240 pair of colliding galaxies. The bottom plot shows *IRS* Short-Low and Long-Low (a), Short-High (b) spectra from Armus et al. (2006).

sion. This is why my PhD work initially focused on this source. In other H$_2$-luminous sources, the energy source is less clear.

Interacting and infrared galaxies

The first H$_2$ luminous galaxy, NGC 6240, was identified from ground based near-IR H$_2$ spectroscopy by Joseph et al. (1984). Later, Hawarden et al. (2002) report the discovery of four Seyfert 2 galaxies (optically classified as LINERs[7]) whose near-IR spectra are dominated by ro-vibrational emission of

---

[7]Low Ionization Emission Regions

H$_2$.

In Fig. 1.3 we show two iconic infrared galaxies, NGC 6240 and M82 that show strong H$_2$ emission. NGC 6240 is a ultra-luminous infrared merger ($\mathcal{L}_{IR} \approx 6 \times 10^{11}$ L$_\odot$) with optical and mid-IR signatures of AGN activity. The outstanding property of NGC 6240 is the presence of a double-AGN (Komossa et al., 2003). Lutz et al. (2003) report mid- and far-IR spectroscopy with the *ISO* SWS[8] and LWS[9] instruments, and find unusually strong H$_2$ mid-IR lines. This result is confirmed by Armus et al. (2006), who find $\approx 2 \times 10^9$ M$_\odot$ of warm H$_2$ within the $11.3'' \times 4.7''$ aperture of the SH[10] slit of the *IRS*, that include the two nuclei and part of an extended region where near-IR ro-vib H$_2$ emission is detected (van der Werf et al., 1993; Max et al., 2005).

The M82 starburst galaxy is not *stricto sensu* an H$_2$ luminous galaxy, but we show it in Fig. 1.3 because it may provide insights for the interpretation of other H$_2$-luminous objects. The well-known *Spitzer* image reveals the dust emission in the starburst-driven wind. Interestingly, H$_2$ is detected in the outflow of the galaxy (Engelbracht et al., 2006). Veilleux et al. (2009) also detected emission in the H$_2$ 1-0S(1) 2.12 μm rovibrational line from the starburst-driven wind. M82 is clear example where H$_2$ gas and dust coexist with the hot plasma outflowing gas.

Up to now, Stephan's Quintet is the only example among the Hickson Compact Groups (HCGs) catalog (Hickson, 1982) that show powerful emission (Appleton et al., 2006; Cluver et al., 2009). HCGs are isolated high-surface-brightness galaxy groups containing at least 4 members within a narrow optical magnitude range ($\approx 13 - 14$ mag), and almost all of them involve extreme galaxy tidal interactions (Hickson, 1982; Sulentic et al., 2001). A *Spitzer* observations have been carried on to search for H$_2$ in HCGs and the data are being analysed (see chapter 9).

Radio-galaxies

The first H$_2$-luminous radio-galaxy, 3C326, was discovered by Ogle et al. (2007). It is one of the most extreme H$_2$-luminous sources (see Fig. 1.2). We will discuss this object in more detail in chapter 9. 3C326 is one example of a sample of H$_2$-luminous radio-galaxies (selected such that $z < 0.22$) from the 3CR[11] catalog, reported in Ogle et al. (2009). They find that, among 57 sources, 17 ($\approx 30\%$) have strong H$_2$ rotational lines. These galaxies are the red triangles in Fig. 1.2. In Fig. 1.4 we show four examples of *IRS* spectra. Note the strong H$_2$ lines, as opposed to the weakness of the PAH features and the absence of silicate absorption. The summed H$_2$ S(0)-S(3) line luminosities are $\mathcal{L}(H_2) = 10^{32} - 2 \times 10^{35}$ W. Ogle et al. (2009) estimate the mass of warm molecular gas in these galaxies to be[12] $M(H_2) = 10^5 - 2 \times 10^{10}$ M$_\odot$.

Radio-galaxies have an AGN and a source of mechanical energy that is the AGN-driven jet. It is not clear how the H$_2$ luminosity is powered. The large majority (16/17) of these radio-galaxies seem to belong to pairs or clusters (see the *HST* images on the right of Fig. 1.4). This suggests that galaxy

---

[8]Short Wavelength Spectrometer.

[9]Long Wavelength Spectrometer.

[10]Short High module of the Infrared Spectrometer onboard the *Spitzer* space telescope, see http://ssc.spitzer.caltech.edu/irs/ for informations about the spectrometer.

[11]Third Revised Cambridge Catalog, http://3crr.extragalactic.info/

[12]They estimate by fitting the H$_2$ S(0) to S(7) rotational line fluxes with 3 temperatures components with thermalized H$_2$ excitation and ortho-to-para ratios. See chapters 3 and 9 for details.
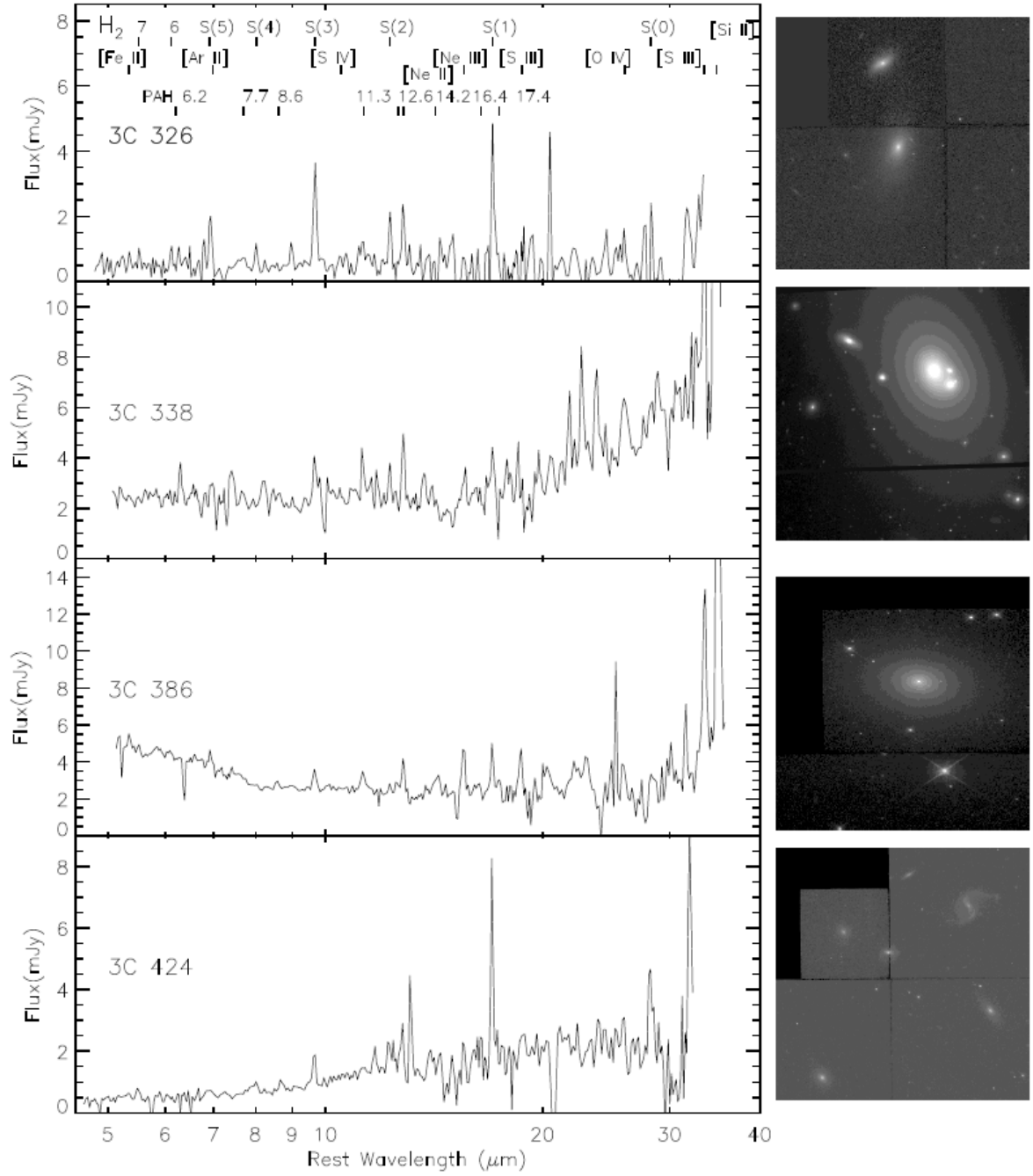
Figure 1.4: Examples of *Spitzer IRS* low-resolution spectra of MOHEGs (3C 326, 338, 386, 424). These sources show no silicate absorption and very weak PAH emission. On the right, we show *HST WFPC2* and *ACS* images. Taken from Ogle et al. (2009).

interaction may also play a role in powering the H₂ emission, although radio activity may be triggered by interactions.
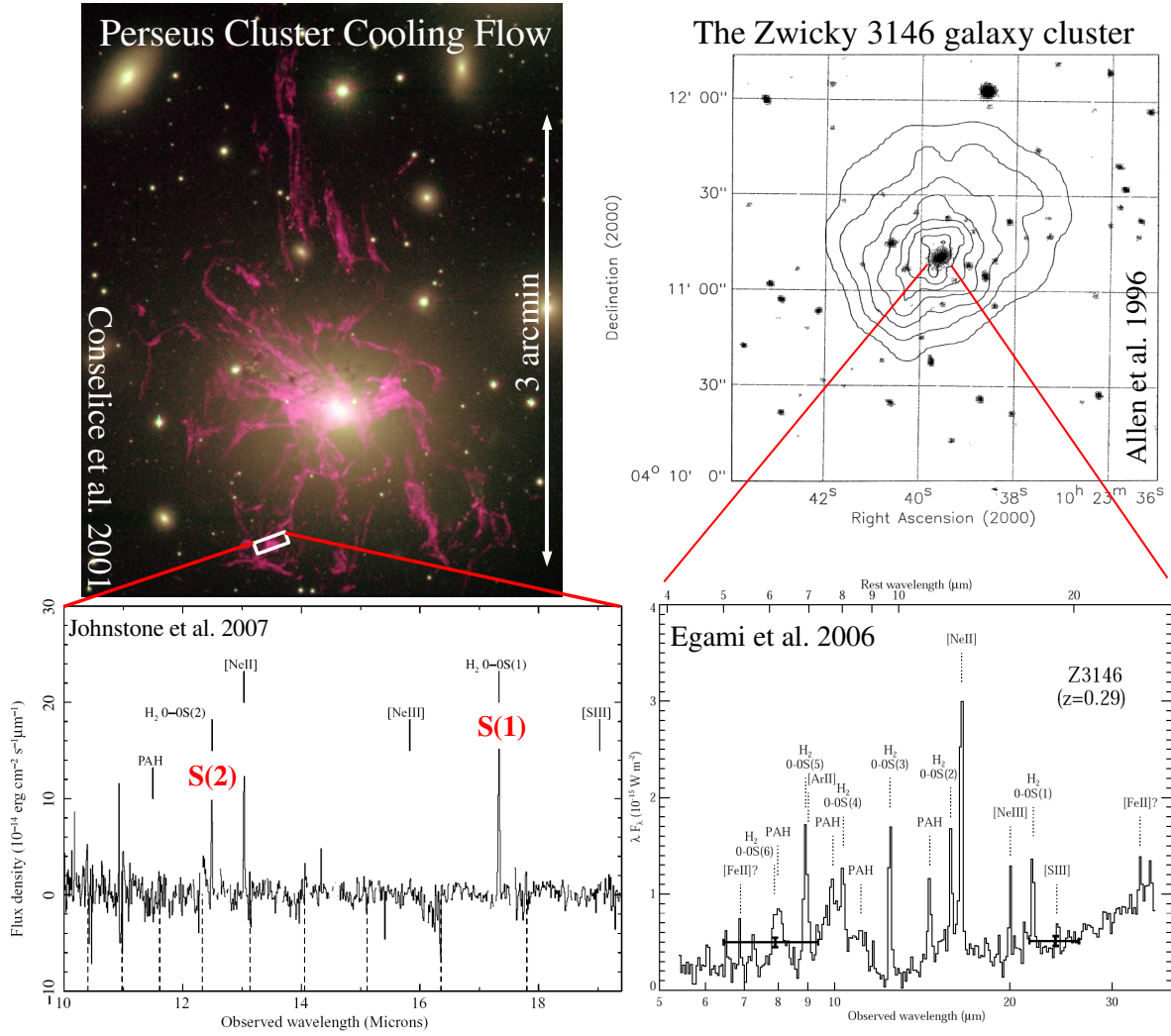
Figure 1.5: The Perseus A (NGC 1275) and Zwicky galaxy clusters illustrate the presence of H₂ in the gas that flows in/out galaxies. *Left:* In the Perseus A cooling flow, luminous H₂ line emission (see inset spectrum, Johnstone et al., 2007) is associated with the network of filaments of ionized gas in the halo (Hα image Conselice et al., 2001). These observations suggest that the cooling of the inter-cluster gas may occur through a phase transition from hot to molecular gas. *Right:* the top panel shows an R-band image of the $z = 0.3$ cluster Z3146 taken with the ESO 3.6-m telescope with X-ray *ROSAT* contours overlaid from Allen et al. (1996). The mid-IR spectrum shows powerful H₂ line emission (Egami et al., 2006).

Cooling flows in clusters of galaxies

Spitzer observations reveal that warm ($\approx 10^{2-3}$ K) H₂ is present in the central regions of galaxy clusters. The most striking examples, shown on Fig. 1.5, are the Zwicky 3146 (Egami et al., 2006) and the Perseus A (NGC 1275) (Johnstone et al., 2007) clusters. In the case of Perseus A, the H₂ emission seems to be associated with an extended network of optical line filaments (see the beautiful Hα image in Fig. 1.5), the so-called "cooling flows". These filaments are commonly found in X-ray

luminous clusters (e.g. Heckman et al., 1989), but their origin is still debated. de Messières et al. (2009) report the detection with *Spitzer IRS* of strong H_2 rotational line emission from nine cool-core galaxy clusters, with surprisingly weak dust features in 6 (out of 9) of them. Again, the H_2 detection in these hostile environments show that warm molecular gas is coexisting with the hot (a few million K) intra-cluster gas.

Elliptical galaxies

Kaneda et al. (2008) report the detection of strong H_2 emission in a sample of dusty elliptical galaxies. These galaxies are reported in the left plot of Fig. 1.2 (light blue open circles). They also show an enhancement of the $\frac{\mathcal{L}(H_2)}{\nu \mathcal{L}_\nu(24\,\mu m)}$ luminosity ratio with respect to star-forming galaxies, in spite of prominent PAH features. Many of them have radio-loud AGN. These elliptical galaxies were previously detected by the *IRAS*[13] satellite (Goudfrooij and de Jong, 1995).

1.3 Main questions addressed in this dissertation

1.3.1 Astrophysical implications of observations of H_2-galaxies

The observations of H_2-luminous galaxies are puzzling for several reasons, and raise these two main astrophysical questions:

Why is H_2 present in violent phases of galaxy evolution?

First, in galaxy clusters or high-speed galaxy collisions like Stephan's Quintet, the presence of large quantities of warm H_2 gas in a hot gas environment is unexpected. In starburst-driven winds like M82, or AGN-driven outflows like radio-galaxies (3C326 in particular), it is not clear whether the H_2 gas is molecular material that has been entrained from the galactic disk by radiation pressure and/or the outflow ram pressure, or whether it is formed *in situ*, meaning formed out of warm outflowing gas. Observations of H_2-luminous galaxies thus raise the question of the origin and the physical state of the molecular gas in these environments. In particular, is the warm H_2 physically associated with a more massive reservoir of cold ($T \lesssim 100$ K) molecular gas, as it is the case in "standard" galaxies?

How is the H_2 emission powered?

In H_2-luminous galaxies, H_2 lines appear to have an unexpected contribution to the gas cooling. The energy source powering the H_2 emission and the dominant H_2 excitation mechanisms remains to be identified. In the Stephan's Quintet galaxy collision, the astrophysical context is clearer than in distant objects, essentially because it has been extensively observed, from X-ray to radio wavelengths. This allows to study in more details the physics of the H_2 formation and emission, and to infer a physical framework to interpret other observations of H_2-luminous sources.

In conclusion, the core of this thesis is to understand the origin of the H_2 emission in these H_2-luminous objects, to identify and to study the underlying physical processes that drive H_2 formation and excitation in these hostile environments.

---

[13]InfraRed Astronomical Satellite, http://irsa.ipac.caltech.edu/IRASdocs/iras.html

Why is the H₂ gas inefficient at forming stars?

In the introduction, we have stated that, up to now, H₂ observations have been mostly associated with stellar activity. H₂-luminous galaxies are revealing molecular gas in a physical state where it is inefficient at forming stars, which does not straigthforwardly fit with our current understanding of the link between molecular gas and star formation. These H₂ observations raise the question of the identification of the physical processes that inhibit star formation in H₂-luminous galaxies. I have addressed this question within the context of the Stephan Quintet galaxy collision (see chapters 5, 7 and 8), and the 3C326 radio galaxy (chapter 9).

1.3.2   What can we learn from H₂ galaxies?

A common characteristic links the heterogeneous sample of H₂-luminous galaxies presented above: they are all in active and key phases of galaxy evolution, dominated by accretion, galaxy interactions, energy plus gas ejection due to star formation or to the action of the central black hole on its environment (AGN feedback). The exceptional H₂ luminosities observed in this variety of sources suggest that molecular gas is "responding" to these active phases of galaxy evolution. The discovery of H₂ luminous galaxies then suggests that molecular gas has an important impact on the energetics of galaxy formation and evolution, which is, up to now, largely unexplored. Most of the analytical models or simulations that describe galaxy evolution within the context of cosmological structure formation ignore the physics of the molecular gas.

Although H₂ emission does not trace the bulk of the molecular mass directly, these H₂ observations reveal key aspects of the energetic interplay between galaxies and the intergalactic medium, and between stars and their nascent clouds, that are missed by CO observations. The low star-formation efficiency observed in H₂-luminous galaxies may also provide insights in the processes that trigger or regulate star formation.

To sum up, H₂-luminous objects may represent an unexplored step in galaxy evolution, which provide insights in the role molecular gas plays in galaxy evolution.

1.4   Outline of the dissertation

The three following chapters present the background needed to tackle the problems raised above. Chapter 2 discusses the dynamics and thermal properties of the multiphase ISM, as well as the result of the calculation of the time-dependent cooling of a dusty plasma, taking into account dust destruction processes. In Chapter 3 I describe the properties of the H₂ molecule, focusing on its excitation mechanisms. The physics and chemistry of shocks in a multiphase ISM are presented in chapter 4. In particular, the codes used to interpret the observations are introduced, with emphasis on some results about molecular emission in MHD shocks.

In the second part of this dissertation, I essentially focus on the Stephan's Quintet galaxy collision. Chapter 5 presents the observational discovery of H₂ emission in the group, and the scenario I propose to explain the presence of H₂ in this violent environment. Then I address the question of H₂ excitation (chapter 6), and extend the analysis to the emission from the ionized gas in the SQ shock. Chapter 7 present the results of an observational campaign I have conducted to search for the CO counterpart of

the H_2 emission, and chapter 8 discusses dust emission. This part ends with chapter 9, which presents an extension of this work to the H_2-luminous radio galaxy 3C326, and discusses the role molecular gas plays in galaxy evolution.

The third part of this thesis is dedicated to MIRI, the Mid-IR Instrument that will be part of the scientific payload of the James Webb Telescope. Chapter 10 introduces the JWST and describes the MIRI instrument, and chapter 11 presents my contribution to the testing of the instrument, focusing on the analysis of the Point Spread Function (PSF) of the instrument. In the context of the scientific preparation of the guaranteed time projects for MIRI, we have proposed to use MIRI to study high-redshift H_2-luminous sources (chapter 12). Finally, I discuss the observational and theoretical perspectives of this work (chapter 13).

Chapter 2

Gas and dust in galaxies

If there's a bright center of the universe, you're on the planet that it's farthest from.

Luke Skywalker to C-3PO

Abstract

The astrophysical questions raised by the observational discovery of H_2-luminous galaxies involve the rich physics and chemistry of the interstellar medium (ISM). The presence and excitation of molecular gas (H_2) in the ISM heated by the release of mechanical energy on galactic scales (e.g. galaxy interactions, starburst and AGN feedback, cooling flows in galaxy cluster cores, etc.) is related to thermal and dynamical interactions between the phases of the ISM. This chapter gives an overview of the ISM phases and of the dynamical and thermal processes that drive mass and energy exchange between these phase. As H_2 forms on the surface of interstellar grains, dust evolution processes are also described in the context of this dynamical picture. This chapters ends with a description of the calculation of the cooling of a dusty, hot plasma. This result provides interesting results on dust survval in a multiphase ISM, and will be used in chapter 5 to interpret the observations of Stephan's Quintet.

Contents

2.1 Introduction

Although William Herschel and Edward Barnard produced the first images of dark nebulae silhouetted against the background star field of the galaxy (e.g. Barnard, 1919), the first direct detection of diffuse matter in interstellar space was made by Hartmann (1904) through absorption spectroscopy of the K-line of calcium at 3934 Å toward the line of sight of the δ-Orionis star. This discovery lauched more than one century of studies on the interstellar medium (henceforth ISM).

The ISM, the matter that exists between the stars, plays a crucial role in astrophysics precisely because of its intermediate role between stellar and galactic scales. The study of the ISM is closely related to the lifecycle of stars. Stars form within molecular clouds, and replenish the ISM with matter and energy when they die, through supernovae explosions, planetary nebulae, stellar winds, etc. This interplay between stars and the ISM helps determine the rate at which a galaxy depletes its gaseous content, and therefore its lifespan of active star formation.

Much of my PhD work is dedicated to the modeling of the formation of molecular hydrogen and its emission in H_2-luminous sources (these sources have been introduced in chapter 1). This involves the physics of the gas and dust in the ISM of these galaxies. In particular, this modeling is based on the heating and cooling mechanisms of the gas, and on the exchanges of energy between the different phases of the ISM.

This chapter is not an exhaustive review of ISM physics. We direct the reader to the books by (Dopita and Sutherland, 2003; Lequeux, 2005; Tielens, 2005) and to the review by Ferrière (2001). I introduce here some of the key astrophysical processes on which we will rely in the following chapters. In section 2.2 we present the different gaseous phases of the ISM and their interactions. Section 2.3 focuses on dust evolution in galaxies. Then I focus on the modeling of the cooling of a dusty, hot plasma. This calculation is illustrated within the context of H_2 studies in the multiphase medium of the Stephan's Quintet galaxy collision (see chapter 5), but *(i)* it can apply to many other astrophysical situations, and *(ii)* it provides interesting results on dust survival in the multiphase ISM.

2.2   The multiphase interstellar medium (ISM) in galaxies

Interstellar matter comprises of gas, mostly composed of hydrogen, and solid particles of dust that contain half of the elements heavier than Helium, the so-called "metals" in astrophysics. The matter consists of about 99% gas and 1% dust by mass. If the ISM fills most of the volume of a galaxy, it only represents a tiny fraction of its mass (5% of the stellar mass, and 0.5% of the total mass of the galaxy that is dominated by the dark matter).

2.2.1   Constituents, phases, and structure of the ISM

Because of the variety of processes involved in the ISM, an extremely wide range of physical conditions are present in the interstellar gas. The average density of the ISM is 1 particle per cm^3 in the Milky Way Galaxy[1], but this value varies by 8 orders of magnitude, from the hot ($T > 10^6$ K), tenuous plasma produced by supernovae shocks, to cold ($T < 10$ K) prestellar condensations.

In table 2.1 we gather the physical conditions (density, temperature, etc.) of the different components of the ISM. In the following I describe these components from an observational point of view. This description, based on observations, is very schematic, the ISM properties being a continuuous distribution.

The Hot Ionized Medium (HIM): this hot, ionized, volume-filling phase has been introduced by Spitzer (1956) to explain the stability of the cold clouds that are not gravitationally bound. This phase results mostly from supernovae explosions, that produce hot (10^{5-7} K) bubbles of

---

[1]This average density of 1 particle per cm^{-3} in the ISM is 10^{19} less than the air we are breathing!

McKee & Ostriker, 1977 *Spitzer* view at the ISM
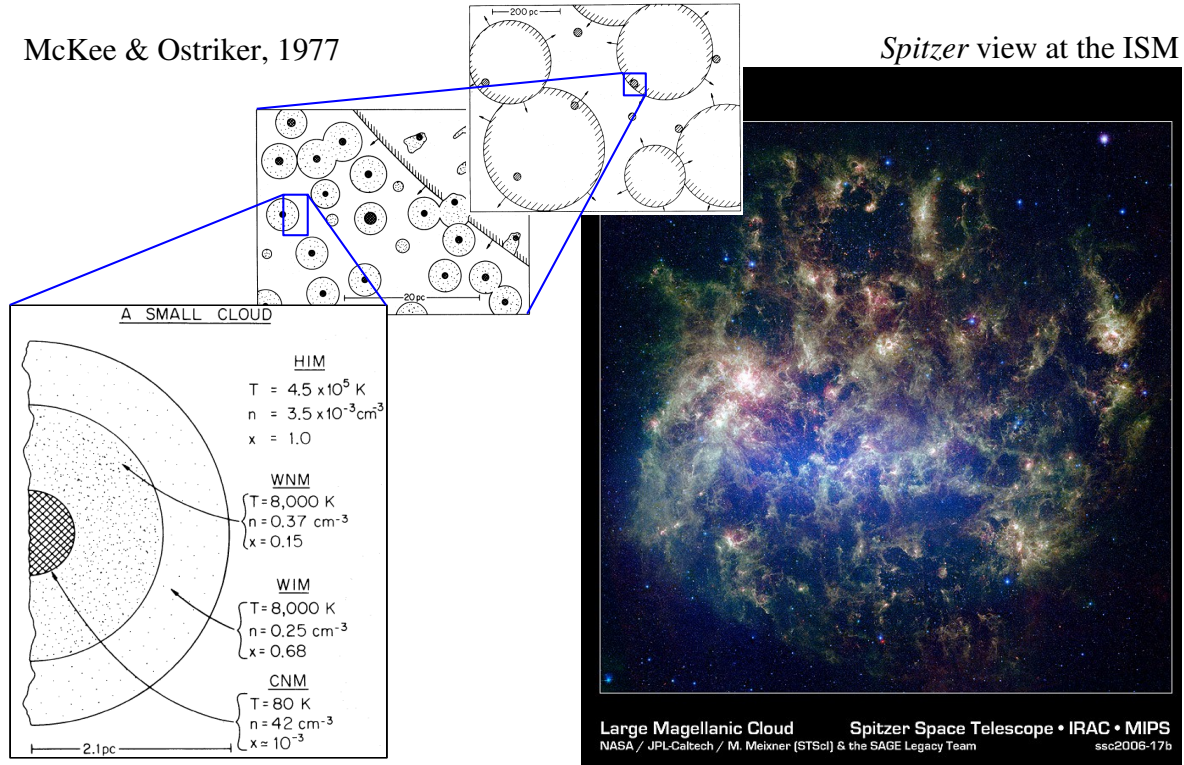
Figure 2.1: The structure of the ISM as seen by McKee and Ostriker (1977) and the *Spitzer* telescope. In the schematic view *(left)*, diffuse clouds have an *onion-like* structure, in which teneous and hotter phases are surrounding denser and colder phases. The *Spitzer* image of the ISM in the Large Magellanic Cloud *(right)* shows a contrasted view, where the ISM is a complex network of filaments, sheets and cavities, structured by star formation.

Table 2.1: Description of the phase components of the interstellar medium[a].

Phase	Density [cm^{-3}]	Temperature [K]	Volume fraction	Mass[b] [M$_\odot$]	Hydrogen[c]
Molecular Cloud	$10^2 - 10^6$	$20 - 50$	$< 1\%$	$\approx 10^9$	H$_2$
Cold Neutral Medium	$1 - 10^3$	$50 - 100$	$1 - 5\%$	1.5×10^9	H I
Warm Neutral Medium	$0.1 - 10$	$10^3 - 10^4$	$10 - 20\%$	1.5×10^9	H I
Warm Ionized Medium	10^{-2}	$10^3 - 10^4$	$20 - 50\%$	$\approx 10^9$	H II
H II region	$10^2 - 10^4$	10^4	10%	5×10^7	H II
Hot Ionized Medium	$10^{-4} - 10^{-2}$	$10^5 - 10^7$	$30 - 70\%$	$\approx 10^8$	H II

[a]This is a very schematic classification, and the separation between phases is debated. The numbers are orders of magnitudes.

[b]These masses are rough estimates for our Galaxy.

[c]This column lists the main state of the hydrogen atom in the different phases.

expanding gas, or stellar winds. The gas at $\approx 10^5$ K is predominantly traced by soft (< 1 keV) X-ray emission and UV absorption lines (OVI, NV, etc.). Hotter gas ($\approx 10^6$ K) can be seen through X-ray emission lines (OVII, OVIII). This diffuse, hot plasma phase is also characterized by a thermal continuum (free-free ot free-bound) X-ray emission.

The Warm Ionized Medium (WIM): this diffuse phase is mostly produced by the ionization of the diffuse neutral medium (by stellar radiation or shocks) or by ejection of matter from HII regions (Yorke et al., 1989). This gas at 10^{3-4} K is traced by recombination of forbidden line emission. In the McKee and Ostriker (1977) view, the WIM is associated with the external shell of a cloud.

H II regions: unlike the HIM and the WIM, this hot, ionized gas phase is *localized* around the hot stars (O- or B-type) that create ionized shells by their UV radiation. An idealized model for these regions is the Strömgren sphere, which results from the equilibrium between the ionizing flux (> 13.6 eV) and the electronic recombination rate. Some of these regions can be compact (less than 1 pc) or extremely extended (1 kpc or more) in case of very massive star clusters. These regions are traced by free-free or free-bound emission (see the book by Osterbrock, 1989, for details), like in the HIM, and by UV absorption and IR emission due to the heating of dust by the star. Diverse optical recombination lines are also produced (like Hα) and also forbidden lines ([NII], [SII], [OIII], etc.).

The Warm Neutral Medium (WNM): within the inner shells of the clouds, the gas is shielded from the background ionizing radiation and is mostly neutral, while photoelectric heating maintains the gas at temperatures around 8000 K. This phase is mostly traced by H I 21 cm line emission.

The Cold Neutral Medium (CNM): its atomic component is traced by the H I 21 cm line emission, while UV absorption spectroscopy reveals *diffuse* H$_2$ gas (Richter et al., 2003). This gas is cold because it is denser than the WNM.

Molecular Clouds (MCs): these gravitationally bound structures result from the condensation of a diffuse cloud under the effect of gravity. These clouds are dense enough for hydrogen to be molecular (H$_2$). MCs occupy a tiny fraction of the total ISM volume (1%), but account for a substantial fraction of the total mass of the ISM ($30 - 60\%$). Molecular clouds are structured over a wide range of spatial scales, from giant complexes (GMCs) of more than 10^6 M$_\odot$ and sizes of 100 pc, to smaller condensations of 50 M$_\odot$ (< 1 pc).

Classically, the ISM has been modeled by a mixture of different phases. Field et al. (1969) put forward a static *two-phase* equilibrium model to explain the observed properties of the ISM. Their modeled ISM consists of a cold dense phase ($T < 300$ K), made of clouds of neutral and molecular hydrogen, and a warm intercloud phase ($T \approx 10^4$ K), consisting of rarefied neutral and ionized gas. McKee and Ostriker (1977) added a third phase that represents the hot ($T \gtrsim 10^6$ K) gas which is shock heated by supernovae and constitutes most of the volume of the ISM. This schematic view at the ISM is presented on the left panel of Fig. 2.1. These phases are associated with temperatures where heating and cooling can reach a stable equilibrium, except for the hot phase which is metastable and needs to be continuously replenished. Their paper formed the basis for further study over the past three decades!

Today, our view at the ISM is dynamical and based on numerical simulations. The dynamical evolution of the multiphase ISM in galaxies has been extensively investigated with numerical simulations, within the context of the injection of mechanical energy by star formation, in particular supernovae explosions (de Avillez and Breitschwerdt, 2005; Dib et al., 2006). This injection of energy by supernovae is shown to be able to maintain a fragmented, multiphase and turbulent ISM, in which the gas phases are not in pressure equilibrium. Theoretical studies and numerical simulations of a supersonically turbulent isothermal gas show that the pressure may vary over two orders of magnitude, the distribution function of the pressure values being lognormal, with a dispersion that increases with the Mach number (Vazquez-Semadeni, 1994; Padoan et al., 1997; Passot and Vázquez-Semadeni, 1998; Mac Low et al., 2005).

2.2.2 Structuring the ISM

The CNM, WNM, WIM and HIM form the *diffuse* ISM phases. In the McKee and Ostriker (1977) equilibrium model, the diffuse clouds are structured like "onions", or "Russian dolls". Due to heat conduction, the teneous phases surround the denser ones. However, as shown in Fig. 2.1, the ISM structure is much more complex. It is organized in filaments, or sheets, continuously stirred by turbulent motions. This structure is observed from large scales (see the *Spitzer* image of the LMC[2] in Fig. 2.1) to small scales around the solar neighbourhood. This *self-similar* structure is also observed within molecular clouds (e.g. Falgarone, 2002).

It has often been proposed that the condensation of matter by *thermal instability*, that will be discussed in sect. 2.2.5, was the origin of the multiphase structure of the ISM (e.g. McKee and Ostriker, 1977; Wolfire et al., 1995). On the other hand, since almost 30 years, it is known that the ISM is a turbulent medium (Larson, 1981; Scalo, 1987). Measurements of line velocity dispersions (Solomon et al., 1987; Caselli and Myers, 1995) show that supersonic flows permanently skim through the ISM. These observations led to models where the ISM clouds are not the product of thermal condensation, but the result of short-lived over-densities due to turbulent motions. It has even been proposed that the pressure equilibrium between the ISM phases was not relevant for the ISM (Ballesteros-Paredes et al., 1999; Vázquez-Semadeni et al., 2000). However, these statements are moderated by Hennebelle and Pérault (1999); Audit and Hennebelle (2005), who show that thermal instability can be triggered by large-scale motions in the ISM. Therefore, it seems that both thermal instability and turbulence are not exclusive with each other in the role they play in the structuring of the ISM (e.g. Dib and Burkert, 2002).

2.2.3 Energy content of the ISM

The ISM is penetrated by photons and high-energy particles. In addition, it is dynamically tied to the magnetic field of the galaxy. I briefly summarize here the main energetic components of the ISM

In the solar neighbourhood, the average total *electromagnetic energy* density is $\approx 1\,\mathrm{eV\,cm^{-3}}$. This radiation is dominated by the UV and visible stellar radiation, and also the strong infrared radiation. In addition, the cosmological blackbody radiation of the Universe at 2.7 K correspond to $0.26\,\mathrm{eV\,cm^{-3}}$.

---

[2]Large Magellanic Cloud

The average strength of the *magnetic field* is $B \approx 5 \, \mu$G (Heiles and Troland, 2005), which corresponds to an average magnetic energy density of ≈ 1 eV cm^{-3}. Although partly organized at the galactic scale, the magnetic field in the ISM comprises of a random component and a regular component, both of comparable strengths.

Cosmic-rays are high-energy (mostly relativistic) particles (electrons, protons, heavier atoms) propagating through the ISM gas with little interactions (except at energies $\lesssim 0.1$ MeV). Assuming equipartition of energy between cosmic-ray and magnetic energy densities, the average cosmic-ray energy density derived from synchrotron emission is ≈ 1 eV cm^{-3}.

The *kinetic* energy may be non-thermal (for instance in case of supersonic motions of the gas) or thermal, and the distribution between the two forms of kinetic energy depends on the gas phase. In the CNM, the non-thermal energy is observed to dominate the thermal energy. Assuming an average density in the solar neighbourhood of $n_{\rm H} \simeq 25$ cm^{-3} and a temperature of $T \simeq 100$ K, the average thermal energy is ≈ 0.3 eV cm^{-3}.

All the energy densities listed above (photons, magnetic field, cosmic-rays, random motions) are commensurate, and of the order of 1 eV cm^{-3} in the vicinity of the Sun. This is not a fortuitous coincidence, but the result of energy transfers between this different forms of energy. Consequently, although there are exceptions, one cannot neglect any of these energies, which makes the study of the ISM ~~so difficult~~ so exciting!

2.2.4   Mass and energy transfers between the ISM phases

The ISM is a restless medium. None of the ISM components introduced above is static in time or space. A permanent exchange of matter between stars and the matter between them occurs in the galactic disk, but also between the galaxy and the intergalactic medium. The interstellar matter is thus constantly flowing from one phase to another. Depending on the physical process , and on the spatial scale we consider, the timescales associated with these mass and energy transfers can be very different, from e.g. 10^6 yr to form a protostar out of its parent molecular cloud, to e.g. 10^9 yr to consume all the molecular gas content by star formation on galactic scales.

The lifecycle of interstellar matter

The cycle of interstellar matter, sketched in Fig. 2.2, is closely related to the lifecycle of stars. Stars are born in the densest regions of molecular clouds, when the gravity takes over the turbulent motions and condenses the gas. During their life, they emit UV radiation and hot winds that create local H II regions, and may eventually break through the parent cloud and fuel the WIM and HIM phases. Some of these stars, at the end of their life, explode in supernovae. The supernovae shocks heat and ionized the gas, enriching the gas with metals, and may eventually destroy the molecular cloud from which they were born. When the ionizing source has switched off, recombination occurs and, in turn, the WIM and HIM can cool. Under the effect of gravitational contraction, diffuse neutral and molecular clouds may re-form. Within this dynamical picture of the gas evolution, the dust is also experiencing a lifecycle, which contributes to its evolution and this to the evolution of the galaxy properties in general. This will be discussed in sect. 2.3.

The galactic "ecosystem", or the cycle of interstellar matter

Hot Ionized Medium (HIM)

Metal enrichment M_{ISM}/M_{tot} decreases

Neutral atomic medium

Supernovae

Molecular clouds

Star-forming regions

→ Recombination, condensation, molecule formation
→ Dissociation, ionization (UV, shocks)
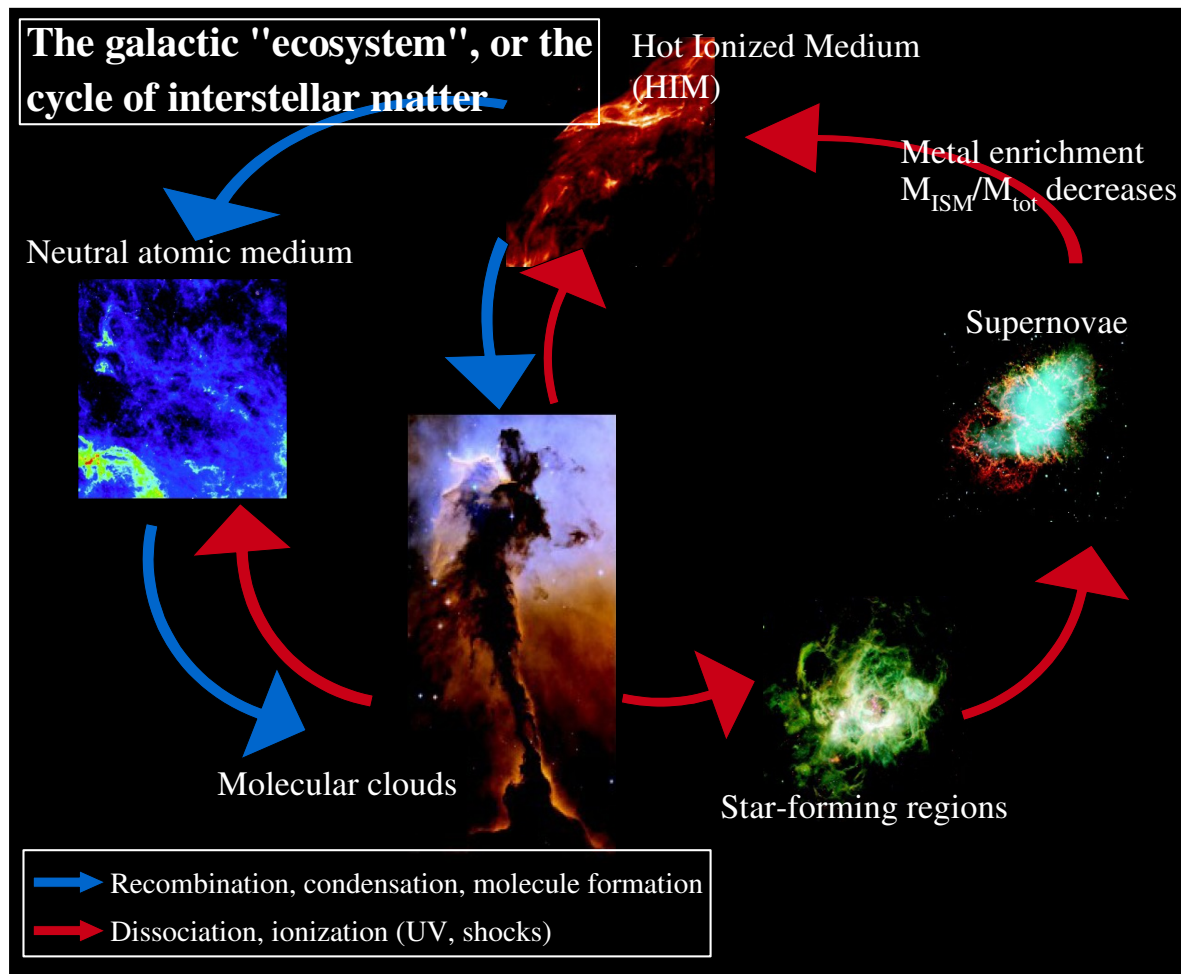
Figure 2.2: The cycle of the interstellar matter within a galaxy. The ISM is not a passive substrate within which stars evolve. It constitutes their direct partner in the "ecosystem of a galaxy", continually exchanging matter and energy with them. It is the spatial distribution ot the interstellar material together with its thermal and chemical characteristics that determines the locations where new stars form as well as their mass and luminosity spectra. Therefore, the lifecycle of interstellar matter governs the overall structure and emission properties of a galaxy.

To sum up, the physical processes involved in the mass and energy transfers between ISM phases can be splitted into two categories:

Dynamical processes: large- and small-scale fluid motions in a multiphase medium transfer momentum and kinetic energy from one phase to another. Large-scale motions are dominated by galaxy interactions, disk-halo circulation, galactic rotation, stellar-driven winds and supernovae, and gravitational collapse of giant molecular complexes. At small scales, the dynamics of the ISM is controlled by turbulence and fluid instabilities (Kelvin-Helmholtz and Rayleigh-Taylor). As introduced in sect. 2.2.1, the fact that the structure of the ISM is fragmented and self-similar[3],

---

[3]This property is true over four orders of magnitude in size, from galactic to proto-stellar scales.

suggest that turbulence plays an important role in the dynamical coupling between the different scales of the ISM. The kinetic energy cascade from the bulk motions on large scales to small-scale turbulence is a key aspect of ISM dynamics that is still poorly understood (see Elmegreen and Scalo, 2004; Scalo and Elmegreen, 2004, for reviews about interstellar turbulence).

Thermal processes: thermal exchanges (heating and cooling mechanisms) correspond to a transfer of thermal energy to or from atoms, molecules and ions of the interstellar gas. Most of the heating mechanisms involves the release of a suprathermal particle (electron, molecule) from a gas or grain specie by an energetic particle or a photon. This suprathermal particle heats the gas by thermalization through collisions. The cooling mechanisms mainly occur through inelastic collisions between light gaseous colliders (e^-, H, H^+, etc.) and heavier atoms, molecules, or grains. If energy levels of these targets can be excited by the collider, the collider loses kinetic energy and the gas cools by thermalization with the collider. The target then dissipates its energy through the emission of radiation. In the neutral ISM, this line emission mostly occur in the infrared (rotational or fine-structure line emission of e.g. C^+, C, O, H_2, CO, H_2O, etc. in the cold phase). Except in dense molecular clouds, the opacity of the medium is small in the infrared, so that the radiation can escape and the gas can effectively cool.

The heat conduction allows to redistribute the thermal energy content from one thermal phase to another. Heat conduction occurs through electron conduction (collisions) or turbulent transport. We will study these processes in more detail in sect. 4.5.2 when we will discuss the fate of molecular gas in a hot plasma, which is particularly relevant for H_2 studies in the multiphase ISM of H_2 galaxies.

Within a range of physical conditions (density, temperature), the gas is *thermally unstable*. A dynamical or thermal perturbation can bring the gas from one stable phase to a thermally unstable state which is sufficiently far from its initial state that it evolves towards another stable phase. The thermal instability appears to be an important source of mass and energy exchange between phases in the ISM. This process is discussed in the next section (sect. 2.2.5).

2.2.5 Thermal balance in the ISM

The ISM is shaped by the gas dynamics and thermal properties. As introduced before, the thermal instability plays an important role in the physics and in structuring the ISM. Thermal instabilities arises from the properties of the thermal equilibrium of the gas. I will not review here all the cooling and heating mechanisms (see e.g. the book by Lequeux, 2005), but rather focus on the properties of a thermally unstable gas.

Thermal instability

I will define the global cooling function [erg s^{-1} H^{-1}], i.e. the net heat loss function, by:

$$\mathcal{L}(\rho, T) = \Lambda - \Gamma \,, \tag{2.1}$$

where Λ and Γ are the total cooling and heating rates, respectively. At thermal equilibrium we have $\mathcal{L}(\rho, T) = \Lambda - \Gamma = 0$, which determines the temperature of the medium for a given density. This
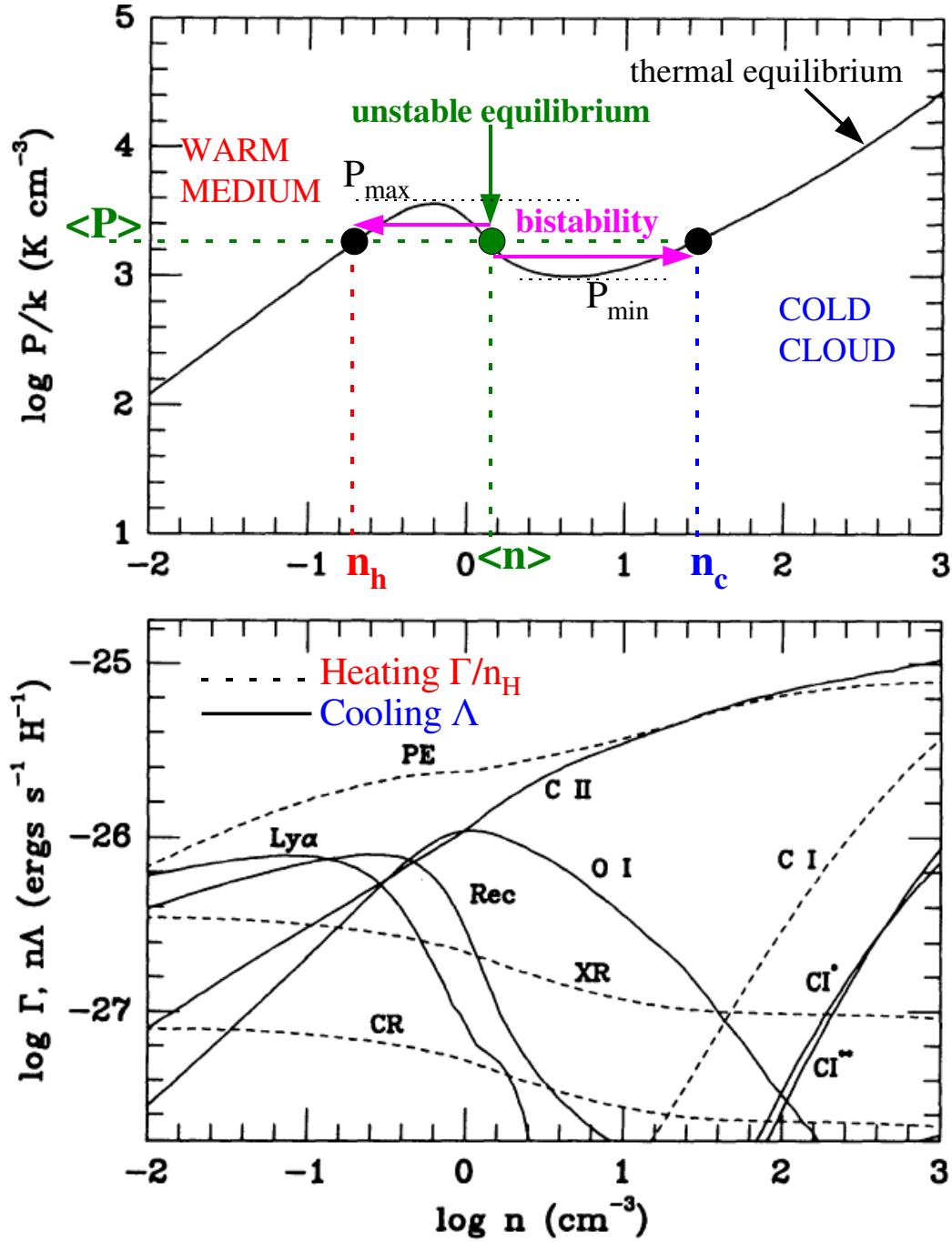
Figure 2.3: Thermal equilibrium and instability in the ISM. *Top:* Thermal pressure P/k_B at equilibrium as a function of hydrogen density n_H in the solar neighbourhood ISM, the X-ray heating being evaluated for $N_H = 10^{19}$ cm^{-2}. If the gas at (P, n_H) is above the curve, the representative point (P, n_H) will move to right because its pressure is too high, and cooling dominates over heating. Inversely, a medium below the equilibrium curve will move to the left. *Bottom:* Contributions of the different heating (Γ/n_H in our notation, dashed lines) and cooling (Λ, solid line) mechanisms. For the *heating*, PE=photoelectric effect on grains; XR=X-ray heating; C I=carbon photoionization. For the *cooling*, C II=cooling by the [C II]$\lambda158\,\mu$m line; O I=cooling by the [O I]$\lambda63\,\mu$m; CI* and CII* =cooling by [C I]$\lambda609\,\mu$m and 370 μm; Lyα =cooling by excitation of Lyman α and other transitions; Rec=cooling by recombination on the grains. Figures adapted from Wolfire et al. (1995).

condition is plotted in the top panel of Fig. 2.3. Above the thermal equilibrium curve, the cooling dominates the heating: $\Lambda > \Gamma$. Below, $\Lambda < \Gamma$. The bottom panel shows the main contributions to the Λ and Γ functions.

The first discussion of thermal instability in low-density media like the ISM has been made in a classical paper by Field (1965). I will follow his analysis to derive the thermal instability criterion. Let us consider a volume of interstellar gas (the system) in thermal equilibrium at (P, T) and introduce a perturbation of density (or temperature) while keeping constant another thermodynamic variable, A, for instance the pressure or the density. Since the entropy of the medium is defined by

$$\frac{1}{T} = \left[\frac{\partial S}{\partial E} \right]_A , \qquad (2.2)$$

E being the internal energy of the system. The perturbation yields to a change $\delta\mathcal{L}$ in the cooling efficiency:

$$\mathcal{L} \longrightarrow \mathcal{L} + \delta\mathcal{L} \qquad (2.3)$$

Rewriting Eq. 2.2, the associated change δS in the entropy can be expressed as follows

$$d(\delta S) = -\frac{1}{T}\, \delta\mathcal{L}\, dt , \qquad (2.4)$$

which can be re-written as

$$\frac{d(\ln|\delta S|)}{dt} = -\frac{1}{T} \left[\frac{\delta\mathcal{L}}{\delta S} \right]_A , \qquad (2.5)$$

This equation gives the time-evolution of the perturbation of the entropy of the system. If this perturbation δS grows with time, the thermal equilibrium of the system is *unstable*. This *criterion of thermal instability* can thus be written as

$$\left[\frac{\delta\mathcal{L}}{\delta S} \right]_A < 0 \qquad (2.6)$$

For the isobaric case, $A = P$, and since $TdS = c_P dT$, the instability criterion can be re-written as

$$\left[\frac{\delta\mathcal{L}}{\delta S} \right]_P < 0 \iff \left[\frac{\delta\mathcal{L}}{\delta T} \right]_P < 0 \iff \left[\frac{\delta P}{\delta\rho} \right]_{\mathcal{L}=0} < 0 . \qquad (2.7)$$

The last form of the instability criterion[4] can be interpreted by looking at the top panel of Fig 2.3. Let us consider the green point, located in the portion of the equilibrium curve where its slope is negative. If density increases, the pressure of the system diminishes, and becomes smaller than the ambient, external pressure. Thus the system is compressed, and the density further increases. The equilibrium is *unstable* in this zone. This *positive feedback* will stop when the gas reaches a stable equilibrium (the black point to the right in this case).

---

[4]This last form is obtained by using $\left(\dfrac{d\log P}{d\log\rho} \right)_{\mathcal{L}=0} = \left(\dfrac{\partial\mathcal{L}}{\partial T} \right)_P \Big/ \left(\dfrac{\partial\mathcal{L}}{\partial T} \right)_\rho .$

When thermal instability becomes bi-stability

The thermal instability is the core of the Field et al. (1969) two-phase model of the ISM, and I have sketched the principle of the bi-stability in the top panel of Fig. 2.3. Let us consider again our green point, at $(\langle P \rangle, \langle n_H \rangle)$. Any perturbation will make the system leave this unstable equilibrium and evolves toward a stable one. If the pressure of the system falls within the $[P_{min}, P_{max}]$ range, Fig. 2.3 shows that there are three equilibrium configurations: an unstable one (green point), and two stable (black points). The stable configurations are identified as the *warm intercloud medium* and the *cold atomic clouds* by Field et al. (1969).

A few remarks need to be given about this simple model. First, the range of pressures observed in the ISM is not always compatible with the unstable part of the thermal equilibrium curve. Secondly, the pressure equilibrium is not always reached. This is the case at small scales, because the timescale of the propagation of the perturbation (speed of sound times the length-scale) is shorter than the characteristic interval between two perturbation (typically a few 10^5 yr for supernovae explosions, yielding to sizes of 0.4 pc for the CNM and 4 pc for the WNM). Third, in the warm medium, the cooling time is larger than the perturbation time, and therefore the thermal equilibrium may not be reached for the WNM. In addition, note that the criterion for thermal instability has to be modified for *dynamical* systems, out of thermal equilibrium. The interested reader can refer to Balbus (1986). And last, depending on the cooling/heating process at work, the metallicity of the gas, the presence of dust or not, the shape of the cooling function may vary as function of the environment, and sometimes it may not exhibit and unstable part. We will come back to this point in sect. 2.4.

2.3   Evolution of interstellar dust

2.3.1   The importance of dust for our study of H$_2$-luminous galaxies

Dust grains are nanometer- to micrometer-sized solid particles that are mixed with the interstellar gas[5]. Although dust represents only $\approx 1\%$ of the total mass of the ISM, it plays a central role in the physics and chemistry of this medium. Dust grains are particularly important for our study for two main reasons:

H$_2$ formation: dust grains are the sites for H$_2$ formation (this will be discussed in chapter 3). More generally, dust grains act as catalysts for chemical reactions in the ISM.

Thermal balance of the gas: dust grains participate to the heating (via the photoelectric effect) and the cooling of the hot gas (via inelastic collisions with electrons).

Within the cycle of interstellar matter (sect. 2.2.4 and Fig. 2.2), dust is prone to evolutionary processes, being constructive and destructive, which lead to an exchange of metals with the gas. Dust nucleation occurs in cool atmospheres of dying stars, in supernovae, and dust grains grow in size in the ISM by condensation of metals. They are released to the diffuse medium by stellar winds or

---

[5]At the end of the 18th century, William Herschel made the first observations of "dark nebulae" (dusty interstellar clouds). It is only at the beginning of the 20th century that astronomers began to consider the absorption and scattering of light by dusty clouds. Today, dust particles are known to be ubiquitous in galaxies.

supernovae explosions, where they experience processing (in particular by shock-waves). Dust is then re-incorporated into newly-forming stars out of molecular clouds.

In the multiphase ISM of H_2-luminous galaxies, we also expect dust destruction to occur. On the other hand, the presence of dust is required for H_2 formation. Therefore, within the framework of my modeling of the gas cooling and H_2 formation, I have been driven to study and model dust destruction processes. I have carried on a detailed calculation of the time-dependent cooling of a shock-heated dusty plasma, taking into account dust destruction. This calculation has been published in the appendix of Guillard et al. (2009c) (hereafter paper I) in the context of the Stephan's Quintet galaxy collision. Before presenting these results, that may apply to other astrophysical situations, we introduce the properties of interstellar dust that are relevant for dust evolution modeling (sect. 2.3.2), and the physical processes of dust destruction (sect. 2.3.3).

2.3.2   Dust composition and size distribution

The composition of dust is only loosely constrained by observations. The most direct information on the composition of dust[6] comes from spectral features observed in absorption or emission[7].

Dust extinction and size distribution

The left panel of Fig 2.4 shows the *extinction law* (absorption plus scattering) from the Weingartner and Draine (2001) model. The extinction A_λ, which is the ratio of the flux $I(\lambda)$ after crossing the dust cloud to the incident flux $I_0(\lambda)$, is, in terms of magnitude,

$$I(\lambda) = I_0(\lambda) \, 10^{-A_\lambda/2.5} = I_0(\lambda) \, e^{-\tau_\lambda} \, , \tag{2.8}$$

where $\tau_\lambda = 0.921 \, A_\lambda$ is the *optical depth*. Observationally, the extinction is mostly obtained by comparing the reddened spectrum of stars to the relevant intrinsic spectrum from a library of spectral models (e.g. Fitzpatrick and Massa, 1990). This gives a relative curve, which is usually normalized to the extinction in some broad spectral bands, like B and V. For instance, A_λ is often divided by the *color excess* $E(B - V) = A_B - A_V$ or simply by A_V like in Fig. 2.4.

The extinction curve provides constrains on the size distribution of dust particles. Mathis et al. (1977) showed that the average interstellar extinction could be satisfactorily reproduced by a grain model containing two components: graphite grains and silicate grains. Remarkably, the extinction curve was reproduced very well if both grain components had power-law size distribution, so-called MRN[8] *distribution*:

$$dn_i = A_i n_H a^{-3,5} da \, , \tag{2.9}$$

where dn_i is the number of grains of the species i which radii between a and $a + da$, n_H is the reference hydrogen nuclei density, and A_i is a normalization constant. This distribution is truncated at a minimum grain size $a_{min} \simeq 50$ Å and a maximum size $a_{max} \simeq 2500$ Å. The right panel of Fig 2.4

---

[6]Although meteorites provide us with genuine specimens of interstellar grains for examination, these are subject to severe selection effects, and cannot necessarily be considered representative of interstellar grains.

[7]The amplitude of the radiated electromagnetic field from small dust particles depends not only on the incident radiation, but also on the size, shape, refractive index and polarizability of the grain.

[8]Mathis J.S., Rumpl W., Nordsieck K.H.
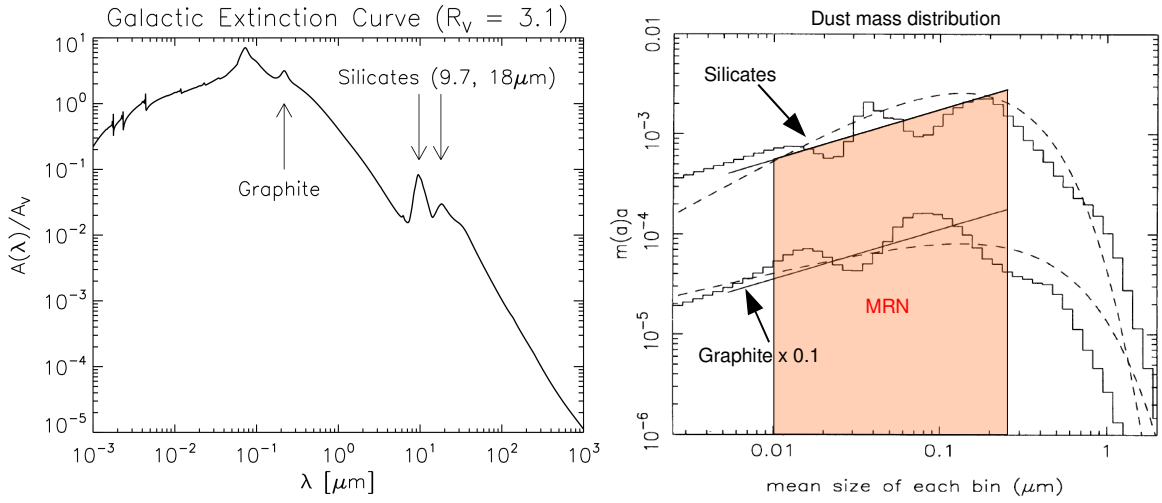
Figure 2.4: Dust extinction and mass distribution[a]. *Left:* Extinction law computed from the Weingartner and Draine (2001) model fitted to the Galactic extinction curve. *Right:* Mass distributions of interstellar grains for the difuse interstellar medium ($R_V = A_V/E(B-V) = 3.1$), expressed relative to the mass of hydrogen. The power-law ($n(a) \propto a^{-3.5}$ or $m(a) \propto a^{-0.5}$) is the MRN distribution. The histograms show the mass distributions deduced by Kim et al. (1994) from the extinction curve. The upper histogram is for silicates, and the lower for graphite (scaled down by a factor of 10 for clarity).

---

[a]Note that the two plots presented in this figure do not belong to the same model. These plots are used here for an illustration purpose.

shows the MRN mass distribution, overlaid on calculations by Kim et al. (1994). Although big grains are less numerous than small ones, they carry the bulk of the dust mass.

The extinction curve is often represented by plotting the optical depth per unit total hydrogen column density N_H. This quantity is linked to the extinction by the relation between the color excess and the hydrogen column density: $N_H/E(B-V) = 5.8 \times 10^{21}$ atoms cm^{-2} mag^{-1}. We briefly give the principle of the theoretical calculation of the extinction law. The optical depth can be written as

$$\tau_\lambda = \sum_i \int_{a_{min}}^{a_{max}} Q_e(a_i, \lambda) \pi a_i^2 N_i(a_i) da_i , \qquad (2.10)$$

where $N_i(a_i)$ is the grain column density for the species i and Q_e is the extinction efficiency. For spherical particles of radius a, these quantities can be expressed from the absorption and scattering cross sections: $\sigma_a = \pi a^2 Q_a$ and $\sigma_s = \pi a^2 Q_s$. The calculation of Q_a and Q_s as a function of the grain properties and the wavelength was first performed by Mie (1908). The success of the Mathis et al. (1977) grain model led Draine and Lee (1984) to refine the optical constants and extend the treatment into the mid- and far-infrared. In a more recent study, Weingartner and Draine (2001) added very small carbonaceous grains which play a role in the UV extinction and IR emission (Fig. 2.4).

Composition of interstellar dust

Interstellar dust grain models have been improved for 30 years in order to fit observational constraints such as elemental abundances of the heavy elements, UV, visible and infrared absorption and scattering properties, infrared emission, polarization properties of the absorbed and emitted light. The models include *a mixture of silicate grains and carbonaceous grains*, each with a wide size distribution ranging from molecules containing tens of atoms to large grains $\gtrsim 0.1\,\mu$m in diameter that can be coated with ices in dense clouds (Désert et al., 1990; Li and Draine, 2001).

Immediately following the discovery of the 2175 Å bump by Stecher (1965), Stecher and Donn (1965) pointed out that small graphite particles would produce absorption very similar to the observed feature. However, the presence of crystalline grains is considered unlikely in interstellar space where grains are exposed to cosmic rays. Other forms of carbonaceous grains (PAHS, amorphous carbons, and organic mantles on silicate grains) are being considered.

The absorption feature at $\sim 9.7\,\mu$m is due to interstellar silicate minerals, these having strong resonances near 10 μm due to the Si-O stretching mode. This conclusion is strengthened by the fact that a 10 μm emission feature is observed in outflows from cool oxygen-rich stars (which would be expected to condense silicate dust) but not in the outflows from carbon-rich stars (where silicates do not form because all of the oxygen is locked up in CO). There is also a broad feature at 18 μm that is presumed to be the O-Si-O bending mode in silicates (McCarthy et al., 1980).

The extinction curve is strongly modified when one looks along different directions, which probe the spatial variations of the dust grain properties. Some of these variations may correspond to the coagulation into bigger grains (Dominik and Tielens, 1997; Stepnik et al., 2003), or on the contrary to some erosion or destruction of grains.

2.3.3   Dust processing in shocks

I focus here on the dust destruction mechanisms relevant for the calculation of the cooling of a dusty, shock-heated plasma. I direct the reader to the review by Jones (2004) and references therein for an exhaustive presentation of all the destruction processes in the ISM evoked above. For a detailed modeling of dust evolution in shocks, please see the PhD thesis of Guillet, V. (2008).

The Fig. 2.5 gathers the mechanisms responsible for dust processing in shocked gas. Grain processing arises from interactions between the grain and "particles" (grain, atom, ion, atomic nucleus, electron, photon). They can be *destructive*, i.e. leading to a transfer of the grain atoms to the gas and thus to a net mass loss from the grain, or *non-destructive*, the grain size distribution being modified but the total dust mass conserved. These processes are counterbalanced by formation, like the accretion and nucleation, but also coagulation between grains.

Destructive processes: destructive interactions can expulse directly atoms and ions from the grain surface (via *sputtering*, ion field emission[9] or direct Coulomb explosion via extreme charging effects, coming from electron-grain interactions or photoelectric effect), or vaporize/sublimate the grain in case of $\gtrsim 20$ km s^{-1} grain-grain collisions. Vaporisation/sublimation via absorption of energetic photons (UV, γ) or interaction with cosmic rays, may also be an important destruction mechanism for volatile material, such as ice mantles.

---

[9]direct expulsion of atoms and ions from the surface at extreme surface irregularities (Draine and Salpeter, 1979b)
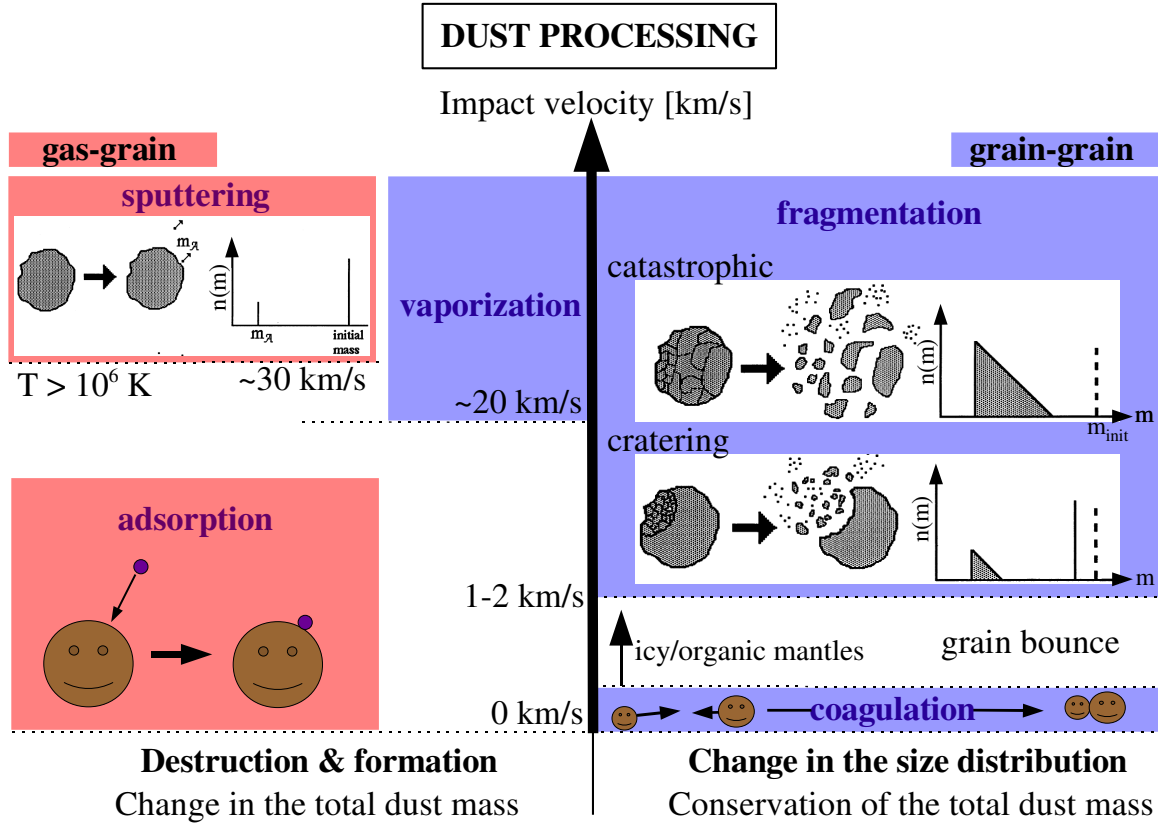
Figure 2.5: Overview of the dust processing in shocks[a]. The mechanisms are ordered as a function of the impact velocity and separated in two groups: those which modify the total dust mass (formation or destruction), and those which affect the size distribution while conserving the total dust mass. The small inset figures are from Borkowski and Dwek (1995) and show schematic description of the processing of refractory grains: sputtering, craterisation (with partial vaporization), and catastrophic fragmentation (accompanied with total vaporization). On the right of the cartoons the mass distribution of the fragments is sketched. Note that the velocity threshold for coagulation (that may lead to formation of icy and organic mantles) depends on the grain size.

---

[a]This figure is inspired from a slide of Vincent Guillet.

Non-destructive processes: Grain-grain collisions at velocities $\gtrsim 1-2\,\mathrm{km\,s^{-1}}$ lead to *fragmentation* (or *shattering*) of both grains (see Fig. 2.5 and Tielens et al., 1994). The size distribution of the fragments is a power-law, suggesting that dust fragmentation in shocks is responsible for the observed power-law (MRN) in the diffuse ISM. By definition, fragmentation is not a destructive process. It re-distributes the dust mass towards smaller grains, increasing the total cross-section of the distribution of grains, and therefore the optical and UV extinction.

In the following I will focus on the sputtering of grains by ion-grain interaction because it is the dominant destructive process in a hot ($T = 10^6 - 10^8$ K) plasma (e.g. Draine and Salpeter, 1979b; Dwek and Smith, 1996).
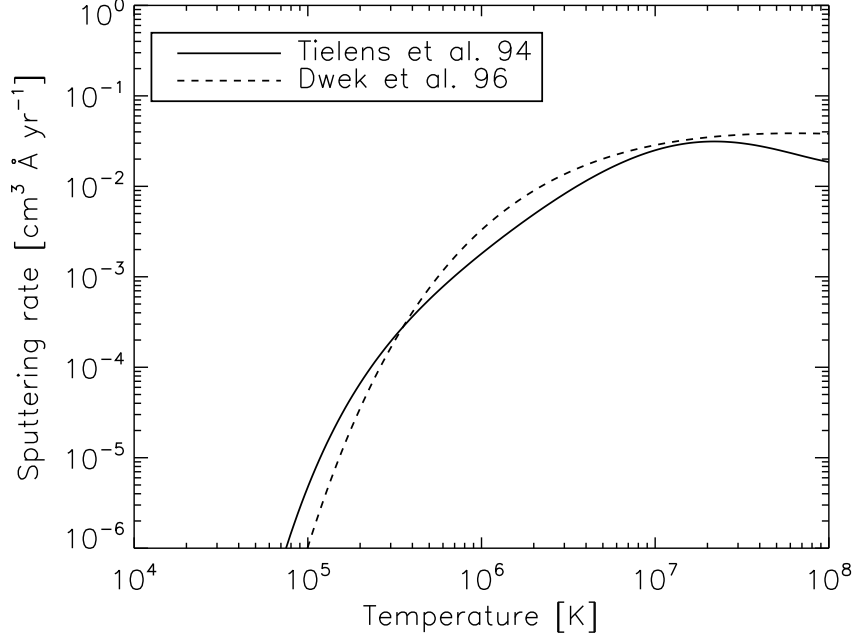
Figure 2.6: Thermal sputtering rates $\frac{1}{n}\frac{da}{dt}$ for silicate grains as a function of the gas temperature we use in our calculation of the time-dependent cooling of a dusty plasma (see sect. 2.4). The solid line shows the sputtering rates I adopt in my modeling (from Tielens et al., 1994). For comparison, the dashed line show the exponential form (Arrhenius law) of Dwek and Smith (1996) that is practical for analytical calculations. Impacts with H, He, C, N and O are considered in the calculations. Below 10^6 K, the sputtering of dust grains in a hot gas drops drastically.

Sputtering of interstellar grains

Behind a shock, gaseous ions impacting on a grain at high velocities will sputter atoms from the surface layer. We distinguish 2 cases of sputtering, depending on the nature of the shock and physical conditions of the environment.

- For high velocity ($V_s > 300\,\mathrm{km\,s^{-1}}$), grains are dragged to rest with respect to the gas before the postshock gas cools and compresses, so that sputtering arises from the *thermal motion* of ions in the gas. It is then the most abundant H^+ protons that dominate this *thermal* sputtering. This case happens in a hot gas ($T \gtrsim 10^6$ K), for example in the postshock of a supernova-generated bubble. Therefore, for $V_s > 300\,\mathrm{km\,s^{-1}}$, thermal sputtering dominates over inertial sputtering, so we ignore inertial sputtering. In this case, the grain sputtering rate is nearly constant for $T \gtrsim 3 \times 10^6$ K and strongly decreases at lower temperatures (see Fig. 2.6 and Draine and Salpeter, 1979b; Tielens et al., 1994; Dwek and Smith, 1996). The rate of decrease in grain size through sputtering is given by

$$\dot{a}_s = \frac{da}{dt} = -\frac{m_{\mathrm{sp}}}{2\,\rho_g}\,n_{\mathrm{H}}\sum A_i\,\langle Y_i\,v\rangle\;,\qquad\qquad (2.11)$$

where $m_{\rm sp}$ and ρ_g are the average mass of the sputtered atoms and the density of the grain material, A_i the abundance of impacting ion i and Y_i is the sputtering yield[10] of ion i. The quantity $\langle Y_i\,v\rangle$ is the impacting ion velocities v times the velocity-dependent yield averaged over the Maxwellian distribution. Fig. 2.6 shows the sputtering rates I use in my modeling. These yields are from Tielens et al. (1994). Then, assuming that the grains are spherical, the rate of grain mass destruction by sputtering, $\dot{m}_s$, can be easily calculated from $\dot{m}_s = 4\pi a^2 \rho_g \dot{a}_{\rm s}$.

- For low velocity ($v_s \leq 300\,{\rm km\,s^{-1}}$) shocks, grains are moving at high velocities with respect to the gas[11]. The relative gas-grain velocities result in atoms and ions collisions on grain surfaces. These collisions lead to the so-called *nonthermal* or *inertial* sputtering. If a grain is moving through a stationary gas, all particles incident upon the grain have the same relative velocity. This occurs in shock waves where the gas is rapidly swept up but the dust lags due to its greater inertia. In general, the He$^+$ ions dominate the erosion process (Tielens et al., 1994; Jones and Tielens, 1994). In the case of inertial sputtering, the parametrization of the erosion rate of the grain is more complex. I have followed the empirical approach detailed in Borkowski and Dwek (1995) to compute the rate of destruction of a grain slowing down in a dusty gas. In the following, I give the principle of this calculation.

The deceleration of a grain through the gas by collisions with the atoms or ions of the gas can be written as

$$\frac{dv_g}{dt} = -\frac{\beta\,\pi\,a^2\,\rho\,v_g^2}{m}\,, \tag{2.12}$$

where v_g is the grain velocity with respect to the gas, m and a are its mass and radius, ρ is the gas density, and β is the enhancement of the collisional drag in a plasma relative to that of a neutral medium. The initial grain velocity is set to $3/4$ of the shock velocity (Jones and Tielens, 1994). We take $\beta = 1$, which maximizes the dust destruction[12]. Therefore, our computation of the dust survival is conservative. As the grain is decelerating through the gas, it also experiences collisions with the other grains, which results in craterization or complete vaporization of the grain (see Fig. 2.5). Along its trajectory, the rate of reduction of the grain mass is the sum of the inertial sputtering and craterization rates:

$$\frac{dm}{dt} = \dot{m}_{is} + \dot{m}_{cr} \tag{2.13}$$

For a given initial grain size, I have calculated the evolution of the dust-to-gas mass ratio by integrating Eq. 2.12 and 2.13. The inertial mass sputtering rate is given by (Tielens et al., 1994)

$$\dot{m}_{is} = 2\pi a^2 m_{\rm sp}\,v_g\,n_{\rm H} \sum A_i Y_i \tag{2.14}$$

and the mass erosion rate due to cratering collisions with dust particles (field) of mass m_f and mass distribution $n(m_f)$ can be expressed as (Borkowski and Dwek, 1995)

$$\dot{m}_{cr} = -\mathcal{A}m_{\rm H}n(m_f)\pi a_g^2 v_g Y_{cr} = -n(m_f)\pi a^2 v_g f_c m_g\,, \tag{2.15}$$

---

[10]The yield is the number of atoms ejected from the grain surface per incident particle.

[11]In this case, charged grains are betatron-accelerated, because of their gyration around the magnetic field lines.

[12]The collisional drag of the grain in an ionized plasma can be enhanced ($\beta > 1$) because of charge effects (see Shull, 1978; Draine and Salpeter, 1979a)

where a_g and m_g are the radius and mass of the target grain, and v_g is the relative velocity between the target grain and the impinging dust particles (m_f). $\mathcal{A}$ is the mean atomic mass in a.m.u. of a constituent atom of the fragments. Y_{cr} is a dimensionless cratering yield equal to $m_f v^2/2E_{cr}$, where E_{cr} is the specific energy in eV atom^{-1} for the ejection of one atom in a cratering event. The quantity $\mathcal{A}m_{\mathrm{H}}Y_{cr}$ represents the average mass excavated in each collision, which can be written as $f_c m_g$, where f_c is the fraction of the target grain mass m_g that is ejected in the collision. We have adopted $f_c = 0.1$ and $E_{cr} = 2$ eV for silicate grains (see Borkowski and Dwek, 1995, for details).

I have described the physical processes that are taken into account for dust destruction and detailed how I have calculated the evolution of the dust-to-gas mass ratio in the postshock gas. This calculation was based on previous studies. Let us now couple this calculation to that of the cooling of shock-heated gas.

2.4   Time-dependent cooling of a dusty plasma

In the extreme environments of H_2-luminous galaxies, like the Stephan's Quintet galaxy collision, starburst- or AGN-driven winds, galaxy cluster cores, the warm H_2 gas is coexisting with a hot ($T > 10^6$ K) plasma. I have computed the time-dependent cooling of a gas that is shock-heated to these high temperatures. Initially, the gas is dusty, with a Galactic dust-to-gas mass ratio. The calculation of dust destruction detailed above is coupled to that of the gas cooling. This calculation is presented in the appendix of Guillard et al. (2009c). I briefly remind the principle of the calculation and summarize the main results, emphasizing some points that were not stressed in the paper.

2.4.1   Calculation method

The time-dependent total cooling function is the sum of the dust cooling (weighted by the remaining fraction of dust mass at the time t) and the gas cooling contributions. From a range of postshock temperatures up to more than 10^7 K, the isobaric gas cooling is calculated by integrating the energy balance equation which gives the rate of decrease of the gas temperature:

$$\frac{5}{2} \, k_{\mathrm{B}} \, \frac{dT}{dt} = -\mu \, n_e \, (f_{\mathrm{dust}} \, \Lambda_{\mathrm{dust}} + \Lambda_{\mathrm{gas}}) \; , \tag{2.16}$$

where μ is the mean particle weight ($\mu = 0.6$ a.m.u for a fully ionized gas), n_e is the electron density, k_{B} the Boltzman constant, f_{dust} the dust-to-gas mass ratio, Λ_{dust} and Λ_{gas} are respectively the dust and gas cooling efficiencies per unit mass of dust and gas, respectively. For the gas cooling efficiency, Λ_{gas}, I use the recent non-equilibrium, isobaric cooling curves calculated by Gnat and Sternberg (2007). The dust cooling efficiency (dust heating by electrons), Λ_{dust} is calculated following the method of Dwek (1987). The calculation is stopped when the gas has cooled to 10^4 K.

At each time step, the fraction of dust remaining in the gas f_{dust}, is computed in parallel to the postshock gas cooling:

$$f_{\mathrm{dust}} = \left(\frac{a}{a_{\mathrm{eff}}} \right)^3 \text{ with } \mathrm{a} = \mathrm{a_{eff}} - \int_{\mathrm{t_0}}^{\mathrm{t}} \dot{\mathrm{a}} \, \mathrm{dt} \; , \tag{2.17}$$
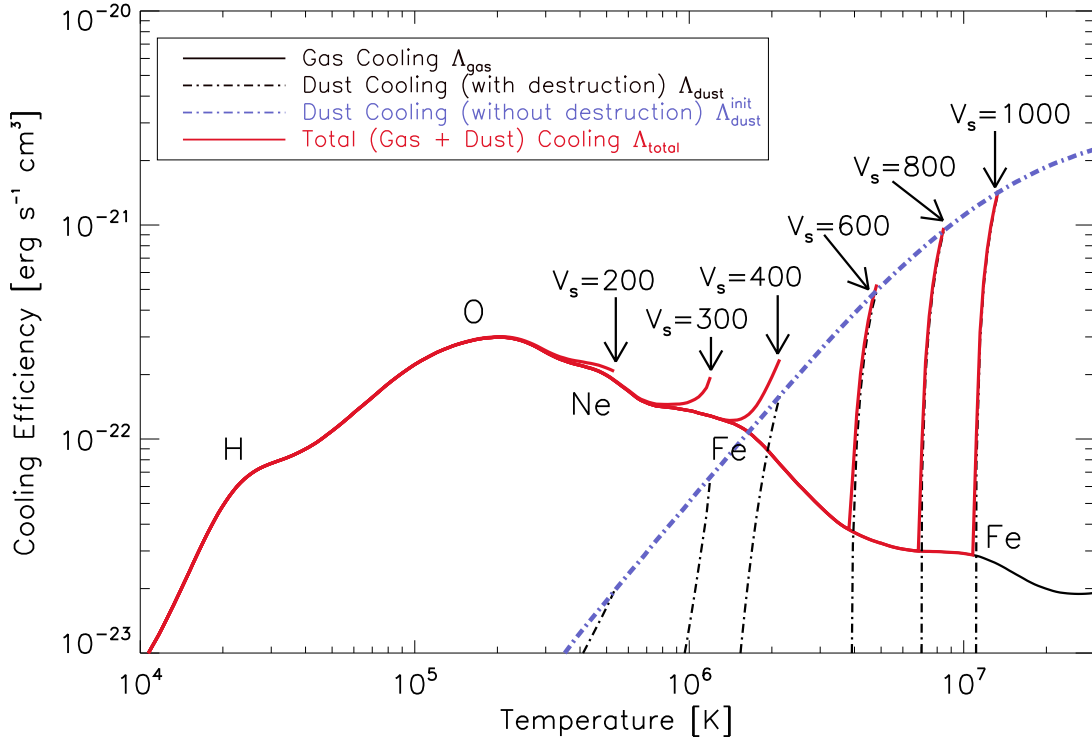
Figure 2.7: Time-dependent cooling efficiency [erg cm^3 s^{-1}] as a function of temperature during the gas cooling, for different initial conditions. The blue dashed line, $\Lambda_{\mathrm{dust}}^{\mathrm{init}}(T)$, represents the *initial* cooling function of the gas including the dust contribution, computed for a MRN interstellar dust size distribution (0.01 to 0.25 μm dust particles). The black dashed lines are the dust cooling functions for different shock velocities (i.e. different initial temperatures) which take into account the destruction by sputtering during the cooling. The cooling function due to atomic processes, $\Lambda_{\mathrm{gas}}(T)$, is displayed for an isobaric and non-equilibrium (time-dependent) cooling, and for solar metallicities ($Z = 1$). The dominant cooling elements at various temperatures are indicated on the curves. The red lines are the total cooling functions, $\Lambda_{\mathrm{total}} = \Lambda_{\mathrm{dust}} + \Lambda_{\mathrm{gas}}$, for different initial temperatures or shock velocities. The shock velocities are indicated in km s^{-1}. Their starting points are indicated by the arrows.

where $\dot{a} = da/dt$ is the rate of reduction of grain size that we have parametrized above. In the following, it is assumed that dust grains have an initial radius equal to the effective (mean) radius of $a_{\mathrm{eff}} = 0.05 \, \mu$m. This radius is the effective mean radius computed for the MRN dust size distribution.

2.4.2 Results

The resulting cooling functions are shown on Fig. 2.7. The different initial temperatures corresponds to different shock velocities. The blue dashed curve is the dust cooling function assuming a constant dust-to-gas mass ratio. The red curves are the time-dependent cooling curves taking into account dust processing.

I only briefly summarize here the main results, discussed in more detail in paper I. If the preshock

gas is dusty, the dust is initially the most efficient coolant. Indeed, at temperature hotter than $\approx$ 3×10^6 K, the dust cooling function (blue curve on Fig. 2.7), dominates the gas cooling. This produces a "flash" of IR emission. The duration of this "flash" depends on the initial gas temperature and dust-to-gas mass ratio. This collisional heating of dust is likely to be responsible for the far-IR emission in the intracluster medium of galaxy groups (see Popescu et al., 2000, for a model of dust emission within the contet of the Virgo cluster).

Significant dust emission from a hot gas does not last forever. As discussed in Smith et al. (1996) and in Guillard et al. (2009c) (paper I), the dust cooling efficiency drops with time because of the reduction of dust mass (black dashed line in Fig. 2.7). When the grains are significantly sputtered, the dust cooling efficiency becomes lower than that of the gas. This is why the total cooling curve (red line) "rejoins" the gas cooling curve (black line). As a result, the cooling times of the dusty plasma are significantly longer than those calculated with a constant dust-to-gas mass ratio (see Fig. B.2 of paper I). Consequently, the cooling timescale of the hot gas is longer than the survival timescale of dust grains (see Fig. 2 of paper I).

Looking at the cooling functions shown on Fig. 2.7, we can see that the reduction of the dust-to-gas mass ratio in a cooling plasma also favors the development of thermal instability. If the dust-to-gas mass ratio was constant, the slope of the total ($\Lambda_{\mathrm{total}} = \Lambda_{\mathrm{dust}} + \Lambda_{\mathrm{gas}}$) cooling function would be almost always positive, whereas in the case of dust destruction, the total cooling curve has an unstable part over a wide range of t emperatures, between $\approx 10^5 - 10^7$ K.

Note that a significant dust mass can still remain in the hot gas, because very large grains may survive sputtering in the hot gas. These results are in very good agreement with that of Smith et al. (1996), whom treat carefully the effect of the dust size distribution, but only consider thermal sputtering (which is anyway the dominant destruction mechanism for shock-heated plasma by high velocity ($V_{\mathrm{s}} \gtrsim 300$ km s^{-1}) shocks.

Chapter 3

The H$_2$ molecule

Some scientists claim that hydrogen, because it is so plentiful, is the basic building block of the universe. I dispute that. I say that there is more stupidity than hydrogen, and that is the basic building block of the universe!

Frank Zappa

Abstract

The hydrogen molecule, H$_2$, is the simplest and most abundant molecule in the Universe. H$_2$ has a key-role in many astrophysical processes, from galaxy formation in the primordial universe to star and planet formation. As an efficient coolant of the ISM, it is an actor of the formation of cold and dense molecular clouds, the fuel for star formation, and participates to the formation of more complex molecules. In this introductory chapter, we review the basic properties of H$_2$, highlighting its formation mechanisms and excitation processes. We also present the tools for observing molecular gas in space, and detail how to derive key parameters of the gas physical conditions (temperature, gas masses, ortho-to-para ratio, etc.) from observations.

Contents

3.1   Introduction: the role of H$_2$ in the Universe

Today, molecules are known to be ubiquitous in the Universe, with more than 150 different molecules detected in the interstellar medium (henceforth ISM). H$_2$ is the simplest one, and the most abundant in the Universe. From an astrophysical point of view, H$_2$ is an efficient cooling agent in a large variety of environments, which is perhaps the "guiding thread" of this PhD work. Therefore, H$_2$ occupies a central place in astrophysics, from large- to small-scale processes. It is impressive how such a simple molecule can touch most of the important questions in astronomy! In the following list, I briefly summarize some of the "hot topics" where H$_2$ has a word to say.

- Stars are made from the gravitational condensation of molecular gas. Then H$_2$ can be viewed as the fuel for star formation. Consequently, the star formation efficiency in "standard" galaxies correlates with the mass surface density of H$_2$ gas. This translates in a relationship between H$_2$ and IR luminosities, which has been inferred from *Spitzer* data. Furthermore, these observations disclosed the existence of sources with enhanced H$_2$ emission with weak spectroscopic signatures (dust or ionized gas lines) of star formation (the H$_2$-luminous galaxies presented in chapter 1). In these galaxies, H$_2$ seems to be a tracer of mechanical energy dissipation associated with gas accretion, galaxy collisions, or feedback. This is the core topic of this PhD work.

- H$_2$ was the first neutral molecule to be formed in the Universe, and it had influenced the collapse of the first cosmological objects, and thus had an important impact on the energetics of the formation of cosmological structures and galaxies (see chapter 9 and Abel and Haiman, 2000, for a short review).

- Most of the baryons in the Universe are "dark". Indeed, the mass of observed baryonic matter (stars and gas) in galaxies makes up at most 8 % of the total mass expected from dynamics or weak lensing studies (Fukugita and Peebles, 2004). Although alternative scenarii are being proposed, H$_2$ is now considered as a potential significant contribution to the problem of missing baryons in galaxies (e.g. Pfenniger et al., 1994; Combes and Pfenniger, 1997). Some of the missing baryons may be in the form of H$_2$ lying beyond the optical galactic disk. This gas would have remained undetected in CO because it is metal poor, clumpy, or too cold to be seen in emission. First evidence for the presence of warm H$_2$ in the outer parts of galaxies comes from the detection of H$_2$ S(0) and S(1) emission with $T \sim 80$ K in the outer disk of NGC 891, as far out as 11 kpc (Valentijn and van der Werf, 1999).

- For a star to be made, the turbulent kinetic energy of the parent molecular cloud has to be dissipated so that the gravity takes over and further condense the gas. The ranges of gas temperatures ($\approx 10^{2-3}$ K) and velocities ($\approx 1 - 10$ km s^{-1}) in the parent turbulent cloud make H$_2$ a major agent of the dissipation of this energy. Once stars have formed, they emit jets and winds that in turn inject some turbulent kinetic energy in their nascent cloud. This stellar *feedback* process remains largely unexplored. Again, H$_2$, as a tracer of dissipative processes, is certainly a key to understand what controls the star formation efficiency. The importance of H$_2$ in star formation is confirmed by observations of H$_2$ in galactic star forming regions (e.g. Orion), in protostellar molecular outflows, or infrared luminous galaxies.

- H$_2$ is also a major ingredient of giant planet formation. Planets are thought to form in the circumstellar disks that surround proto-stars and pre-main-sequence stars. Such disks, a natural outcome of the star formation process, are composed of 99 % of gas (mostly H$_2$) and 1 % of dust. H$_2$ is therefore the building block of giant planets. H$_2$ dominates the disk mass and dynamics while the dust is the main source of opacity and controls the thermodynamics of the disk. H$_2$ observations in protoplanetary disks may be used to constrain the scenario of planet formation, which is, up to now, not well determined.

- H$_2$ initiates a complex chemistry within the shielded interiors of dense clouds. Some of these reactions take place at the surface of dust grains, and the formed molecules can become constituents of protoplanetary disks, where they contribute to the formation of icy planetesimals such as the comets in our Solar System. The richness of molecular chemistry in dense gas is highlighted by observations of large organic molecules in proto-stellar cores heated by nascent stars, where ices return to the gas, and in the circumstellar environment of evolved stars (e.g. Cernicharo et al., 2001). H$_2$, as tracer of the sites of formation of complex molecules, may be a key to elucidate the open question about the connection between molecular species present in circumstellar environments and those present in the ISM.

All these astrophysical questions are closely related to the dynamics and energetics of dense gas, of which H$_2$ is the main consituent. To understand why H$_2$ is a probe as such a variety of astrophysical processes, this chapter introduces the basis of the radiative and collisional properties of H$_2$. We will rely on these properties in the next chapters. Part of my PhD work is dedicated to the modeling of H$_2$ formation and excitation in the extreme environments of H$_2$-luminous galaxies (chapters 5 and 9) by mean of shock and chemical network models (Flower et al., 2003) described in chapter 4. While going through H$_2$ properties, I will give details about how some specific processes are treated in our shock model. In particular, we discuss the ortho-to-para ratio of H$_2$ (sect. 3.2.2), and describe H$_2$ formation (sect. 3.3) and excitation mechanisms (sect. 3.4). This chapter ends with a discussion about how to observe molecular gas in space (sect. 3.5).

3.2 Portrait of the H$_2$ molecule

This section introduces some basic properties of the H$_2$ molecule that are of astrophysical interest. We direct the reader to Shull and Beckwith (1982) for an historical review, and to the specialized books by Bransden and Joachin (1983) and Flower (2007) for a fully developed theory of rotational and vibrational excitation of linear molecules. In this manuscript, we will mainly focus on the rovibrational transitions of H$_2$ in its electronic ground state, denoted[1] $X^1\Sigma_g^+$.

3.2.1 H$_2$ rovibrational transitions

H$_2$, the simplest molecule, consists of two hydrogen atoms linked by a covalent bond. H$_2$ is an homonuclear molecule, i.e. the barycenter of its electrical charges concides with its center of mass. So

---

[1]The notation is $^{2S+1}\Lambda$, where $S = 0$ or 1 is the total electronic spin and Λ is the projection of electronic orbital angular momentum on the internuclear axis
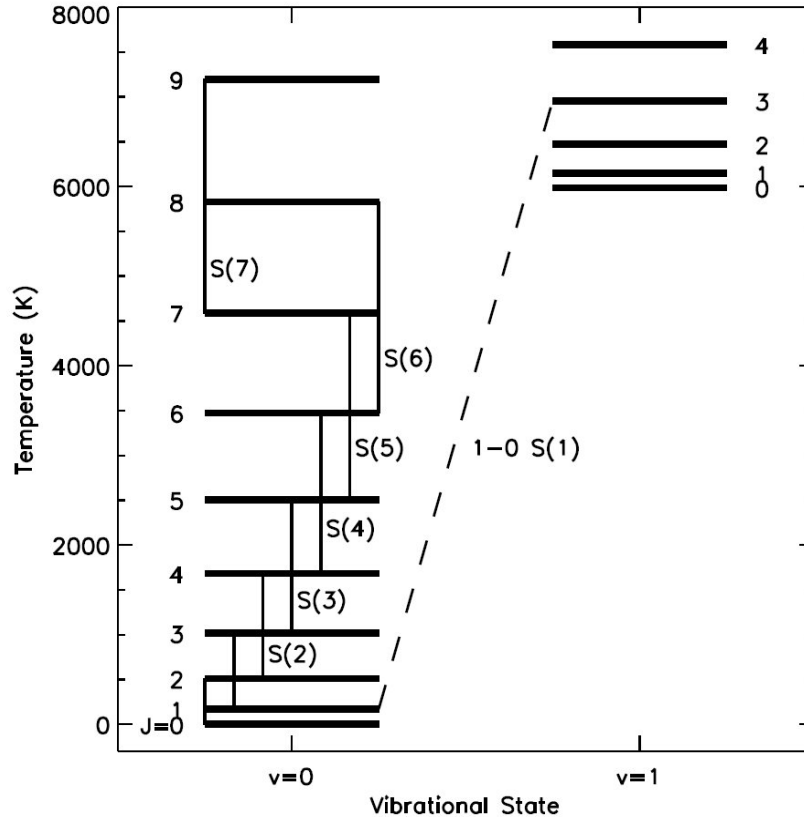
Figure 3.1: Rovibrational energy level diagram for molecular hydrogen with rotational J states labeled. The S(0) to S(7) transitions available to *Spitzer IRS* observations are indicated with solid lines. All "S" transitions are from the upper to lower J state with $\Delta J = 2$. The $v = 1$-0S(1) transition commonly observed at 2.12 μm is plotted as a das hed line. Note that the S(7) transition traces a higher upper excitation state than the 1-0 S(0) and S(1) lines commonly observed in the near-infrared. Taken from Hewitt et al. (2009).

H_2 has no permanent dipole moment and rovibrational transitions are forbidden electric quadrupole transitions. Molecular hydrogen thus exists in two different forms, depending on the value of its nuclear spin, S:

para H_2 the $S = 0$ singlet state, where the two protons have opposite directions of spin (anti-parallel). This corresponds to *even* values of J.

ortho H_2 the $S = 1$ triplet state, where the proton spins are parallel to each other. This corresponds to *odd* values of J.

The the parity (oddness or evenness) of the rotational quantum number J is constrained by the fact that the nuclear wave function must be asymmetric under exchange of protons.

Another consequence of the absence of permanent dipole moment is that rovibrational transitions within the $X^1\Sigma_g^+$ electronic ground state occur by electronic quadrupole radiation ($\Delta J = 0, \pm 2$). These quadrupole transitions do not allow to go from one H_2 form to another (from ortho to para). Because the electronic potential is anharmonic, there are no selection rules for vibrational quantum

numbers, v. Within the harmonic approximation and if we neglect the centrifugal distorsion, the energy of the rovibrational levels are given by

$$E(v, J) = BJ(J + 1) + \hbar\omega\left(v + \frac{1}{2}\right), \tag{3.1}$$

where B is the rotational constant of the molecule and ω is characteristic vibration pulsation, and $\hbar = h/2\pi$ the reduced Planck's constant. B is related to the moment of inertia of the molecule, $\mathcal{I}$, and ω can be expressed as a spring pulsation:

$$B = \frac{h}{8\pi^2 c \mathcal{I}} \quad \text{and} \quad \omega = \sqrt{\frac{k}{\mu}}, \tag{3.2}$$

where μ is the reduced mass (here it is half the mass of an hydrogen atom, $\mu = 0.5 m_{\mathrm{H}}$) and k is the spring force constant of the Hooke's law. Because H$_2$ is a light molecule, it has a small moment of inertia, and therefore a large rotational constant $B/k_{\mathrm{B}} = 85.25$ K. Its rotational levels are thus widely spaced. The diagram of Fig. 3.1 shows the level energies of the $v = 0$ and $v = 1$ vibrational states of H$_2$, with the relevant lines for our study. The $J = 2$ state lies 510 K above the $J = 0$ state, and $J = 3$ lies 845 K above $J = 1$. Consequently, the rotational excitation of H$_2$ becomes important only for temperatures $T \gtrsim 100$ K. The $v = 1$ vibration level is ≈ 6000 K above the ground state, so that rovibrational excitation (such as that at the 2.2 μm line) requires kinetic temperatures $T > 1000$ K.

The statistical weight of a given level is

$$g(J)g(I) \;\; = \;\; (2J + 1)(2I + 1) \tag{3.3}$$
$$g_J \;\; = \;\; 2J + 1 \qquad \text{for the para state} \tag{3.4}$$
$$= \;\; 3 \times (2J + 1) \quad \text{for the ortho state} \tag{3.5}$$

Under the assumption of Local Thermodynamic Equilibrium (LTE), the level populations are proportional to the statistical weight and the Boltzman factor, so that the rotational partition function is written

$$Z_{\mathrm{rot}} = \sum_J g_J \, e^{\dfrac{-E(v, J)}{k_{\mathrm{B}} T}} \tag{3.6}$$

However, because of the low temperature and density conditions in the ISM, the LTE hypothesis is not valid, and the populations of the (v, J) levels do not follow the Boltzman distribution.

In this manuscript, we will mostly focus on the first pure rotational lines of H$_2$ ($v = 0$). In Table 3.1 we list the properties of the main rovibrational lines we will consider. These transitions are within the near- and mid-infrared part of the spectrum. A transition is denoted by first writing the vibrational transition followed by the relevant branch and the lower rotational level. Thus the transition from $v = 1$ to $v = 0$, $J = 3$ to $J = 1$ is written 1-0S(1). More generally, the S-branch corresponds to $\Delta J = -2$, the Q-branch to $\Delta J = 0$, and the O-branch to $\Delta J = +2$. Table 3.1 also list the Einstein coefficients (see Eq. 3.14) and line ratios assuming LTE (see Eq. 3.6) for 4 different gas temperatures.

Table 3.1: Properties of important near- and mid-infrared H$_2$ transitions [a]

| line | Wavel. | Freq. | g_J | E_{upper} | A | LTE | $\mathcal{I}_{line}/\mathcal{I}_{1-0S(1)}$ | | |
name	[μm]	[cm^{-1}]		[K]	10^{-7} s	1000 K	2000 K	3000 K	4000 K
0-0 S(0)	28.221	354.35	5	510	0.0003	0.001			
0-0 S(1)	17.035	587.04	21	1015	0.0048	0.065	0.003	0.001	0.001
0-0 S(2)	12.279	814.43	9	1682	0.0276	0.11	0.008	0.003	0.002
0-0 S(3)	9.6649	1034.67	33	2504	0.0984	0.84	0.091	0.043	0.030
0-0 S(4)	8.0258	1245.98	13	3474	0.264	0.40	0.071	0.040	0.030
0-0 S(5)	6.9091	1447.36	45	4586	0.588	1.19	0.36	0.25	0.20
0-0 S(6)	6.1088	1636.97	17	5829	1.14	0.29	0.16	0.13	0.12
0-0 S(7)	5.5115	1814.40	57	7197	2.00	0.47	0.53	0.56	0.57
1-0 S(0)	2.2235	4497.41	5	6471	2.53	0.27	0.21	0.19	0.19
1-0 S(1)	2.1218	4712.91	21	6956	3.47	1.00	1.00	1.00	1.00
2-1 S(0)	2.3556	4245.15	5	12095	3.68	0.001	0.017	0.041	0.063
2-1 S(1)	2.2477	4448.95	21	12550	4.98	0.005	0.083	0.21	0.33
2-1 S(2)	2.1542	4642.04	9	13150	5.60	0.001	0.031	0.086	0.14

[a]We list the wavelength (in vacuum) of the line, the wave number, the statistical weight of the upper level (degeneracy), the energy of the upper level E_{upper}, the Einstein coefficient A. References: Turner et al. (1977); Dabrowski and Herzberg (1984); Black and van Dishoeck (1987); Wolniewicz et al. (1998)
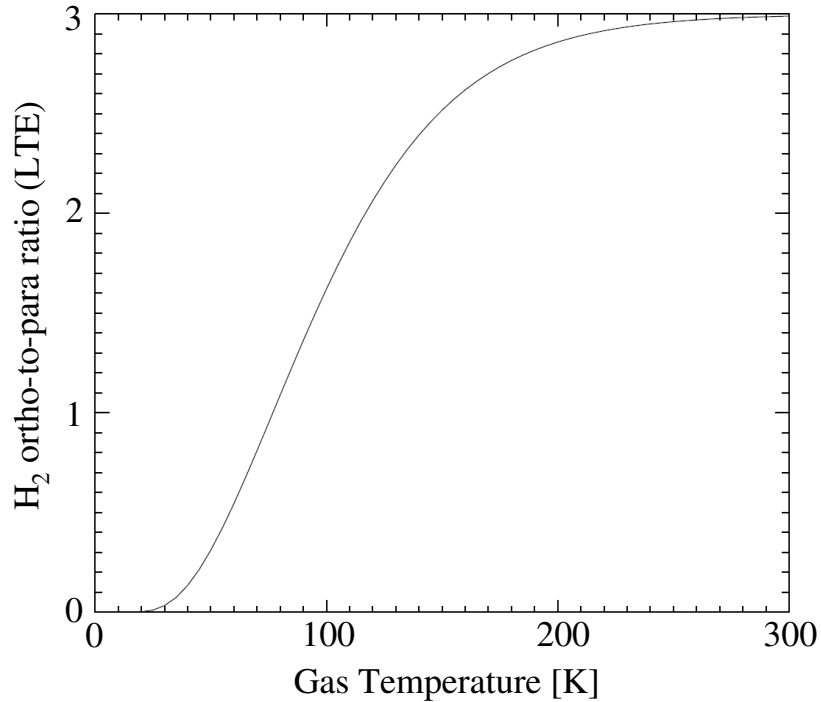
Figure 3.2: H$_2$ ortho-to-para ratio as a function of the gas temperature, assuming Local Thermodynamic Equilibrium (LTE) conditions. Below 50 K, the ortho-to-para ratio can be expressed as in Eq. 3.8.

3.2.2 H₂ ortho-to-para ratio

Definition and LTE values

The *local* H$_2$ ortho-to-para ratio (hereafter o/p) is the relative abundance of the ground state ortho- and para-H$_2$. In conditions of LTE, this ratio can be written as

$$\frac{Z_{\text{ortho}}}{Z_{\text{para}}}(\text{LTE}, T) = \frac{\displaystyle\sum_{J \text{ odd}} 3(2J + 1)e^{-E_J/(k_{\text{B}}T)}}{\displaystyle\sum_{J \text{ even}} (2J + 1)e^{-E_J/(k_{\text{B}}T)}} \tag{3.7}$$

At "high" temperatures, $T \gtrsim 300$ K, the o/p ratio tends towards the value of 3, which is the ratio of the statistical weights of all the odd and even levels. This is illustrated in Fig. 3.2, where we show the ortho-to-para ratio as a function of T. At low temperatures, $T \lesssim 50$ K like in a quiet molecular cloud, only the levels $(v = 0, J = 0, 1)$ are populated, so that, at low T and in LTE conditions, the ortho-to-para ratio can be written

$$\frac{Z_{\text{ortho}}}{Z_{\text{para}}}(\text{LTE}, T \lesssim 50\,\text{K}) = \frac{\text{Z}(\text{J} = 1)}{\text{Z}(\text{J} = 0)} = 9 \times e^{\frac{-170.5}{\text{T}}}, \tag{3.8}$$

where we get $\frac{2\,B}{k_{\text{B}}} = \frac{\hbar^2}{k_{\text{B}}\mathcal{I}} = 170.5$ K.

The o/p ratio is an important astrophysical parameter to characterize the physical state, and the history of the molecular gas. The o/p ratio of a given molecular cloud indeed depends on its age and on the timescale of para-ortho conversion, $\tau_{\text{o/p}}$. If the age of the molecular cloud is longer than the o/p conversion timescale, the o/p ratio equals its LTE value at the given temperature (Fig. 3.2). Otherwise, if the cloud age is shorter than the o/p conversion timescale, the o/p ratio keeps its value during the process of H$_2$ formation. Our model assumes that H$_2$ molecules are formed with an o/p ratio of 3, although this value is poorly constrained. The conversion mechanisms are briefly discussed in the following paragraph.

Ortho to para conversion

The conversion ortho-H$_2$ $\longleftrightarrow$ para-H$_2$ can occur through four main mechanisms:

1. the proton exchange with H$^+$, H$_3^+$, or other cations (Dalgarno et al., 1973):

$$\text{H}_2(\text{J} = 1) + \text{H}^+ \rightleftarrows \text{H}_2(\text{J} = 0) + \text{H}^+(+170.5\,\text{K}) \tag{3.9}$$
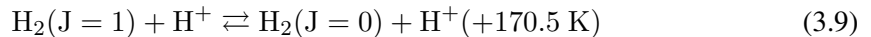
This is the dominant process at low ($T \lesssim 50$ K) temperatures (Flower et al., 2006). The reaction rates are of the order of $k_{\text{H}^+,\text{H}_2} = k_{\text{H}_3^+,\text{H}_2} \simeq 3 \times 10^{-10}$ cm^3 s^{-1} (Gerlich, 1990). For instance, in a molecular cloud of hydrogen density $n_{\text{H}} = 10^4$ cm^{-3} and temperature $T = 10$ K, H$_3^+$ being more abundant than H$^+$, H$_3^+$ − H$_2$ reactions will set the o/p conversion timescale to be of the order of

$$\tau_{\text{o/p}} = \frac{1}{n(\text{H}_3^+)\,k_{\text{H}_3^+,\text{H}_2}} \tag{3.10}$$

$$= 3 \times 10^6 \left(\frac{4 \times 10^{-5}\,\text{cm}^{-3}}{n(\text{H}_3^+)}\right)\left(\frac{3 \times 10^{-10}\,\text{cm}^3\,\text{s}^{-1}}{k_{\text{H}_3^+,\text{H}_2}}\right)\,[\text{yr}] \tag{3.11}$$

Flower and Watt (1984) carried on detailed calculations of the evolution of the o/p ratio as a function of the cosmic-ray ionization rate, which has an impact on the proton density, and therefore on the rate of Eq. 3.9, and on the chemical history of the cloud.

2. the atom exchange between H_2 and H:

$$H_2(\text{para}) + H \rightleftarrows H_2(\text{ortho}) + H \tag{3.12}$$
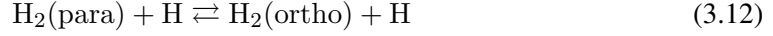
Schofield (1967) give an estimate of the collision rate of the order of

$$k_{H,H_2} \simeq 8 \times 10^{-11} e^{\frac{-3900}{T}} \ [\text{cm}^3 \ \text{s}^{-1}] \ . \tag{3.13}$$

Because of the high activation energy of ≈ 3900 K, this process is negligible in cold molecular clouds. In a cold dark cloud at $T = 10$ K, $n_H = 10^4$ cm^{-3}, for a typical cosmic-ray ionization rate $\zeta = 5 \times 10^{-17}$ s^{-1} H^{-1}, and an initial degree of ionization of $\approx 10^{-8}$, it will take more than 10^7 years to go from an o/p ratio of 3 to the equilibrium value at 10 K of $\approx 3 \times 10^{-7}$. The conversion timescale is only weakly dependent on density (Kristensen et al., 2007).

However, this mechanism can be important, and even dominant, when molecular gas is subject to heating and compression by a shock wave. Because the reaction 3.12 is rapid, the o/p ratio in the hot postshock gas may differ significantly from the o/p ratio in the cold ambient medium. The evolution of the o/p ratio in shocks has been discussed by Wilgenbus et al. (2000). For application of these studies to H_2 observations in star forming regions, we direct the reader to the PhD thesis by Kristensen (2007). The reactive collision rates used in the Flower et al. (2003) shock model are more complex, and are described in Le Bourlot et al. (1999).

3. the interaction of the H_2 nuclear spin with the inhomogeneous magnetic field at the surface of dust grains (Tielens and Allamandola, 1987). An upper limit of the ortho-to-para conversion rate by this process is given by the accretion rate of H_2 onto dust grains, and Timmermann (1998) show that this mechanism is inefficient in low-velocity (a few 10 km s^{-1}) molecular shocks.

4. the ortho to para conversion may occur when an H_2 molecule is destroyed and then reformed onto the surface of a dust grain. However, given that the H_2 formation is slow, this process is negligible here.

3.2.3   Critical densities: H_2 as a thermometer

The LTE hypothesis is valid when the density of the medium reaches a threshold density, so-called *critical density*, n_{crit}, above which collisionnal deexcitations dominate over radiative deexcitations. For a $j \to i$ transition, this condition can be written

$$nq_{j \to i} \gg A_{j \to i} = n_{\text{crit}}q_{j \to i} \ , \tag{3.14}$$

where $A_{j \to i}$ [s^{-1}] is the probability of radiative deexcitation (or so-called Einstein coefficient), and $q_{j \to i}$ the probability of collisional deexcitation [m^3 s^{-1}]. $A_{j \to i}$ is proportional to $(E_j - E_i)^5$, so for
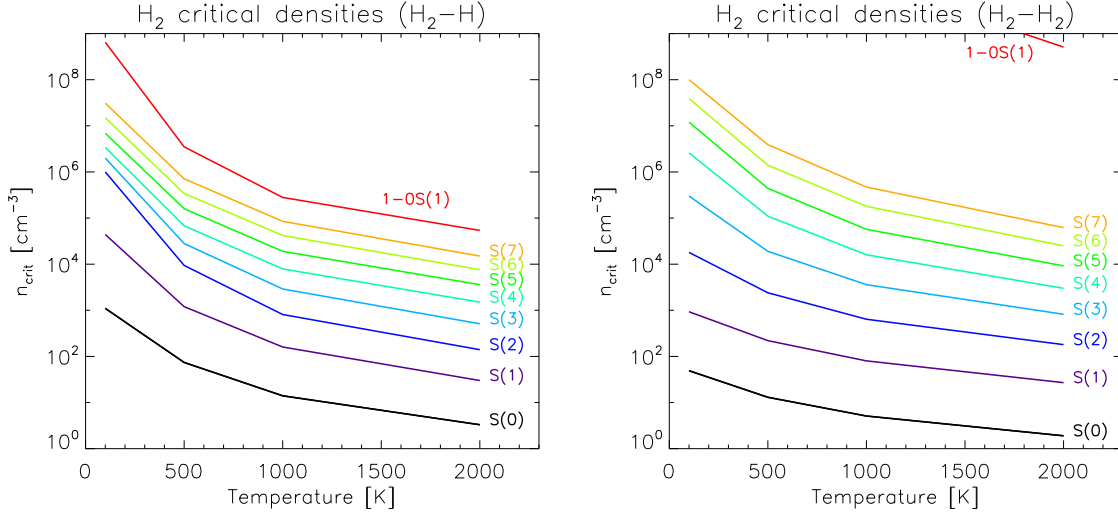
Figure 3.3: Critical densities, n_{crit}, for the S(0) to S(7) H_2 rotational lines, and the 1-0S(1) rovibrational line. The corresponding upper J levels are thermalized if the gas density is higher than n_{crit}. The collisional partner is H on the *left* plot and H_2 on the *right*. The critical densities are calculated at 100, 500, 1000 and 2000 K from Wrathmall et al. (2007).

high values of J, we have $A_{j\to i} \propto J^5$, which shows that the lowest energy levels (with smallest J values) are thermalized first.

This is illustrated in Fig. 3.3, which shows the critical densities, n_{crit}, at which the probabilities of collisional and radiative deexcitation are equal, for the first 7 rotational lines of H_2 and the 1-0S(1) rovibrational line. The collisional partner is H on the left panel and H_2 on the right[2]. At a given temperature, a given level is thermalized if the gas density is higher than n_{crit}. On the other hand, if the gas density is much less than the critical density, collisional excitation is followed by radiative decay, and so the collisional excitation rates determine the emission line intensities. The critical densities decrease with temperature because the collision rates also decrease with T. Note that higher densities appear necessary to thermalize rovibrational (not shown here) as compared with pure rotational transitions.

The excitation and deexcitation collisional rates of H_2 with H we use in our shock model are discussed extensively in Le Bourlot et al. (1999, 2002); Wrathmall et al. (2007), and we also refer the reader to the PhD thesis by Gusdorf (2008) for more details and calculations of n_{crit} with other collisional partners (H, H_2, He).

3.3 H₂ formation and chemistry

In spite of the simplicity of the H_2 molecule, its formation process in space has been a source of puzzles since more than 40 years, and H_2 formation is still an active research topic. I summarize here some of the basic ideas about H_2 formation that are crucial to have in mind for the next chapters, when

---

[2]Note that a similar figure can be found in Roussel et al. (2007), but the collision rates used in that paper are outdated, which lead to significant differences with the critical densities indicated here.
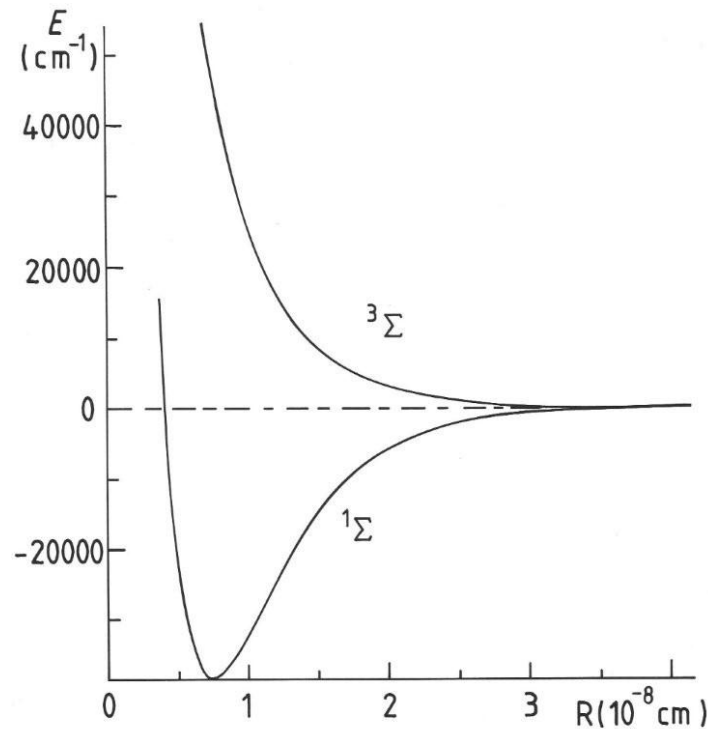
Figure 3.4: The lowest electronic potential energy curves of H$_2$. The curves shows the energy of the H(1s) + H(1s) system at large internuclear separation R. The singlet and triplet molecular states are denoted $^1\Sigma$ and $^3\Sigma$ because the projection of the electronic orbital angular momentum $\Lambda = 0$. The $^1\Sigma$ state is attractive whilst the $^3\Sigma$ is repulsive. Figure taken from the book by Flower (2007), with kind permission.

we will deal with H$_2$ formation issues in the extreme environments of H$_2$-luminous galaxies.

3.3.1   H$_2$ formation in the gas phase?

We will briefly demonstrate that the direct formation H$_2$ with gaseous elements only cannot explain the observed presence of molecular hydrogen in the ISM. The first process would consist in a *radiative association of two hydrogen atoms*:

$$\mathrm{H} + \mathrm{H} \longrightarrow \mathrm{H}_2 + h\nu \ (4.478 \ \mathrm{eV}) \tag{3.15}$$
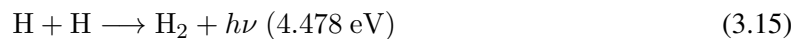
The Fig. 3.4 shows the electronic potential energy curves of an association of two hydrogen atoms as a function of their distance. Initially, H atoms are unbound and their total energy E is positive. To stabilize, the system must lose energy so that $E \leqslant 0$. This formation process would be possible if the molecule forms in a state that can deexcite to the ground state in order to lose its excess of energy by the emission of a photon $h\nu$. However, Fig. 3.4 shows that a molecule formed by an encounted or two H atoms may be formed in a repulsive state. Transitions between the $^3\Sigma$ and $^1\Sigma$ levels are forbidden to electronic dipole radiation because they would involve a change in the total spin quantum number. Rotational and vibrational transitions are also forbidden because H$_2$ has no permanent dipole moment.

Therefore, the molecule formed by radiative association can only dissociate. H_2 cannot be formed by radiative association of two hydrogen atoms.

The formation H_2 in the gas phase (meaning only with gaseous collision partners) cannot occur through *three-body collisions*, because the probability of a simultaneous encounter between 3 Hydrogen atoms is extremely small. When a sufficient abundance of electrons and ions exists, ion-atom reactions can be effective. Two routes for H_2 formation are then possible. The "H_2^+ route", that is a radiative association followed by a charge exchange reaction:

$$H + H^+ \longrightarrow H_2^+ + h\nu \tag{3.16}$$

$$H_2^+ + H \longrightarrow H_2 + H^+ \tag{3.17}$$

The alternative route is through H^-, with a radiative attachment followed by a associative detachment:

$$H + e^- \longrightarrow H^- + h\nu \tag{3.18}$$

$$H^- + H \longrightarrow H_2 + e^- \tag{3.19}$$

These reactions require very high densities (comparable to the density of a star) to be probable and contribute significantly to H_2 formation. Such processes are likely to be important for the chemistry of the primordial Universe, and we direct the reader to Stancil et al. (1998); Galli and Palla (1998) for more details, in particular about the reaction rates. However, densities in the ISM, even in the denser molecular clouds, are too small for this process to be probable.

3.3.2   The H_2 formation on interstellar dust grains

We have shown that the H_2 formation in the ISM cannot occur only with gaseous contituants. To overcome this difficulty, it has been proposed by Gould and Salpeter (1963); Hollenbach and Salpeter (1971); Jura (1975) that interstellar dust grains play the role of catalysts for H_2 formation:

$$\text{grain} + H + H \longrightarrow \text{grain} + H_2 + E_f \; (4.478 \text{ eV}) \tag{3.20}$$
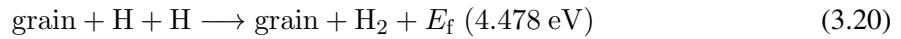
The grain plays the role of the third-body in a three-body reaction. The mechanism for H_2 through grain surface reactions is poorly known, as well as the distribution of the energy released by the formation, $E_f \approx 4.5$ eV, among the internal, kinetic and grain energy components. The part that goes into H_2 internal energy contribute to H_2 excitation, and we will come back to this point in sect. 3.4.3.

Two main mechanisms exist for the heterogeneous catalysis on a solid:

The Langmuir-Hinshelwood reaction: H_2 is formed by physisorption, i.e. through a reaction between two atoms (or radicals) that are already adsorbed on the grain surface.

The Eley-Rideal reaction: H_2 is formed by chemisorption, i.e. by the direct interaction of an adsorbed radical with an atom hitting it upon arrival from the gas phase.

In both cases, the H_2 formation rate per unit volume can be written as

$$R(H_2) = R_f(H_2) \times n_H \times n_{\text{gr}} \quad [\text{cm}^{-3} \text{ s}^{-1}] \; , \tag{3.21}$$

where $R_f(\mathrm{H_2})$ [cm^3 s^{-1}] is the H$_2$ formation rate, n_H is the gas hydrogen density, and n_gr is the number density of grains. Empirically the H$_2$ formation rate [cm^3 s^{-1}] is often expressed as:

$$R_f(\mathrm{H_2}) = \frac{1}{2}\sigma v_\mathrm{H} \times S(T) \times f \times \eta \tag{3.22}$$

$$= \pi a_\mathrm{gr}^2 \left(\frac{8k_\mathrm{B}T}{\pi m_\mathrm{H}}\right)^{1/2} \times S(T) \times f \times \eta \quad , \tag{3.23}$$

where σ is the average cross-section [cm^2] of the interaction between H atoms and grains, v_H is the velocity of H, $S(T)$ is the temperature-dependent probability that an H atom sticks onto the grain surface, f is the probability that the incident H atom stays on the grain and migrates towards the other adsorbed H atom, and η is the probability of recombination to form H$_2$. σ is calculated by averaging the quantity $\left\langle \frac{n_\mathrm{gr}(a_\mathrm{gr})}{n_\mathrm{H}} \pi a_\mathrm{gr}^2 \right\rangle$ over the grain size distribution (a_gr is the grain radius). It is generally assumed that the newly-formed H$_2$ molecule has a probability of 1 to be ejected from the grain because the potential wells of the physisorption (≈ 50 meV) and chemisorption (≈ 1 eV) are much smaller than the energy released by the formation (4.5 eV).

Several expressions have been proposed for the dependence of the sticking coefficient on the temperature. In our model we use the following expression, given in (Hollenbach and McKee, 1979):

$$S(T) = \frac{1}{1 + 0.04\sqrt{T + T_\mathrm{gr}} + 2 \times 10^{-3}\,T + 8 \times 10^{-6}\,T^2} \ , \tag{3.24}$$

where T is the kinetic gas temperature and T_gr is the grain temperature. In addition, we assume $f = \eta = 1$.

From UV observations of diffuse interstellar clouds with the Copernicus satellite[3], Jura (1975) estimates an H$_2$ formation rate of $R_f(\mathrm{H_2}) \approx 3 \times 10^{-17}$ cm^3 s^{-1} at $T = 70$ K. For more details about H$_2$ formation and recent estimates of $R_f(\mathrm{H_2})$ from photo-dissociation regions (PDRs), we direct the reader to the the PhD thesis by Habart (2001) and to Habart et al. (2004).

Note that, in cold clouds, the dust grains may be covered by ices, primarily composed of H$_2$O and CO, whereas in hotter regions, such as circumstellar environments or shock-heated gas, the icy mantles evaporate. The nature of the grain surface affects the H$_2$ formation rate, and an active experimental work is being done on this topic (e.g. Pirronello et al., 1997; Manicò et al., 2001; Hornekær et al., 2003; Amiaud et al., 2007).

3.3.3 H$_2$, initiator of an impressive molecular complexity

We have stated in the introduction that H$_2$ initiates the formation of more complex molecules in cold clouds. Obviously, I will not review here the full theory of the formation of heavy molecules in the ISM (see the book by Duley and Williams, 1984, for details). I will only briefly give the tracks towards this molecular complexity that we observe in the ISM.

In fact, the formation of molecules more complex than H$_2$ requires the H$_3^+$ ion, which is primarily formed by cosmic-ray (CR) ionization of H$_2$ (Herbst and Klemperer, 1973):

$$\mathrm{H_2 + CR \longrightarrow H_2^+ + e^- + CR} \tag{3.25}$$

---

[3] http://heasarc.gsfc.nasa.gov/docs/copernicus/copernicus_about.html
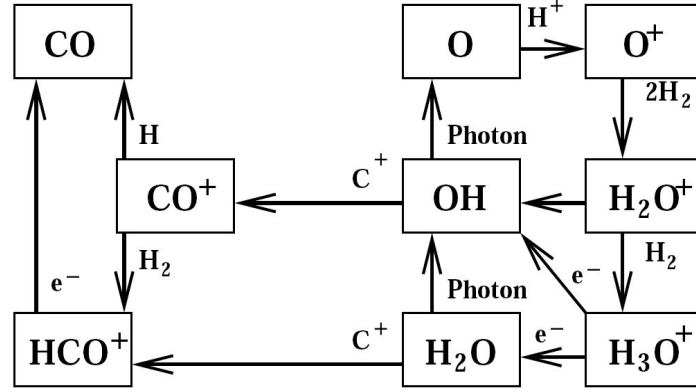
Figure 3.5: H_2 as an initiator of the formation of CO. This figure sketches the CO formation routes in a low UV radiation field. Destruction is still dominated by photo-dissociation. From Nehmé et al. (2008).

This reaction is rapidly followed by

$$H_2^+ + H_2 \longrightarrow H_3^+ + H \tag{3.26}$$

Then, the way for complex chemistry is open. Heavier molecules can form via proton transfer reactions. Let us give one example of a chain of reactions which leads to the formation of CO. The CO formation routes are schematically illustrated in Fig. 3.5. One of the possibilities, the "H_2O route", can be summarized as:

$$
\begin{aligned}
2O^+ + 3H_2 &\longrightarrow 2H_3O^+ \\
H_3O^+ + e^- &\longrightarrow H_2O + H \\
C^+ + H_2O &\longrightarrow HCO^+ + H \\
HCO^+ + e^- &\longrightarrow CO + H
\end{aligned}
\tag{3.27}
$$
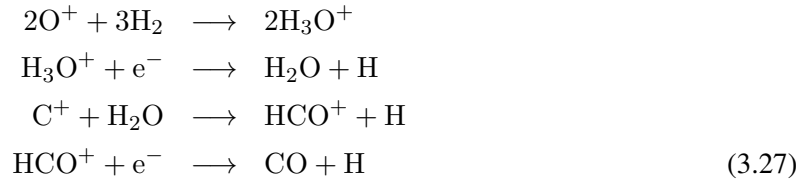
CO is then formed! The importance of the CO molecule is stressed in sect. 3.5, and we will come back to CO emission in Stephan's Quintet in chapter 7.

3.4 H₂ excitation mechanisms and diagnostics

Excitation of rotation-vibration levels of H_2 can occur through different mecanisms, which can be separated in three categories: collisional excitation, radiative (UV pumping) excitation, or excitation directly in the process of forming the molecule. Obviously, it would be impossible to give an exhaustive review about each processes here. We summarize the main ideas and classify these processes by order of relevance for our astrophysical context. I also give a few details about the chemical reaction rates incorporated in the shock model we use in the following chapters (in particular chap. 4 and 5).

3.4.1 Collisional excitation and dissociation

H_2 levels may be excited by collisions in warm gas, and the resulting spectrum is often invoked as an indicator that shocks are occurring. The calculation of the collisional rates is complex because

it involves detailed quantum mecanics calculations of the interaction potential between the collision partner and the target. For a comprehensice description of the collisional processes in the ISM, we direct the reader to the book by Flower (2007).

H$_2$ collisions with atoms or molecules

The most important collisional partners for H$_2$ excitation with atoms or molecules are the light and most abundant partners H, He, ortho- and para-H$_2$, that lead to rotational and vibrational excitation of H$_2$. The cross sections for rovibrational transitions of H$_2$, induced by collisions with H and He atoms have been discussed in Le Bourlot et al. (1999, 2002). An update of H$_2$-H collision rates is given in Wrathmall and Flower (2007). H$_2$-H$_2$ collisions are treated in (Flower, 1998). For the particular interest of this PhD work, the reader will find the cross-sections and rate coefficients that are used in our models for collisional excitation of H$_2$ rotational transitions in the appendices of Flower (2007).

Collision with H can also lead to the dissociation of H$_2$. The rate coefficient calculated by Dove and Mandy (1986) can be fitted as a function of the temperature of the neutral fluid, by the following form (Flower et al., 1996):

$$k_{\text{diss.}}^{\text{H-H2}}(T_n) = 10^{-10} \times e^{\dfrac{-5.2 \times 10^4}{T_n}} \quad [\text{cm}^3\,\text{s}^{-1}] , \tag{3.28}$$

where the temperature of 5.2×10^4 K in the exponential corresponds to the dissociation energy of H$_2$ (4.48 eV). In our model, the above expression has been adapted to allow for the excitation energy $E(v, J)$ of the initial rovibrational level (v, J). The following rate is adopted in the code (Le Bourlot et al., 2002):

$$k_{\text{diss.}}^{\text{H-H2}}(T_n) = \frac{10^{-10}}{n(\text{H}_2)} \sum_{v,J} n(v, J) e^{\dfrac{-(56\,644 - E(v, J))}{T_n}} \quad [\text{cm}^3\,\text{s}^{-1}] , \tag{3.29}$$

where $E(v = 4, J = 29) = 56\,644$ K is the energy of the highest bound level of H$_2$, relative to the $v = 0$, $J = 0$ ground state (Dabrowski, 1984). $n(v, J)$ is the level population density. By definition,

$$n(\text{H}_2) = \sum_{v,J} n(v, J) \ . \tag{3.30}$$

The rate coefficient for the collisional dissociation of H$_2$ by H$_2$ is taken to be (Jacobs et al., 1967):

$$k_{\text{diss.}}^{\text{H2-H2}} = \frac{k_{\text{diss.}}^{\text{H-H2}}}{8} \tag{3.31}$$

The rate coefficient for the collisional dissociation of H$_2$ by He is taken to be (Le Bourlot et al., 2002):

$$k_{\text{diss.}}^{\text{H2-He}} \approx \frac{k_{\text{diss.}}^{\text{H-H2}}}{10} \tag{3.32}$$
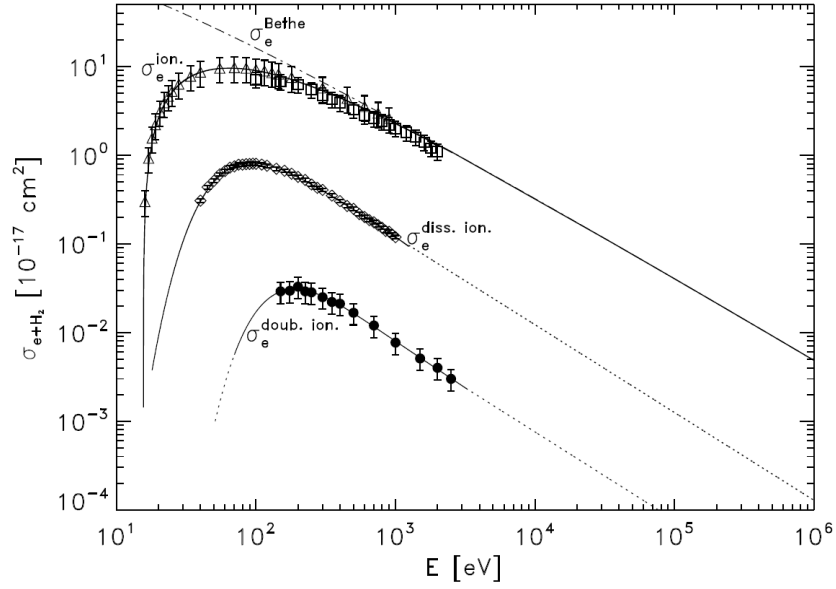
Figure 3.6: Cross sections for electron impact on H_2 from Padovani et al. (2009): ionization cross section $\sigma_P^{\text{ion.}}$ (Rudd 1991), dissociative ionization $\sigma_P^{\text{diss.ion.}}$, and double ionization cross section $\sigma_P^{\text{doub.ion.}}$. The solid curves are polynomial fits. For comparison, the dot-dashed line shows the Bethe ionization cross section multiplied by a factor of 2. The points are experimental data (see Padovani et al. (2009) for references).

Cosmic-ray ionization of H₂

H_2 excitation by electrons is a process that occurs in the astrophysical context of the interaction of cosmic rays or X-ray photons or cosmic rays with molecular gas. When X-ray photons or cosmic ray particles (electrons, protons, and heavy nuclei) penetrate into a molecular cloud, photoelectrons or secondary electrons are produced (see Padovani et al., 2009, for a review). Let us consider the direct ionization of H_2 by a cosmic-ray particle (electrons, protons, and heavy nuclei) impact:

$$H_2 + CR \longrightarrow H_2^+ + e^- + CR \tag{3.33}$$

The Fig. 3.6 shows the theoretical and experimental cross-sections for the impact of electrons onto H_2 from Padovani et al. (2009). The experimental data for electron-impact ionization of H_2 have been reviewed by Liu and Shemansky (2004). The curves show a semi-empirical model developped by Rudd (1991). Note that the Bethe (1933) cross section for primary ionization of atomic hydrogen, multiplied by a factor of 2, reproduces very well the behavior of the ionization cross section at energies above a few tens of keV.

Collisional excitation of H₂ by electrons

The scattering of these photoelectrons or secondary electrons on H_2 molecules can lead to thermal (Lepp and McCray, 1983) or non-thermal excitation to singlet and triplet electronic states of H_2. The triplet states lead to dissociation but in some fraction of the excitations the singlet states cascade down

by allowed radiation transitions into the array of rotation-vibration levels of the ground electronic state.

We will show below that the H_2 excitation by thermal electrons can be very important in shocked molecular gas because of the shock-induced rise of the electron temperature. We give a brief review of the theoretical studies about H_2 excitation by collision with thermal and non-thermal electrons, and we give some key-examples of excitation rates incorporated in the shock code we use later. The global properties of the efficiencies of H_2 excitation by cosmic or X-rays will be addressed in section 3.4.2.

The rate of production of secondary electrons by cosmic ray ionization of hydrogen is approximately $\zeta n(H_2)$, where ζ is the cosmic ray ionization rate (a few 10^{-17} s^{-1} is a classical value in molecular clouds) and $n(H_2)$ the number density of H_2 molecules. Typically, $\sim 15\%$ of the secondary electrons subsequently excite H_2 molecules by collision (Cravens et al., 1975; Sternberg et al., 1987). Therefore the rate of H_2 excitation by secondary electrons is $0.15\zeta n(H_2)$.

We consider now the H_2 excitation by thermal electrons. If we denote k_1 the rate coefficient for the excitation of the singlet states, then the rate of excitation can be written as $n_e n(H_2) k_1(T_e)$. The cross-sections for the excitation of singlet states of H_2 by thermal electrons are linear as a function of energy for the dominant B and C states (Ajello et al., 1984). Flower et al. (1996) provide the following form for the rate coefficient for electron excitation of the B and C states:

$$k_1(T_e) = 10^{-16} \left(\frac{8k_{\mathrm{B}}T_e}{\pi m_e} \right)^{1/2} \left(0.429 + 6.14 \times 10^{-6}\, T_e \right) \times e^{\dfrac{-1.4 \times 10^5}{T_e}} \quad \mathrm{cm^3\,s^{-1}} \qquad (3.34)$$

The factor $\left(\frac{8k_{\mathrm{B}}T_e}{\pi m_e} \right)^{1/2}$ represents the mean velocity of electrons at temperature T_e. The 1.4×10^5 K temperature in the exponential factor is the mean excitation temperature of the B and C states from the $X^1\Sigma_g^+$ ground state.

Therefore, the total rate of H_2 excitation by (thermal + non-thermal) electrons, $R_1(T_e)$ [cm^{-3} s^{-1}], is

$$
\begin{aligned}
R_1(T_e) \;=\;& 0.15\,\zeta\,n(H_2) + n_e\,n(H_2)\,k_1(T_e) \hspace{6cm} (3.35)\\[2mm]
\approx\;& 7.5\,10^{-15}\frac{n_{\mathrm{H}}}{10^4}\left[\frac{\zeta}{10^{-17}} + 2\,10^6\frac{n_e/n_{\mathrm{H}}}{10^{-7}}\frac{n_{\mathrm{H}}}{10^4}\frac{T_e}{10^5}\left(0.43 + 0.61\frac{T_e}{10^5}\right) e^{\dfrac{-1.4}{T_e/10^5}} \right] \quad (3.36)
\end{aligned}
$$

This is the rate we use in our model for the H_2 excitation by electrons. In eq. 3.36 we have assumed that the gas is molecular, so $n(H_2) = 0.5 n_{\mathrm{H}}$. For a gas of density $n_{\mathrm{H}} = 10^4$ cm^{-3} and fractional ionization $n_e/n_{\mathrm{H}} = 10^{-7}$, the H_2 excitation rate by thermal electrons exceeds by a factor 10^6 the cosmic ray electrons rate if we assume $T_e = 10^5$ K. If $T_e = 10^4$ K, the two contributions are comparable. More generally, because magneto-hydrodynamical shocks can easily increase the electron temperature above 10^4 K, the photodissociation and photoionization of molecular species induced by a shock wave can greatly exceed the rate of cosmic ray-induced processes (Flower et al., 1996).
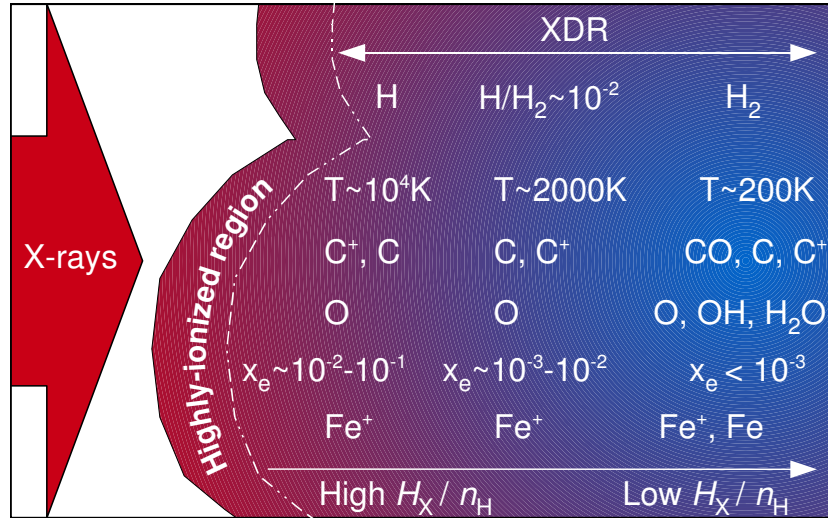
Figure 3.7: Schematic structure of an X-ray dissociation region (XDR), where an X-ray flux *(arrow on the left)* illuminates a molecular cloud *(on the right)*. As we penetrate into the XDR, we indicate the approximate temperature, chemical composition and ionization fraction x_e as a function of the ratio of the local X-ray energy deposition rate per particule, H_X, to the total hydrogen density n_H.

3.4.2 X-ray and cosmic-ray heating efficiencies

X-rays

The excitation by X-ray photons was quantified by a number of authors (e.g. Voit, 1991; Tine et al., 1997; Dalgarno et al., 1999). Let us estimate the maximum X-ray to H₂ luminosity conversion factor. We consider that an X-ray source heats the H₂ gas (see Fig. 3.7 for a sketch of an XDR), by assuming that 100 % of the X-ray flux penetrates into the molecular gas. Models of X-ray dissociation regions (XDRs) show that $30 - 40$ % of the absorbed X-ray flux goes into photoelectron heating (Maloney et al., 1996). The atomic photoelectric cross section is a steep decreasing function of the energy ($E^{-8/3}$). Photoionization in the energy range $1 - 30$ keV are the most important. At a temperature of 200 K for the H₂ gas, the cooling by H₂ rotational lines in XDRs models is ~ 2 % of the total cooling (see Fig 3a and 5 of Maloney et al., 1996). The maximum X-ray to H₂ luminosity conversion factor is therefore

$$\frac{\mathcal{L}(\mathrm{H_2}\ 0\text{-}0\mathrm{S}(0)\text{-}\mathrm{S}(3))}{\mathcal{L}_\mathrm{X}(2 - 10\ \mathrm{keV})} < 8 \times 10^{-3} \tag{3.37}$$

This estimate will be useful in the next chapter to see whether X-rays can power the observed H₂ emission in the extreme environments of H₂-luminous galaxies.

H₂ heating by cosmic-ray ionization

We estimate the molecular heating associated with cosmic-ray ionizations (see sect. 3.4.1 for a description of the process). Each ionization of a hydrogen molecule is associated on average with 40.1 eV energy loss by electrons, of which 11 % ends up as heat (Dalgarno et al., 1999). This gives a heating energy of 4 eV per ionization. This is the value adopted in the Meudon PDR code (Le Petit

et al., 2006). If we add the energy associated with the recombination of H_3^+ that may follow the H_2 dissociation, another 8 eV is released per recombination (Maloney et al., 1996). Thus, each ionization of a hydrogen molecule is associated with the deposition of 12 eV into the gas. In the *CLOUDY*[4] gas code, last described by Ferland et al. (1998), the heating efficiency increases with the ionization fraction of the gas. For an ionization fraction of 10^{-4}, a classical value for the diffuse ISM (Shaw et al., 2005), the heating energy per H_2 ionization is $\approx 7\ eV$. As the ionization rate per hydrogen nucleus is half the H_2 ionization rate ζ_H, the heating rate per hydrogen nucleus Γ/n_H is $\approx 14\,\text{eV} \times \zeta_H$, or

$$\Gamma/n_H = 2.2 \times 10^{-33} \frac{\zeta_H}{10^{-15}\,\text{s}^{-1}} \quad \text{W} . \tag{3.38}$$

Using the cooling rates calculated by Neufeld et al. (1995) for $n(H) = 10^4$ cm^{-3} and $N(H)/\Delta v = 10^{22}$ cm^{-2} km^{-1} s, the equilibrium temperatures are approximately 50, 150, and 300 K for $\zeta_H = 10^{-15}, 10^{-14}$, and 10^{-13} s^{-1}, respectively.

3.4.3   Excitation during the H₂ formation process

During the H_2 formation process on grain surfaces (see sect. 3.3.2), the binding energy of H_2 ($\approx$ 4.5 eV, or 51 000 K) is released and partitioned among the grain (internal heating), kinetic energy of the ejected H_2 (gas heating), and internal energy in H_2 (i.e. the molecule is formed in a rovibrationally excited state). Therefore, H_2 excitation can also occur directly during the process of its formation.

How is the H_2 binding energy divided between the constituents? What is the internal energy distribution? What the ortho-to-para ratio of the newly-formed molecule? In spite of many theoretical work and experiments (e.g. Hornekær et al., 2003; Amiaud et al., 2007), all these questions remain open.

In our model, we choose to distribute the H_2 binding energy with *equipartition*: one third of the formation energy (1.4927 eV, or 17249 K) goes into internal energy of H_2 and levels are populated in proportion to the Boltzmann factor at a temperature of 17249 K. Another third goes into kinetic energy and the last third goes into grain heating. In our model we assume that the H_2 molecule is formed with an ortho-to-para ratio of 3.

Several surveys of cold dark clouds have been performed to observe directly the H_2 excitation by formation, but so far without results (see Tiné et al., 2003, and references therein).

3.4.4   Radiative excitation of H₂ (UV pumping)

When a UV source is present, for instance in Photo-Dissociation Regions (PDRs), H_2 may be excited rovibrationally by first being UV-pumped to an electronically excited state (Black and Dalgarno, 1973; Black and van Dishoeck, 1987) via the Lyman and Werner transitions within the range $912 - 1110$ Å(see also Hollenbach and Tielens, 1997, for a review about dense PDRs). The excited molecule will then deexcite (fluorescence) back into vibrationally excited levels of the ground electronic state. If the densities are not too large ($n_H < n_{crit} \approx 10^{4-5}$ cm^{-3}) these levels will cascade down through rovibrational transitions. The corresponding UV spectrum has been calculated by Sternberg (1989). This fluorescence occurs with a probability of $\approx 90\%$. If $n_H > n_{crit}$, the collisional

---

[4]http://www.nublado.org/

deexcitation of H_2 contributes to heat the gas. In $\approx 10\,\%$ of the electronic excitations, the molecule will dissociate because the absorption of a UV photon is followed by a cascade towards rovibrational levels of the ground electronic state.

3.4.5 H₂ excitation diagrams

Excitation diagrams are a way to represent the SED of the H_2 emission that provides a practical visualization of the physical conditions of the emitting medium. We detail how one builds an excitation diagram and we give canonical examples within the context of H_2 emission in shocks.

Building excitation diagrams

Excitation diagrams plot the logarithm of the column densities of the upper H_2 rovibrational levels (v, J) divided by their statistical weights, $\ln(N_{vJ}/g_J)$, against their excitation energies, E_{vJ}/k_B, expressed in K. The column density is expressed in cm^{-2}. The statistical weight $g_J = g_s\,(2J + 1)$ is the product of the nuclear spin statistical weight, g_s, which has value of 1 and 3 for even and odd rotational levels J, respectively, and the rotational statistical weight, which is $2J + 1$.

Such diagrams are very useful to get a first idea of the temperature conditions that exist in the emitting gas. If one assumes that a given line is optically thin to H_2 emission, one can calculate the gas column density, N from the observed brightness of the line, $\mathcal{I}$. The probability for spontaneous emission is given by the Einstein A-coefficient. The measured H_2 line intensities $\mathcal{I}_{vJ}$ are converted into column densities N_{vJ} as follows:

$$N_{vJ} = \frac{4\,\pi}{h\,c}\frac{\lambda}{A_{vJ}}\mathcal{I}_{vJ} \tag{3.39}$$

where λ is the central wavelength of the line transition, A_{vJ} the transition probability (Einstein coefficient) for the rovibrational level $(v; J)$, h is Planck's constant, and c is the velocity of light in the vacuum.

To estimate whether the assumption that the line is optically thin, we may calculate the optical depth, τ, for a transition $j \to i$ between an upper j and lower i level:

$$\tau = \frac{A_{vJ}}{8\pi}\frac{1}{\Delta v}\frac{g_j}{g_i}\lambda^3\,N_{vJ} \tag{3.40}$$

where Δv is the linewidth (dispersion velocity) and g_j, g_i are the degeneracies of the upper and lower levels, respectively. For the $v = 0$-0 S(1) transition we find

$$\tau = 3.94 \times 10^{-5}\left(\frac{10\,\mathrm{km\,s^{-1}}}{\Delta v}\right)\left(\frac{N_H}{10^{20}\,\mathrm{cm^{-2}}}\right)\;. \tag{3.41}$$

Therefore the assumption that the line is optically thin to H_2 emission is fulfilled for most of the situations in the ISM.

Column densities can then be compared with those expected from thermal excitation. The method is the following one. In a thermal distribution, N_{vJ} is proportional to the statistical weight g of the level and to the Boltzmann factor $e^{-\frac{E_{vJ}}{k_B T_{\mathrm{exc}}}}$, where E_{vJ} is the excitation energy of the respective level.
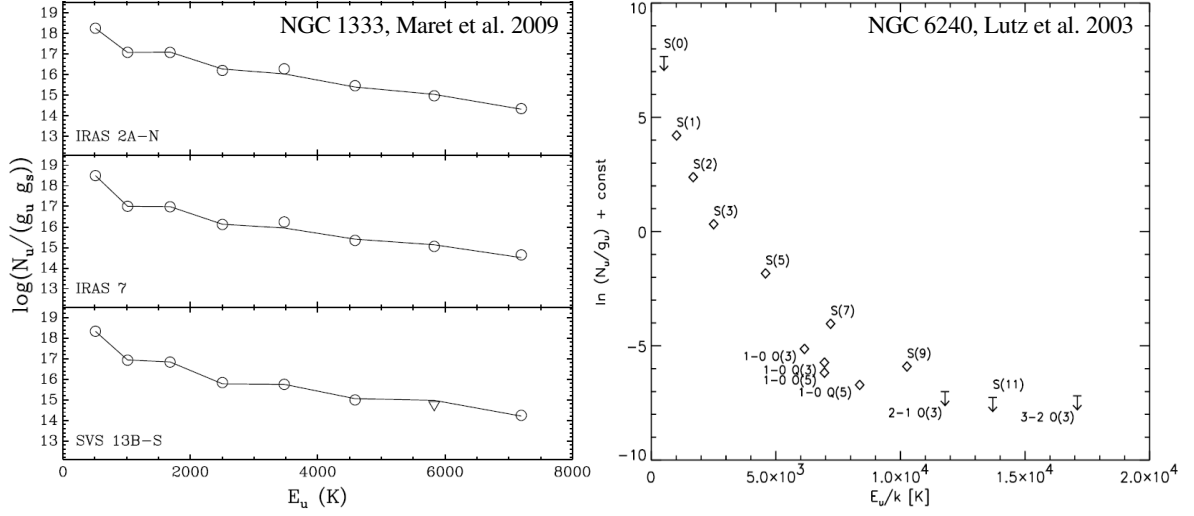
Figure 3.8: Examples of observed H$_2$ excitation diagrams in NGC 1333 and 6240. *(Left)* Excitation diagrams of pure rotational H$_2$ lines observed with *Spitzer* of three sub-regions in NGC 1333, a starforming region with molecular outflows (from Maret et al., 2009). *(Right)* H$_2$ excitation diagram of NGC 6240, a luminous infrared galaxy observed with *ISO*, by Lutz et al. (2003).

The Boltzman law allows to define the excitation temperature associated to a transition $j \rightarrow i$, T_{exc} from the ratio of the level populations:

$$e^{-\dfrac{h\nu}{k_{\text{B}}T_{\text{exc}}}} = \dfrac{g_j/n_j}{g_i/n_i} \tag{3.42}$$

where ν is the frequency associated to the $j \rightarrow i$ transition, and n the level populations associated to the connected levels. In a situation of local thermal equilibrium, the excitation temperature equals that of the gas. For a uniform excitation temperature, the values $\ln N_{vJ} = g_J$ should thus all fall on a straight line plotted versus E_{vJ}, with a slope proportional to T_{exc}^{-1}. This diagram thus allows to roughly estimate the temperature conditions in the emitting gas.

From an observational point of view, deriving the excitation temperature is a rough estimate of the temperature conditions in the considered region. With this diagram, deviations from LTE can be easily be probed. Generally, multiple temperature fits are done, corresponding to several excitation temperatures. In a shocked medium, this reflects the distribution of temperatures involved in the postshock medium.

Examples of observed H$_2$ excitation diagrams

For illustration, we show in Fig. 3.8 two examples of observed excitation diagrams of pure rotational H$_2$ lines in very different environments. NGC 1333 (on the *left*) is a Galactic star forming region comprising mutiple outflows (Neufeld et al., 2006; Maret et al., 2009). The diagrams show a "zigzag" pattern, indicating that the ortho-to-para ratio is lower than 3, the high-temperature limit (see sect. 3.2.2). In addition, the curvature of the diagram show that the observed values cannot be

fitted with a single LTE excitation temperature. This suggest that the gas, shocked by the proto-stellar outflows, is a mixture of multiple temperature gas components.

NGC 6240, an IR-luminous merger, shows the same non-linear decline of the H_2 excitation diagram than what is commonly seen in shocks within the Galaxy, as well as in external galaxies (e.g. Rigopoulou et al., 2002; Lutz et al., 2003).

3.5 Observing H₂ in space

3.5.1 Direct H₂ observations

The first detection of H_2 beyond the Solar System was made by Carruthers (1970) through absorption spectroscopy of UV light with a rocket-borne UV spectrometer. This discovery was followed by UV observations with the Copernicus space mission that demonstrated the presence of the hydrogen molecule in diffuse interstellar clouds (for a first review on this subject, see Spitzer and Jenkins, 1975, and references therein). These observations revolutionized our understanding of the origin of astronomical objects.

A decade later, Gautier et al. (1976) detected H_2 in emission for the first time through near-infrared rovibrational lines from a massive young stellar object in the Orion Nebula. This demonstrated the importance of H_2 in dense environments as well. However, because of lack of sensitivity, such observations remained of limited scope over the next three decades. Today, the near-infrared rovibrational transitions are routinely imaged from ground-based telescopes.

The H_2 mid-infrared rotational transitions, which trace warm ($\approx 10^{2-3}$ K) molecular gas, must be observed from space (see Fig. 3.9, right panel). Indeed, the Earth's atmosphere is mostly opaque to the mid-IR lines of ortho and para H_2. For the transitions occurring at wavelengths where the atmosphere is partially transparent, the thermal background from the warm telescope, its spectrometer, and the sky, limit the sensitivity. The H_2 infrared lines were observed by *ISO* and *Spitzer* with limited imaging capabilities and low spectral resolution. The next future (≈ 2015) of mid-IR H_2 observations will the James Webb Space Telescope (JWST, see Fig. 3.9) in which I am involved (see chapters 10 to 12). On a longer timecale, the *SPICA* mission[5] (Swinyard et al., 2009), an actively-cooled *Herschel*-like telescope, would be capable of doing MIR and FIR spectroscopy at high spectral resolution with an unprecedent sensitivity.

Boulanger et al. (2009) have proposed a mission to the Cosmic Vision 2015-2025 call, so-called *H₂Ex,* dedicated to wide-field ($20' \times 20'$) observations of the lowest H_2 rotational transition lines, S(0) to S(3), at high spectral resolution (up to $\lambda/\Delta\lambda \approx 30\,000$, in our Galaxy and up to redshift $2 - 3$. Actually, the start of my PhD work about modeling H_2 formation and emission in active phases of galaxy evolution was motivated by the preparation of this Cosmic Vision proposal, which was not selected, unfortunately.

3.5.2 CO, a proxy for H₂

The bulk of the molecular hydrogen in a galaxy is cold ($10 - 20$ K), too cold to be seen in emission. This is why the presence of cold H_2 is inferred essentially from carbon monoxyde (CO) observations.

---

[5]Space Infrared Telescope for Cosmology and Astrophysics
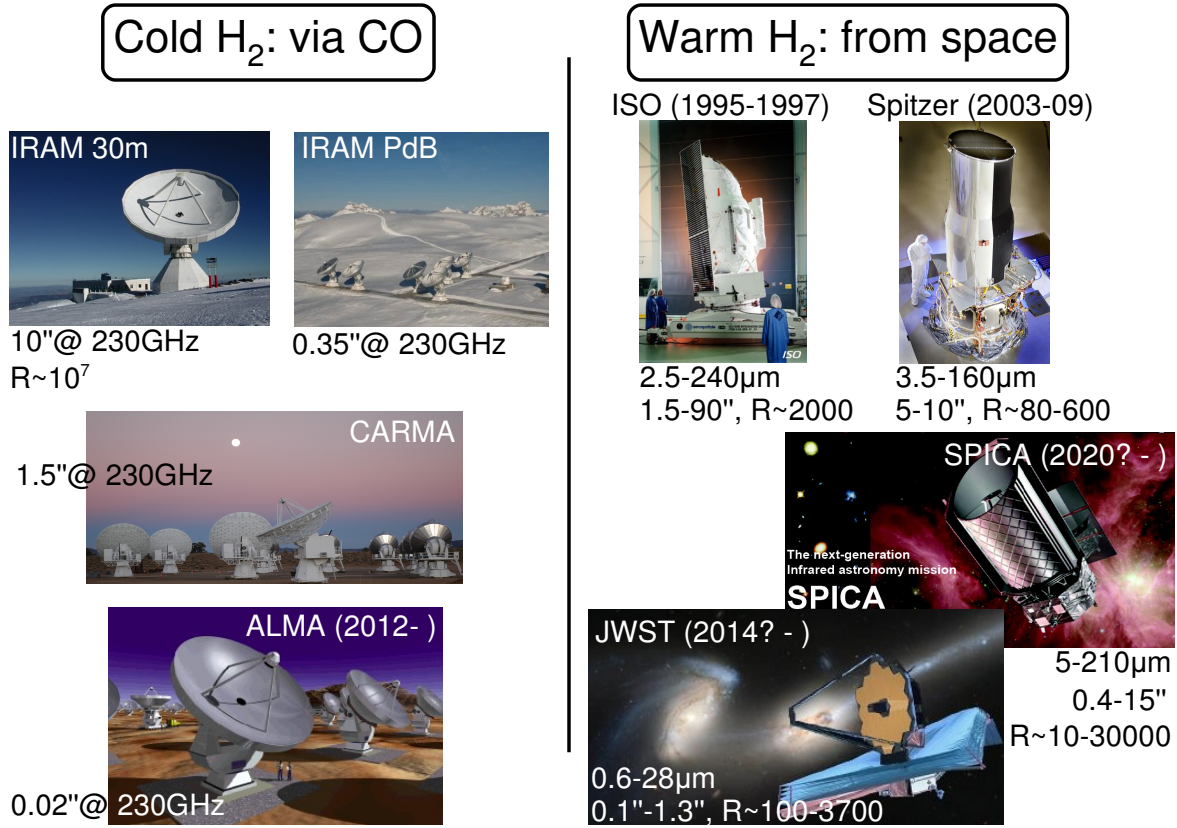
Figure 3.9: Cold and warm molecular gas are observed with two different kinds of observatories. Cold molecular gas is essentially derived from CO ground-based observations with single-dish radio-telescopes or interferometers. On the other hand, the IR emission from warm H$_2$ must be observed from space. This figure shows a few examples (past, present and future) of these observatories, with their basic characteristics (wavelength coverage, spatial and spectral resolution).

CO is the most abundant molecule after H$_2$. Its dipole moment is small (0.1 Debye), so CO is easily excited. The emission of the CO(1-0) line at 2.6 mm (corresponding to its first level at 5.52 K) is ubiquitous in galaxies.

The CO lines (mainly 1-0 at 115 GHz and 2-1 at 230 GHz) are observed with radiotelescopes (see left panel of Fig. 3.9), being single-dish or interferometers. During my PhD, I have made use of the IRAM 30m single-dish telescope. The high spectral resolution of radiotelescopes provides crucial information about the molecular gas kinematics which, in general, cannot be inferred from mid-IR H$_2$ line observations alone because of limited spectral resolution.

In order to derive the cold H$_2$ masses, we generally assume a fixed CO luminosity to H$_2$ mass conversion factor, the so-called $X = N(\mathrm{H}_2)/\mathcal{I}_{\mathrm{CO}}$ factor, where $N(\mathrm{H}_2)$ is the column density of H$_2$ and $\mathcal{I}_{\mathrm{CO}}$ the integrated CO line intensity. Several methods are employed to derive the X factor (see Solomon and Barrett, 1991), leading to similar results. In our Galaxy, the most common value is Dame et al. (2001):

$$X = \frac{N(\mathrm{H}_2)\ [\mathrm{cm}^{-2}]}{\mathcal{I}_{\mathrm{CO}}\ [\mathrm{K\ km\ s}^{-1}]} = 2.2 \times 10^{20}\ \mathrm{cm}^{-2}\ [\mathrm{K\ km\ s}^{-1}]^{-1} \qquad (3.43)$$

In extragalactic environments, the CO(1-0) line luminosity seems also to be a reliable mass tracer (e.g. Dickman et al., 1986; Solomon and Barrett, 1991). This allows us to convert the integrated line flux of CO(1-0) line into molecular gas mass. Including a factor of 1.36 to account for helium, the gas mass bound into molecular clouds can be calculated as:

$$M_{\mathrm{gas}} = 2.94 \times 10^7 \left(\frac{\mathcal{F}_{\mathrm{CO(1-0)}}}{1\,\mathrm{Jy\,km\,s^{-1}}} \right) \left(\frac{X}{2.2 \times 10^{20}} \right) \left(\frac{d}{50\,\mathrm{Mpc}} \right)^2 \mathrm{M}_\odot \ . \tag{3.44}$$

We will make use of this useful expression later in this manuscript.

Chapter 4

Shocks and chemistry in the multiphase ISM

Nothing shocks me. I'm a scientist.

Indiana Jones, *in Indiana Jones and the Temple of Doom*

Abstract

H_2-luminous galaxies appear to be in active phases of their evolution (galaxy collisions, galaxy cluster cooling flows, starburst- or AGN-driven winds, etc., see chapter 1) that release a large amount of kinetic energy in the interstellar medium . Shocks are thus expected to be ubiquitous in these media, and may account for a significant, if not dominant, part of the powerful H_2 emission observed in these sources. Consequently, I have been driven to study H_2 emission in shocks, and use MHD shock models to interpret these observations. This has been done first within the context of the Stephan's Quintet galaxy collision (chapter 5 and 6), and is being extented to other astrophysical objects (chapter 9). In this chapter, I present the necessary background on the physics and chemistry of MHD shocks, as well as a few results extracted from the grid of shock models I have built to interpret the observations. Then the discussion is extented to shocks in inhomogeneous media. I focus on two situations: the evolution of a shocked dense cloud, and the collision between two gas streams. The physical processes that control the evolution of the shocked gas will be discussed, as well as recent results for numerical simulations.

Contents

4.1   Introduction

Shock waves are ubiquitous in the interstellar matter settled in galactic disks, but also in the intergalactic medium. They are produced by violent pressure disturbances such as star- or AGN-driven jets and winds, supernovae explosions, collisions between molecular clouds or, at larger scales, between galaxies.

A shock wave is *an overpressure region that propagates in the fluid at a supersonic velocity*. These shock waves accelerate, heat and compress the gas. This condensation may lead to star formation, as it is the case for giant shock waves propagating in the spiral arms of a galaxy. On the other hand, shocks may have destructive effects on the molecular clouds, thus quenching star formation, as it is perhaps the case in AGN jets driven in the ISM of their host galaxy.

Shocks have an important impact on the evolution of the interstellar medium (ISM), from a dynamical but also from a chemical point of view. By heating the gas, shocks driven into molecular clouds initiate chemical reactions that would not occur in peaceful, cold molecular gas. These chemical processes play a role in the thermal balance of the shock, which in turn has an impact on the gas dynamics.

H$_2$ appears to be a dominant coolant of MHD shocks. H$_2$-luminous galaxies (chapter 1) are be precisely in some of the energetic phases of strong dissipation of kinetic energy quoted above. Therefore, a large part of my modeling work of the dissipation of mechanical energy involves the physics and chemistry of shocks.

In the multiphase environment of these H$_2$-luminous galaxies, different types of shocks are expected. Fast shocks, heating the gas to high ($T \approx 10^6 - 10^8$ K), produce EUV and X-ray photons that photoionize the tenuous medium. These shocks are one source of energy that produce the HIM[1] in galaxies. On the other hand, low-velocity shocks (typically $\lesssim 50$ km s^{-1}) are known to *(i)* initiate the

Photograph of a bullet in supersonic flight, published by Ernst Mach in 1887.

Jet launched by a newly forming star in the Carina Nebula (*HST*)

Giant bow-shaped shock wave in the Bullet cluster (Red=X-rays, Blue=dark matter)

---
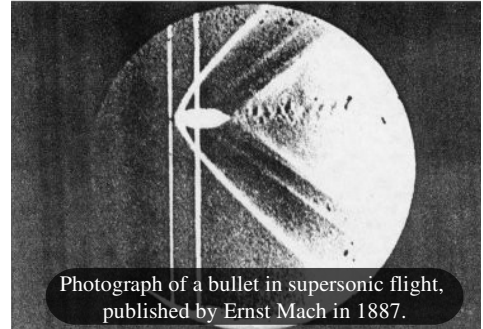
[1]Hot Ionized Medium, see chapter 2, sect. 2.2.1.

formation of molecules in the gas that cools behind the shock (e.g Hollenbach and McKee, 1979), and *(ii)* be a very efficient process to excite molecules, especially H_2, via collisions in the dense gas compressed and heated by the shock.

To interpret the H_2 observations presented in chapter 1, I have been driven to study the formation of H_2 during the cooling of a shock-heated gas, and H_2 excitation in magnetohydrodynamical (MHD) shocks driven into dense molecular gas. I have used the Flower et al. (2003) shock model, a 1-D^2 MHD code coupled to a extensive network of chemical reactions, to build a large grid of shock models for different values of key parameters such as the shock velocity, the pre-shock density, the magnetic field, etc. In particular, the results of the modeled emission of molecular hydrogen (whose treatment is included inside the shock code) to the observations.

For a review about the physics and chemistry of interstellar shocks, I direct the interested reader to Draine (1980); McKee and Hollenbach (1980); Chernoff (1987); Hollenbach and McKee (1989); Draine and McKee (1993); Hartigan (2003). For a comprehensive and didactic presentation of hydrodynamical and MHD shocks, the reader will consult the PhD thesis (in french) by Guillet, V. (2008). I assume that the reader is familiar with the basic properties of hydrodynamical shocks (in which the magnetic field is absent $B = 0$). This chapter first focuses on the basic properties of MHD (*single-fluid* or *multi-fluids*) shocks (sect. 4.2). I present the shock code and the grid of shock models I use in the following chapters (sect. 4.3), and mainly discuss H_2 cooling in MHD shocks (sect. 4.3.3). Then I extend the discussion to shocks into multiphase media. I describe the evolution of a cloud (embedded in a tenuous gas) that is overrun by a shock wave, from a theoretical and numerical simulation point of view. Finally, I consider the collision between two gas stream and point out the main differences between 1-D and 3-D models.

4.2 Magnetohydrodynamic (MHD) shocks in an homogeneous medium

In the presence of a magnetic field, ubiquitous in the ISM, the shock wave satisfies not only the equations of the fluid dynamics, but also the Maxwell's equations. The magnetic field does not interact the same way with charged and neutral particles, which can result in a *decoupling* of the charged (ions and electrons) and neutral fluids. Indeed, the magnetic field modifies directly the dynamics of the charged particles[3] (ions, electrons or grains), whereas it affects only indirectly the neutrals through collisions with the positive ions (and electrons). Therefore, the magnetic field and the ionization fraction of the gas have thus an important impact on the structure of shock waves.

Before discussing the structure of MHD shocks, I shall recall the basic properties of the types of MHD waves that can propagate in a plasma.

4.2.1 Waves propagating into a plasma

In a magnetized plasma, different types of waves can propagate at distinct velocities:

---

[2]One dimension

[3]For instance, if the magnetic field is oriented parallel to the shock front, the Lorentz's force will make the particles girate around the magnetic field lines, thus leading to a coupling of the charged fluid to the magnetic field.

Sound waves are (*longitudinal*) compression waves that propagate pressure disturbances at a speed

$$c_{\mathrm{s}} = \sqrt{\frac{\gamma k_{\mathrm{B}} \mathrm{T}}{\bar{\mu}}} \, , \tag{4.1}$$

where γ is the *adiabatic index* (the heat capacity ratio, with $\gamma = 5/3$ for a monoatomic gas and $\gamma = 7/5$ for a diatomic gas). T is the gas temperature and $\bar{\mu}$ is the mean molecular mass[4] in atomic mass unit (amu).

Alfvn waves are *transverse* waves that propagate the distortion of the magnetic field lines *along* these lines (Alfven, 1950). Alfvn waves are thus incompressible, dispersionless waves. The neutral species can propagate Alfvn waves because of their coupling to the charged fluid. The *Alfvn speed* of these waves are thus

$$V_{\mathrm{A}}^{n} = \sqrt{\frac{B^2}{\mu_0 \rho_n}} \ \text{ for the neutrals } \ \text{ and } \ V_{\mathrm{A}}^{c} = \sqrt{\frac{B^2}{\mu_0 \rho_c}} \ \text{ for the charged fluid }, \tag{4.2}$$

where ρ_n and ρ_c are the mass density of the neutral and charged (ions, electrons, grains) fluids, respectively.

Magnetosonic waves are *longitudinal*, *compressible*, dispersionless waves that propagate pressure variations in the direction perpendicular to the magnetic field lines. The propagation of these waves involves variations of the strength of the magnetic field. In the neutral fluid (most of the gas mass), the magnetosonic speed is

$$V_{\mathrm{ms}}^{n} = \sqrt{c_{\mathrm{s}}^2 + \frac{B^2}{4\pi\rho_n}} \simeq \frac{B}{\sqrt{4\pi\rho_n}} \tag{4.3}$$

In the charged fluid, magnetosonic waves can propagate at a speed

$$V_{\mathrm{ms}}^{c} = \sqrt{c_{\mathrm{s}}^2 + \frac{B^2}{4\pi\rho_c}} \simeq \frac{B}{\sqrt{4\pi\rho_c}} \gg V_{\mathrm{ms}}^{n} \, , \tag{4.4}$$

In a typical molecular cloud, $\rho_c \approx 10^{-2}\rho_n$ because the dust grains are charged. So $V_{\mathrm{ms}}^{c} \approx 10 V_{\mathrm{ms}}^{n}$.

In the following I will only consider *stationary* shocks, where the structure of the shock (density, temperature profiles) in the reference shock frame do not evolve with time. In addition, *the direction of the magnetic field is perpendicular to the direction of propagation of the wave*, or parallel to the shock front. In this case, the magnetic field limits the compression of the gas at a maximum efficiency, since the fluid cannot flow along the magnetic field lines.

---

[4]$\bar{\mu} = 0.6$ amu for a fully ionized gas, or 2.33 for a molecular gas. 1 amu $= 1.66 \times 10^{-24}$ g

4.2.2   C- and J- type shocks

Depending on the intensity of B and the ionization fraction of the gas, we distinguish between two types of MHD shocks, C- and J-types:

J-shocks: if the B is weak or absent, or if the ionization fraction of the gas is high, the collisional coupling between charged and neutral particles is strong. These particles behave like a *single fluid*, coupled to the magnetic field. The properties of these shocks are similar to that of the hydrodynamical shocks. Across the shock front, the variables (pressure, density, velocity, etc.) change abruptly (see the top plot of Fig. 4.1). The transition region, which scale is of the order of the mean free path, is much narrower than the other dimensions in the gas. This transition is treated as a discontinuity, where the change of the variables of the gas is discrete (J being for *Jump*). The preshock and postshock values of the gas density, pressure and temperature are related by the Rankine-Hugoniot jump conditions (see sect. 4.2.2).

C-shocks: if the magnetic field is present and the ionization fraction low (typically $x_e = 10^{-7} - 10^{-8}$ in dense $n_H = 10^3 - 10^4$ cm^{-3} molecular clouds), the neutral and charged fluids are decoupled from each other. These shocks are named *multi-fluids* or $C-$shocks (Mullan, 1969, 1971), C being for *Continuous*, because in this case the discontinuity is smoothed and the gas parameters vary continuously across the shock front (see details below and Fig. 4.1).

Structures of C- and J-shocks

The Rankine-Hugoniot relations are conservations laws between any points behind and ahead of the shock front. They do not give any information about the internal structure of the shock. This structure depends on the strength of the magnetic field and the ionization fraction of the gas, and has a direct impact on the characteristics of the excitation of species in the shock, in particular H$_2$. This is why I briefly discuss here the Fig. 4.1, which shows schematically the structure of a stationary shock as a function of the preshock strength of the (transverse) magnetic field.

As shown in Eq. 4.4, in a molecular cloud of density $n_H = 10^4$ cm^{-3} and ionizing fraction $\chi \approx 10^{-5} - 10^{-9}$, magnetosonic waves propagate faster in the charged fluid than the shock front. Typically for this medium we have:

$$c_s \lesssim V_A^n < V_s \ll V_A^c \; , \tag{4.5}$$

where c_s is the sound speed, V_s is the shock velocity, V_A^n and V_A^c being the Alfvn speed for the neutral and charged fluids, respectively. So, if the strength of the magnetic field is high enough, the information can be transported ahead of the shock by the charged fluid, and a so-called *magnetic precursor* appears. This precursor slows and compresses the charged fluid of the preshock gas before the arrival of the shock front, on spatial scales much larger than the mean free path. This magnetic precursor decouples the neutral and charged fluid, generating *ambipolar diffusion*. The resulting friction between the fluids heats mostly the charged fluid. The variables of the charged fluid are continuous across the shock front, whereas those of the neutral fluid are discontinuous. Such a shock is called *J-shock with magnetic precursor*. This is the case *(c)* of Fig. 4.1.
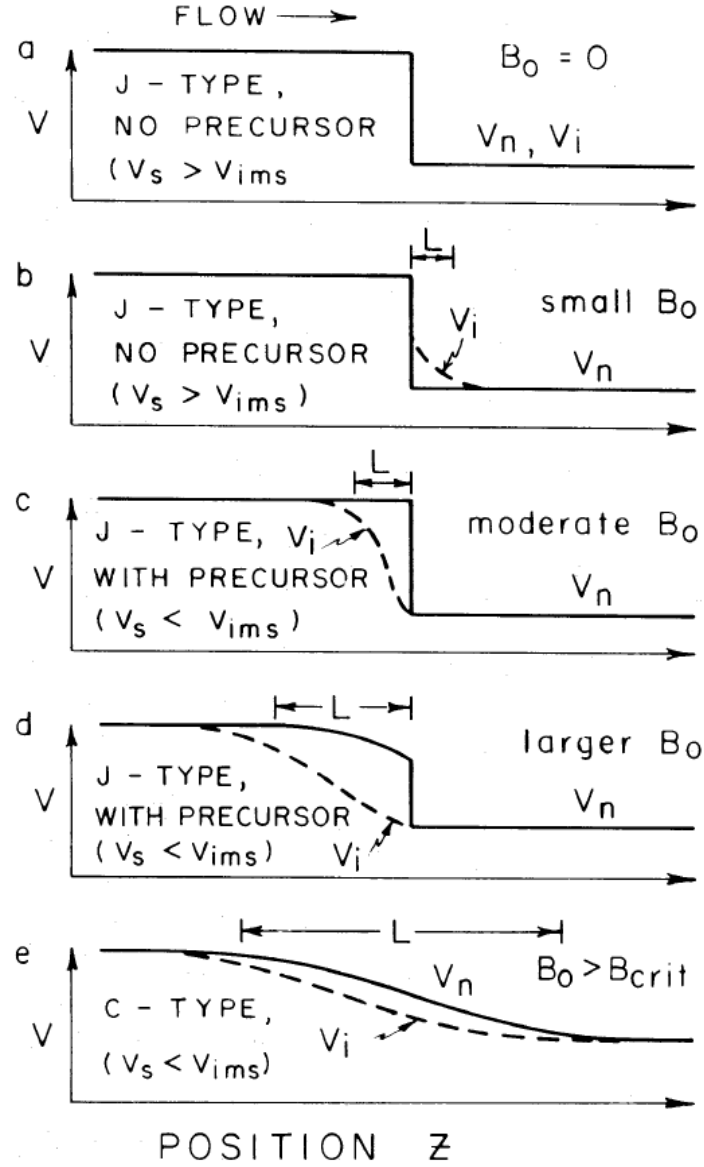
Figure 4.1: Schematic structure of the velocity of a stationary shock wave in poorly ionized medium, as a function of the local magnetic field strength B_0. B_0 increases from top to bottom. The velocities are given in the frame where the shock front is idle: V_n is the neutral velocity in the propagation direction of the shock, V_i that of the ions and electrons. The preshock medium is on the left hand side of the shock front, the postshock on its right hand side. L is the shock length, and V_{ims} is the ions magnetosonic speed given by Eq. 4.4 (the dust grains are ignored in this model). Taken from Draine (1980).

If the magnetic field is more intense, the magnetosonic speed further increases and the length of the magnetic precursor, L, too. The exchanges of momentum and energy between the neutral and the charged fluids in the precursor are more important, and the neutral fluid itself is likely to be heated, compressed and slowed before the arrival of the shock front, through elastic collisions with

the charged fluid. Because of this slowing down, the neutral fluid also undergoes a velocity jump of a smaller amplitude than in the situation where there is no magnetic field. This is the case *(d)*, in Fig. 4.1.

When the magnetic field strength is higher than a critical value, B_{crit}, the flow of the neutral fluid becomes continuous across the shock front. The discontinuity vanishes, and the shock turns into a C shock (case *(e)* in Fig. 4.1).

Rankine-Hugoniot jump conditions for an adiabatic MHD shock

The jump conditions across an MHD shock or discontinuity are referred as the Rankine-Hugoniot equations for MHD. Before giving these equations, let us recall some thermodynamical relations and definitions. We denote by c_{P} and c_{V} the specific heats of the gas at constant pressure and volume respectively. The *adiabatic index* is defined by $\gamma = c_{\mathrm{P}}/c_{\mathrm{V}}$. In the case of a perfect gas, the pressure P, density ρ and temperature T are connected by the classical equation

$$ \mathrm{P} = \frac{\rho R \mathrm{T}}{\bar{\mu}\, m_{\mathrm{H}}} \tag{4.6} $$

where $R = 8.31 \, \mathrm{J\,K^{-1}\,mol^{-1}}$ is the universal gas constant, $\bar{\mu}$ is the mean molecular mass in atomic mass unit (amu) and m_{H} is the mass of an hydrogen atom. For an adiabatic evolution, the additional relation holds:

$$ \mathrm{P} = K \rho^{\gamma} \tag{4.7} $$

where K is a constant. Apart from a constant, the entropy of a perfect gas is defined as

$$ \mathrm{S} = c_{\mathrm{V}} \log \left(\frac{\mathrm{P}}{\rho^{\gamma}} \right) \tag{4.8} $$

We place ourselves then in the reference frame of the shock (the surface discontinuity is at rest), and we take the suffixes $_1$ and $_2$ to refer to the preshock and postshock regions, respectively. The jump conditions are obtained by developing the conservation laws for mass, momentum, and enthalpy[5], with the few relations above (see e.g. the book by Shu, 1991):

$$ \rho_1 v_1 = \rho_2 v_2 \tag{4.9} $$

$$ \rho_1 v_1^2 + \mathrm{P}_1 + \frac{B_1^2}{8\pi} = \rho_2 v_2^2 + \mathrm{P}_2 + \frac{B_2^2}{8\pi} \tag{4.10} $$

$$ \left(\rho_1 \frac{v_1^2}{2} + \frac{\gamma}{\gamma - 1} \mathrm{P}_1 + \frac{B_1^2}{4\pi} \right) v_1 = \left(\rho_2 \frac{v_2^2}{2} + \frac{\gamma}{\gamma - 1} \mathrm{P}_2 + \frac{B_2^2}{4\pi} \right) v_2 \tag{4.11} $$

where v the velocity of the flow in the reference frame of the shock, ρ the mass density, and P the thermal pressure of the gas. The term $B^2/8\pi$ is the magnetic pressure that is added to the thermal pressure in the direction perpendicular to the magnetic field lines. The terms $\gamma \mathrm{P}/(\gamma - 1)$ and $B^2/4\pi$ are the specific enthalpy[6] and the magnetic energy, respectively. The conservation of momentum

---

[5]Because of the pressure forces on the fluid element, the enthalpy fux is conserved, not the energy flux

[6]entropy per unit volume.

(Eq. 4.10) can also be viewed as the conservation of the sum of the ram pressure (ρv^2) and the thermal pressure P.

We remind that the preshock (respectively postshock) flow is *supersonic* (resp. *subsonic*) in the reference frame of the shock front. In this frame, the gas appears to be decelerated. Knowing the Rankine-Hugoniot relations, and considering the relation defining the entropy for a perfect gas (see above Eq. 4.8), one can show that the entropy increases during the shock if and only if $P_2 > P_1$, i.e. whenever a shock can form (e.g. Zeldovich and Raizer, 1966). It follows that all transverse shock waves lead to compression of the gas. In the reference frame of the preshock medium, a fluid parcel that crosses the shock front, is compressed ($P_2 > P_1$), accelerated and heated ($T_2 > T_1$) by the work of the pressure forces applied by the postshock gas, just behind the shock front.

Frozen magnetic field

In the interstellar medium, the characteristic time of diffusion of the magnetic field is generally much longer than the characteristic time of advection. One can therefore assume that the field is *frozen* in the charged fluid. The charged grains are also coupled to the magnetic field because their slowing-down time in the shock is longer than their timescale of gyration around the magnetic field lines (Pineau des Forets et al., 1997). For a one-dimension (1D) transverse shock, the jump relations for the magnetic field are the following:

$$B_2 = B_1 \frac{v_1}{v_2} = B_1 \frac{\rho_2}{\rho_1} \tag{4.12}$$

The compression of the magnetic field follows that of the charged fluid.

Compression rate and postshock temperature

Roberge and Draine (1990) gives the compression factor of the gas:

$$\chi = \frac{\rho_2}{\rho_1} = \frac{2(\gamma+1)}{D + \sqrt{D^2 + 4(\gamma+1)(2-\gamma)M_A^{-2}}} = \frac{v_1}{v_2} \tag{4.13}$$

$$D = (\gamma-1) + 2M_s^{-2} + \gamma M_A^{-2} \ , \tag{4.14}$$

where $M_s = V_s/c_1$ is the sonic Mach number, V_s being the shock velocity (velocity of the shock front in the reference frame of the preshock medium) and c_1 the sound speed in the preshock gas. M_A is the Alfvn Mach number $M_A = V_s/V_A$.

For a *single-fluid* MHD shock, the postshock temperature (and thus the postshock pressure) can be expressed as a function of the compression factor $\chi = \rho_2/\rho_1$ (Roberge and Draine, 1990):

$$T_2 = \frac{\bar{\mu}_2 V_s^2}{k_B} \frac{1}{\chi} \left(1 + \frac{1}{\gamma M_s^2} - \frac{1}{\chi} + \frac{1}{2M_A^2}(1-\chi^2)\right) \tag{4.15}$$

More generally, in case of hydrodynamical shocks ($B = 0$), or single-fluid MHD shocks, the physical preshock and postshock quantities can be expressed as a function of the pressures P_1 and P_2, or as a function of the Mach number of the shock M_s (see Landau and Lifshitz, 1959; Roberge and Draine, 1990).

4.3   Modeling MHD shocks in molecular gas

My interpretation work of H_2 emission in H_2-luminous galaxies has involved the use of a sophisticated shock model developed by David Flower, Guillaume Pineau des Forts and Jacques Le Bourlot. The first paper describing the code is Flower et al. (1985), and the most recent developments are published in Le Bourlot et al. (2002); Flower et al. (2003); Flower and Pineau des Forêts (2003).

I run a grid of shock models that I use to fit the observations (see chapters 5, 6 and 9). In this section, I present illustrative results for C and J shock models, and focus on molecular emission (especially H_2) in C shocks, which are relevant for our study.

4.3.1   The Flower et al. code and the grid of shock model

In a few words, this 1-D[7] code integrates[8] the dynamical and chemical rate equations, together with those for the level populations of the rovibrational levels of the electronic ground state of H_2. In my grid of models, I use 137 chemical species, connected by a set of 1040 chemical reactions. The code can be used to model hydrodynamic shocks or transverse MHD shocks (C- or J-type).

The code has been described extensively in many papers and PhD thesis, so I will not repeat this description in this manuscript. The interested reader will consult Flower et al. (1985) for a first description of the equations solved by the code, and to the PhD thesis by Guillet, V. (2008) for a detailed formulation of these equations closer to the current version of the code. For a description of the treatment of H_2 in the code, please see Flower et al. (1986), Le Bourlot et al. (2002) and the PhD thesis by Gusdorf et al. (2008) for comparison of the model predictions with observations of proto-stellar outflows and a description of other chemical aspects. For the treatment of dust grains, see Flower and Pineau des Forêts (2003) and Guillet, V. (2008); Guillet et al. (2009) for the implementation of a sophisticated module that treats in details the dynamics and evolution of the dust.

Hypothesis

In this section I consider MHD shocks *without radiative precursor*, i.e. the shock velocities are low enough (typically $V_\mathrm{s} \lesssim 80$ km s^{-1} in molecular gas Hollenbach and McKee, 1989). Shocks with radiative precursor will be considered later in sect. 4.4. In the following, I list a few important features and assumptions used in the MHD shock model I have been using.

Stationary shock: the model assumes that a *stationary state* is reached in the 1D flow at velocity $v_n(z)$ (neutrals velocity) in the z-direction, so that $d/dt = v_n d/dz$. The flow time, t, of the neutrals is thus related to the distance, z, by the relation:

$$t = \int \frac{1}{v_n} \, dz \qquad (4.16)$$

The following results often present the physical quantities as a function of the flow time.

---

[7]The Flower et al. code is a one dimensional code, i.e. it considers a plane-parallel geometry.
[8]The algorithm is base on the VODE integrator (Brown et al., 1989).

Preshock magnetic field: we adopt the classical scaling relation for the preshock magnetic field
strength:

$$\frac{B_0}{1\,\mu\text{G}} = b\sqrt{\frac{n_\text{H}}{1\,\text{cm}^{-3}}}\ , \tag{4.17}$$

where b is the magnetic scaling factor and n_H the preshock hydrogen density ($n_\text{H} = n(\text{H}) + 2n(\text{H}_2)$). This expression is in agreement with the Zeeman effect observations of galactic molecular clouds that lead to $B \propto n_\text{H}^{0.47\pm0.08}$ (Crutcher, 1999). This observational result seems to be in agreement with numerical simulations of the condensation of molecular clouds under the effect of ambipolar diffusion (Fiedler and Mouschovias, 1993; Hennebelle et al., 2008), although the densities considered in these studies (prestellar cores) are much higher than those we consider here. For the following illustrative results, we adopt $b = 1$ for C-shocks, and $b = 0$ for J-shocks (no magnetic field).

For C-type shocks, the gas is treated as 3 fluids consisting of neutral species, positively and negatively charged species. We assume that the transverse magnetic field remains frozen into the charged fluid of the preshock gas all through the shock (see sect. 4.2.2).

H$_2$ is treated in a detailed manner in the code. The excitation mechanisms taken into account in
the model, as well as associated hypothesis, have been presented in chapter 3. We remind that
collisional excitation with H, H$_2$ and He is included. When an H$_2$ molecule forms on the surface
of a grain, we assume that the binding energy of H$_2$ is distributed with equipartition between
heating of the grain, kinetic energy of the newly-formed H$_2$ molecule, and internal energy of
H$_2$.

Dust grains are assumed to be composed of olivine-like material, (same stoechiometry as MgFeSiO$_4$).
The size distribution is assumed to be the MRN (Mathis et al., 1977) distribution $dn_g(a)/da \propto a^{-3.5}$, where $dn_g(a)$ is the density of grains having a radius between a and $a + da$. The radius
is taken to be in the range of $10 - 300$ nm. The total mass density (including mantles) of the
grains is taken to be $8.5 \times 10^{-3} \times 1.4\,n_\text{H}m_\text{H}$, where 8.5×10^{-3} is the dust-to-gas mass ratio.
The grain temperature is not calculated in the models but remains constant at a user specified
value. Here we use 15 K. The rate coefficients for charge transfer with grains is also taken into
account into the model, allowing for the grain charge distribution to be calculated for each step
of the model.

In the version I use, gas-grain collisions are also taken into account (Flower and Pineau des
Forêts, 2003), which may lead to sputtering of icy mantles and grain cores. It is possible to
release the grain core elements (Mg, Fe, Si and O) into the gas phase through sputtering. Sputtering yields are given in May et al. (2000). It is an important process both in J- and C-type
shocks. In J-type shocks the high kinetic temperature ensures that sputtering is an efficient
process, while in C-type shocks it is due to the velocity difference between neutral and charged
species.

An artificial viscosity is added to the terms of momentum and energy in the case of J-shocks. This
allows, rather than applying the Rankine-Hugoniot jump conditions at the shock discontinuity,
to integrate and resolve the discontinuity

Table 4.1: Description of the parameter space of the grid of MHD shock models

parameter	values
shock velocity	$V_s = 3 - 50$ km s^{-1} (step: 1 km s^{-1})
preshock density	$n_H = 10^2, 10^3, 10^4, 10^5$ cm^{-3}
Magnetic scaling factor[a]	J-shocks: $b = 0, 0.1$
	C-shocks: $b = 1$
Initial H$_2$ ortho/para ratio	o/p = LTE value[b] at 10 K, 0.01, 0.1, 3
dust to gas mass ratio	$Z = 7.5 \times 10^{-3}$ (Galactic), 7.5×10^{-4}
cosmic-ray ionization rate	$\zeta = 5 \times 10^{-17}, 5 \times 10^{-16}, 5 \times 10^{-15}, 5 \times 10^{-14}$ s^{-1}

[a]The strength of the preshock magnetic field is given by Eq. 4.17.
[b]The LTE value at low temperatures is given in chapter 3, Eq. 3.8. In a molecular cloud at 10 K, o/p $= 3.5 \times 10^{-7}$.

Table 4.2: Initial repartition of the refractory elements in the gas phase and in the grain mantles and cores used in the shock code[a].

element	fractional abundance[b]	gas phase	grain mantles	grain cores
C	3.55×10^{-4}	8.27×10^{-5}	5.53×10^{-5}	2.17×10^{-4}
O	4.42×10^{-4}	1.24×10^{-4}	1.78×10^{-4}	1.40×10^{-4}
Mg	3.70×10^{-5}			3.70×10^{-5}
Si	3.37×10^{-5}			3.37×10^{-5}
Fe	3.23×10^{-5}	1.50×10^{-8}		3.23×10^{-5}

[a]A more complete table can be found in Table 1 of Flower and Pineau des Forêts (2003).
[b]relative to Hydrogen: n_X/n_H with $n_H = n(H) + 2n(H_2)$.

Description of the grid of models

I have run a grid of C- and J- shock models by varying the shock velocity, preshock density, magnetic scaling factor, initial H$_2$ ortho-to-para ratio, and dust-to-gas mass ratio. This grid was primarily designed to interpret the H$_2$ observations in the Stephan's Quintet galaxy collision, where we expect significant dust destruction (chapters 5 and 6). Note that the output also includes atomic lines such as the intensity of the far-IR [O I]λ 63.2 μm line to be observed with the *Herschel Space Telescope*. The Table 4.1 lists the range of physical parameters of the grid of shock models.

The initial abundances of the 137 species are determined before any shock model calculation, by running a chemical steady-state model where we do not include adsorption on grains to avoid complete freezeout of molecules onto grains. The output abundances of this chemical steady-state model are then used as input abundances in the shock models.

I do not give here a complete review of all the model results of the grid, but I rather comment a few examples. The comparison with observations is presented in the following chapters. For a description of an other extensive grid of models, the interested reader may consult the PhD thesis by Kristensen (2007).

In the following illustrative results, I have used the initial elemental abundances of Flower and
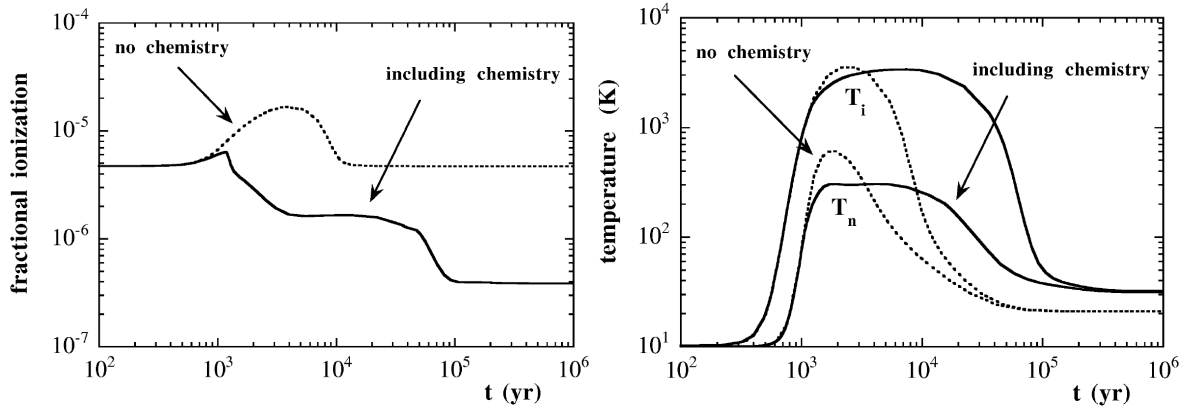
Figure 4.2: Impact of the chemistry on the fractional ionization (*left*) and temperature (*right*) of a C-shock. The shock velocity is 10 km s^{-1}. The preshock medium is molecular, at a density $n_{\rm H} = 10^3$ cm^{-3}. The preshock magnetic strengh is $B_0 = 25\,\mu$G, perpendicular to the direction of propagation of the shock. T_n and T_i are the temperatures of the neutral and ionized fluids, respectively. The plots show model results with (*solid line*) and without (*dotted line*) chemical reactions. Taken from Pineau des Forets et al. (1997).

Pineau des Forêts (2003), listed in Table 4.2. These abundances are those given by the output of the steady-state calculation. The initial repartition of the chemical species in the grain mantles can be found in Table 2 of Flower and Pineau des Forêts (2003). The preshock medium is molecular gas at $n_{\rm H} = 10^4$ cm^{-3}. The cosmic-ray ionization rate is the standard value $\zeta = 5 \times 10^{-17}$ s^{-1}.

4.3.2   Impact of the chemistry on the shock structure

Fig. 4.2 illustrates the impact of the chemical processes on the shock structure. Chemistry plays a role in the thermal balance of the shock, which in turn impacts the number of reactions the shock can initiate and the reaction rates. Fig. 4.2 shows the difference of the results obtained with or without taking the chemistry into account:

without chemistry, the ionization fraction varies only through the differential compression of the ionized and neutral fluids by the shock wave, and has the same value in the preshock and postshock regions.

with chemistry, the ionization degree of the postshock in one order of magnitude lower. This is essentially due to the neutralization of C$^+$ into C, initiated by H$_2$:

$$C^+ + H_2 \longrightarrow CH^+ + H \tag{4.18}$$

followed by a chain of reactions, which balance is

$$CH^+ + e^- \longrightarrow C + H \tag{4.19}$$

Consequently, the ion-neutral coupling is weaker, hence broadening the size of the precursor (the width of the shock is ≈ 5 times larger). Since the energy is dissipated on a larger region
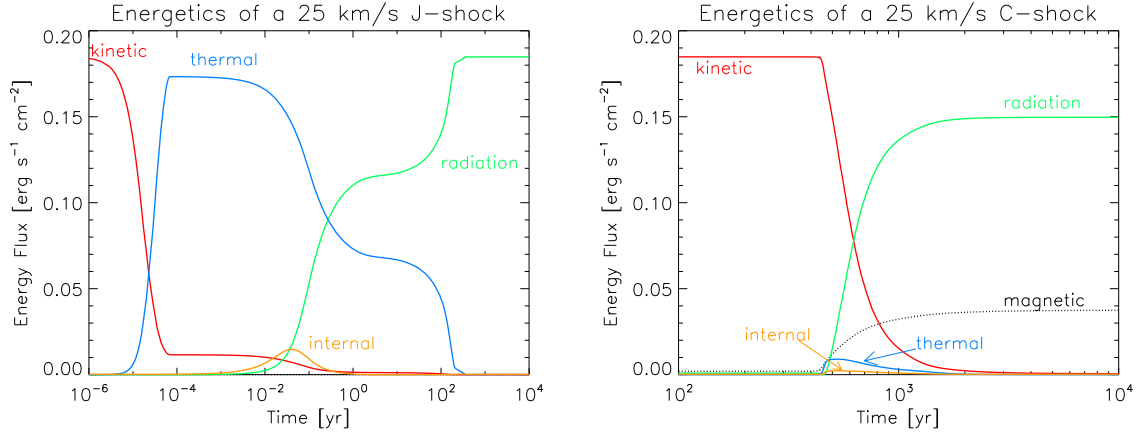
Figure 4.3: Contributions of the kinetic, thermal, internal and magnetic energies as a function of the flow time for *J*- (*left*) and *C*-shock (*right*), both at $V_s = 25$ km s^{-1}. The two shocks have the same total energy. The preshock medium is molecular, at a density $n_H = 10^4$ cm^{-3}. The preshock magnetic strengh is $B_0 = 100\,\mu$G for the *C*-shock and $B_0 = 0$ for the *J*-shock. The magnetic field is perpendicular to the direction of propagation of the shock.

> as compared to the first case, the maximum temperature is lower (here approximately twice lower).

This shows that chemistry and hydrodynamics are coupled, and have to be treated in parallel.

Dust grains, through gas-grain interactions, have also an important impact on the physical and chemical properties of the shock. They participate to the formation or removal of molecules of the gas, and their inertia can modify the propagation of the shock[9], especially in the case of *C*-shocks. Some details about the nature and treatment of the grains in the model have been given in sect. 4.3.1. A detailed review of the processes involving grains taken into account in the code, as well as their impact on the structure of *C*-shocks can be found in Flower and Pineau des Forêts (2003). For detailed calculations of the evolution of the dust size distribution in MHD shocks, please consult the PhD thesis by Guillet, V. (2008).

4.3.3 Energetics and molecular emission in shocks

In this section, a few results from my grid of models are presented.

Energy budgets

Fig. 4.3 compares the energy budgets for two types of shocks (*C* and *J*) of the same energy. In the reference frame of the shock front, the energy of the preshock gas is pure bulk kinetic energy. In the hydrodynamic case (*J*-shock with $B_0 = 0$), when the gas crosses the shock front, most (15/16) of the bulk kinetic energy is converted into thermal energy. Then, at $t \approx 10^{-4}$ yr on the left panel of Fig. 4.3, the shock dissipates its energy in radiation form (collisional excitation of species in the shock, followed by radiative deexcitation).

---

[9]The mass of the dust grains makes the bulk of the mass of the ions.

In C-shocks, the thermal energy stays low as compared to other forms of energy. The reason is that the dissipation of energy is not instantaneous and occurs over a timescale comparable to the cooling time through radiation. The heating of the neutral gas is due to inelastic collisions with the charged fluid. Unlike hydrodynamic shocks, part of the postshock gas energy is stored as *magnetic energy*. This magnetic energy can even dominate the postshock energy budget for very low-velocity shocks (< 7 km s^{-1} for $n_{\mathrm{H}} = 10^4$ cm^{-3}). The internal energy corresponds to the excitation of molecules, essentially H_2.

Temperature, velocity and abundance profiles

Fig. 4.4 compares two shocks of same energy, one J- and one C-shock. The profiles show some important physical quantities across the shock as a function of the flow time. The reference frame is the shock front. On the left colum we show J-shock profile with no magnetic field. On the right column, we show C-shock profiles with a preshock $B_0 = 100\,\mu$G. The models are the same than those used to make Fig. 4.3. In both cases, the shock velocity is $V_{\mathrm{s}} = 25$ km s^{-1} and the preshock gas density $n_{\mathrm{H}} = 10^4$ cm^{-3}. To facilitate the comparison, the y-axis are the same for both shocks. The x-axis has been extended to much shorter flow times for the J-shock, as the physical quantities start to vary much faster than for C-shocks.

The top panel of Fig. 4.4 shows the temperature of the neutrals and velocities (of the neutrals, V_n, and the charged species, V_i in the case of the multi-fluids shock). As discussed in sect. 4.2.2 (see also Fig. 4.1), the gas is slowed down abruptly when crossing the shock front, whereas in C-shocks the charged fluid, and then the neutrals by friction, slow down progressively.

In C-shocks, the energy is dissipated over a longer timescale than in J-shocks, which implies that the maximum temperature attained in C-shocks (≈ 2000 K here) is much lower than in J-shocks ($\approx 30\,000$ K). For strong ($M_{\mathrm{s}} \gg 1$) shocks with $B = 0$, the postshock temperature is given by (see e.g. Draine and McKee, 1993):

$$T_{\mathrm{ps}} = \frac{2(\gamma - 1)}{(\gamma + 1)^2}\, \frac{\bar{\mu}}{k_{\mathrm{B}}}\, V_{\mathrm{s}}^2 \simeq 2.6 \times 10^4 \left(\frac{V_{\mathrm{s}}}{25\ \mathrm{km\,s^{-1}}}\right)^2\ \mathrm{K}\ , \tag{4.20}$$

where V_{s} is the velocity of the shock wave, μ the mean molecular weight, k_B the Boltzmann constant and γ the adiabatic index. $\gamma = 7/5$ in a fully molecular medium in which the internal (rotational) degrees of freedom are thermalized. In the second member of Eq. 4.20, we indicate typical values for shocks driven into molecular gas. Thus we assume $\bar{\mu} = 2.33$ a.m.u. and $\gamma = 1.44$, since we take into account the presence of atomic Helium[10], with a fractional abundance $n(\mathrm{He})/n_{\mathrm{H}} = 0.1$.

The *middle panel* of Fig. 4.4 shows the evolution of the fractional abundances of a few important species (H_2, O, H_2O, H, H^+) in the shock. The J-shock is fast enough to dissociate H_2 (4.5 eV), but not enough to ionize significantly H (13.6 eV). H_2 molecules reform over a short timescale in the postshock cooling gas, which releases energy in the gas, and induces a small "knee" at ≈ 300 K on the temperature profile.

Unlike J-shocks, C-shocks do not generate significant dissociation of molecular hydrogen, as shown on the profiles of the fractional abundances[11]. The most active molecular chemistry takes

---

[10]instead of $\gamma = 1.4$ for a pure H_2 gas.

[11]The fractional abundances shown here are defined relative to hydrogen: $n(X)/n_{\mathrm{H}}$.
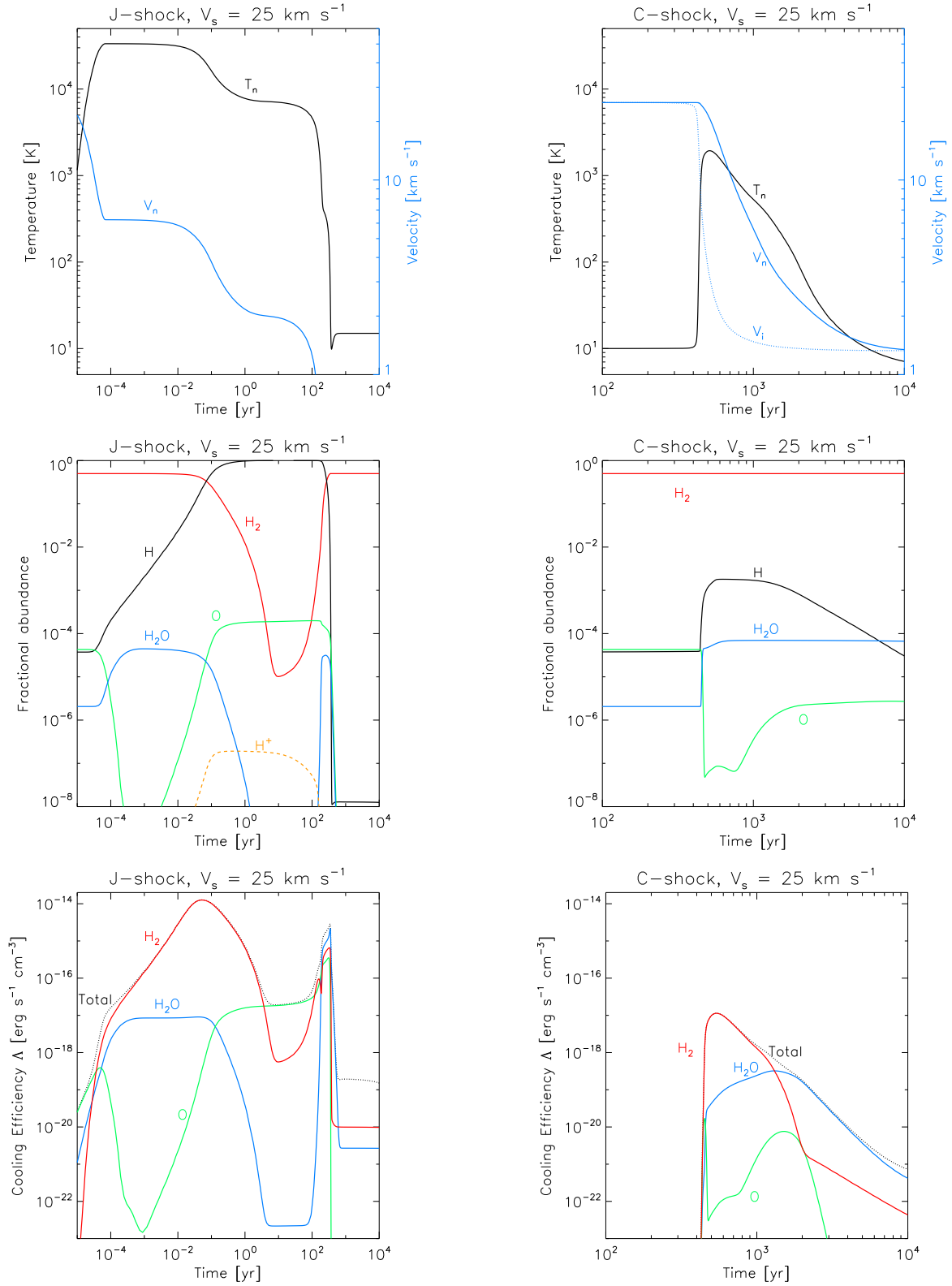
Figure 4.4: Comparison between J (*left*) and C (*right*) shock profiles. The shock velocity is 25 km s^{-1} and the preshock gas density $n_H = 10^4$ cm^{-3} for both shocks. The preshock magnetic field is $B_0 = 0\,\mu$G for the J shock and $B_0 = 100\,\mu$G for the C shock. Abundances are relative to H $(n(X)/n_H)$. See text for details.
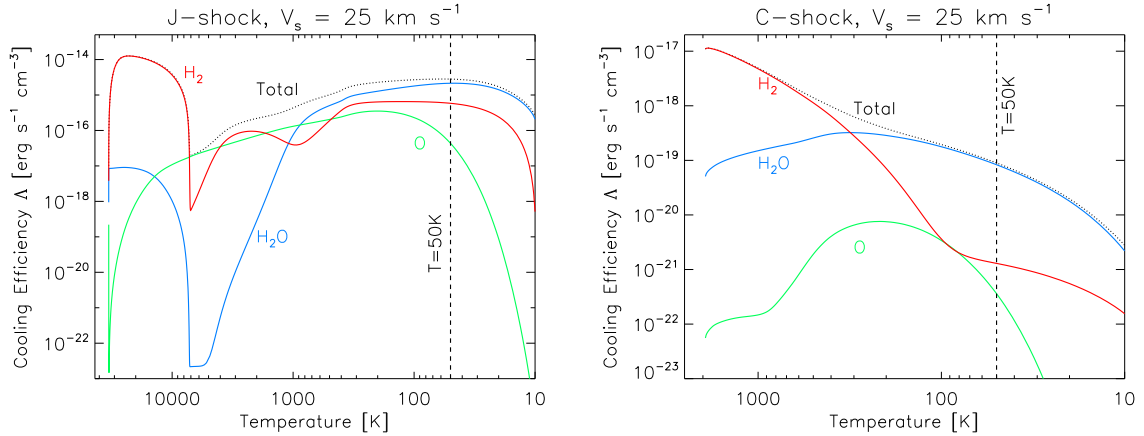
Figure 4.5: Contribution of the main coolants to the total cooling function as a function of the gas temperature for 25 km s^{-1} J- (*left*) and C- (*right*) shocks. The models are the same than in Fig. 4.3 and 4.4. The gas is cooling from the left to the right of the plots, from the maximum postshock temperature to 10 K.

place within these shocks, as the temperature jump is high enough to trigger endothermic chemical reactions without disrupting the involved molecules. Therefore I shall concentrate on C-shocks.

Note that depletion of gaseous species onto dust grain surfaces in the postshock region reduces the abundances of some of the newly formed molecules. This affects the thermal balance of the shock. This is clearly seen for the cooling rates profiles of the J-shock, where cooling efficiency of all the molecules drops at about $t = 3 \times 10^3$ yr because of adsorption onto dust grains.

Both kinds of shocks generate an intensive grain processing, that is still the subject of studies (Flower et al., 2003; Guillet et al., 2007), and depletion onto dust grain surfaces in the postshock region. This depletion reduces the abundances of some of the newly formed molecules.

Cooling functions and main coolants

We now discuss the radiative properties of the shock. The *bottom panel* of Fig. 4.4 shows the local cooling rates of the main coolants relevant for our study, as a function of the flow time. Fig. 4.5 shows these cooling efficiencies as a function of the temperature of the cooling postshock gas. More generally, the main coolants are O, H$_2$, H$_2$O, C$^+$, OH, CO. Their relative contributions to the cooling depend on the shock profile, and determine the radiative properties of the shock, which are very different in J and C shocks.

For J-shocks, the cooling is first dominated by H$_2$ over very short period of time, at high temperatures where it experiences dissociation. Then, at $\approx$ 8000 K, the [O I]λ6300 Å line takes over. When the gas has cooled down sufficiently, H$_2$, H$_2$O, O and C$^+$ dominate the cooling. More precisely, at $T \approx 1000$ K, the fine-structure line [O I]λ63.2 μm dominates. Other important lines in this temperature range are [C I], [N I]λ5200 Å, [C II]λ158 μm, [N II]λ121.8 μm, [S II]λ6731 Å and [Fe II]. At lower temperatures, the oxygen is converted into CO, H$_2$O, and OH, which become the dominant coolants.

For C-shock, H$_2$ is the main coolant for $T > 300$ K, which is the excitation range of the mid-IR
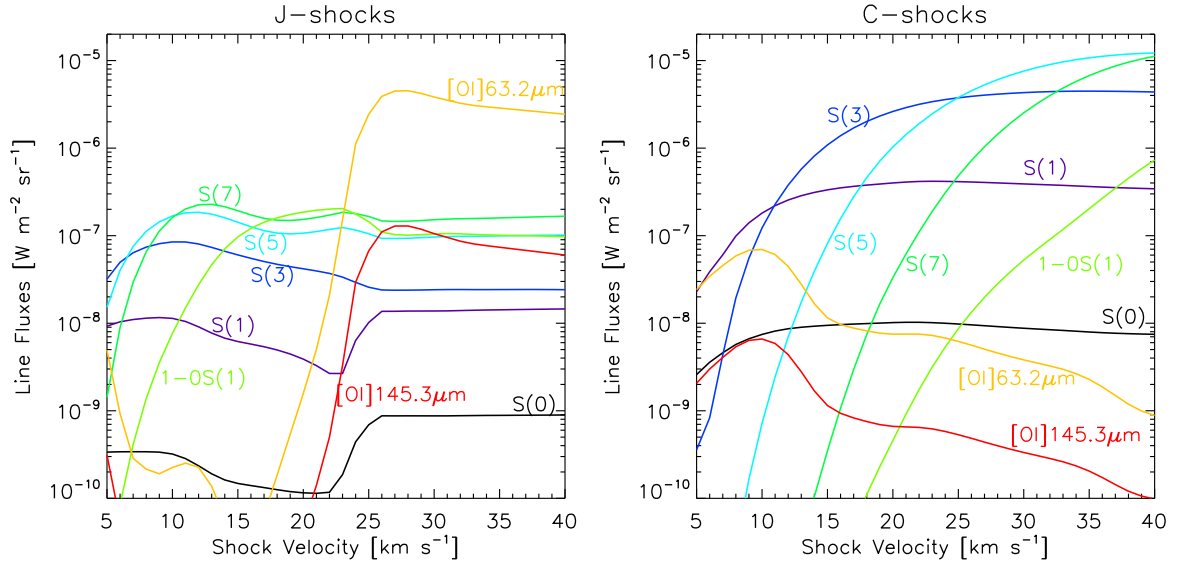
Figure 4.6: Integrated line fluxes as a function of shock velocity for *J*- (*left*) and *C*- (*right*) transverse shocks. The models are the same than in Fig. 4.3 and 4.4 (preshock density $n_H = 10^4$ cm^{-3}). The integrated line fluxes are calculated after a cooling down to 50 K.

rotational lines in which we are interested for our study. Remarkably, the cooling is dominated by H$_2$O emission at $T < 200$ K.

Line fluxes

The Fig. 4.6 shows the integrated (down to 50 K) line intensities as a function of shock velocity, for the two types of shock (*C* and *J*). Note that in *J*-shocks, the higher H$_2$ rotational excitation levels, like the corresponding upper levels of the S(5) and S(7) lines, are populated efficiently for low-velocity shocks. For *J*-shocks of velocities such that $25 < V_s < 40$ km s^{-1}, the integrated intensities are roughly constant with shock velocity, whereas for *C*-shocks, line fluxes increases smoothly with shock velocity.

Note that the [O I]λ 63 μm and 145 μm lines are good tracers to distinguish between the two types of shock (see Fig. 4.6). These lines are particularly sensitive to low velocity ($V_s \lesssim 20$) shocks, where their intensities are much higher for MHD shocks than for pure hydrodynamical shocks ($B_0 = 0$).

Examples of H$_2$ excitation diagrams for C- and J-type shock models

The Fig. 4.8 shows theoretical H$_2$ diagrams for our two shock models (see chapter 3, sect. 3.4.5 for the definition and calculation of the diagram). This diagram is computed at a temperature of 50 K in the postshock gas. If the gas temperature is below 50 K, almost no H$_2$ emission is produced. The integrated H$_2$ line intensities at 50 K are converted into column densities using Eq. 3.39. I only show on the plot the first 8 rotational levels relevant for our study, corresponding to the upper levels of the S(0) to S(7) transitions, plus three rovibrational levels, corresponding to the upper levels of the
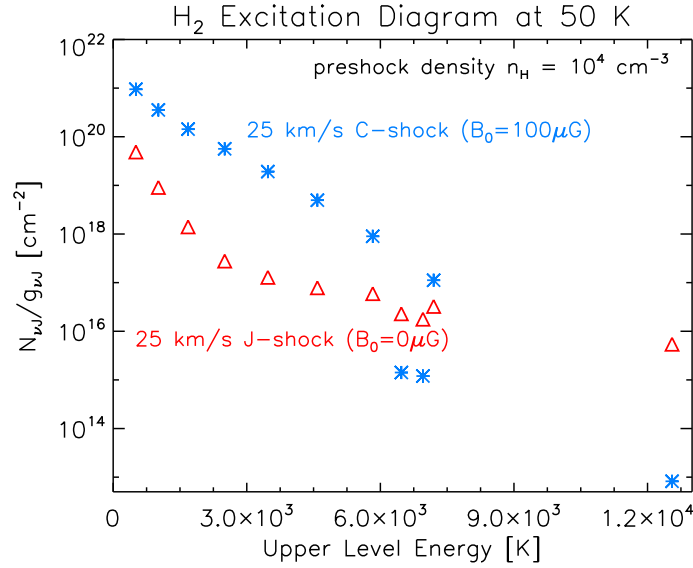
Figure 4.7: H_2 excitation diagram for 25 km s^{-1} C- and J-shocks. The preshock medium is molecular, at a density $n_H = 10^4$ cm^{-3}. The preshock magnetic strengh is $B_0 = 100 \, \mu$G for the C-shock and $B_0 = 0 \, \mu$G for the J-shock. The first 8 rotational levels of H_2, corresponding to the upper levels of the S(0) to S(7) transitions, plus three rovibrational levels, corresponding to the upper levels of the 1-0S(0), 1-0S(1), and 2-1S(1) lines (these are the 3 blue points at the bottom of the plot for the C-shock, showing that pure rotational levels are not thermalized with rovibrational levels).

1-0S(0), 1-0S(1), and 2-1S(1) lines. The characteristics of these lines have been given in chapter 3, Table 3.1.

This figure illustrates the impact of the type of shock on the excitation of H_2. For the C-shock, the rotational lines are much brighter than for the J-shock, because the temperature is lower and the shock is broader, thus increasing the column density of emitting gas (see the bottom panel of Fig. 4.4). The high temperatures reached in the J-shock favor the ro-vibrational lines. Note that if the J-shock velocity further increases, the dissociation of H_2 will be so important that the ro-vibrational excitation will be much weaker.

To conclude, MHD low-velocity shocks, driven into molecular gas, are very efficient in channelling the kinetic energy of the shock into the rotational H_2 lines. This characteristic is essential within the framework of my interpretation of H_2 emission in H_2-luminous sources.

I have used these diagrams to characterize the excitation characteristics in H_2-luminous objects, such as the Stephan's Quintet and the 3C326 radio galaxy. This will be discussed in details in chapters 5, 6 and 9. Flower et al. (2003); Giannini et al. (2004, 2006) provide examples of celestial sources (proto-stellar outflows, Herbig-Haro objects) for which use was made of such excitation diagrams to describe both the type of shock that is occuring and the physical parameters in these regions.
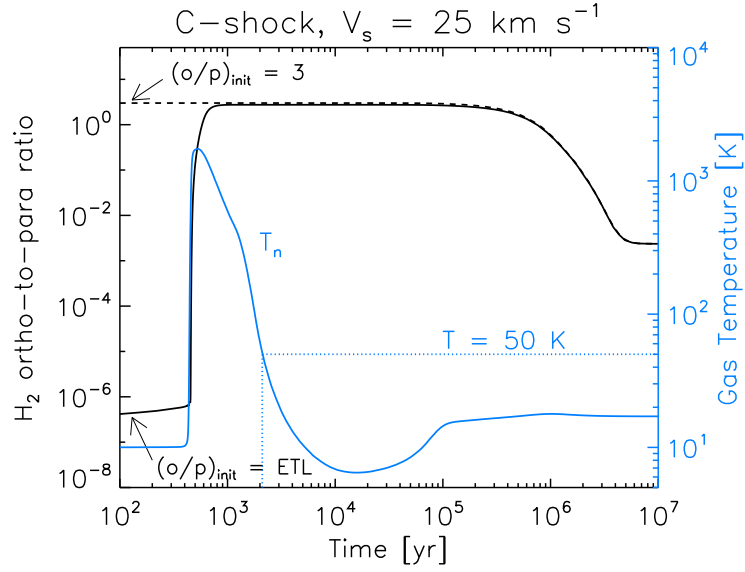
Figure 4.8: Evolution of the H_2 ortho-to-para ratio and temperature (in blue, labeled on the right) for a 25 km s^{-1} C-shock. Two initial values of the o/p ratio are shown: the Local Thermodynamical Equilibrium (LTE) value at 10 K (3.5×10^{-7}), and the high-temperature limit (3). The preshock medium is molecular, at a density $n_H = 10^4$ cm^{-3}. The preshock magnetic strengh is $B = 100 \, \mu$G, perpendicular to the direction of propagation of the shock.

Evolution of the H_2 ortho-to-para ratio in C-shocks

So far, the initial H_2 ortho-to-para ratio is assumed equal to the statistical equilibrium value of 3 in our shock models. I also adopt this value in the following chapters because the H_2 excitation diagrams observed in Stephan's Quintet or in the 3C326 radio-galaxy do not show any significant departure from this value, which would result in a systematic displacement of the ortho with respect to the para levels ("zig-zag pattern").

However, we have shown in chapter 3, sect. 3.2.2 that the LTE value of the o/p ratio is 3.5×10^{-7} at $T = 10$ K, and 0.03 at $T = 30$ K. To justify the high value of the initial o/p ratio, I briefly discuss the timescale of H_2 o/p conversion in shocks. This point has been discussed in more details by Wilgenbus et al. (2000) and Kristensen et al. (2007).

Fig. 4.8 illustrates the evolution of the H_2 o/p ratio in a 25 km s^{-1} C-shock, for two initial values of the o/p ratio: 3.5×10^{-7} (the LTE value at 10 K) and 3 (high-temperature limit). In the case of the low initial value, the interconversion between para- and ortho-H_2 starts when the temperature is rising, and, excepted within the first 10^3 years, the evolution of the o/p ratio is similar for both cases. The timescale of thermalization of the H_2 o/p ratio is long, $\approx 4 \times 10^6$ yr in this case, which is in good agreement with Eq. 3.10.

As a result, if the molecular gas experiences multiple shocks, and if the time interval between two shocks is smaller than the H_2 o/p conversion timescale, the o/p will not have time to thermalize to the low equilibrium value in the cold H_2. This may be the case in the H_2-luminous objects I have studied. Note that there are objects that favor a low initial o/p value, like proto-stellar bipolar outflows for

instance (Wilgenbus et al., 2000).

The initial value of the H_2 ortho-to-para ratio has an impact on the H_2 line brightnesses. Generally speaking, the lower the initial o/p ratio, the lower the brightness is. This impact is a timescale effect, and is more important in C-shocks than in J-shocks. The fact that the ortho-H_2 levels cannot begin to be populated until the temperature reaches ≈ 800 K causes a delay. This delay is responsible for the lower brightness in transitions between ortho-levels at low initial o/p ratio. Inversely, the brightness from transitions between para-levels is higher for low initial o/p ratio.

4.4   Fast shock models

So far, we have mostly discussed low-velocity shocks driven into dense molecular gas, that power molecular emission. These shocks are well traced through rotational line emission of H_2. Obviously, much faster shocks are likely to occur in the violent environments of H_2-luminous galaxies. Within the framework of understanding their multi-wavelength observations, I have been driven to use an other shock model that describes *fast shocks with radiative precursor*. This section briefly discuss the properties of these shocks, very different from the shocks discussed above.

4.4.1   Structure of a fast shock with radiative precursor

Fig. 4.9 schematically illustrates the structure of the fast shocks we now consider. In fast shocks, the shocked medium emits UV of soft X-ray radiation that propagates in all directions, including that of the preshock gas. This UV emission produces a *radiative precursor* that heats, dissociates (for $V_s \gtrsim 90$ km s^{-1}) and ionizes (for $V_s \gtrsim 120$ km s^{-1}) the preshock gas before it is shocked (see Hollenbach and McKee, 1989).

4.4.2   The MAPPINGS shock model library

In my PhD work, I have made use of the shock model library named *MAPPINGS III*, described in Allen et al. (2008), which is an updated version of the *MAPPINGS II* code described in Sutherland and Dopita (1993). I do not give a complete review of this model. Here I only present a short description of the basic properties and underlying physics included or not included in the model. The theory of fast, photoionizing shocks is described in Sutherland and Dopita (1993); Dopita and Sutherland (1995, 1996). I also direct the reader to the complementary book by Dopita and Sutherland (2003).

Modeling technique

Shocks with radiative precursor are difficult to solve numerically because

1. the UV radiation inside the shock imposes to carry on radiative transfer calculations to compute the ionization state of the gas, as well as the excitation state of the species in the shock

2. the shock has a *feedback* effect on the preshock gas in which it propagates. Therefore, one cannot integrate the shock structure (meaning integrate the MHD and chemical rate reactions) starting from any point in the preshock.
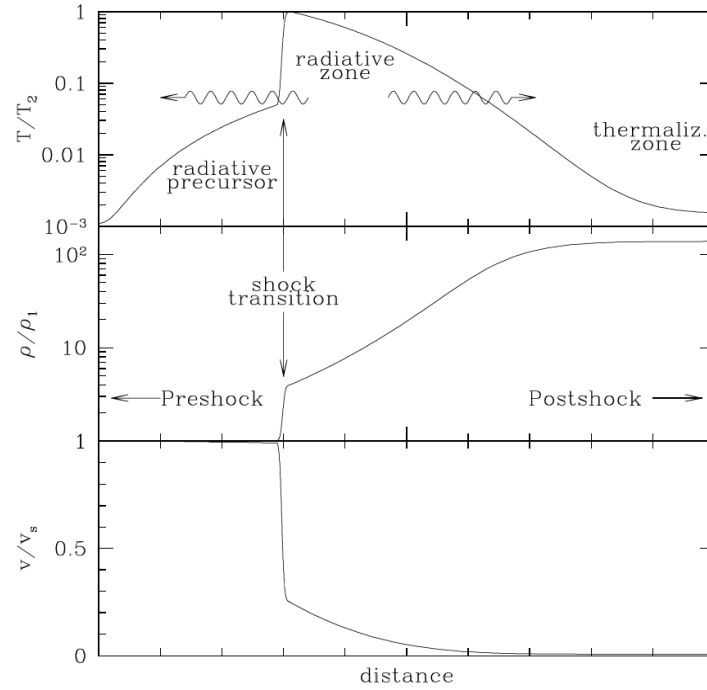
Figure 4.9: Stationary profile of a shock with radiative precursor, in the reference frame of the shock front. In this reference frame, the preshock gas comes from the left at a high speed, and is slowed down in the shock front (*bottom*), compressed (*middle*) and heated (*top*). The radiative emission of the postshock gas produces a *radiative precursor* that heats and ionize the gas ahead of the shock. Taken from Draine and McKee (1993).

The MAPPINGS 1-D code couples an MHD shock code to a radiative transfer photoionizing code. At each time step of the integration of the dynamical conservation equations in the flow, the rate equations for non-equilibrium ionization, recombination, excitation, and radiative transfer and cooling are solved at each time step of the flow. A total of four iterations (shock integration followed by calculation of the precursor) are performed to allow the temperature and ionization state of the precursor gas to stabilize at a constant value.

The physics included in the code

The cooling and radiative emission is calculated using a very large atomic data set (16 atoms) which allows treatment of all ionization stages (225 ions), up to fully ionized nickel.

- *The atomic processes affecting the ionization balance* of the plasma taken into account in the code are photoionization, ionization by electron collision, charge transfer reactions, and various forms of recombination channels, including radiative and dielectronic recombination,

- *Radiative processes* includes fine-structure, inter-system, and forbidden emission, as well as resonance transitions and continuum calculations. Fine-structure, inter-system and resonance lines are approximated by a two-level system. The model assumes that the resonance lines are

primarily excited by collisions. The continuum calculations includes free-free, free-bound and two-photon processes.

- *Additional heating and cooling processes*, including recombination and Compton heating, are integrated over the electron thermal distribution or the photon spectral distribution.

Physically, the ionizing radiation produced in the cooling zone behind the shock front shock is mostly composed of thermal bremsstrahlung (free-free) continuum, resonance lines, bound-free continuum of hydrogen, and the strong hydrogen two-photon continuum produced mostly by the down-conversion of Ly α photons trapped in the recombination region of the shock structure. Recombination lines and bound-free continuum from Helium and heavier elements are also contrinution to the ionizing radiation of the precursor.

The hydrogen ionizing radiation flux, $\mathcal{L}_{\mathrm{UV}}$, integrated for all energies $h\nu > 13.6$ eV, and over 2π sr follows the following scaling relation (Allen et al., 2008):

$$\mathcal{L}_{\mathrm{UV}} = 2.44 \times 10^{-7} \left(\frac{V_{\mathrm{s}}}{100\,\mathrm{km\,s^{-1}}} \right)^{3.02} \left(\frac{n_{\mathrm{H}}}{1\,\mathrm{cm^{-3}}} \right) \; [\mathrm{W\,m^{-2}}] \qquad (4.21)$$

which is almost scaled as $n_{\mathrm{H}} V_{\mathrm{s}}^3$.

What is not included: shortcomings

- *Dust grains* are ignored in these models. The shocks propagate in a dust-free gas. However, we have seen in sect. 4.3 that grains have an important impact on the structure, and thereby on the emission, of MHD shocks. The main difference is that in fast (> 200 km s^{-1} shocks, the dust destruction is expected to be very efficient. As shown in chapter 2, sect. 2.4, if the postshock temperature is hotter than $\approx 10^6$ K, dust grains may affect the *initial* stages of the cooling of the postshock gas, and thus the structure of the shock. However, their cooling efficiency will drop rapidly because of thermal sputtering.

- *Molecules* are not included although the computation of the shock structure is allowed to proceed until the gas has cooled to 1000 K. Therefore, the cooling functions are valid for $T \gtrsim 10^4$ K.

The shock model library is available online[12]. In my PhD work, I have used this library to produce diagnostics of mid-IR fine-structure line ratios in order to contrain the physical properties of the ionized gas in the Stephan's Quintet. Examples of line ratio diagnostics and comparison to observations are discussed in chapter 6.

I have also used these shock models to obtain a synthetic ionizing spectrum to model the emission from dust that would be heated by this radiation. This modeling has been performed within the context of the Stephan's Quintet, and this is discussed in chapter 8.

---

[12]http://cdsweb.u-strasbg.fr/~allen/mappings_page1.html

4.5 Shocks propagating into an inhomogeneous medium

So far, we have considered the ideal case of a shock that propagates in an homogeneous medium. However, as introduced in chapter 2, the interstellar or intergalactic media have a multiphase and a self-similar structure. The interaction of shock waves with density inhomogeneities (I will call them "clouds") in the ISM is thought to be an important dynamical process in a multiphase medium (e.g. McKee and Ostriker, 1977). As discussed in chapter 2, it contributes to mass exchange between the dense and diffuse phases. On one hand, it may trigger gravitational collapse and star formation (e.g. Elmegreen and Scalo, 2004). On the other hand, shocks may have a net destructive effects on molecular clouds, suppressing star formation.

Chapter 5 and Guillard et al. (2009c) (paper I) discuss the formation and excitation of H_2 in the context of the Stephan's Quintet galaxy collision, where observations indicate that these processes may be the response of a multiphase medium to a galactic-scale shock. It would be impractical to give an exhaustive review of the abundant litterature on such a vast topic. I will rather focus on two situations that are relevant for the context of H_2-galaxies, but also in many other astrophysical environments: the evolution of a cloud hit by a strong shock wave (sect. 4.5.2), and the supersonic collision between two gas streams of different densities and velocities (sect. 4.5.3). Before describing these two situations and the associated physical processes, I shall recall a few properties of a shock wave that encounters a discontinuity of density.

4.5.1 Reflexion and transmission of a shock through a discontinuity

When the propagation medium in which the shock wave is going through changes, the shock wave may enter

1. *a denser medium:* a reflected shock wave is driven back into the postshock flow of the incident wave. A shock wave is transmitted into the dense medium, and the initial discontinuity is accelerated. This case is schematically presented in Fig. 4.10. The reflected and transmitted postshock gas, separated by the contact discontinuity, are in pressure equilibrium.

2. *a less dense medium, or a medium that moves in the same direction of the shock:* a rarefaction wave is reflected into the postshock gas of the incident shock, and a transmitted shock is produced. The contact discontinuity is also accelerated.

In the following I shall consider the case (1), illustrated in Fig. 4.10. I take the suffixes $_i$ and $_c$ to refer to the inter-cloud and cloud media. If the age of the incident shock is much shorter than its cooling timescale (*adiabatic* shock), McKee and Cowie (1975) estimate that the velocity of the transmitted shock into the cloud, V_c, is of the order of [13]

$$V_c \simeq \sqrt{\frac{n_i}{n_c}} \, V_i = \frac{V_i}{\sqrt{\chi}} \qquad (4.22)$$

where V_i is the shock velocity in the inter-cloud medium, and n_c and n_i are the densities of the cloud and intercloud medium, respectively. The ratio between the densities in the two media is $\chi = \dfrac{n_c}{n_i} > 1$.

---

[13]This approximate relation is obtained from the conservation of the kinetic pressure ρV^2. More detailed expressions are given in Klein et al. (1994a)
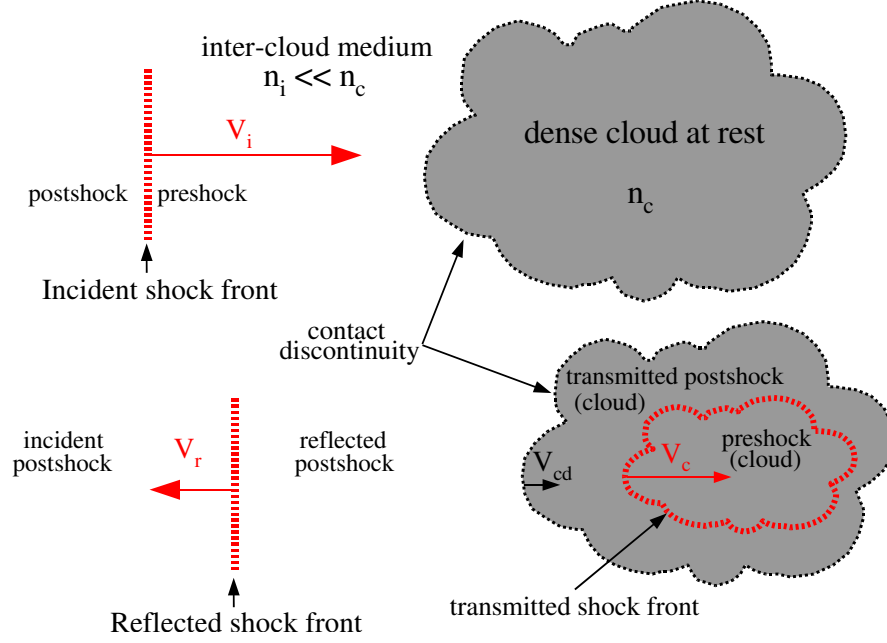
Figure 4.10: Reflexion and transmission of a shock through a discontinuity of density (cloud of density $n_{\mathrm{H}} = n_{\mathrm{c}}$). The incident shock wave propagates in the tenuous inter-cloud medium ($n_{\mathrm{i}} \ll n_{\mathrm{c}}$). The incident shock is transmitted into the cloud and reflected into the inter-cloud medium because of the abrupt density contrast. The initial contact discontinuity remains and is being accelerated at a velocity V_{cd} in the direction of the propagation of the incident shock wave. The postshock media of the reflected and transmitted shocks are in pressure equilibrium and propagate at the same velocity V_{cd}.

Note that if the shock is *isothermal*, i.e. if the shock has cooled down through radiation significantly to reach the preshock temperature, and if the incident shock is fast enough (such that $M_{\mathrm{i}} \gg \sqrt{\chi}$), the shock is not slowed down when penetrating into the cloud (Miesch and Zweibel, 1994):

$$V_{\mathrm{c}} \simeq V_{\mathrm{i}} \quad \text{if} \quad M_{\mathrm{i}} = \frac{V_{\mathrm{i}}}{c_{\mathrm{i}}} \gg \sqrt{\chi} \,, \tag{4.23}$$

where M_{i} is the Mach number of the inter-cloud shock and c_{i} the sound speed of the inter-cloud medium. This puzzling result can be understood as follows. If the incident shock is isothermal, the compression factor is much higher (M_{i}^2) than for the adiabatic case (equal to 4). If $M_{\mathrm{i}}^2 \gg \chi$, the incident postshock gas (the piston) is denser than the cloud[14]. Therefore, the ram pressure ρV^2 of the incident postshock gas, which is much higher for the isothermal than for the adiabatic case, drives the transmitted shock into the cloud at a higher velocity than the adiabatic shock.

To conclude, a shock wave that hits a medium that is denser than its propagation medium, is slowed down at the boundary of the dense medium (adiabatic phase) and then travels into the denser inner regions of the cloud at a quasi-constant velocity (isothermal phase).

---

[14]The density of the piston is $M_{\mathrm{i}}\rho_i \gg \chi\rho_i = \rho_c$. This is not the case for the adiabatic case if $\chi > 4$, where the density of the piston is lower than the shocked cloud ($4\rho_i < \chi\rho_i$).

4.5.2 Evolution of a shocked molecular cloud

I will now introduce the relevant timescales for the description of the evolution of a cloud that is run over by a fast shock wave, illustrated in Fig. 4.10. How does the shock wave propagate inside and outside the cloud? What happens to the cloud? This section first adresses these questions, both from an analytical and numerical point of view.

This problem has been extensively studied by means of numerical simulations, which is the only quantitative way to study the development of instabilities that are produced when the flow of background gas establishes around the cloud and interacts with it. The 2D dynamical evolution of such a cloud has been described in many papers, and I direct the interested reader to Klein et al. (e.g. 1994a); Mac Low et al. (e.g. 1994); Poludnenko et al. (e.g. 2002).

It is important to realize that the evolution of a shocked cloud does not only depend only on the dynamics, but also on its thermal and radiative properties. Thermal and radiative properties are just being explored in multi-dimensional numerical simulations, and have been largely neglected in the past. I will briefly discuss these recent numerical results.

I shall consider here the case of a spherical, cooling cloud, of radius R_c and mass density $\rho_c = m_H n_c$. The cloud is initially in pressure equilibrium with the inter-cloud medium (background gas). The density contrast between the two media is $\chi = \rho_c/\rho_i > 1$. The evolution of the shocked cloud consists of three phases:

1. Initially, the shock runs over the cloud. The time scale for this is the *shock passing time*,

$$t_{sp} = \frac{2R_c}{V_i} \tag{4.24}$$

$$\simeq 2 \times 10^5 \left(\frac{R_c}{10\,pc}\right)\left(\frac{V_i}{100\,km\,s^{-1}}\right)^{-1} \, [yr] \tag{4.25}$$

   where V_i is the velocity of the passing shock in the inter-cloud medium.

2. The second phase is the compression phase, in which the cloud finds itself inside the high pressure cocoon. It is now underpressured compared to its environment. Shock waves are transmitted into the cloud, and start to travel into it from all sides. The timescale for the cloud compression is named the *cloud crushing time* and is simply given by

$$t_{crush} = R_c/V_c \simeq \sqrt{\chi}\frac{R_c}{V_i} \tag{4.26}$$

$$= 3.1 \times 10^6 \left(\frac{\chi}{10^3}\right)^{1/2}\left(\frac{R_c}{10\,pc}\right)\left(\frac{V_i}{100\,km\,s^{-1}}\right)^{-1} \, [yr] \tag{4.27}$$

   where V_c is the velocity of the shock travelling into the cloud, which can be calculated from Eq. 4.22 (see sect. 4.5.1).

3. The third phase starts when the transmitted shocks have passed over the cloud. During this phase the cloud is subject to both *Rayleigh-Taylor* and *Kelvin-Helmholtz* instabilities. Meanwhile, during phases 2 and 3, the radiative cooling of the cloud impacts the evolution of the gas, which may also become *thermally unstable*. These processes lead to a fragmentation of the shocked cloud, and the fragments may end up mixed with the inter-cloud gas. Taking a first, qualitative look at Fig. 4.11, one can clearly see the effect of fragmentation on the shocked cloud.

In the following I discuss the key physical processes introduced above that control the evolution of the shocked cloud and its fragments.

Cloud acceleration and growth of Rayleigh-Taylor instabilities   The growth of the Rayleigh-Taylor instability[15] is related to the acceleration of the cloud by the postshock background gas. The acceleration timescale is the amount of time it takes to accelerate the cloud gas to the velocity of the postshock background. Let us write the momentum transfer from an inter-cloud gas flowing by a spherical cloud (of cross-sectional area $\pi R_{\rm c}^2$) at a relative velocity $V_{\rm ps,i}$. The postshock force acting on the cloud can be written

$$F \;=\; \pi R_{\rm c}^2 \rho_i V_{\rm ps,i}^2 \tag{4.28}$$

$$\;=\; \pi R_{\rm c}^2 \rho_i \frac{3}{4} V_{\rm i}^2 \;, \tag{4.29}$$

where I have assumed the jump condition $\rho_{ps,i} = 4\rho_i$ with $\gamma = 5/3$. Then the *acceleration timescale* is given roughly by $t_{\rm acc} = V_{\rm i}/(F/M_{\rm c})$, $M_{\rm c}$ being the mass of the cloud. We find that

$$t_{\rm acc} \;=\; \frac{4}{3} \frac{\rho_{\rm c}}{\rho_i} \frac{R_{\rm c}}{V_{\rm i}} = \frac{4}{3} \sqrt{\chi}\, t_{\rm crush} \tag{4.30}$$

$$\;\simeq\; 1.3 \times 10^8 \left(\frac{\chi}{10^3}\right) \left(\frac{R_{\rm c}}{10\,{\rm pc}}\right) \left(\frac{V_{\rm i}}{100\,{\rm km\,s^{-1}}}\right)^{-1} \;[{\rm yr}] \tag{4.31}$$

The above equation show that it is very difficult to couple dynamically dense gas with a background flow of tenuous gas. The crushing time to acceleration time ratio is $t_{\rm crush}/t_{\rm acc} = 3/4\sqrt{\chi}$, which shows that as soon as the density contrast is higher than $\approx 10^2$, the cloud will be compressed on a timescale much shorter than the acceleration time. The *growth timescale of Rayleigh-Taylor instabilities* is given by $t_{\rm RT} = (a\,k)^{-1/2}$, where a is the acceleration of the cloud and $k = 1/\lambda$ is the wavenumber of the perturbation (Chandrasekhar, 1961). In our case, $a \sim V_{\rm i}/t_{\rm acc}$, so we obtain

$$t_{\rm RT} = \frac{t_{\rm crush}}{\sqrt{k\,R_{\rm c}}} \approx t_{\rm crush} \;. \tag{4.32}$$

Perturbation wavelengths such that $k\,R_{\rm c} \sim 1$ are the most disruptive[16], so we conclude that Rayleigh-Taylor instabilities develop on a timescale comparable to the crushing timescale, and more than one order of magnitude shorter than the acceleration timescale for $\chi \gtrsim 100$.

Growth timescale of Kelvin-Helmholtz instabilities   A similar analysis can be applied to derive the growth timescale of the Kelvin-Helmholtz instabilities[17], $t_{\rm KH}$. For a high density contrast ($\chi \gg 1$),

---

[15]The Rayleigh-Taylor instability (after Lord Rayleigh and G. I. Taylor), is an instability of an interface between two fluids of different densities, which occurs when the lighter fluid is pushing the heavier fluid. As the instability develops, downward-moving irregularities ("dimples") are quickly magnified into sets of inter-penetrating Rayleigh-Taylor "fingers". The upward-moving, lighter material is shaped like mushroom caps. This phenomenon is clearly visible in the Crab and Helix nebulae.

[16]The growth rate of the RT instabilities is highest for the shortest wavelengths ($\lambda \ll R_{\rm c}$), but the amplitude of these perturbations ($\sim \lambda$) saturates rapidly.

[17]The Kelvin-Helmholtz instability occurs when velocity shear is present within a continuous fluid or, when there is sufficient velocity difference across the interface between two fluids.

$t_{\mathrm{KH}} = \sqrt{\chi}/kv_{\mathrm{rel}}$, where v_{rel} is the relative velocity between the postshock background and the cloud (Chandrasekhar, 1961). Assuming that $v_{\mathrm{rel}} \approx V_{\mathrm{ps,i}} = \frac{3}{4}V_{\mathrm{i}}$, we obtain:

$$t_{\mathrm{KH}} \simeq \frac{t_{\mathrm{crush}}}{\sqrt{k\,R_{\mathrm{c}}}} \approx t_{\mathrm{crush}} \;. \tag{4.33}$$

As Rayleigh-Taylor instabilities, Kelvin-Helmholtz instabilities growth on a timescale comparable to the cloud crushing time.

To sum up, if we assume an adiabatic evolution of the gas, the timescales calculated above suggest that the cloud is destroyed over a timescale comparable to the compression timescale, or crushing time. Destruction is enhanced by the fact that the shocks travelling into the cloud meet and interact, or reach the opposite boundary of the cloud. This produces a rarefaction wave travelling through the shocked cloud material. The cloud, which was compressed by the hot cocoon, now starts expanding again. This increases the pressure contrast between the compressed cloud and the postshock external gas, effectively accelerating the growth of destructive instabilities.

Impact of the magnetic field on the evolution of the shocked cloud Because of the coupling between the magnetic field and the cloud material, the magnetic field may have strong effects on the cloud evolution and on the development of instabilities. This effect is subtle, because it depends on the local orientation of the magnetic field in the inter-cloud medium.

If the background medium is magnetized, then magnetic field lines can become trapped in deformations on the surface of the cloud. As these field lines are stretched, the magnetic pressure along the leading edge of the cloud can increase enough to accelerate the disruption of the cloud through the Rayleigh-Taylor instability (Gregori et al., 1999). On the other hand, tangled magnetic fields within the clouds would act to resist compression, potentially reducing cooling and enhancing cloud destruction by shocks.

The left panel of Fig. 4.11 shows the results of two 3D MHD simulations, one being for a weak magnetic field, the other for a strong one (Shin et al., 2008). The effect of the magnetic field seems important only in the late stages of the evolution of the cloud. This figure illustrates that at late times, strong fields substantially alter the dynamics of the cloud, suppressing fragmentation and mixing by stabilizing the interface at the cloud surface. Even weak magnetic fields can drastically alter the evolution of the cloud compared to the hydrodynamic case.

In addition, the topology of the magnetic field has a strong impact on the thermal conduction for clouds in hot ($> 10^6$ K) gas, because in this case the conduction is carried on by the electrons (see the discussion about the thermal conduction below). Indeed, the magnetic field channels the electron conductivity along the field lines.

Impact of the cooling of the cloud and thermal instability The above conclusion that clouds are destroyed in a time comparable to the cloud crushing time is drastically changed if the cloud is able to cool through radiative processes over a timescale t_{cool} shorter than the dynamical timescale of destruction, t_{crush} (Mellema et al., 2002; Fragile et al., 2004). Mellema et al. (2002) define a cooling-dominated regime by $t_{\mathrm{cool}} < \frac{t_{\mathrm{crush}}}{10}$, in which the evolution of the cloud is dominated by radiative processes. A simple estimate of the cooling time (Fragile et al., 2004) leads to the following
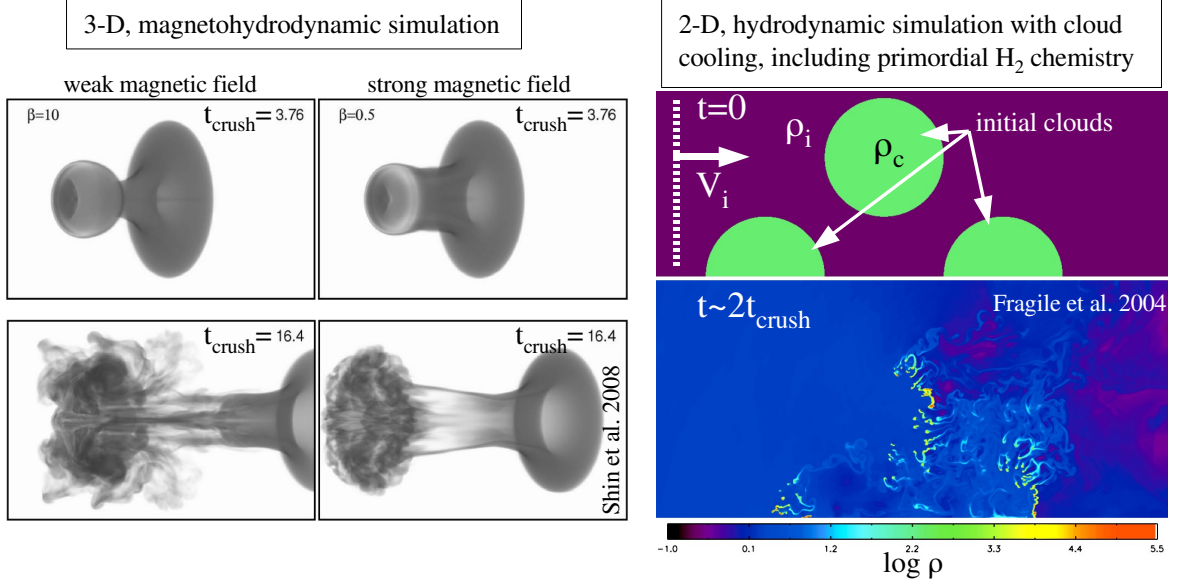
Figure 4.11: Numerical simulations of shocked clouds. *Left:* 3-D MHD simulation of a non-cooling cloud (Shin et al., 2008). The plots show volumetric renderings of the cloud density for a weak magnetic field value[a] ($\beta = 10$, left column) and strong-field ($\beta = 0.5$, right column) parallel shock simulations. The Mach number of the shock is $M_s = 10$. The cloud boundary is not a discontinuity but a smooth density gradient. The density contrast between the cloud and the inter-cloud medium is $\chi = \rho_c/\rho_i = 10$. *Right:* 2-D hydrodynamical simulation ($B = 0$) of three cooling clouds hitted by a shock wave (Fragile et al., 2004). The above plot shows the initial conditions. The dimensions of the computational grid are 900×400 pc. The initial cloud radii are 100 pc and their temperature 10^4 K. The initial cloud density is $\rho_c = 1.7 \times 10^{-24}$ g cm^{-3} ($n_c = 1$ cm^{-3}), with a density contrast of $\chi = 10^3$. The bottom plot shows contours of the logarithm of gas density, in units of 6.7×10^{-27} g cm^{-3} on the scale. The shock velocity in the inter-cloud medium is $V_s = 7.4 \times 10^3$ km s^{-1}, for a Mach number of $M_s = 20$.

---

[a]β is the ratio of the gas to magnetic pressures.

condition:

$$R_c > 1.2 \times 10^{-2} \left(\frac{\chi}{10^3}\right)^{-2} \left(\frac{V_i}{10^3\,\mathrm{km\,s^{-1}}}\right)^4 \left(\frac{n_c}{1\,\mathrm{cm^{-3}}}\right)^{-1} \,, \qquad (4.34)$$

which shows that cooling will generally govern evolution for moderate cloud densities and shock velocities. However, sufficiently high shock velocities ($V_i \gtrsim 10^4$ km s^{-1}) can suppress the effect of cooling over the cloud destruction time. Cooling is also negligible at low densities ($n_c \lesssim 10^{-4}$ cm^{-3} for $V_i \gtrsim 10^3$ km s^{-1}).

Heating and cooling processes may generate thermally unstable gas in the cloud (see Fig. 2.3 or later in Fig. 4.13). The thermal instability adds to the Rayleigh-Taylor and Kelvin-Helmholtz instabilities, and is an important fragmentation mechanism. The thermal instability has been discussed in chapter 2, sect. 2.2.5). Below $\sim 10^6$ K, the gas is thermally unstable. Numerical simulations show that the thermal instability generates complex inhomogeneous structures, dense regions that cool and low density voids (Sutherland et al., 2003; Audit and Hennebelle, 2005). This fragmentation

occurs on the gas cooling timescale. In most numerical simulations, the thermal instability is ignored because simplifying assumptions are made on the equation of state of the gas (adiabatic, isothermal or polytropic evolution).

The lifetime of the fragments in the hot gas depends on their ability to cool. An efficient gas cooling stabilizes the clouds. As H_2 is a major coolant in the warm molecular gas, it may have an important impact on the survival of molecular clouds hitted by strong shocks. This is illustrated in the right panel of Fig. 4.11, that shows numerical simulations of multiple clouds overtaken by a shock wave that takes into account the radiative properties of the clouds, as well as primordial gas-phase formation of H_2. These simulations show that the cloud first breaks into fragments. Because of the cloud cooling, these fragments become dense enough to be able to survive over a timescale of the order of a few million years Mellema et al. (2002); Fragile et al. (2004).

These numerical simulations ignore in particular the H_2 formation on grains, which may greatly enhance the cooling efficiency of the cloud, provided that dust can survive the transmitted shock. If it is the case, the cloud fragments may be even further stabilized.

Thermal conduction and evaporation timescale   The heat conduction has an important and subtle impact on the evolution of the shock cloud. Depending on how the heat flux is treated and whether cloud cooling is included, heat conduction may or may not lead to the evaporation of the cloud fragments.

The heat flux is carried by electrons in hot or ionized gas, and by H in cold or warm neutral gas. This heat flux is proportional to the temperature gradient (Fourier's law):

$$\dot{\mathbf{q}} = -\kappa \, \nabla \mathbf{T} \, , \tag{4.35}$$

which defines the *thermal conductivity*[18] κ. In case of a steep temperature gradient between the cloud and intercloud medium, the heat flux is limited by the ability of the electrons or H atoms to diffuse across the boundary. If the spatial scale of the temperature variation is smaller than the mean free path of the electrons, the heat flux *saturates*, and its value can be reduced up to a factor ~ 10 as compared with the classical heat flux given by Spitzer (1962). The saturation of the conduction thus reduces the evaporation of the cloud (Cowie and McKee, 1977).

In the case of saturated heat flux, the rate at which the cloud evaporates can be written analytically (Cowie and McKee, 1977; Klein et al., 1994a):

$$\dot{M}_c \approx 4\pi R_c^2 \, \rho_i \, c_i \tag{4.36}$$

where ρ_i and c_i are the mass density and sound speed in the inter-cloud medium. One can define an *evaporation timescale*

$$t_{ev} = \frac{M_c}{\dot{M}_c} \approx \frac{\sqrt{\chi} \, t_{crush}}{7} \, , \tag{4.37}$$

which shows that for $\chi \sim 10^2$, the clouds will evaporate in a time comparable with the compression timescale (cloud crushing time).

---

[18]The mean free path of the specie that carries the heat flux determines the temperature dependence of the thermal conductivity: $\kappa \propto T^{5/2}$ for electron conductivity and $\kappa \propto T^{0.8}$ for H. Note that the charge transfer reactions strongly limits the H mean free path. Thereby, ionization reduces conductivity in partially ionized warm gas.

Vieser and Hensler (2007a) performed numerical simulations of static clouds embedded within a hot gas, taking the saturated heat flux. The main result is that the evaporation timescale is at least one order of magnitude longer than the analytical value given by Eq. 4.37. The reason is that a transition zone forms at the cloud edge in which the steep temperature and density gradients are reduced. This results in a lower evaporation rate than predicted.

Simulations that include both thermal conduction and radiative cooling (and heating) processes show an even more dramatic effect. The clouds can even gain material if radiative cooling exceeds the energy input by heat conduction. Vieser and Hensler (2007a) show that matter from the hot inter-cloud medium can condensate onto the clouds in a regime of cloud parameters where evaporation is requested from the analytical approach. The reason is that the additional energy driven by heat conduction from the hot background gas into the cloud can be transported away from the interface and radiated off efficiently from the inner parts of the cloud.

Turbulent mixing   Another important mean to transport the energy from the hot background gas to the cool medium is through *mixing of gas phases at boundary layers*. This mixing is expected to occur wherever there is a velocity shear is present at the interface of cloud phases. A schematic description of such a boundary layer is given in Fig. 4.12. Such velocity shears occur in many astrophysical situations, including outflows of hot gas driven into the ISM by supernovae explosions, starburst or AGN, but also galaxy mergers, etc.

A turbulent mixing layer at the boundary of the cloud develops through the growth of Kelvin-Helmholtz instabilities, that drive transverse waves along the boundary between the two fluids. The energy of these waves is dissipated at small scales, and a layer of gas at intermediate temperatures is produced at the interface (see Begelman and Fabian, 1990; Slavin et al., 1993). The intermediate temperature, $\bar{T}$, in the turbulent mixing layer is determined by the temperatures of the hot (T_h) and cloud (T_c) phases, the evaporation rate of the cold gas into the intercloud medium, $\dot{m}_c$, and the entrainment rate of hot gas into the mixing layer, $\dot{m}_h$:

$$\bar{T} = \frac{\dot{m}_h T_h + \dot{m}_c T_c}{\dot{m}_h + \dot{m}_c} = \zeta \sqrt{T_c T_c} \, , \tag{4.38}$$

where ζ is a dimensionless factor of the order of unity (see Begelman and Fabian, 1990). Typically, for warm ($T \approx 10^4$ K) clouds embedded within a hot ($T \approx 5 \times 10^6$ K), the temperature of the mixing layer is $T_{\mathrm{mix}} \approx 10^{5-5.5}$ K.

The intermediate-temperature gas may be thermally unstable and any dynamical disturbance will cause the gas to rejoin the hot or warm phase (see Fig. 4.13). This length of the boundary layer is obtained by assuming a stationary mixing layer, in which the energy flux input by turbulent motions is balanced by the cooling rate per unit area.

The right panel of Fig. 4.12 illustrates the situation of a cold neutram medium (CNM) cloud embedded within a stream of hot gas. The two sub-panels compare the results with our without thermal conduction. These simulations have been performed by J. Slavin (private communication). When thermal conduction is ignored *(right)*, the Kelvin-Helmholtz instabilities are developped. The comparison between the two figures clearly shows that the conduction reduces the growth rate of Kelvin-Helmholtz instabilities. When conduction is taken into account, the evaporative outflow prevents instabilities from developing at the interface with the flow. With conduction, the cloud is less
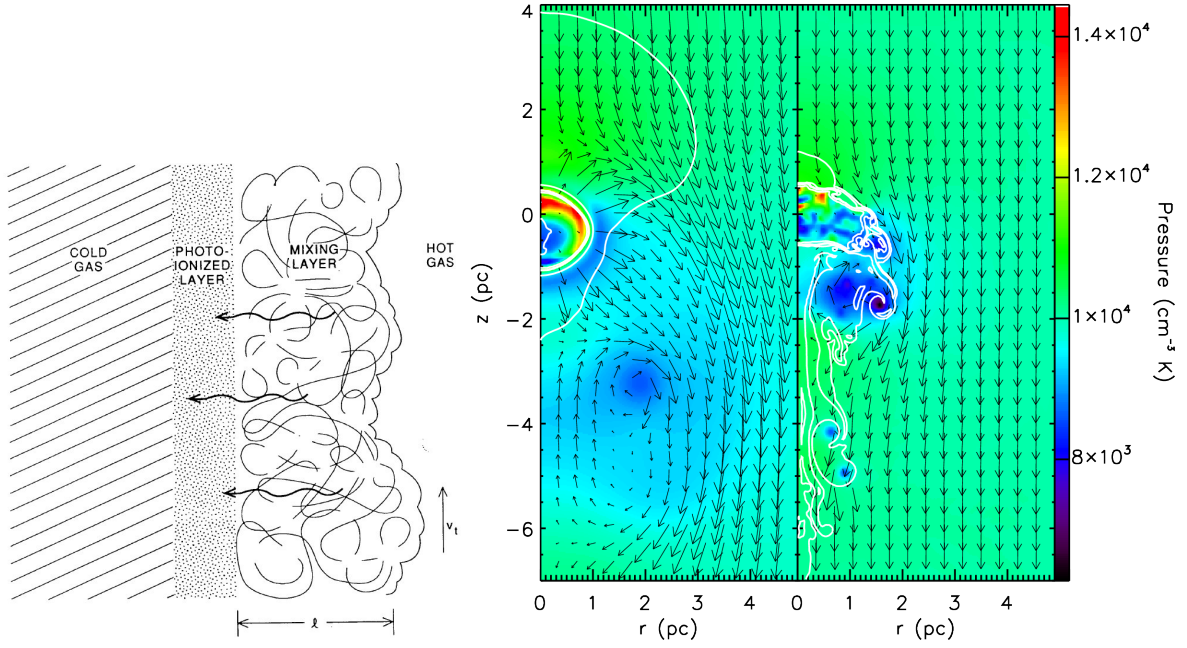
Figure 4.12: *Left:* Schematic description of a turbulent mixing layer from Slavin et al. (1993). *Right:* Numerical simulations of a CNM cloud embedded in a hot plasma stream (J. Slavin, private communication). The colors indicate the gas pressure, and the arrows the velocity field. In the *left* panel, heat conduction is taken into account, whereas in the *right* panel not. The cloud with thermal conduction (*left*) is much less disrupted than the cloud with conduction turned off (*right*). The hot gas has a speed of 50 km s^{-1} relative to the cloud and a temperature 10^6 K. The initial cloud density is $n_{\rm H} = 0.6$ cm^{-3} and its radius 1 pc. The cloud to hot gas density contrast is $\chi = 125$. The ambient pressure is 10^4 K cm^{-3}. No cooling processes are included in these simulations.

disrupted but loses its mass faster. These illustrative results are in agreement with other simulations performed by Vieser and Hensler (2007b,a), and we direct the reader to those papers for a detailed discussion of the impact of thermal conduction on the evolution of a cloud embedded in hot gas.

4.5.3 Supersonic collision between two gas streams

Let us consider now the collision between two gas streams at different densities and velocities. This situation may be relevant in the case of galaxy collisions, where the ISM of the galaxies are colliding with each other. I briefly discuss the plane-parallel situation, which can be solved analytically, and move to a brief discussion of numerical simulations that provide some useful feeling about how the gas and shocks behave in such collisions.

Plane-parallel collision between two gas streams

We consider the situation of Fig. 4.14. Two plane-parallel flows of preshock densities ρ_1 and ρ_2 are colliding at $t = 0$, which produces the contact discontinuity (CD). Fig. 4.14 shows the situation where $\rho_1 = 4\rho_2$, $P_1 = P_2$ and $v_1 = -v_2$. To simplify the expressions of the post-collision quantities, we
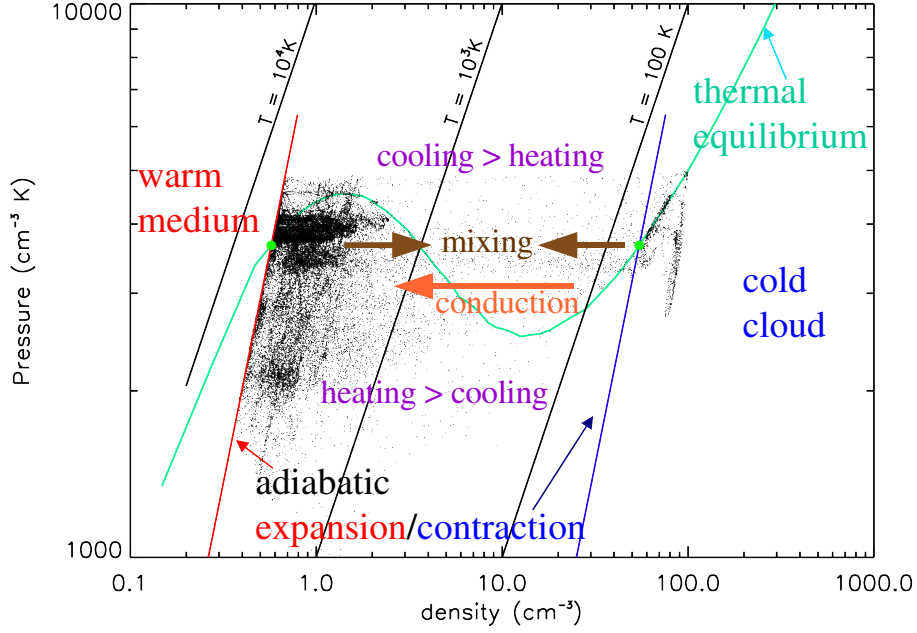
Figure 4.13: CNM Clouds in a WNM stream: thermal balance. The diagram shows the phase proper-
ties of a CNM cloud being destroyed by turbulent mixing in a WNM flow. Points are gas parcels from
the hydro-dynamical simulation shown on Fig. 4.12, at $t = 3.5 \times 10^5$ yr (J. Slavin, private communi-
cation). Part of the gas is located on the thermally unstable branch of the equilibrium cooling curve.
Dynamical processes (turbulent mixing) lead to departures from equilibrium (stable or unstable). The
WNM gas has a speed of 5 km s^{-1} relative to the cloud and a temperature 6 300 K. The initial cloud
density is $n_{\mathrm{H}} = 55$ cm^{-3} and its radius 0.1 pc. The cloud to hot gas density contrast is $\chi \sim 100$. The
ambient pressure is 3660 K cm^{-3}. No thermal conduction is included in these simulations.

place ourselves in the case where the two flows are identical, i.e. $\rho_1 = \rho_2$ ($\chi = 1$). The case presented
in Fig. 4.14 is more general. The corresponding equations for the general case can be found in Lee
et al. (1996). Since the pressure and velocity are continuous across the surface discontinuity, we have:

$$P_3 = P_4 = \frac{4}{3}\rho_1 v_1^2 \quad \text{and} \quad \mathrm{v}_3 = \mathrm{v}_4 = \mathrm{v}_{\mathrm{CD}} \;, \tag{4.39}$$

where v_{CD} is the velocity of the contact discontinuity. For this simplified case, the bulk kinetic energy
to thermal energy conversion rate can be written as

$$R = \frac{\frac{4}{3}\rho_1 v_1^3}{\frac{1}{2}\rho_1 v_1^3 + \frac{1}{2}\rho_2 v_2^3} = \frac{4}{3} \;, \tag{4.40}$$

which is the largest value attained for $\gamma = 5/3$ when the two colliding flows are identical. The fact
that R is greater than 1 is not surprising. Since the postshock gas is at rest in the lab frame, all the
bulk kinetic energy of the gas that passes through the shock is converted into thermal energy. But the
shocks move outward from the discontinuity, so R is actually the ratio between the shock velocity
relative to the upstream flow in region 1 to the shock velocity v_1, which is $4/3$ for $\gamma = 5/3$.

We will now consider the similar situation of the collision between two gas streams, but from the
point of view of 3D simulations. This allows to point out the main differences between the 1D and
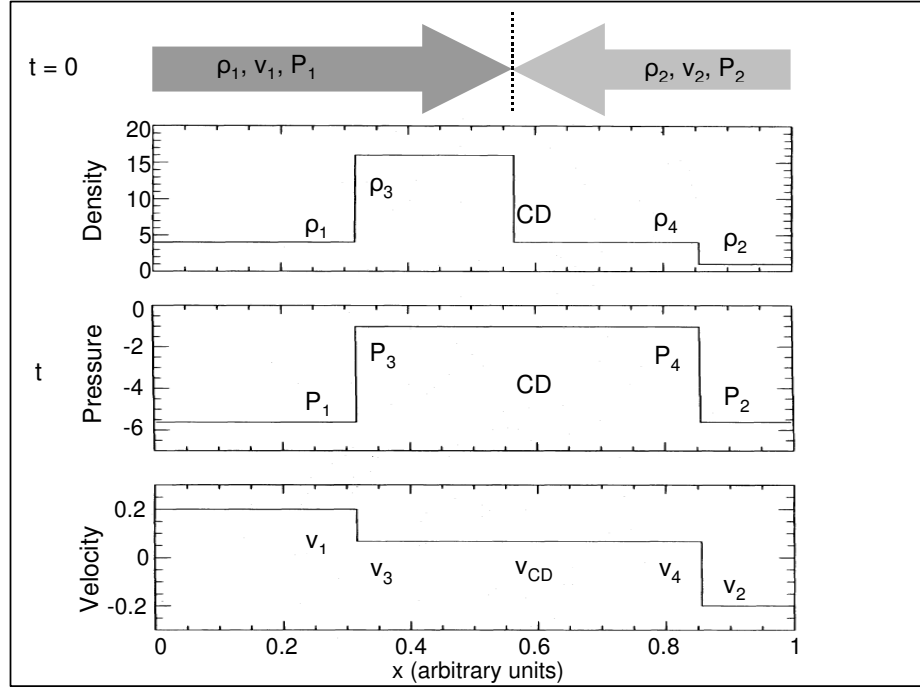
Figure 4.14: Flow structure of a one-dimensional (plane-parallel) collision between two gas streams. The parameters ρ_1, v_1, P_1 and ρ_2, v_2, P_2 of the two flows indicate the pre-collision parameter to the left and right of the contact discontinuity (CD). Two shocks propagate away from the discontinuity. Adapted from Lee et al. (1996).

the 3D cases, in particular in terms of conversion of energy from the bulk pre-collision energy to the postshock kinetic energy.

3D simulations of an oblique collision between two gas streams

Fig. 4.15 shows the result of 3D hydrodynamic simulations of the oblique collision between two gas streams. These simulations are performed by Lee et al. (1996) within the context of the collision of gas streams produced by the disruption of a massive star around a black hole. Obviously, these simulations do not directly apply to the SQ collision, in particular because in the simulations the gas flows are homogeneous and radiative processes are ignored. However, these simulations provide interesting insights about the dynamical evolution of the flows and the geometry of the shock fronts produced by the collision.

The pressure map (left panel of Fig. 4.15) shows that oblique shocks are produced around the initial contact surface. The position of these shock fronts are indicated on Fig. 4.15 by the solid red arrows. In the case of a one dimensional (1D) collision of two stream at the same velocity v_{st}, the two shocks produced at the discontinuity surface propagate back to the upstream flows at a velocity $V_{\text{sh}} = \frac{4}{3}v_{\text{st}}$ (see above for an analytical description of the 1D case). In the 3D case, the shock speed is $\sim v_{\text{st}}$ and the shock fronts stand off near the initial contact surface because the shocked gas can escape in the direction perpendicular to the stream flow. For instance, if we assume two identical gas
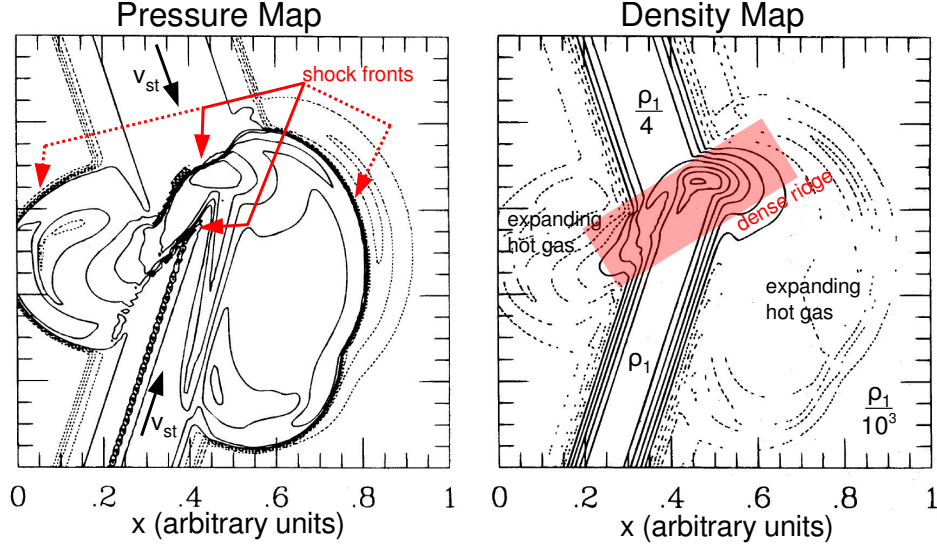
Figure 4.15: 3D numerical simulations of an oblique, supersonic collision between two homogeneous gas streams. The plots show pressure *(left)* and density *(right)* maps of a slice cut in the simulation cube. The angle between the flows is 143˚and their velocities and pressure are identical. The bottom flow is four times denser than the top stream. The streams propagate in a background medium that is 10^3 times less dense and pressurized. The figures are adapted from Lee et al. (1996).

streams with a relative velocity of $1000\,\mathrm{km\,s^{-1}}$, the shock velocity is $\sim 500\,\mathrm{km\,s^{-1}}$. The density map (right panel) show that the shocked gas is accumulated in a dense ridge (red rectangle) between the shocks and accelerated into the ambient medium. This hot gas is expanding adiabatically and drives other shocks in the background medium (dashed red arrows).

We have discussed above the conversion of the mechanical energy of the colliding gas flows into thermal energy of the gas for a plane-parallel (1D) collision. We remind that the ratio of the thermal energy flux produced by the shock to the flux of kinetic energy, R, is maximum ($R = 4/3$) for a 1D collision between two identical stream flows. Lee et al. (1996) find drastic differences between one- and three-dimensional cases. In 3D, most of the bulk kinetic energy of the flows is converted into the kinetic energy of the accelerating hot gas instead of thermal energy. For the 3D simulations, Lee et al. (1996) compute the time-dependent energy conversion rate, $R(t)$, as the ratio of the increase in the total thermal energy of the gas in the computational box to the kinetic energy added in the box through the discontinuity:

$$R(t) = \frac{E_{\mathrm{th}}(t) - E_{\mathrm{th}}(0)}{\frac{1}{2}(\rho_1\sigma_1 v_1 t)v_1^2 + \frac{1}{2}(\rho_2\sigma_2 v_2 t)v_2^2} \ , \tag{4.41}$$

where ρ_1, v_1 and ρ_2, v_2 are the pre-collision mass densities and the velocities of the gas flows. σ_1 and σ_2 are the cross-sections of the two colliding streams, so the quantity $\rho\,\sigma\,v\,t$ represents the mass of gas that passes through the boundary within the simulation time t. For the model shown on Fig. 4.15, Lee et al. (1996) find $R \sim 0.1$ at the end of the simulation. This value is one order of magnitude smaller than the one-dimensional model. This is due to the possibility for the gas to expand in directions perpendicular to the gas streams. This illustrative result suggests that the dynamical and thermal

properties of the shocked gas are very different between 1D and 3D models.

4.5.4   Concluding remarks and limitations of existing codes

The modeling of shocks in inhomogeneous media is very complex, and this is due to the richness of the physical processes at work (listed above), and the fact that they almost all operate on a comparable timescale. Here I would like to stress some key processes that one cannot ignore when describing the survival on shocked molecular gas, as it is one key aspect of the study presented here.

So far, most of the 3D numerical simulations focus on the development of hydrodynamical instabilities and the effect of the magnetic field. They generally predict the complete destruction of clouds by fast shocks in a timescale comparable with the compression (*crushing*) timescale of the cloud. This is essentially because these simulations do not include a realistic treatment of the thermal properties of the shocked gas, including H_2 formation on dust and H_2 cooling. On the other hand, models that are used for the comparison with observations, in which chemical processes are included, are limited to 1D geometry. Here I summarize a few important points among which some of them remain largely unexplored in numerical simulations:

1. thermal processes have a very important impact on the fate of shocked gas, perhaps more important than the effect of the magnetic field. The thermal instability, so far ignored in numerical simulations, triggers gas cooling and thereby stabilizes the cloud phase. Both cooling and thermal conduction seem to limit evaporation of cold and dense gas embedded in the hot and tenuous postshock medium. In the case of molecular gas, H_2, as a main coolant of the gas, may be a key-actor. In addition, the production of thermally unstable gas in turbulent mixing layers (at the cloud-intercloud interface) may also help in balancing the evaporation with condensation of material from the hot to the warm/cold phase.

2. the 3D geometry also influences the dynamical and thermal properties of the shocked gas. One should keep in mind that 1D models assume a maximum compression of the gas by the shock, leading to a maximum conversion of the bulk kinetic energy of the shock to thermal energy. In 3D, this conversion may be less efficient. This is perhaps the main limitation of the models that I have been using (the Flower et al. and the MAPPINGS shock codes) to interpret observations.

All the effects listed above would tend to increase the lifetime of shocked clouds compared to pure hydrodynamical simulations.

Part II

Detailed studies of H$_2$-luminous sources in space

Chapter 5

Powerful H$_2$ emission from the Stephan's Quintet galaxy-wide shock

Life is a series of collisions with the future; it is not the sum of what we have been, but what we yearn to be.

Jose Ortega y Gasset

Abstract

The Stephan's Quintet (SQ) is a compact group of interacting galaxies and a spectacular example of H$_2$ luminous source. The Spitzer Space Telescope indeed detected a powerful mid-infrared H$_2$ line emission from the X-ray bright galaxy-wide shock created by the high-velocity (~ 1000 km s^{-1}) collision between a galaxy and the tidal tail of an other member of the group. Observations show that the H$_2$ gas is extremely turbulent and that the H$_2$ luminosity exceeds that of the X-rays. The core of my PhD work is dedicated to the interpretation and modeling of these observations. In this chapter I present the observational discovery of H$_2$ in the shock, and address the following question: Why is H$_2$ present in such a violent environment? I propose a scenario where H$_2$ forms out of shocked gas, and present my results on the modeling of the cooling of the multiphase postshock gas and associated H$_2$ formation.

Contents

5.1 Introduction

Stephan's Quintet (hereafter SQ) is a fascinating example of an interacting galaxy system (Fig. 6.2). Perhaps not as famous as Arp 220 or M82, SQ is a well-known astrophysical target for amateur or professional astronomers. It is a nearby (94 Mpc) compact group of galaxies situated in the Pegasus constellation, at about half a degree to the South-West of NGC 7331[1]. SQ has been observed in almost all wavebands, and it keeps revealing surprises when being looked at by new instruments. SQ belongs to a peculiar class of interacting systems of galaxies: the compact groups (Hickson, 1982) that are characterized by aggregates of more than 4 galaxies in implied space densities as high as those in galaxy cluster cores.

SQ is a complex web of galaxy-galaxy and galaxy-intragroup medium (henceforth IGM) interactions that have triggered different types of phenomena related to the interactions, including an IGM starburst, long tidal tails (> 100 kpc) with tidal dwarf candidates, and a large scale shock (~ 40 kpc long). This shock is materialized by a giant X-ray and radio-bright *ridge*, attributed to the collision of an intruding galaxy with the tidal tail of another member of the group.

In 2006, *Spitzer Space Telescope* observations revealed a powerful mid-IR H_2 rotational line emission in the SQ shock structure. This discovery makes SQ the first known example of an *"H_2-luminous source"*, amongst the emerging class of H_2-galaxies presented in chapter 1. This was perhaps one of the most exciting results of extragalactic spectroscopic observations carried out with the *Spitzer* mission.

This surprising observational result was published at the start of my PhD thesis. Much of my PhD work was dedicated to its interpretation. I have devoted a significant part of my time in building a theoretical model that attempts to explain the formation and excitation of H_2 in the SQ galaxy collision within the broader framework of the numerous multi-wavelength observations of the system. It was not an easy task (!), and I will try to show that our current understanding is the result of a long path, along which several working hypothoses have been explored before coming to what we think to be a "coherent" scenario.

This work has been published in Guillard et al. (2009c) (hereafter paper I). In this manuscript, I will introduce the two questions of H_2 formation and excitation almost independently. In this chapter, I only discuss H_2 formation. The interpretation work carried out in paper I is based on the single-pointing observations of Appleton et al. (2006). After the publication of that paper, we have obtained new *Spitzer* observations that now cover the full area of the SQ ridge. I have re-visited my previous analysis of the H_2 excitation in this extended region, and complemented it by an analysis of mid-IR fine-structure lines diagnostics. These new observations and the modeling results are presented in the next chapter (chap. 6).

After reading chapters 5 and 6, I hope that the reader will be convinced that SQ is an outstanding source to study in detail phenomena such as large scale shocks and high velocity galaxy collisions. SQ is a beautiful example of astrophysical source where detailed and rich micro-physics of the ISM are needed to understand the global observational picture. These studies have implications for our understanding of the dynamics and energetics of the molecular gas in galaxy evolution.

In this chapter, I present the observational discovery of H_2 emission in SQ (sect. 5.2), and point

---

[1] http://antwrp.gsfc.nasa.gov/apod/ap071124.html

out the set of astrophysical questions raised by these observations (sect. 5.2.2). Then sect. 5.3 adresses the question of the H$_2$ formation in the SQ shock. I present the long route that drove us to our current interpretation of these observations and introduce our paper I. A quick summary of the results and concluding remarks end this chapter (sect. 5.4)

5.2 Observations of warm H$_2$ gas in Stephan's Quintet

The first mid-IR spectroscopic observations of the SQ shock were performed by Appleton et al. (2006). We present the observational discovery based on single-pointing observations (sect. 5.2.1), and their extension to new spectral maps are presented in chapter 6.

5.2.1 The discovery: an H$_2$-bright giant shock!

The *Spitzer* Infra-Red Spectrograph (*IRS*) observations of the SQ galaxy-wide collision led to the unexpected detection of extremely bright mid-IR H$_2$ rotational line emission from warm ($\sim 50 - 10^3$ K) molecular gas in the center of the X-ray emitting ridge (Appleton et al., 2006). The observational results about the first detection of H$_2$ in the SQ shock are summarized in Fig. 5.1. The left panel shows the position of the *IRS* slits (SH, LH and SL modules; see caption for the slit sizes) overlaid on a *R*-band image with radio *VLA* contours. The high-resolution modules are placed close to the "center" of the radio-bright ridge. The SL slit is oriented along the radio filament that traces the shock structure.

The right panel of Fig. 5.1 gathers the low- and high-resolution spectra extracted in the SQ shock. These spectacular spectra are dominated by the mid-IR rotational emission of H$_2$. The 0-0 S(0) to S(5) lines are detected, plus atomic lines of [Ne II] at $12.8\,\mu$m and [Si II] at $34.8\,\mu$m. No PAH emission is seen[2] and the thermal dust continuum is very weak. This is the first time an almost pure H$_2$ line spectrum has been seen in an extragalactic object.

A two-temperatures fit of the observed H$_2$ excitation diagram reproduces the data satisfactorily and gives a rough estimation of the excitation temperatures of the gas. The warm molecular gas is constrained by the S(0)/S(1) line ratio and is consistent with $T_{\mathrm{exc}} = 185 \pm 30$ K and an H$_2$ column density of 2.06×10^{20} cm^{-2}. The higher order S(3)/S(5) [ortho] transitions give $T_{\mathrm{exc}} = 675 \pm 80$ K and an H$_2$ column density of 1.54×10^{18} cm^{-2}. Appleton et al. (2006) assume an ortho-to-para ratio of 3 and note no obvious deviations from this value in the data.

The SL spectroscopy shows that the H$_2$ emission is extended on the scale of 52" (24 kpc). Assuming that the extra, undetected H$_2$ lines represent 40% of the flux detected by *Spitzer*, Appleton et al. (2006) derive an total H$_2$ luminosity of 8.4×10^{33} W from the SH slit area (11.3×4.7 arcsec^2).

The bottom right inset of Fig. 5.1 shows one of the remarkable results of these observations: the H$_2$ $17\,\mu$m 0-0 S(1) line is resolved, though the relatively low resolution ($\mathcal{R} = 600$) of the *IRS*. The S(1) line is extremely broad, with a FWHM linewidth of $\Delta v = 870 \pm 60$ km s^{-1}. This is the broadest H$_2$ line ever observed! The high velocity dispersion of the warm molecular gas suggest that the postshock medium in the ridge is extremely turbulent. This is a puzzling result since H$_2$ is a fragile molecule and easily dissociated in $V_{\mathrm{s}} > 50$ km s^{-1} shocks.

---

[2]this conclusion will be revised in chapter 6. New *Spitzer IRS* observations indeed show PAH emission in the ridge(Cluver et al., 2009)
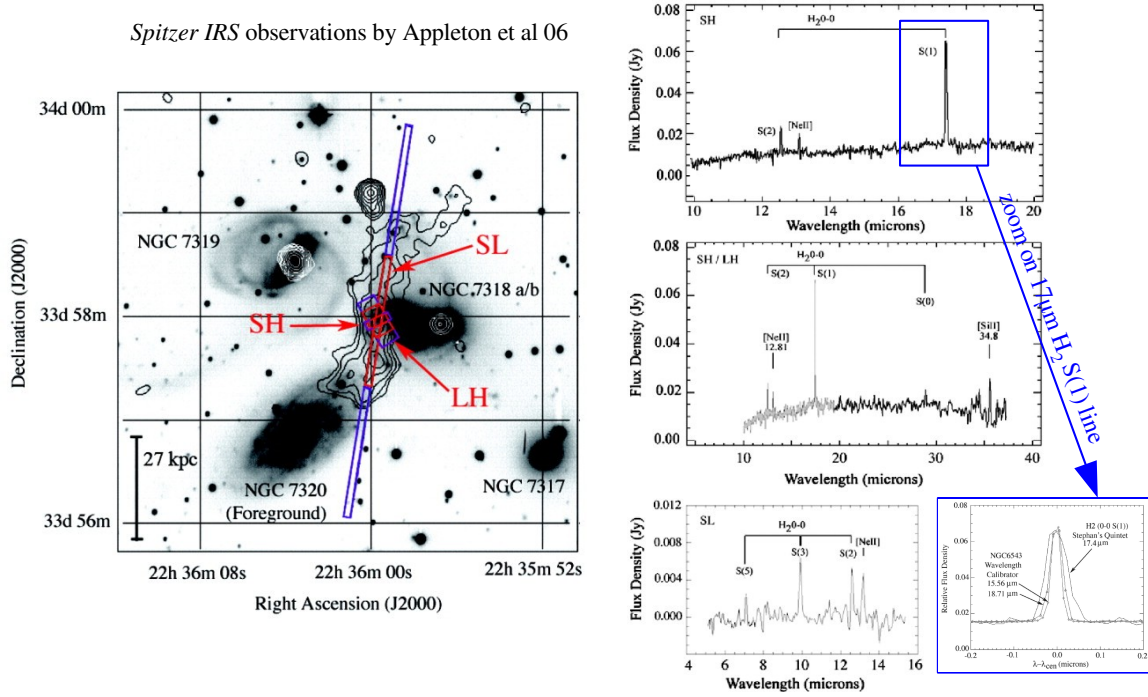
Figure 5.1: *Spitzer IRS* H₂ observations by Appleton et al. (2006). *Left:* Positioning of the *IRS* slits overlaid on an R-band image and *VLA* radio contours at 1.4 GHz by Xu et al. (2003). The slits are centered on $\alpha_{J2000} = 22h35m59s.57$, $\delta_{J2000} = 33^o58'1.8"$. Only the central portion of the slits (red boxes) were common to the two separate observing (nod) positions made in each IRS module slit (the purple shows the full coverage). $SL = 57 \times 3.6$ arcsec², $SH = 11.3 \times 4.7$ arcsec², and $LH = 22.3 \times 11.1$ arcsec². *Right:* top: IRS SH spectrum of the brightest radio/IR point in the shock front. Middle: Combined SH (gray line) and LH (black line) spectrum of the same target region. Bottom left: SL spectrum at the same position. SL2 is the gray line, and SL1 is the black line. Bottom right: zoom on the 17 μm H₂ 0-0 S(1) line (detected with a signal-to-noise ratio of 33) showing that the line is resolved (intrinsic FWHM of 870 ± 60 km s⁻¹) as compared with two unresolved spectral lines ($\mathcal{R} = 600$) in the planetary nebula NGC 6543 at 15.6 and 18.7 μm that bracket the H₂ line (gray line).

We summarize the main unexpected results from the Appleton et al. (2006) observational paper:

1. the H₂ gas is coexisting with a hot ($\sim 5 \times 10^6$ K), X-ray emitting plasma.

2. the velocity dispersion of the H₂ gas seems unusually large and of the order of the velocity of the galaxy collision ~ 900 km s⁻¹, which is of the order of the velocity of the galaxy collision.

3. the total H₂ line luminosity within the SH slit aperture exceeds that of the X-rays in this area by a factor of 3.

4. the spectroscopic signatures (dust or ionized gas lines) of star formation are much fainter than the H₂ emission. This is unlike what is observed in star forming galaxies where the H₂ lines are much weaker than the mid-IR dust features (Rigopoulou et al., 2002; Higdon et al., 2006; Roussel et al., 2007).

5.2.2 Astrophysical questions

These surprising observations raise the following questions:

- Why is there H_2 gas is the extreme environment of the SQ postshock gas?

- How can we account for the H_2 excitation characteristics?

- Why is H_2 a dominant coolant?

Much of my thesis work has been driven by these astrophysical questions, which are addressed in Guillard et al. (2009c) (paper I). In the following, I only discuss the scenario proposed to explain the formation of H_2 in the SQ shock. The two last issues will be discussed in the next chapter (chap. 6), where I extend the analysis of paper I, which was based on the single-pointing observations presented above, to the full area of the SQ ridge.

5.3 How does H_2 form in the Stephan's Quintet giant shock?

In this section we focus on the first out of our three astrophysical questions: the formation of H_2 in the SQ ridge. We introduce the scenario presented in Guillard et al. (2009c) (paper I). I will first show that we have explored several working hypothesis before coming to this scenario. Obviously, our scenario may not be the right solution, but, to our knowledge, this is the first quantitative model that attempt to explain the H_2 formation and emission within the broader context of multi-wavelength observations of SQ. Up to now, it has not been invalidated by observations.

5.3.1 A long route to a coherent scenario. . .

The main difficulty in understanding the presence of H_2 in the SQ shock is to explain how the gas can cool and become molecular in a hot plasma, and how it can survive in such a violent environment. Inspired by previous studies, Appleton et al. (2006) evoke two possibilities: *(i)* an *oblique* shock geometry, and *(ii)*, the presence of *dust* in the hot plasma. Both ingredients will help diminishing the gas temperature and make its cooling easier to form H_2 within the age of the collision. These hypothesis may also explain why the gas temperature in the ridge is not much hotter than that of the underlying halo (see sect. 6.3.3 and Trinchieri et al., 2003; Xu et al., 2003; O'Sullivan et al., 2009b). However, these ingredients alone are not sufficient enough to explain the coexistence of warm molecular gas with a hot plasma. I will show that the multiphased nature of the shocked gas is a key to interpret multi-wavelength observations of SQ.

An oblique shock geometry?

The collision between the new intruder, NGC 7318b, and the intra-group tidal tail is not necessarily head-on. The shock associated with this collision may be oblique, i.e. the upstream fluid crosses the shock front with an incident angle $\phi \neq 90°$ (see sect. 4.5.3 for a description of oblique supersonic collisions between two gas streams). This hypothesis is considered by Trinchieri et al. (2003); O'Sullivan et al. (2009b) to explain with there is so little difference between the gas temperature in the radio

ridge (6.9×10^6 K) and outside, in the halo (5.7×10^6 K). Trinchieri et al. (2003); O'Sullivan et al. (2009b) assume a shock velocity equal to the relative line-of-sight velocity between the new intruder and NGC 7319's tidal tail ($900 - 1000$ km s^{-1}). In the case of a perpendicular shock, a 1000 km s^{-1} shock would lead to a post shock temperature of $\sim 1.4 \times 10^7$ K (see Eq. 6.4), which is twice the temperature derived from X-ray observations in the ridge. If the incoming flow forms an angle ϕ with the shock surface, then the shock velocity is reduced by a factor $\sin \phi$. In this case, the postshock temperature can be written as

$$T_{\mathrm{ps}} = \frac{2(\gamma - 1)}{(\gamma + 1)^2} \frac{\mu}{k_{\mathrm{B}}} V_{\mathrm{s}}^2 \sin^2 \phi \simeq 6.9 \times 10^6 \left(\frac{V_{\mathrm{s}}}{1000 \ \mathrm{km \, s^{-1}}} \right)^2 \sin^2 \left(\frac{\phi}{30^\circ} \right) \ \mathrm{K} \, , \qquad (5.1)$$

where V_{s} is the velocity of the shock wave, μ the mean particle mass (equals to 10^{-24} g for a fully ionized gas), k_B the Boltzmann constant and $\gamma = 5/3$. Therefore, an incidence of $\phi \sim 30°$ would be required to match the observed temperature of the hot gas in the ridge.

The possibility that the large-scale shock is oblique may be an argument to reduce the X-ray power with respect to the more luminous H$_2$ emission in the ridge. However, it does not explain why part of the gas has cooled down efficiently to form H$_2$, and part of the gas is still hot and emits X-rays.

A significant cooling of the hot gas by the dust?

Based on *ISO* IR observations, Xu et al. (2003) suggest that dust grains are the main coolant of the hot gas, which produce FIR emission. After subtraction of the IR emission from the individual sources in the group, they detect a residual IR emission from the shock. The IR emission is extended, its morphology is similar to the radio emission in the ridge, and is one order of magnitude more luminous than the X-ray emission. They interpret this IR emission by collisional heating of dust grains by the hot electrons and ions of the plasma. Assuming a constant dust-to-gas mass ratio of 6×10^{-3}, they estimate a cooling time scale of $t_{\mathrm{cool}} \sim 2 \times 10^6$ yr, which is two orders of magnitude shorter than if the plasma is dust-free (see sect. 2.4). They use the collisional heating model of Popescu et al. (2000) and find that the expected FIR luminosity is in agreement with observations.

The problem is that the cooling timescale is so short that we should observe cool gas around the shock, which is not seen on the X-ray temperature maps (O'Sullivan et al., 2009b). This scenario has difficulties to explain why we observed both a diffuse hot ($6 - 7 \times 10^6$ K) component in the ridge and in its outskirts, and warm ($100 - 1000$ K) molecular gas. In fact, at the beginning of our study, we started to work in the direction of Xu et al. (2003) to explain the cooling of the gas by the dust grains in the ridge. This is why I decided to carry on a detailed calculation of the time-dependant cooling of the hot gas, taking into account dust destruction. This modeling has been presented in sect. 2.4 and in paper I. The results lead us to revise the conclusions of Xu et al. (2003), and we discuss the application of this modeling to the case of SQ in sect. 5.3.2.

We find that the cooling timescale of the hot gas in the ridge is more than one order of magnitude longer than the shock age. We conclude that it is very unlikely that the H$_2$ gas results from the direct cooling of the hot gas. This result has driven us to the idea that, if the H$_2$ formation was induced by the galaxy collision, it must have cooled down from much lower temperatures. Then the gas in the ridge must have been shocked by a wide distribution of shock velocities, a thus of postshock temperatures. This is how we came to consider that the preshock medium was inhomogeneous. In the following, we

present our scenario for H$_2$ formation. New IR observations and modeling of the dust emission in the SQ shock within the framework of this scenario will be discussed in chapter 8.

5.3.2 H$_2$ formation out of multiphase postshock gas

The difficulties evoked above suggest that it is very difficult to explain H$_2$ formation from homogeneous shocked gas at high-speed. In our view, the presence of H$_2$ in the SQ ridge is closely related to the multiphase structure of the preshock gas and may result from two possibilities:

1. molecular clouds are present in the preshock gas and embedded within the pre-existing halo of hot gas. Because of the density contrast between the tenous gas and the clouds, slower shocks are driven into the clouds (see sect. 4.5), and H$_2$ molecules may or may not be dissociated, depending on the shock velocity. If the shock transmitted into the cloud is dissociative, H$_2$ molecules may reform in the postshock medium (see sect. 4.2 and Hollenbach and McKee, 1979). If gravitationally bound molecular clouds are present in the preshock medium, we expect the shock to trigger their collapse, which would lead to star formation (Jog and Solomon, 1992). This process is perhaps what is happenning in the northern region of the shock, SQ-A, where optical and IR imaging show that a starburst is occuring (Xu et al., 1999).

   The weakness of tracers of star formation in the region of the main shock (Xu et al., 2003) suggests that preshock GMCs are not a major source of the observed postshock H$_2$ gas in the ridge. Although we do not exclude pre-existing molecular gas in the ridge, we explore the following second possibility.

2. H$_2$ gas forms out of preshock H I gas. Appleton et al. (2006) also evoke this scenario by proposing that a large-scale shock overruns a clumpy preshock medium. H$_2$ molecules would form in the denser regions that experience slower shocks compared with the high-speed shock in the tenuous gas. In the following we summarize and complete the results presented in our paper I.

Supersonic collision between two inhomogeneous gas streams

Multiwavelength observations of SQ suggest that two multiphase gas flows are colliding (see paper I for an introduction to the past observations and to the astrophysical context that are relevant for our study[3]). One stream is associated with the intruding galaxy (NGC 7318b), and the other is associated with the tidal tail of NGC 7319. Both gas streams are likely to contain hot (a few million K), H I and perhaps molecular clouds. Therefore we consider the collision of two flows of multiphase dusty gas. The relative velocity between the flow is $900 - 1000$ km s^{-1}, constrained by H I observations and optical line spectroscopy. Our model quantifies the gas cooling, dust destruction, and H$_2$ formation in the postshock medium within this framework.

If the colliding gas flows are inhomogeneous, the rise of pressure in the hot, tenuous gas drives slower shocks into the denser clouds (see sect. 4.5). Each cloud density corresponds to a shock velocity. The galaxy collision generates a range of shock velocities and postshock gas temperatures. The state of the postshock gas is related to the preshock gas density. Schematically, low density

---

[3]A more complete review of SQ observations is differed to the sect. 6.3.3 of chapter 6 because this observational context is needed to interpret our new extended observations of SQ.

(preshock at $n_{\rm H} \lesssim 3 \times 10^{-3}\,{\rm cm}^{-3}$) gas is shocked at high speed ($\gtrsim$ 700 km s^{-1}) and accounts for the X-ray emission. Denser H I gas ($n_{\rm H} \gtrsim \times 10^{-2}$) is heated to lower ($\lesssim 10^6$ K) temperatures. The fig. 1 of paper I sketches this scenario. The rise of pressure in the hot gas triggers the compression of the H I clouds that are the sites for H$_2$ formation.

In the following we compute the isobaric cooling, the evolution of the dust-to-gas mass ratio, and the formation of molecules in this multi-temperature postshock gas (see chapter 2 and chapter 4 for a description of the microphysics included in the calculation). We show that the hot plasma did not have time to cool down significantly since the collision was initiated, whereas the denser gas has time to cool and form H$_2$.

Gas cooling, dust survival and H$_2$ formation in the SQ ridge

We summarize here the context and main results of our calculation of the time-dependence of the gas temperature and dust-to-gas mass ratio. We start the computation with a galactic dust-to-gas mass ratio and equilibrium ionization. We assume that the metallicity of the gas is solar and that the cooling gas is in pressure equilibrium with the hot, volume-filling gas (the average thermal pressure of the hot plasma is $P/k_{\rm B} = 2 \times 10^5$ K cm^{-3}). As the gas cools, it condenses. In paper I we explore the possibility that the gas pressure vary around this average value (see in particular Fig. 3).

The H$_2$ formation, gas cooling, and dust destruction timescales are plotted as a function of the postshock temperature in the key-figure 2 of paper I. The gas cooling timescale is defined as the time at which the temperatures coolds down to 10^4 K. The H$_2$ formation timescale is the time when the H$_2$ fractional abundance reaches 90% of its final (end of cooling) value, including the gas cooling time from the postshock temperature to 10^4 K. The dust destruction timescale is the time when 90% of the dust mass is destroyed and returned to the gas. We remind that a given initial postshock temperature is associated to a given preshock density. The relative values of the timescales with respect to the collision age define three gas phases:

The hot plasma: the preshock gas at $n_{\rm H} \lesssim 6 \times 10^{-3}$ cm^{-3} is shocked at $V_{\rm s} > 500$ km s^{-1} and therefore heated to temperatures $T_{\rm ps} > 5 \times 10^6$ K. Our estimate of the cooling timescale of the hot plasma takes into account the time-dependence of the dust-to-gas mass ratio. Fig. 2 of paper I shows that, because the dust grains are efficiently sputtered in the hot gas, the cooling timescale is much longer ($t_{\rm cool} = 2 \times 10^7$ yr for $T_{\rm ps} = 7 \times 10^6$ K) than if one estimates it for a constant dust-to-gas mass ratio ($t_{\rm cool} = 2 \times 10^6$ yr as estimated by Xu et al., 2003). The cooling timescale of the hot gas is longer than the age of the collision, so the tenuous, shocked gas has not yet cooled down significantly. This is the X-ray emitting plasma indicated by the red thick line. Note that this hot gas may still contain some dust because the largest grains (representing most of the mass) may not have been completely sputtered within the collision age. However, these grains are the less numerous, so their contribution to the gas cooling is weak (see chapter 2, sect. 2.3 and 2.4 for a quantitative discussion of these processes).

The molecular gas: The preshock gas at $n_{\rm H} \gtrsim 3 \times 10^{-2}$ cm^{-3} is shocked at $V_{\rm s} < 250$ km s^{-1} and therefore heated to temperatures $T_{\rm ps} \lesssim 8 \times 10^5$ K. In this case, the gas cooling timescale to 10^4 K and the H$_2$ formation timescale are shorter than the collision age, whereas the dust

destruction timescale is longer. Therefore, this gas keeps a significant fraction of its initial dust content and becomes H_2 gas (blue thick line) within the age of the collision.

Atomic and ionized gas: for intermediate densities ($6 \times 10^{-3} \lesssim n_H \lesssim 3 \times 10^{-2}$) and therefore intermediate postshock temperatures ($8 \times 10^5 < T_{ps} < 5 \times 10^6$ K), the gas has time to cool down but it loses its dust content and does not have time to form H_2 within the collision age. This phase is indicated with the grey thick line and may represents H I and H II gas phases.

This description of the multiphase postshock ignores the fragmentation of the clouds by thermal and hydrodynamical instabilities (Rayleigh-Taylor and Kelvin-Helmholtz) that develop when a cloud is shocked. As discussed in sect. 4.5.2, this fragmentation can lead to the mixing (evaporation), and therefore the destruction, of the clouds with the background hot plasma. The powerful H_2 emission in the SQ shock suggest that warm molecular gas is formed before the clouds mixing timescale. In sect. 3.3 of paper I we compare the H_2 formation timescale to the fragmentation and mixing timescales. The conclusions are the following:

Cloud fragmentation: we show that for a wide range and preshock cloud densities and sizes (see Fig. 4, paper I), the crushing time is longer than the cooling, so the gas fragments by thermal instability as the shock penetrates into the cloud. H_2 forms before the shock has crossed the cloud, and therefore before hydrodynamical instabilities start to develop.

Cloud evaporation: analytical and numerical studies suggest that the typical evaporation timescale of warm ($\sim 10^4$ K) H I clouds in hot ($> 10^6$ K) gas is a few million years (see sect. 4.5.2 for a description of turbulent mixing and references). This is long enough for H_2 to form within the lifetime of the fragments. The cloud lifetime may be even longer because they are stabilized by the efficient H_2 cooling. Up to now, none of the simulations include both the detailed microphysics (realistic cooling functions and H_2 formation on dust grains), and the full dynamic range of spatial scales and densities that are involved in the evolution of clouds embedded into a flow of hot gas (see sect. 4.5.2 for the description of the state-of-art simulations).

5.4 Summary and conclusions

One of the most interesting features of the Stephan's Quintet compact group is the presence of a galaxy-wide shock in the halo of the group, created by an intruding galaxy colliding with a tidal tail at a relative velocity of $\sim 1\,000$ km s^{-1}. Evidence for a group-wide shock comes from observations of X-rays from the hot postshock gas in the ridge strong radio synchrotron emission from the radio emitting plasma and shocked-gas excitation diagnostics from optical emission lines. *Spitzer* observations show that this gas also contains molecular hydrogen with an extreme velocity dispersion. The H_2 luminosity is larger than the X-ray emission from the same region, thus the H_2 line emission dominates over X-ray cooling in the shock. As such, it plays a major role in the energy dissipation and evolution of the postshock gas.

The interpretation of these observations is the core of my PhD work. I present a scenario where H_2 gas forms out of the postshock gas that results from the supersonic collision between two multiphase gas streams. This collision leads to a multiphase medium with a distribution of shock velocities,

related to the variations of the density in the preshock medium. The H_2 formation in the SQ ridge environment is quantified by calculating the time-dependent isobaric cooling of the gas, including dust destruction mechanisms. I show that H_2 forms out of the dense regions where dust survives the shocks. The bulk kinetic energy of the molecular gas is the main energy reservoir of the postshock gas, and it has to be dissipated within the H_2 gas to explain the poserful H_2 excitation. I propose that supersonic turbulence is sustained within the molecular gas by a transfer of momentum induced by cloud-cloud collisions and the relative shear motions between the molecular gas and the hot plasma. A phenomenological model of low-velocity MHD shocks driven into the dense H_2 gas is capable of explaining the observed excitation characteristics.

Within this framework, dust is a key ingredient. It is required for H_2 formation. Our model has implications on the expected dust emission in the SQ halo and on dust survival in a multiphase environment. These points are adressed in chapter 8.

5.5 Publication: paper I

In the following, we reproduce the Guillard et al. (2009c) paper, *H_2 formation and excitation in the Stephan's Quintet galaxy-wide collision*, 2009, A&A, 502, 515. This paper contain key-figures that I have discussed in this chapter, and a lot of details that I have intentionally not repeated in this manuscript.

**Astronomy
&
Astrophysics**

H$_2$ formation and excitation in the Stephan's Quintet galaxy-wide collision*

P. Guillard[1], F. Boulanger[1], G. Pineau des Forêts[1,3], and P. N. Appleton[2]

[1] Institut d'Astrophysique Spatiale (IAS), UMR 8617, CNRS, Université Paris-Sud 11, Bâtiment 121, 91405 Orsay Cedex, France
e-mail: pierre.guillard@ias.u-psud.fr
[2] NASA *Herschel* Science Center (NHSC), California Institute of Technology, Mail code 100-22, Pasadena, CA 91125, USA
[3] LERMA, UMR 8112, CNRS, Observatoire de Paris, 61 Avenue de l'Observatoire, 75014 Paris, France

ABSTRACT

Context. The *Spitzer Space Telescope* has detected a powerful ($L_{\rm H_2} \sim 10^{41}$ erg s^{-1}) mid-infrared H$_2$ emission towards the galaxy-wide collision in the Stephan's Quintet (henceforth SQ) galaxy group. This discovery was followed by the detection of more distant H$_2$-luminous extragalactic sources, with almost no spectroscopic signatures of star formation. These observations place molecular gas in a new context where one has to describe its role as a cooling agent of energetic phases of galaxy evolution.
Aims. The SQ postshock medium is observed to be multiphase, with H$_2$ gas coexisting with a hot ($\sim 5 \times 10^6$ K), X-ray emitting plasma. The surface brightness of H$_2$ lines exceeds that of the X-rays and the 0−0 S(1) H$_2$ linewidth is ~ 900 km s^{-1}, of the order of the collision velocity. These observations raise three questions we propose to answer: *(i)* why is H$_2$ present in the postshock gas? *(ii)* How can we account for the H$_2$ excitation? *(iii)* Why is H$_2$ a dominant coolant?
Methods. We consider the collision of two flows of multiphase dusty gas. Our model quantifies the gas cooling, dust destruction, H$_2$ formation and excitation in the postshock medium.
Results. *(i)* The shock velocity, the post-shock temperature and the gas cooling timescale depend on the preshock gas density. The collision velocity is the shock velocity in the low density volume-filling intercloud gas. This produces a $\sim 5 \times 10^6$ K, dust-free, X-ray emitting plasma. The shock velocity is lower in clouds. We show that gas heated to temperatures of less than 10^6 K cools, keeps its dust content and becomes H$_2$ within the SQ collision age ($\sim 5 \times 10^6$ years). *(ii)* Since the bulk kinetic energy of the H$_2$ gas is the dominant energy reservoir, we consider that the H$_2$ emission is powered by the dissipation of kinetic turbulent energy. We model this dissipation with non-dissociative MHD shocks and show that the H$_2$ excitation can be reproduced by a combination of low velocities shocks (5−20 km s^{-1}) within dense ($n_{\rm H} > 10^3$ cm^{-3}) H$_2$ gas. *(iii)* An efficient transfer of the bulk kinetic energy to turbulent motion of much lower velocities within molecular gas is required to make H$_2$ a dominant coolant of the postshock gas. We argue that this transfer is mediated by the dynamic interaction between gas phases and the thermal instability of the cooling gas. We quantify the mass and energy cycling between gas phases required to balance the dissipation of energy through the H$_2$ emission lines.
Conclusions. This study provides a physical framework to interpret H$_2$ emission from H$_2$-luminous galaxies. It highlights the role that H$_2$ formation and cooling play in dissipating mechanical energy released in galaxy collisions. This physical framework is of general relevance for the interpretation of observational signatures, in particular H$_2$ emission, of mechanical energy dissipation in multiphase gas.

Key words. ISM: general – ISM: dust, extinction – ISM: molecules – shock waves – Galaxy: evolution – galaxies: interactions

1. Introduction

Observations with the infrared spectrograph (henceforth *IRS*) onboard the *Spitzer Space Telescope* of the Stephan's Quintet (HCG92, hereafter SQ) galaxy-wide collision led to the unexpected detection of extremely bright mid-infrared (mid-IR) H$_2$ rotational line emission from warm ($\sim 10^2$−10^3 K) molecular gas (Appleton et al. 2006). This is the first time an almost pure H$_2$ line spectrum has been seen in an extragalactic object. This result is surprising since H$_2$ coexists with a hot X-ray emitting plasma and almost no spectroscopic signature (dust or ionized gas lines) of star formation is associated with the H$_2$ emission. This is unlike what is observed in star forming galaxies where the H$_2$ lines are much weaker than the mid-IR dust features (Rigopoulou et al. 2002; Higdon et al. 2006; Roussel et al. 2007).

The detection of H$_2$ emission from the SQ shock was quickly followed by the discovery of a class of H$_2$-luminous galaxies that show high equivalent width H$_2$ mid-IR lines. The first H$_2$-luminous galaxy, NGC 6240, was identified from ground based near-IR H$_2$ spectroscopy by Joseph et al. (1984), although this galaxy also exhibits a very strong IR continuum. Many more of H$_2$ bright galaxies are being found with *Spitzer* (Egami et al. 2006; Ogle et al. 2007), often with very weak continuua, suggesting that star formation is not the source of H$_2$ excitation. These H$_2$-luminous galaxies open a new perspective on the role of H$_2$ as a cold gas coolant, on the relation between molecular gas and star formation, and on the energetics of galaxy formation, which has yet to be explored.

SQ is a nearby H$_2$-luminous source where observations provide an unambigious link between the origin of the H$_2$ emission, and a large-scale high-speed shock. The SQ galaxy-wide shock is created by an intruding galaxy colliding with a tidal tail at a relative velocity of ~ 1000 km s^{-1}. Evidence for a group-wide

---

* Appendices are only available in electronic form at
http://www.aanda.org

shock comes from observations of X-rays from the hot postshock gas in the ridge (Trinchieri et al. 2003, 2005; O'Sullivan et al. 2008), strong radio synchrotron emission from the radio emitting plasma (Sulentic et al. 2001) and shocked-gas excitation diagnostics from optical emission lines (Xu et al. 2003). *Spitzer* observations show that this gas also contains molecular hydrogen and that it is turbulent with an H$_2$ linewidth of 870 km s^{-1}. The H$_2$ surface brightness is higher than the X-ray emission from the same region, thus the H$_2$ line emission dominates over X-ray cooling in the shock. As such, it plays a major role in the energy dissipation and evolution of the postshock gas.

These observations raise three questions we propose to answer: *(i) why is there* H$_2$ *in the postshock gas? (ii) How can we account for the* H$_2$ *excitation? (iii) Why is H$_2$ a dominant coolant?* We introduce these three questions, which structure this paper.

(i) H$_2$ formation. The detection of large quantities of warm molecular gas in the SQ shock, coexisting with an X-ray emitting plasma, is a surprising result. Appleton et al. (2006) invoked an oblique shock geometry, which would reduce the shock strength. However, with this hypothesis, it is hard to explain why the temperature of the postshock plasma is so high (5×10^6 K, which constrains the shock velocity to be ~600 km s^{-1}). Therefore the presence of H$_2$ is likely to be related to the multiphase, cloudy structure of the preshock gas.

One possibility is that molecular clouds were present in the preshock gas. Even if the shock transmitted into the cloud is dissociative, H$_2$ molecules may reform in the postshock medium (Hollenbach & McKee 1979). An alternative possibility is that H$_2$ forms out of preshock H clouds. Appleton et al. (2006) proposed that a large-scale shock overruns a clumpy preshock medium and that the H$_2$ would form in the clouds that experience slower shocks. In this paper we quantify this last scenario by considering the collision between two inhomogeneous gas flows, one being associated with the tidal tail and the other associated with the interstellar medium (hereafter ISM) of the intruding galaxy.

(ii) H$_2$ excitation. Several excitation mecanisms may account for high equivalent width H$_2$ line emission. The excitation by X-ray photons was quantified by a number of authors (e.g. Tine et al. 1997; Dalgarno et al. 1999). The energy conversion from X-ray flux to H$_2$ emission is at most 10% for a cloud that is optically thick to X-ray photons. The absorbed fraction of X-ray photons may be even smaller if the postshock H$_2$ surface filling factor is smaller than 1. *Chandra* and *XMM* observations (0.2−3 keV) show that, within the region where *Spitzer* detected H$_2$ emission, the H$_2$ to X-ray luminosity ratio is ~5 (O'Sullivan et al. 2008; Trinchieri et al. 2005). Therefore, the excitation of H$_2$ by 0.2−3 keV X-ray photons cannot be the dominant process.

H$_2$ excitation may also be produced by cosmic ray ionization (Ferland et al. 2008). However, radio continuum observations of SQ show that the combined cosmic ray plus magnetic energy is not the dominant energy reservoir.

SQ observations suggest that only a fraction of the collision energy is used to heat the hot plasma. Most of this energy is observed to be kinetic energy of the H$_2$ gas. Therefore we consider that the H$_2$ emission is most likely to be powered by the dissipation of the kinetic energy of the gas. This excitation mechanism has been extensively discussed for the Galactic interstellar medium. It has been proposed to account for H$_2$ emission from solar neighbourhood clouds (Gry et al. 2002; Nehmé et al. 2008), from the diffuse interstellar medium in the inner Galaxy (Falgarone et al. 2005) and from clouds in the Galactic center (Rodríguez-Fernández et al. 2001).

(iii) H$_2$ cooling. For H$_2$ to be a dominant coolant of the SQ postshock gas, the kinetic energy of the collision in the center of mass rest-frame has to be efficiently transfered to the molecular gas. In the collision, the low density volume filling gas is decelerated but the clouds keep their preshock momentum. The clouds, which move at high velocity with respect to the background plasma, are subject to drag. This drag corresponds to an exchange of momentum and energy with the background plasma. This transfer of energy between clouds and hot plasma has been discussed in diverse astrophysical contexts, in particular infalling clouds in cooling flows of clusters of galaxies (Pope et al. 2008) and galactic halos (Murray & Lin 2004), as well as cometary clouds in the local interstellar medium (Nehmé et al. 2008) and the Helix planetary nebula tails (Dyson et al. 2006).

The dynamical evolution of the multiphase interstellar medium (ISM) in galaxies has been extensively investigated with numerical simulations, within the context of the injection of mechanical energy by star formation, in particular supernovae explosions (e.g. de Avillez & Breitschwerdt 2005a; Dib et al. 2006). The injection of energy by supernovae is shown to be able to maintain a fragmented, multiphase and turbulent ISM. Numerical simulations on smaller scales show that the dynamical interaction between gas phases and the thermal instability feed turbulence within clouds (Sutherland et al. 2003; Audit & Hennebelle 2005; Nakamura et al. 2006). The SQ collision releases ~10^{56} erg of mechanical energy on a collision timescale of a few million years. This is commensurate with the amount of mechanical energy injected by supernovae in the Milky Way (MW) over the same timescale. The main difference is in the mass of gas, which is two orders of magnitude lower in the SQ shock than in the MW molecular ring. None of the previous simulations apply to the context of the SQ collision, but they provide physics relevant to our problem. In this paper, based on this past work, we discuss how the dynamical interaction between the molecular gas and the background plasma may sustain turbulence within molecular clouds at the required level to balance the dissipation of energy through the H$_2$ emission lines.

The structure of this paper is based on the previous 3 questions and is organised as follows: in Sect. 2, we gather the observational data that set the luminosity, mass and energy budget of the SQ collision. In Sect. 3, the gas cooling, dust destruction, and H$_2$ formation in the postshock gas are quantified. In Sect. 4 the dissipation of kinetic energy within the molecular gas is modeled, in order to account for the H$_2$ emission in SQ. Section 5 presents a view of the dynamical interaction between ISM phases that arises from our interpretation of the data. In Sect. 6 we discuss why H$_2$ is such a dominant coolant in the SQ ridge. Section 7 discusses open questions including future observations. Our conclusions are presented in Sect. 8.

2. Observations of Stephan's Quintet

This section introduces the observational data that set the luminosity, mass and energy budgets of the SQ shock. Relevant observational numbers and corresponding references are gathered in Table 1. Note that all the quantities are scaled to the aperture $\mathcal{A}$ used by Appleton et al. (2006) to measure H$_2$ luminosities: $\mathcal{A} = 11.3 \times 4.7$ arcsec^2, which corresponds to 5.2×2.1 kpc^2. The equivalent volume associated with this area is $\mathcal{V}_{\mathcal{A}} = 5.2 \times 2.1 \times l_z$ kpc^3, where l_z [kpc] is the dimension along the line-of-sight. For the X-ray emitting gas, O'Sullivan et al. (2008) assume a cylindrical geometry for the shock, which gives $l_z \sim 4.5$ kpc. This dimension may be smaller for the H$_2$ emitting gas, which could be concentrated where the gas density is

Table 1. Mass, energy and luminosity budgets of the preshock and postshock gas in the Stephan's Quintet galaxy-wide shock, directly inferred from observations[a].

	P	G		P	G			
	Hot Plasma[b]	H [d]	H$_2$	Hot Plasma[b]	H [c]	H [d]	Warm H$_2$[e]	Cold H$_2$
Density n_H [cm^{-3}] Temperature T [K] Pressure P/k_B [K cm^{-3}] N_H [cm^{-2}]				0.02 5×10^6 2×10^5				<10^2
N_H [cm^{-2}]		3×10^{20}			1.4×10^{19}	<5.8×10^{19}	2×10^{20}	
Temperature (Warm H$_2$)							185	
Mass Budget [$M_\odot$]	Hot Plasma[b] 6×10^6	H [d] 2–6×10^7	H$_2$	Hot Plasma[b] 1.4×10^7	H [c] 1.2×10^6	H [d] <5×10^6	Warm H$_2$[e] 3×10^7	Cold H$_2$
Energy Budget [erg]	Thermal (Plasma in halo) 1.7×10^{55}	Bulk Kinetic (Shocked H gas) 1–3×10^{56}		Thermal (X-ray emitting plasma) 4×10^{55}			Bulk Kinetic[f] (Turbulent H$_2$) $\gtrsim 1.2 \times 10^{56}$	
Flux [W m^{-2}]	X-rays 2.3×10^{-18}			X-rays 1.1×10^{-17}	Hα 5.1×10^{-18}	O 3.6×10^{-18}	H$_2$[e] 5.5×10^{-17}	
Luminosity[g] [erg s^{-1}]	2.5×10^{39}			1.2×10^{40}	5.4×10^{39}	3.8×10^{39}	5.8×10^{40}	

[a] All the numbers are scaled to our aperture ($\mathcal{A} = 5.2 \times 2.1$ kpc^2) where *Spitzer* observations were performed. The preshock gas is mainly the H gas contained in the tidal tail of NGC 7319. After the shock, the mass is distributed between the hot X-ray emitting plasma and the H$_2$ gas (see text for details). Before the shock, most of the energy available is the kinetic energy of the H gas that will be shocked. The shock splits the energy budget in two parts: thermal and kinetic energy. The former is stored in the hot plasma whereas the latter goes into turbulent motions that heat the H$_2$ gas. Observations show that mechanical energy is the dominant energy reservoir.
[b] XMM-Newton observations of the extended X-ray emission in the shock and the tidal tail (Trinchieri et al. 2005).
[c] Hα and O optical line observations by Xu et al. (2003).
[d] Based on extrapolation of H observations in the tidal tail by Sulentic et al. (2001); Williams et al. (2002).
[e] From *Spitzer IRS* observations. The H$_2$ line flux is summed over the S(0) to S(5) lines (Appleton et al. 2006).
[f] This bulk kinetic energy is a lower limit because an unknown mass of turbulent cold molecular gas can contribute to this energy.
[g] Luminosities are indicated assuming a distance to SQ of 94 Mpc.

largest. To take this into account, we use a reference value of $l_z = 2$ kpc. Since this number is uncertain, the explicit dependence of the physical quantities on this dimension are written out in the equations.

2.1. Astrophysical context

Since its discovery (Stephan 1877), the Stephan's Quintet (94 Mpc) multigalaxy compact group has been extensively studied, although one member of the original quintet (NGC 7320) is now presumed to be a foreground dwarf galaxy and will not be discussed further here. Later studies have restored the "quintet" status with the discovery of a more distant member. The inner group galaxies are shown on the left-hand side of Fig. 1.

H observations exhibit a large stream created by tidal interactions between NGC 7320 and NGC 7319 (Moles et al. 1997; Sulentic et al. 2001). It is postulated that another galaxy, NGC 7318b (hereafter called the "intruder"), is falling into the group with a very high relative velocity, shocking a 25 kpc segment of that tidal tail (Xu et al. 2003). The observed difference in radial velocities between the tidal tail and the intruder is ~1000 km s^{-1}. If this picture of two colliding gas flows is correct, we expect two shocks: one propagating forward into the SQ intergalactic medium, and another reverse shock driven into the intruding galaxy.

Over the shock region, no H gas is detected, but optical line emission from H gas is observed at the H tidal tail velocity. X-ray (Trinchieri et al. 2003, 2005; O'Sullivan et al. 2008) observations resolve shock-heated plasma spatially associated with the optical line and 21 cm radio continuum (Sulentic et al. 2001). The width of this emission is ~5 kpc, which is commensurate with the width of the Hα emission. Dividing this shock width

by the collision velocity (assumed to be 1000 km s^{-1}), we obtain a collision age of $t_{coll} \sim 5 \times 10^6$ yr.

Spectral energy distribution fitting of *Chandra* and *XMM* observations of SQ show that the temperature of the hot plasma is $T_X \sim 5 \times 10^6$ K (Trinchieri et al. 2003, 2005; O'Sullivan et al. 2008). The postshock temperature is given by (see e.g. Draine & McKee 1993):

$$T_{ps} = \frac{2(\gamma - 1)}{(\gamma + 1)^2} \frac{\mu}{k_B} V_s^2 \simeq 5 \times 10^6 \left(\frac{V_s}{600 \text{ km s}^{-1}} \right)^2 \text{ K}, \qquad (1)$$

where V_s is the velocity of the shock wave, μ the mean particle mass (equals to 10^{-24} g for a fully ionized gas), k_B the Boltzmann constant and $\gamma = 5/3$. Therefore, the postshock temperature of the hot plasma allows us to estimate a shock velocity of ~600 km s^{-1}. This shock velocity is consistent with the gas velocity in the center of mass frame, which would be approximately half of the observed relative velocity if the mass of the gas reservoirs on the intruder and SQ tail sides are commensurate.

2.2. Mass budgets

Observations show that the preshock and postshock gas are multiphase. We combine H$_2$, H , H and X-ray gas luminosities to estimate gas masses.

2.2.1. Preshock gas

The H preshock gas is contained on both the SQ tidal tail side (at a velocity of ~6700 km s^{-1}) and the intruder galaxy side (~5700 km s^{-1}). On both sides, this gas is seen outside the shock
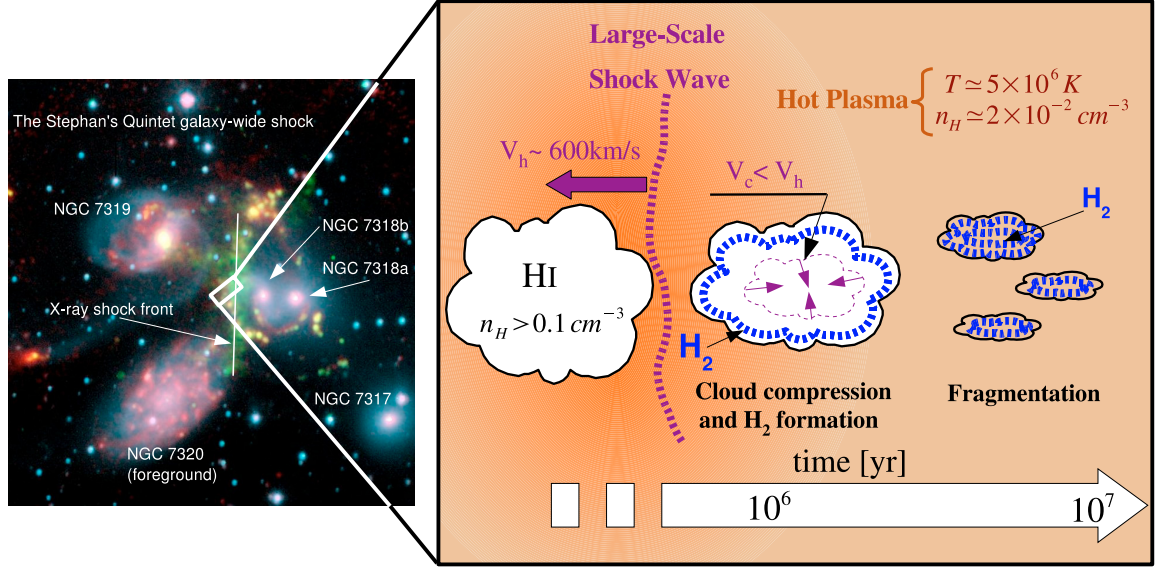
Fig. 1. A schematic picture of a galactic wide shock in an inhomogeneous medium. *Left*: a three data set image of the Stephan's Quintet system (visible red light (blue), Hα (green) from the Calar Alto Observatory in Spain, and 8-micron infrared light (red) from *Spitzer*'s InfraRed Array Camera (*IRAC*). The white box represents the aperture $\mathcal{A}$ where *Spitzer* spectroscopic observations were performed. *Right*: schematic view of the proposed scenario for the H₂ formation in the SQ galaxy-wide collision. In the hot/tenuous medium, the shock is propagating fast ($V_h \sim$ 600 km s^{-1}), whereas in the clouds a lower velocity shock ($V_c < V_h$) is driven. The cloud compression triggers gas cooling and H₂ formation in the postshock clouds. Thermal instability and dynamical interaction with the hot plasma lead to molecular gas fragmentation (see Sect. 3.3).

area (Sulentic et al. 2001; Williams et al. 2002). On the SQ intra-group side, the tidal tail H column densities are in the range $N_H = 1-3 \times 10^{20}$ cm^2. These two values bracket the range of possible preshock column densities. Neutral hydrogen observations of SQ show H at the intruder velocity to the South West (SW) of the shock area. The H column density of the SW feature and that of the tidal tail are comparable. By multiplying the column densities by the area $\mathcal{A}$, we derive a total mass of H preshock gas in the aperture $\mathcal{A}$ of $2-6 \times 10^7 M_\odot$.

Deep *Chandra* and *XMM-Newton* observations show a diffuse "halo" of soft X-ray emission from an extended region around the central shock region (Trinchieri et al. 2005; O'Sullivan et al. 2008). We consider that this emission traces the preshock plasma, which may have been created by a previous collision with NGC 7320c (Sulentic et al. 2001; Trinchieri et al. 2003). The mass of hot gas, within the equivalent volume $V_\mathcal{A}$ associated with the aperture $\mathcal{A}$, is derived from the X-ray luminosity and the temperature T_X:

$$M_X \simeq 6 \times 10^6 \left(\frac{L_X}{2.5 \times 10^{39}}\right)^{1/2} \left(\frac{3 \times 10^{-23}}{\Lambda(T_X)}\right)^{1/2} \left(\frac{l_z}{2 \text{ kpc}}\right)^{1/2} M_\odot, \quad (2)$$

where L_X [erg s^{-1}] is the X-ray luminosity, $\Lambda(T_X)$ [erg s^{-1} cm^3] the gas cooling efficiency at the plasma temperature T_X. The X-ray luminosity in the halo is derived from Trinchieri et al. (2005) and is 2.5×10^{39} erg s^{-1}. We assume a solar metallicity (Xu et al. 2003) and a cooling efficiency of $\Lambda(T_X) = 3 \times 10^{-23}$ erg s^{-1} cm^3 at $T_X = 5 \times 10^6$ K (see Appendix B.1 and Gnat & Sternberg 2007, for more details).

2.2.2. Postshock gas

The galaxy-wide collision creates a multi-phase interstellar medium where molecular and H gas are embedded in a hot X-ray emitting plasma.

No postshock H gas is detected in the shocked region where H₂ was observed. We derive an upper limit of $5 \times 10^6 M_\odot$ based on the lowest H contour close to the shock. A two-temperature fit of the H₂ excitation diagram gives $T = 185$ K and $T = 675$ K for the two gas components. Most of the gas mass is contained in the lower temperature component, which represents a mass of warm H₂ of $3 \times 10^7 M_\odot$ (Appleton et al. 2006) within the aperture $\mathcal{A}$. Published CO observations do not constrain the total H₂ mass in the preshock and postshock gas. Given the uncertainties on the preshock gas masses, one cannot infer a precise mass of cold molecular gas.

The mass of hot plasma is derived from the O'Sullivan et al. (2008) *Chandra* observations in the region observed by *Spitzer*. The absorption-corrected X-ray luminosity is 1.2×10^{40} erg s^{-1} within the aperture $\mathcal{A}$. Using Eq. (2), this corresponds to a mass of $1.4 \times 10^7 M_\odot$. This is 2–3 times the mass of the preshock hot plasma. O'Sullivan et al. (2008) report variations of the average proton density in the range $n_H = 1.2-2.3 \times 10^{-2}$ cm^{-3}. The density peaks close to the area $\mathcal{A}$. We adopt a hot plasma density of $n_H \simeq 0.02$ cm^{-3} where H₂ has been detected. This is in agreement with the value obtained by Trinchieri et al. (2005). The postshock gas pressure is given by

$$\frac{P_{ps}}{k_B} = 2.2 \times 10^5 \frac{0.6 \times m_H}{\mu} \left(\frac{n_H}{0.02 \text{ cm}^{-3}}\right) \left(\frac{T_{ps}}{5 \times 10^6 \text{ K}}\right) \text{ K cm}^{-3}. \quad (3)$$

In the tenuous gas this pressure remains almost constant during the collision time scale since the plasma does not have the time to cool nor to expand significantly. The isobaric gas cooling time scale can be estimated as the ratio of the internal energy of the gas to the cooling rate:

$$t_{cool} = \frac{5/2 \, k_B \, T_X}{n_H \, \Lambda(T_X)} \simeq 9 \times 10^7 \left(\frac{T_X}{5 \times 10^6 \text{ K}}\right)^{1.54} \left(\frac{0.02 \text{ cm}^{-3}}{n_H}\right) \text{ yr.} \quad (4)$$

This cooling time is significantly longer than the age of the shock. In the right hand side of Eq. (4), we use the power-law fit of the $Z = 1$ cooling efficiency given in Gnat & Sternberg (2007) (consistent with Sutherland & Dopita 1993). If the metallicity of the pre-shocked tidal filament was sub-solar, this would increase the cooling time of the gas still further. O'Sullivan et al. (2008) found a best fit to their X-ray spectrum for $Z = 0.3 \, Z_\odot$.

The mass of the ionized H gas is derived from the emission measure of Hα observations:

$$M_{\rm HII} \simeq 1.2 \times 10^6 \left(\frac{\mathcal{F}_{\rm H\alpha}}{5.1 \times 10^{-18}} \right) \left(\frac{T}{10^4 \, \rm K} \right)^{0.92} \left(\frac{10 \, \rm cm^{-3}}{n_{\rm H}} \right) M_\odot \quad (5)$$

where $\mathcal{F}_{\rm H\alpha}$ [W m^{-2}] is the flux of the H_α line scaled to the aperture $\mathcal{A}$ and $n_{\rm H}$ the gas proton density. For SQ, the observed H_α flux is $\mathcal{F}_{\rm H\alpha} = 5.1 \times 10^{-18}$ W m^{-2} (Xu et al. 2003). At the SQ postshock pressure, the gas density at 10^4 K is $n_{\rm H} \simeq 10$ cm^{-3}.

2.3. Extinction and UV field

Xu et al. (2003) have interpreted their non-detection of the H$_\beta$ line as an indication of significant extinction ($E(\rm H_\beta - H_\alpha) > 1.2$, i.e. $A(\rm H_\alpha) > 2.4$). However, more sensitive spectroscopy[1] by Duc et al. (private communication) show that the H$_\beta$ line is detected over the region observed with *IRS* at two velocity components ($\sim$5700 and 6300 km s^{-1}, corresponding to the intruder and the intra-group gas velocities). These observations show that the extinction is much higher ($A_V = 2.5$) for the low-velocity gas component than for the high-velocity one. There are also large spatial variations of the extinction value for the intruder gas velocity close to this position, suggesting clumpiness of the gas within the disturbed spiral arm of NGC 7318b. An extinction of $A_V = 0.3-0.9$ is derived from the Balmer decrement for the intra-group tidal tail velocity, with much lower spatial variation. After subtraction of the foreground galactic extinction ($A_V = 0.24$), this gives an SQ ridge extinction A_V in the range 0.1–0.7.

A low extinction for the H$_2$-rich, intra-group gas is also consistent with measured UV and far-IR dust surface brightness observations. Using the published value of FUV extinction (Xu et al. 2005) and the Weingartner & Draine (2001) extinction curve, we derive $A_V = 0.29$, which is in agreement with the new Balmer-decrement study. *GALEX* observations show that the radiation field is $G \sim 1-2 \, G_0$ in the shocked region, where G_0 is the interstellar radiation field (ISRF) in Habing units[2]. We obtain the higher value using the flux listed in Table 1 of Xu et al. (2005). This flux is measured over an area much larger than our aperture $\mathcal{A}$. It provides an upper limit on the UV field in the shock because this area includes star forming regions in the spiral arm of NGC 7318b. ISO observations show a diffuse 100 μm emission at a 2.2 MJy sr^{-1} level in the shocked region (Xu et al. 2003). Using the Galactic model of Draine & Li (2007) for $G = 2 \, G_0$, the 100 μm FIR brightness corresponds to a gas column density of 1.5×10^{20} cm^{-2}. For $G = G_0$, we obtain $N_{\rm H} = 3.3 \times 10^{20}$ cm^{-2}, which corresponds to $A_V = 0.18$ for the Solar neighbourhood value of the $A_V/N_{\rm H}$ ratio. Since this value is low, no extinction correction is applied.

---

[1] Observations made at the Cerro Tololo Inter-American Observatory (CTIO).

[2] $G_0 = 2.3 \times 10^{-3}$ erg s^{-1} cm^{-2} at 1530 Å, Habing (1968).

2.4. Energy reservoirs

The bulk kinetic energy of the pre- and postshock gas are the dominant terms of the energy budget of the SQ collision (Table 1). Assuming that the preshock H mass is moving at $V_s = 600$ km s^{-1} in the center of mass rest frame, the preshock gas bulk kinetic energy is $1-3 \times 10^{56}$ erg. Note that this is a lower limit since a possible contribution from preshock molecular gas is not included. The thermal energy of the X-ray plasma represents $\sim$10% of the preshock kinetic energy.

The shock distributes the preshock bulk kinetic energy into postshock thermal energy and bulk kinetic energy. The *Spitzer* IRS observations of SQ (Appleton et al. 2006) show that the $0-0$ S(1) 17 μm H$_2$ line is resolved with a width of 870 ± 60 km s^{-1} (*FWHM*), comparable to the collision velocity. We assume that the broad resolved line represents H$_2$ emission with a wide range of velocities, by analogy with the O [6300 Å] emission seen in the same region by Xu et al. (2003) (see Appleton et al. 2006, for discussion). Then the results imply a substantial kinetic energy carried by the postshock gas. The kinetic energy of the H$_2$ gas is estimated by combining the line width with the warm H$_2$ mass. This is a lower limit since there may be a significant mass of H$_2$ too cold to be seen in emission. The H$_2$ kinetic energy is more than 3 times the amount of thermal energy of the postshock hot plasma. This implies that most of the collision energy is not dissipated in the hot plasma, but a substantial amount is carried by the warm molecular gas.

Radio synchrotron observations indicate that the postshock medium is magnetized. Assuming the equipartition of energy between cosmic rays and magnetic energy, the mean magnetic field strength in the SQ shocked region is $\simeq$10 μG (Xu et al. 2003). The magnetic energy and thereby the cosmic ray energy contained in the volume $V_\mathcal{A}$ is $\frac{B^2}{8\pi} V_\mathcal{A} = 2.7 \times 10^{54}$ erg. This energy is much lower than the bulk kinetic energy of the H$_2$ gas.

Thus, the dominant postshock energy reservoir is the bulk kinetic energy of the molecular gas. We thus propose that the observed H$_2$ emission is powered by the dissipation of this kinetic energy. The ratio between the kinetic energy of the warm H$_2$ gas in the center of mass frame and the H$_2$ luminosity is:

$$t_{\rm diss} \simeq 10^8 \left(\frac{1.5 \times 10^7 \, L_\odot}{L_{\rm H_2}} \right) \rm yr. \quad (6)$$

The H$_2$ luminosity of $1.5 \times 10^7 \, L_\odot$ is summed over the S(0)$-$S(5) lines. This dissipation timescale is of the order of the cooling time of the hot X-ray emitting plasma. Therefore, the dissipation of the kinetic energy of the SQ collision can power the H$_2$ emission on a timescale more than one order of magnitude longer than the collision age ($t_{\rm coll} \sim 5 \times 10^6$ yr). The timescale of energy dissipation will be longer if the total amount of molecular gas is larger than the warm H$_2$ mass derived from *Spitzer* observations. On the other hand, it will be shorter by a factor of 2 if we consider cooling through the emission of the H gas.

The line emission of the ionized gas could also contribute to the dissipation of energy. We estimate the total luminosity of the postshock H gas from the Hα luminosity (Heckman et al. 1989):

$$L_{\rm HII} = \frac{13.6 \, \rm eV}{0.45 \times E_{\rm H\alpha}} L_{\rm H\alpha}, \quad (7)$$

where $E_{\rm H\alpha}$ is the energy of an $H\alpha$ photon. Therefore, the luminosity of the postshock H gas is $L_{\rm HII} = 2.1 \times 10^7 \, L_\odot$ within the aperture $\mathcal{A}$. This represents $16 \times L_{\rm H\alpha}$ and is comparable to the H$_2$ luminosity.

3. Why is H₂ present in the postshock gas?

Observations show that the pre-collision medium is *inhomogeneous*. The gas in the SQ group halo is observed to be structured with H clouds and possibly H₂ clouds embedded in a teneous, hot, intercloud plasma (Sect. 2.1). On the intruder side, the galaxy interstellar medium is also expected to be multiphase. We consider a large-scale collision between two flows of multiphase dusty gas (Fig. 1). In this section we quantify H₂ formation within this context. The details of the microphysics calculations of the dust evolution, gas cooling and H₂ formation are given in Appendices A−C.

3.1. Collision between two dusty multiphase gas flows

This section introduces a schematic description of the collision that allows us to quantify the H₂ formation timescale. The collision drives two high-velocity large-scale shocks that propagate through the teneous volume filling plasma, both into the tidal arm and into the intruder. The rise in the intercloud pressure drives slower shocks into the clouds (e.g. McKee & Cowie 1975). The velocity of the transmitted shock into the clouds, V_c, is of the order of $V_c \simeq \sqrt{n_h/n_c} \, V_h$, where V_h is the shock velocity in the hot intercloud medium, and n_c and n_h are the densities of the cloud and intercloud medium[3], respectively. Each cloud density corresponds to a shock velocity.

The galaxy collision generates a range of shock velocities and postshock gas temperatures. The state of the postshock gas is related to the preshock gas density. Schematically, low density ($n_H \lesssim 10^{-2}$ cm^{-3}) gas is shocked at high speed ($\gtrsim 600$ km s^{-1}) and accounts for the X-ray emission. The postshock plasma did not have time to cool down significantly and form molecular gas since the collision was initiated. H gas ($n_H \gtrsim 3 \times 10^{-2}$) is heated to lower ($\lesssim 10^6$ K) temperatures. This gas has time to cool. Since H₂ forms on dust grains, dust survival is an essential element of our scenario (see Appendix A). The gas pressure is too high for warm neutral H to be in thermal equilibrium. Therefore, the clouds cool to the temperatures of the cold neutral medium and become molecular.

The time dependence of both the gas temperature and the dust-to-gas mass ratio, starting from gas at an initial postshock temperature T_{ps}, has been calculated. We assume a galactic dust-to-gas ratio, a solar metallicity and equilibrium ionization. In the calculations, the thermal gas pressure is constant. As the gas cools, it condenses. Below ~10^4 K, the H gas recombines, cools through optical line emission, and becomes molecular. The gas and chemistry network code (Appendix C) follows the time evolution of the gas that recombines. The effect of the magnetic field on the compression of the gas has been neglected in the calculations and we assume a constant thermal gas pressure.

Under the usual flux-freezing ideas, the magnetic field strength should increase with volume density and limit the compression factor. However, observations show that the magnetic field in the cold neutral medium (CNM) is comparable to that measured in lower density, warm ISM components (Heiles & Troland 2005). 3D MHD numerical simulations of the supernovae-driven turbulence in the ISM also show that gas compression can occur over many orders of magnitude, without increasing the magnetic pressure (e.g. Mac Low et al. 2005; de Avillez & Breitschwerdt 2005b). The reason is that the lower density ($n_H \lesssim 10^3$ cm^{-3}) gas is magnetically sub-critical and mainly flows along the magnetic field lines without compressing

---

[3] More detailed expressions are given in Klein et al. (1994).

the magnetic flux. The magnetic field intensity increases within gravitationally bound structures at higher gas densities ($n_H \gtrsim 10^3$ cm^{-3} (e.g. Hennebelle et al. 2008). This result is in agreement with observations of the magnetic field intensity in molecular clouds by Crutcher (1999) and Crutcher et al. (2003).

3.2. Gas cooling, dust destruction and H₂ formation timescales

The physical state of the post-shock gas depends on the shock age, the gas cooling, the dust destruction, and the H₂ formation timescales. These relevant timescales are plotted as a function of the postshock temperature in Fig. 2. Given a shock velocity V_h in the low-density plasma, each value of the postshock temperature T_{ps} corresponds to a cloud preshock density $n_{c,p}$:

$$T_{ps} = 2.4 \times 10^5 \left(\frac{n_h}{0.02 \text{ cm}^{-3}}\right)\left(\frac{0.1 \text{ cm}^{-3}}{n_{c,p}}\right)\left(\frac{V_h}{600 \text{ km s}^{-1}}\right)^2 \text{ K.} \quad (8)$$

Dust destruction is included in the calculation of the H₂ formation timescale. The H₂ formation timescale is defined as the time when the H₂ fractional abundance reaches 90% of its final (end of cooling) value, including the gas cooling time from the postshock temperature. The dust destruction timescale is defined as the time when 90% of the dust mass is destroyed and returned to the gas. At $T < 10^6$ K, this timescale rises steeply because the dust sputtering rate drops (see Appendix A for details). The dust destruction timescale increases towards higher temperatures because, for a fixed pressure, the density decreases.

The present state of the multiphase postshock gas is set by the relative values of the three timescales at the SQ collision age, indicated with the horizontal dashed line and marked with an arrow. The ordering of the timescales depends on the preshock density and postshock gas temperature. By comparing these timescales one can define three gas phases, marked by blue, grey and red thick lines in Fig. 2.

1. *The molecular phase*: for $T_{ps} \lesssim 8 \times 10^5$ K, the dust destruction timescale is longer than the collision age and the H₂ formation timescale is shorter. This gas keeps a significant fraction of its initial dust content and becomes H₂ (blue thick line).
2. *Atomic* H *and ionized* H *gas phase*: for intermediate temperatures ($8 \times 10^5 < T_{ps} < 3 \times 10^6$ K), the gas has time to cool down but loses its dust content. The H₂ formation timescale is longer than the collision age. This phase is indicated with the grey thick line.
3. *X-ray emitting plasma*: at high temperatures ($T_{ps} > 3 \times 10^6$ K), the postshock gas is dust-free and hot. This is the X-ray emitting plasma indicated by the red thick line.

In Fig. 2 it is assumed that, during the gas cooling, the molecular gas is in pressure equilibrium with the hot, volume filling gas. The gas pressure is set to the measured average thermal pressure of the hot plasma (HIM). Theoretical studies and numerical simulations show that the probability distribution function of the density in a supersonically turbulent isothermal gas is lognormal, with a dispersion which increases with the Mach number (Vazquez-Semadeni 1994; Padoan et al. 1997; Passot & Vázquez-Semadeni 1998; Mac Low et al. 2005). Based on these studies, the SQ postshock pressure in the turbulent cloud phase is likely to be widely distributed around the postshock pressure in the HIM (2×10^5 K cm^{-3}). The H₂ formation timescale would be longer in the low pressure regions and shorter in high pressure regions.
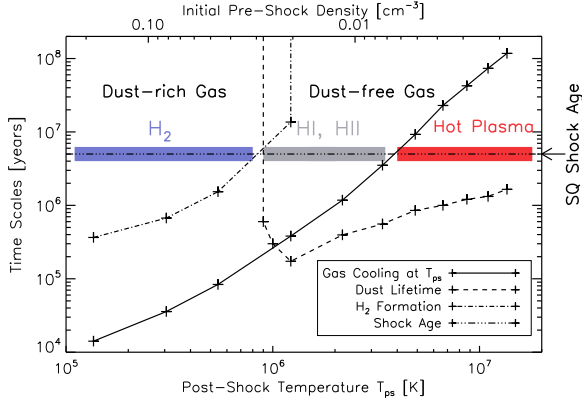
Fig. 2. The multiphasic postshock medium. The dust lifetime, H$_2$ formation and gas cooling (solid line) time scales in the SQ postshock gas are plotted as a function of the postshock temperature and preshock density (top axis). The state of the multiphase postshock gas is set by the relative values of these timescales at the SQ collision age ($\sim 5 \times 10^6$ yr, indicated with the horizontal dashed line and marked with an arrow). By comparing these timescales one can define three gas phases, marked by blue, grey and red thick lines. In particular, the comparison of the H$_2$ formation time scale with the SQ collision age show where H$_2$ molecules can form (blue thick line).

Fig. 3. Cooling and H$_2$ formation timescales for ionized gas at 10^4 K as a function of the gas density and pressure (top axis). The grey horizontal bar indicates the SQ collision age, and the blue vertical bar shows the gas thermal pressure at which the H$_2$ formation timescale equals the collision age. The vertical green bar indicates the thermal pressure of the hot plasma. A power-law fit to the H$_2$ formation timescale is indicated (Eq. (9)). The H$_2$ formation timescale is shorter than the collision age for pressures larger than 1/10 of the hot plasma pressure.

To quantify this statement, we run a grid of isobaric cooling models for different gas thermal pressures. Figure 3 shows the gas cooling time and the H$_2$ formation timescale as a function of the gas thermal pressure. A Solar Neighborhood value of the dust-to-gas ratio is assumed. The H$_2$ formation time scale roughly scales as the inverse of the gas density at 10^4 K and can be fitted by the following power-law:

$$t_{\mathrm{H}_2} \; [\mathrm{yr}] \simeq 7 \times 10^5 \, f_{\mathrm{dust}} \left(\frac{2 \times 10^5 \; [\mathrm{K \, cm^{-3}}]}{P_{\mathrm{th}}} \right)^{0.95}, \tag{9}$$

where P_{th} is the thermal gas pressure and f_{dust} the dust mass fraction remaining in the gas (In Fig. 3, $f_{\mathrm{dust}} = 1$).

Figure 3 shows that for a wide range of gas thermal pressures ($> 3 \times 10^4$ K cm^{-3}, i.e. $P_{\mathrm{th}}(\mathrm{CNM}) > \frac{1}{10}P_{\mathrm{th}}(\mathrm{HIM})$), H$_2$ can form within less than the collision age (5×10^6 yrs). Numerical simulations of supernovae-driven turbulence in the ISM show that this condition applies to a dominant fraction of the gas mass (see Fig. 10 of Mac Low et al. 2005). Numerical studies by Glover & Mac Low (2007) show that the pressure variations induced by the turbulence globally reduce the time required to form large quantities of H$_2$ within the Galactic CNM.

3.3. Cloud crushing and fragmentation timescales

In Sect. 3.2, the microphysics of the gas has been quantified, ignoring the fragmentation of clouds by thermal, Rayleigh-Taylor and Kelvin-Helmholtz instabilities. In this section, we introduce the dynamical timescales associated with the fragmentation of clouds and compare them with the H$_2$ formation timescale.

3.3.1. Fragmentation

When a cloud is overtaken by a strong shock wave, a flow of background gas establishes around it, and the cloud interacts with the low-density gas that is moving relative to it (see Fig. 1). The dynamical evolution of such a cloud has been described
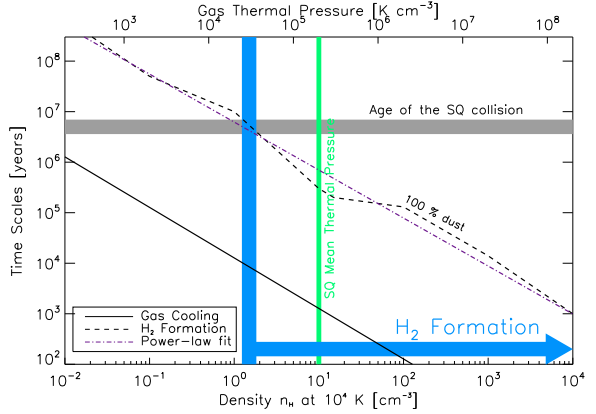
in many papers (e.g. Klein et al. 1994; Mac Low et al. 1994). Numerical simulations show that this interaction triggers clouds fragmentation. The shock compresses the cloud on a *crushing time* $t_{\mathrm{crush}} = R_c/V_c$, where V_c is the shock velocity in the cloud and R_c its characteristic preshock size. The shocked cloud is subject to both Rayleigh-Taylor and Kelvin-Helmholtz instabilities.

Gas cooling introduces an additional fragmentation mechanism because the cooling gas is thermally unstable at temperatures smaller than $\sim 10^6$ K. The thermal instability generates complex inhomogeneous structures, dense regions that cool and low density voids (Sutherland et al. 2003; Audit & Hennebelle 2005). This fragmentation occurs on the gas cooling timescale. In most numerical simulations, the thermal instability is ignored because simplifying assumptions are made on the equation of state of the gas (adiabatic, isothermal or polytropic evolution).

In Fig. 4, the H$_2$ formation and gas cooling timescales are compared to the crushing time and collision age, as a function of the initial density and size of the cloud. The pressure of the clouds is 2×10^5 K cm^{-3}. The red zone indicates where the H$_2$ formation timescale is longer than the SQ collision age. In this domain, clouds do not have time to form H$_2$. The blue hatched zone defines the range of sizes and densities of the clouds which become molecular within 5×10^6 yr. In this zone, the crushing time is longer than the cooling time. Gas fragments by thermal instability as the shock moves into the cloud. H$_2$ forms before the shock has crossed the cloud and therefore before Rayleigh-Taylor and Kelvin-Helmholtz instabilities start to develop. The black dashed line is where the cloud crushing timescale equals the SQ collision age (5×10^6 yr). To the right of this line, the clouds have not been completely overtaken and compressed by the transmitted shock.

Preshock Giant Molecular Clouds (hereafter GMCs) of size $\gtrsim 30$ pc and mean density $\gtrsim 3 \times 10^2$ cm^{-3}, like those observed in spiral galaxies, fall within the yellow zone in Fig. 4. The bottom boundary corresponds to the density at which the free-fall time equals the age of the SQ collision. For densities higher than this limit, the free-fall time is shorter than the SQ collision age. The left boundary of this area is the maximum cloud size set by the Bonnor-Ebert criterion for a pressure of 2×10^5 K cm^{-3}. Clouds
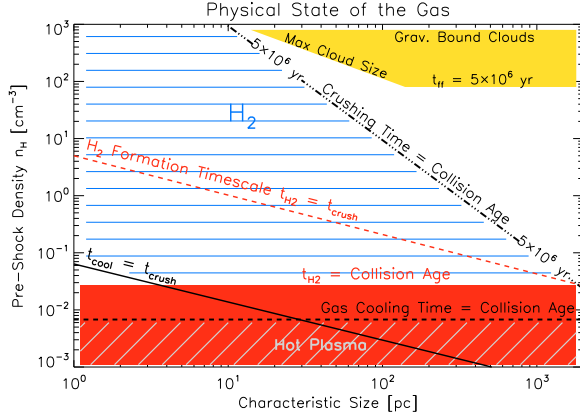
Fig. 4. The gas cooling and H$_2$ formation timescales compared to the cloud crushing time and SQ collision age as a function of the cloud parameters (size and preshock density). The solid black line indicates where the gas cooling time t_{cool} equals the crushing time t_{crush}. The black dashed line shows where the cloud crushing timescale equals 5×10^6 yr (i.e. the SQ collision age). The red dashed line defines the location where the H$_2$ formation timescale t_{H_2} equals the crushing timescale. The red area indicates where the H$_2$ formation timescale is greater than the collision age, whereas the blue hatched zone show the parameter space where H$_2$ can form. The yellow zone is the location of gravitationally bound, unstable clouds that have a free-fall time shorter than the collision age.

with larger sizes are gravitationally unstable. Such clouds are expected to form stars.

A natural consequence of pre-existing GMCs would be that the shock would trigger their rapid collapse and star formation should rapidly follow (e.g. Jog & Solomon 1992). The absence (or weakness) of these tracers in the region of the main shock (Xu et al. 2003) suggests that fragments of preshock GMCs disrupted by star formation are not a major source of the observed postshock H$_2$ gas. However, it is possible that some of the gas in the intruder did contain pre-existing molecular material. The star formation regions seen to the North and South of the ridge are consistent with this hypothesis.

3.3.2. Survival of the fragments

The breakup of clouds can lead to mixing of cloud gas with the hot background plasma (Nakamura et al. 2006) and thereby raises the question of whether the cloud fragments survive long enough for H$_2$ to form. Fragments evaporate into the background gas when their size is such that the heat conduction rate overtakes the cooling rate. The survival of the fragments thus depends on their ability to cool (Mellema et al. 2002; Fragile et al. 2004). Gas condensation and H$_2$ formation are both expected to have a stabilizing effect on the cloud fragments, because they increase the gas cooling power (Le Bourlot et al. 1999).

So far, no simulations include the full range of densities and spatial scales and the detailed micro-physics that are involved in the cloud fragmentation and eventual mixing with the background gas. Slavin (2006) reports an analytical estimate of the evaporation time scale of tiny H clouds embedded in warm and hot gas of several million years. This timescale is long enough for H$_2$ to form within the lifetime of the gas fragments.

4. H$_2$ excitation

This section addresses the question of H$_2$ excitation. The models (Sect. 4.1) and the results (Sect. 4.2) are presented.

4.1. Modeling the dissipation of turbulent kinetic energy by MHD shocks

Given that the dominant postshock energy reservoir is the bulk kinetic energy of the H$_2$ gas (Sect. 2.4), the H$_2$ emission is assumed to be powered by the dissipation of turbulent kinetic energy into molecular gas. Radio synchrotron observations indicate that the postshock medium is magnetized (Sect. 2.4). In this context, the dissipation of mechanical energy within molecular gas is modeled by non-dissociative MHD shocks. In the absence of a magnetic field, shocks are rapidly dissociative and much of the cooling of the shocked gas occurs through atomic, rather than H$_2$, line emission. We quantify the required gas densities and shock velocities to account for the H$_2$ excitation diagram.

The H$_2$ emission induced by low velocity shocks is calculated using an updated version of the shock model of Flower & Pineau des Forêts (2003). In these models, we assume a standard value for the cosmic ray ionization rate of $\zeta = 5 \times 10^{-17}$ s^{-1}. In its initial state, the gas is molecular and cold ($\sim$10 K), with molecular abundances resulting from the output of our model for the isobaric cooling (Sect. C.2 and Fig. C.2). A grid of shock models has been computed for shock velocities from 3 to 40 km s^{-1} with steps of 1 km s^{-1}, two values of the initial H$_2$ ortho to para ratio (3 and 10^{-2}), and 3 different preshock densities ($n_{\rm H} = 10^2$, 10^3, and 10^4 cm^{-3}). We adopt the scaling of the initial magnetic strength with the gas density, $B(\mu G) = b \sqrt{n_{\rm H} [{\rm cm}^{-3}]}$ (Crutcher 1999; Hennebelle et al. 2008). In our models, $b = 1$.

4.2. Results: contribution of MHD shocks to the H$_2$ excitation

Results are presented in terms of an H$_2$ excitation diagram, where the logarithm of the column densities $N_{vJ}[{\rm cm}^{-2}]$, divided by the statistical weight g_{vJ}, are plotted versus the energy of the corresponding level. The excitation diagrams are calculated for a gas temperature of 50 K, since the molecular gas colder than 50 K does not contribute to the H$_2$ emission. Figure 5 shows the H$_2$ excitation diagram for both observations and model. The SQ data from Appleton et al. (2006) is indicated with 1σ error bars. The H$_2$ line fluxes have been converted to mean column densities within our area $\mathcal{A}$.

The observed rotational diagram is curved, suggesting that the H$_2$-emitting gas is a mixture of components at different temperatures. The data cannot be fitted with a single shock. At least two different shock velocities are needed. A least-squares fit of the observed H$_2$ line fluxes to a linear combination of 2 MHD shocks at different velocities V_{s1} and V_{s2} has been performed. For a preshock density of 10^4 cm^{-3}, the best fit is obtained for a combination of 5 and 20 km s^{-1} shocks with an initial value of the ortho to para ratio of 3 (Fig. 5 and Table 2). Note that no satisfactory fit could be obtained with the low value of the initial H$_2$ ortho-to-para ratio. The contributions of the 5 (green dashed line) and 20 km s^{-1} (orange dashed line) shocks to the total column densities are also plotted. Qualitatively, the 5 km s^{-1} component dominates the contribution to the column densities of the upper levels of S(0) and S(1) lines. The 20 km s^{-1} component has a major contribution for the upper levels of S(3) to S(5). For S(2), the 2 contributions are comparable. The red line shows the weighted sum of the two shock components (best fit). The
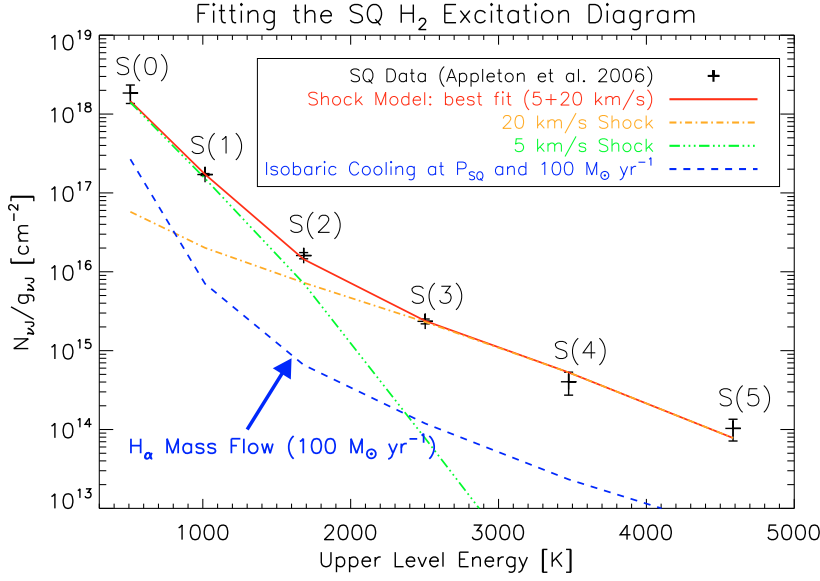
Fig. 5. H$_2$ excitation diagram fit by shock models. The data (Appleton et al. 2006) are the black crosses with their 1-σ error bars. The blue dashed line show the modeled excitation associated with the H$_2$ formation during the isobaric cooling of the postshock gas. The pressure is 2×10^5 K cm^{-3}. The model column densities correspond to a mass flow of recombining gas of 100 $M_\odot$ yr^{-1}. The green and orange dashed lines show the contribution of 5 and 20 km s^{-1} shocks to the best fit model (red line), multiplied by the weights determined when fitting the line fluxes, respectively. Shocks are driven into molecular gas of preshock density $n_H = 10^4$ cm^{-3}. The red line shows the linear combination of the two magnetic shocks (with velocities of 5 and 20 km s^{-1}).

Table 2. Overview of the emission of the SQ postshock gas, from observations and model predictions[a]. The models are the same as those used in Fig. 5.

	Mass Flow [$M_\odot$ yr^{-1}]	P/k_B [K cm^{-3}]	V_s[b] [km s^{-1}]	Cooling Time[c] [yr]	F O [63 μm]	S H$_2$ rot.[d]	F H$_2$ 1–0 S(1)	(10^{-18} W m^{-2}) O 6300 Å[e]	H$_\alpha$[e]
Observations						55 ± 3		3.6	5.3
Isobaric Cooling	100 (WIM, H$_\alpha$)[f]	2×10^5		1.2×10^4	3.9	1.4	0.05	0.5	5.3
	640 (WNM, O)[g]	2×10^5		1.5×10^5	25.8	9.1	0.3	3.6	
Shock Models	5.7×10^3	4.5×10^7	5	1.8×10^4	13	27	0.3	10^{-5}	
	270	5.6×10^8	20	3.7×10^3	0.04	25	0.01	5×10^{-3}	

[a] All line fluxes are scaled to the aperture $\mathcal{A} = 11.3 \times 4.7$ arcsec^2. For isobaric cooling calculations, the pressure is set to the SQ postshock gas value. For MHD shock models, both contributions of the 2 shock velocities to the emission are indicated, as well as the pressure for the warm H$_2$ phase in the shock.
[b] MHD Shock velocity.
[c] Cooling time computed down to 50 K.
[d] Sum of the H$_2$ S(0) to S(5) rotational lines (from Appleton et al. 2006).
[e] From optical observations by Xu et al. (2003).
[f] Mass flow derived from H α observations, ignoring ionization. It represents the isobaric cooling of the recombining H gas.
[g] Cooling mass flow derived from O observations and model calculations at the ambient SQ pressure. This mass flow does not depend much on the pressure since the critical density of the O line is high (2×10^6 cm^{-3}).

warm H$_2$ pressure ρV^2 in the two shocks is 4.5×10^7 K cm^{-3} (respectively 5.6×10^8 K cm^{-3}) for the 5 km s^{-1} (resp. 20 km s^{-1}) shock.

Our grid of models shows that this solution is not unique. If one decreases the density to 10^3 cm^{-3}, we find that one can fit the observations with a combination of MHD shocks (at 9 and 35 km s^{-1}). If one decreases the density to 10^2 cm^{-3}, the rotational H$_2$ excitation cannot be fitted satisfactorily. At such low densities, MHD shocks fail to reproduce the S(3) and S(5) lines because the critical densities for rotational H$_2$ excitation increase steeply with the J rotational quantum number (Le Bourlot et al. 1999). Both warm and dense (i.e. high pressure) gas is needed to account for emission from the higher J levels.

The data fit gives an estimate of the shock velocities required to account for the H$_2$ excitation. The velocities are remarkably low compared to the SQ collision velocity. The fact that energy dissipation occurs over this low velocity range is an essential key to account for the importance of H$_2$ cooling. High velocity shocks would dissociate H$_2$ molecules.

5. The cycling of gas across ISM phases

An evolutionary picture of the inhomogeneous postshock gas emerges from our interpretation of the data. The powerful H$_2$ emission is part of a broader astrophysical context, including optical and X-ray emission, which can be understood in terms of mass exchange between gas phases. A schematic diagram of the evolutionary picture of the postshock gas is presented in Fig. 6. It illustrates the cycle of mass between the ISM phases that we detail here. This view of the SQ postshock gas introduces
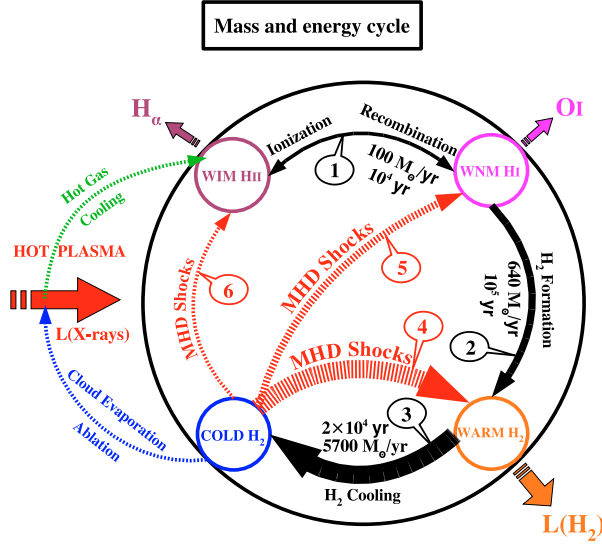
Fig. 6. Schematic view of the evolutionary cycle of the gas proposed in our interpretation of optical and H$_2$ observations of Stephan's Quintet. Arrows represent the mass flows between the H, warm H, warm and cold H$_2$ gas components. They are numbered for clarity (see text). The dynamical interaction between gas phases drives the cycle. The values of the mass flows and associated timescales are derived from the Hα, [O 6300 Å], H$_2$ observed luminosities and model calculations (cf. Table 2). Heating of the cold H$_2$ gas (red dashed arrows) is necessary to account for the increasing mass flow from the ionized gas to cold H$_2$ phases.

a physical framework that may apply to H$_2$ luminous galaxies in general.

5.1. Mass flows

The H$_2$ gas luminosity is proportional to the mass of gas that cools per unit time, the so-called mass flow. We compute the mass flow associated with one given shock, dividing the post-shock column density, associated with the gas cooling to a temperature of 50 K, by the cooling time needed to reach this temperature. Gas cooler than 50 K does not contribute to the H$_2$ emission.

The two-component shock model has been used to deduce the mass flows needed to fit the data. The cooling timescale (down to 50 K) is set by the lowest shock velocity component. For a shock velocity of 5 km s^{-1}, the cooling time is $\sim 2 \times 10^4$ yr. This gives a total mass flow required to fit the H$_2$ emission of $\dot{M}_3 = 5.7 \times 10^3 \, M_\odot$ yr^{-1}. For comparison, for the 20 km s^{-1} shock, the cooling time down to 50 K is $\sim 4 \times 10^3$ yr and the associated mass flow is $\dot{M} = 270 \, M_\odot$ yr^{-1}.

These mass flows are compared to the mass flow of recombining gas that can be estimated from the Hα luminosity $L_{H\alpha}$:

$$L_{H\alpha} = 0.45 \times E_{H\alpha} \times \Phi_{Rec}, \tag{10}$$

where $E_{H\alpha}$ is the energy of an Hα photon and Φ_{Rec} is the number of hydrogen atoms that recombine per second (Heckman et al. 1989). For our reference area $\mathcal{A}$, we find a mass flow of recombining gas $\dot{M}_{H\alpha} = m_H \Phi_{Rec} \simeq 100 \, M_\odot$ yr^{-1}. If the ionizing rate of warm gas is smaller than Φ_{Rec}, most of the recombining gas cools. In this case Φ_{Rec} provides the estimate of the mass flow

needed to compute the cooling gas H$_2$ luminosity. Φ_{Rec} is an upper limit if we suppose that some of the H$_\alpha$ emission arises from collisional excitation of neutral hydrogen or if some of the warm gas is re-ionized before it has time to cool.

The H$_2$ emission integrated over the isobaric cooling sequence is calculated. The blue dashed curve of Fig. 5 corresponds to the model results for a mass flow of $\dot{M} = 100 \, M_\odot$ yr^{-1} and a pressure $P_{SQ} = 2 \times 10^5$ K cm^{-3}. The model results do not depend much on the pressure. The model reproduces well the shape of the observed excitation diagram, but the emission is a factor ~ 25 below the observations. The model also fails to reproduce the [O] 6300 Å line emission by a factor of 7. Therefore, the cooling of the warm H gas produced by H recombination cannot reproduce the observed H$_2$ emission nor the [O] 6300 Å line emission. A larger amount of energy needs to be dissipated within the molecular gas to account for the H$_2$ emission. This is why the total mass flow associated with the 2-component MHD shocks is much larger than the mass flow of recombining gas.

5.2. The mass cycle

This section describes the mass cycle of Fig. 6. Black and red arrows represent the mass flows between the H, warm H, warm and cold H$_2$ gas components of the postshock gas. The large red arrow to the left symbolizes the relative motion between the warm and cold gas and the surrounding plasma. Each of the black arrows is labeled with its main associated process: gas recombination and ionization (double arrow number 1), H$_2$ formation (2) and H$_2$ cooling (3). The values of the mass flows and the associated timescales are derived from observations and our model calculations (Sect. 5.1 and Table 2).

A continuous cycle through gas components is excluded by the increasing mass flow needed to account for the Hα, O , and H$_2$ luminosities. Heating of the cold H$_2$ gas towards warmer gas states (red arrows) must occur. The postshock molecular cloud fragments are likely to experience a distribution of shock velocities. Arrow number 4 represents the low velocity MHD shock excitation of H$_2$ gas described in Sect. 4.1. A cyclic mass exchange between the cold molecular gas and the warm gas phases is also supported by the high value of the H$_2$ ortho to para ratio (Sect. 4.1). More energetic shocks may dissociate the molecular gas (arrows number 5). They are necessary to account for the low O luminosity. Even more energetic shocks can ionize the molecular gas (arrow number 6). This would bring cold H$_2$ directly into the H component. Such shocks have been proposed as the ionization source of the clouds in the Magellanic Stream by Bland-Hawthorn et al. (2007) based on hydrodynamic simulations of their interaction with the Galactic halo plasma.

Turbulent mixing of hot, warm and cold gas is an alternative route to mass input of H gas. Turbulent mixing layers have been described by Begelman & Fabian (1990) and Slavin et al. (1993). They result from the shredding of the cloud gas into fragments that become too small to survive evaporation due to heat conduction. It is represented by the thin blue and green arrows to the left of our cartoon. Turbulent mixing produces intermediate temperature gas that is thermally unstable. This gas cools back to produce H gas that enters the cycle (thin green arrow). It is relevant for our scenario to note that cold gas in mixing layers preserves its dust content. It is only heated to a few 10^5 K, well below temperatures for which thermal sputtering becomes effective. Further, metals from the dust-free hot plasma brought to cool are expected to accrete on dust when gas cools and

condenses. Far-UV O line observations are needed to quantify the mass flow rate through this path of the cycle and thereby the relative importance of photoionization (arrow 1), ionizing shocks (arrow 6), and turbulent mixing with hot gas in sustaining the observed rate ($\simeq$100 $M_\odot$ yr^{-1}) of recombining H gas.

Within this dynamical picture of the postshock gas, cold molecular gas is not necessarily a mass sink. Molecular gas colder than 50 K does not contribute to the H$_2$ emission. The mass accumulated in this cold H$_2$ gas depends on the ratio between the timescale of mechanical energy dissipation (on which gas is excited by shocks through one of the red arrows 4−6) and the cooling timescale along the black arrow 3.

6. Why is H$_2$ a dominant coolant of the postshock gas?

This section sketches the energetics of the molecular gas in relation to its interaction with the background plasma. An efficient transfer of the bulk kinetic energy of the gas to turbulent motions of much lower velocities within molecular clouds is required to make H$_2$ a dominant coolant of the postshock gas. We consider that the bulk kinetic energy of the clouds drives the gas cycling through the warm/cold H , H and H$_2$ states of multiphase fragmentary clouds and feeds the cloud turbulence. This hypothesis is supported by the fact that the mechanical energy is the main energy reservoir (Sect. 2.4). The energetics of the gas are discussed within this framework.

6.1. Cloud dynamics and energy transfer

In the collision, the clouds do not share the same dynamics as the lower density intercloud gas. The clouds keep their preshock momentum and move at high velocity with respect to the background plasma. The kinetic energy recorded in the 900 km s^{-1} H$_2$ line width is dominated by the bulk motion of the H$_2$ clouds in the plasma rest frame. The turbulent velocities required within clouds to excite H$_2$ have a much smaller amplitude (relative fragment velocities up to 20 km s^{-1}). The cloud turbulence needs to be continuously sustained to balance energy dissipation. An efficient transfer of the bulk kinetic energy to low velocity turbulence of the molecular gas is required to make H$_2$ a dominant coolant of the postshock gas. Dissipation within either the hot plasma or warm atomic gas, leading to radiation at X-ray or optical wavelengths that is not efficiently absorbed by the molecular gas, has to be minor.

We are far from being able to describe how the energy transfer occurs. We can only make qualitative statements that would need to be quantified with numerical simulations in future studies. The cloud motion is subject to drag from the background flow (Murray & Lin 2004). This drag corresponds to an exchange of momentum and energy with the background plasma which drives turbulence into the clouds.

The fragmented, multiphase structure of the clouds is likely to be a main key of the energy transfer. The dynamical interaction with the background plasma flow generates relative velocities between cloud fragments because their acceleration depends on their mass and density. The relative motion between cloud fragments can lead to collisions, which results in the dissipation of kinetic energy (Sect. 4.1). This dissipation will occur preferentially in the molecular gas because it is the coldest component with the lowest sound speed. The magnetic field is likely to be important because it binds the cloud H$_2$ fragments to the lower density cloud gas which is more easily entrained

by the background plasma flow. The mass cycle between cloud gas states contributes to the energy transfer in two ways. (1) Gas cooling transfers the turbulent energy of the warm H and H to the H$_2$ gas. (2) The thermal instability which occurs when the gas cools both from 10^6 K and from 10^4 K transfers a significant fraction of the gas thermal energy to turbulent kinetic energy. Numerical simulations (Sutherland et al. 2003; Audit & Hennebelle 2005) show that the thermal instability inhibits energy-loss through radiation from the warmer gas and feeds turbulence in the cooler gas. The turbulent velocities generated by the thermal instability are found to be commensurate with the sound speed in the warmer gas and are thus supersonic for the colder gas.

6.2. Gas energetics

The turbulent energy of the cloud and the dissipated power per H$_2$ molecule may be written as

$$E_T = \frac{3}{2} m_{H_2} \sigma_T^2 \tag{11}$$

$$P_T = \frac{E_T}{t_T} = 0.24 \left(\frac{\sigma_T}{10 \text{ km s}^{-1}} \right)^2 \left(\frac{t_T}{10^5 \text{ yr}} \right)^{-1} \frac{L_\odot}{M_\odot}, \tag{12}$$

where m_{H_2} is the mass of the H$_2$ molecule and σ_T the cloud turbulent velocity dispersion. The second equation introduces an effective dissipation timescale, t_T which is often written as the ratio between the cloud size, L, and σ_T. The reference value of σ_T used in the second equation is commensurate with the shock velocities inferred from the fitting of the H$_2$ excitation diagram in Sect. 4.1.

If dissipation of turbulent energy powers the H$_2$ emission, the energy dissipation rate must be at least equal to the power radiated by H$_2$. Using the H$_2$ emission and the warm H$_2$ mass in Table 1, we estimate the luminosity to mass ratio of the warm H$_2$ gas in SQ to be 0.5 $L_\odot/M_\odot$. The dissipated power P_T may be somewhat larger if it powers the dissociative and ionizing shocks represented by the arrows 5 and 6 in Fig. 6. This calculation implies a dissipation timescale of ~5 × 10^4 yr which is not much higher than the cooling time of the lower excitation warm H$_2$ gas that accounts for the S(0) and S(1) line emission (Sect. 5.1). Cold H$_2$ gas would thus be heated by turbulent dissipation on timescales comparable to the gas cooling time. If this is correct, the cold molecular gas mass should not be much higher than the warm H$_2$ mass inferred from the *Spitzer* observations. The turbulence dissipation timescale is more than three orders of magnitude smaller than the ratio between the H$_2$ gas bulk kinetic energy and H$_2$ luminosity (Sect. 2.1). Thereby, the dissipation of the collision energy must involve a large ($\gtrsim$1000) number of cycles where H$_2$ gas fragments are accelerated and dissipate their kinetic energy in shocks.

7. Future tests of the model and open questions

In this section, we provide a few observational predictions of the model related to questions that remain open. For each point, we discuss which observations could test these predictions.

7.1. Dust emission

Dust is a key element in our scenario. It must be present in the postshock clouds for H$_2$ to form. Xu et al. (1999, 2003) present results from infrared imaging observations carried out with the

Infrared Space Observatory (ISO). Far-infrared (FIR) emission was detected in the shock region and Xu et al. (2003) proposed that it arises from large dust grains in the hot X-ray emitting plasma. Clearly, the *Spitzer* detection of molecular gas opens a new perpective on the origin of this emission. In our model, we expect that some of the thermal dust emission comes from the molecular gas. Outside the local UV enhancements associated with star formation seen in *GALEX*[4] observations (Xu et al. 2005), dust emission should appear spatially correlated with the H$_2$ emission. Given that the value of the radiation field in the shock is low ($G \sim 1-2$ G$_0$ Sect. 2.3), we expect rather faint dust emission in the SQ ridge. This accounts for the weakness of the Polycyclic Aromatic Hydrocarbons (PAH) features in the *Spitzer* spectra. Deep *Spitzer* imaging observations have been undertaken and will allow us to test this prediction. Moreover, observations with the *Herschel Space Observatory* will have the required angular resolution and sensitivity to detect the long wavelength emission of the dust in the SQ shock.

7.2. Mass budget

The *Spitzer* H$_2$ observations only trace the warm molecular gas ($T \gtrsim 150$ K). This warm gas could be physically connected to a more massive reservoir of cold H$_2$ gas. This is a major open question about the physical state of the molecular gas, as well as about the mass and energy budget. In a forthcoming paper, we will report the detection of CO(1$-$0) and (2$-$1) emision from cold molecular gas associated with the H$_2$ emitting molecular gas. The physical state of the shocked gas is likely to be different to that of GMCs in galactic disks which are gravitationally bound. It is thus not clear that the standard CO emission to H$_2$ mass conversion factor applies. *Herschel* observations of the dust emission will provide an estimate of the mass of cold gas, independent of the CO/H$_2$ ratio.

7.3. Shock energetics

Spitzer observations of the low-excitation H$_2$ rotational lines do not provide a complete budget of the kinetic energy dissipation. To constrain the present scenario, observations of both higher and lower excitation lines are required. Rovibrational H$_2$ lines would probe dissipation in more energetic shocks than those inferred from the H$_2$ pure rotational lines. If the molecular gas only experiences low-velocity MHD shocks, our model predicts a 1$-$0 S(1) line flux of 3.6×10^{-19} W m^{-2} within the aperture $\mathcal{A}$ (Table 2). This is likely to be a strict lower limit since the dynamical interaction between the gas phases may well drive higher shock velocities (Sect. 3.1). Observations of the O [63 μm] line would provide constraints on the physical state of colder molecular gas. The luminosity ratio of H$_2$ rotational lines to O depends on the shock velocity and the gas density. For the SQ ridge, the observed H$_2$ 0$-$0 S(1) line flux within the area $\mathcal{A}$ is 2×10^{-17} W m^{-2}, and our model predicts a H$_2$ 0$-$0 S(1) to O [63 μm] luminosity ratio of 2.5. The Integral Field Spectrometer of the PACS[5] instrument onboard the *Herschel* satellite should be able to detect the O [63 μm] line in one hour of integration. The spectral resolution of these observation will be a factor $\sim$5 higher than *Spitzer*. The O [63 μm] line profiles will allow us to compare the kinematics across the different temperatures of the gas. If the emission arises from multiphase

clouds where warm and cold components are mixed down to small scales, their kinematics should be the same.

7.4. Star formation in the postshock gas

Many galaxy collisions and mergers are observed to trigger IR-luminous bursts of star formation. However, the absence or weakness of spectroscopic signatures of photoionization (dust or ionized gas lines) in the center of the SQ ridge (Xu et al. 2003), where bright H$_2$ emission was detected by *Spitzer*, show that star formation does not occur in this region. Within the physical framework of dynamical interaction between gas phases described in Sects. 5 and 6, these observations suggest that most of the H$_2$ emission arises from molecular fragments that are not massive enough or not long-lived enough to collapse. Star formation may also be quenched by continuous heating of the molecular gas and/or by the magnetic pressure if the dense cloud fragments are not magnetically supercritical (Sect. 3.1). Star-forming regions possibly associated with the galaxy collision are present away from the center of the shock (Xu et al. 1999; Gao & Xu 2000; Smith & Struck 2001; Lisenfeld et al. 2002; Xu et al. 2003).

In our model, star formation may arise from the collapse of pre-existing GMCs (see Sect. 3.3). An alternative route to star formation may be the formation of gravitationally unstable postshock fragments. This second possibility has been quantified with numerical simulations that introduced the concept of turbulence-regulated star formation (Mac Low & Klessen 2004). Krumholz & McKee (2005) present an analytical description of the results of simulations, where the star formation rate depends on the Mach number of the turbulence within clouds and the ratio between their gravitational and turbulent kinetic energy. The star formation rate increases with the Mach number, but it is low even for high Mach numbers when the ratio between binding and turbulent energy is low. In the center of the SQ ridge, the star formation may be low because the average gas density is low (see Table 1), even if the amount of turbulent energy is high. The low gas density and large-scale dynamical context (high-velocity dispersion) does not favor the formation of gravitationnally bound molecular clouds, such as galactic GMCs.

8. Conclusions

Spitzer Space Telescope observations led to the surprising detection of H$_2$ luminous extragalactic sources whose mid-infrared spectra are dominated by molecular hydrogen line emission. The absence or weakness of dust features or lines of ionized gas suggests the presence of large quantities of warm molecular gas with no or very little star formation. This work focuses on one of these H$_2$ luminous galaxies: the Stephan's Quintet (SQ) galaxy-wide shock, created by the collision between an intruding galaxy and a tidal arm at a relative speed $\sim$1000 km s^{-1}. SQ observations place molecular gas in a new context where one has (1) to account for the presence of H$_2$ in a galaxy halo; (2) to characterize its physical state and (3) to describe its role as a cooling agent of an energetic phase of galaxy interaction. The aim of the paper is to answer three main questions: *(i) Why is there H$_2$ in the postshock gas? (ii) How can we account for the H$_2$ excitation? (iii) Why is H$_2$ the dominant coolant?* We summarize the main results of our work along these three points and present perspectives for future studies.

We presented and quantified a scenario where H$_2$ forms out of shocked gas. H$_2$ formation results from the density structure of the preshock gas. The collision velocity, $\sim$600 km s^{-1} in the

---

[4] Galaxy evolution explorer.
[5] Photodetector Array Camera and Spectrometer.

centre of mass frame of the collision, is the shock velocity in the low density ($n_H \lesssim 10^{-2}$ cm^{-3}) volume-filling gas. This produces a ~5×10^6 K, dust-free, X-ray emitting plasma. The pressure of this background plasma drives slower shocks into denser gas within clouds. Gas heated to temperatures lower than ~10^6 K keeps its dust and has time to cool within the 5×10^6 yr collision age. Because the postshock pressure is too high for the warm neutral medium to be thermally stable, the gas cools to cold neutral medium temperatures, condenses and becomes molecular. We show that for a wide range of postshock pressures, as well as realistic preshock cloud sizes and densities, the H$_2$ formation timescale is shorter than the collision age and also than the turbulent mixing timescale of the warm gas with the background plasma.

Observations show that the H$_2$ non-thermal kinetic energy is the dominant energy reservoir. It is higher than the thermal energy of the plasma. We propose that the H$_2$ emission is powered by the dissipation of this kinetic energy. The H$_2$ excitation can be reproduced by a combination of low velocity (~5 to 20 km s^{-1}) MHD shocks within dense ($n_H > 10^3$ cm^{-3}) H$_2$ gas. In this interpretation, the pressure of the warm H$_2$ gas is much higher than the ambient pressure set by the background plasma. Such a pressure enhancement is required to account for the higher excitation H$_2$ S(3) and S(5) rotational lines. For this shock velocity range, the warm H$_2$ pressure in the shocks is ~$0.5-5 \times 10^8$ K cm^{-3}, 2$-$3 orders of magnitude higher than the ambient pressure (2×10^5 K cm^{-3}).

The thermal, Rayleigh-Taylor and Kelvin-Helmhotz instabilities contribute to produce fragmentary postshock clouds where H$_2$, H and H gas are mixed on small scales and embedded in the hot plasma. In our scenario, the H$_2$ excitation is related to the dynamical interaction between gas phases which drives an energy transfer between these phases. An efficient transfer of the kinetic energy associated with the bulk displacement of the clouds to turbulent motions of much lower velocity within molecular gas, is required to make H$_2$ a dominant coolant of the postshock gas.

We present a global view of the postshock gas evolution that connects H$_2$, warm H and H gas emission to mass cycling between these gas components. Within this dynamical picture of the postshock gas, cold molecular gas is not necessarily a mass sink. The fact that there is no star formation in the shocked region where H$_2$ is detected suggests that molecular fragments are not long-lived enough to collapse and become gravitationally unstable.

This global description provides a physical framework of general relevance for the interpretation of observational signatures, in particular H$_2$ emission, of mechanical energy dissipation in multiphase gas. This study highlights the need to take into account H$_2$ formation and the mechanical energy dissipation within cold molecular gas in the physics of turbulent mixing of gas phases.

Future observations of Stephan's Quintet will contribute to testing the proposed interpretation and better characterize some of its aspects. Some of these observations have been briefly discussed. Further work is needed to explore the impact of key physical parameters (such as gas pressure, radiation field, mechanical energy deposition, thermal to mechanical energy ratio, metallicity) on gas evolution and on energy dissipation, to investigate the diversity of relevant galaxy-wide environments and mechanical energy sources (gas accretion, galaxy interaction and feedback from starburst and active galactic nuclei). The analytical approach presented here should be pursued to compute how the timescales of the relevant physical processes depend on these parameters. The non-linear dynamical interaction between gas phases, in particular the driving of cloud turbulence, can only be investigated quantitatively through numerical simulations.

References

Appleton, P. N., Xu, K. C., Reach, W., et al. 2006, ApJ, 639, L51
Audit, E., & Hennebelle, P. 2005, A&A, 433, 1
Begelman, M. C., & Fabian, A. C. 1990, MNRAS, 244, 26P
Bland-Hawthorn, J., Sutherland, R., Agertz, O., & Moore, B. 2007, ApJ, 670, L109
Borkowski, K. J., & Dwek, E. 1995, ApJ, 454, 254
Crutcher, R., Heiles, C., & Troland, T. 2003, 614, 155
Crutcher, R. M. 1999, ApJ, 520, 706
Dalgarno, A., Yan, M., & Liu, W. 1999, ApJS, 125, 237
de Avillez, M. A., & Breitschwerdt, D. 2005a, A&A, 436, 585
de Avillez, M. A., & Breitschwerdt, D. 2005b, ApJ, 634, L65
Dib, S., Bell, E., & Burkert, A. 2006, ApJ, 638, 797
Draine, B. T., & Li, A. 2007, ApJ, 657, 810
Draine, B. T., & McKee, C. F. 1993, ARA&A, 31, 373
Draine, B. T., & Salpeter, E. E. 1979, ApJ, 231, 77
Dwek, E. 1986, ApJ, 302, 363
Dwek, E. 1987, ApJ, 322, 812
Dwek, E., & Werner, M. W. 1981, ApJ, 248, 138
Dwek, E., Foster, S. M., & Vancura, O. 1996, ApJ, 457, 244
Dyson, J. E., Pittard, J. M., Meaburn, J., & Falle, S. A. E. G. 2006, A&A, 457, 561
Egami, E., Rieke, G. H., Fadda, D., & Hines, D. C. 2006, ApJ, 652, L21
Falgarone, E., Verstraete, L., Pineau Des Forêts, G., & Hily-Blant, P. 2005, A&A, 433, 997
Ferland, G. J., Fabian, A. C., Hatch, N. A., et al. 2008, MNRAS, 386, L72
Flower, D. R., & Pineau des Forêts, G. 2003, MNRAS, 343, 390
Flower, D. R., Le Bourlot, J., Pineau des Forêts, G., & Cabrit, S. 2003, MNRAS, 341, 70
Fragile, P. C., Murray, S. D., Anninos, P., & van Breugel, W. 2004, ApJ, 604, 74
Gao, Y., & Xu, C. 2000, ApJ, 542, L83
Glover, S. C. O., & Mac Low, M.-M. 2007, ApJ, 659, 1317
Gnat, O., & Sternberg, A. 2007, ApJS, 168, 213
Gry, C., Boulanger, F., Nehmé, C., et al. 2002, A&A, 391, 675
Habing, H. J. 1968, Bull. Astron. Inst. Netherlands, 19, 421
Heckman, T. M., Baum, S. A., van Breugel, W. J. M., & McCarthy, P. 1989, ApJ, 338, 48
Heiles, C., & Troland, T. H. 2005, ApJ, 624, 773
Hennebelle, P., Banerjee, R., Vázquez-Semadeni, E., Klessen, R. S., & Audit, E. 2008, A&A, 486, L43
Higdon, S. J. U., Armus, L., Higdon, J. L., Soifer, B. T., & Spoon, H. W. W. 2006, ApJ, 648, 323
Hollenbach, D., & McKee, C. F. 1979, ApJS, 41, 555
Jog, C. J., & Solomon, P. M. 1992, ApJ, 387, 152
Jones, A. P., Tielens, A. G. G. M., Hollenbach, D. J., & McKee, C. F. 1994, ApJ, 433, 797
Joseph, R. D., Wade, R., & Wright, G. S. 1984, Nature, 311, 132
Klein, R. I., McKee, C. F., & Colella, P. 1994, ApJ, 420, 213
Krumholz, M. R., & McKee, C. F. 2005, ApJ, 630, 250
Le Bourlot, J., Pineau des Forêts, G., & Flower, D. R. 1999, MNRAS, 305, 802
Lisenfeld, U., Braine, J., Duc, P.-A., et al. 2002, A&A, 394, 823
Mac Low, M.-M., & Klessen, R. S. 2004, Rev. Mod. Phys., 76, 125
Mac Low, M.-M., McKee, C. F., Klein, R. I., Stone, J. M., & Norman, M. L. 1994, ApJ, 433, 757
Mac Low, M.-M., Balsara, D. S., Kim, J., & de Avillez, M. A. 2005, ApJ, 626, 864
Mathis, J. S., Rumpl, W., & Nordsieck, K. H. 1977, ApJ, 217, 425
McKee, C. F., & Cowie, L. L. 1975, ApJ, 195, 715
Mellema, G., Kurk, J. D., & Röttgering, H. J. A. 2002, A&A, 395, L13
Moles, M., Sulentic, J. W., & Marquez, I. 1997, ApJ, 485, L69
Murray, S. D., & Lin, D. N. C. 2004, ApJ, 615, 586
Nakamura, F., McKee, C. F., Klein, R. I., & Fisher, R. T. 2006, ApJS, 164, 477

Nehmé, C., Gry, C., Boulanger, F., et al. 2008, A&A, 483, 471

Ogle, P., Antonucci, R., Appleton, P. N., & Whysong, D. 2007, ApJ, 668, 699

O'Sullivan, E., Giacintucci, S., Vrtilek, J. M., Raychaudhury, S., & David, L. P. 2008, arXiv e-prints

Padoan, P., Nordlund, A., & Jones, B. J. T. 1997, MNRAS, 288, 145

Passot, T., & Vázquez-Semadeni, E. 1998, Phys. Rev. E, 58, 4501

Pope, E. C. D., Hartquist, T. W., & Pittard, J. M. 2008, MNRAS, 389, 1259

Rigopoulou, D., Kunze, D., Lutz, D., Genzel, R., & Moorwood, A. F. M. 2002, A&A, 389, 374

Rodríguez-Fernández, N. J., Martín-Pintado, J., Fuente, A., et al. 2001, A&A, 365, 174

Roussel, H., Helou, G., Hollenbach, D. J., et al. 2007, ApJ, 669, 959

Slavin, J. D. 2006, in BAAS, 38, 114

Slavin, J. D., Shull, J. M., & Begelman, M. C. 1993, ApJ, 407, 83

Smith, B. J., & Struck, C. 2001, AJ, 121, 710

Smith, R. K., Krzewina, L. G., Cox, D. P., Edgar, R. J., & Miller, W. W. I. 1996, ApJ, 473, 864

Stephan, M. 1877, CR Acad. Sci. Paris, 84, 641

Sulentic, J. W., Rosado, M., Dultzin-Hacyan, D., et al. 2001, AJ, 122, 2993

Sutherland, R. S., & Dopita, M. A. 1993, ApJS, 88, 253

Sutherland, R. S., Bicknell, G. V., & Dopita, M. A. 2003, ApJ, 591, 238

Tielens, A. G. G. M., McKee, C. F., Seab, C. G., & Hollenbach, D. J. 1994, ApJ, 431, 321

Tine, S., Lepp, S., Gredel, R., & Dalgarno, A. 1997, ApJ, 481, 282

Trinchieri, G., Sulentic, J., Breitschwerdt, D., & Pietsch, W. 2003, A&A, 401, 173

Trinchieri, G., Sulentic, J., Pietsch, W., & Breitschwerdt, D. 2005, A&A, 444, 697

Vazquez-Semadeni, E. 1994, ApJ, 423, 681

Weingartner, J. C., & Draine, B. T. 2001, ApJ, 548, 296

Williams, B. A., Yun, M. S., & Verdes-Montenegro, L. 2002, AJ, 123, 2417

Xu, C., Sulentic, J. W., & Tuffs, R. 1999, ApJ, 512, 178

Xu, C. K., Iglesias-Páramo, J., Burgarella, D., et al. 2005, ApJ, 619, L95

Xu, C. K., Lu, N., Condon, J. J., Dopita, M., & Tuffs, R. J. 2003, ApJ, 595, 665

Appendix A: Modeling dust evolution

Interstellar dust plays a major role in the evolution of the post-shock gas because its survival is required for H_2 formation. For a constant dust-to-gas mass ratio, the dust dominates the cooling efficiency of the gas at high ($T > 10^6$ K) temperatures (Dwek 1987), but for such high temperatures, the timescale for dust destruction is shorter than the gas cooling time (Smith et al. 1996). This Appendix details how the evolution of the dust-to-gas mass ratio in the postshock gas is calculated. This calculation is coupled to that of the gas cooling, detailed in Appendix B.

The dominant dust destruction process depends on the shock velocity. In this study, we consider the effect of thermal and inertial sputtering by grain-ion collisions. This is the dominant mode of destruction in a hot ($\sim 10^6 - 10^8$ K) plasma, resulting from fast ($100 - 1000$ km s^{-1}) intergalactic shocks (e.g. Draine & Salpeter 1979; Dwek et al. 1996).

It is assumed that dust grains have an initial radius equal to the effective (mean) radius of $a_{\rm eff} = 0.05$ μm. This radius is calculated from the MRN dust size distribution (Sect. B.1). At each time step, the fraction of dust remaining in the gas $f_{\rm dust}$, is computed in parallel to the postshock gas cooling:

$$f_{\rm dust} = \left(\frac{a}{a_{\rm eff}}\right)^3 \text{ with } a = a_{\rm eff} - \int_{t_0}^t \dot{a}\,{\rm d}t, \qquad (A.1)$$

where $\dot{a} = {\rm d}a/{\rm d}t$. For a shock velocity $V_s > 300$ km s^{-1}, thermal sputtering dominates over inertial sputtering, so we ignore inertial sputtering. In this case, the grain sputtering rate is nearly constant for $T \gtrsim 3 \times 10^6$ K and strongly decreases at lower temperatures (Draine & Salpeter 1979; Tielens et al. 1994; Dwek et al. 1996). The rate of decrease in grain size is given by

$$\frac{{\rm d}a}{{\rm d}t} = \frac{m_{\rm sp}}{2\rho_0} n_{\rm H} \sum A_i \langle Y_i v \rangle, \qquad (A.2)$$

where $m_{\rm sp}$ and ρ_0 are the average mass of the sputtered atoms and the density of the grain material, A_i the abundance of impacting ion i and Y_i is the sputtering yield[6] of ion i. The quantity $\langle Y_i v \rangle$ is the average of the impacting ion velocities v times the yield over the Maxwellian distribution. The right hand side of this equation is computed from the results given in Tielens et al. (1994).

For $V_s < 300$ km s^{-1}, we integrate the equation of deceleration of the dust grains with respect to the gas

$$\frac{{\rm d}v_{\rm g}}{{\rm d}t} = -\frac{\beta \pi a^2 \rho v_{\rm g}^2}{m}, \qquad (A.3)$$

where $v_{\rm g}$ is the grain velocity with respect to the gas, m and a are its mass and radius, ρ is the gas density, and β is the enhancement of the collisional drag in a plasma relative to that of a neutral medium. The initial grain velocity is set to $3/4$ of the shock velocity (Jones et al. 1994). We take $\beta = 1$, which maximizes the dust destruction (see Borkowski & Dwek 1995, for details). Therefore, our computation of the dust survival is conservative. When inertial sputtering is the dominant destruction process, the erosion rate is given by (Tielens et al. 1994)

$$\frac{{\rm d}a}{{\rm d}t} = \frac{m_{\rm sp}}{2\rho_0} v_{\rm g} n_{\rm H} \sum A_i Y_i. \qquad (A.4)$$

By integrating these differential equations, the radius of the dust grains as a function of their velocity has been deduced (see Borkowski & Dwek 1995, for a complete parametrization of ${\rm d}a/{\rm d}t$ in the case of inertial sputtering).

---

[6] The yield is the number of atoms ejected from the grain surface per incident particle.
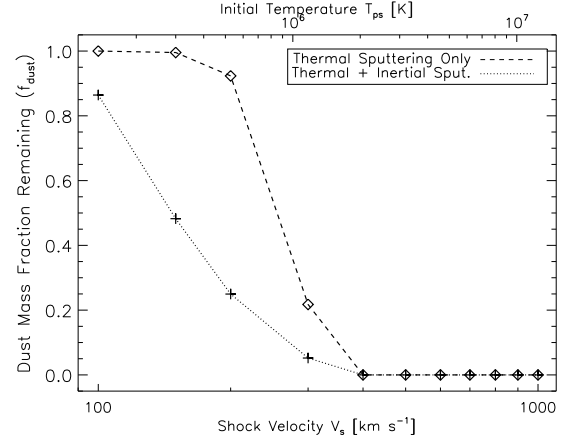

Fig. A.1. Dust mass fraction as a function of the initial (postshock) temperature, after isobaric cooling to 10^4 K. The pressure is fixed to $P_{\rm ps}/k_{\rm B} = 2.3 \times 10^5$ [cm^{-3} K]. The dotted line shows the result of the model which includes both inertial and thermal sputtering. As a comparison, the dashed line only shows the effect of thermal sputtering.

Figure A.1 shows the dust mass fraction remaining in the gas after isobaric cooling from the postshock temperature $T_{\rm ps}$ to 10^4 K as a function of the shock velocity. The dotted line includes both thermal and inertial sputtering. For comparison, the dashed line only includes dust destruction by thermal sputtering. Our calculation for thermal sputtering with a single grain size ($a_{\rm eff} = 0.05$ μm) is in very good agreement with the study by Smith et al. (1996) who used a grain size distribution. For $T_{\rm ps} > 2 \times 10^6$ K, i.e. $V_s > 400$ km s^{-1}, most of the dust is destroyed before the gas has cooled to 10^4 K. The gas that is heated to less than $\sim 10^6$ K keeps a major part of its dust content and may therefore form H_2.

Appendix B: Modeling the cooling of hot gas

This Appendix details how we model the cooling of the hot gas. The cooling functions used in the calculations are presented in Sect. B.1. The results are discussed in Sect. B.2.

The time dependence of both the gas temperature and the dust-to-gas mass ratio has been calculated. We start from gas at an initial postshock temperature $T_{\rm ps}$ with a galactic dust-to-gas ratio, a solar metallicity and assume equilibrium ionization. From a range of postshock temperatures up to 10^4 K, the isobaric gas cooling is calculated by integrating the energy balance equation which gives the rate of decrease of the gas temperature:

$$\frac{5}{2} k_{\rm B} \frac{{\rm d}T}{{\rm d}t} = -\mu\, n_{\rm e} \left(f_{\rm dust}\, \Lambda_{\rm dust} + \Lambda_{\rm gas} \right), \qquad (B.1)$$

where μ is the mean particle weight ($\mu = 0.6$ a.m.u for a fully ionized gas), $n_{\rm e}$ is the electron density, $k_{\rm B}$ the Boltzman constant, $f_{\rm dust}$ the dust-to-gas mass ratio, $\Lambda_{\rm dust}$ and $\Lambda_{\rm gas}$ are respectively the dust and gas cooling efficiencies per unit mass of dust and gas, respectively.

The time-dependent total cooling function is the sum of the dust cooling (weighted by the remaining fraction of dust mass, see Appendix A) and the gas cooling contributions. We neglect the effect of the magnetic field on the compression of the gas. This assumption is in agreement with observations and numerical simulations, provided that the gas is not gravitationally
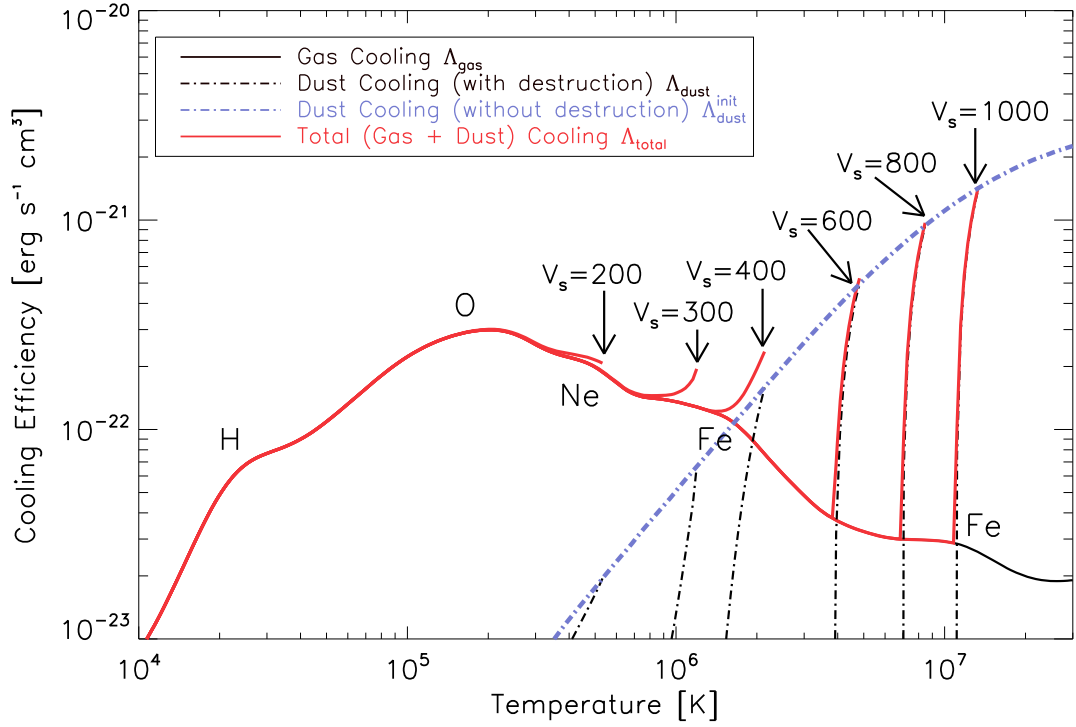
Fig. B.1. Time-dependent cooling efficiency [erg cm^3 s^{-1}] as a function of temperature during the gas cooling, for different initial conditions. The blue dashed line, $\Lambda_{\text{dust}}^{\text{init}}(T)$, represents the *initial* cooling function of the gas including the dust contribution, computed for a MRN interstellar dust size distribution (0.01 to 0.25 μm dust particles). The black dashed lines are the dust cooling functions for different shock velocities (i.e. different initial temperatures) which take into account the destruction by sputtering during the cooling. The cooling function due to atomic processes, $\Lambda_{\text{gas}}(T)$, is displayed for an isobaric and non-equilibrium (time-dependent) cooling, and for solar metallicities ($Z = 1$). The dominant cooling elements at various temperatures are indicated on the curves. The red lines are the total cooling functions, $\Lambda_{\text{total}} = \Lambda_{\text{dust}} + \Lambda_{\text{gas}}$, for different initial temperatures or shock velocities. The shock velocities are indicated in km s^{-1}. Their starting points are indicated by the arrows.

bound (see Sect. 3.1 for details and references). The thermal gas pressure P_{th} is constant in the calculations.

B.1. Physical processes and cooling functions

B.1.1. Cooling by atomic processes in the gas phase

The calculations of the non-equilibrium (time-dependent) ionization states and isobaric cooling rates of a hot, dust-free gas for the cooling efficiency *by atomic processes* has been taken from Gnat & Sternberg (2007). The electronic cooling efficiency, Λ_{gas}, includes the removal of electron kinetic energy via recombination with ions, collisional ionization, collisional excitation followed by line emission, and thermal bremsstrahlung. Λ_{gas} is shown in Fig. B.1 (black solid line[7]) and reproduces the standard "cosmic cooling curve" presented in many papers in the literature (e.g. Sutherland & Dopita 1993). Note that most of the distinct features that appear for the ionization equilibrium case are smeared out in the nonequilibrium cooling functions and that the nonequilibrium abundances reduce the cooling efficiencies by factors of 2 to 4 (Sutherland & Dopita 1993; Gnat & Sternberg 2007). The chemical species that dominate the gas cooling are indicated in Fig. B.1 near the Λ_{gas} cooling curve. Over most of the temperature range, the radiative energy losses are dominated by electron-impact excitation of resonant line transitions

in metal ions. At $T \simeq 2 \times 10^4$ K, the cooling is mainly due to the collisional excitation of hydrogen Lyα lines. For $T \gtrsim 10^7$ K, the bremsstrahlung (free-free) radiation becomes dominant.

B.1.2. Cooling by dust grains

Following the method of Dwek (1987), the cooling function of the gas *by the dust* via electron-grain collisions has been calculated. We adopt an MRN (Mathis et al. 1977) size distribution of dust particles, between 0.01 to 0.25 μm in grain radius. All the details can be found in Dwek (1986, 1987), and we briefly recall here the principles of this calculation. For temperatures lower than 10^8 K, electron – dust grain collisions cool the gas with a cooling efficiency, $\Lambda_{\text{dust}}(T)$ [erg s^{-1} cm^3], given by:

$$\Lambda_{\text{dust}}^{\text{init}}(T) = \frac{\mu \, m_H \, Z_d}{\langle m_d \rangle} \left(\frac{32}{\pi \, m_e} \right)^{1/2} \pi (k_B T)^{3/2} \int a^2 h(a, T) f(a) \, \mathrm{d}a \quad \text{(B.2)}$$

where Z_d is the dust-to-gas mass ratio, m_H the mass of an hydrogen atom, m_e the mass of electron, μ the mean atomic weight of the gas (in amu), $f(a)$ the grain size distribution function (normalized to 1) in the dust size interval, $\langle m_d \rangle$ the size-averaged mass of the dust, and $h(a, T)$ the effective grain heating efficiency (see e.g. Dwek & Werner 1981; Dwek 1987). This *initial* cooling efficiency is shown with the *blue* dashed line of Fig. B.1 for an MRN dust size distribution and the solar neighbourhood dust-to-gas mass ratio of 7.5×10^{-3}.

---

[7] The black solid line (gas cooling efficiency) is merged with the total cooling curve (red line) for $T \lesssim 10^7$ K.
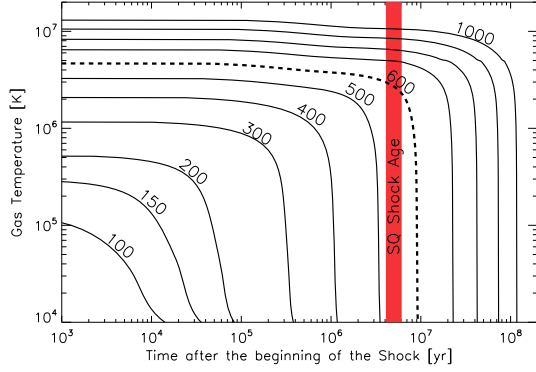
Fig. B.2. Evolution of the gas temperature with time at constant pressure, from the postshock temperature to 10^4 K for different shock velocities (indicated on the curves in km s^{-1}). The dashed line is for $V_s = 600$ km s^{-1}, which corresponds to the SQ hot (5×10^6 K) plasma. The red vertical thick line at 5×10^6 yr indicates the collision age.
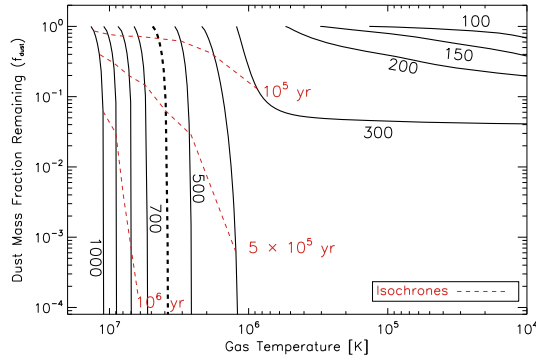

Fig. B.3. Dust mass fraction remaining as a function of the gas temperature, from the postshock temperature to 10^4 K for different shock velocities V_s [km s^{-1}] labelled on the curves. The gas cooling is isobaric, and the thermal gas pressure is set to the average pressure of the SQ hot gas $P_{ps}/k_B \simeq 2.3 \times 10^5$ cm^{-3} K. The dashed line is for $V_s = 600$ km s^{-1}. The red dashed lines are the cooling isochrones at 10^5, 5×10^5 and 10^6 yr.

The comparison in Fig. B.1 of the *initial* cooling efficiency by the dust, $\Lambda_{dust}^{init}(T)$, and by atomic processes, Λ_{gas}, shows that, for a dust-to-gas mass ratio of $Z_d = 7.5 \times 10^{-3}$, the dust is initially the dominant coolant of the hot postshock gas for $T \gtrsim 10^6$ K. During the gas cooling, we calculate how much the grains are eroded and deduce the mass fraction of dust that remains in the cooling gas as a function of the temperature. The total cooling function (*red* curves in Fig. B.1) is deduced by summing the gas and dust cooling rates. We show different cooling efficiencies for different initial temperatures, corresponding to different shock velocities.

B.2. Results: evolution of the hot gas temperature and dust survival

The temperature profiles are shown in Fig. B.2 for different shock velocities (100 to 1000 km s^{-1}), which corresponds to a range of preshock densities of ~0.2 to 2×10^{-3} cm^{-3} for a postshock pressure of 2×10^5 K cm^{-3}.

Figure B.3 shows the remaining fraction of dust mass as a function of the gas temperature. In this plot, the thermal gas pressure is constant and equals the measured average thermal
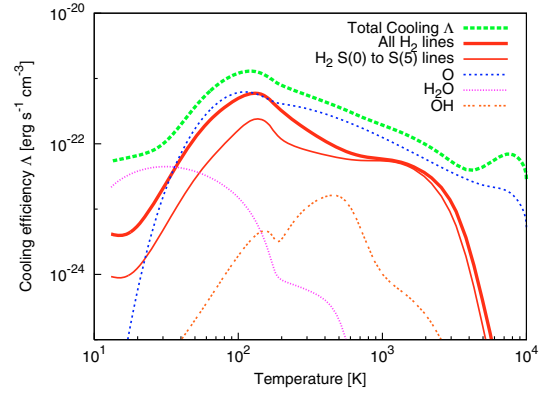
Fig. C.1. Cooling efficiency [erg s^{-1} cm^{-3} by H$_2$ S(0) to S(5) rotational lines (thin red line) and all H$_2$ lines (thick red line) for the gas cooling at constant thermal pressure. Initially, the gas is ionized (see text for details), the density is $n_H = 10$ cm^{-3} and temperature is $T = 10^4$ K. For comparison, the local cooling rate of all the coolants is shown (green dashed line).

gas pressure of the Stephan's Quintet hot gas $P_{ps}/k_B \simeq 2 \times 10^5$ [cm^{-3} K]. This plot illustrates a dichotomy in the evolution of the dust to gas mass ratio. On the top right side, a significant fraction of the dust survives in the gas, whereas on the left side, almost all the dust is destroyed on timescales shorter than the collision age (5×10^6 yr). In the intercloud gas shocked at high velocities ($V_s > 400$ km s^{-1}), the dust mass fraction drops rapidly. In clouds where the gas is shocked at $V_s < 300$ km s^{-1}, the gas retains a large fraction of its dust content (>20%). For the gas that is heated to temperatures $T > 10^6$ K, the dust lifetime is shorter than the gas cooling time and most of the dust is destroyed. At lower temperatures ($T < 10^6$ K), the dust cooling rate is lower than the gas cooling rate. Then, the dust never contributes significantly to the cooling of the postshock gas. This last result is in agreement with the earlier study by Smith et al. (1996).

Appendix C: Modeling H$_2$ formation

C.1. Cooling function for $T < 10^4$ K

This section describes the cooling of clouds below 10^4 K and H$_2$ formation. We use the chemistry, and the atomic and molecular cooling functions described in Flower et al. (2003) and references therein. The principal coolants are O, H$_2$, H$_2$O and OH (see Fig. 3 in Flower et al. 2003). The time evolution of the gas temperature and composition is computed at a fixed thermal gas pressure equal to that of the intercloud gas (2×10^5 K cm^{-3}). The metallicity and the gas-to-dust mass ratio are assumed to be the solar neighbourhood values. The initial ionization state of the gas is the out-of-equilibrium value resulting from cooling from higher temperatures (Gnat & Sternberg 2007). We assume a standard value for the cosmic ray ionization rate of $\zeta = 5 \times 10^{-17}$ s^{-1} and the UV radiation field is not considered here (see Sect. 2.2). The initial temperature is 10^4 K and density $n_H = 10$ cm^{-3}. Hydrogen is initially highly ionized. During the postshock gas cooling, hydrogen recombination occurs, the neutral gas cools, H$_2$ starts to form and further cools and condenses the gas.

Figure C.1 presents the contribution of H$_2$ line emission to the total cooling function as a function of the gas temperature.
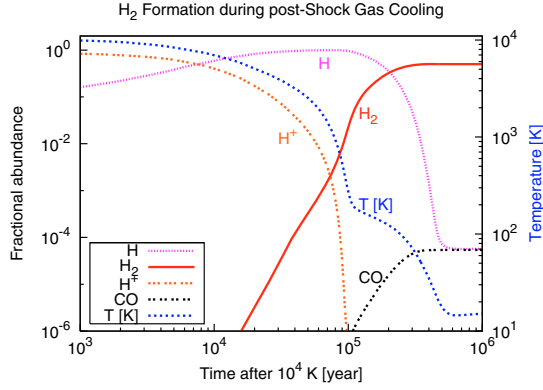
Fig. C.2. Isobaric cooling of the postshock gas and H$_2$ formation. The temperature (blue line, labeled on the right side) and abundance profiles relative to n_H are shown. The initial conditions and model are the same as in Fig. C.1. The final density of the molecular gas is $n(H_2) = 2 \times 10^4$ cm^{-3}, for a temperature of ~10 K.

It shows the cooling functions of *(i)* all the H$_2$ lines (thick red line); *(ii)* the H$_2$ rotational lines S(0) to S(5) detected by *Spitzer* (thin red line); *(iii)* the total cooling efficiency in which all elements are included (green dashed line). The cooling efficiencies of some other major coolants (O in blue, H$_2$O in purple, and OH in orange) are also indicated. H$_2$ excitation at low temperatures (~10 K) is dominated by the contribution associated with H$_2$ formation.

C.2. H$_2$ formation

The chemical abundance profiles in the postshock gas are illustrated in Fig. C.2 as a function of time, for the same model as in Fig. C.1 From the time when the gas attains 10^4 K, it takes $\sim 3 \times 10^5$ yrs to form H$_2$. This time scales inversely with the dust-to-gas mass ratio. The H$_2$ formation gives rise to a shoulder in the temperature profile around 200 K. At this point, the energy released by H$_2$ formation is roughly balanced by the cooling due to atomic oxygen (see Fig. 3 in Flower et al. 2003).

Chapter 6

Mapping the mid-IR line cooling in Stephan's Quintet

It's just like when you've got some coffee that's too black, which means it's too strong. What do you do? You integrate it with cream, you make it weak. But if you pour too much cream in it, you won't even know you ever had coffee. It used to be hot, it becomes cool. It used to be strong, it becomes weak. It used to wake you up, now it puts you to sleep.

Malcolm X

Abstract

The observations of H_2 rotational line emission from the Stephan's Quintet (SQ) galaxy collision presented in chapter 5 are extended to a complete, and high signal-to-noise spectral mapping of the SQ giant shock. We find that the H_2 line emission is extended over the full ridge ($\approx 15 \times 35\ kpc^2$). I present these recent observations and the new astrophysical questions they raise, in particular on the dynamical history of the group. I thus introduce some observational background needed to elucidate these questions. Then, I present an update of the mass and energy budgets of the galaxy collision based on these new data. I also performed a complete re-analysis of the new data with shock models, and discuss the issue of H_2 excitation in the shock. This analysis is complemented by the use of fast shocks models to interpret the fine-structure line emission from the ionized gas.

Contents

6.1 Introduction

The interpretation of H_2 observations presented in the previous chapter (chap. 5) and in Guillard et al. (2009c) (paper I) is based on the single-pointing observations by Appleton et al. (2006),

who first detected H_2 emission from the Stephan's Quintet (henceforth SQ) shock. The spectacular result of Appleton et al. (2006) led us to propose a new set of *Spitzer* observations to obtain a full mid-IR spectral map of the X-ray bright shock region. I have participated in the preparation of this proposal (P.I.: P.N. Appleton) by performing the model calculations that support it. It was accepted and observed in December 2007 and January 2008. Both mid-infrared (mid-IR) imaging and spectroscopy were performed.

These new observations were reduced by M. Cluver and P. Appleton at the SSC and the results are presented in Cluver et al. (2009) (hereafter paper II). I have participated to the interpretation of these data and to the writing of this paper. Thanks to this new *IRS* spectral mapping of the SQ ridge, we have now an almost complete census of the mid-IR warm H_2 emission, fine-structure line and dust emission in the SQ shock. These observations allow to complement the mass and energy budget of the collision presented in paper I, which was resticted to a small area of the giant shock. This energy budget is the first step to understand the mechanisms that produce the high H_2 luminosity over such a large area ($\approx 40 \times 15$ kpc). This leads me to do a complete re-analysis of the H_2 data, based on my previous interpretation work. I have also complemented this work by an interpretation of the emission from the ionized gas in the group (optical and fine-structure mid-IR lines).

This chapter extends and re-visits the analysis presented in chapter 5 and in paper I for the full area of the SQ shock. In sect. 6.2 I briefly present the results of the spectral maps, focussing on H_2. Obviously, these new observations raise new astrophysical questions, formulated in sect. 6.2.2. In sect. 6.2.3, I present an updated mass and energy budget in the SQ shock, similar to that presented in paper I, but for the full extension of the ridge. Section 6.3 describes past observations of SQ to set the astrophysical observational context, focusing on the complex dynamics of the galaxy group. This background seems crucial for the understanding of our new set of *Spitzer* observations. Then I extend my modeling of the H_2 excitation for the whole ridge (sect. 6.4). Pursuing the work of paper I, I discuss the dynamical picture of the energy transfer between the ISM phases that emerges from this interpretation, and the physical mechanisms that may explain how the bulk kinetic energy of the galaxy collision is transfered into the warm H_2 (sect. 6.5). Then I complement the H_2 analysis by a study of the excitation of the mid-IR fine structure lines in sect. 6.6. Section 6.7 comments about the AGN member of the group, NGC 7319, which shows an interesting H_2 feature revealed by our new *IRS* spectral maps. A quick summary and concluding remarks end this chapter (sect. 6.8).

The paper II is reproduced at the end of this chapter because it contains the figures I will rely on in this chapter, and a lot of information that I have intentionally not repeated in this manuscript.

6.2   Spectral mapping of the H_2 line emission in the SQ shock

The *Spitzer IRS* mapping strategy is summarized in Fig. 6.1. The SL and LL modules were used to map the entire shock region, the SL slits being oriented along the shock structure and the LL slits perpendicular to it. The spectral mapping aims at spatially resolving the H_2 and dust across the shock.

6.2.1 H_2 spatial distribution

The new spectral maps are reported in Cluver et al. (2009) (hereafter paper II). We summarize here the main observational results, focusing on the distribution and characteristics of the H_2 emission in
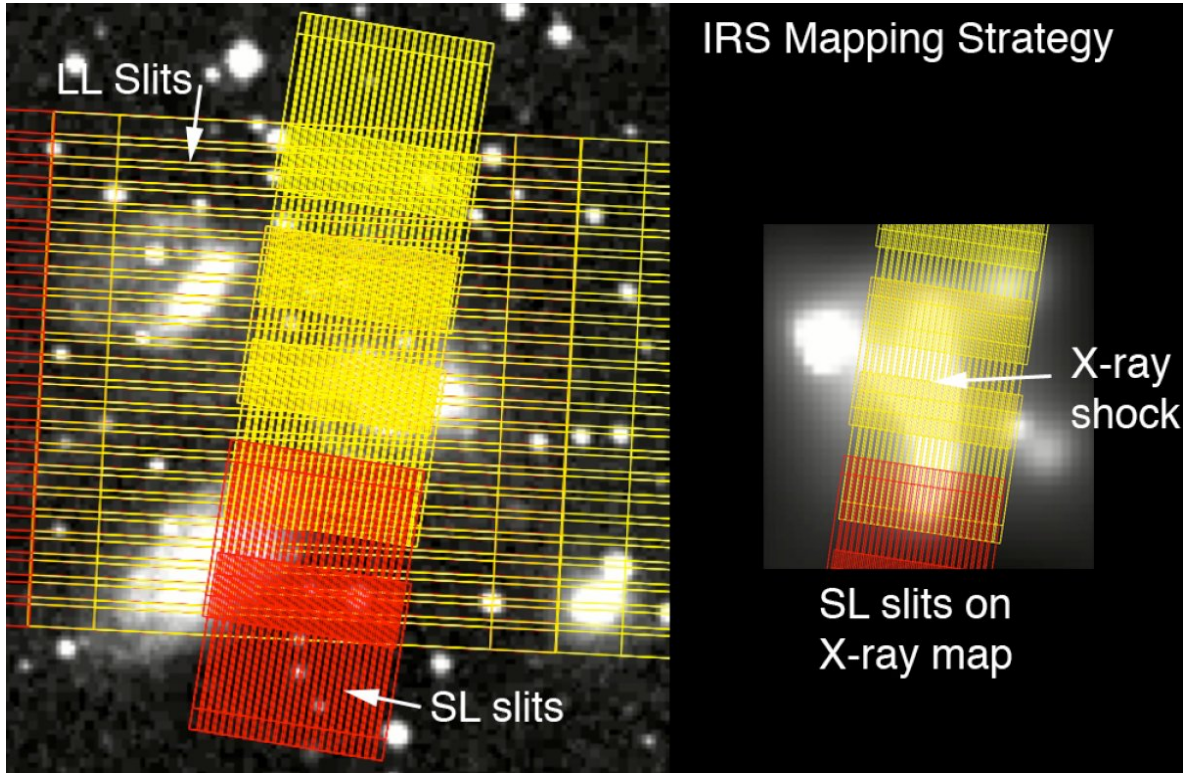
Figure 6.1: The IRS mapping strategy. *Left Panel:* The SL and LL slits superimposed over the DSS image of Stephan's Quintet. The SL map covers most of the intruder galaxy NGC 7318b. *Right Panel:* The same SL slit-mapping superimposed on the Chandra image of the shock. The shock is the vertical X-ray structure. NGC 7318b does not show up in the X-ray image, although the brighter of the two X-ray sources just on the right-edge of the SL region is associated with NGC 7318a.

the SQ intra-group. The main results regarded the mapping of other mid-IR fine-structure lines are discussed later in sect. 6.6.2.

A remarkably extended H₂ emission!

Fig. 2 of paper II shows contours of the H_2 S(0)-S(5) line emission overlaid on an R-band image. The S(0) and S(1) lines were mapped by the LL modules, while S(2) - S(5) transitions were mapped by the SL modules of the *IRS*. These spectral maps show an extended emission from a giant filament ($\sim$ 40 kpc long) oriented north-south along the direction of the *"main shock"*. This "H_2 ridge" spatially correlates very well with the radio or the X-ray emission. This provides an unambigious link between the origin of the H_2 emission, and a large-scale high-speed shock generated by the galaxy collision between NGC 7318b and the tidal tail of NGC 7319. We define the main shock aperture as a $\mathcal{A}_{MS} = 77'' \times 30''$ rectangular aperture, corresponding to $\sim 13.7 \times 35.1$ kpc^2, centered on the coordinates $\alpha = 22$h35m59.6s, $\delta = +33°58'05.7''$.

H_2 emission from the star forming region, SQ-A, as well as associated with NGC 7319 is also detected. We note that the $28.2\,\mu$m S(0) line emission appears to be concentrated towards the SQ-A northern region. The maps also show an H_2 structure running eastward, from the center of the

main shock to NGC 7319. We call this the *"H$_2$ bridge"*, because it connects the ridge to the core of NGC 7319. This feature is also visible in radio, Hα, and is and faintly detected in X-rays. The origin of this bridge feature is not clear, and we will come back to this point later (sect. 6.7).

Enormous H$_2$ fluxes!

The spectra (see Fig. 8 of paper II) and the H$_2$ line fluxes (see sect. 4 and table 2) have been calculated for different apertures in the ridge (Fig. 7). The spectra show the striking dominance of the H$_2$ lines in the mid-IR range of the *IRS*. The thermal dust continuum is very weak in the center of the shock and in the bridge structure, whereas it is stronger for the northern region SQ-A where star formation is likely occurring. For the main shock structure, the 0-0S(1) line luminosity alone, the sum of the S(0) to S(5), and the total H$_2$ (accounting for $\approx 30\,\%$ of the flux in undetected lines) luminosities are respectively

$$\mathcal{L}_{\mathrm{S(1)}}(\mathrm{H}_2) \quad \approx \quad 2.3 \times 10^{34} \text{ W} \tag{6.1}$$

$$\mathcal{L}_{\mathrm{S(0)-S(5)}}(\mathrm{H}_2) \quad \approx \quad 7 \times 10^{34} \text{ W} \tag{6.2}$$

$$\mathcal{L}_{\mathrm{tot.}}(\mathrm{H}_2) \quad \approx \quad 9 \times 10^{34} \text{ W} \tag{6.3}$$

This exceptional power in the molecular hydrogen lines is one order of magnitude brighter than the next brightest mid-IR line, [Si II]$\lambda 34.82\mu$m, with a line luminosity of $\mathcal{L}(\mathrm{SiII}) = 8.5 \times 10^{33}$ W.

The mid-IR spectral mapping will allow us to map the excitation of the H$_2$ along and across the X-ray shock. We have started to work on a two-dimensional modelling of the H$_2$ excitation. We will create maps the H$_2$ excitation temperature across the shock, and correlate this with dust emission SEDs, in order to test models we are developing to explain the extreme H$_2$ power observed. This work will be pursued during my postdoc.

6.2.2   Astrophysical questions raised by the new observations

The new spectral maps described above reveal the wide extension of the H$_2$ emission in the halo of the SQ group, as well as the spatial distribution of the mid-IR emission from dust and fine-structure lines. They essentially raise the main following questions:

- Why is the H$_2$ emission so extended? In particular, what is the origin of the H$_2$ emission in the bridge feature between the main shock and the AGN (NGC 7319) of the group?

- Which mechanisms power the mid-IR fine-structure lines detected in the ridge? Is H$_2$ really the dominant coolant in the shock?

- Where does the emission come from? From the hot gas in the halo of the group, or from the molecular gas?

The first issue is related to the geometry and dynamics of the galaxy interactions in the group. This is why we discuss this point in sect. 6.3. The second point is discussed in paper II and I have complemented this discussion in sect. 6.6. The dust emission in SQ is tackled in chapter 8. Before addressing the two first questions, it is important to assess the energy content of the extended SQ shock.

6.2.3 Updated mass and energy budgets for the whole ridge

In Guillard et al. (2009c), we use the multiwavelength observations (see sect. 6.3) to estimate the masses, thermal and mechanical energy, and luminosities in the preshock and postshock medium (see table 1 of paper I). At that time, only the single-pointing H_2 observations by Appleton et al. (2006) were available, so the mass and energy budgets were calculated within the *IRS* SH slit aperture. Now that we have a complete spectral mapping of the ridge, we are able to estimate the physical quantities within the full shock region. The details on how we determine the quantities from the observations are given in sect. 2.2 and 2.4 of paper I. The new results for the whole ridge are gathered in table 6.1. All the quantities are estimated within the "main shock" $77'' \times 30''$ aperture defined above.

The conclusions are the same as those of Guillard et al. (2009c). In the preshock medium, the thermal energy of the hot plasma ($\frac{3}{2}\frac{M_X}{m_H}T_X$) is only a few percent of the bulk kinetic energy of the H I gas. In the postshock medium, the main energy reservoir is the mechanical energy associated with the high-velocity dispersion of the warm H_2 gas. All the mechanical energy of the collision is not dissipated in the hot plasma, but a substantial amount is carried by the warm H_2. We show that the bulk kinetic energy of the molecular gas is > 2 times the thermal energy of the postshock plasma.

6.3 A complex astrophysical context: SQ observational constrains

I describe here the SQ group of galaxies and give an overview of its multi-wavelength data (sect. 6.3). This review is focused on the dynamics of the group and on the evidence for a high-speed, galaxy-wide shock. This is crucial to understand the complexity of this interacting system and to set the context for the interpretation of the extended H_2 emission.

6.3.1 Are there five musicians playing in the Stephan's Quintet?

SQ was discovered in 1877 by the french astronomer Edouard Jean-Marie Stephan ($1837 - 1923$) at the Observatory of Marseille, France (Stephan, 1877). He discovered a group of four "elliptical nebulae", today known as SQ, much earlier than anyone knew the existence of galaxies outside the Milky Way! When one looks at a SQ image, one actually sees 6 galaxies: NGC 7317, NGC 7318a, NGC 7318b, NGC 7319, NGC 7320 and NGC 7320c (see Fig. 6.2). So how many galaxies belong to the group, 4, 5 or 6?

The first estimates of the redshifts of the SQ members were done through optical spectroscopy, and observations show a wide range of values among the galaxies within the group (Humason et al., 1956; Ambartsumian, 1958; Limber and Mathews, 1960; Burbidge and Burbidge, 1961a). In particular, NGC 7320 has a recession velocity of ~ 6000 km s^{-1} less than NGC 7317, NGC 7318a and NGC 7319 that are at ~ 6600 km s^{-1} (see table 6.2). In addition, NGC 7318b and NGC 7320c have respectively "redshift" ~ 900 and ~ 700 km s^{-1} less than the three members at ~ 6600 km s^{-1}. This puzzling result was the start of a long debate about the population of Stephan's Quintet. Do all the galaxies belong to the group? How many galaxies are in gravitational interaction?

Burbidge and Burbidge (1961b) reported that the difference in redshift of ~ 6000 km s^{-1} between the high- and low-redshift members of SQ could only means one of two things: *(i)* NGC 7320 is a foreground galaxy, or *(ii)* NGC 7320 is literally exploding away from the other members. They

Table 6.1: Mass, energy and luminosity budgets of the preshock and postshock gas in the SQ ridge[a].

	PRESHOCK GAS			POSTSHOCK GAS				
	Hot Plasma[b]	HI[d]	H$_2$	Hot Plasma[b]	HII[c]	HI[d]	Warm H$_2$[e]	Cold H$_2$
n_H [cm^{-3}]	3.2×10^{-3}			1.17×10^{-2}				
T [K]	5.7×10^6			6.9×10^6				
P/k_B [K cm^{-3}]				1.9×10^5			$>10^2$	$<10^2$
N_H [cm^{-2}]		3×10^{20}			1.4×10^{19}	$<5.8\times10^{19}$	2×10^{20}	
Masses [M$_\odot$]	2.4×10^8	$0.8-2.5\times10^9$		5.3×10^8	4.9×10^7	$<2\times10^8$	1.2×10^9	
Energy [erg]	Thermal (Plasma in halo) 3.4×10^{56}	Bulk Kinetic (Shocked HI gas) $0.4-1.2\times10^{58}$		Thermal (X-ray emitting plasma) 9×10^{56}			Bulk Kinetic[f] (Turbulent H$_2$) $\gtrsim1.8\times10^{57}$	
Flux [W m^{-2}]	X-rays 6.6×10^{-17}			X-rays 31.4×10^{-17} 7.8×10^{-17}	Hα 5.5×10^{-17}	OI 74.6×10^{-17}	H$_2$[e]	
$\mathcal{L}^g$ [erg s^{-1}]	6.2×10^{40}			X-rays 2.95×10^{41} 6.5×10^{40}	Hα 4.6×10^{40}	OI 8×10^{41}		

[a] All the numbers are scaled to our main shock aperture ($A_{MS} = 70'' \times 30'' = 33.8 \times 13.2$ kpc^2) where *Spitzer* mapping was performed. The preshock gas is mainly the HI gas contained in the tidal tail of NGC 7319. After the shock, the mass is distributed between the hot plasma and the H$_2$ gas (see text for details). Before the shock, most of the energy available is the kinetic energy of the HI gas that will be shocked. The shock splits the energy budget in two parts: thermal and kinetic energy. The former is stored in the hot plasma whereas the latter goes into turbulent motions that heat the H$_2$ gas. Observations show that mechanical energy is the dominant energy reservoir.

[b] *Chandra* observations of the extended X-ray emission in the shock and the tidal tail (O'Sullivan et al., 2009b).

[c] Hα and OI optical line observations by Xu et al. (2003).

[d] Based on extrapolation of HI observations in the tidal tail by Sulentic et al. (2001); Williams et al. (2002).

[e] From *Spitzer IRS* observations. The H$_2$ line flux is summed over the S(0) to S(5) lines (Cluver et al., 2009).

[f] This bulk kinetic energy is a lower limit because an unknown mass of turbulent cold molecular gas can contribute to this energy.

[g] Luminosities are indicated assuming a distance to SQ of 94 Mpc.

Table 6.2: Characteristics of the galaxies lying in the Stephan's Quintet field of view [a]

	NGC 7317	NGC 7318a	NGC 7318b	NGC 7319	NGC 7320c	NGC 7320
Type [b]	E4	E2 pec	SB(s)bc pec	SB(s)bc pec (Sy2 [f])	(R)SAB(s)0/a	SA(s)d
RA, α	22 35' 51.9"	22 35' 56.8"	22 35' 58.5"	22 36' 03.7"	22 36' 20.4"	22 36' 03.6s
DEC, δ	+33 56' 40.5"	+33 57' 54.3"	+33 57' 55.4"	+33 58' 31.1"	+33 59' 06"	+33 56' 52.7"
Distance [c]	93.3 ± 6.5	93.7 ± 6.6	82.0 ± 5.8	95.4 ± 6.7	84.9 ± 5.9	13.7 ± 1.0
B-mag [d]	15.3	14.4	14.06	14.8	17	13.8
Ang. Size [e]	0.512 × 0.512	0.512 × 0.512	1.862 × 1.348	1.737 × 1.348	0.575 ± 0.489	2.041 × 1.148
Velocity	6564 ± 47	6597 ± 32	5727 ± 24	6578 ± 49	5932 ± 11	738 ± 48
Redshift	0.02214 ± 0.00016	0.02225 ± 0.00011	0.019289 ± 0.00009	0.02219 ± 0.00016	0.019987 ± 0.000037	0.00247 ± 0.00016

[a] Data extracted from the Simbad and NED databases. See Fig. 6.2 for an image of SQ.
[b] Morphological type. E stands for elliptical galaxy, S for spiral.
[c] Galactocentric distance in Mpc
[d] Magnitude in the B-band (0.83 μm)
[e] Angular size: major axis [arcmin] × minor axis [arcmin].
[f] NGC 7319 is a Seyfert 2 galaxy showing a weak Active Galactic Nucleus (AGN) activity (Durret, 1994)
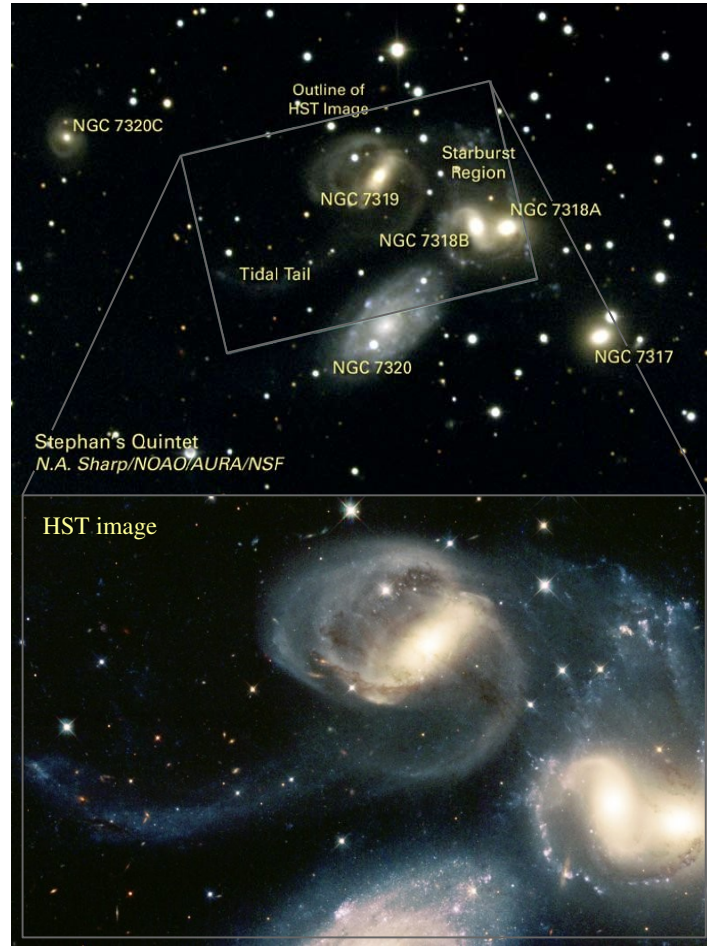
Figure 6.2: The main elements of Stephan's Quintet (North is up, East is left). The top panel shows a CCD image (NOAO[a], Kitt Peak) of SQ. The five members of the quintet are: NGC 7317, NGC 7318a, NGC 7318b, NGC 7319, ans NGC 7320c. The NGC 7320 galaxy is a foreground. The bottom panel is the HST image[b] of the center of SQ (Gallagher et al., 2001), which shows that stars are forming outside of the galactic disks of the group members, in the SQ halo.

[a]National Optical Astronomy Observatory, http://www.noao.edu/
[b]http://hubblesite.org/newscenter/archive/releases/2001/22

estimated the probability of *(i)* being true is $\sim 1/1500$. On the other hand, they stated that conclusion *(ii)* "is outside conventional ideas about the [dynamics] of galaxy groups". Arp (1973b) reports the first Hα interference filter images of SQ. These images clearly separate the low- and high-redshifts systems, associated with the foreground galaxy NGC 7320 (~ 800 km s^{-1}) and the SQ group (~ 6000 km s^{-1}). Based on the analysis of the distribution and diameters of the H II regions, Arp (1973b); Arp and Lorre (1976) argued that NGC 7320 is physically associated with other SQ galaxies, and this was a prime case for the existence of non-Dopler redshift.

Tammann (1970); Allen and Sullivan (1980); Moles et al. (1997) provided counter arguments against this claim. First, H I and Hα observations show no evidence for NGC 7320 interaction with other SQ galaxies. Second, redshift independent estimates yield to distances consistent with the red-
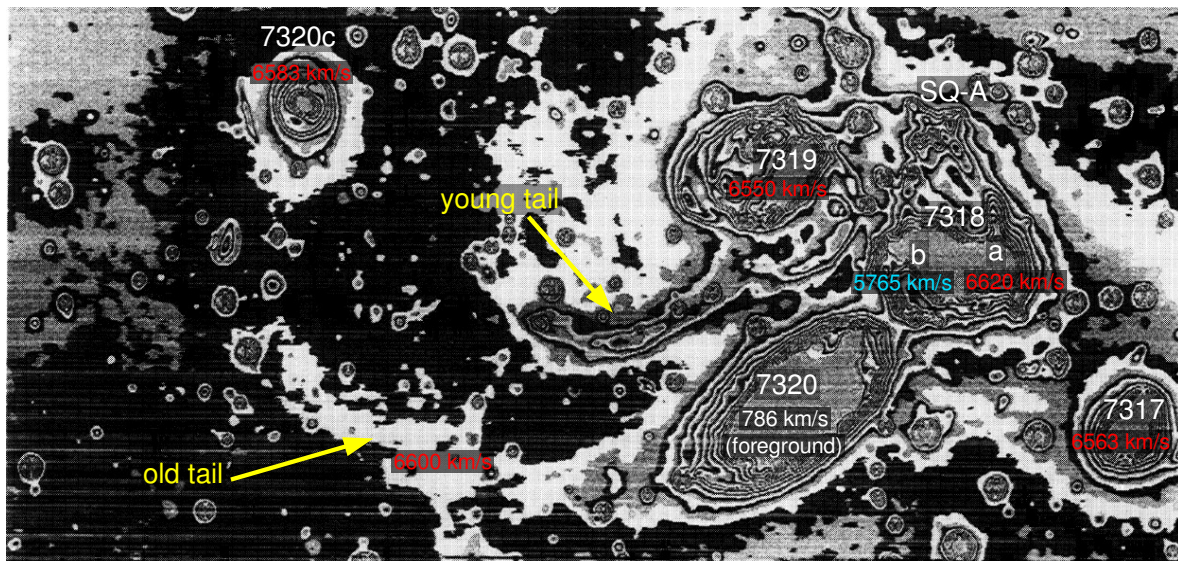
Figure 6.3: Iso-density image of an optical photographic plate (3h of observations) taken with the 200-inch telescope at Palomar (Arp, 1973a). We identify the members of the Stephan's Quintet group and the two tidal tails. Recent measurements of redshifts are indicated.

shifts. Third, the redshift of NGC 7320 is close to that of NGC 7331 (818 ± 5 km s^{-1}), so NGC 7320 appear to be a member of a foreground loose galaxy group which includes the large spiral galaxy NGC 7331. In the following, we thus assume that NGC 7320 is a foreground galaxy and it will not be further discussed hereafter. Arp (1973a) suggested that NGC 7320c, the galaxy lying 4 arcmin to the east of NGC 7319 (see Fig. 6.2, top panel) is linked to the group by optical tidal tails. Therefore the "quintet" status is restored!

In the bottom panel of Fig. 6.2 we show a recent mosaic picture taken by Gallagher et al. (2001) with the Wide Field and Planetary Camera 2 (WFPC2) onboard the *Hubble Space Telescope* (*HST*), on Dec. 30, 1998 and June 17, 1999. One clearly sees on the image that galaxy interactions have distorted the galaxies' shapes, creating elongated spiral arms and long, gaseous streamers. Interestingly, this spectacular image reveals that star clusters are forming outside the galactic disks, in the SQ halo. Some of these star cluster contain a few millions of stars.

In the following, we assume the distance to the SQ group to be 94 Mpc (with a Hubble constant of 70 km s^{-1} Mpc^{-2}) and a systemic velocity for the group as a whole of $6\,600$ km s^{-1}. At this distance, 10 arcsec$= 4.56$ kpc.

6.3.2 The complex dynamical history of Stephan's Quintet

The first deep optical images taken by Arp and Kormendy (1972); Arp (1973a); Arp and Lorre (1976) show two concentrating parallel tidal tails, both starting from NGC 7319 and extending to NGC 7320c, with the more diffuse one passing through the low redshift galaxy NGC 7320. Fig. 6.3 presents an example of a photographic plate taken at the 200-inch Palomar telescope, where these two tidal tails are clearly visible. This is the first indication of a long list of observations that show that the group has a complex dynamical history.

As its population, the dynamical history of SQ has been a long debate that is not entirely solved yet. In the following, we first summarize the scenario of past and present dynamical interactions that emerges from multi-wavelengths observations. Then we detail the different arguments that support it, and we point out the remaining uncertainties.

Summary of the scenario: multiple galaxy collisions

In the past, an "old intruder", NGC 7320c, stripped most of the gas from group members (essentially NGC 7319 and NGC 7318a), and a new intruder, NGC 7318b is currently colliding with this gas and triggering a large scale shock. The old intruder passed the core of SQ twice, first $\sim 5-7 \times 10^8$ yrs ago and creating the "old tail" (the southern tail in Fig. 6.3), and second about 2×10^8 yrs ago, triggering the "young tail" (the narrower one in Fig. 6.3).

Observational constrains on past interactions with NGC 7320c

The "two-intruders" scenario summarized above was clearly formulated by Moles et al. (1997) and further confirmed by Sulentic et al. (2001), who discussed in detail the link between the two tidal tails and the two passages of NGC 7320c through the kernel of the group.

The *HST* image (Fig. 6.2) highlights that star birth occurs mainly in three dynamically-perturbed sub-regions of the group: the long, sweeping tail and spiral arms of NGC 7319 [left]; the gaseous debris of the galaxy pair NGC 7318a and b [bottom right]; and an area north of those galaxies, the so-called SQ-A starburst region [top right]. Since galaxy interactions are known to trigger star formation, the SQ star formation history is closely linked to its dynamical history. Photometric analysis of the *HST* images shows that the ages of these star clusters span over a wide range, spanning from $\sim 2 \times 10^6$ yrs to $\sim 3 \times 10^9$ yrs, which shows past and recent star formation (Gallagher et al., 2001). The southern, diffuse tail mostly contains an old population of star clusters, whereas the northern one is comprised of younger stars.

X-ray observations also support multiple episods of galaxy interaction in the SQ group. A very extended halo of hot ($\sim 6 \times 10^6$ K) gas was first detected by Bahcall et al. (1984). They state that the extent of the halo is too big and its temperature too low to have been produced by the collision of the new intruder. They also show that the X-ray luminosity of the halo ($\mathcal{L}_X(0.1 - 3 \text{ keV}) = 5 \times 10^{42}$ erg s^{-1}) is 10 times the expected luminosity from the combined five SQ galaxies. Later, Moles et al. (1997); Sulentic et al. (2001); O'Sullivan et al. (2009b) suggest that this X-ray emitting hot intracluster gas was produced by previous galaxy encounters (with NGC 7320c for instance). We will further discuss X-ray observations in sect. 6.3.3.

The discovery of a galaxy-wide shock in Stephan's Quintet

The first evidence for the recent collision between the intruder NGC 7318b and the IGM comes from two discoveries in the radio band, both made with the Westerbork Synthesis Telescope, Netherlands.

The first is a giant (~ 40 kpc long) radio continuum ridge found in the IGM between NGC 7319 and NGC 7318b (Allen and Hartsuiker, 1972). Among other possible interpretations, Allen and Hartsuiker (1972) suggested this may be a large scale shock triggered by an on-going collision between NGC 7318b (the recent intruder) and the rest of the group. The collision velocity is about

one million mph (1000 km s^{-1})! A one hundred thousand light-year long giant shock is produced! Stephan's Quintet is thus a multi-galaxy collision caught in action!

The second (Allen and Sullivan, 1980; Shostak et al., 1984) is the revelation that nearly all the H I gas associated with SQ is lying outside galaxy disks, in the group halo. This represents a mass of neutral gas of $\sim 10^{10}$ M$_{\odot}$. These observations suggest that this gas has been stripped from late type galaxy disks due to an earlier interaction (a few 10^8 yr ago) either between NGC 7319 and NGC 7318a (Allen and Sullivan, 1980), or between NGC 7319 and NGC 7320c (Shostak et al., 1984). In sect. 6.3.3 we discuss more recent observations of the radio-emitting ridge.

Ongoing debate about the origin of the "young" tidal tail

If most of the litterature now agrees on the origins of the old tail and of the main shock, the origin of the "young tail" is more debated. Instead of the "two step" scenario proposed by Moles et al. (1997); Sulentic et al. (2001), Xu et al. (2005) proposed a "three-intruders" scenario based on new UV observations.

They argue that it is unlikely that the young tail is also triggered by NGC 7320c. This is because the recently measured redshift of NGC 7320c (6583 km s^{-1} Sulentic et al., 2001) is almost identical to that of NGC 7319, indicating a slow passage (Sulentic et al., 2001) rather than a fast passage ($\sim$ 700 km s^{-1} Moles et al., 1997). In order for NGC 7320c to move to its current position, the NGC 7319/7320c encounter must have occurred $\gtrsim 5 \times 10^8$ yr ago. This is close to the age of the old tail, but older than that of the young tail. They suggested that the young tail is triggered by a close encounter between the elliptical galaxy NGC 7318a and NGC 7319. The projected distance between NGC 7318a/7319 is only $\sim 1/3$ of that between NGC 7320c/7319. Therefore the time argument is in favor of the new scenario.

Numerical N-body simulations are certainly needed to explore and test the dynamical scenarios inferred from observations. Recent work within the specific context of SQ has been made by Renaud (2007), and has to be pursued. We will not further discussed this debate and shall concentrate on the main shock.

6.3.3 Further evidence for a galaxy-wide shock

In the following we further discuss multi-wavelength observations of Stephan's Quintet. These data sets allow to establish the energy and mass budget of the SQ galaxy collision, which is gathered in the Table 1 of Guillard et al. (2009c) (paper I).

Radio observations

The galaxy-wide radio ridge discovered by Allen and Sullivan (1980) has been confirmed by VLA[1] observations by van der Hulst and Rots (1981); Williams et al. (2002); Xu et al. (2003). Fig. 6.4 presents radio observations of SQ at 1.416 and 4.86 GHz. O'Sullivan et al. (2009a) extend these observations to lower frequencies (327 and 610 MHz) with the GMRT telescope. Fig. 6.5 shows

---

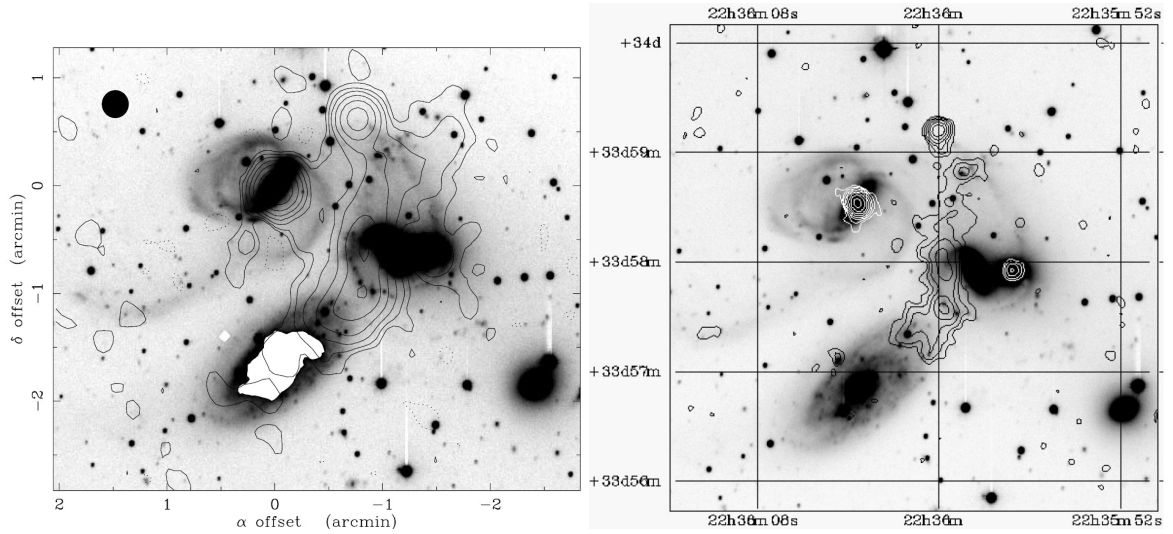[1]Very Large Array http://www.vla.nrao.edu/

Figure 6.4: Radio continuum observations of SQ. *(Left):* Contour map of the 21 cm continuum emission at 1.4 GHz overlaid on an R-band image obtained by J. Sulentic at the 3.5 m Calar Alto telescope. The contours are $-0.2, 0.2, 0.4, 0.8, 1.6, 3.2, 6.4, 13$, and 26 mJy beam^{-1}, for an rms noise level of 0.1 mJy beam^{-1} (0.3 K). The synthesized beam, $15.4'' \times 14.8''$, is shown on the upper left corner. Coordinate offsets are with respect to the optical nucleus of NGC 7319 at α_{J2000} 22 36' 03.7", δ_{J2000} +33 58' 31.1". From Williams et al. (2002). *(Right):* Contours of the radio continuum at 4.86 GHz (VLA B configuration) overlaid on an R-band CCD image (from Xu et al., 2003). The lowest contour is 50 μJy beam^{-1}, and the spacing is equal to 2 in ratio. The FWHM of the synthesized beam is 6".
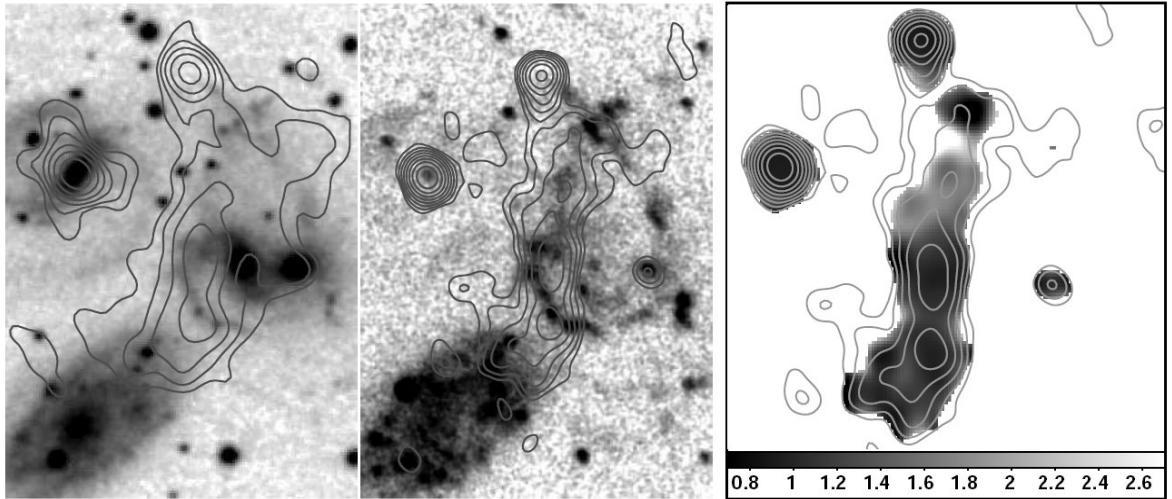
Figure 6.5: GMRT low-frequency observations of SQ by O'Sullivan et al. (2009a). *Left:* 327 MHz GMRT contours overlaid on POSS blue image of the core of Stephan's Quintet. Contours start from $3\sigma = 0.9$ mJy beam^{-1}, HPBW (Half Power Beam Width) is $12'' \times 10''$. *Center:* 610 MHz GMRT contours overlaid on a Swift UVOT UVW2-band image (~ 200 nm). *Right:* $1400 - 610$ MHz spectral index map (HPBW of $6'' \times 5''$) with 610 MHz contours overlaid.

GMRT radio contours overlaid on optical and UV images of the group core, and on a $1400 - 610$ MHz spectral index map. We summarize the main results:

- there is a bright north-south linear ridge of radio emission running in between NGC 7319 and NGC 7318b. The diffuse radio emission is more extended at lower frequencies, including areas west of the ridge. The 1.4 GHz image shows that faint emission connects this extended ridge to NGC 7319. A faint extension to the northwest, coinciding with Hα emission (Plana et al., 1999; Sulentic et al., 2001), is also detected. The total flux density associated with the extended radio ridge is 48 ± 7 mJy (Williams et al., 2002).

- The spectral index map shows that the southern part of the ridge has an index of $0.7 - 0.8$, while the northern part has a steeper spectrum (O'Sullivan et al., 2009a). Some of the brightest spots of radio emission corresponds with knots of UV emission in the south-eastern spiral arm of NGC 7318b. In this region the spectral index is consistent with star formation, so the underlying extended radio emission arising from shocks may be enhanced by star formation in some areas.

- the core of the Seyfert 2 NGC 7319 shows a radio source with a flux 28.5 ± 0.5 mJy. Both images also show that there is a radio source associated with the nucleus of NGC 7318a (0.95 ± 0.05 mJy Xu et al., 2003).

- note that the bright source lying to the north of SQ-A is a backgroung distant binary source seen in projection behind SQ (van der Hulst and Rots, 1981; Williams et al., 2002).

The total luminosity emitted by the radio ridge at 1.4 GHz is $\mathcal{L}_{1.4\text{GHz}} \sim 4 \times 10^{31}$ W from a volume extending about $90'' \times 15''$. This luminosity is 10 times the radio-luminosity of all star-forming regions in SQ (NGC 7318a, SQ-A, and a possible non-AGN component from 7319). van der Hulst and Rots (1981) proposed that the radio emission in the ridge is produced by an intra-cluster starburst. This would imply a star-formation rate of ~ 30 M$_\odot$ yr^{-1}, which is uncompatible with optical spectroscopy, Hα imaging, or mid-IR observations (see chapter 8).

The radio ridge must be associated with synchrotron emission of relativistic electron accelerated in the giant shock created by the NGC 7318b galaxy that is entering into NGC 7319's tidal tail. The ridge is the interface between the interloper NGC 7318b and the group. Indeed, the shocked, ionized gas is predicted to produce significant amounts of synchrotron emission (van der Hulst and Rots, 1981; Allen and Hartsuiker, 1972). The synchrotron life time for the radiating electrons is estimated to be rather short, a few times 10^7 yr, which is comparable to the crossing time for the collision.

Assuming the equipartition of energy between gas internal energy, cosmic rays and magnetic energy, Xu et al. (2003) estimate the magnetic field strength to be $B_{\text{eq}} \simeq 10 \,\mu$G. The corresponding energy density of relativistic particles plus the magnetic fields is $\mathcal{U}_{\text{min}} \sim 10^{11}$ erg cm^{-3}. This is significantly lower than the thermal energy density implied by X-ray observations (see below).

Kinematics of the H I gas

Fig. 6.6 shows 21 cm observations of the H I line at two velocities, that of the intruding galaxy, ~ 5700 km s^{-1}, and that of NGC 7319, ~ 6700 km s^{-1}. The H I contours are overlaid on Hα interference filter images centered at the intruder and intra-group velocities. These images will be
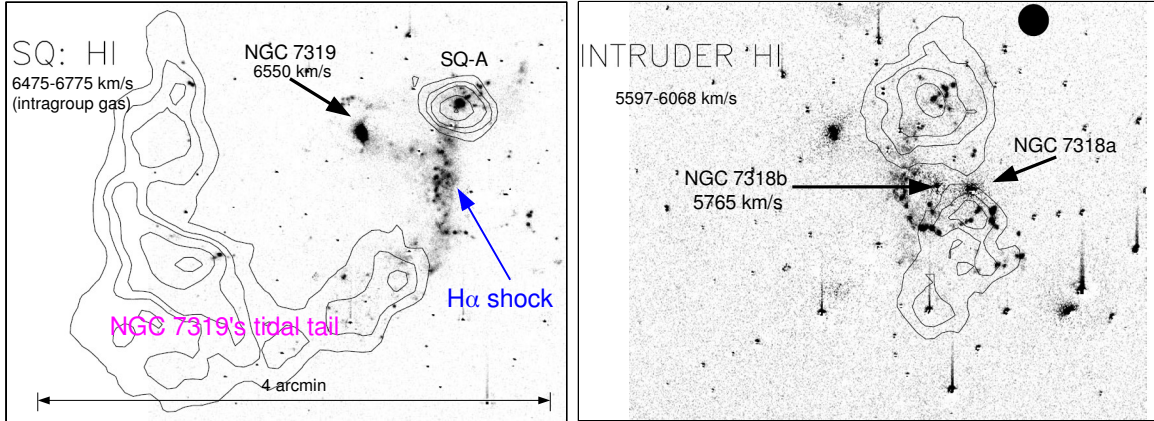
Figure 6.6: H I 21 cm radio contours superposed on Hα interference filter images. *Left:* H I contours for velocities in the SQ range $6475 - 6755$ km s^{-1}. *Right:* H I contours for velocities in the new intruder range ($5597 - 6068$ km s^{-1}). H I contours levels correspond to [0.526, 1.58, 2.63, 5.26, 7.89]$\times 10^{20}$ cm^{-2} with last contour shown only in the left panel. Adapted from Sulentic et al. (2001).

discussed later, in sect. 6.6.1. On Fig. 6.7, the H I contours are overlaid on an optical R-image. In colors we show the radial velocities of the gas. HI observations exhibit a large stream created by tidal interactions between NGC 7320c, and NGC 7319 (Moles et al., 1997; Sulentic et al., 2001). This stream corresponds to the "old tidal tail" (see Fig. 6.3) and the velocity of the gas in the tail is $6600 - 6700$ km s^{-1}. No H I gas is detected in the younger tail. The SQ-A starburst region both contains H I gas at the intragroup (tidal tail) velocity (~ 6600 km s^{-1}) and at a velocity slightly higher that the intruder velocity (~ 6000 km s^{-1}), which suggests that this gas was accelerated by the shock. Some H I gas associated with the intruder velocity (~ 5700 km s^{-1}) is detected to the south of NGC 7318a/b.

The observed difference in radial velocities between the H I tidal tail and the intruder is about $1\,000$ km s^{-1}. On Fig. 6.6, the 21 cm contours are overlaid on an Hα Fabry-Pérot image. At the velocity of the intra-group medium, the Hα image (left panel) clearly shows the linear feature associated with the shock. Over the shock region, no H I gas is detected, but optical line emission from H II gas is observed at the H I tidal tail velocity. This suggests that *the H I gas present in the ridge before the recent galaxy collision was ionized by the shock induced by the collision between the two gas flows*. It is likely that the H I gas at ~ 6600 km s^{-1} in SQ-A was physically connected to the H I tail. We infer the preshock H I gas masses based on the I column densities observed on both sides of the ridge (see paper I).

X-ray observations

The first X-ray observations of SQ were performed with the *Einstein Observatory* and were reported by Bahcall et al. (1984). They found an extended halo but the spatial resolution was not high enough to resolve the structure of the ridge. The presence of shock-heated gas in the SQ halo was confirmed by X-ray *ROSAT*, *Chandra* and *XMM* observations. X-ray maps (Pietsch et al., 1997; Sulentic et al., 2001) revealed an extended and diffuse hot halo, plus features associated with the radio ridge and

Figure 6.7: The of H I column density contours and first-order moment of the radial velocity (lines and numbers in km s^{-1}) for low (cyan and blue), intermediate (green and orange) and high (red and black) velocity ranges. The galaxies velocities are from Sulentic et al. (2001). This image is taken from Renaud (2007).

with galaxy members of the group. The extent of the underlying X-ray emitting halo is too big to have been produced by the new interaction of NGC 7318b with the tidal tail, strongly suggesting that it must have been heated during previous dynamical encounters (Moles et al., 1997; Sulentic et al., 2001; O'Sullivan et al., 2009b). One third of the total X-ray luminosity, $\mathcal{L}_X = 5 \times 10^{41}$ erg s^{-1}, is associated with the intergalactic ridge. The comparison of the relative structures in radio and X-ray bands (Fig. 6.4 and 6.8) show that the X-ray emission is brightest in the northern part of the ridge, while the radio emission is brightest in the south.

High spatial resolution maps (Trinchieri et al., 2003, 2005; O'Sullivan et al., 2009b) and optical narrow-band Hα/[N II] maps (Vilchez and Iglesias-Paramo, 1998; Ohyama et al., 1998; Xu et al., 1999; Plana et al., 1999; Sulentic et al., 2001) show a similar structure, in both the hot gas and the ionized gas. The left panel of Fig. 6.8 shows a spectacular *Chandra* image (blue) overlaid on an optical CFHT image.The right panel shows a zoomed gray-scale B-band image overlaid with *Chandra*

Figure 6.8: Chandra X-ray observations of SQ *(Left)*: $0.3 - 2.0$ keV image (curved, light blue ridge running down the center of the image) overlaid on a deep CFHT image. *(Right):* A zoomed X-ray contour map ($0.5 - 3$ keV) of the main concentration of X-ray photons (from Trinchieri et al., 2003). Contours are superimposed on a CFHT B-band image of the field. The X-ray data are smoothed with an adaptive filter (FFT method) and $2.5\,\sigma$ as the lowest significance of the signal within the kernel.

$0.5 - 3$ keV iso-contours.

The width of the radio or X-ray emission in the shock is ~ 5 kpc, which is commensurate with the width of the H α ridge. Dividing the width of the ridge by the collision velocity (assumed to be $1\,000$ km s^{-1}), we get a collision age of the order of $t_{\rm coll} \sim 5 \times 10^6$ yr.

Spectral energy distribution fitting of *Chandra* and *XMM* observations of SQ show that the temperature of the hot plasma in the ridge is $T_{\rm X} = 6.9 \times 10^6$ K (Trinchieri et al., 2003, 2005; O'Sullivan et al., 2009b). The postshock temperature for a perpendicular shock is given by (see chapter 4, Eq. 4.20 or e.g. Draine and McKee, 1993):

$$T_{\rm ps} = \frac{2(\gamma - 1)}{(\gamma + 1)^2} \frac{\mu}{k_{\rm B}} V_{\rm s}^2 \simeq 6.94 \times 10^6 \left(\frac{V_{\rm s}}{715 \text{ km s}^{-1}}\right)^2 \text{ K} , \qquad (6.4)$$

where $V_{\rm s}$ is the velocity of the shock wave, μ the mean particle mass (equals to 10^{-24} g for a fully ionized gas), k_B the Boltzmann constant and $\gamma = 5/3$. Therefore, the postshock temperature of the hot plasma allows us to estimate a shock velocity of ~ 700 km s^{-1}. We expect the shock velocity to be equal to the gas velocity in the center of mass frame. If the volume-averaged gas densities are the same on the intruder side and on the side of the tidal tail (see sect. 6.3.3 for details), the shock velocity would be approximately half of the observed relative velocity, so $1000/2 = 500$ km s^{-1}. This is significantly lower than the shock velocity we deduce from X-ray observations, suggesting that the mass of the gas in the intruding galaxy is higher than in the tidal tail.

The fact that the shock velocity agrees with the line-of-sight relative velocity of the intruder suggests that its transverse velocity component is small. Sulentic et al. (2001) also argue that the distribution of the H I and H II emissions support the idea of an ongoing collision of NGC 7318b with the tidail tail almost parallel to the line of sight. This conclusion has been revised by Trinchieri et al. (2003); O'Sullivan et al. (2009b) who argued for an oblique shock geometry. They find that the temperature in the ridge (6.9×10^6 K) is close to that of the underlying hot halo (5.7×10^6 K). As they

are assuming a shock velocity of $900 - 1000$ km s^{-1}, they conclude that the temperature in the ridge is too low. The hypothesis of an oblique shock may help to decrease the main shock velocity and therefore the postshock temperature. This will be further discussed in sect. 5.3.1.

The only sign for any interaction between NGC 7317 with other members of SQ is a common halo linking it to the binary NGC 7318, found in the deep X-ray and optical R-band images (Trinchieri et al., 2005).

6.4 How can we account for the H$_2$ excitation?

In this section we address the question of the H$_2$ excitation in the ridge. Thanks to the *IRS* spectral mapping of the ridge presented in sect. 6.2, we have a complete census of the warm H$_2$ excitation over the extended region of the SQ ridge. I have extended and re-visited the analysis presented in chapter 5 and in paper I for the full area of the SQ shock.

6.4.1 Possible H$_2$ excitation mechanisms in the SQ shock

H$_2$ can be excited by several mechanisms: X-ray heating, cosmic-ray heating and shock excitation. We have discussed the micro-physics of these processes in sect. 3.4 and we discuss here which are the dominant processes for H$_2$ excitation in the environment of the SQ ridge.

X-ray heating

The physics of the H$_2$ excitation by X-rays is discussed in sect. 3.4.1 and 3.4.2. We show that the energy conversion from X-ray flux to the bolometric H$_2$ emission is at most 10 % for a molecular cloud that is optically thick to X-ray photons. This excitation efficiency may be even smaller because the absorbed fraction of X-ray photons may be smaller than 1. We indeed expect that the surface filling factor of the postshock H$_2$ gas is smaller than 1.

The *Spitzer* observations show that the H$_2$ line luminosity domines the X-ray emission from the SQ shock region. This result is true for the whole SQ ridge, but also for sub-regions extracted in the center of the ridge or in the "H$_2$ bridge structure" towards NGC 7319 (see sect. 6.2 and paper II). For the main shock, the total X-ray flux is $\mathcal{F}_X(0.001 - 10\,\mathrm{kev}) \approx 2.8 \times 10^{-16}$ W m^{-2}, which corresponds to a luminosity of $\mathcal{L}_X(0.001 - 10\,\mathrm{kev}) \approx 2.95 \times 10^{34}$ W. Therefore, we find an H$_2$ to X-ray luminosity ratio of

$$\frac{\mathcal{L}_{\mathrm{tot.}}(\mathrm{H_2})}{\mathcal{L}_X(0.001 - 10\,\mathrm{keV})} \approx 3 \tag{6.5}$$

Given the X-ray to H$_2$ flux conversion estimated previously, this ratio shows that the H$_2$ gas cannot be predominantly excited by the X-ray photons of the hot plasma.

Cosmic ray heating

Warm H$_2$ gas may also be heated by relativistic particles in the radio ridge. The physical processes related to H$_2$ excitation by cosmic-ray ionization have been discussed in sect. 3.4.1 and 3.4.2. An enhanced cosmic ray density has been proposed to account for the high temperatures of molecular clouds in the Milky Way nuclear disk (Yusef-Zadeh et al., 2007) and for the mid-IR H$_2$ emission in

the filaments of the Perseus A (3C 84) cool core cluster (Ferland et al., 2008). Is the cosmic-ray heating can explain the powerful H_2 emission in the SQ ridge?

Let us estimate the cosmic-ray ionization rate ζ that is needed to balance the cooling of the gas by H_2 line emission. In the SQ ridge, the total H_2 line luminosity is 9×10^{34} W (see eq. 6.3) and the estimated total mass of H_2 is 1.2×10^9 $M_\odot$ (see sect 6.2.3, table 6.1). Therefore, the average total line emission per H_2 molecule is

$$\mathcal{L}_{H_2}(\text{SQ}) \approx 1.3 \times 10^{-31} \quad \text{W H}_2^{-1} \tag{6.6}$$

We assume that each H_2 ionization releases $\mathcal{E}_{\text{ion.}}(H_2) \approx 7$ eV of energy to heat the molecular gas (see sect. 3.4.2 for the determination of this value). Therefore, the H_2 line cooling is balanced by cosmic ray heating for an ionization rate per hydrogen equal to

$$\zeta = 1.2 \times 10^{-13} \left(\frac{\mathcal{L}_{H_2}(\text{SQ})}{1.3 \times 10^{-31}\,\text{W}} \right) \left(\frac{7\,\text{eV}}{\mathcal{E}_{\text{ion.}}(H_2)} \right) \quad -1\,\text{H}^{-1} \tag{6.7}$$

Therefore, the cosmic-ray ionization rate needed to balance the H_2 line cooling in the SQ ridge is $\approx 5 \times 10^3$ times higher than the standard Galactic rate (Shaw et al., 2005). For a cosmic ray energy density $\approx 5 \times 10^3$ times higher the the Milky Way mean value, the cosmic ray pressure would be a factor 400 higher than the mean cosmic ray pressure in the Milky Way disk ($P_{\text{cos}}(\text{MW}) \approx 10^4$ K cm^{-3}, Boulares and Cox, 1990) and ≈ 20 times larger than the thermal gas pressure. Such a high difference in the pressures is unlikely on large scales. It would imply large departures from the g as equilibrium and from the equipartition of energy on a very large volume, which does not seem to be confirmed by radio observations (see Xu et al., 2003; O'Sullivan et al., 2009a, and paper I).

However, enhanced cosmic-ray ionization rates may be produced at small scales, for instance in turbulent mixing layers. This turbulent mixing occurs when the flow of the background hot plasma interacts with the molecular clouds. At the interface, cosmic-ray particles can be accelerated efficiently (see Scalo and Elmegreen, 2004, for a review of these processes). For such a high value, cosmic rays are the main destruction mechanism of H_2 molecules, and the molecular gas fraction depend on the ionization rate to gas density ratio ζ/n_H. The models by Ferland et al. (2008) show that for $\zeta \approx 10^{-13}$ s^{-1}, the gas is molecular for $n_H > 10^4$ cm^{-3} (see their figure 2). Given that the warm H_2 temperature inferred from the S(1) to S(0) line ratio is ≈ 160 K (see fig. 9 of paper II) in the main shock region, the pressure of the warm molecular gas would be $> 2 \times 10^6$ K cm^{-3}, which is physically possible in the SQ environment.

H_2 emission associated with its formation

The formation of H_2 during the cooling of the dense postshock gas (discussed in sect. 5.3.2) must be accompanied by H_2 emission. The excitation mechanism associated with H_2 formation is discussed in sect. 3.4.3. Can this excitation explain the powerful H_2 excitation in the SQ ridge? To quantify this, we calculate the H_2 emission associated with its formation during the isobaric cooling of the gas from 10^4 K to ≈ 10 K. This calculation has been discussed in sect. 5 of paper I and we summarize here our results.

Within the framework of a multiphase postshock medium, we assume that the gas that is forming H_2 comes from hotter, ionized gas that has recombined. We find that the observed H_2 rotational line

ratios are well reproduced by the model. Fig. 5 of paper I shows that the shape of the H$_2$ excitation diagram associated with H$_2$ formation during the gas cooling matches the observations very well (blue dashed curve). However, we find that the mass flow of cooling gas (the mass of gas that recombines per unit time, $\dot{M}_{\rm rec} = dM_{\rm rec}/dt$) needed to reproduce the absolute level of H$_2$ emission in the SQ shock is 25 times larger than the mass flow derived from Hα observations. We use the following expression to derive $\dot{M}_{\rm rec.}$ from the Hα luminosity:

$$
\begin{aligned}
\dot{M}_{\rm rec} &= m_{\rm H} \times \dot{N}_{\rm rec} & (6.8) \\
&= m_{\rm H} \times \frac{\mathcal{L}_{\rm H\alpha}}{0.45 \times E}_{\rm H\alpha} & (6.9) \\
&= 1263 \times \frac{\mathcal{L}_{\rm H\alpha}}{6.5 \times 10^{33}\,{\rm W}} \quad {\rm M}_\odot\,{\rm yr}^{-1} \ , & (6.10)
\end{aligned}
$$

where $\dot{N}_{\rm rec}$ is the number of hydrogen atoms that recombine per second, $E_{\rm H\alpha}$ is the energy of an Hα photon and $\mathcal{L}_{\rm H\alpha}$ is the Hα luminosity (see Heckman et al., 1989, for details). To match the observed H$_2$ line fluxes with this model would require a mass flow of recombining gas of ≈ 30300 M$_\odot$ yr^{-1}, which is not compatible with the mass rate derived from Hα observations (≈ 1260 M$_\odot$ yr^{-1}). This model also fails to reproduce the [OI] 6300Å line emission by a factor of 7. Therefore, the cooling of the warm H I gas produced by H II recombination cannot reproduce the observed H$_2$ emission nor the [OI] 6300Å line emission. A larger amount of energy needs to be dissipated within the molecular gas to account for the H$_2$ emission.

Shocks

In paper I we show that, within the *IRS* SH slit aperture centered in the ridge, the dominant energy reservoir of the postshock gas is the bulk kinetic energy of the molecular gas. In sect. 6.2.3 we have extended the mass and energy budget of the SQ galaxy collision and shown that the mechanical H$_2$ energy is at least a factor of 2 higher than the thermal energy of the hot plasma for the whole shock. If we assume the equipartition of energy between cosmic rays and magnetic energy, the mean magnetic field strength in the SQ shocked region is $\simeq 10\,\mu$G (Xu et al., 2003). The magnetic energy and thereby the cosmic ray energy $\dfrac{B^2}{8\,\pi}\,V_{\rm MS}$, contained in the volume of the main shock region, $V_{\rm MS} = \mathcal{A}_{\rm MS} \times l_z$, is

$$
\mathcal{E}_{\rm mag.}({\rm SQ}) \approx 2 \times 10^{56} \left(\frac{\rm B}{10\,\mu{\rm G}}\right)^2 \frac{\mathcal{A}_{\rm MS}}{446\,{\rm kpc}^2} \frac{{\rm l_z}}{4\,{\rm kpc}} \ , \quad (6.11)
$$

where l_z is the dimension along the line-of-sight and $\mathcal{A}_{\rm MS}$ the area of the main shock region defined in paper II and sect. 6.2. Assuming $l_z \approx 4$ kpc (O'Sullivan et al., 2009b), we conclude that the equipartition energy of cosmic-rays is one order of magnitude smaller than the bulk kinetic energy of the H$_2$ gas. So the bulk kinetic energy of the warm H$_2$ gas greatly domines the overall energy budget of the entire SQ ridge structure.

This conclusion drives us to the following interpretation of the extreme H$_2$ power in the SQ ridge: we propose that the H$_2$ emission is powered by the dissipation of turbulent kinetic energy into molecular gas. In the turbulent postshock medium, we expect that the relative motion between the backgroung plasma and the H$_2$ gas, but perhaps also the relative motion between the molecular clouds themselves, supply supersonic turbulence in the H$_2$ gas. Since the postshock medium is magnetized (as indicated

by radio synchrotron observations, see sect. 6.3.3), we phenomenologically model this dissipation of mechanic energy by shocks. In sect. 4.3.3 we have discussed extensively the molecular cooling in shocks. Non-dissociative MHD shocks are a very efficient way to channel the mechanical energy of the shock to the rotational excitation of H_2. Then we favor this process. In the absence of a magnetic field, shocks are rapidly dissociative and much of the cooling of the shocked gas occurs through atomic, rather than H_2, line emission.

6.4.2 Low-velocity MHD shocks and H_2 excitation

We quantify the required gas densities and shock velocities to account for the H_2 rotational line fluxes. In paper I, we present in details the result for the single-pointing observations by Appleton et al. (2006). Here we use our spectral mapping data to extend our analysis on the whole region of the SQ ridge. We compare these new results with our previous analysis in the center of the SQ shock.

The H_2 emission induced by low velocity shocks is calculated using an updated version of the shock model of Flower et al. (2003), presented in chapter 4, sect. 4.3. We use the same grid of models presented in paper I, i.e. shock velocities from 3 to 40 km s^{-1} with steps of 1 km s^{-1}, two values of the initial H_2 ortho to para ratio (3 and 10^{-2}), and three different preshock densities ($n_H = 10^2$, 10^3, and 10^4 cm^{-3}). In this models, we assume a standard value for the cosmic ray ionization rate of $\zeta = 5 \times 10^{-17}$ s^{-1}. In its initial state, the gas is molecular and cold (~ 10 K), with molecular abundances resulting from the output of our model for the isobaric cooling (see sect. 5.3.2 and paper I for details). We adopt the scaling of the preshock magnetic strength with the gas density, $B(\mu G) = b \sqrt{n_H [\text{cm}^{-3}]}$ (Crutcher, 1999; Hennebelle et al., 2008). In our models, $b = 1$. Since the molecular gas colder than 50 K does not contribute to the H_2 emission, we stop the integration when the gas has cooled to 50 K, and we calculate the line fluxes at this point.

In paper I we present the result in terms of H_2 excitation diagram (see sect. 3.4.5 for the details about how it is calculated). In this manuscript we present the observed and model spectral energy distribution (SED) of the H_2 line fluxes for *(i)* the same data as in paper I, and *(ii)* the new data of paper II for the main shock region.

We detail how we fit the H_2 line fluxes with shock models. In the models presented here, the preshock gas density is $n_H = 10^4$ cm^{-3}. The shock velocity is the only shock parameter that we allow to vary. From the output of the shock model we derive the H_2 line brightnesses $\mathcal{B}^{50\,\text{K}}(H_2)$ at 50 K, in units of [W m^{-2} sr^{-1}]. We perform a least-squares fit of the observed H_2 line fluxes to a linear combination of two MHD shocks at different velocities V_{s1} and V_{s2} has been performed. These fits provide a scaling factor for each of the shocks which represents a mass flow $\dot{M} = dM/dt$, the amount of gas traversing the shocks per unit time. The H_2 gas luminosity is proportional to this mass flow. For a given H_2 line of upper rotational level J, the model line flux is derived as follows:

$$\mathcal{F}_J^{\text{mod.}}(H_2) = \frac{1}{4\pi d^2} \frac{\dot{M}}{m_H} \frac{4\pi \mathcal{B}_J^{50\,\text{K}}(H_2)}{n_H V_s} \quad [\text{W m}^{-2}], \tag{6.12}$$

where d is the distance to the source (94 Mpc for SQ), m_H is the mass of an hydrogen atom, $\dot{M}$ the hydrogen mass flow [kg s^{-1}], and $n_H V_s$ represents the flow of hydrogen atoms per unit surface [H m^{-2} s^{-1}].
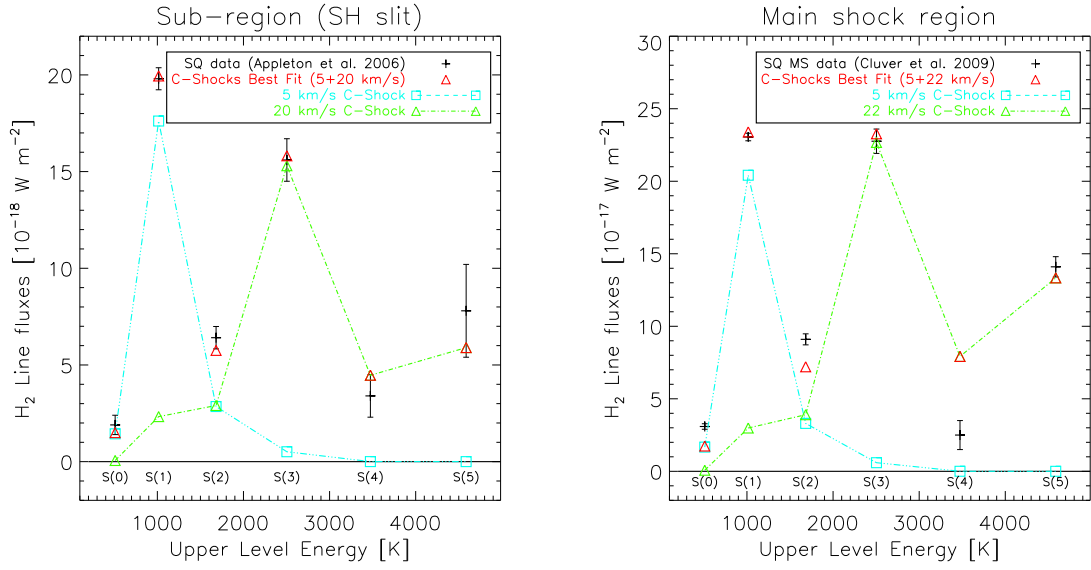
Figure 6.9: Fit of the Stephan's Quintet H_2 spectral energy distribution with 2 shocks at fixed density $n_H = 10^4$ cm^{-3}. *Left:* data from Appleton et al. (2006), extracted within the *IRS* SH slit aperture in the center of the ridge. *Right:* data from Cluver et al. (2009) (paper II) for the main shock region. The 2 shock components account for comparable fractions of the total H_2 luminosity but the less energetic component accounts for most of the warm H_2 mass (see table 6.3 and 6.4).
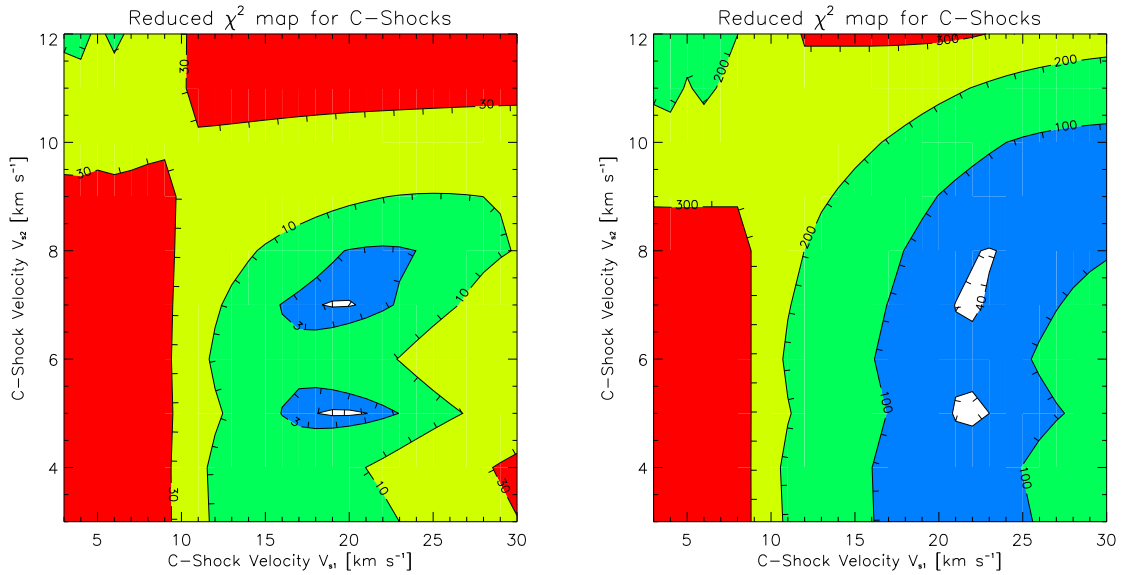
Figure 6.10: Reduced χ^2 map for the fit of the Stephan's Quintet H_2 spectral energy distribution with 2 shocks at fixed density $n_H = 10^4$ cm^{-3}. *Left:* data from Appleton et al. (2006), extracted within the *IRS* SH slit aperture in the center of the ridge. The χ^2 contours are 1.5, 3, 10, 30. *Right:* data from Cluver et al. (2009) (paper II) for the main shock region. The χ^2 contours are 40, 100, 200, 300.

Table 6.3: MHD shock model parameters, mass flows and cooling times for the Appleton et al. (2006) data [a].

V_s [b]	Mass Flow	COOLING TIMES		GAS MASSES	
		$t_{\rm cool}(150{\rm K})$ [c]	$t_{\rm cool}(50{\rm K})$ [c]	(150 K)	(50 K)
[km s^{-1}]	[M$_\odot$ yr^{-1}]	[yr]	[yr]	[M$_\odot$]	[M$_\odot$]
5	5870	14460	18160	8.5×10^7	1.07×10^8
20	260	2375	3230	6.2×10^5	8.5×10^5

[a]This table lists the mass flows, cooling time to 150 K and 50 K, and molecular gas masses, associated with each shock velocity components. The models are the same as those used in the left panel of fig. 6.9.
[b]MHD Shock velocity.
[c]Cooling time computed down to 150 K and 50 K.

The data cannot be fitted with a single shock. For the six H$_2$ lines detected S(0)$-$S(5), we obtain a good fit for two different shock velocities, V_{s1} and V_{s2}. The Fig. 6.9 shows the observed and modeled H$_2$ line fluxes for the Appleton et al. (2006) data (left panel, corresponding to the fig. 5 of paper I) and for the main shock region (data from paper II). For a preshock density of 10^4 cm^{-3}, the best fit is obtained for a combination of 5 and ≈ 20 km s^{-1} shocks (22 km s^{-1} for the main shock region) with an initial value of the ortho to para ratio of 3. Note that no satisfactory fit could be obtained with the low value of the initial H$_2$ ortho-to-para ratio. The red line shows the weighted sum of the two shock components (best fit). The contributions of the 5 (blue dashed line) and ≈ 20 km s^{-1} (green dashed line) shocks to the total column densities are also plotted. The 5 km s^{-1} component dominates the contribution to the column densities of the upper levels of S(0) and S(1) lines. The 20 km s^{-1} component has a major contribution for the upper levels of S(3) to S(5). For S(2), the 2 contributions are comparable.

The fig. 6.10 shows the reduced chi-square contour maps of the two-velocities shock fit for the two apertures used. These maps allow the visualize which are the best combinations of shock velocities to fit the data. As compared to the small aperture in the center of the shock, there are bigger discrepancies between the best-fit model and the data for the extended ridge aperture. We note that the agreement between the model and the data is very good for the odd J values of upper H$_2$ levels, whereas much larger differences are seen for the even-levels. The error bars on the H$_2$ line fluxes are also much smaller for the main shock aperture because data is much deeper than the previous observations by Appleton et al. (2006), so the χ^2 value are thus much higher. The extended ridge aperture is more contaminated by star-forming regions than the small aperture (see chapter 8 for a discussion of star formation in the ridge), which may explain why the fit is poorer.

Some of the key-parameters derived from the fit are gathered in tables 6.3 and 6.4 for the two sets of data. We indicate the best-fit shock velocities, the mass flows $\dot{M}$ that are required to explain the absolute H$_2$ line fluxes, and the gas cooling times $t_{\rm cool}$ at 150 K and 50 K. The gas masses are derived from $M = \dot{M} \times t_{\rm cool}$. For the main shock region, we find a mass of gas at temperatures larger than $T = 150$ K of 9.8×10^8 M$_\odot$, which is a factor of 2 larger than the mass derived from a three-temperatures fit of the excitation diagram (see sect. 4 of paper II, fig. 9). This difference essentially comes from the fact that multi-temperatures fits assume that the H$_2$ ortho-to-para ratio

Table 6.4: MHD shock model parameters, mass flows and cooling times for the Cluver et al. (2009) main shock region data [a].

V_s [b]	Mass Flow	COOLING TIMES		GAS MASSES	
		$t_{\mathrm{cool}}(150\mathrm{K})$ [c]	$t_{\mathrm{cool}}(50\mathrm{K})$ [c]	(150 K)	(50 K)
[km s^{-1}]	[M$_\odot$ yr^{-1}]	[yr]	[yr]	[M$_\odot$]	[M$_\odot$]
5	6.8×10^4	14460	18160	9.8×10^8	1.23×10^9
22	3545	2100	2910	7.5×10^6	1.03×10^7

[a]This table lists the mass flows, cooling time to 150 K and 50 K, and molecular gas masses, associated with each shock velocity components. The models are the same as those used in the right panel of fig. 6.9.
[b]MHD Shock velocity.
[c]Cooling time computed down to 150 K and 50 K.

Table 6.5: MHD shock model parameters and predicted H$_2$ line fluxes for the Appleton et al. (2006) data in the center of the SQ ridge [a] for SQ.

V_s [b]	H$_2$ LINE FLUXES [10^{-18} W m^{-2}]						$\mathcal{F}_{\mathrm{H}_2}$ [d]	$\mathcal{F}_{\mathrm{bol}}$ [e]
[km s^{-1}]	S(0)	S(1)	S(2)	S(3)	S(4)	S(5)		
5	1.44	17.61	2.85	0.51	0.0028	0.0012	22.42	38.05
20	0.06	2.33	2.90	15.30	4.47	5.90	30.96	33.15
2 shocks	1.50	19.94	5.75	15.81	4.47	5.90	53.38	71.20
Spitzer obs.	1.9 ± 0.5	19.8 ± 0.6	6.4 ± 0.6	15.6 ± 1.1	3.4 ± 1.1	7.8 ± 2.4	54.9 ± 3.1	

[a]This table lists the shock model velocities, the predicted H$_2$ rotational line fluxes, and bolometric luminosities associated with each shock velocity components. The models are the same as those used in the lesft panel of Fig. 6.9.
[b]MHD best fit shock velocities.
[d]Sum of the H$_2$ S(0) to S(5) rotational lines in 10^{-18} W m^{-2}
[e]Sum over all the lines (bolometric luminosity of the shock)

is thermalized, which is not the case in shock models. In addition, one of the advantages of shock models in estimating the gas masses is that it includes the mass of gas at lower temperatures which has sufficient time too cool before being reheated. The total mass of gas at temperatures above 50 K is 1.2×10^9 M$_\odot$.

The gas luminosities are listed in Table 6.5 and 6.6 for the Appleton et al. (2006) small aperture and for the extended shock region. We list the H$_2$ S(0) to S(5) line fluxes from each best-fit shock model velocity and the sum of the two shocks. The observed values are indicated at the bottom line. The two last rows show the total H$_2$ S(0)$-$S(5) flux and the bolometric flux of the shocks obtained by integrating the emission in all lines. The bolometric luminosities are smaller than the kinetic luminosities

$$\mathcal{L}_{\mathrm{kin.}} = \frac{1}{2}\,\dot{M}\,V_{\mathrm{s}}^2 \tag{6.13}$$

because some of the mechanical energy of the shock is transferred to the magnetic energy. The H$_2$ line luminosities are close to the bolometric values obtained by integrating the emission in all lines because the H$_2$ rotational lines are the main cooling lines of magnetic shocks (see sect. 4.3.3 for a discussion of the energetics of magnetic shocks). Summing over the two shocks, we estimate a total

Table 6.6: MHD shock model parameters and predicted H_2 line fluxes for the Cluver et al. (2009) main shock region [a] for SQ.

V_s [b]	H_2 LINE FLUXES $[10^{-17}$ W m$^{-2}]$						$\mathcal{F}_{H_2}$ [d]	$\mathcal{F}_{bol}$ [e]
[km s^{-1}]	S(0)	S(1)	S(2)	S(3)	S(4)	S(5)		
5	1.67	20.41	3.30	0.59	0.003	0.001	26.0	44.1
22	0.07	2.98	3.90	22.67	7.92	13.33	50.9	55.5
2 shocks	1.74	23.4	7.20	23.26	7.92	13.34	76.9	99.6
Spitzer obs.	3.09 ± 0.19	23.05 ± 0.26	9.10 ± 0.38	22.76 ± 0.84	2.5 ± 1.0	14.1 ± 0.7	74.6 ± 1.6	

[a]This table lists the shock model velocities, the predicted H_2 rotational line fluxes, and bolometric luminosities, associated with each shock velocity components, for the main shock region (aperture $\mathcal{A}_{MS} \approx 2310$ arcsec^2). The models are the same as those used in the right panel of Fig. 6.9.

[b]MHD Shock velocity.

[d]Sum of the H_2 S(0) to S(5) rotational lines in 10^{-17} W m^{-2}

[e]Sum over all the lines (bolometric luminosity of the shock)

luminosity of 8.2×10^{34} W for the S(0)$-$S(5) H_2 lines, which is excellent agreement with the observed value ($8.0 \pm 0.2 \times 10^{34}$ W).

Our grid of models shows that this solution is not unique. If one decreases the density to 10^3 cm^{-3}, we find that one can fit the observations with a combination of MHD shocks (at 9 and 35 km s^{-1}). If one decreases the density to 10^2 cm^{-3}, the rotational H_2 excitation cannot be fitted satisfactorily. At such low densities, MHD shocks fail to reproduce the S(3) and S(5) lines because the critical densities for rotational H_2 excitation increase steeply with the J rotational quantum number (see sect. 3.2.3). The warm H_2 pressures ρV^2 in the two shocks are 4.5×10^7 K cm^{-3} and 5.6×10^8 K cm^{-3}) for the 5 km s^{-1} and 20 km s^{-1} shocks, respectively. These pressure are much higher than the pressure of the background hot plasma ($\approx 2 \times 10^5$ K cm^{-3}). Both warm and dense (i.e. high pressure) gas is needed to account for emission from the higher J levels.

Though the fit is not unique, it gives an estimate of the relevant range of shock velocities required to account for the H_2 excitation. The velocities ($\approx 5 - 20$ km s^{-1}) are remarkably low compared to the SQ collision velocity (≈ 1000 km s^{-1}) and to the velocity dispersion of the warm molecular gas (≈ 900 km s^{-1}). If our interpretation of the H_2 emission in terms of shock-driven dissipation of energy within the warm molecular gas is right, such a contrast in velocities is a beautiful illustration of turbulent cascade, from high-velocities at large scales, to low-velocity at small scales. The fact that energy dissipation occurs over this low velocity range is an essential key to account for the importance of H_2 cooling. High velocity shocks ($> 40 - 50$ km s^{-1}) in dense ($n_H > 10^4$ cm^{-3}) molecular gas would dissociate H_2 molecules. However, we are far from understanding in details how the transfer of energy from the background plasma (shocked at high speed, ≈ 700 km s^{-1}, see sect. 6.3.3) to the molecular gas. This is discussed qualitatively in sect. 5 and 6 of paper I, and we will come back to this question in sect. 6.5.

6.4.3 Future observational tests: near-IR H_2 line emission

A missing piece of the puzzle of the SQ shock is the near-IR spectrum. This would allow to have access to both ro-vibrational H_2 cooling lines and atomic lines, and therefore to gain a more complete
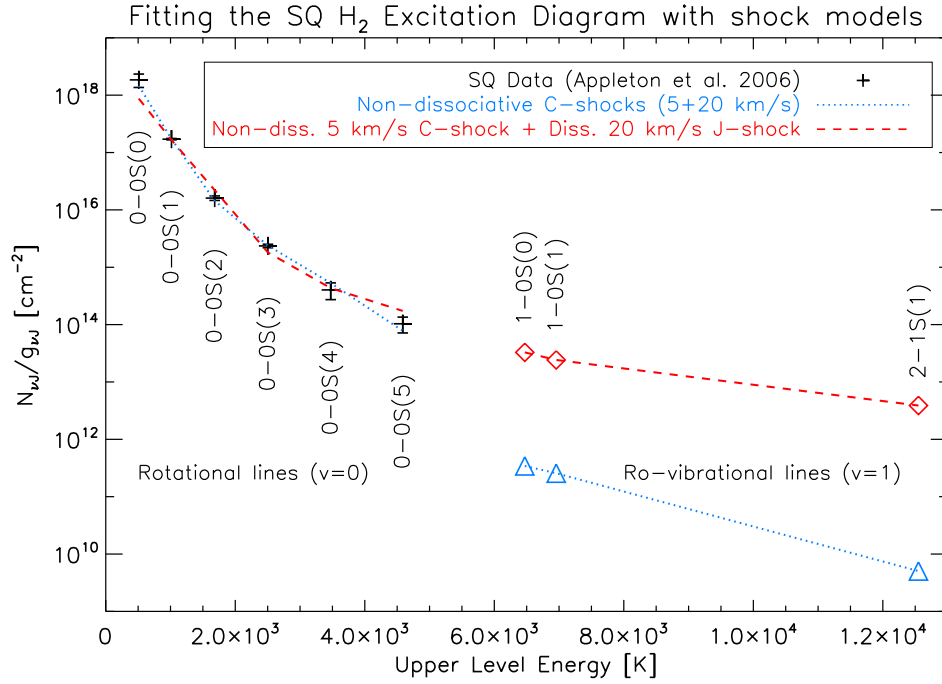
Figure 6.11: The excitation diagram of H_2 emission in Stephan's Quintet from observations (black symbols from Appleton et al., 2006) compared with a model of the post-shock gas from (Guillard et al., 2009c). The model predicts fluxes for the ro-vibrational lines in the range $0.2 - 14 \times 10^{-18}$ W m^{-2} over a solid angle of 5×10 arcsec^2, depending on the kind of shock. Observations in the near-IR can significantly limit the kinds of shocks capable of explaining the excitation diagram. These will influence our picture of how eneregy is funnelled down to 20 km s^{-1} shocks from the large-shock ($V_s \sim 600$ km s^{-1}) which creates the X-ray emission.

picture of the total line cooling in the SQ shock. The near-IR ro-vibrational lines sample much hotter H_2 gas than the Spitzer data (see chapter 3). In particular, near-IR spectroscopy will allow us to extend the H_2 excitation diagram into the hotter regime, where we can start to distinguish between dissociative or non-dissociative type of shocks. This would have important implications for how the energy cascades down from the large scale turbulence to the small cloud fragments.

A proposal has been written to perform near-IR spectroscopy with the *TripleSpec* instrument installed on the Palomar 200-inch telescope (P.I.: P.N. Appleton). The spectral ($\mathcal{R} = 2600$ or $\Delta v = 115$ km s^{-1}) and spatial (1") resolution of TripleSpec is far superior to that of the *Spitzer IRS*, and is crucial to determine if the large velocity spread seen in the Mid-IR H_2 lines ($\sigma \approx 800 - 900$ km s^{-1}) represents a single broad line or two separate narrow lines indicating both pre-and post shocked material.

Fig 6.11 shows example of dissociative and non-dissociative shock predictions from the shock model grid presented in paper I. The blue dotted curve is our best fit model for C-shocks presented in sect. 6.4.2, Fig. 6.9 (left panel). The red curve is a model where the higher velocity component (20 km s^{-1}) is dissociative (J-type). In this case, the ro-vibrational line fluxes are much higher than

the non-dissociative case because the gas reaches higher temperatures. Near-IR spectroscopy should provide constrains on the contribution from non-ionizing shocks to the H_2 emission. This would help in determining if these shocks can contribute to other line emission, like [O I] 6300Å for instance.

I participated to our first observation run at Palomar observatory to perform near-IR spectroscopy with the newly-commissioned *TripleSpec* instrument in November 2008 with Phil Appleton and Patrick Ogle. Unfortunately the weather was very bad and we have only detected, through the clouds, some H_2 emission from the NGC 7319 Seyfert galaxy. The proposal was re-submitted and accepted for a new observation run in August 2009.

6.5   Why is H_2 such an important coolant?

Our interpretation of mid-IR line emission, but also optical and X-ray emission, within the context of a multiphase postshock gas, suggests that observations can be understood in terms of dynamical interactions between the ISM phases (sect. 6.5.1). Exchanges of mass and energy between the gas phases seem a key to elucidate why the H_2 power is so high in the ridge. An efficient transfer of the bulk kinetic energy of the gas to turbulent motions of much lower velocities within molecular clouds seems required to make H_2 a dominant coolant of the postshock gas (sect. 6.5.2). Here we briefly summarize and update the discussion of paper I (sect. 5 and 6).

6.5.1   Mass and energy cycle between ISM phases

In the Stephan's Quintet shock region, observations and modeling suggest that the dissipation of the mechanical energy of the collision between a galaxy and a tidail tail is the main source to power the X-ray emission, the optical, and mid-IR line emission from the gas in the ridge. The relative luminosities from the different gas components depend on the dynamical coupling between the gas phases. In this section we propose a scenario for the postshock gas evolution that sketches the dynamical interaction between ISM phases. This interpretation introduces a physical framework that may apply to other astrophysical situations (AGN-driven jets in radio-galaxies, supernova remnants, starburst-driven winds, etc.).

Fig. 6.12 sketches our view at the mass and energy exchanges between the different gas phases that control the evolution of the postshock gas. This cartoon is the same as Fig. 6 of paper I except that the values of the mass flows are updated for the full SQ ridge. Black and red arrows represent the mass flows between the H II, H I, warm and cold H_2 gas components of the post-shock gas. The large arrow to the left symbolizes the relative motion between the warm and cold gas and the surrounding plasma. Each of the black arrows is labeled with its main associated process: gas recombination and ionization (arrow number 1), H_2 formation (2) and H_2 cooling (3). The values of the mass flows and the associated timescales are derived from observations and our model calculations.

The total mass flow associated with the low-velocity component of MHD shocks required to reproduce the H_2 line fluxes is much larger (≈ 68000 $M_\odot$ yr^{-1}) than the mass flow of recombining gas derived from Hα observations (≈ 1260 $M_\odot$ yr^{-1}). The mass rates needed to account for the H$_\alpha$, OI, and H_2 luminosities increases. Therefore, one cannot explain the H_2 luminosity with only a continuous cycle through the gas components, from H II to cold H_2. Heating of the cold H_2 gas towards warmer gas states (red arrows) needs to occur.
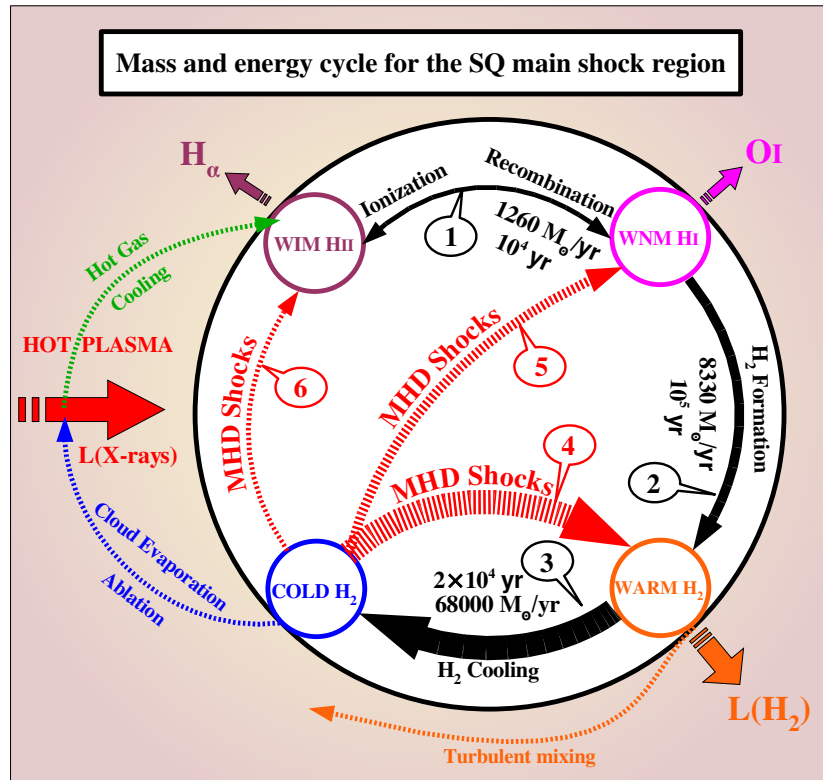
Figure 6.12: Schematic view at the gas evolutionary cycle proposed in our interpretation of Stephan's Quintet optical and H_2 observations. Arrows represent the mass flows between the H II, warm H I, warm and cold H_2 gas components. They are numbered for clarity. The dynamical interaction between gas phases drives the cycle. The mass flow values and associated timescales are derived from the H_α, OI, and H_2 luminosities and model calculations. Heating of the cold H_2 gas (red arrows) is necessary to account for the increasing mass flow from the ionized gas to cold H_2 phases.

The main energy reservoir that can power these red arrows is the mechanical energy of the galaxy collision. We propose that mass and energy are transfered from cold molecular gas via shocks. The post-shock molecular cloud fragments are likely to experience a distribution of shock velocities, depending on their size and density. Arrow number 4 represents the low velocity magnetic shocks excitation of H_2 gas that can account for the H_2 emission (described in sect. 6.4.2). More energetic shocks may dissociate the molecular gas (arrows number 5). They are necessary to account for the low H_α to [O I] 6300 Å luminosity ratio. Even more energetic shocks may ionize the molecular gas (arrow number 6). This would bring cold H_2 directly into the H II reservoir.

The H II gas can also be produced by the turbulent mixing of the warm and cold gas with the hot background plasma (see sect. 4.5.2 for a description of turbulent mixing layers). This is represented by the thin blue and orange arrows from the cold and warm molecular gas reservoirs to the hot plasma. This mixing produces gas at intermediate temperature (a few 10^5 K) that is thermally instable. At these temperatures, the thermal sputtering of the dust is uneffective, so dust is preserved. This gas cools back to produce H II gas that re-enters the cycle (thin green arrow).

An important question is to know whether there is a significant mass of cold (< 50 K) molecular

gas associated with the warm H_2. This cold gas does not contribute to the H_2 emission. The mass accumulated in this cold H_2 reservoir depends on the ratio between the timescale of mechanical energy dissipation (on which gas is excited by shocks through one of the red arrows 4, 5 and 6) and the cooling timescale along the black arrow 3.

Following the calculation made in sect. 6 of paper I, we estimate the timescale of dissipation of the turbulent energy, t_{turb}, and compare it to the cooling time of the warm H_2 gas. We assume that the dissipation of turbulent energy powers the H_2 emission, so the energy dissipation rate P_{turb} must be at least equal to the power radiated by H_2, $\mathcal{L}_{H_2}$. Thus we write the turbulent dissipation timescale as the ratio of the total turbulent energy of the warm H_2 gas, E_{turb}, to the total H_2 power:

$$
\begin{aligned}
t_{\mathrm{turb}} &= \frac{E_{\mathrm{turb}}}{P_{\mathrm{turb}}} & (6.14) \\
&= \frac{\frac{3}{2} M_{H_2} \sigma_{\mathrm{turb}}^2}{\mathcal{L}_{H_2}} & (6.15) \\
&= 1.14 \times 10^4 \left(\frac{M_{H_2}}{1.2 \times 10^9 \, M_\odot} \right) \left(\frac{\sigma_{\mathrm{turb}}}{10 \, \mathrm{km \, s^{-1}}} \right)^2 \left(\frac{10^{35} \, \mathrm{W}}{\mathcal{L}_{H_2}} \right) \quad [\mathrm{yr}] & (6.16)
\end{aligned}
$$

In Eq. 6.16, M_{H_2} is the total warm H_2 mass and σ_{turb} is the turbulent velocity dispersion within the warm H_2 gas. Using the H_2 luminosity and the warm H_2 mass in Table 6.1, we estimate a turbulent dissipation timescale of $\approx 10^4$ yr for a typical dispersion velocity of ≈ 10 km s^{-1}. This estimate of the turbulent dissipation timescale is a lower limit since the dissipated power P_{turb} may be larger if it powers the dissociative and ionizing shocks represented by the arrows 5 and 6 in Fig. 6.12. Therefore, cold H_2 gas would be heated by turbulent dissipation on timescales comparable to the cooling time of the warm H_2 gas that accounts for the S(0) and S(1) line emission (1.8×10^4 yr, see table 6.4). If this is correct, the cold molecular gas mass should not be much higher than the warm H_2 mass inferred from the *Spitzer* observations.

We compare the turbulent dissipation timescale to the dissipation timescale of the total bulk kinetic energy of the warm H_2 gas, t_{TDK}, which can be written as the ratio between the H_2 gas bulk kinetic energy and H_2 luminosity:

$$
t_{\mathrm{TDK}} = 5.7 \times 10^8 \left(\frac{E_{\mathrm{kin}}(H_2)}{1.8 \times 10^{51} \, \mathrm{J}} \right) \left(\frac{10^{35} \, \mathrm{W}}{\mathcal{L}_{H_2}} \right) \quad [\mathrm{yr}] \tag{6.17}
$$

The turbulence dissipation timescale t_{turb} is more than three orders of magnitude smaller than t_{TDK}. Therefore, the dissipation of the mechanical energy of the galaxy collision must involve a large ($\gtrsim$ 1 000) number of cycles where H_2 gas fragments are accelerated and dissipate their kinetic energy in shocks.

6.5.2 Physics of the energy transfer: qualitative discussion

We have shown that the bulk kinetic energy of the gas accelerated by the shock induced by the galaxy collision has to be transfered efficiently within molecular gas to explain the powerful H_2 emission. However, how this energy transfer occurs is far from being known. We discuss here two possible processes: *(i)* the momentum transfer induced by the motion of clouds in the hot plasma, and *(ii)* the production of cosmic rays in the turbulent mixing layers. The first process is discussed in more details in sect. 6.1 of paper I.

Supersonic turbulence sustained by the motion of clouds

We remind that in our interpretation of the H_2 emission in the SQ halo, the formation of H_2 gas arises from the compression of shocked H I gas. The two pre-collision H I complexes, one associated with the intruding galaxy NGC 7318b and the other with NGC 7319's tidal tail, move at a relative velocity of ≈ 900 km s^{-1} with respect to each other. While they are compressed and becoming H_2 clouds, the clouds move at high velocity with respect to the background plasma because they keep their preshock momentum. In the collision, the clouds do not share the same dynamics as the lower density intercloud gas, and the kinetic energy recorded in the ≈ 900 km s^{-1} H_2 line width is dominated by the bulk motion of the H_2 clouds in the plasma rest frame.

The background flow applies drag forces on the clouds (Murray and Lin, 2004). Because of the viscosity of the fluid, the dynamical friction (shear forces) between the cloud and the hot flow also lead to a transport of momentum from the fast flow into the cloud. Analytical and numerical studies of shock-cloud interactions, or studies of the interaction between an outflow and molecular clouds seem to show that the injection of momentum within cloud can feed supersonic turbulence within clouds (e.g. Kornreich and Scalo, 2000; Matzner, 2007; Carroll et al., 2009). The turbulent energy injected into the clouds is dissipated by low-velocity shocks into the dense molecular material. Besides, the relative motion between cloud fragments can lead to cloud-cloud collisions, which results in the dissipation of kinetic energy preferentially in the molecular gas because it is the coldest component with the lowest sound speed.

In addition to dynamics, the thermodynamics of the multiphase gas is a key to understand the energy transfers between the phases. First, the cooling of the gas transfers the turbulent energy of the hotter H II and H I phases to the H_2 gas. Secondly, the thermal instability is also an efficient mechanism to convert the thermal energy to turbulent kinetic energy. Numerical simulations (Sutherland et al., 2003; Audit and Hennebelle, 2005) show that the thermal instability inhibits energy-loss through radiation from the warmer gas and feeds turbulence in the cooler gas. The turbulent velocities generated by the thermal instability are found to be of the order of the sound speed in the warmer gas and are thus supersonic for the colder gas.

H₂ heating by cosmic rays produced in turbulent mixing layers

An alternative mecanism to transfer the bulk kinetic energy of the gas to H_2 heating is the production of cosmic-ray particles in the turbulent mixing layers that would scatter within the molecular clouds and excite H_2 molecules (see sect. 3.4 for a description of H_2 excitation by cosmic rays). In sect. 6.4.1 we show that the average cosmic-ray ionization rate in the SQ ridge is likely to be too low to balance the H_2 cooling. The advantage of cosmic-ray acceleration in mixing layers is that cosmic-ray particles are produced *locally* and can diffuse into the H_2 gas. Cosmic rays are accelerated by the Fermi mechanism and can in turn generate turbulence and MHD waves into the molecular gas if they are accelerated to velocities faster than the local Alfvén speed. These processes are reviewed by Scalo and Elmegreen (2004) (see their sect. 4) and we direct the reader to this review for references.

The two processes discussed above (shocks induced by momentum transfer or cosmic ray excitation produced by turbulent mixing) are two alternative means to cascade the bulk kinetic energy of the gas on large scales to small-scale dissipation withinthe H_2 gas. From an astrophysical point of view,
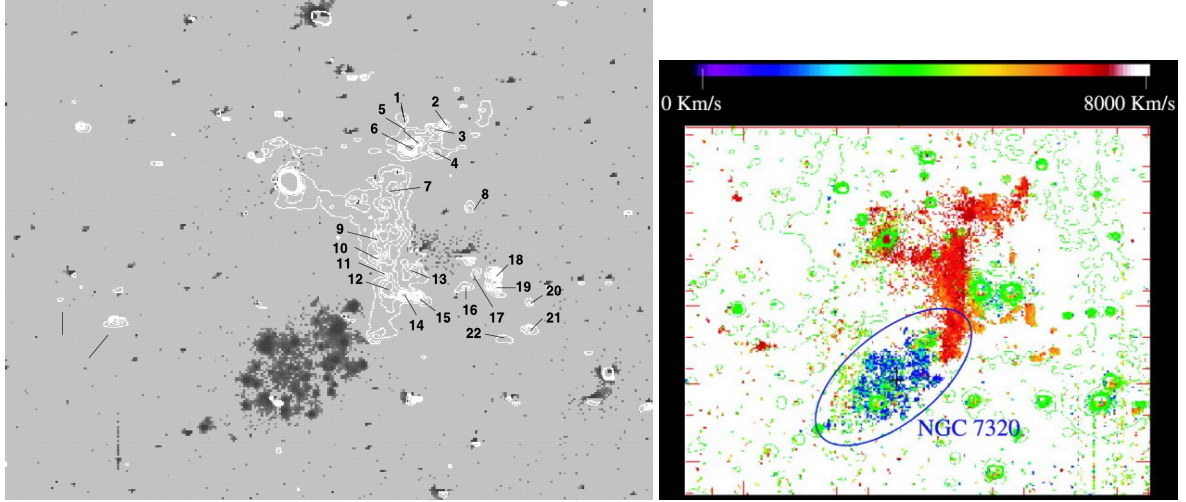
Figure 6.13: Hα contours and velocity maps of SQ. *Left:* High-velocity (> 5500 km s^{-1}, white contours) and low-velocity (~ 800 km s^{-1}, gray scale) Hα maps of Stephan's Quintet. *Right:* Velocity map obtained from the low-v and high-v Hα images. Figures taken from Gutiérrez et al. (2002).

the most important point is that the H$_2$ emission traces the dissipation of the bulk kinetic energy of the system.

6.6   Optical and mid-IR fine structure line diagnostics

In the previous sections we have shown that the dominance of the H$_2$ line cooling in the SQ shock region would require an efficient cascade of energy from the large-scale, bulk kinetic energy of the gas to small-scale turbulent motions within the H$_2$ gas. However, the H$_2$ rotational lines observed by *Spitzer* do not provide a complete budget of the kinetic energy dissipation in the SQ ridge. These low-excitation lines trace gas between $\approx 50 - 1000$ K, and therefore they only sample a narrow range of shock velocities. Within the framework of our interpretation of the H$_2$ emission (the high-speed collision of two flows of multiphase gas), we expect a broad distribution of shock velocities.

Fast shocks may lead to the line emission from ionized gas, which, up to now, has not been considered. This section adresses the following questions: is the emission from the ionized gas an important component of the energetics in the SQ ridge? Is H$_2$ really a dominant coolant? We first describe optical imaging and spectroscopy, as well as mid-IR fine-struture line maps from our new *Spitzer IRS* observations. We use line ratios diagnostics to infer the shock properties from the ionized gas.

6.6.1   Hα imaging and optical line spectroscopy

Moles et al. (1997); Vilchez and Iglesias-Paramo (1998); Xu et al. (1999); Plana et al. (1999); Sulentic et al. (2001); Gutiérrez et al. (2002) present narrowband filter and Fabry-Pérot images that show a chaotic morphology of emission-line regions and complex H II gas kinematics. The left panel of Fig. 6.13 shows Hα maps of SQ from Gutiérrez et al. (2002). The white contours result from com-

bination of four narrowband filter images centered at different wavelengths (from 6667Å to 6737Å), covering the full velocity range of the SQ galaxies ($4760 - 7960$ km s^{-1}). The grey-scale background image is a combination of two images centered at 6569Å (280 km s^{-1}) and 6611Å (2200 km s^{-1}), and thus mainly exhibits the NGC 7320 foreground galaxy. The white contours clearly show an extended and clumpy North-South Hα filament that spatially correlates with the radio emission in the ridge, as well as an East-West feature (we called it the "bridge") that connects the nucleus of the Seyfert 2 NGC 7319 with the North-South ridge. In addition, emission-line regions associated with the new intruder and with the northern SQ-A region are detected.

The two background images on Fig. 6.6 show Hα Fabry-Pérot images from Sulentic et al. (2001), centered at ~ 6600 km s^{-1} (left panel) and ~ 5600 km s^{-1} (right panel). These images show different morphologies. The 6600 km s^{-1} image shows the North-South clumpy, linear shock structure, the core of NGC 7319 and its "bridge", and the SQ-A starburst. On the 5600 km s^{-1} image, the intragroup emission has an "arc shape", with brighter emission in the southern region. This southern arc is comprised of a string of Hα knots that connects to the east end of the faint bar in the new intruder NGC 7318b. This southern arc may be material disrupted from NGC 7318b that has been compressed by the shock. This arc almost connects to a fainter string starting from the core of NGC 7318a, then forming a peculiar "smily face" (the cores of NGC 7318 a and b would be the eyes of this giant smiley!), also clearly visible on the UV (see the central panel of Fig. 6.5) and mid-IR (see chapter 8) images. Note that in some regions, the two velocities components have similar morphologies (see also Fig. 2 of Xu et al., 1999). This emission may arise from gas at intermediate velocities (~ 6000 km s^{-1}) that may be shock-accelerated material from the new intruder.

Up to now, very few high signal-to noise optical spectra in the SQ ridge have been published. Xu et al. (2003) performed optical spectroscopy with the Palomar 200" telescope at several positions along the SQ ridge. In the center of the shock the flux ratios are:

$$\mathcal{F}([\text{O I}]\,\lambda6300)/\mathcal{F}(\text{H}\,\alpha + [\text{N II}]) \quad = \quad 0.53 \tag{6.18}$$

$$\mathcal{I}([\text{S II}]\,\lambda6717, \lambda6731)/\mathcal{I}(\text{H}\,\alpha + [\text{N II}]) \quad = \quad 1.09 \tag{6.19}$$

$$\mathcal{I}([\text{O III}]\,\lambda5007)/\mathcal{I}(\text{H}\,\beta) \quad > \quad 1\,. \tag{6.20}$$

These ratios are different from those observed in H II regions, and suggest shock excitation. Based on the shock models by Dopita and Sutherland (1995), Xu et al. (2003) conclude that these lines are predominantly excited by fast ($V_{\text{s}} > 100$ km s^{-1}) shocks. In fact, the [O I] / Hα line ratio is so high that it is difficult to explain this ratio only with fast shock models (see sect. 6.6.3).

Optical emission lines are mainly detected at three velocities (6800, 6100, and 6400 km s^{-1}). The Hα, [N II], [S II] and [O II] lines are detected predominently at 6100 km s^{-1}, and the [O III] $\lambda5007$ line is detected at 6800 km s^{-1}. The [O I] $\lambda6300$ Å line is centered at 6400 km s^{-1}, and is remarkably broad, with a FWHM $\Delta v \simeq 1130$ km s^{-1}. The width of the line is commensurate with the relative velocity between the intruder and the tidal tail.

Dopita and Sutherland (1996) give the following relation for the total energy flux of a radiative shock:

$$\mathcal{F}_{\text{tot}} = 2.28 \times 10^{-6} \left(\frac{V_{\text{s}}}{100 \text{ km s}^{-1}} \right)^3 \left(\frac{n_{\text{H}}}{\text{cm}^{-3}} \right) \text{ W m}^{-2}\,, \tag{6.21}$$

where n_{H} is the preshock hydrogen number density and V_{s} the shock velocity. We use the aperture

$\mathcal{A}_{\mathrm{MS}}$ corresponding to the SQ "main shock region" (30×77 arcsec^2, corresponding to $\sim 13.7 \times 35.1$ kpc^2). Therefore, the total mechanical luminosity of the SQ high-speed shock propagating into the tenuous intra-group medium is given by:

$$\mathcal{L}_{\mathrm{tot}} = 5.48 \times 10^{36} \left(\frac{V_{\mathrm{s}}}{700 \ \mathrm{km \, s^{-1}}} \right)^3 \left(\frac{n_{\mathrm{H}}}{3.2 \times 10^{-2} \ \mathrm{cm^{-3}}} \right) \left(\frac{\mathcal{A}_{\mathrm{MS}}}{2310 \ \mathrm{kpc^2}} \right) \ \mathrm{W} \qquad (6.22)$$

From X-ray observations, Trinchieri et al. (2003, 2005); O'Sullivan et al. (2009b) estimate the average hydrogen density of the hot plasma in the ridge to be $n_{\mathrm{H}} \simeq 1.17 \times 10^{-2}$ cm^{-3}. For a fast shock, the postshock density is about 4 times the preshock density (sect. 4.2), so we estimate a preshock density of the tenuous gas of $n_{\mathrm{H}} \simeq 3.2 \times 10^{-3}$ cm^{-3}. The total mechanical energy flux for the SQ main shock is thus $\mathcal{F}_{\mathrm{tot}} \simeq 2.6 \times 10^{-6}$ W m^{-2}.

If we assume that this luminosity is radiated over a galaxy crossing time (the shock age) of 5×10^6 yr, the intruder/IGM collision deposits $\sim 8.7 \times 10^{57}$ erg of energy in the SQ shock region. This energy is equivalent to the kinematic energy of $\sim 10^7$ supernovae.

6.6.2 Distribution of the fine-structure line emission

Appleton et al. (2006) reported the detection of the [Ne II] $\lambda 12.8 \, \mu$m and [Si II] $\lambda 34.8 \, \mu$m lines. Thanks to the deeper spectral maps, we have access to the spatial distribution of emission from the [Fe II] $\lambda 25.99 \, \mu$m and [O IV] $\lambda 25.89 \, \mu$m blend, [S III] $\lambda 33.48 \, \mu$m, [Si II] $\lambda 34.82 \, \mu$m, [Ne II] $\lambda 12.8 \, \mu$m and [Ne III] $\lambda 15.56 \, \mu$m lines.

Fig. 4 and 5 of paper II show the intensity contours of these fine-structure lines overlaid on H$_2$ S(1) and X-ray maps. The strong [Si II]$\lambda 34.82 \, \mu$m emission spatially correlates with the H$_2$ and X-ray emission, whereas the [Fe II]$\lambda 25.99 \, \mu$m line emission is only detected towards the AGN NGC 7319 and the center of the ridge, where there is a bright spot of X-ray emission. We direct the reader to sect. 3.2 of paper II for a detailed description of these fine-structure line emission maps. We now discuss the interpretation of these observations with models that allow to constrain the gas physical conditions and the dominant excitation mechanisms (shocks, X-rays, photoionization).

6.6.3 Optical and mid-IR fine structure lines as shock diagnostics

The deep mid-IR spectral mapping data presented above allow to complement the analysis of the rotational H$_2$ lines with the fine-structure line emission from the SQ ridge (see sect. 6.2 for a description of the observational results). These metal lines provide complementary diagnostics to probe the physical conditions of the emitting gas and more energetic excitation mechanisms. Since the main shock region (the X-ray ridge) also contains star forming regions, we have selected a sub-region of our extended *IRS* spectral mapping, so-called *"center"* because it is located in the central region of the ridge, that has less contamination by star-forming regions (see sect. 4, Fig. 7 of paper II). We compare the line ratio diagnostics within these two apertures.

Optical spectroscopy diagnostics show that the SQ shock can be classified as a LINER (Low Ionization Excitation Region). We will show in this section that the gas must be heated to $\gtrsim 10^5$ K by collisional excitation to explain the optical and mid-IR fine-structure line emission.

We use the Allen et al. (2008) shock model library described in sect. 4.4 to compare models with the fine structure line ratios measured with *Spitzer IRS* data. The model results depend on the preshock
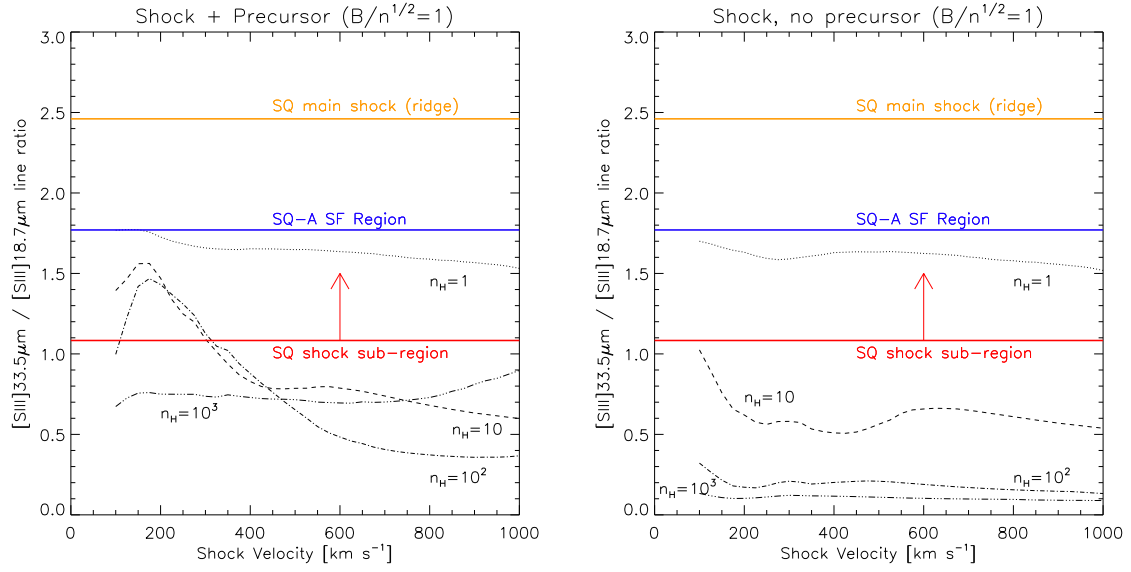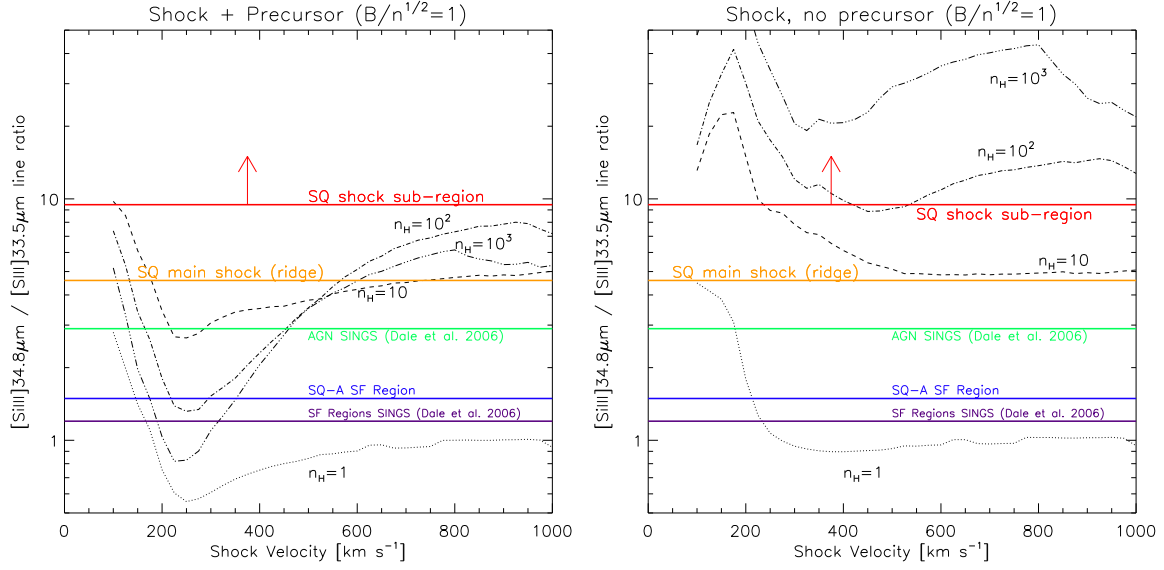
Figure 6.14: The fine-structure line ratios measured in the SQ shock (full ridge and sub-region in the center) are compared with shock calculations (broken curves) from Allen et al. (2008). The model values are shown for shock velocities between 100 and 1000 km s^{-1} (with steps of 25 km s^{-1}), four preshock gas densities ($n_H = 1$, 10, 100 and 1000 cm^{-3}) for a magnetic parameter $B/\sqrt{n_H} = 1$. Observed values are the horizontal solid lines in colors.

magnetic parameter $b = B/\sqrt{n_H}$, where B is the magnetic field strength and n_H the preshock gas density. In the models presented here, we assume $b = 1$, which is slightly lower than the equipartition value of 3.23. We compare the model results with and without the radiative precursor. The radiative precursor of a fast shock moving into low-density gas adds an emission component which has the spectral characteristics of photoionized gas with a high ionization parameter. To neglect the precursor may be relevant if the shock is propagating in a clumpy medium because only a fraction of the ionizing photons will interact with the molecular gas (see sect. 4.5).

The [S III] lines ratios are shown on Fig. 6.14 as a function of the shock velocity. The broken curves are the shock models for different preshock gas densities ($1 - 1000$ cm^{-3}). The solid coloured lines are the observed values. The electron critical densities of the [S III]$\lambda 33.48\,\mu$m and [S III]$\lambda 18.71\,\mu$ lines are $n_e = 1.2 \times 10^3$ cm^{-3} and $n_e = 10^4$ cm^{-3}, respectively. The observed ratio for the full ridge (2.46) is close to the low density limit ($n_e < 100$ cm^{-3}, see Fig. 6.15 and details in Martín-Hernández et al., 2002). The comparison with shock models show that the gas preshock density is smaller than ~ 1 cm^{-3}. The lower limit for the shock sub-region is compatible with preshock gas densities smaller than 100 cm^{-3} and shock velocities $100 < V_s < 300$ km s^{-1}. The [S III] lines ratio diagnostic clearly shows that the mid-IR line emission from the ionized gas originates from moderate shocks (of the order of 100 km s^{-1}) in low-density (≈ 1 km s^{-1}). Faster shocks in denser gas would not be compatible with the available ram pressure in the surrounding hot plasma ($\approx 2 \times 10^5$ K cm^{-3}).

XDRs[2] models show that the [Si II] line is one of the major mid-IR cooling line from gas exposed

---

[2]X-ray Dissociation Regions

Figure 6.15: Ionization potentials and critical densities of important mid-IR fine structure lines. The electron critical densities, indicated for every line in italic, are given in units of cm^{-3} and are expressed as $a(b) = a \times 10^b$. Figure taken from Martín-Hernández et al. (2002).

to X-rays (see Fig. 8 of Maloney et al., 1996). XDRs models have been used to interpret the line emission from AGN. Powerfull [Si II] line emission can also be produced by shock excitation, whereas the [S III] mid-IR lines are mostly tracers of H II regions. Therefore, the [Si II] / [S III] line ratio measures the ratio between the X-rays or shocks and photoionization excitation powers.

Fig. 6.16 shows the observed (solid, coloured lines) and model (broken curves) [Si II]$\lambda 34.82\,\mu$m / [S III]$\lambda 33.48\,\mu$m and [S III]$\lambda 33.48\,\mu$m / [S III]$\lambda 18.71\,\mu$m line flux ratios as a function of the shock velocity, and for different preshock gas densities ($1 - 1000$ cm^{-3}). The [S III]$\lambda 33.48\,\mu$m line is not detected in the sub-region in the center of the shock, so we indicate an lower limit for the line ratios (red line). For comparison, the average line ratios observed in local AGN and extragalactic star-forming regions (from the *SINGS*[3] survey) are shown.

The [Si II] / [S III] SQ line ratios stand out above typical values observed in star-forming regions or AGN, and cannot be accounted for by PDRs or XDRs models. They are rather consistent with the line ratios observed in supernova remnants (see sect. 5 of paper II), suggesting shock-excitation. The lower limit of the [Si II]$\lambda 34.82\,\mu$m / [S III]$\lambda 33.48\,\mu$m line ratio observed in the SQ shock sub-region

---

[3]*Spitzer* Infrared Nearby Galaxies Survey, http://sings.stsci.edu/

Figure 6.16: The fine-structure line ratios measured in the SQ shock (full ridge and sub-region in the center) are compared with shock calculations (broken curves) from Allen et al. (2008). The model values are shown for shock velocities between 100 and 1000 km s^{-1} (with steps of 25 km s^{-1}), four preshock gas densities ($n_H = 1$, 10, 100 and 1000 cm^{-3}) for a magnetic parameter $B/\sqrt{n_H} = 1$. Observed values are the horizontal solid lines in colors.
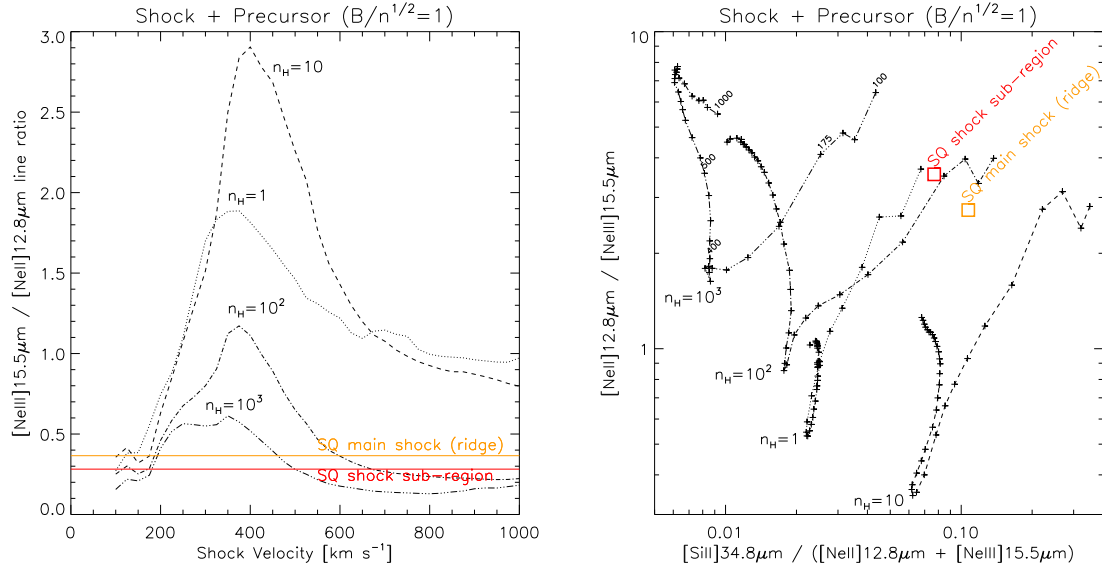
Figure 6.17: Observed mid-IR line ratios compared with shock models (same as Fig. 6.16. The model values are shown for shock velocities between 100 and 1000 km s^{-1} (with steps of 25 km s^{-1}), four preshock gas densities ($n_H = 1$, 10, 100 and 1000 cm^{-3}) for a magnetic parameter $B/\sqrt{n_H} = 1$. Observed values are the horizontal solid lines in colors. The Ne line ratios shown on the *left* panel contrain the shock velocities to be of order of $100 - 200$ km s^{-1}. This result is confirmed by the Ne and S line diagnostic plot on the *right panel*. Note that the radiative precursor is included in both panels.
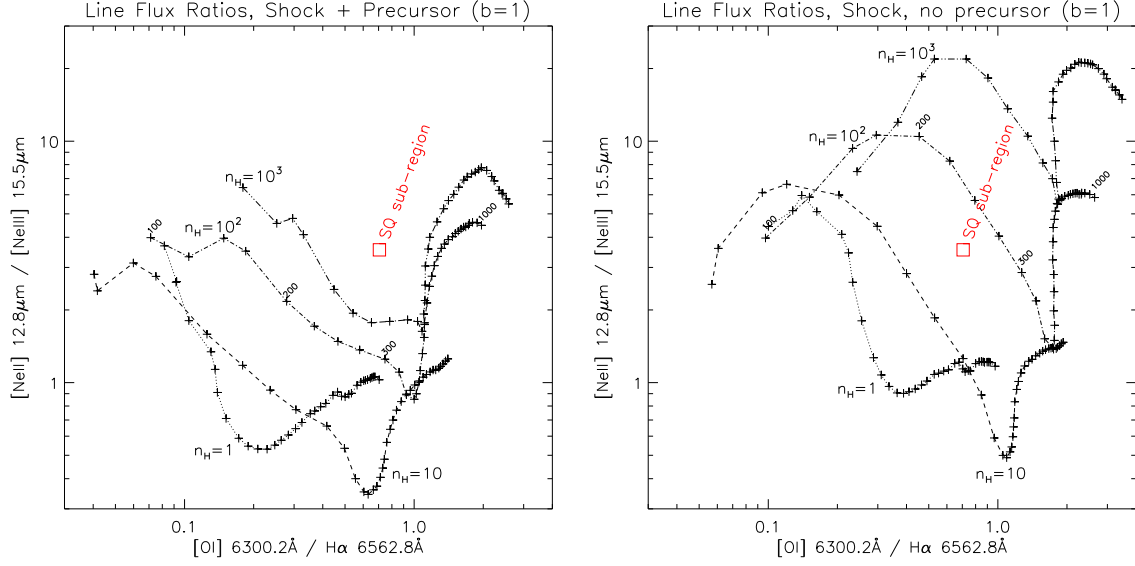
Figure 6.18: Ne fine-structure line ratio vs. optical line ratio measured in the SQ shock (sub-region in the center) as compared with shock calculations (broken curves) from Allen et al. (2008). The model values are shown for shock velocities between 100 and 1000 km s^{-1} (with steps of 25 km s^{-1}), four preshock gas densities ($n_H = 1, 10, 100$ and 1000 cm^{-3}) for a magnetic parameter $B/\sqrt{n_H} = 1$. In the *left* panel, the radiative precursor is included, whereas in the *right* panel, only the shock contribution is plotted.

seems to be consistent with ~ 100 km s^{-1} shocks into $n_H \simeq 10$ cm^{-3} gas. Unlike the sub-region, the SQ-A starburst line ratios are consistent with the values observed in standard extragalactic star-forming regions. This shows that photoionization must be the dominant process in this region, with a minor contribution from shocks.

The Fig. 6.17 shows the [Ne III]$\lambda15.56$ / [Ne II]$\lambda12.8$ line flux ratio as a function of the shock velocity (left panel) or as a function of the [Si II] / ([Ne II] + [Ne III]) line ratio. For our range of preshock densities ($1-1000$ cm^{-3}), the shock models show that the observed line ratios are consistent with shock velocities of $\sim 100 - 200$ km s^{-1}.

Xu et al. (2003) suggest that the optical lines ratios observed in the center of the ridge (see sect. 6.6.1) are evidence for a dominant shock excitation. The mid-IR fine structure lines detected by *Spitzer* confirm this conclusion. However, the large value of the [O I] / Hα line ratio observed in the ridge, $\mathcal{F}([\text{O I}]\,\lambda6300)/\mathcal{F}(\text{H}\,\alpha + [\text{N II}]) = 0.53$, is difficult to explain with fast shocks models. Fig. 6.18 shows the [Ne II] to [Ne III] ratio as a function of the [O I] / Hα optical line ratio. In the left panel, where the precursor is included, the observed value do not match with the models. The mid-IR [Ne II] to [Ne III] line ratio in SQ suggest a low ionization parameter, whereas the radiative precursor produces a highly-ionized medium ahead of the shock. This apparent contradiction can be solved if the SQ intragroup medium is clumpy. In this case, a large fraction of the ionizing photons can escape from the medium without interacting with the dense phase. If we neglect the radiative precursor (right panel), we find a much better agreement with the models. The line ratios are reproduced for a preshock density of $n_H = 10 - 10^2$ cm^{-3} and a shock velocity of $V_s = 200 - 250$ km s^{-1}. These

conditions imply high values of the postshock pressure as compared with the ambient value. Note that a significant contribution from non-ionizing J-shocks contribute to the optical lines, in particular to the [O sc i] 6300Å line (see sect. 4.3.3). This will be further discussed in sect. 6.5.1.

In sect. 6 of paper II we discuss the [Fe II] $\lambda 25.99\,\mu$m and [Si II]$\lambda 34.82\,\mu$m line emission. The fact that the observed [Fe II] / [Ne II] and [Si II] / [Ne II] line ratios are both smaller than the shock model values can be interpreted as evidence for Si and Fe depletion onto dust grains (see Fig. 11 of paper II). This supports our idea that dust survives in the dense gas phases that are the sites for H_2 formation. This will be further discussed in chapter 8 where we model the dust emission from the molecular gas in SQ.

6.6.4 Conclusion: a distribution of shock velocities

The X-ray, optical and mid-IR line emissions from the SQ shock suggest that the gas experiences a wide distribution of shock velocities. We relate this distribution of shock velocities with a distribution of preshock gas densities, due to the multiphasic nature of the preshock medium (paper I). The denser gas phases are associated with the smaller shock velocities.

Very fast shocks ($V_s \sim 700$ km s^{-1}) driven into preshock gas of a few 10^{-3} cm^{-3} are responsible for the bright X-ray emission in the ridge. Optical lines and mid-IR fine-structure lines are likely to be produced by intermediate ($100 < V_s < 300$ km s^{-1}) ionizing J-shocks. A significant contribution from non-ionizing J-shocks can also contribute to these lines, in particular to the [O I] 6300Å (which may help in explaining the very high value of [O I]/ H α), [Fe II] $\lambda 25.99\,\mu$m and [Si II]$\lambda 34.82\,\mu$m lines. And last but not least, low-velocity ($5 - 20$ km s^{-1}), non-dissociative C-shocks driven into dense gas ($> 10^3$ cm^{-3}) are associated to the rotational H_2 emission seen by *Spitzer*.

6.7 Remarks about the NGC 7319 Seyfert galaxy

6.7.1 Observational context: and AGN in the SQ group

In this short paragraph I gather some observational results about the NGC 7319 galaxy. Although not related to the SQ main shock itself, these results are helpful to interpret our recent, extended IR and CO observations of SQ.

van der Hulst and Rots (1981) first detected the NGC 7319 AGN with radio continuum VLA observations of SQ at 20cm. They detected a bright compact source with a jet-like extension, and suggested this might be related to those found in Seyfert galaxies. Huchra et al. (1982) obtained the optical spectrum which shows clearly Sy2-type emission-line features. Based on the stellar velocity dispersion, Woo and Urry (2002) estimated a black hole mass of 2.4×10^7 M$_\odot$. Aoki et al. (1999) made VLA A-array radio continuum observations, complimented with an archival HST optical image. They found a chain of 3 radio sources, interpreted as the nucleus and its two jets on opposite sides. Optical features are found in the HST image closely related to the radio jets, interpreted as gas compressed and excited by bow shocks driven into the ambient medium by the jets. This is different from the so-called extended emission line regions (EELR) which are supposedly excited by the AGN radiation (Aoki et al., 1996).

Even higher resolution (0.16") radio continuum observations at 1658 MHz, using MERLIN, were reported by Xanthopoulos et al. (2004). They compared the data with an HST/ACS U-band (F330W) image, and found extended UV emission around the nucleus and the northern jet. They argued that this indicates star formation triggered by the jet/ISM interaction. By assuming the diffuse radio emission outside the compact sources is due to the star formation, they estimated that the SFR in the circum-nuclear region is 8.4 $M_\odot$ yr^{-1}. However, all of the optical spectra of emission line regions in the circum-nuclear region show Seyfert or LINER line ratios and none is H II region-like (Aoki et al., 1996), indicating that most of the radio and UV radiation is related to the AGN and/or the shocks. Comparing the UV and MIR observations, Xu et al. (2005) found the AGN and the surrounding region is highly obscured, with an FUV extinction of $A_{\rm FUV} = 5.4$ mag, consistent with the Sy2 classification.

6.7.2   The H$_2$ bridge: AGN-driven outflow or tidal interactions?

Our new *Spitzer* spectral maps presented in sect. 6.2 show that the H$_2$ emission extends from the ridge to the core of the AGN NGC 7319. This "H$_2$ bridge" feature is also seen on the 1.4 GHz radio image (see Fig. 6.4 and Williams et al., 2002), on Hα maps (see Fig. 6.13 and Xu et al., 1999; Plana et al., 1999; Sulentic et al., 2001; Gutiérrez et al., 2002), and faintly detected in X-rays (see Fig. 6.8 and Trinchieri et al., 2003, 2005). The distribution of the H$_2$ emission seems to correlate with that of the radio emission.

The origin of the "H$_2$ bridge" is unclear. Is it related to the AGN activity of NGC 7319, or is it related to past or recent galaxy interactions? Optical spectroscopy (Aoki et al., 1996) and VLA radio observations (Aoki et al., 1999) seem to support the first hypothesis. Indeed, Aoki et al. (1996) interpret the large velocity gradients between the AGN core and the South-West bridge as an high-speed (~ 500 km s^{-1}) jet-induced outflow of gas. The very high electron density in the outflow (~ 600 cm^{-3}, twice that of the nucleus) and the multiple radio structure in the jet suggest that the outflow is interacting with interstellar matter. The H$_2$ emission in this bridge may then be powered by jet-driven shocks within dense clouds or/and AGN radiation. Cluver et al. (2009) propose an alternative explanation: the bridge is a remnant of previous tidal interactions. This scenario is suggested by the similarity between the mid-IR spectrum and X-ray properties of the *ridge* and *bridge* regions. This picture fits in the context of multiple shock heating events proposed by Moles et al. (1997); Sulentic et al. (2001); O'Sullivan et al. (2009b). The two scenarios (AGN-driven outflow and galaxy-wide shock) are difficult to disentangle because they lead to similar observational signatures. Our new CO observations in the ridge and in the bridge set a new light on this question, and we will discuss this further in sect. 7.3.

6.8   Summary and conclusions

One of the most interesting features of the Stephan's Quintet compact group is the presence of a galaxy-wide shock in the halo of the group, created by an intruding galaxy colliding with a tidal tail at a relative velocity of $\sim 1\,000$ km s^{-1}. Evidence for a group-wide shock comes from observations of X-rays from the hot postshock gas in the ridge strong radio synchrotron emission from the radio emitting plasma and shocked-gas excitation diagnostics from optical emission lines. *Spitzer* observations show

that this gas also contains molecular hydrogen with an extreme velocity dispersion. The H_2 luminosity is larger than the X-ray emission from the same region, thus the H_2 line emission dominates over X-ray cooling in the shock. As such, it plays a major role in the energy dissipation and evolution of the postshock gas.

The interpretation of these observations is the core of my PhD work. I present a scenario where H_2 gas forms out of the postshock gas that results from the supersonic collision between two multiphase gas streams. This collision leads to a multiphase medium with a distribution of shock velocities, related to the variations of the density in the preshock medium. The H_2 formation in the SQ ridge environment is quantified by calculating the time-dependent isobaric cooling of the gas, including dust destruction mechanisms. I show that H_2 forms out of the dense regions where dust survives the shocks. The bulk kinetic energy of the molecular gas is the main energy reservoir of the postshock gas, and it has to be dissipated within the H_2 gas to explain the poserful H_2 excitation. I propose that supersonic turbulence is sustained within the molecular gas by a transfer of momentum induced by cloud-cloud collisions and the relative shear motions between the molecular gas and the hot plasma. A phenomenological model of low-velocity MHD shocks driven into the dense H_2 gas is capable of explaining the observed excitation characteristics.

Within this framework, dust is a key ingredient. It is required for H_2 formation. Our model has implications on the expected dust emission in the SQ halo and on dust survival in a multiphase environment. These points are adressed in chapter 8, as well as a discussion of star formation in the SQ group.

6.9 Publication: paper II

In the following, we reproduce the Cluver et al. (2009) paper, entitled *Powerful H_2 line-cooling in Stephan's Quintet : I- Mapping the dominant cooling pathways in group-wide shocks*, accepted for publication in ApJ. This paper contain some figures I have discussed in this chapter, and a lot of details that I have intentionally not repeated in this manuscrit.

POWERFUL H₂ LINE-COOLING IN STEPHAN'S QUINTET : I- MAPPING THE DOMINANT COOLING PATHWAYS IN GROUP-WIDE SHOCKS

M.E. Cluver[1], P.N. Appleton[2,3], F. Boulanger[4], P. Guillard[4], P. Ogle[1], P.-A., Duc[5], N. Lu[2], J. Rasmussen[6], W.T. Reach[1], J.D. Smith[7], R. Tuffs[8], C.K. Xu[2], M.S. Yun[9]

Draft version July 21, 2009

ABSTRACT

We present results from the mid-infrared spectral mapping of Stephan's Quintet using the *Spitzer Space Telescope*. For the first time the large-scale distribution of warm molecular hydrogen emission is revealed in the group, as well as its close association with known shock structures. In the main shock region alone we find $2.8 \times 10^8 \, \mathrm{M_\odot}$ of warm H₂ spread over $\sim 480 \, \mathrm{kpc^2}$ and additionally report the discovery of a second major shock-excited H₂ feature, likely a remnant of previous tidal interactions. This brings the total H₂ line luminosity of the group in excess of $10^{42} \, \mathrm{erg \, s^{-1}}$. In the main shock, the H₂ line luminosity exceeds, by a factor of three, the X-ray luminosity from the hot shocked gas, confirming H₂ as the dominant cooling pathway in the shock. The H₂ emission requires dust to survive in dense clumps. [Si II] emission, detected at a luminosity of 1/10th of that of the H₂, appears to trace the group-wide shock closely and in addition, we detect weak [Fe II] from the most X-ray luminous part of the shock. Comparison with shock models reveals that this emission is consistent with regions of fast shocks ($100 < V_s < 300 \, \mathrm{km \, s^{-1}}$) experiencing depletion of iron and silicon onto dust grains.

Star formation in the shock (as traced via nebula lines, PAH and dust emission) appears in the intruder galaxy, but most strikingly at either end of the radio shock. The shock ridge itself shows little star formation, consistent with a model in which the tremendous H₂ power is driven by turbulent energy transfer from motions in a post-shocked layer which suppresses star formation. The dominance of the molecular hydrogen lines over other sources of cooling in fast galaxy-scale shocks may have crucial implications for the cooling of gas in the assembly of the first galaxies.

Subject headings: galaxies: evolution – galaxies: individual (NGC 7318b; NGC7319) – galaxies: interactions – intergalactic medium – compact groups – shocked H₂ emission

1. INTRODUCTION

Stephan's Quintet (hereafter SQ) is a strongly interacting compact group which has produced a highly disturbed intragroup medium (IGM) (Xu et al. 2003, 2005) through a complex sequence of interactions and harrassment (Allen & Sullivan 1980; Williams et al. 2002). This interplay has produced a large-scale intergalactic shockwave, first observed as a narrow filament in the radio continuum (Allen & Hartsuiker 1972), and subsequently detected in the X-ray (Pietsch et al. 1997; Trinchieri et al. 2005). The high-velocity ($\sim$1000 km s^{-1}) collision of an intruder galaxy, NGC 7318b, with the intergalactic medium of the group (Sulentic et al. 2001; Xu et al.

2003) is believed to be responsible for the shock-heating of the X-ray emitting gas. Optical emission lines associated with the structure provide clear evidence of high-excitation and broad-line widths are indicative of turbulent shocks (Xu et al. 2003; Duc et al. 2009, in preparation).

In Figure 1 we show schematically the main elements of Stephan's Quintet. Central to the system is the primary shock, as shown by the 20 cm contours, with NGC 7318b, the intruder galaxy, lying West of the shock. NGC 7319, the Seyfert 2 galaxy (Durret 1994), lies to the East and the extranuclear star formation region, SQ-A (Xu et al. 1999, 2003), lies to the North of the primary shock.

The unexpected discovery of extremely powerful, pure-rotational H₂ line emission from the center of the shock using the *Spitzer Space Telescope* (Appleton et al. 2006), hereafter *Spitzer* [10], has sparked intense interest in the SQ system. Warm molecular hydrogen emission was found with a line luminosity exceeding the X-ray luminosity from the shock. The mid-infrared (MIR) H₂ line-width was resolved ($\sigma = 870$ km s^{-1}) suggesting that the H₂-emitting clouds carry a large bulk-kinetic energy, tapping a large percentage of the energy available in the shock. A recent model of SQ, involving the collision between two inhomogeneous gas flows, describes H₂ forma-

[1] Spitzer Science Center, IPAC, California Institute of Technology, Pasadena, CA 91125
[2] NASA Herschel Science Center, IPAC, California Institute of Technology, Pasadena, CA 91125
[3] Visiting Astronomer, Institute d'Astrophysique Spatiale, Université Paris Sud 11, Orsay, France
[4] Institute d'Astrophysique Spatiale, Universite Paris Sud 11, Orsay, France
[5] Laboratoire AIM, CEA/DSM - CNRS - Université Paris Diderot, DAPNIA/Service d'Astrophysique, CEA/Saclay, F-91191 Gif-sur-Yvette Cedex, France
[6] Carnegie Observatories, 813 Santa Barbara St., Pasadena, CA 91101, Chandra Fellow
[7] Department of Physics and Astronomy, Mail Drop 111, University of Toledo, 2801 West Bancroft Street, Toledo, OH 43606
[8] Max-Planck-Institut für Kernphysik, Saupfercheckweg 1, 69117 Heidelberg,Germany
[9] Department of Astronomy, University of Massachusetts, Amherst, MA
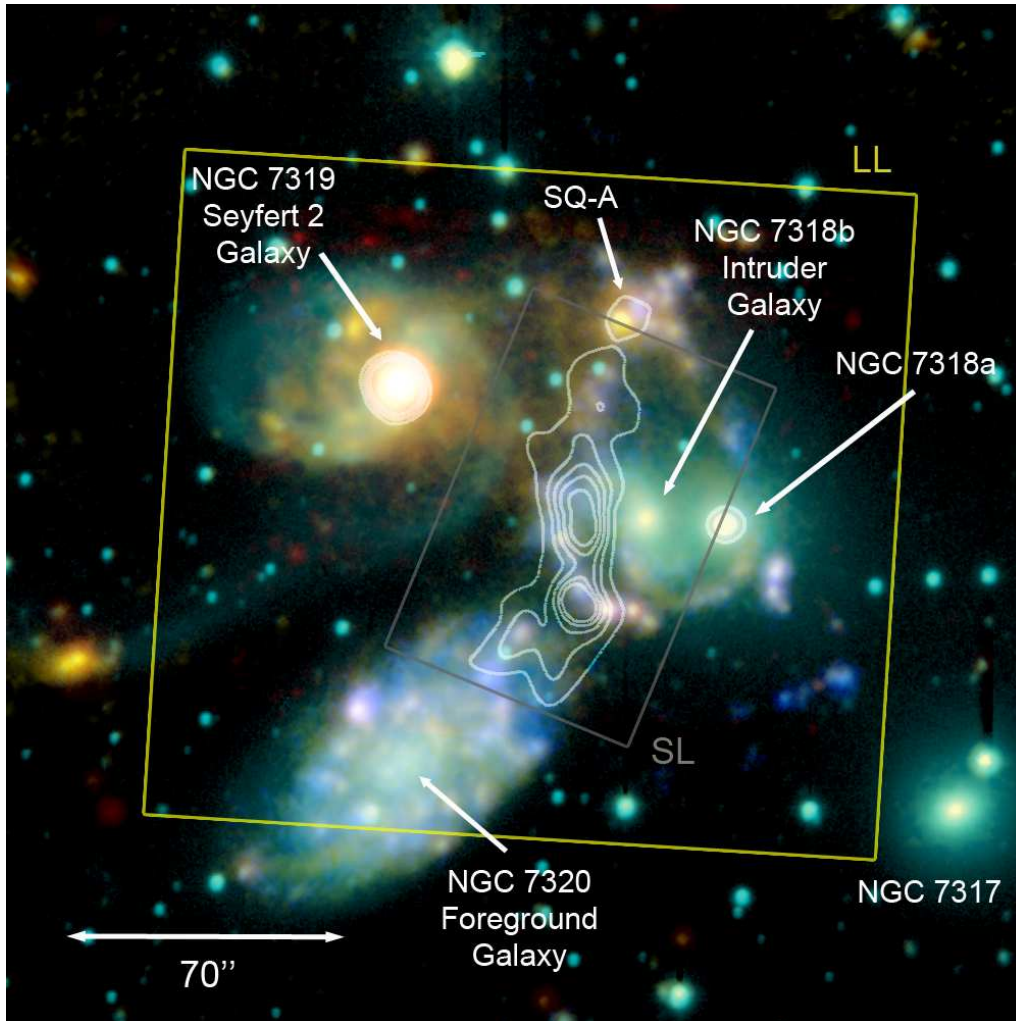
Fig. 1.— Schematic composite image of Stephan's Quintet consisting of a *Galex* Near-UV image, an optical R-band image from Xu et al. (1999), an IRAC 8μm image and an image from the 16μm IRS Peak-up Array. The contours show the 20 cm emission associated with the shock as obtained by the VLA (Xu et al. 2003). The boundaries of the *Spitzer* IRS Spectral Mapping coverage (this paper) are shown as boxes. A color version of this image is available in the online publication.

tion out of the multiphase, shocked gas, and an efficient cooling channel for high-speed shocks as an alternative to X-ray emission (Guillard et al. 2009)

Since the SQ detection, several other systems showing similarly strong H_2 emission have been discovered. Ogle et al. (2007, 2009) find that a large-subset of the local 3CR radio galaxies have extremely dominant MIR rotational H_2 lines, often seen against a very weak thermal continuum. The low-powered AGN continuua and very low star formation rates indicate an alternative excitation mechanism generating the high H_2 line luminosities ($10^{41} < L_{H_2} < 5 \times 10^{42}$ ergs s^{-1}). In addition, H_2 luminosities exceeding 10^{43} ergs s^{-1} have been detected associated with central cluster galaxies (Egami et al. 2006) and filaments in clusters (Hatch et al. 2005). The study of nearby prototypes may provide valuable insight into the nature of these more distant systems. The large-scale (~ 30 kpc) nature of the SQ shock is well-suited for such a study.

In this Paper I, we extend the single pointing observations of Appleton et al. (2006) to full spectral maps of SQ in the SL and LL modules of the IRS instrument on *Spitzer*. This shows, for the first time, the astonishing extent and spatial distribution of warm H_2 and places the emission in the context of the known shocked X-ray gas and the compact group as a whole. The new observations have revealed the detection and distribution of [Fe II]25.98μm and [Si II]34.81μm emission from the shock, as well as PAH (polycyclic aromatic hydrocarbon) and dust emission from star forming regions. In Paper II, we will present detailed 2-dimensional excitation maps of the H_2 emission across the face of the X-ray emitting shock, and compare them with models. In addition, several other papers are being prepared by our team which will discuss the relationship between the UV/X-ray emission and emission from dust.

In Section 2, we present our observations and data reduction methods. In Section 3 we discuss the mapping

results for various detected lines. In Sections 4, 5 and 6 we present our discussion on the properties of the system and in Section 7 the implication for galaxy formation. In Section 8 we present our conclusions. Additional material is included as appendices, with a discussion on NGC 7319 in Appendix A, and a reanalysis of the high resolution MIR spectrum of the shock, as well as renanalysis of the X-ray data presented in Appendix B and C, respectively.

Throughout this paper, we assume a systemic velocity of $v = 6600 \, \mathrm{km \, s^{-1}}$ for the group, corresponding to a distance of 94 Mpc with $H_\mathrm{o} = 70 \, \mathrm{km \, s^{-1} Mpc^{-1}}$.

2. OBSERVATIONS AND DATA REDUCTION

Mid-infrared spectroscopy of the shock region in SQ was obtained using the IRS instrument (Houck et al. 2004) onboard *Spitzer*. Observations were done in low-resolution mapping mode, using the Short-Low ($R \sim 60 - 127$; $5.2 - 14.5 \, \mu$m) and Long-Low ($R \sim 57 - 126$; $14.0 - 38.0 \, \mu$m) modules and taken on January 11 2008 and December 10 2007, respectively. Figure 1 shows an outline of the areas observed superimposed on a composite image of the group.

The SL spectral mapping consists of two separate, partially overlapping maps, centered North and South on the X-ray emission associated with the shock. The map was constructed with 23 steps of $2.8''(0.75 \times \text{slit width})$ perpendicular to the slit and one parallel step of $7.2''$. Observations consisted of 60 s integrations with 5 cycles per step.

The LL module was used to map an area of $\sim 2.8' \times 3.2'$ using 21 steps of $8.0''$ ($0.75 \times$ slit width) perpendicular to the slit and a parallel step of $24.0''$. An integration time of 120 s was used with 3 cycles per step.

Primary data reductions were done by the *Spitzer* Science Center (SSC) pipeline, version S17.0.4 and S17.2.0 for SL and LL respectively, which performs standard reductions such as ramp fitting, dark current subtraction and flat-fielding. Background subtraction for LL data was performed by subtracting dedicated off-source observations, with the same observing mode, taken shortly after the mapping sequence. In the case of SL, where for scheduling reasons the dedicated "off" observations were too far away in time to be optimal, backgrounds were generated from observations at the periphery of the map that contain no spectral line signatures.

Unlike standard pipeline processing, we did not perform the stray-light correction to account for potential spillover from the peak-up arrays onto the SL1/2 spectral apertures. This was due to the stray-light-corrected images containing wavelength-dependent over-corrections in some of the images due to a high background of cosmic rays during the SL portion of the mapping. However, we were able to show that after background subtraction, any uncorrected stray light in the SL spectral extraction areas was unmeasurable at the $< 2 - 3\%$ level. Thus stray-light correction was unneccesary, and the resulting Basic Calibrated Data (BCD) images used were of better quality than the standard BCDs.

For all modules, individual frames for each pointing were median-combined and obvious "bad" pixels were replaced using customised software that allows for manual "average" replacement. The spectra were assembled into spectral cubes for each module using the software

tool, CUBISM (Smith et al. 2007). Further bad pixel removal was performed within CUBISM. Spectral maps were generated by making continuum maps on either side of a feature and subtracting the averaged continuum map from the relevant emission line map. One dimensional spectra were further extracted from the data cubes using matched apertures.

Broad-band images at 16 and 24μm were obtained with the *Spitzer* IRS blue Peak-up Imager (PUI) and the MIPS instrument. The PUI was obtained in a 5 x 5 map with 3 cycles of 30s duration each on 2007 December 10. The MIPS instrument (Rieke et al. 2004) on *Spitzer* obtained 24μm imaging of SQ on 2008 July 29, achieving a spatial resolution of $\sim 6''$. Primary data reduction was done by the *Spitzer* Science Center (SSC) science pipeline (version S18.0.2) run through the MOPEX software, and for the MIPS image a smooth 2D polynomial background was further removed to correct for a large-scale background gradient. *Spitzer* IRAC (3.6, 4.5, 5.8 and 8.0 μm) data of SQ (P.I. J.R. Houck) were obtained from the SSC archive; these were reduced using science pipeline version S18.0.2. The final mosaics have a pixel scale of $0.61''$.

3. RESULTS

3.1. *The Molecular Hydrogen Distribution*

The pure rotational transitions of molecular hydrogen can be excited by several mechanisms. These include FUV (Far Ultraviolet) induced pumping, and possible additional collisional heating, of the H$_2$ in photodissociation regions associated with star formation (e. g. Black & Dishoeck 1987, Hollenbach & Tielens 1997), hard X-rays penetrating and heating regions within molecular clouds, which in turn excite H$_2$ via collisions with electrons or hydrogen atoms (Lepp & McCray 1983; Draine & Woods 1992) and finally collisional excitation of H$_2$ due to acceleration produced by shocks (e.g. Shull & Hollenbach 1978). The pure rotational MIR line ratios are not especially good diagnostics for distinguishing between these mechanisms, since all three mechanisms discussed can lead to well thermalized level distributions of lower-level rotational states. The low-J rotational H$_2$ emission lines do, however, allow us to trace gas at different temperatures and compare with model predictions (this will be the main emphasis of Paper II). Higher level transitions 0-0 S(3)-S(5) tend to trace warmer gas, whereas the S(0) and S(1) lines are sensitive to the "coolest" warm H$_2$.

Although the line ratios themselves cannot be used directly as shock diagnostics, in Stephan's Quintet the distribution of large-scale X-ray and radio emission, plus optical emission line diagnostics, provide strong evidence that the giant filament shown in Figure 1 is the result of a strong shock. In Appleton et al. (2006) this fact was used to determine the surprising association of detected H$_2$ emission with the shock. However, in this paper we can make a more definitive association of the emission with the shock by means of spectral maps.

The spectral cubes were used to extract maps of all the pure rotational emission lines of molecular hydrogen that were detected, namely the 0-0 S(0), S(1), S(2), S(3), S(4) and S(5) lines at 28.22, 17.03, 12.28, 9.67, 8.03 and 6.91μm, respectively. Specific intensity contour maps of these lines are shown in Figure 2 overlaid on a *R*-band
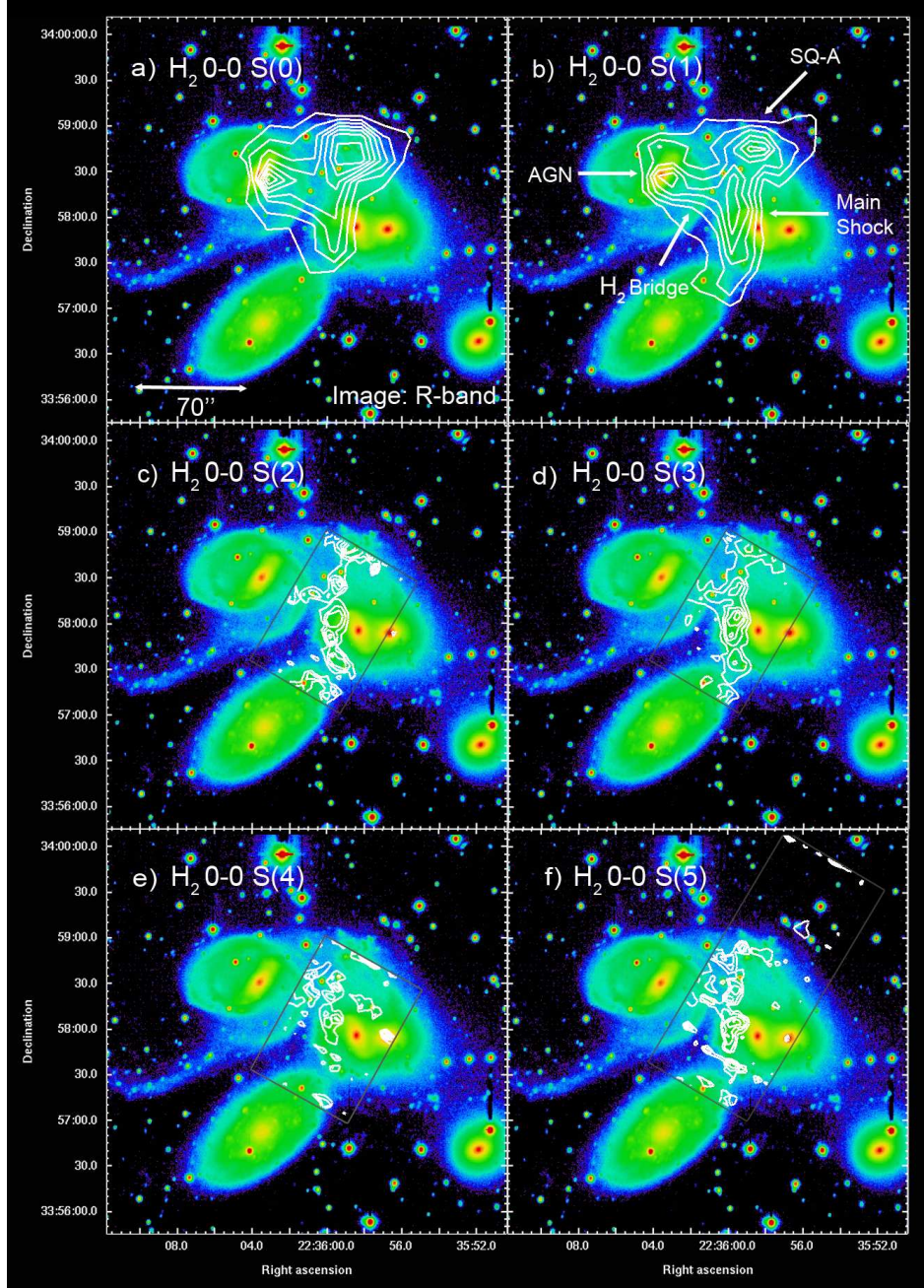
FIG. 2.— The large-scale distribution of warm H_2 in Stephan's Quintet with each detected 0-0 transition overlaid on an R-band image from Xu et al. (1999). The grey box indicates the limit of the SL module coverage. Contour levels are as follows (all in units of MJy/sr): (a) 0.1, 0.14. 0.19, 0.28, 0.32, 0.37, 0.41, 0.46, 0.5, (b) 0.3, 0.53, 0.75, 0.98, 1.2, 1.43, 1.65, 1.88, 2.1, (c) 0.3, 0.4, 0.5, 0.6, 0.7, (d) 0.25, 0.42, 0.58, 0.75, 0.92, 1.08, 1.25, (e) 0.11, 0.19, 0.27, 0.36, 0.44, 0.52, 0.6 and (f) 0.3, 0.46, 0.61, 0.77. 0.93, 1.09, 1.24, 1.4. We note that the SL coverage for (f) is larger due to incorporating the "parallel mode" SL2 slit observations from the "off-target" positions when SL1 mapping observations were the primary observing mode.

image of the region from Xu et al. (1999). The S(0) and S(1) lines were mapped by the LL modules, while S(2) - S(5) transitions were mapped by the SL modules of the IRS. As shown in Figure 1, the SL observations were concentrated on the main shock to provide high signal to noise (S/N) measurements there. As a result these maps do not fully cover SQ-A or NGC 7319. We note that the S(4) line at 8.03μm (Fig. 2e) is faint, and also suffers from contamination from the PAH bands at 7.7μm and 8.6μm.

The contours show powerful, widespread emission running North-South along the shock ridge (as shown in Fig. 1). In addition we also see strong emission from the star forming region, SQ-A, as well as associated with NGC 7319. We discuss further details of the AGN-like MIR emission lines from NGC 7319 in Appendix A.

Figures 2a-d show clearly a new H$_2$ structure running eastward from the "main" shock ridge. In what follows, we refer to this feature as the "bridge". We note that it is seen faintly in the *Chandra* (Trinchieri et al. 2003) and XMM (Trinchieri et al. 2005) X-ray images and detected as faint Hα emission by Xu et al. (2003), but is not seen in radio continuum images.

As is evident in Figure 2, there is distinct variation in the distribution of the warm H$_2$ emission. The brightest 0-0 S(0) emission (Fig. 2a) appears to be concentrated towards the North of the shock, whereas the 0-0 S(1) transition emission (Fig. 2b) appears more concentrated towards the center. We note that both the S(0) and S(1) maps show that the H$_2$ in the bridge terminates in a large clump a few arcsecs west of the nucleus of the Seyfert 2 galaxy NGC 7319, and in a small detour to the North (especially in the S(1) map which has the highest S/N).

The S(2) through S(5) lines clearly show that the warm H$_2$ emission breaks into clumps in the shock. Despite the limited coverage compared to the LL mapping, the base of the "bridge" is visible and SQ-A is partially covered. SQ-A is fully covered by the SL2 module (because of fortuitous "off observation" coverage) and hence the S(5) emission line shows that in SQ-A the H$_2$ emission is also clumpy.

The molecular-line maps provide considerable information about the excitation of the H$_2$ along and across the X-ray shock, but these discussions will be deferred to a full 2-D modelling of the H$_2$ excitation in Paper II (Appleton et al. 2009, in preparation). Instead we shall limit ourselves to global properties of the H$_2$ here. In Section 4 we shall present spectra of some selected regions of the emission and discuss a global excitation diagram for the shock.

To further demonstrate the close connection between the H$_2$ emission and the main global shock-wave in SQ, we now consider the distribution of warm H$_2$ in relation to the X-ray and radio emission. In Figure 3a and b we show the S(0) and S(3) contours overlaid on an XMM-Newton X-ray image (Trinchieri et al. 2005) of Stephan's Quintet. We see that the warm molecular hydrogen is distributed along the length of the main North-South (NS) X-ray shock ridge and along the "bridge", showing the remarkable projected coexistence of energetic X-rays and the seemingly fragile molecular hydrogen. Although the H$_2$ appears to follow the X-ray, there are subtle differences. We see that the cooler S(0) line has emission concentrated to the North and follows the X-ray less closely

compared to the warmer S(3) line. The S(3) line shows a clear correspondence to the X-ray, notably at the center of the shock, where we find peaks at both wavelengths. This implies that regions of greater shock heating (as traced by the X-ray) are producing warmer H$_2$ emission (this will be discussed further in Paper 2). The intergalactic star formation region SQ-A, is essentially absent in X-ray emission, as seen in Figure 3a, but is strongly detected in H$_2$.

We find a similar picture at 20 cm (Fig. 3c & d) with the S(0) line showing correspondence with the main shock, but dominated by emission in the North where we see less powerful radio emission. The S(3) (and S(2)–see Fig. 2c) line shows a much tighter correlation with regions of the shock that are more radio luminous than the lower-J transitions. However, the correlation breaks down for the warmest gas which would be represented by the S(4) and S(5) lines. The radio emission is quite likely sensitive to the most compressed regions of the shock where cosmic ray particles are accelerated more strongly (Helou & Bicay 1993; Appleton et al. 1999), whereas the brightest X-ray patches are likely due to the fastest regions of the shock (Guillard et al. 2009). As already mentioned the "bridge" emission is seen faintly in X-rays, but absent at radio continuum wavelengths, possibly suggesting older shock heating in the "bridge" compared with the main shock.

3.2. *Shock-related Fine-structure Line Emission*

Emission from fine-structure lines provide key diagnostics that trace the interplay between the various constituents of the shocked interstellar medium. In Appleton et al. (2006) the spectra shown were limited to the very core of the shock and only weak emission was detected from all but two metal lines, namely [Ne II]λ12.81μm and [Si II]λ34.81μm (this data has been reanalysed and it shown in Appendix B). In this section we discuss the spatial distribution of emission from the [Fe II], [O IV], [S III], [Si II], [Ne II] and [Ne III] lines located at rest λ 25.99, 25.89, 33.48, 34.82, 12.81 and 15.56 μm, respectively.

In Figure 4 we show the specific intensity contours of the [Fe II]25.99μm and [O IV]25.89μm blend, [S III]33.48μm and [Si II]34.82μm emission lines. Given the low spectral resolution of the SL and LL modules of *Spitzer*, we cannot distinguish between emission from [Fe II]25.99μm and [O IV]25.89μm. However, except in the direction of the Seyfert II galaxy NGC 7319, the emission near 26μm seen in Figure 4a is likely to be pure [Fe II] with little contamination from [O IV] as there is no evidence from the spectra of high-excitation emission from the intragroup medium in SQ. For example, [O IV] has an excitation potential of 56 eV (compared to 7.9 eV of [Fe II]), and yet Appleton et al. (2006) have shown that the [Ne III]/[Ne II] ratio is low suggesting low-excitation conditions for the ions in the shock, further supported in Section 5. We note faint emission from [Fe II]25.99μm at the location of the center of the shock (as defined by the X-ray "hotspot" in Fig. 3a). The energetic requirements for shocks to produce strong [Fe II] emission are usually present in J shocks while the ion abundance in C shocks are low in comparison (Hollenbach & McKee 1989). We will discuss the production of [Fe II] in the shock in Section 6.2.
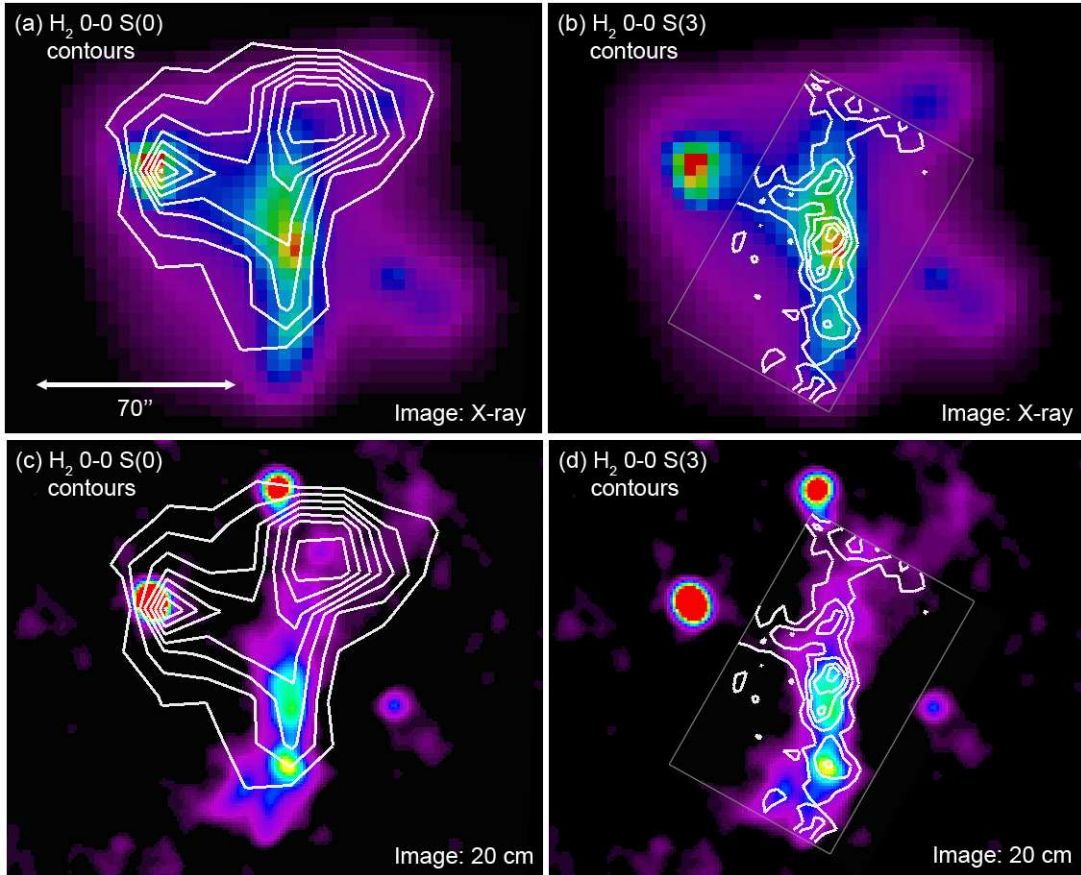
FIG. 3.— X-ray image from XMM-Newton (Trinchieri et al. 2005) in the 1.5−2.5 keV band with (a) H₂ S(0) contours and (b) H₂ S(3) contours overlaid. Also shown are 1.4 GHz radio continuum images from the VLA (Xu et al. 2003) with (c) H₂ S(0) contours and (d) H₂ S(3) contours overlaid. Contours levels are as in Fig 2.

The [S III]33.48μm distribution is shown in Figure 4b. This fine structure line acts as a strong tracer of H II regions (Dale et al. 2006) and we see emission from SQ-A and from other regions of star formation in the South (see section 3.3). We note that in the primary shock region the distributions of [Fe II] and [S III] are anti-correlated.

In strong contrast to the weak [Fe II] emission, we see copious [Si II]34.82μm emission (Fig. 4c), which follows the S(1) distribution closely with respect to the primary shock, as mapped by X-ray emission (Fig. 4d).

Although [Si II] is commonly found in normal H II regions, we will show below that, apart from in SQ-A, the strong silicon emission does not correlate with regions of strong PAH emission (tracing star formation) in SQ, but instead closely follows the H₂ and X-ray (shock) distributions. [Si II] acts as an efficient coolant of X-ray-irradiated gas and is predicted to be one of the top four cooling lines under these circumstances (Maloney et al. 1996). We will discuss the excitation of [SiII] in the shock in Section 6.2.

[Ne II]12.81μm (with an ionisation potential of 21.6 eV) is also represented in the shock, as shown in Figure 5a, although it is also emitted from some H II regions associated with star formation, such as SQ-A and the star-forming region South of NGC 7318b (see Section 3.3).

The [Ne III]15.56μm contours (with an ionisation potential of 41 eV) are shown in Figure 5b and are associated with excitation in the shock, as well as from regions of star formation (see Section 3.3). We see that the higher ionisation line of [Ne III] is much weaker in the shock ridge, but regions of emission correspond closely to peaks seen for the H₂ S(3) line. The [Ne II] emission, however, shows clearly extended emission with regions of greatest luminosity matching those seen for the H₂ S(3) line. The [Ne II] emission suggests excitation from the shock, with [Ne III] found at the location of the center of the shock, similar to what is seen for [Fe II].

3.3. Star Formation Tracers and Dust Emission in Stephan's Quintet

Previous observations of SQ and spectroscopy have shown (Xu et al. 2005) that there are some regions of star formation associated with the spiral arms of the intruder galaxy NGC 7318b. We show in this section how these regions, which have a different distribution from the shocked gas, are correlated with the PAH emission we detect in the IRS spectra.

In Figure 6a we show strong correlation between the 11.3μm PAH distribution (from the IRS cube) superimposed on a Near-UV image from *Galex* (Xu et al. 2005)
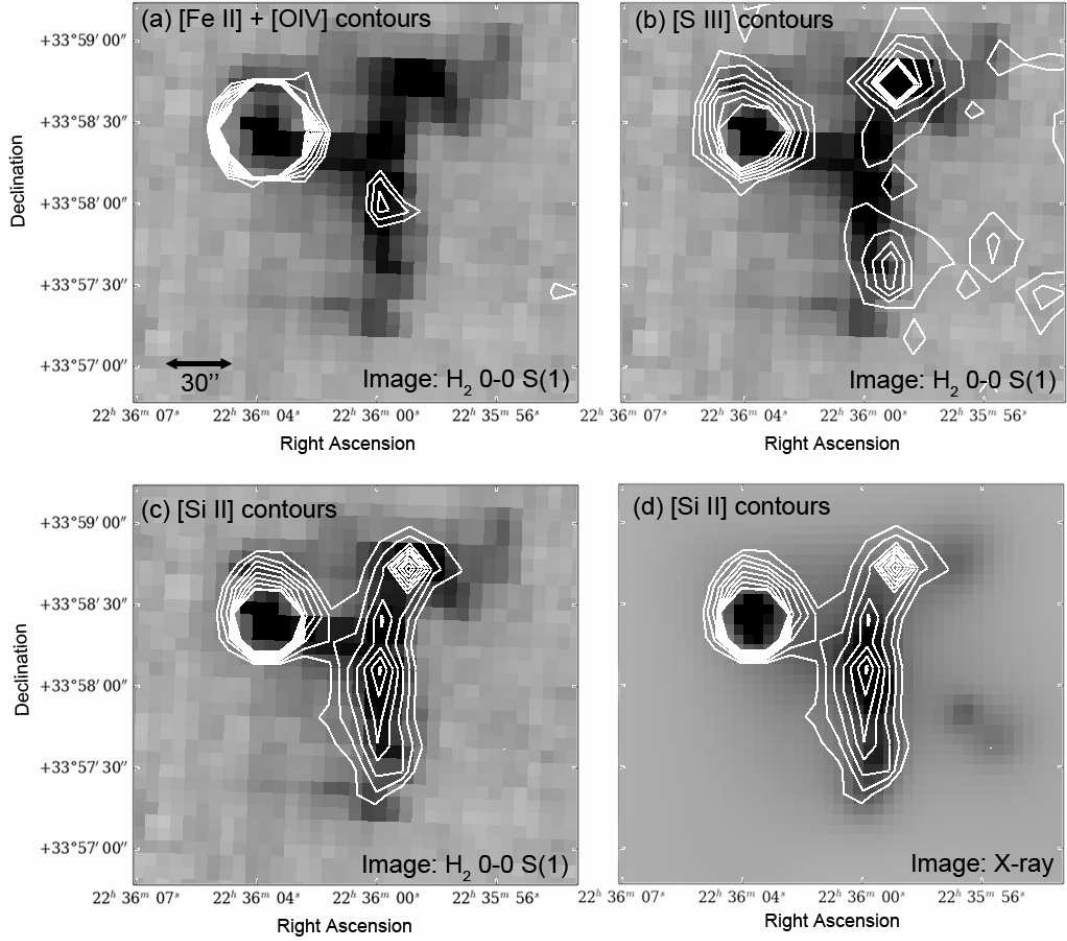
FIG. 4.— Fine structure emission ([Fe II]25.99μm and [O IV]25.89μm blend, [S III]33.48μm and [Si II]34.82μm) compared to the distribution of H$_2$ S(1) emission. Also shown are [Si II]34.82μm contours compared to X-ray 0.5-1.5 keV emission. Contour levels are as follows (all in units of MJy/sr): (a) 0.08, 0.1, 0.13, 0.15, 0.165, 0.18, 0.2, 0.22, 0.23, 0.25, (b) 0.2, 0.33, 0.47, 0.6, 0.73, 0.87, 1.0 with (c) and (d) having levels of 0.5, 0.66, 0.83, 0.99, 1.15, 1.31, 1.48, 1.6, 1.8.

which maps the UV emission from hot stars associated with weak star formation from the system. A similar close correlation is also seen in Figure 6b where we overlay the 11.3μm contours on the IRAC 8μm band, which is dominated by the 7.7 and 8.6 μm feature. The strong correlation between the 11.3μm map and the UV image suggests that the PAH molecules are excited by star formation.

We can also compare the 11.3μm PAH map to the distribution of thermal dust in Figure 6c, which shows the MIPS 24μm map of SQ. Again, it is clear that there is a good correlation between the PAH emission and the thermal dust, most of which seems only poorly correlated with the shock ridge. The lack of conspicuous star formation in the ridge was also observed by Xu et al. (2003).

The main point we emphasize here is that the dust, PAH and UV emission appears to be associated with previously known star formation regions and no additional star formation is seen in the shock; this can be seen in Figure 6d showing the H$_2$ 0-0 S(1) emission overlaid on

an IRAC 8μm image. We see little correspondence between the H$_2$ emission in the shock and 8μm (hot dust plus PAH) image. This is important because it implies that there is very little triggered star formation in the molecular gas associated with the shock-excited H$_2$.

Figure 6c shows that there is only faint dust emission at 24μm from the shock ridge. The presence of dust in the shock is required in the model of Guillard et al. (2009) to explain the formation of H$_2$ behind the shock and we do see evidence of dust reprocessing (see Section 6.2). Thus the faint 24μm emission could be the result of destruction of Very Small Grains (VSGs), with only larger grains surviving, or indicate that the grains are cold and radiating more strongly at longer wavelengths, where *Spitzer* has the least spatial resolution. A more detailed description of the current evidence for dust and faint PAH emission in the SQ group is discussed in separate papers (Guillard et al. 2009 in prep.; Natale et al. 2009 in prep.). A definitive understanding of the likely existence of cool dust in the shock will probably require an observatory like the *Herschel Space Observatory*.
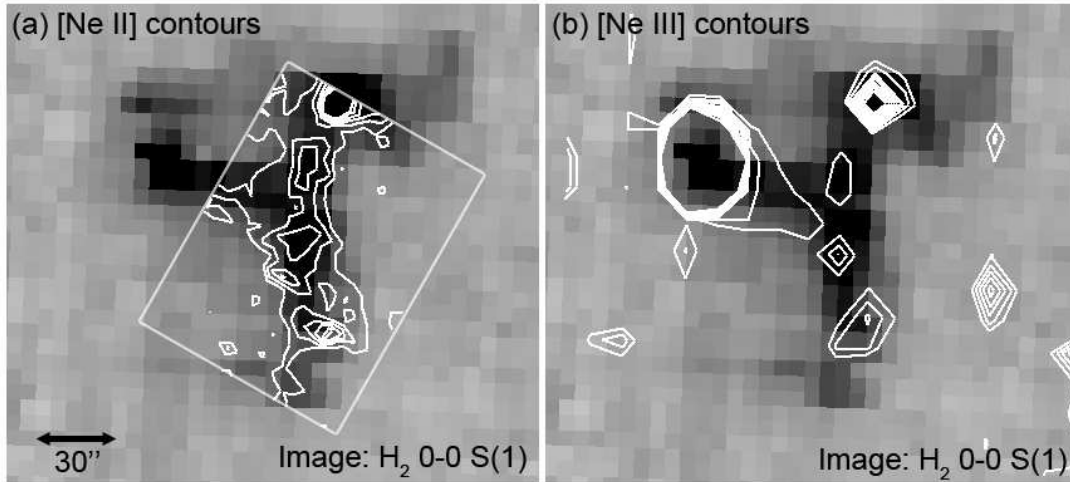
FIG. 5.— [Ne II]12.81μm and [Ne III]15.56μm emission compared to the distribution of H$_2$ S(1) emission. Contour levels are as follows (in units of MJy/sr): (a) 0.22, 0.4, 0.57, 0.75, 0.92, 1.1 and (b) 0.06, 0.08, 0.1, 0.13, 0.16, 0.18, 0.2, 0.23, 0.25.

Despite the faintness of emission from the main shock, the 24μm map shows a new result, which was less obvious in previous studies, namely that the dominant regions of star formation in SQ lie not in the galaxies themselves (with the possible exception of NGC 7319) but in two strikingly powerful, almost symmetrically disposed regions at either end of the shock. The region to the North is the well studied SQ-A, but the region to the South (which we refer to as 7319b-south) is also very powerful and both regions lie at the ends of the shock, as defined by the H$_2$ distribution. This may not be a coincidence, and we will discuss this further in Section 6.1.

The [Ne II]12.81μm, [Ne III]15.56μm and [S III]33.48μm fine-structure lines, as mentioned above, are also tracers of star formation in SQ as these lines are often associated with H II regions. The [Ne II]12.81μm emission appears to follow *both* the H$_2$ and the star formation regions (see Fig. 5a), appearing more extended in the South than the corresponding H$_2$ emission and flaring out where star formation regions, especially 7318b-south, are seen optically, and through PAH emission (see Fig. 6).

4. GLOBAL PROPERTIES OF THE MOLECULAR HYDROGEN IN SQ

We have demonstrated that the warm molecular hydrogen in Stephan's Quintet follows the X-ray distribution in the main shock (as defined by the radio emission) and in the "bridge" structure. This might suggest that the molecular hydrogen is excited directly by the X-ray heating. However, we will show that the H$_2$ emission exceeds by at least a factor of 3 the X-ray luminosity from the various shocked filaments, thus ruling out direct X-ray excitation from the shock.

To measure the strength of the H$_2$ emission, we extract spectra from various rectangular sub-areas of SQ which are defined in Figure 7. The spectra were extracted from CUBISM cubes built from each IRS module, and joined to make a continous spectrum–no scaling was necessary to join the spectra.

Figures 7 a, b and c show spectral extraction regions of the main NS shock, a sub-region of the shock and

a characteristic part of the "bridge". The shock sub-region is chosen to be just North of the center of the shock, avoiding regions contaminated by star formation in the intruder. Spectra for these extractions are shown in Figure 8 a, b and c. All three spectra, share the common property that they are dominated by molecular hydrogen emission. The shock sub-region (Fig. 8b), unlike Figure 8a, is less contaminated by the star forming regions discussed in the previous section. The MIR continuum of the main shock appears stronger than the shock sub-region indicating stronger emission from warm dust; this is likely the result of contamination from star-forming regions in the main shock extraction. The bridge shows similarly weak continuum emission compared to the shock sub-region.

Figure 8 b shows the photometry from the 16μm Peak-up Image (PUI) and MIPS-24μm measurements of the same area superimposed on the IRS spectrum. The results strongly confirm the accuracy of the background subtraction and calibration of the IRS spectra. Stellar light in the extraction area, from an extended spiral arm of NGC 7318b, produces contamination of the shock spectrum, seen as continuum emission shortwards of 6μm, in both Figure 8a and b.

The striking similarity between the mid-IR spectrum of all three regions (powerful H$_2$ lines, weak PAH emission, and low excitation weak emission from fine structure lines) confirms that these properties, seen in the Appleton et al. (2006) observations of the shock core, extend to both the full extent of the main shock and the "bridge". This, and the fact that the "bridge" has similar X-ray properties to the main shock (see later) suggests that the "bridge" is a "scaled-down" version of the main shock. Thus the new IRS observations seem to suggest that more than one large-scale group-wide shock is present in the group. This could be the result of previous tidal interactions and imply multiple shock heating events have taken place in SQ, consistent with what is seen in the X-ray (O'Sullivan et al. 2009).

Figures 7d and 8d present the extraction region and
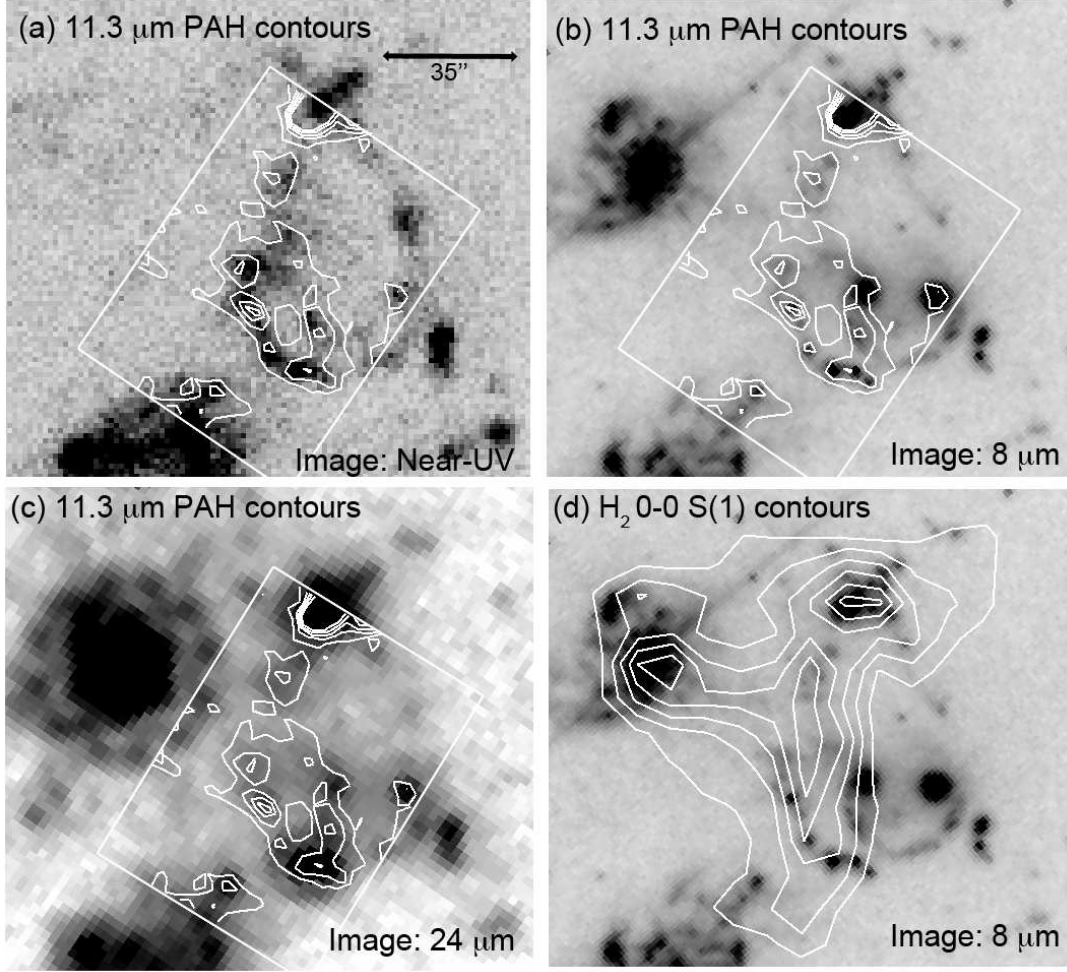
Fig. 6.— Dust as tracers of star formation. This shows 11.3μm PAH contours overlaid on (a) the Near-UV, (b) an 8μm image and (c) a 24μm image. By comparison the H$_2$ 0-0 S(1) contours show little correlation with the 8μm image (as shown in d). Contour levels are as follows (in units of MJy/sr): (a), (b) and (c) are 0.2, 0.35, 0.5, 0.65, 0.8. Contour levels for (d) are as in Fig. 2b.
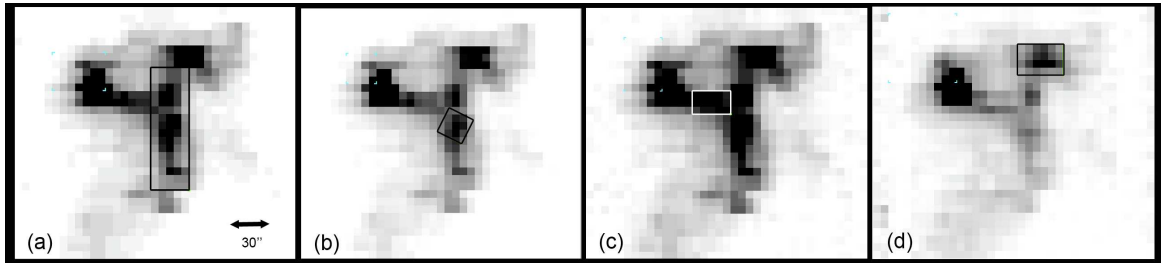
Fig. 7.— We show here the rectangular sub-regions extracted from the main components of the SQ shock system overlaid on the H$_2$ 0-0 S(1) line emission. a) The Main Shock region centered on 22^{h}35^{m}59.6^s, +33°58$'$05.7$''$. b) A region in the main shock centered on 22^{h}35^{m}59.97^s, +33°58$'$23.3$''$ and chosen to have limited contamination from star forming regions in SQ. c) Extraction of the H$_2$ "bridge" feature centered on 22^{h}36^{m}0.14^s, +33°58$'$23.3$''$. d) An extraction of the SQ-A star forming region centered on 22^{h}35^{m}58.85^s, +33°58$'$50.4$''$.

(a) Main Shock Region

(b) Shock Sub-region

(c) "Bridge"

(d) SQ-A
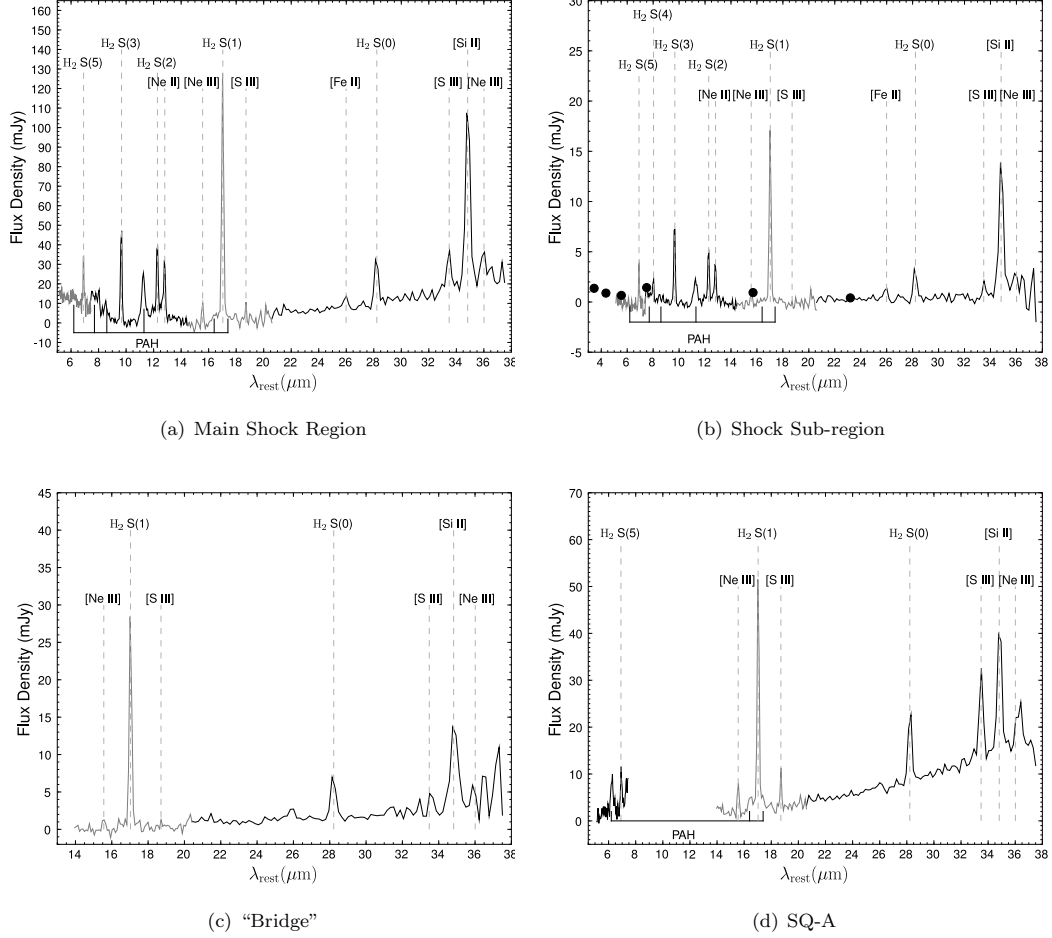
FIG. 8.— Extracted Spectra (low resolution) of the regions shown in Fig. 7 combining all IRS modules having coverage of the areas. The key emission features are labeled with measurements and sizes of extraction areas given in Table 2, which provides H_2 line fluxes, and Table 3 listing the PAH and fine-structure measurements. The shock sub-region (shown in b) shows the IRAC, $16\mu m$ PUI and $24\mu m$ MIPS measurements for the same area. The $16\mu m$ flux is 0.939 ± 0.047 mJy, which includes emission from the $17.03\mu m$ H_2 line covered by the filter, while the $24\mu m$ flux is 0.408 ± 0.046 mJy; photometry was performed using a circular aperture with no aperture correction applied to compensate for contamination from the surrounding emission. The corresponding IRAC fluxes are 1.362 ± 0.068, 0.885 ± 0.045, 0.659 ± 0.036 and 1.434 ± 0.073 mJy for the 3.6, 4.5, 5.8 and 8.0 μm bands, respectively. The extraction of SQ-A (shown in d) also has coverage from the SL2 module due to the orientation of the IRS during the SL1 observation.

spectrum of SQ-A, the extragalactic star-forming region. In this case, although H_2 lines are still strong, a rising continuum and an increase in the strength of the metal lines relative to the H_2 shows a spectrum that is increasingly dominated by star formation–a result which is already known from previous optical observations (Xu et al. 2003). Line fluxes for all the H_2 and metal lines in the spectra are presented in Table 2 and Table 3, respectively.

In order to place the H_2 emission from SQ in perspective, we estimate the luminosity emitted from the H_2 lines in the main aperture shown in Figure. 8a. The emission from the 0-0 S(1) line alone can be calculated from Table 2 (for D = 94 Mpc) to be 2.3×10^{41} erg s^{-1}. Summing the emission seen in the observed lines for the main shock (0-0 S(0) through S(5) lines) and including an extra 28% emission from unobserved lines (see model fit to excitation diagram below), yields a total H_2 line luminosity from the main shock of 9.7×10^{41} erg s^{-1}. This phenomenal power in the molecular hydrogen lines dwarfs by a factor of ten the next brightest mid-IR line, which is [Si II]34.82μm with a line luminosity of $L_{SiII} = 0.85 \times 10^{41}$ erg s^{-1}.

Figure 9 presents the excitation diagram of the low-J 0-0 H_2 transitions for the main shock extraction. The points are well fit by a model including three temperature components ($T_1 = 158\pm6$ K, $T_2 = 412\pm4$ K, and $T_3 = 1500\pm200$ K). It is likely that in reality, many different temperature components are present in the shock, and the three-temperature fit is only an approximation. However, it does allow us to provide an estimate of the total mass of warm H_2 of $5.0\pm1\times10^8$ M$_\odot$. Temperature T_2 is more uncertain than formally represented by the fit because it depends on the value of the S(4) flux, which may be systematically too low due to PAH contamination (see Fig. 9). In Paper II we will present a more complete two-dimensional map of the excitation of the H_2 in SQ and explore variations in the shape of the excitation diagram along and across the shock in more detail.

Our observations have shown that H_2 is the dominant line coolant in the MIR. However, how does it compare with the most important coolant in high-speed shocks–namely the X-ray emission? In Appleton et al. (2006) we had suggested that the H_2 emission was stronger than the X-ray emission at the shock center. We are now in a position to evaluate this over the whole group.

We present a complete reanalysis of the XMM-Newton observations of SQ using the latest calibrations (see Appendix C for full details) in order to determine the fluxes and luminosities of the X-ray emission to match our spectral extractions. The results show the striking dominance of the H_2 line luminosities compared with the X-ray emission from the same regions. For the main shock, the X-ray "Bolometric" flux $L_{X(0.001-10kev)} = 2.8 \times 10^{-13}$erg s^{-1}cm^{-2}, which corresponds to 2.95×10^{41} erg s^{-1}, or $L(H_2)/L_{X(0.001-10kev)} = 2.9$. This is probably a lower limit since we have not attempted to remove the contribution to the main shock aperture of an extended group-wide X-ray component upon which the emission from the shock lies. Nevertheless, it is clear that the H_2 line luminosity dominates over the X-ray emission from the entire shock by a factor ≥ 3. Similar calculations can be done for the other regions for

which H_2 spectra have been extracted. For example, in the "bridge" region, which we have already indicated has many of the same characteristics as the main shock, we find $L(H_2)/L_{X(0.001-10kev)} = 2.5$. These values show that throughout the extended regions of the SQ system, the dominant coolant in these high-speed shocks is molecular hydrogen. This is a very significant result, upturning the traditional view that X-ray emission always dominates cooling in the later stages of evolution in compact groups of galaxies.

5. EMISSION LINE DIAGNOSTICS

The fine-structure flux ratios (see Table 3) can be used to probe the conditions within the extracted regions of SQ. The [Si II] 34.82μm/[S III]33.48μm ratio provides an indication of the sources of excitation within the system. As mentioned previously, [S III] is mainly a tracer of H II regions, whereas enhanced [Si II] emission can be generated via several mechanisms, including thermal excitation by X-rays (XDR), or in shocks. In the main shock, the [Si II] 34.82μm/[S III]33.48μm ratio of ~ 4.59 is high compared to, for example, the low-luminosity AGN in SINGS which have an average value of ~ 2.9 (Dale et al. 2006). However, this large aperture is contaminated by star formation emission from SQ-A. A better measure is to take the smaller shock sub-region, where the [Si II] 34.82μm/[S III]33.48μm ratio in the shock sub-region is ~ 9.5. Thus it is clear that the [Si II] emission is well outside the normal range of values, even for local well-studied AGN. Using the upper limit found for [S III] 33.48μm in the "bridge" structure, we find a ratio of > 5–again values well outside the range of normal galaxy disk emission. Indeed, these high values are typical of galactic supernova remnants where shock excitation is well determined (e.g. Hewitt et al. 2009, find a range of $2.7 - 18$ for 6 remnants). We will argue in the next section that silicon is being ionised in regions experiencing fast shocks $100 < V_s < 300$ km s^{-1} and depleted onto dust grains . For the extragalactic star forming region SQ-A, [Si II] 34.82μm/[S III] 33.48μm $\sim$1.49, only slightly higher than the average of ~ 1.2 found for star-forming regions in the SINGS sample (Dale et al. 2006), another indication that SQ-A is dominated by star formation.

In star-forming galaxies the [Ne III] 15.56μm/[Ne II] 12.81μm ratio can be used as a measure of the hardness of the radiation field as it is sensitive to the effective temperature of the ionising sources. In the main shock, we find a value of ~ 0.36 which would be considered typical compared to, for example, those found in starburst systems, which range from $\sim 0.03 - 15$ (Verma et al. 2003; Brandl et al. 2006), and in supernovae remnants (0.07 - 1.24 for the sample of Hewitt et al. 2009). The shock subregion has a ratio of only ~ 0.14 indicating a lower intensity radiation field North of the shock center. However, it is clear that most of the neon is not originating from star formation, and so shocks are an obvious source of excitation.

Using [Ne II] 12.81μm/[Ne III] 15.56μm ratio as a measure of shock velocity (from the models of Hartigan et al. 1987), the ratio of ~ 2.74 for the main shock corresponds to shock speeds of 200 km s^{-1}, 100 km s^{-1} and/or 80 km s^{-1} and the shock sub-region value corresponds to a shock of 80 km s^{-1}. Using the shock model library of Allen et al. (2008) we find that
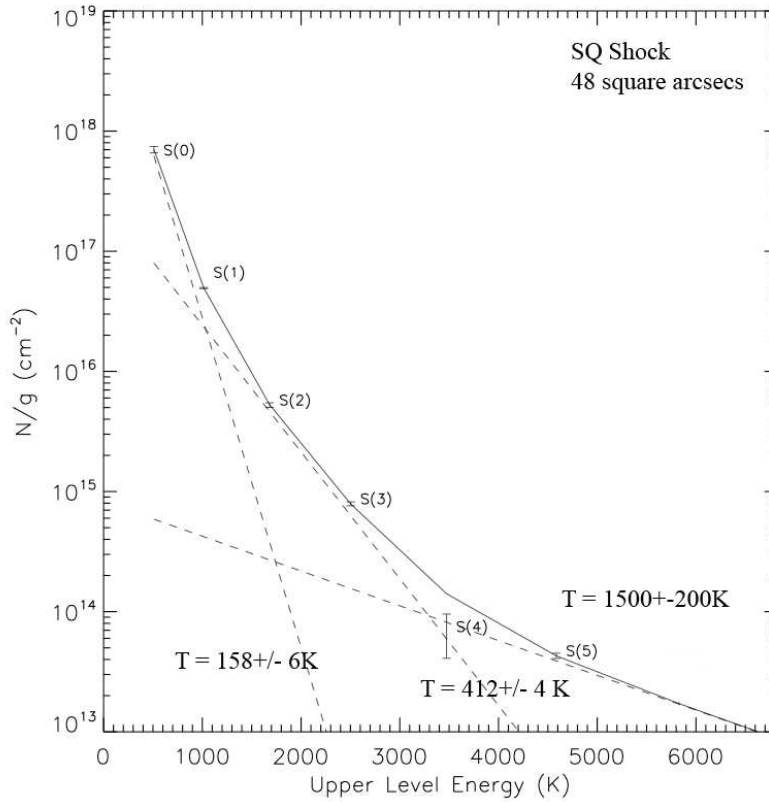
FIG. 9.— Excitation Diagram of the Main Shock region in Stephan's Quintet. The ordinate (N/g) represents the column density divided by the statistical weight of the rotational state.

the [Ne III] 15.56μm/[Ne II] 12.81μm ratio for the main shock corresponds to shock velocities between 100 and $300\,\mathrm{km\,s^{-1}}$ (using preshock densities, n, between 0.01 and 10 cm^{-3} and magnetic parameter[11] $B/n^{\frac{1}{2}} = 1$). We shall use this in Section 6.2 to explore dust reprocessing in the shock.

We estimate the average electron density from the [S III]18.71μm/[S III]33.48μm (two lines of the same ionisation state) ratio. For SQ-A we find a ratio of $\sim$0.56, and in the main shock $\sim$0.41. This corresponds to an electron density of $100 - 200$ cm^{-3} (Martín-Hernández et al. 2002) i.e. in the low-density limit for this diagnostic (Smith et al. 2009).

6. THE GROUP-WIDE SHOCKS

6.1. *Origin of the H$_2$ and X-ray emission*

Our observations have shown that the molecular hydrogen and X-ray emitting plasma seem to follow a similar distribution, and we have ruled out the possibility that this is a consequence of X-rays heating the H$_2$, since the H$_2$ has the dominant luminosity. How then can we explain the similar distributions? Are these results consistent with the hypothesis that the shock is formed where the intruding galaxy NGC 7318b collides with a preexisting tidal filament of H I drawn out of NGC 7319 in a

[11] This value is less than the nominal equipartition value of 3.23. See Allen et al.(2008)

previous interaction with another group member (Moles et al. 1997; Trinchieri et al. 2003)?

This basic mechanical picture seems plausible as can be seen in Figure 10 which shows that the H$_2$ distribution "fills in" the gap in the H I tidal tail as seen by the VLA (Williams et al. 2002). The implication is that the H I has been converted into both a hot X-ray component and a warm H$_2$ component by the collision of the intruder with the now missing H I .

Part of the puzzle of how this high-speed ($V_s \sim 700 - 1000$ km s^{-1}) shock can lead to both X-ray and very strong molecular line emission is presented in a model by Guillard et al. (2009). The high-speed collision of NGC 7318b with the H I filament (assumed to be composed of a multi-phase medium) leads to multiple shocks passing through and compressing denser clumps (which become dusty nucleation sites for H$_2$ formation) at the expense of the lower-density gas which is shock-heated to X-ray temperatures. The H$_2$ therefore forms in denser clouds experiencing slower shocks. Thus the coexistence of both hot X-ray gas, and cooler molecular material is a natural consequence of the multi-phase medium of the pre-shocked material.

Modeling of the H$_2$ excitation by Guillard et al. (2009) shows that the emission can be reproduced by low velocity ($\sim 5 - 20\,\mathrm{km\,s^{-1}}$) magnetohydrodynamic shocks within the dense ($n_\mathrm{H} > 10^3\,\mathrm{cm^{-3}}$) H$_2$ gas. The denser clouds survive long enough to be heated by turbulence

Fɪɢ. 10.— Schematic Diagram of the H I distribution in Stephan's Quintet, from Williams et al. (2002), and the H_α emission (Xu et al. 1999), with the H₂ 0-0 S(1) emission overlaid. The grey dots represent the locations of the core galaxies in the group as shown in Fig. 1.

in the hot-gas component, tapping into the large available kinetic energy of the shock. This picture also explains the broad $870\,\mathrm{km\,s^{-1}}$ H₂ line width discovered in the shocked molecular component (Appleton et al. 2006). Intermediate pre-shock densities and post-shock temperatures result in regions of H I and H II that have cooled, but where the dust content has been destroyed (Guillard et al. 2009). Similarly, pre-existing Giant Molecular Clouds (GMCs) embedded in the H I gas could become compressed by the shock, but not destroyed, causing instabilities that culminate in a burst of star formation. This triggering mechanism, proposed for SQ-A by Xu et al. (2003), could also apply to 7318b-south, however it seems unlikely for two GMCs to coincidentally lie at either end of the shock ridge. The star formation in SQ-A has been shown to have two components, in the IGM as well as in the ISM of the intruder (Xu et al. 2003), whereas 7318b-south appears to be associated with the intruder only (Xu et al. 2005). It may be that due to the geometry of the shock, these regions are dynamically more favourable for star formation as the postshock medium here is less turbulent and molecular gas has had time to cool and collapse. Detailed kinematic modeling of the collision may be possible with future improved resolution and data and remains to be explored.

6.2. Origin of [Fe II] and [Si II] emission

As outlined above, the combination of emission seen in the shock region of SQ can be understood in terms of a spectrum of shock velocities. The fastest shock velocities ($V_s \sim 600\ \mathrm{km\,s^{-1}}$) are associated with the lowest den-

sity pre-shock regions and the post-shock X-ray emitting plasma. These are fast J shocks and represent a discontinuous change of hydrodynamic variables and are often dissociative (Hollenbach & McKee 1989). C shocks have a broad transition region such that the transition from pre-shock to post-shock is continuous and are usually non-dissociative (Draine et al. 1983). The lowest velocity shocks associated with the turbulent H₂ emission are $\sim 5 - 20\ \mathrm{km\,s^{-1}}$ C shocks (Guillard et al. 2009).

We see that the [Fe II] emission associated with the shock region in SQ is relatively weak, but coincides with the most energetic part of the shock as traced by the X-rays (Fig. 4). We also see abundant [Si II] emission associated with the main shock.

Silicon and iron have very similar first and second ionization potentials. Their first ionization potentials (7.9 and 8.15 eV for Fe and Si, respectively) are lower than that of hydrogen but their second ionization potential is higher (16.19 and 16.35 eV). The MIR [Fe II] and [Si II] line emission observed from the SQ shock could thus arise from neutral as well as ionized gas. We discuss the contribution from the ionized gas using the [Fe II](26.0μm)/[Ne II](12.8μm) and [Si II](34.8μm)/[Ne II](12.8μm) line ratios. The high [Ne II](12.8μm)/[Ne III](15.6μm) mid-IR line ratio (see Section 5) implies that [Ne II] is the dominant ionization state of Ne in the SQ shock. Unlike Fe and Si, Ne is not much depleted on dust (Simpson et al. 1998); its MIR line has a high critical density ($n_e = 4.3 \times 10^5$ cm^{-3}, Ho and Keto 2007).

The optical line emission from the SQ shock is dis-
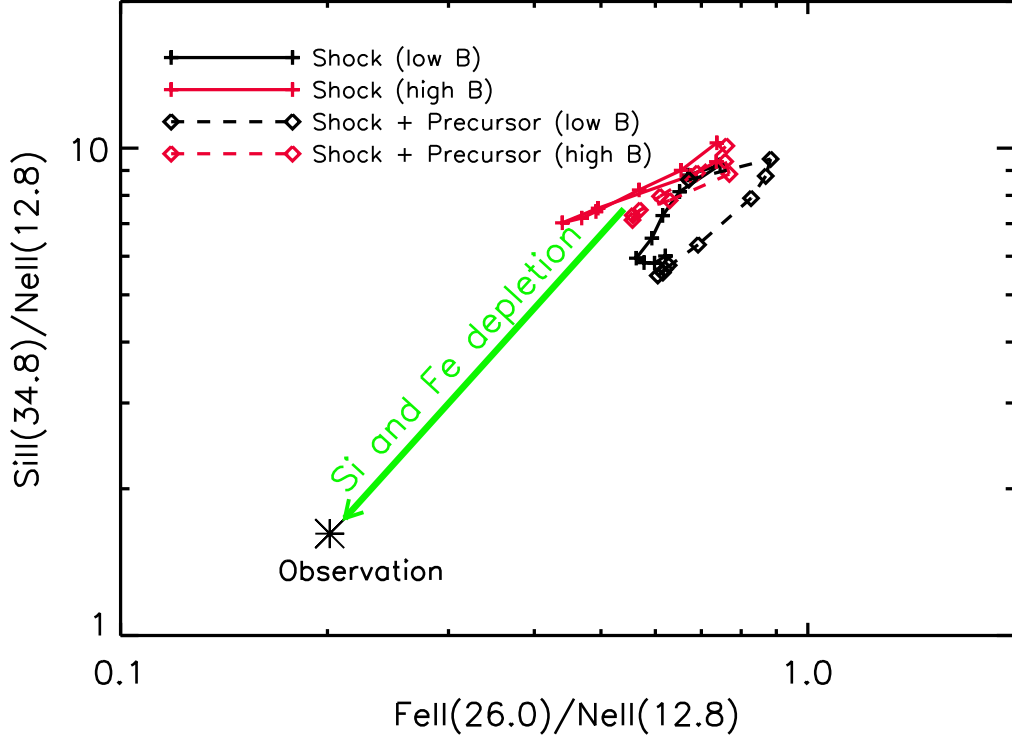
FIG. 11.— The line ratios measured in the Main SQ shock between the [Ne II](12.8μm), [Fe II](26.0μm), and [Si II](34.8μm) lines are compared with shock calculations from Allen et al. (2008). We show the model values for a shock velocity range $100 - 300 \ \mathrm{km\,s^{-1}}$, a gas density of $1 \, \mathrm{cm^{-3}}$ and two values of the magnetic parameter $B/n^{0.5} = 3$ and 0.5. Both line ratios, [Si II]/[Ne II] and [Fe II]/[Ne II], are lower than the model values which we interpret as evidence for Si and Fe depletion onto dust grains.

cussed in detail in Xu et al. (2003). The high values of the [O I](6300Å) and [N II](6584Å) lines to Hα line ratios are evidence of shock ionization. The optical [S II](6716Å/6731Å) line ratio as well as the MIR [S III] line ratio correspond to the low density limit (see Section 5) and comparison with the shock models of Allen et al. (2008) constrain the pre-shock gas density to be about $1 \, \mathrm{cm^{-3}}$ or smaller.

In Figure 11 we show the observed MIR ratios, as well as the expected emission from the shock models of Allen et al. (2008), with model values for both the shock and the shock plus its radiative precursor displayed for a pre-shock gas density of 1 cm^{-3} and for two values of the magnetic parameter, $B/n^{\frac{1}{2}} = 0.5$ and 3. The shock velocity ranges from 100 to $300\,\mathrm{km\,s^{-1}}$ in steps of $25\,\mathrm{km\,s^{-1}}$. For clarity of the figure, we have discarded higher velocities shocks which do not match the observed [Ne II]/[Ne III] line emission ratio (see Section 5). We note that Xu et al. (2003) find optical emission line ratios consistent with shock models that do not include a radiative precursor (Dopita & Sutherland 1995), but include it for comparison.

The observed [Fe II](26.0μm)/[Ne II](12.8μm) and [Si II](34.8μm)/[Ne II](12.8μm) are both smaller than the shock values. The iron and silicon lines are not dominant

cooling lines of ionizing shocks. The gas abundances of these elements do not impact the thermal structure of the shock and the line intensities roughly scale with the gas phase abundances. We thus interpret the offset between the IRS observation and model values as evidence for Fe and Si depletion. We consider the magnitude of the depletions indicated by the arrow in Figure 11 as lower limits since there could be a contribution to the [Fe II] and [Si II] line emission from non-ionizing J-shocks into molecular gas (Hollenbach & McKee 1989). Such shocks could also contribute to the [O I](6300Å) line emission as discussed in Guillard et al. (2009). Forthcoming observations of the H$_2$ ro-vibrational line emission in the near-IR should allow us to estimate whether they may be significant. A contribution from non-ionizing shocks to the [Fe II] and [Si II] line emission will raise the depletion of both Fe and Si as well as the Fe/Si depletion ratio because non-ionizing shocks do not produce [Ne II] line emission and the [Fe II](26.0μm)/[Si II](34.8μm) line emission ratio in J-shocks within dense gas is larger than for shocks plotted in Figure 11. Note that an increase of the Fe/Si depletion ratio would put the SQ depletion in better agreement with the ratio ~ 2 observed on average in the Milky Way (Sembach & Savage 1996).
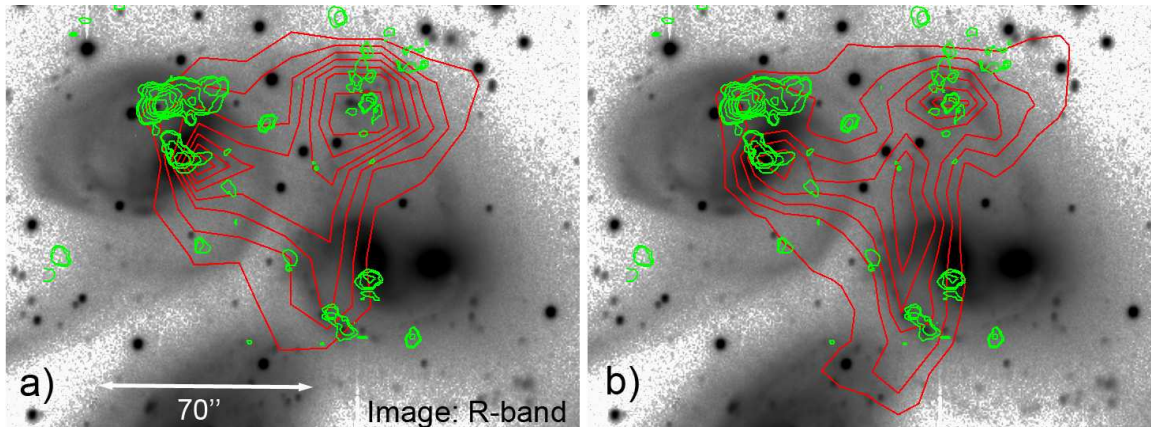
FIG. 12.— CO (1-0) contours from Gao & Xu (2000) shown on an R-band image (Xu et al. 1999) of the group. Contour levels correspond to 2.4σ, 3.0σ, 4.0σ, 5.0σ, 6.0σ, 7.0σ and 8σ ($1.0\sigma \sim 0.025$ Jy). In (a) we show the H$_2$ contours for the S(0) line and in (b) the S(1) line (with contour levels as in Fig. 2a and b respectively). This figure is available in colour in the online publication.

6.3. Comparison with Cold H$_2$ Distribution

A key aspect to understanding the emission we observe in SQ, as well as a test of the proposed model of H$_2$ excitation, is the amount and distribution of cold H$_2$, as measured by CO. A reservoir of cold H$_2$ associated with the warm gas observed in SQ would provide key insight into conditions within the intragroup medium. In Figure 12 we show the BIMA CO (1-0) integrated intensity contours from Gao & Xu (2000), shown with the H$_2$ S(0) and S(1) emission contours, overlaid on an optical image of SQ. These interferometric observations use the large primary beam of 110″, centered on the shock, to determine areas of high column densities in the group. We see that the CO traces areas of known star formation seen at $24\mu m$ and in the NUV (see section 3.3), notably SQ-A and 7318b-south. As seen by Yun et al. (1997), the CO around NGC 7319 is concentrated in two regions. The dominant complex is North of the nucleus residing in a dusty tidal feature. The nuclear CO is elongated perpendicular to the stellar disk indicating a deficiency of ongoing star formation in the disk.

We see that the CO distribution does not correlate with the warm H$_2$ emission, particularly around NGC 7319. The cold H$_2$ complexes are clearly offset from the concentrations of warm H$_2$. Even the S(0) emission line (see Fig. 12a), which follows the coldest warm H$_2$, does not have peaks corresponding to the strongest CO detections.

Lisenfeld et al. (2002) mapped CO in several regions of the IGM of SQ using the IRAM 30 m antenna, focusing mainly on the starbursts SQ-A and SQ-B. They did, however, detect narrow-line width CO emission above 3σ ($T_{mb} \sim 9$ mK) along the N-S shock ridge (as defined by th 20 cm and X-ray maps) North of NGC 7318b, with most of the gas at a velocity of 6000 km s^{-1}, but also detected at 6700 km s^{-1}.

In a forthcoming paper, we will report the recent detection of ^{12}CO(1-0) and (2-1) emission, associated with the warm H$_2$ in the SQ shock, using the single-dish 30m IRAM telescope (Guillard et al. 2009, in preparation). These observations suggest that most of the CO emis-

sion in the shock has been missed by the interferometers (because of the broad-line width) and show that the CO emission is both present in the shock, and extends along the H$_2$-emitting bridge and towards NGC 7319 (in the so-called H$_2$-bridge).

The kinematics of the CO gas lying outside of star-forming regions, in the new observations, appears to be highly disturbed with a broad line-width in agreement with the Appleton et al. (2006) interpretation that the MIR H$_2$ lines were intrinsically very broad and resolved by the high resolution module of IRS. The CO data also agrees with our re-analysis of the Appleton et al. (2006) data (see Appendix B) using more recent and reliable wavelength calibration, which places the bulk of the H$_2$ gas at velocities intermediate of that of the intruder and the group—supporting the idea that the H$_2$ gas is accelerated in the shock.

6.4. Turbulent Suppression of Star Formation in the H$_2$ filaments

In Section 3.3 we discussed the star forming regions seen in SQ and noted that there was very little evidence for star formation in the shock, associated with the warm H$_2$ emission. As discussed in Section 4, the main shock contains a large quantity of warm molecular hydrogen (5.0×10^8 M$_\odot$) providing a reservoir of fuel for star formation once it cools. We investigate star formation in the warm H$_2$-dominated medium by considering the shock sub-region, chosen to avoid star forming regions in the intruder galaxy, but likely still subject to some contamination from these regions.

PAH emission is a classical tracer of star formation, but the molecules are fragile and easily destroyed in hard radiation fields. We note that in the spectra of the main shock and subregion (Fig. 8a and b) we see that the PAH emission bands at 6.2 μm, 7.7 μm and 8.6 μm are far weaker compared to the 11.3 μm bands, which when strong are predominantly produced by neutral PAH molecules (Draine & Li 2001). In the shock subregion we find an upper limit flux for the 6.2 μm PAH of 0.47×10^{-17} W m^{-2} and fluxes of 0.87×10^{-17} W m^{-2}

and 2.49×10^{-17} W m^{-2} for the 7.7 and 11.3 μm bands respectively. This corresponds to a 7.7μm/11.3μm PAH ratio of 0.35, very low compared to the median value found for the SINGS sample of 3.6 (Smith et al. 2007).

The suppression of the 7.7μm/11.3 μm PAH ratio is seen in low-luminosity AGN in the SINGS sample and Smith et al. (2007) suggest the selective destruction of the PAH molecules small enough to emit at 7.7μm, implying that the ionisation state in this environment modifies the PAH grain size distribution. The PAH dust properties and its implications for the ionisation state in the shock are discussed in more detail by Guillard et al. (2009, in preparation).

Dust emission in the mid- and far-infrared can be used to infer the amount of star formation taking place (Kennicutt 1998). We measure a 24μm flux in this region of 0.408 mJy, corresponding to a spectral luminosity (νL_ν) of $L_{24} = 1.38 \times 10^7 L_\odot$. This low luminosity is consistent with the MIR continuum seen in its spectrum (Fig. 8b), arising from emission from VSGs.

We can combine this with a measurement of the Hα emission in this region to obtain a star formation rate (SFR), given that they are complimentary (Hα tracing the young stellar population and 24μm as a measure of dust-absorbed stellar light). We find $L_{H\alpha} = 2.03 \times 10^6 L_\odot$, but caution that H$\alpha$ emission in SQ is also the result of shock-excitation (Xu et al. 2003) and must be considered an upper limit for measuring star formation. When we combine $L_{H\alpha}$ with L_{24}, using the relation of Calzetti et al. (2007), we find a SFR of 0.05 $M_\odot$ yr^{-1}.

A further quantitative measure of star formation can be obtained from the PAH strength. Using the relation of Houck et al. (2007), derived from the starburst sample of Brandl et al. (2006), we can use the 7.7μm flux density as a measure of star formation. The shock subregion has a 7.7μm flux density of 0.73 mJy which corresponds to a SFR of $\sim 0.08 M_\odot$ yr^{-1}, in good agreement with our previous calculation, but also an upper limit as some PAH emission is contamination from known star formation regions in the group. Comparing the $L_{PAH}(7.7\mu m)/L_{24}$ ratio to the galaxies in SINGS, we find that the value of ~ 0.17 is typical of star-forming galaxies (Ogle et al. 2009), which suggests that both measures of star formation are low, but self-consistent.

The low *upper limits* for the SFR in the shock suggests that star formation is being quenched, likely the result of cooled molecular hydrogen being reheated by MHD shocks in the turbulent medium.

The cold molecular gas clouds may therefore be too short-lived or undersized to facilitate collapse and produce significant star formation (Guillard et al. 2009). The extent of a cold reservoir of molecular gas in the shock is a key consideration in this scenario, as discussed in Section 6.3.

7. IMPLICATIONS FOR HIGH-Z GALAXY FORMATION

The present observations suggest that molecular line cooling in high-speed shocks driven into a clumpy medium represents a significant fraction of the kinetic energy available in the shock. For reference, and to provide a glimpse of what this group might look like at high redshift when filling a single beam, we show in Figure 13 the spectrum extracted for the entire group (i.e. including the three neighbouring galaxies and the shock).

The total H$_2$ line emission from the whole group exceeds 10^{42} erg s^{-1} and is still the most dominant MIR line. Indeed the luminosity of the rotational H$_2$ lines is sufficient that it could be detected at very high redshift with future far-infrared or sub-mm instrumentation like SPICA or SAFIR (see Appleton et al. 2009). How likely is it, however, that high-speed shocks play a role in the assembly of galaxies?

There is growing evidence that galaxies at high redshift are turbulent (Förster Schreiber et al. 2006; Genzel et al. 2008) and increasingly clumpy (e.g. Conselice et al. 2005, Elmegreen & Elmegreen 2005). Indeed Bournaud & Elmegreen (2009) discuss the importance of the growth instabilities in massive gas clumps in forming disks at z > 1, and favor at least a large fraction of the clump systems being formed in smooth flows, perhaps similar to those discussed by Dekel et al. (2009). Certainly, in the early universe, gas flowing into the more massive dark halos will experience strong shocks, most likely in an inhomogenious medium (e. g. Greif et al. 2008)–thus it begs the question as to how important H$_2$ cooling may be in these cases.

Although models of the collapse of the first structures predict strong metal lines as the dominant coolant (Bromm, et al. 2001, Santoro & Shull 2006) once the medium is polluted by the first stars, it is also clear that these models do not include the consequences of strong, shock-driven molecular line cooling in the early phases of gas accretion. Our observations suggest that future models of gas accretion onto galaxies or massive halos should include the effects of molecular line cooling through shocks. This will not be a trivial problem, since our best model of Stephan's Quintet (Guillard et al 2009) involves the formation of H$_2$ in a complex multiphase turbulent medium in which shocks destroy dust in some places, but allow survival in others–thus encouraging H$_2$ formation. In the early universe, this enhanced cooling, which has so far been neglected, will depend on the distribution and nature of the first dust grains, in concert with the formation, temperature and abundance of gas, and the feedback effects from the first stars and AGN.

8. CONCLUSION

In this paper we have presented the results of the mid-infrared spectral mapping of the Stephan's Quintet system using the *Spitzer* Space Telescope. We highlight here our five main conclusions:

- The powerful H$_2$ emission seen by Appleton et al. (2006) surprisingly represents only a small fraction of the group-wide warm H$_2$ (with a lower limit luminosity of 1.1×10^{42} erg s^{-1} spread over $\sim$ 975 kpc^2) that dominates the mid-infrared emission of system. We also see evidence for another shock-excited feature, the so-called H$_2$ bridge, which is likely a remnant of past tidal interactions within the group. The subtle variation in the distribution of the H$_2$ 0-0 transitions implies differences in temperature and excitation in the shocked system - this will be explored fully in Paper II.

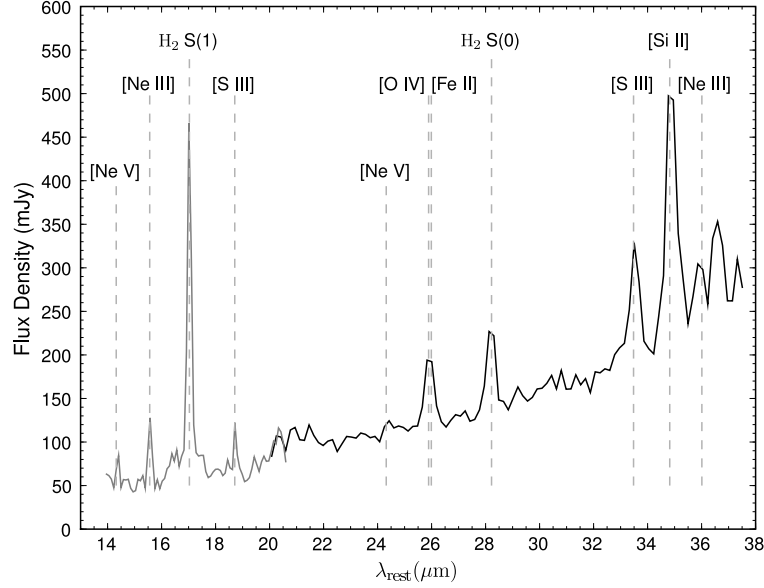- The global L(H$_2$)/L$_{X(0.001-10keV)}$ ratio in the main shock is >= 3, and $\sim$2.5 in the new "bridge" fea-

FIG. 13.— Low resolution spectrum of the entire SQ region mapped by the IRS. This extraction is a rectangular box corresponding to an area of 94 kpc × 56 kpc centered on $22^h35^m59.97^s$, $+33°58'12.7''$, and includes the main shock, H$_2$ bridge, NGC 7319, SQ-A and NGC 7318a and NGC 7318b.

ture. The results confirm that H$_2$, not X-ray emission, is the dominant coolant over the shock structures, indicating a new cooling pathway seen on a large scale in SQ. This modifies the traditional view that X-rays dominate cooling at all times in the later stages of compact group evolution. Since H$_2$ forms on the surfaces of dust grains, we expect dust emission associated with these regions, but a low intensity radiation field and/or VSG destruction produces only weak emission at 24μm.

- We do, however, see evidence of dust reprocessing in the shock. The [Si II] and [Fe II] emission associated with the shock is consistent with regions of fast shocks $(100 < V_s < 300\,\mathrm{km\,s^{-1}})$ experiencing depletion onto dust.

- Star formation in SQ is dominated by SQ-A and 7318b-south, located at the extreme ends of the shock ridge seen at radio wavelengths, suggesting they are both shock triggered starbursts. However, regions dominated by warm H$_2$ emission show suppressed star formation, consistent with a turbulent model where H$_2$ is significantly reheated and cool

clouds are too short-lived or undersized to collapse.

- In SQ we see the projected coexistence of [Si II] and H$_2$ being produced by $\sim$200 km s^{-1} and $\sim$20 km s^{-1} velocity shocks, respectively. Our observational results are consistent with a model of a multi-phase postshock medium produced by a galaxy-wide collision (Guillard et al. 2009).

The cooling pathway of warm H$_2$ emission we observe group-wide in SQ is clearly a significant, albeit surprising, mechanism in shock systems. It is plausible that the diverse environments seen producing strong warm H$_2$ emission have this in common. Stephan's Quintet provides the ideal laboratory for probing a mechanism potentially crucial in systems ranging from ULIRGs to supernovae remnants.

REFERENCES

Allen, M.G., Groves, B.A., Dopita, M.A., Sutherland, R.S., & Kewley, L.J. 2008, ApJ, 178, 20
Allen, R.J., & Hartsuiker, J.W. 1972, Nature, 239, 324
Allen, R.J., & Sullivan, W.T.,III. 1980, A&A, 84, 181
Appleton, P., et al. 2009, Astro2010: The Astronomy and Astrophysics Decadal Survey, Science White Papers, 2010, 2
Appleton, P.N. et al. 2006, ApJ, 639, L51
Appleton, P.N., Charmandaris, V., Horrelou, C., Mirabel, I.F., Ghigo, F., Higdon, J.L., & Lord, S., ApJ, 527, 143
Armus, L. et al. 2006, ApJ, 640, 204
Arp, H., & Kormendy, J. 1972, ApJ, 178, L101

Bournaud, F., & Elmegreen, B. G. 2009, ApJ, 694, L158
Brandl, B.R. et al. 2006, ApJ, 653, 1129
Bromm, V., Ferrara, A., Coppi, P. S., & Larson, R. B. 2001, MNRAS, 328, 969
Buchanan, C. L., Gallimore, J. F., O'Dea, C. P., Baum, S. A., Axon, D. J., Robinson, A., Elitzur, M., & Elvis, M. 2006, AJ, 132, 401
Calzetti, D., et al., 2007, ApJ, 666, 870
Conselice, C. J., et al. 2005, ApJ, 633, 29
Dale, D.A., et al. 2009, ApJ, 693, 1821
Dale, D.A., et al. 2006, ApJ, 646, 161

Dekel, A., Sari, R., & Ceverino, D. 2009, arXiv:0901.2458 (astro-ph)

Deo, R.P., et al. 2007, ApJ,, 671, 124

Desai, V., et al. 2007, ApJ, 669, 810

Dopita, M. A., & Sutherland, R. S. 1995, ApJ, 455, 468

Draine, B.T., Roberge, W.G., & Dalgarno, A. 1983, ApJ, 264, 485

Draine, B.T., & Li A. 2001, ApJ, 551, 807

Durret, F. 1994, A&AS, 105, 57

Egami, E., Rieke, G.H., Fadda, D. & Hines, D.C. 2006, ApJ, 652, L21

Elmegreen, B. G., & Elmegreen, D. M. 2005, ApJ, 627, 632

Förster Schreiber, N. M., et al. 2006, ApJ, 645, 1062

Gao, Y. & Xu, C. 2000, ApJ, 542, L83

Genzel, R., et al. 2008, ApJ, 687, 59

Genzel , R., et a. 1998, ApJ, 498, 579

Greif, T. H., Johnson, J. L., Klessen, R. S., & Bromm, V. 2008, MNRAS, 387, 1021

Guillard, P., Boulanger, F., Pineau des Forêts, G., & Appleton, P.N. 2009, A&A, in press

Haas, M.R., Hollenbach, D., & Erickson, E.F. 1991, ApJ, 374, 555

Hartigan, P., Raymond, J., & Hartmann, L. 1987, ApJ, 316, 323

Hatch, N.A., Crawford, C.S, Fabian, A.C., & Johnstone, R.M. 2005, MNRAS, 358, 765

Helou, G., & Bicay, M.D. 1993, ApJ, 415, 93

Hewitt, J.W., Rho, J., Andersen, M., & Reach, W.T. 2009, ApJ, 694, 1266

Ho, L.C., & Keto, E. 2007, ApJ, 658, 314

Hollenbach, D., & McKee C.F. 1989, ApJ, 342, 306

Houck, J.R., Weedman, D.W., Le Floc͂h, & Hao, L. 2007, ApJ, 671, 323

Houck, J.R. et al. 2004, ApJS, 154, 18

Kennicutt Jr., R.C., 1998, ARA&A, 36, 189

Lisenfeld, U., Braine, J., Duc, P. -A., Leon, S., Charandaris, V., & Brinks, E. 2002, A&A, 394, 823

Maloney, P.R., Hollenbach, D.J., & Tielens, A.G.G.M. 1996, ApJ, 466, 561

Martín-Hernández, N.L., Vermeij, R., Tielens, A.G.G.M., van der Hulst, J.M., & Peeters, E. 2002, A&A, 389, 286

Moles, M., Sulentic, J.W., & Márquez, I. 1997, ApJ, 485, L69

Pietsch W., Trinchieri, G., Arp, H., & Sulentic, J.W. 1997, A&A, 322, 89

Ogle, P., Antonucci, R., Appleton, P., & Whysong, D. 2007, ApJ, 668, 699

Ogle, P. et al. 2009, ApJsubmitted

O'Sullivan, E.O. et al. 2009, arXiv:0906.5610v1 (astro-ph)

O'Sullivan, E.O., Giacintucci, S., Vrtilek, J.M., Raychaudhury, S., & David, L.P. 2008, arXiv:0812.0383v1 (astro-ph)

Rieke, G. et al., 2004, ApJS, 154, 204

Rigopoulou, D., Kunze, D., Lutz, D., Genzel, R., & Moorwood, A.F.M., 2002, A&A, 389, 374

Santoro, F., & Shull, J. M. 2006, ApJ, 643, 26

Sembach, K. R., & Savage, B. D. 1996, ApJ, 457, 211

Shostak, G.S., Sullivan, W.T., III, & Allen, R.J. 1984, A&A, 139, 15

Simpson, J. P., Witteborn, F. C., Price, S. D., & Cohen, M. 1998, ApJ, 508, 268

Smith, J.D.T. et al. 2007, PASP, 119, 1133

Smith, J.D.T. et al. 2009, ApJ, 693, 713

Van Steenberg, M.E., & Shull, J.M. 1988, ApJ, 330, 942

Stephan, M. 1877, CR Acad. Sci. Paris, 84, 641

Sturm, E., Lutz, D., Verma, A., Netzer, H., Sternberg, A., Moorwood, A.F.M., Oliva, E., & Genzel, R. 2002, A&A, 393, 821

Sulentic, J.W., Rosado, M., Dultzin-Hacyan, D., Verdes-Montenegro, L., Trincheri, G., Xu, C., & Pietsch, W. 2001, AJ, 122, 2993

Trinchieri, G., Sulentic, J., Breitschwerdt, D., & Pietsch, W., 2003, A&A, 401, 173

Trinchieri, G., Sulentic, J., Pietsch, W., & Breitschwerdt, D. 2005, A&A, 444, 697

Verma, A., Lutz, D., Sturm, E., Sternberg, A., Genzel, R., & Vacca, W. 2003, A&A, 403, 829

Weedman, D., et al. 2005, ApJ, 633, 706

White, S.D.M., & Rees, M.J., 1978, MNRAS, 183, 341

Williams, B.A., Yun, M.S., & Verdes-Montenegro, L. 2002, AJ, 123, 2417

Xanthopoulos, E., Muxlow, T.W.B., Thomasson, P., & Garrington, S.T., 2004, MNRAS, 353, 1117

Xu, C., Sulentic, J.W., & Tuffs, R. 1999, ApJ, 512, 178

Xu, C.K., Lu, N., Condon, J.J., Dopita, M., & Tuffs, R.J. 2003, AJ, 595, 665

Xu, C.K., et al. 2005, ApJ, 619, L95

Yun, M.S., Verdes-Montenegro, L., del Olmo, A., & Perea, J. 1997, ApJ, 475, L21

In this Section we discuss the results pertaining to NGC 7319, a Seyfert 2 galaxy (Durret 1994) lying to the East in the SQ group (see Fig. 1). The specific intensity contours for the H$_2$ S(0) and H$_2$ S(1) lines (Fig. 2a and b) show emission associated with the galaxy, seemingly connected to the rest of the group by the H$_2$ "bridge" discussed in Section 3.1. In Figure 3 we see that the nucleus of NGC 7319 produces strong X-ray emission (Trinchieri et al. 2003) and is prominent at radio wavelengths (Xu et al. 2003). However, we note an offset between the peak of the H$_2$ emission near NGC 7319 and the Seyfert nucleus, which suggests that the "bridge" is a separate structure and not being excited by the AGN.

The AGN in NGC 7319 does not have a well-collimated jet, but two extended lobes with compact hotspots, asymetrically distributed along the minor axis of the galaxy (Xanthopoulos et al. 2004). This structure runs NE/SW and we note thats its orientation compared to the H$_2$ filament (which runs EW) is not consistent with causing the excitation of the H$_2$ bridge. This is also evident from the relatively weak power in the AGN, as inferred by the emission line diagnostics shown below, and in the X-ray where it is only a factor of $\sim$2 greater than the emission associated with the main shock and "bridge".

In Figure 4 we show the specific intensity contours of the [Fe II]25.99μm (blended with [O IV]25.91μm), [S III]33.48μm and [Si II]34.82μm emission lines. Given the low spectral resolution of the SL and LL modules of *Spitzer*, we cannot distinguish between emission from [Fe II] and [O IV]. The AGN in NGC 7319 is likely to produce both, with [Fe II] emission likely originating in X-ray dissociation regions (XDRs) surrounding the AGN (Maloney et al. 1996). We note prominent emission from [S III]33.48μm and [Si II]34.82μm due to the high excitation conditions associated with the AGN. Dense PDRs and X-ray dominated regions, powered by AGN, show strong [Si II] emission at 34.82μm, while [S III] 33.48 μm emission acts as a tracer of H II regions.
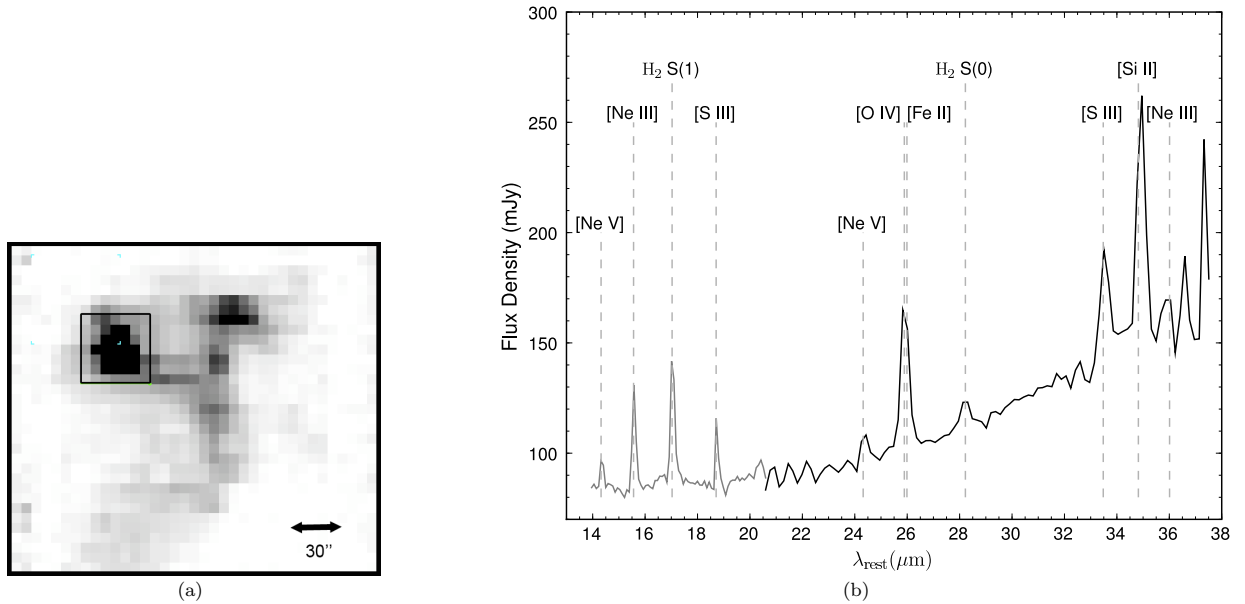
Fig. 14.— The extraction box (a) and low-resolution spectrum (b) of the Seyfert 2 galaxy NGC 7319. The extraction box is centered on $22^{\rm h}36^{\rm m}03.62^{\rm s}$, $+33°58'35.6''$.

We now focus on the emission line properties of NGC 7319. In Figure 14 we show the spectrum extracted from the galaxy and the measured properties of the line ratios are listed in Table 2 and 3. For the first time in the SQ group, we see a spectrum which is no longer dominated by H$_2$ emission, but instead the brightest lines are the high-excitation [O IV]25.91μm and [Fe II]25.98μm blended lines, as well as the [Si II]34.81μm line. [Ne V] is prominent at both 14.32μm and 24.30μm–a line typically seen in AGN. Also, unlike the majority of the extended shocked regions, we see a rising thermal continuum more typical of a starforming galaxy than a classical Seyfert galaxy, although as various studies have shown (Buchanan et al. 2006 ; Deo et al. 2007), Seyfert II galaxies exhibit a variety of MIR spectral characteristics at long wavelengths. NGC 7319's rising continuum is similar to that seen in the Seyfert II galaxy NGC 3079 (Deo et al. 2007), and likely represents a dominant starburst component in the Far-IR. Spitzer imaging shows not only a bright nucleus, but also extended emission regions in the galaxy.

Using the [Si II]34.81μm/[S III]33.48μm ratio as a probe of excitation sources, we find a ratio of $\sim$1.85 which is low compared to the average value found for AGN galaxies ($\sim$ 2.9) in the *Spitzer* Infrared Nearby Galaxy Sample (SINGS),

but high compared to star-forming regions (~ 1.2) in the same sample (Dale et al. 2006). This suggests a relatively weak AGN. The [Ne III] 15.56μm/[Ne II] 12.81μm ratio is a measure of radiation field strength. We find a value of 0.97 indicating a typical radiation field strength compared to other AGN (the sample of Weedman et al. 2005 shows a range of $\sim$0.17 to 1.9). The average electron density, estimated from the [S III]18.71μm/[S III]33.48μm ratio of $\sim$0.56, is $100 - 200$ cm^{-3} (Martín-Hernández et al. 2002), in the low-density limit for this diagnostic (Smith et al. 2009).
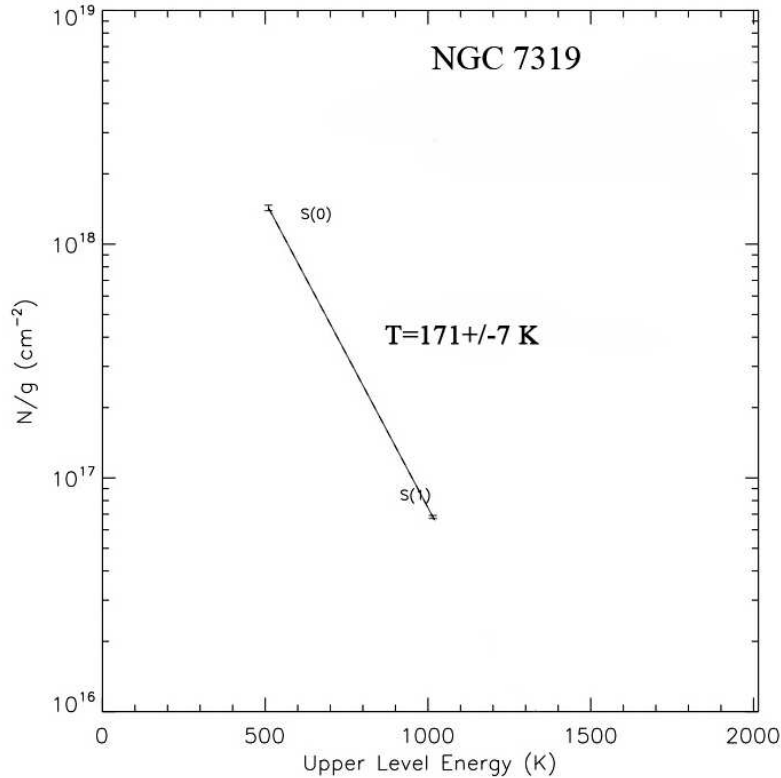
FIG. 15.— Warm H$_2$ Excitation Diagram for NGC 7319. The ordinate (N/g) represents the column density divided by the statistical weight of the rotational state.

The properties of the H$_2$ emission of NGC 7319 are limited to the two long wavelength lines observed by IRS-LL (the galaxy lies outside the region mapped by SL). As a result, the excitation diagram contains only two points allowing only an approximate idea of the H$_2$ mass, since without the SL wavelength coverage to provide information on possible warmer components, we are likely to overestimate the temperature of the H$_2$ by fitting a straight-line to the diagram (shown in Fig. 15). Any warmer component would contribute to the flux of the 0-0 S(1) line thus leading to a reduction of the temperature (and increase in H$_2$ mass) for any cooler component. However, to provide a guide, we estimate the temperature of H$_2$ $<=$171$\pm$8 K (assuming the gas is in thermal equilibrium and thus an ortho-para ratio of 2.65) and a total H$_2$ mass of $3.0\pm7\times10^8\,$M$_\odot$. We consider this a lower limit to the total warm mass if (as is likely) more than one component is present. Gao & Xu (2000) estimated the *cold* molecular hydrogen mass of NGC 7319 based on ^{12}CO (1-0) observations as $> 3.6 \times10^9\,$M$_\odot$, a factor of roughly ten greater than the warm H$_2$ mass. Such a ratio is not atypical of large spiral galaxies Rigopoulou et al. (2002).

APPENDIX B: HIGH RESOLUTION SPECTRUM OF SHOCK CENTRE REANALYSED

The high resolution spectrum at the center of the shock in SQ obtained by Appleton et al. (2006) has been reanalysed using the latest calibrations available for the IRS instrument (SSC pipeline version S17). This has shown that the H$_2$ gas lies at a velocity of 6360($\pm$100) km s^{-1}, between the velocity of the group (6600 km s^{-1}) and the velocity of the intruder (5700 km s^{-1}). This is consistent with a model of gas being accelerated by the shock, as well as the turbulence demonstrated by the broad linewidth of the H$_2$ in the shock (860 km s^{-1}).

The new SH spectrum shows that with the improved calibrations, the 11.3μm PAH feature is detected, although faint. This is consistent with what is found in the larger extractions that show enhanced 11.3μm PAH emission compared to the ionised PAH features.
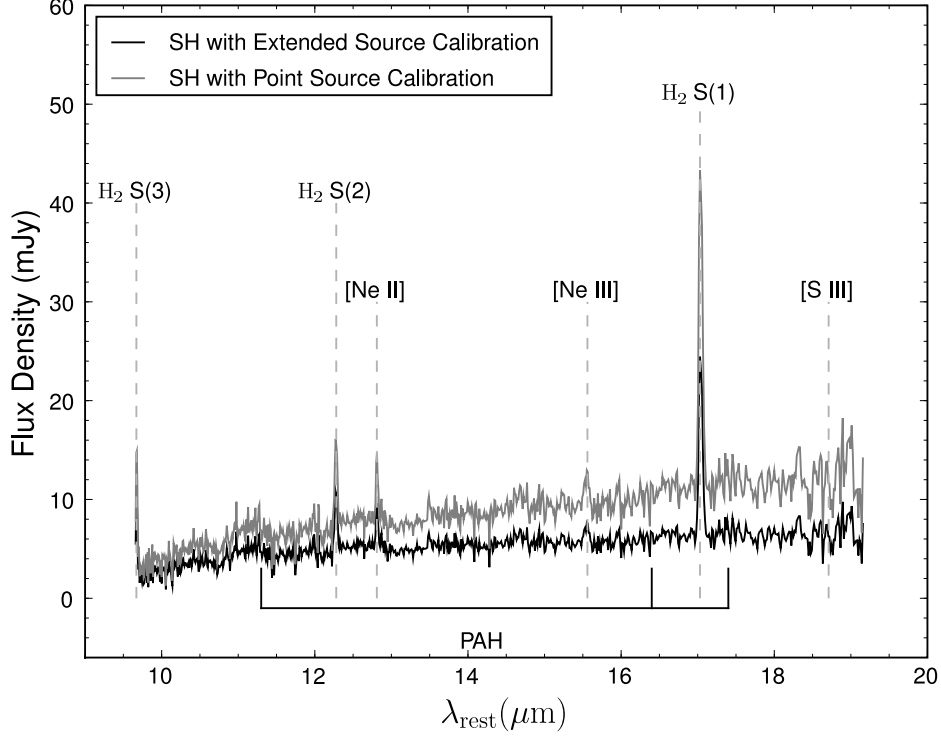
FIG. 16.— *Spitzer* Short-High (SH) Spectrum, centred on $22^h35^m59.57^s$, $+33°58'1.8''$, reanalysed using the latest point source and extended source calibrations.

APPENDIX C: X-RAY FLUXES IN EXTRACTED REGIONS

In this section we determine the X-ray fluxes in the extraction regions shown in Figure 7. The reason for the reanalysis from archival data was to obtain accurate fluxes and luminosities for the X-ray emission over the various apertures matched to our spectral extractions. We use archival XMM-Newton EPIC-pn data (see Trinchieri et al. 2005, for observational details) to obtain the most sensitive measurements. A calibrated event file was generated and filtered using standard quality flags, and subsequently cleaned of background flares. A 0.3–2 keV image was then extracted and corrected for instrumental response. All point-like sources were masked out to $25''$ in the analysis of diffuse emission, and the local background level was estimated within a 5×9 arcmin^2 rectangular region away from the group core. For each region shown in Fig. 7, resulting background-subtracted photon count rates were converted to 0.3–2 keV and "bolometric" (0.001–10 keV) X-ray fluxes assuming an absorbed thermal plasma model of metallicity 0.4 Solar, with temperature as estimated from the map of O'Sullivan et al. (2008), and an absorbing Galactic H$\textsc{i}$ column density of $N_H = 6.2 \times 10^{20}$ cm^{-2}. For NGC 7319, which harbors an AGN, an absorbed power-law spectrum of photon index $\Gamma = 1.7$ was assumed instead. Results are listed in Table 1.

TABLE 1
X-RAY COUNT RATES AND FLUXES FOR EXTRACTED REGIONS

Region	Count Rate (0.3-2 keV) (photons s^{-1})	Flux (0.3-2 keV) erg s^{-1} cm^{-2}	Bolometric Flux (0.001-10 keV) erg s^{-1} cm^{-2}	Adopted Spectral Model
Main Shock	0.102	1.8×10^{-13}	2.8×10^{-13}	$T = 0.7$ keV
Shock Sub-region	0.017	3.3×10^{-14}	5.1×10^{-14}	$T = 0.8$ keV
Bridge	0.017	3.0×10^{-14}	4.5×10^{-14}	$T = 0.6$ keV
NGC 7319	0.051	1.1×10^{-13}	3.7×10^{-13}	$\Gamma = 1.7$
SQ-A	0.013	2.4×10^{-14}	3.7×10^{-14}	$T = 0.6$ keV

NOTE. — Statistical uncertainties on all flux measurements are $< 10\%$.
.

We note that for the main shock (with luminosity 1.9×10^{41} erg s^{-1} in the 0-3-2 keV band) we are within a factor of

2 of the 0.5-2 keV luminosity $\sim 3.1 \times 10^{41}$ erg s^{-1} obtained for a similar, but larger extraction of the shock by Trinchieri et al. (2005). O'Sullivan et al. (2008) obtain a 0.5-2 keV surface brightness of 0.07 L$_\odot$ pc^{-2} in the main shock compared to our value of 0.1 L$_\odot$ pc^{-2} for the 0.3-2 keV surface brightness.

TABLE 2
Observed H$_2$ Line Fluxes in units of 10^{-17} W m^{-2}

Target Region	Aperture (arcsec^2)	H$_2$ 0-0 S(0) $\lambda28.21\mu$m	H$_2$ 0-0 S(1) $\lambda17.03\mu$m	H$_2$ 0-0 S(2) $\lambda12.28\mu$m	H$_2$ 0-0 S(3) $\lambda9.66\mu$m	H$_2$ 0-0 S(4) $\lambda8.03\mu$m	H$_2$ 0-0 S(5) $\lambda6.91\mu$m
Main Shock	2307	3.09±0.19	23.05±0.26	9.10±0.38	22.76±0.84	2.5±1.0	14.1±0.7
Shock Sub-region	242	0.36±0.03	3.13±0.02	1.47±0.08	3.60±0.08	1.04±0.15	2.37±0.30
Bridge	413	0.72±0.04	4.94±0.09	⋯	⋯	⋯	⋯
NGC 7319	1302	2.06±0.26	11.00±0.48	⋯	⋯	⋯	⋯
SQ-A	671	1.83±0.05	8.8±0.13	⋯	⋯	⋯	3.7±0.93

Note. — Upper limits are the 3σ values calculated from the RMS (root mean square) and the expected line profile width.

.

TABLE 3
Observed Fine Structure Line Fluxes in units of 10^{-17} W m^{-2}

Target Region	[NeII] $\lambda12.81\mu$m	[NeV] $\lambda14.32\mu$m	[NeIII] $\lambda15.56\mu$m	[SIII] $\lambda18.71\mu$m	[NeV] $\lambda24.32\mu$m	[FeII]+[OIV] $\lambda25.99+25.89\mu$m	[SIII] $\lambda33.48\mu$m	[SiII] $\lambda34.82\mu$m
Main Shock	5.31±0.30	<0.9	1.94±0.39	0.76±0.13	<0.14	1.07±0.10	1.87±0.15	8.59±0.27
Shock Sub-region	1.04±0.09	<0.18	0.15±0.06	<0.12	<0.14	0.15±0.03	0.13±0.02	1.23±0.04
Bridge	⋯	⋯	0.39±0.04	<0.1	<0.15	0.29±0.04	<0.22	1.1±0.1
NGC 7319	⋯	2.89±0.64	9.47±0.29	2.81±0.40	1.56±0.39	10.9±0.27	5.0±0.42	9.24 ±0.49
SQ-A	⋯	<0.8	1.29±0.16	0.87±0.06	<0.18	<0.17	1.54±0.10	2.3±0.16

Note. — Upper limits are the 3σ values calculated from the RMS and the expected line profile width.

.

Chapter 7

Cold molecular gas in Stephan's Quintet

Continuous eloquence wearies. Grandeur must be abandoned to be appreciated. Continuity in everything is unpleasant. Cold is agreeable, that we may get warm.

Blaise Pascal

Abstract

The warm (> 50 K) H_2 gas detected by Spitzer in the halo of the Stephan's Quintet (SQ) group does not provide a complete inventory of the molecular gas. Gas colder than ≈ 50 K does not contribute to the mid-IR H_2 emission. In order to determine the physical state, the mass and kinematics of the molecular gas in SQ, it is crucial to look for cold molecular gas. This chapter presents the previous CO obervations of the group, and the results of two observation campaigns at the IRAM 30m telescope that I have conducted from the writing of the proposal to the data analysis.

Contents

7.1   Introduction

Within the evolutionary picture of the Stephan's Quintet (SQ) postshock gas presented in sect. 6.5.1, it is fundamental to know whether cold molecular gas (< 50 K) is associated with the warm H$_2$ gas. In star forming galaxies, the warm molecular gas accounts for about a few percent of the total cold H$_2$ gas inferred from the CO luminosity (Roussel et al., 2007). *What is the cold to warm H$_2$ gas mass ratio in SQ?* This is a major open question about the physical state and mass budget of the molecular gas.

According to our model of formation of molecules in the SQ shock, CO should form on the same timescale as H$_2$. However, because the cold gas may be continuously energized by turbulent energy dissipation, the physical state of the shocked gas is likely to be different from that of GMCs in galactic disks. These observations are crucial to test our scenario of H$_2$ formation in the postshock gas and to obtain the kinematics of the molecular gas, which cannot be obtained from the low-resolution Spitzer observations of the H$_2$ alone.

Past interferometric observations do not show any CO signal associated with the H$_2$-emitting ridge. Previous single-dish observations are mostly concentrated on the southern tidal features or on the northern starburst region (SQ-A). Therefore we decided to embark on an observation campaign with the IRAM 30-meter telescope to search for CO emission in the SQ ridge. I have carried on this campain from the beginning (writing of the proposal) to the end (data reduction and analysis), through the observations at the telescope. This was one of the great experiences I had the chance to live during my PhD!

Before presenting our new observations with the IRAM 30-meter telescope (sect. 7.3) and some preliminary results (sect. 7.4), I first review the context of the previous CO observation in the SQ group.

7.2   Previous CO observations of Stephan's Quintet: molecular gas outside galaxies

Before the discovery of warm ($T > 150$ K) molecular hydrogen in SQ (sect. 5.2), CO emitting gas was detected in the group. I summarize here the history and main results of these CO detections.

The first millimeter CO observations only allowed to detect cold molecular gas in NGC 7319 (Yun et al., 1997; Verdes-Montenegro et al., 1998; Leon et al., 1998), which contains 4.8×10^9 M$_\odot$ Smith and Struck (2001). Given its blue luminosity of $\mathcal{L}_\mathrm{B} = 5.5 \times 10^{10}$ L$_\odot$ (Verdes-Montenegro et al.,

Table 7.1: Observed and derived CO properties in Stephan's Quintet from the litterature

Target	Size [arcsec^2]	v_{CO} [km s^{-1}]	Δv_{CO} [km s^{-1}]	$\mathcal{I}_{\text{CO}}$ [K km s^{-1}]	M_{H_2} [a] [$\times 10^8$ M$_\odot$]
NGC 7318a [b]	55×55			< 2.13	
NGC 7318b [c]	55×55	6250 [c]	50	0.3 ± 0.1	2.8
NGC 7319 [b]	55×55	6730	~ 470	1.90 ± 0.15	48
SQ-A (6000) [d]	60×80	6030	70	0.84 ± 0.04	22
SQ-A (6700) [d]	60×80	6700	70	0.33 ± 0.05	8.6
SQ-B [d]	60×40	6625	35	0.54 ± 0.02	7.0
NGC 7320 [e]	55×55	780	22	0.3	0.1

[a] All the H$_2$ gas masses are converted using the Galactic conversion factor of $N(\text{H}_2)/\mathcal{I}_{\text{CO}} = 2 \times 10^{20}$ cm^{-2} [K km s^{-1}]$^{-1}$.

[b] from observations by Smith and Struck (2001) with the NRAO 12m telescope

[c] from interferometric observations by Gao and Xu (2000) with the BIMA array. The velocity of the CO clump do not match with the optical redshift of the galaxy (5760 km s^{-1}). The emission is also offset from the nucleus of NGC 7318b.

[d] from observations by Lisenfeld et al. (2002) with the IRAM 30m telescope

[e] foreground galaxy, from Verdes-Montenegro et al. (1998)

1998), this yields a normal ratio of $\mathcal{L}_{\text{B}}/M_{\text{H}_2} = 11$ (Lisenfeld et al., 2002). Thanks to the BIMA[1] interferometer, Gao and Xu (2000); Petitpas and Taylor (2005) showed that 3/4 of the CO gas in NGC 7319 is lying outside its nuclei, mostly in an extended northern region.

Molecular gas outside galactic disks, associated with the IGM starburst SQ-A, was first detected by Gao and Xu (2000) using BIMA. Then, single dish observations by Smith and Struck (2001) and Lisenfeld et al. (2002) confirmed this spectacular result. Fig. 7.1 presents an overview of these observations and table 7.1 gathers observational results from the litterature. All the cold H$_2$ masses in this table are derived assuming a Galactic CO-to-H$_2$ conversion factor of $N(\text{H}_2)/\mathcal{I}_{\text{CO}} = 2 \times 10^{20}$ cm^{-2} [K km s^{-1}]$^{-1}$, which explains why the values quoted here may be different from those of the litterature. Two velocity components were detected, one centered at ~ 6000 km s^{-1}, and the other at ~ 6700 km s^{-1}. These velocities match the redshifts of the two H I gas systems found in the same region (see sect. 6.3.3). Lisenfeld et al. (2002) found that there is more molecular gas (3.1×10^9 M$_\odot$) in SQ-A than in the H I gas (1.6×10^9 M$_\odot$).

Interestingly, past observations with interferometers have not detected any CO gas in the main shock region. The single-dish observations by Lisenfeld et al. (2002) with the IRAM 30m telescope partially overlap the main shock region and show $> 3\sigma$ detection of CO in the northern region of the ridge. We note that they include this emission in the SQ-A budget. Their observations do not cover entirely the shock region. Gao and Xu (2000); Smith and Struck (2001); Petitpas and Taylor (2005) reported CO emission close to NGC 7318b nucleus (see table 7.1) and from several other regions in the group.

An other interesting feature of SQ is the presence of a CO-rich (Braine et al., 2001; Lisenfeld et al., 2002, 2004, 7×10^8 M$_\odot$) region, SQ-B, located within the young tidail tail, to the south of NGC 7319.

---

[1] Berkeley Illinois Maryland Association, http://bima.astro.umd.edu/bima.html
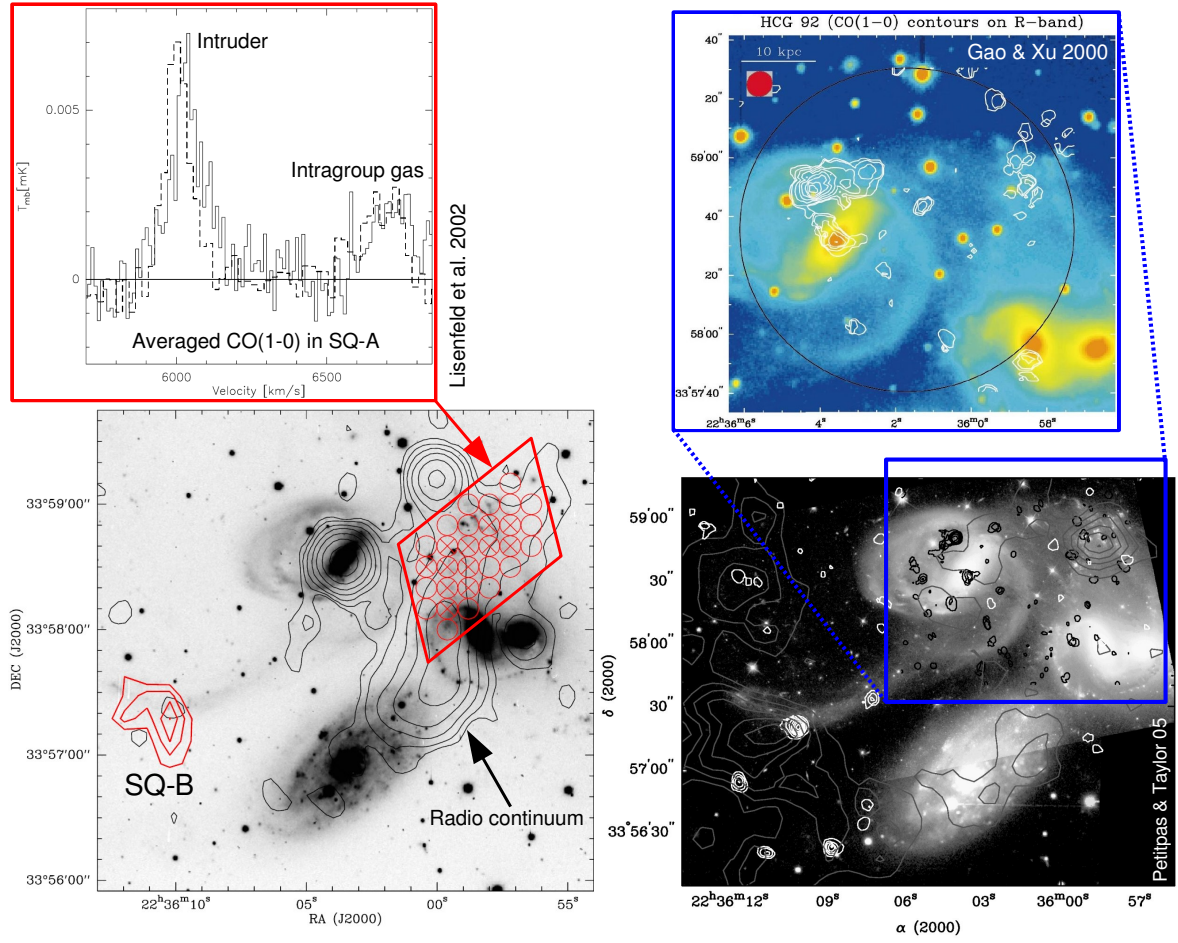
Figure 7.1: Single-dish and interferometric CO observations of Stephan's Quintet. *Left:* The bottom is
an optical image overlaid with contours of the 20 cm radio continuum emission (Williams et al., 2002).
The thick red contours on SQ B and the circles on SQ A show the area observed by Lisenfeld et al.
(2002) with the IRAM 30m telescope. The crosses indicate $> 3\sigma$ CO(1-0) detections. The top inset
shows the CO(1-0) spectrum (full line) in SQ A, with a velocity resolution of 10.6 km s^{-1}, averaged
over the total observed area. The dashed line represents the H I emission with a velocity resolution of
21.4 km s^{-1} in arbitrary units from Williams et al. (2002), averaged over the same area. *Right:* The
top image (Gao and Xu, 2000) show CO(1-0) BIMA contours overlaid on an R-optical image. The
first contour is 2.4σ, the next one is 3σ, and then the contours increase by 1σ. The black circle indicate
the FWHM BIMA primary beam of 110", and the filled red circle the FWHM synthesized beam of
6".The white contours on the bottom image are from Petitpas and Taylor (2005) BIMA observations,
overlaid on an *HST* image. Levels are 0.5, 1.0, 1.5, etc [Jy beam^{-1} km s^{-1}.] The black contours are
the (Gao and Xu, 2000) observations. Gray contours show the H I gas.

This region is also bright in mid-IR (Xu et al., 1999), Hα (Arp, 1973a) and UV (Xu et al., 2005). The
H$_2$ to H I gas mass ratio of 0.5 indicates that SQ-B is a tidal dwarf galaxy (TDG) candidate, i.e. a
small galaxy which is in the process of formation from the material of the NGC 7319's tidal tail.
TDGs will not be further discussed, so we direct the reader to the concise review by Xu (2006) and

references therein.

The gas metallicity in SQ-A and SQ-B is slightly higher than solar (Xu et al., 2003; Lisenfeld et al., 2004) This is a strong indication that the gas in these regions has been pulled out from the inner part of a galaxy disk (or maybe several disks) by tidal interactions.

7.3 New CO observations in the SQ ridge

Since none of the past CO observations in SQ yielded detections from the main area of interaction between the new intruder (NGC 7318b) and the intragroup tidal tail, we decided to search for the CO counterpart of the warm H_2 gas seen by *Spitzer*. Our recent results are the result of an iterative process that has involved three observing runs! Before showing that these results significantly change our view at the molecular gas in SQ (sect. 7.4), I first quickly review the history of our observing runs.

7.3.1 History of our CO observations

In September 2007, we submitted a proposal (P.I.: P. Guillard) to observe the (2-1)CO line from the SQ shock with the multi-beam (3×3 pixels) *HERA* receiver[2] installed on the IRAM[3] 30-meter single-dish telescope in Pico Veleta, Spain. The previous observations by Lisenfeld et al. (2002) did not cover entirely the SQ ridge. Moreover, based on the fact that the H_2 emission is extended, we argued that much of the CO emission associated with the shock has been missed by previous interferometric observations. We thought that *HERA* would provide us both the spatial distribution and kinematics of the molecular gas across the shock front.

François and I performed the observations in January 2008 but we did not detect any obvious signal. No line was clearly detected. The Fig. 7.2 shows the CO(2-1) HERA spectra (in red) averaged on the 9 pixels. Only a constant baseline was subtracted in the data reduction. In the eastern and western (group/intruder) regions there may be weak ($T_A^* \sim 1$ mK) and broad (full width ~ 500 km s^{-1}) lines at the right and left ends of the bandpass, which was ~ 1200 km s^{-1}. In the shock region, these observations set an upper limit on the cold component of the molecular gas of a few 10^{20} H_2 cm^{-2} for a standard H_2/CO conversion factor. This upper limit is roughly the surface density of the warm (~ 200 K) molecular gas detected by Spitzer.

To confirm or not this puzzling result, we wanted to make sure that the CO emission had not been subtracted in the baseline in case it had a large linewidth ($\gtrsim 1000$ km s^{-1}) comparable to that of the ionized gas as measured by optical lines (e.g. the 6300Å O I line). Therefore, we submitted a DDT proposal (P.I.: P. Guillard) to observed the (1-0)CO line with the single-pixel *A-B* receivers, arguing that we would double the bandwidth we had with *HERA* (2-1)CO observations. The proposal was accepted and observed in March 2008 by an astronomer on duty. However, when writing up the proposal, we did not realize that the bandwidth of the *A-B* receivers is half (512 MHz) the bandwidth of *HERA* (1 GHz). So we faced the same problem of baseline fitting! The *top* spectrum in Fig. 7.2 shows the averaged CO(1-0) spectrum obtained with the AB receivers. The spectral resolution is ≈ 13 km s^{-1}. Two very weak lines at 6050 and 6130 km s^{-1} are perhaps detected, but this hypothetic detection is unreliable ($< 3\sigma$).

---

[2]HEterodyne Receiver Array, http://www.iram.es/IRAMES/mainWiki/HeraforAstronomers
[3]Institut de Radio Astronomie Millimétrique, http://www.iram-institute.org
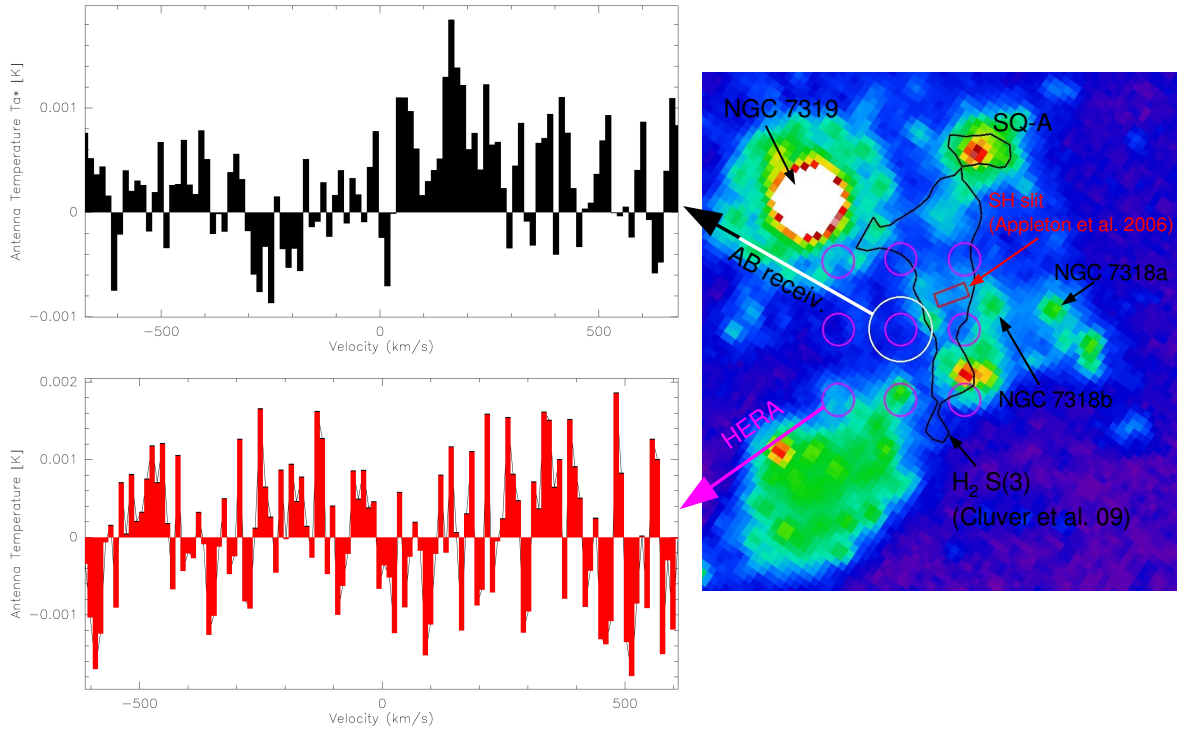
Figure 7.2: Pointing positions and averaged spectra of our two first runs of CO observations, overlaid on a *Spitzer MIPS* 24 μm image. The small magenta circles show the CO(2-1) 11" half-power beams of the HERA 3×3 matrix. The white circle show the CO(1-0) 22" HP beam of the AB receivers for our DDT program. The black contours is the 4σ (0.3 MJy sr^{-1}) H$_2$ S(3) line emission from our paper II, which was not available at the time of these first CO observations. The central velocity is 6400 km s^{-1} on the spectra. Weak lines at 6050 and 6130 km s^{-1} are perhaps detected ($< 3\sigma$) on the CO(1-0) spectrum. On the HERA CO(2-1) spectrum no clear detection of CO gas is seen.

7.3.2   Observations with the new *EMIR* reveiver at IRAM 30m telescope

In March-April 2009, a new heterodyne receiver, *EMIR* [4], was installed and commissioned at the 30m telescope. It replaces the former *ABCD* single-pixel receivers. *EMIR* provides a bandwidth of 4 GHz in each of the two orthogonal linear polarizations for the 3, 2, 1.3 and 0.9 mm atmospheric windows. This increase in bandwith is crucial for our study since we expect that the CO line width to be broad ($\approx 1\,000$ km s^{-1}). The four *EMIR* bands are designated as E090, E150, E230, and E330 according to their approximate center frequencies in GHz.

A proposal was submitted in March 2009 (P.I.: P. Guillard) to observe the CO(1-0) transition. We required 32 hours of observations. Our goal was to reach a 0.3 mK rms noise on the T_A^* scale at 113 GHz, for a spectral resolution of 100 km/s. The proposal was accepted but only 16h were allocated. I carried on the observations in June 28-30, 2009. I briefly give some observational details here and some preliminary results are given in the next paragraph, sect. 7.4.

---

[4]Eight MIxer Receiver, see http://www.iram.es/IRAMES/mainWiki/EmirforAstronomers for details about the instrument

Table 7.2: Pointing positions and integration times of our recent CO observations with the new EMIR receiver at the IRAM 30m telescope.

position	RA (J2000)	DEC (J2000)	integration time [min]
SQ-A [a]	22:35:58.88	+33:58:50.69	150
Bridge [b]	22:36:01.56	+33:58:23.30	250
Ridge 1	22:35:59.85	+33:58:16.55	400
Ridge 2	22:35:59.85	+33:58:04.00	400
Ridge 3	22:35:59.73	+33:57:37.16	120

[a]Starburst region at the northern tip of the SQ ridge
[b]Bridge feature that connects the ridge to the AGN NGC 7319.

Our observations were concentrated on the CO(1-0) line, because of summer weather conditions. In addition, we were able to connect the third and fourth parts of the WILMA backend to the horizontal and vertical polarizations of the E230 band. So we observed the CO(1-0) and CO(2-1) lines at 115.27 GHz and 230.54 GHz. To increase the redundance for the CO(1-0) data, we used in parallel the 4 MHz filterbank with both polarizations connected to the E090 band. The receivers were tuned to 112.86 GHz and 225.72 GHz, which corresponds to a "redshift" of 6400 km s^{-1}. The observations were done in wobbler switching mode, with a wobbler throw of 120" in azimuthal direction. This observation mode provides accurate background subtraction and good quality baselines, which is crucial for our study. Pointing and focus were monitored every 2h in stable conditions and every 1h during sunrise. System temperatures were $\approx 150-200$ K at 115 GHz on the T_A^* scale. The forward effciency of the telescope was 0.94 and 0.91 at 115 and 230 GHz and the beam effciency was 0.78 and 0.58, respectively. Our half-power beam size was 22" at 115 GHz and 11" at 230 GHz.

The data was reduced with the IRAM GILDAS [5] software package (version of July 2009). The lowest quality spectra (typically with $\sigma \gtrsim 30$ mK for a 3 min on-source integration) were rejected. We only subtract a constant when doing baseline fitting. Unfortunately, we experienced problems with the vertical polarization. These spectra show weird features and have been simply removed for this preliminary analysis.

The results are beyond our expectations! The quality of the data was such that we were able to observed five different positions in the SQ shock region. The image in the center of Fig. 7.3 shows the positions of our pointing (blue circles of diameter 22 arcsec, corresponding to the half-power CO(1-0) beam) overlaid on a *Spitzer* 24 μm *MIPS* image of SQ. The three positions in the ridge are designated as "Ridge 1, 2 and 3", from North to South. The two other positions are centered on SQ-A and the middle of the bridge feature in between NGC 7319 and the ridge. The black line shows the 4σ contours of the H$_2$ 0-0S(3) line emission detected by *Spitzer* (see sect. 6.2). Note that the half power beam width at 115 GHz matches very well the width of the H$_2$ emission in the ridge. The red rectangle shows the position of the *IRS* SH slit of the Appleton et al. (2006) observations. The table 7.2 list the coordinates of these positions and the total ON+OFF time spent at each position. A total of ≈ 20 hours has been spent for ON+OFF observations towards SQ.

---

[5]Grenoble Image and Line Data Analysis System, http://www.iram.fr/IRAMFR/GILDAS/

Coming back to the previous observation run...

The reason why we did not detect any clear signal during our previous observations with HERA or the ABCD receivers is not completely clear for us. The possible explanations are the following.

First, for the CO(1-0) ABCD position (see Fig. 7.2) we may have missed the molecular gas rich ridge, because the position was not exactly centered on the H_2 ridge. The central beam position was offset to the East of the Appleton et al. (2006) position because we wanted to avoid the contamination from star-forming regions. However, we did not have the full *IRS* mapping and the mid-IR imaging at that time, so did not have any idea about the extent of the CO emission. So we may have offset our central position too much, thus diluting the signal in the beam. This may explain the non detection if the CO gas is confined to a $\approx 25''$-wide ridge. However, since the H_2 emission seems a bit more extended, the beam dilution does not seem to be a very strong argument.

Second, during our first run, we had lots of problems with the WILMA backend. Several pixels of HERA were not usable, especially pixels 9 and 7, which were, unfortunately, located in the ridge. For the second DDT run with the ABCD receiver, a lot of spectra also show weird features, and I had to throw away $\approx 30\%$ of spurious spectra. These technical problems may also have entrained calibration issues in the data.

The non-detection in our previous HERA and ABCD observations led me to double-check my data reduction for the new EMIR observations. I have checked that the signal is reproductible from one day of observation to another, and search for any spurious features in the spectra. These checks, and the fact that the line velocities are in very good agreement with H I velocities, allow to confirm our new results presented in the following.

7.4   Preliminary results

Since the data has been taken very recently, we present here a preliminary analysis that points out the main observational results about the mass of molecular gas in the system and its kinematics.

7.4.1   Distribution and mass of molecular gas

In Fig. 7.3 we show the averaged CO(1-0) spectra for each of the five observed positions. The spectra are plotted over the full available bandwidth (≈ 8000 km s^{-1} at 115 GHz) at a spectral resolution of 42 km s^{-1}. CO is detected with a high signal-to-noise ratio for all the pointings. This result is in sharp contrast with the previous interferometric observations, where almost no CO was detected in the ridge. It shows that the CO emission is extended and associated with the extended H_2 emission. The noise in the spectra are $\approx 0.5 - 0.7$ mK at a resolution of 42 km s^{-1}. The CO(2-1) is also detected but the quality of the spectra is much poorer than the CO(1-0) because of a shorter integration time and moderate weather conditions. This is why we only show the CO(1-0) spectra here.

The central velocity (0 km s^{-1} on the plots) corresponds to the recession velocity of 6400 km s^{-1} at which the receivers were tuned. The CO(1-0) signal extends over the velocity range $\approx 5700 - 7000$ km s^{-1} (and perhaps until 7400 km s^{-1} for the ridge 1 position, see comment below). Multiple velocity components are detected, pointing out the complexity of the kinematics of the CO gas in the system (see next paragraph below for a discussion of the kinematics). The figures 7.4 and 7.5 shows a
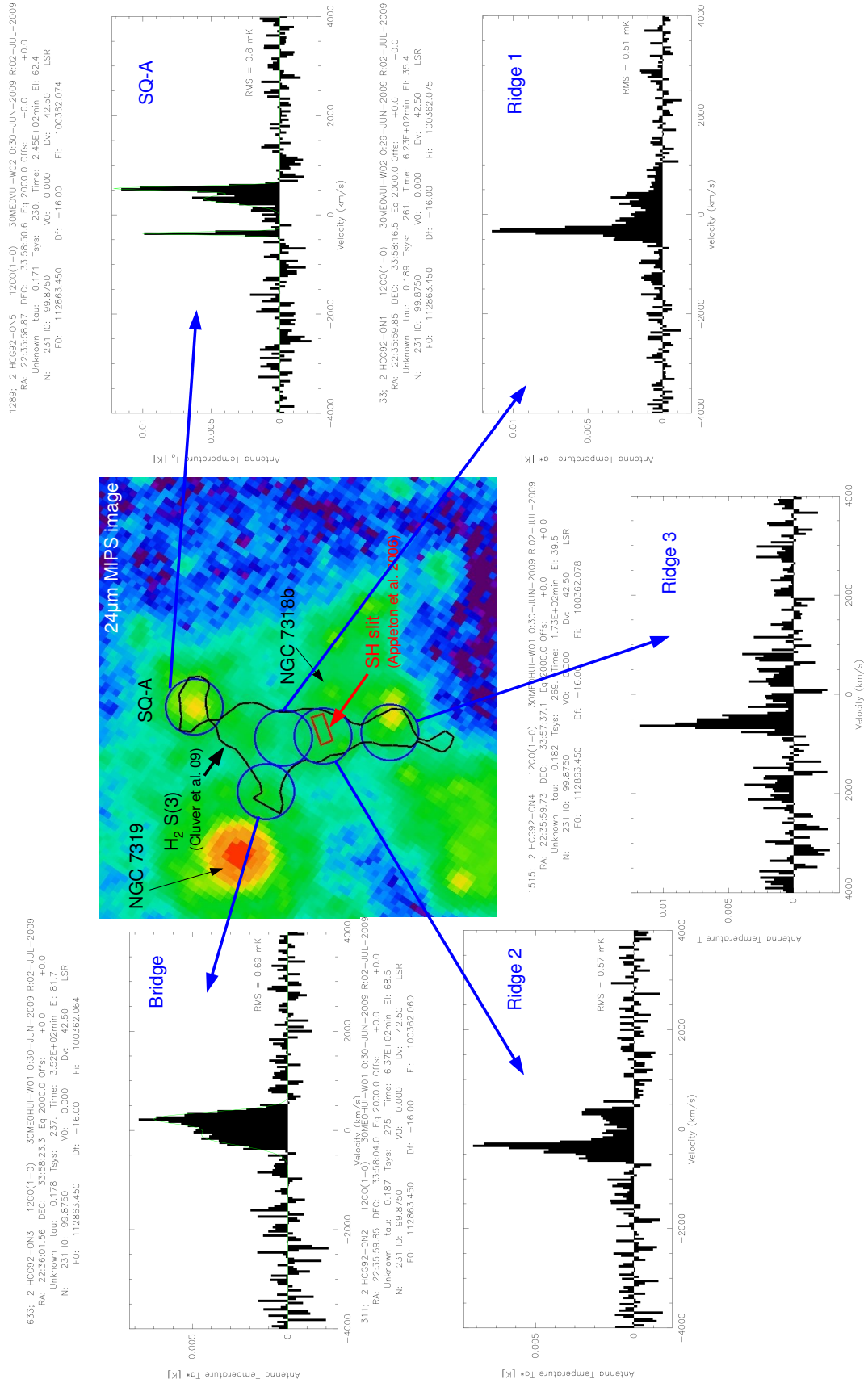
Figure 7.3: New results of CO observations in the SQ group. Extended CO emission is detected in the *ridge* and in the *bridge* feature towards NGC 7319. The spectra show complex kinematics of the CO gas in the SQ halo.
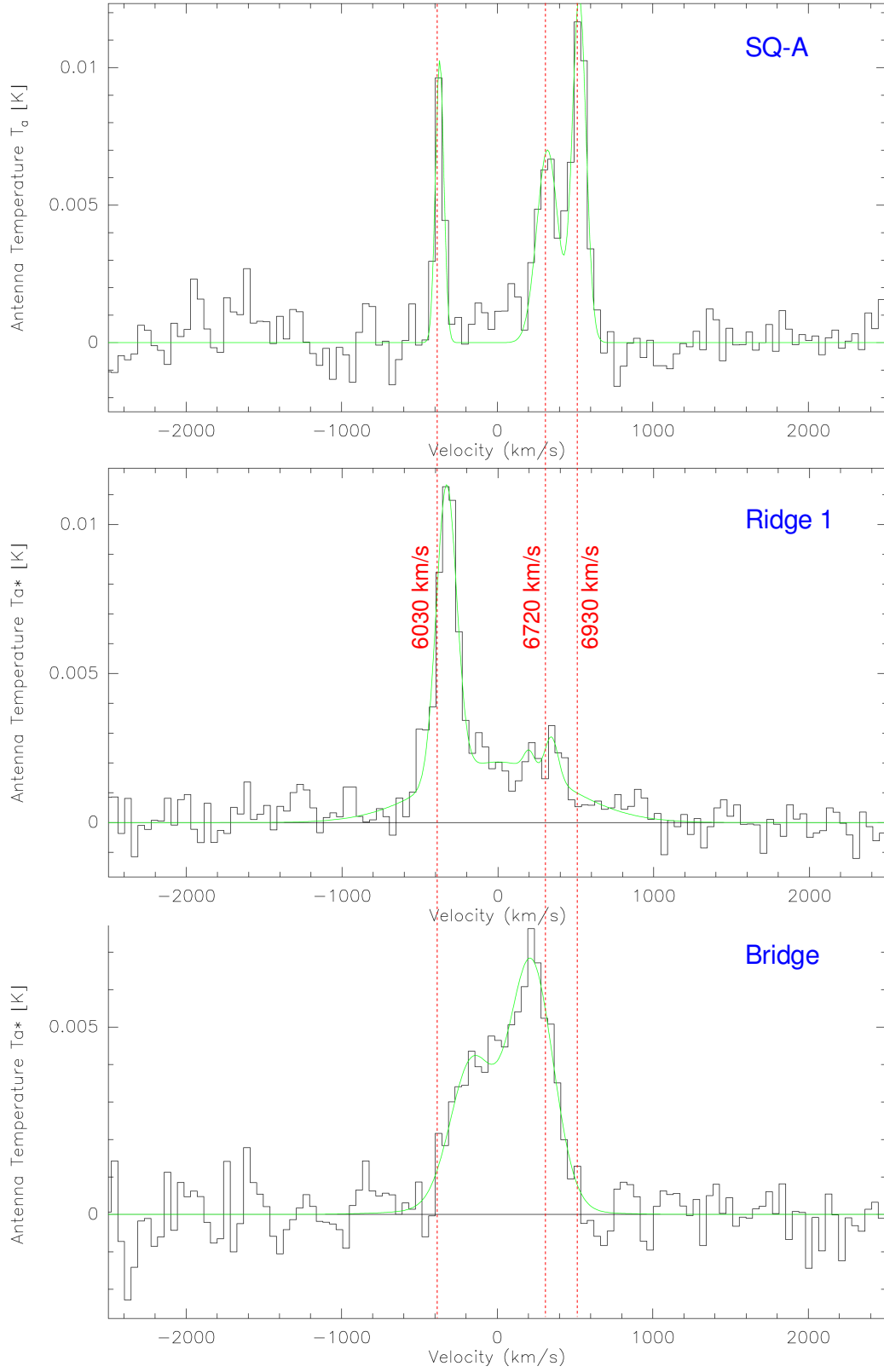
Figure 7.4: CO(1-0) spectra at three positions in the SQ group: SQ-A, Ridge 1, and the in the bridge, from top to bottom. The red dashed lines indicate reference velocities on the SQ-A spectrum, at 6030, 6720 and 6930 km s^{-1}. The green line shows the result of the fitting with three gaussians.
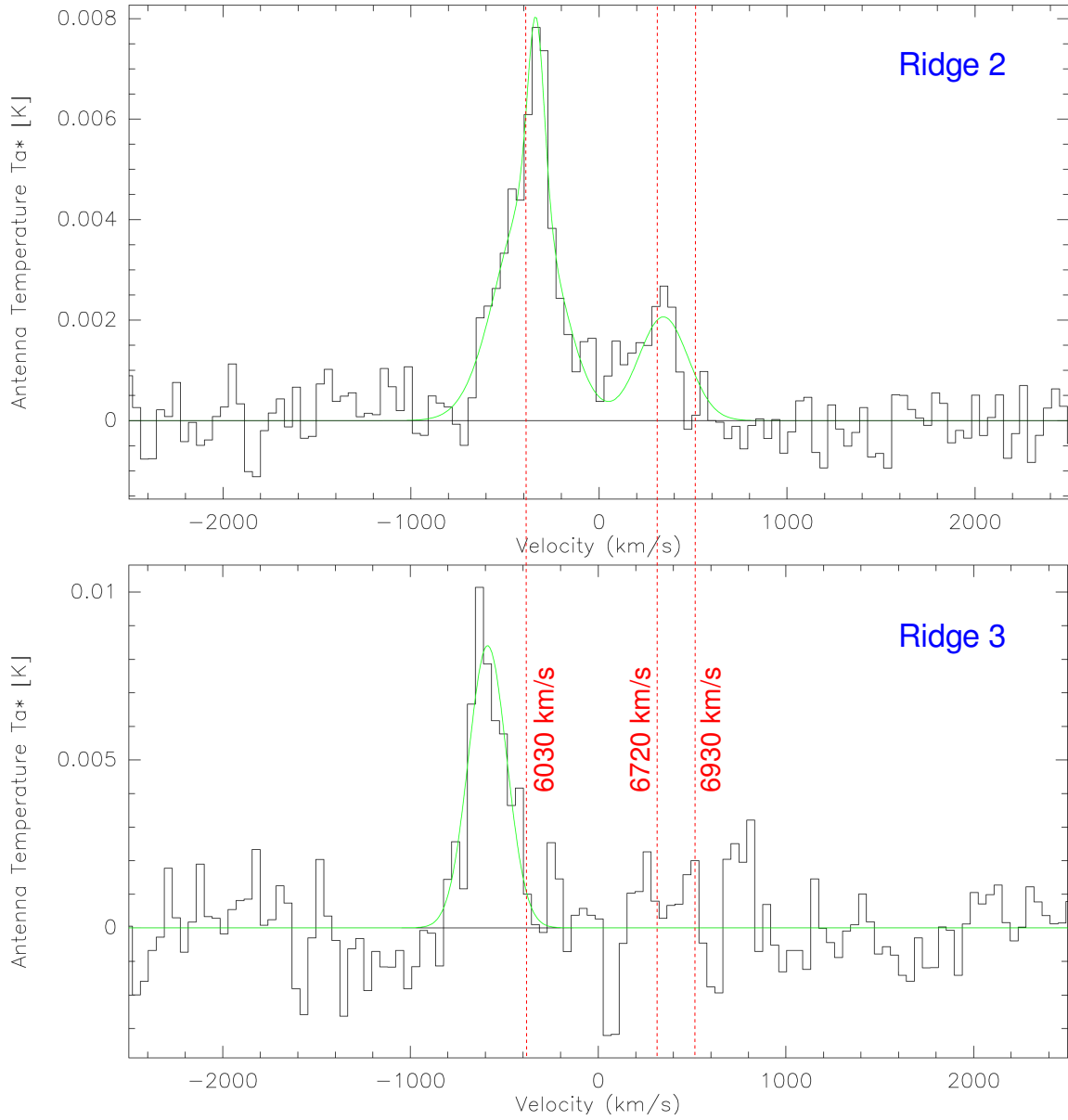
Figure 7.5: Idem Fig. 7.4 for the CO(1-0) spectra at the Ridge 2 and 3 positions.

zoom (bandwidth of $-2500 - 2500$ km s^{-1}) on the spectra with reference velocities of SQ-A overlaid (red dashed lines). The green line shows the result of the multiple gaussian fitting. This fitting is used to derive the central velocities of the CO components, the line widths and integrated intensities. We check that the residuals are below the 2σ level.

In Table 7.3 we gather the CO(1-0) central line velocities, the integrated line intensities, and the derived H$_2$ gas masses for the different observed regions shown on Fig. 7.3 (see Table 7.2 for the coordinates of these positions and the integration times). The molecular gas masses in this table are

Table 7.3: New CO observations of the center of the SQ group[a]: observational results

Target	Area [arcsec^2]	v_{CO} [km s^{-1}]	Δv_{CO} [km s^{-1}]	$\mathcal{I}_{\mathrm{CO}}$ [K km s^{-1}]	$M_{\mathrm{H_2}}$ [b] [$\times 10^8$ M$_\odot$]
SQ-A (6000) [c]		6028 ± 5	63 ± 8	0.60 ± 0.07	2.0 ± 0.2
SQ-A (6700) [c]		6723 ± 12	161 ± 31	0.96 ± 0.15	3.2 ± 0.5
SQ-A (6900) [c]		6927 ± 5	104 ± 12	1.23 ± 0.12	4.1 ± 0.4
SQ-A (tot) [d]				2.8 ± 0.2	9.2 ± 0.7
Ridge 1 (6000)		6069 ± 6	154 ± 10	1.61 ± 0.10	5.3 ± 0.3
Ridge 1 (tot) [d]				1.8 ± 0.1	5.9 ± 0.3
Ridge 2 (6000)		6052 ± 24	405 ± 15	2.3 ± 0.1	7.7 ± 0.4
Ridge 2 (tot) [d]				3.0 ± 0.1	9.9 ± 0.4
Ridge 3 (5700)		5767 ± 35	241 ± 29	2.1 ± 0.2	6.8 ± 0.7
Bridge (tot) [d]				3.9 ± 0.4	12.7 ± 1.4

(Area column, spanning rows: $1.13 \times 22''^2 = 547''^2$)

[a]Recent observations performed with the new EMIR receiver at the IRAM 30m telescope by Guillard et al. (2009b)
[b]H$_2$ gas masses are calculated using the Galactic conversion factor of $N(\mathrm{H_2})/\mathcal{I}_{\mathrm{CO}} = 2 \times 10^{20}$ cm^{-2} [K km s^{-1}]$^{-1}$
[c]Results are given for each velocity components, centered at $\sim$ 6000, 6700 and 6900 km s^{-1}. The last component at 6900 km s^{-1} is a newly discovered feature (see text for details).
[d]All velocity components

calculated using the Galactic conversion factor of $N(\mathrm{H_2})/\mathcal{I}_{\mathrm{CO}} = 2 \times 10^{20}$ cm^{-2} (K km s^{-1})$^{-1}$:

$$M_{\mathrm{H_2}} = \mathcal{I}_{\mathrm{CO}}^{\mathrm{obs}} \times \frac{N(\mathrm{H_2})}{\mathcal{I}_{\mathrm{CO}}} \times d^2 \times \Omega \times 2\,m_{\mathrm{H}} \tag{7.1}$$

$$= 3.3 \times 10^8 \left(\frac{\mathcal{I}_{\mathrm{CO}}^{\mathrm{obs}}}{\mathrm{K\,km\,s^{-1}}} \right) \left(\frac{N(\mathrm{H_2})/\mathcal{I}_{\mathrm{CO}}}{2 \times 10^{20}} \right) \left(\frac{d}{94\,\mathrm{Mpc}} \right)^2 \left(\frac{\theta_{\mathrm{FWHM}}}{21''} \right)^2 \mathrm{M}_\odot \tag{7.2}$$

where $\mathcal{I}_{\mathrm{CO}}^{\mathrm{obs}}$ is the observed velocity integrated CO line intensity expressed in K km s^{-1}, d is the distance to the source in Mpc and Ω is the area covered by the observations in arcsec^2, with $\Omega = 1.13 \times \theta_{\mathrm{HP}}$ for a single pointing with a Gaussian beam of Half Power beam width of θ_{HP}. Note that to derive the total mass of molecular gas, one has to multiply $M_{\mathrm{H_2}}$ by a factor 1.36 to take into account Helium. In the following we briefly discuss the masses of molecular gas detected in the three main area, the ridge, SQ-A, and the bridge.

CO in the SQ ridge Summing over all the velocity components, we derive $\approx 6 \times 10^8$ and 10^9 M$_\odot$ of cold molecular gas in the positions "ridge 1" and 2. For the "ridge 3" position, the spectrum is more noisy because of limited integration time, and we detect ≈ 7 M$_\odot$ of cold H$_2$ at 5700 km s^{-1}. Our pointings do not cover entirely the ridge, but we can safely say that the total mass of molecular gas in the ridge is at least 2.5×10^9 M$_\odot$. It is only a factor of 2 larger than the total warm H$_2$ mass seen by *Spitzer* in the ridge (1.2×10^9 M$_\odot$, see table 6.1). The mass of molecular gas in the SQ shock is larger than in the Milky Way!

CO in SQ-A Within our aperture $\Omega = 547$ arcsec^2 centered on SQ-A, we find a total cold H$_2$ mass of 9.2×10^8 M$_\odot$. Lisenfeld et al. (2002) find $\approx 3 \times 10^9$ M$_\odot$ over a much larger area ($60'' \times 80''$)

that partially overlaps the north of the ridge. However, because of a limited bandwith, they only detect the 6000 and 6700 km s^{-1} velocity components, and they miss the higher velocity component at 6900 km s^{-1} that seem to contain almost half of the mass in the core region of SQ-A (see table 7.3). Based on our new IR maps, we estimate the area of SQ-A to be $\approx 40'' \times 40''$. If we scale the mass we find in our aperture Ω to this larger aperture, we find a total mass of cold H$_2$ of 2.6×10^9 M$_\odot$. This is comparable to the mass derived by Lisenfeld et al. (2002), which is the result of a lucky compensation between two effects, the over-estimate of the mass in SQ-A because of a large aperture, and the under-estimate because of the non-detection of the 6900 km s^{-1} component.

CO in NGC 7319's bridge Summing over all velocities, we find $M_{\mathrm{H}_2} = 1.2 \times 10^9$ M$_\odot$ within our aperture Ω. Note that our aperture matches quite well the width of the bridge, but does not cover its whole extension towards the AGN. Therefore, the total mass of molecular gas in the bridge may be a factor of ≈ 2 larger. Smith and Struck (2001) find $\approx 5 \times 10^9$ M$_\odot$ within a half-power beam of 55" centered on the nucleus of NGC 7319. This beam overlaps our bridge region.

These observations represent a substantial revision of the mass and energy budgets of the collision. The first striking result is that we detect in the ridge and in the bridge features a comparable amount of molecular gas to that of SQ-A. The CO emission in the intragroup medium is then very extended, and in total (SQ-A + ridge + bridge), $\gtrsim 6.5 \times 10^9$ M$_\odot$ of cold H$_2$ gas is lying outside the galactic disks of the group. Although it represents a huge mass of molecular gas, most of this gas appears to be inefficient at forming stars, except in SQ-A (see chapter 8).

Interestingly, assuming a Galactic CO-to-H$_2$ conversion factor, we find that the ratio of the cold to warm H$_2$ masses is ≈ 2 in the ridge. This ratio is much smaller than in galaxies, where the mass of cold molecular gas is $1 - 2$ orders of magnitude greater than the warm H$_2$ mass: $M_{\mathrm{H}_2}(\mathrm{cold}) = 10 - 100 \times \mathrm{M}_{\mathrm{H}_2}(\mathrm{warm})$ (Roussel et al., 2007). This preliminary result seems in agreement with our interpretation of the H$_2$ emission in terms of a continuous heating by dissipation of turbulent energy (see sect. 6.5.1).

7.4.2 Complex kinematics of the CO gas

Fig. 7.3 clearly show the complexity of the kinematics of the CO gas in the SQ group. The shape of the spectra varies a lot from one position to another. Multiple velocity components are detected (see Fig. 7.4 and 7.5 for detailed view at the spectra with some reference velocities overlaid). The four main components are at 5700, 6000, 6700 and 6900 km s^{-1} (see table 7.3 for the precise central line velocities derived from line fitting). Note that the H I velocities detected in SQ are 5700, 6000 (associated with the intruder gas), and 6700 km s^{-1} (associated with the tidal tail to the south of NGC 7319). The velocity component at 6900 km s^{-1} is a new feature that we detect only in the SQ-A region. It was not seen before in CO or H I because of limited velocity coverage. The main general results are the following:

- the gas associated with the intruder NGC 7318b ($5700 - 6000$ km s^{-1}) and with the intragroup medium (the tidal tail, 6700 km s^{-1}) are both detected along the full North-South extension of the ridge, and in the bridge eastern feature towards NGC 7319 as well.

- gas at intermediate velocities, in between that of the intruder and that of the intragroup, is detected. There is a broad component centered at ≈ 6400 km s^{-1} in the ridge 1, 2 and in the bridge positions. Interestingly, this intermediate component seems to be absent (or very weak, $\approx 2\sigma$) in SQ-A and vanishes at the southern end of the main shock region (ridge 3). The 6400 km s^{-1} CO velocity component is consistent with the central velocity of the broad, resolved H$_2$ S(1) line at 6360 ± 100 km s^{-1} (see Appendix B of paper II for a re-analysis of the Appleton et al. (2006) high-resolution *IRS* spectrum). This is the first time CO gas is detected at these intermediate velocities, and this gas is associated with the warm H$_2$ seen by *Spitzer*. This detection support the idea that molecular gas is formed out of gas accelerated in the shock.

- The CO line velocity components are very broad, suggesting that the kinematics of the CO gas is highly disturbed. The FWHM of the main CO(1-0) lines are of the order of $100-400$ km s^{-1}, with an even broader signal (≈ 1000 km s^{-1}) at intermediate velocities (see coments below). This suggests that huge velocity gradients are present in this region. These broad line widths are in agreement with the Appleton et al. (2006) interpretation that the mid-IR H$_2$ lines are intrinsically very broad and resolved by the high resolution module of the *IRS*.

Some specific comments about each regions are given in the following:

SQ ridge In the ridge, the line widths are of the order of $100 - 400$ km s^{-1}, and lines seem to be broader in the center (ridge 2) than at the edges (ridge 1 and 3). In the ridge 1 position (and perhaps ridge 2), the underlying intermediate component at 6400 km s^{-1} is extremely broad (≈ 1000 km s^{-1}, comparable to the relative velocity between the intruder and the intragroup medium), with a hint of emission between 6900 and 7400 km s^{-1} (see ridge 1 spectrum on Fig. 7.4).

SQ-A In SQ-A, three velocity components are detected at 6000, 6700 and 6900 km s^{-1}. The line widths are of the order of 100 km s^{-1}, with the smallest dispersion for the 6000 km s^{-1} line. The broadest component at 6700 km s^{-1} seems to have a left wing extending towards 6400 km s^{-1}. Interestingly, the CO(1-0) line widths are significantly smaller in SQ-A than in the (b)ridge, and this is perhaps a clue to understand why there is much more star formation in this region than in the ridge. This observational picture fits within our interpretation of two colliding gas flows (presented in sect. 5.3.2), where the shear velocities between the flows are maximum in the central region of the contact discontinuity (ridge), and smaller at the edges of the main shock structure (see chapter 4, sect. 4.5.3 and Fig 5 of Lee et al., 1996).

NGC 7319's bridge The spectrum in the bridge is perhaps the most striking. It shows a very broad signal in between the extreme velocities detected in SQ-A (6000 and 6900 km s^{-1}), see Fig. 7.4. This profile is well fitted by a sum of 3 gaussians. As discussed in sect. 6.7, the origin of the molecular gas in the bridge structure is an open question. If an outflow from the AGN is present (as suggested by Aoki et al., 1996), molecular may be entrained from the disk or formed directly in the outflow (see also sect. 6.7 for observational details about NGC 7319). The molecular gas in the bridge may also be the result of a previous tidal interaction (with NGC 7320c for instance) that would have stripped some material from the galactic disk. Then the interaction between

the new intruder and this "tidal bridge" would trigger further molecular gas formation in this region. We do not see any clear-cut argument to favor one of the two possibilities.

7.5 Astrophysical questions raised by CO observations

These CO observations essentially raise two open questions, one related to the dynamical coupling of the molecular gas to the lower density phases, and the other related to star formation. Here are the tracks we are following to tackle these two issues.

7.5.1 How is the molecular gas accelerated?

Observations shows that some of the CO gas lies at intermediate velocities between that of the intruder (NGC 7318b) and that of the target, i.e. NGC 7319's tidal tail. The CO line widths match that of the [O I] $\lambda 6300$ Å line from warm atomic gas. This suggests that the cold molecular gas is dynamically coupled to the lower density components. If the picture of two colliding multiphase gas flows is correct, these observations mean that, in the reference frame of the surface discontinuity between the two gas streams (which may be materialized by the X-ray bright ridge), the dense clouds has been significantly decelerated.

This coupling seems difficult to explain if most of the molecular gas was preshock gas. The high density contrast between cold clouds and the hot, tenuous flow would lead to deceleration timescales longer than the shock age (see sect. 4.5.2), and therefore a weak coupling. In our model of H_2 formation in the shock, the molecular gas is formed out of moderate density medium that is compressed and decelerated while becoming molecular. Therefore, in this context, the coupling is much more efficient because the density contrast is much lower. This *in-situ* formation is perhaps a solution to explain the high velocity dispersion seen in the spectra, although we do not exclude the presence of preshock dense clouds.

7.5.2 Driving Schmidt-Kennicut into a corner

Many galaxy collisions are observed to trigger IR-luminous bursts of star formation. This is not the case in SQ, although a large reservoir of cold molecular gas is present in the area of interaction between the two galaxies. Fig. 7.6 shows a diagram similar to the classical Schmidt-Kennicutt relationship. Based on the empirical correlation between PAH emission and star formation in starbursts (Calzetti et al., 2007; Pope et al., 2008), the 7.7 μm PAH emission is used as a tracer of star formation. The cold H_2 mass is derived from the standard CO(1-0) intensity to H_2 mass conversion factor (see chapter 3, Eq. 3.44). The SQ point corresponds to the ridge 1 position. The PAH luminosity in the SQ shock is integrated over a $18'' \times 15''$ region centered on the CO(1-0) beam of the ridge 1 position (see chapter 8 for details about how the PAH luminosity is calculated).

We find that SQ is offset from the correlation obtained with the SINGs sources (data taken from Roussel et al., 2007). Interestingly, SQ has a similar offset as the H_2-luminous radio galaxies 3C326N and 3C293 (see chapter 9 for a discussion of 3C326N). This plot clearly shows that star formation is suppressed in the center of the shock as compared to star forming galaxies.
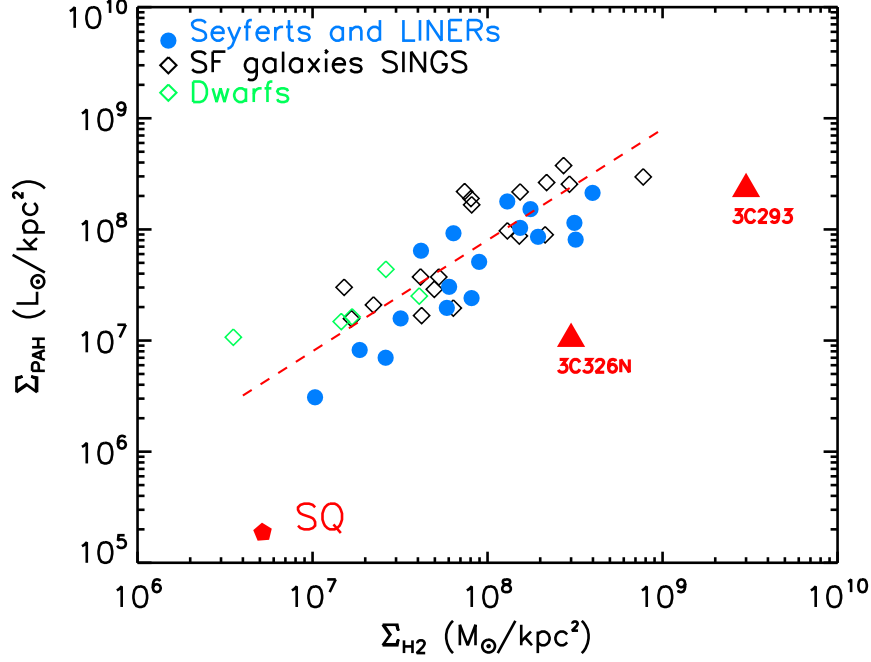
Figure 7.6: Star-formation efficiency (assumed to be traced by the surface luminosity of the PAH emission) as a function of mass of cold H_2, derived from the CO(1-0) line intensity. The hatched line shows the relationship obtained for the SINGS sample, where empty diamonds and filled dots mark dwarf galaxies, star-forming galaxies, and AGN. The SINGS data is from Roussel et al. (2007). The filled pentagon shows the center of the SQ shock. For comparison, the filled triangles mark the H_2-luminous radio galaxies 3C326 N and 3C293.

The molecular gas is observed to be more turbulent in the ridge than in SQ-A, where star formation is occuring. This suggests that the dissipation of the mechanical energy may be an important process in heating the molecular gas and perhaps quenching star formation (see paper I and chapter 8 for a more detailed discussion of star formation in SQ).

7.6   Concluding remarks

These new CO observations provide a more complete inventory of the molecular gas in the SQ intragroup medium. Large amounts of CO emitting gas is detected, both in the main shock region and in the eastern bridge feature. This gas is coexisting with warm H_2, H II gas, and X-ray emitting hot plasma. The CO(1-0) lines are intrinsically broader outside the SQ-A and southern star-forming regions, suggesting that the galaxy collision has disturbed its kinematics within the group halo.

A more detailed analysis and a paper is in preparation to estimate as precisely as possible the mass, excitation characteristics (in particular the CO(2-1) to CO(1-0) line ratio), and the full kinetic energy of the molecular gas in the SQ shock. This will lead to re-evaluate our prior estimate of the dissipation timescale through H_2 line emission. The velocity structure will be used to distinguish

between preshock molecular gas and molecular gas formed out of gas that has been shocked and decelerated in the collision. In addition, we will use MHD shock models (similar to those used to interpret the H_2 line emission) to compute the CO emission in shocks, and compare the results with the observations presented here.

Chapter 8

Dust emission in Stephan's Quintet

I close my eyes
Only for a moment, and the moment's gone
All my dreams
Pass before my eyes with curiosity
Dust in the wind
All they are is dust in the wind

Kerry Livgren, Kansas

Abstract

In chapters 5 and 6, I propose an interpretation to the surprisingly bright H_2 rotational line emission from the Stephan's Quintet (SQ) shock, in which H_2 gas forms out of the multiphase postshock gas. In this scenario, dust is a key-element because its presence is required for H_2 to form. Therefore we expect that some of the dust emission comes from molecular gas. This chapter is a brief introduction to the work I did on the analysis and modeling of new Spitzer imaging and spectroscopy of dust emission in the SQ ridge. The associated paper is reproduced in the manuscript. I have analysed the characteristics of the PAH emission in the shock, built a complete IR spectral energy distribution of the shock, and compare it to that of the diffuse Galactic ISM. In order to try to constrain the physical structure of the molecular gas, a detailed modeling of the dust emission in the SQ ridge has been performed, and the model results compared to observations.

Contents

8.1 Introduction

D ust shapes the spectra of galaxies: dust absorbs[1], scatters stellar light, and re-emits this energy in the infrared domain. It is estimated that 30% or more of the energy emitted as starlight in the Universe is re-radiated by dust in the infrared (see Lagache et al., 2005, for a review about the cosmic IR background).

Molecular hydrogen forms on dust grains. Therefore, dust is a key-element for our interpretation of H_2 emission from the SQ X-ray bright shock structure. In paper I, we show that H_2 gas can form out of the dense gas that is shocked to velocities sufficiently low ($V_s < 300$ km s^{-1}) for dust to survive. One of the consequences of this interpretation is that some of the dust emission comes from molecular gas. Therefore, in order to test this prediction, I have embarked on a study and modeling of the dust emission from the SQ shock, which has been written in paper III (Guillard et al., 2009a), which will be soon submitted to A&A. This chapter will not review the content of the paper, but rather introduce the context of the past observations of dust emission from SQ, as well as their interpretation (sect 8.2.1). Then, I briefly present the context of the new *Spitzer* observations (sect 8.2.2, as well as the paper III. The section 8.4 concludes this chapter by opening the discussion about dust survival in the violent SQ environment, and more generally in the multiphase ISM.

8.2 Observations of dust emission from Stephan's Quintet

8.2.1 Past observations (*ISO*)

IRAS first detected SQ in the infrared (Allam et al., 1996; Yun et al., 1997), but it was barely resolved. The first quantitative study of dust emission in the SQ group was made possible by the *ISO*[2] space observatory. Xu et al. (1999, 2003) reported *ISO* observations that show that most of the mid-IR (11.3 and 15 μm) and Far-IR (60 and 100 μm) emission comes from the disks of NGC 7319 and of the foreground galaxy NGC 7320 (see Fig. 8.1). Two intra-group medium (IGM) starbursts SQ-A and SQ-B, both including several previously detected H II regions, stand out in the 15 μm image due to their strong mid-IR emission. There is evidence for dust emission in the shock front. Xu et al. (2003) have modeled the *ISOPHOT*[3] maps at 60 and 100 μm to isolate emission from the shock (Fig. 8.1). However, the angular resolution is marginally sufficient to separate the shock itself from the SQ-A and SQ-B star forming regions.

Based on *ISO* observations, the total dust luminosity of the shock front is $\mathcal{L}_{dust} = 1.9 \times 10^{35}$ W (Xu et al., 2003). This is about an order of magnitude higher than the X-ray luminosity. Xu et al. (2003) concluded that dust cooling may be a significant cooling mechanism for the shock. They propose that the hot gas is predominantly cooled by electronic collisions with dust grains. This conclusion is based on the comparison between the sputtering time scale of dust grains and the gas cooling

---

[1]The existence of the extinction of stellar light by interstellar dust was found by Trumpler (1930) by measuring the angular diameter of star clusters. They introduce a corrective term, A_λ, in their estimate of the distance to the source, in order to take into account its overestimation due to the presence of dust. Stebbins (1934, 1935) first showed that the extinction follows a λ^{-1} law in the U, B, V bands. This law in the optical shows that the grain size is of the order of the wavelength, i.e. 0.1 to 0.5 μm.

[2]Infrared Space Observatory, http://iso.esac.esa.int/.

[3]Infrared Space Observatory Photopolarimeter http://www.mpia-hd.mpg.de/ISO/welcome.html.

ISO observations of Stephan's Quintet
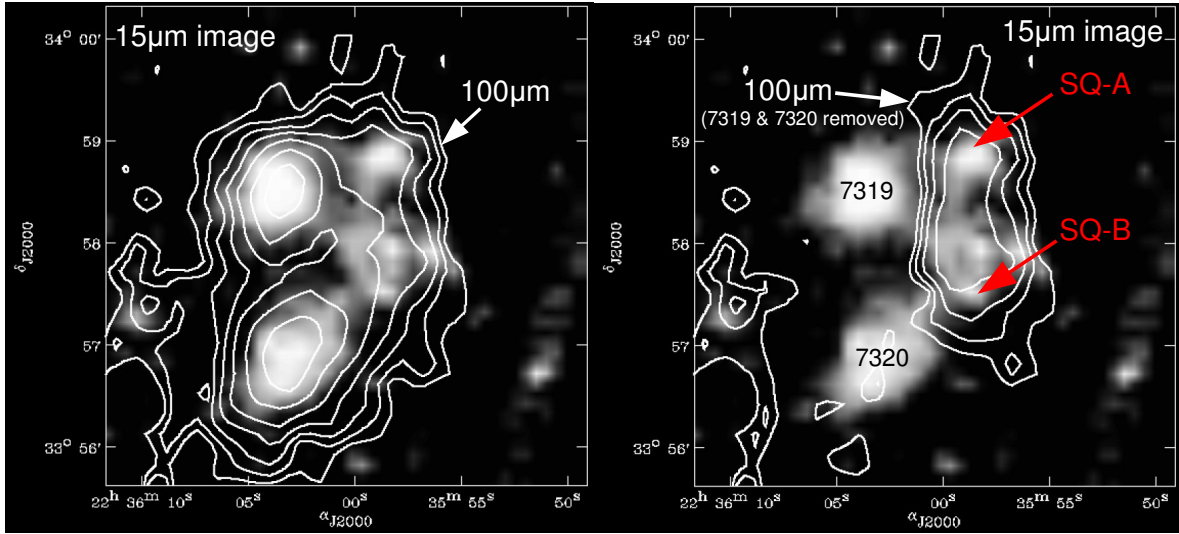
Figure 8.1: *ISO* observations of SQ (15 & 100 μm) by Xu et al. (2003). Contour maps of the IR emission (background subtracted) at 100 μm are overlaid on the *ISO* 15 μm image. *Left:* The contour levels for the 100 μm map are 0.8, 1.12, 1.6, 2.24, 3.2, 4.48, 6.4 MJy sr^{-1}. *Right:* 100 μm emission after the subtraction of NGC 7319 and NGC 7320. The contour levels are 0.8, 1.12, 1.6, 2.24 MJy sr^{-1}.

time. Assuming a constant, Galactic mass-to-dust ratio, the sputtering time of an $a = 0.1 \mu$m grain is 3.7×10^6 yr, compared to the gas cooling time of 2.1×10^6 yr. Hence the big grains can indeed survive the shock long enough. However, as shown in Smith et al. (1996) and Guillard et al. (2009c), the sputtering of dust grains in the hot ($T > 10^6$ K) phase should have reduced significantly the dust to gas mass ratio on a timescale shorter than the gas cooling time (see chapter 2 and discussion later in paper III).

8.2.2 New Spitzer observations

ISO observations have been followed up by *Spitzer* observations. Appleton et al. (2006) release a spectacular composite image with IRAC (see the cover front of this manuscript!) at 3.6, 4.5, 5.8 and 8 μm. Images at 16 and 24 μm were obtained by our team and presented in Cluver et al. (2009) and Guillard et al. (2009a). Longer wavelength images at 70 and 160 μm were obtained by Xu et al. (2008). They claim to detect a significant diffuse dust emission outside individual galaxies, amounting to more than 50% of the total $\mathcal{L}_{160 \, \mu m}$ of SQ (see also Natale, in preparation). Because of the better correspondence between the morphology of the 160 μm map and that of the X-ray map, compared to that between 160 μm and H I, the authors favor the possibility that the grains are collisionally heated in the hot intra-group medium.

The presence of H$_2$ gas in the intragroup set a new perspective on the origin of the dust emission in the ridge. As introduced above, we expect some dust emission from the H$_2$ gas. My work presented in paper III explore this possibility.

8.3 Publication: Paper III

I reproduce here the paper *"Observations and modeling of the dust emission from the H_2-bright galaxy-wide shock in Stephan's Quintet"*, P. Guillard, F. Boulanger, M. Cluver, P.N. Appleton, G. Pineau des Forêts, submitted to A&A. I have intentionally not repeated the content of the paper in this manuscript.

Observations and modeling of the dust emission from the H$_2$-bright galaxy-wide shock in Stephan's Quintet

P. Guillard[1], F. Boulanger[1], M. Cluver[2], P.N. Appleton[3], G. Pineau des Forêts[1,4], and P. Ogle[5]

[1] Institut d'Astrophysique Spatiale (IAS), UMR 8617, CNRS, Université Paris-Sud 11, Bâtiment 121, 91405 Orsay Cedex, France
  e-mail: `pierre.guillard@ias.u-psud.fr`
[2] IPAC, California Institute of Technology, Mail code 100-22, Pasadena, CA 91125, USA
[3] NASA *Herschel* Science Center (NHSC), IPAC, California Institute of Technology, Mail code 100-22, Pasadena, CA 91125, USA
[4] LERMA, UMR 8112, CNRS, Observatoire de Paris, 61 Avenue de l'Observatoire, 75014 Paris, France
[5] *Spitzer* Science Center, IPAC, California Institute of Technology, Mail code 100-22, Pasadena, CA 91125, USA

ABSTRACT

Context. *Spitzer Space Telescope* observations revealed powerful mid-infrared (mid-IR) H$_2$ rotational line emission from the Stephan's Quintet (SQ) X-ray emitting galaxy-wide shock ($\sim 15 \times 35$ kpc^2). Because H$_2$ forms on dust grains, the presence of H$_2$ is physically linked to the survival of dust, and we expect some dust emission to come from the molecular gas.
Aims. To test this interpretation, IR observations and dust modeling are used to identify and characterize the thermal dust emission from the shocked molecular gas.
Methods. The spatial distribution of the IR emission allows us to isolate the faint PAH and dust continuum emission from the H$_2$ gas. We model the spectral energy distribution (SED) of the emission from dust associated with the molecular gas present in the SQ shock, and compare results to the SED derived from *Spitzer* observations. We use a radiation field determined with *GALEX* UV and ground-based near-IR observations and consider two limiting cases for the structure of the H$_2$ gas. It is either diffuse, penetrated by UV radiation, or fragmented into clouds optically thick to UV.
Results. Faint PAH and dust continuum emission are detected in the X-ray shock structure, outside star-forming regions. In both models (diffuse or clumpy H$_2$ gas), the IR SED is consistent with the expected emission from dust associated with the warm (> 150 K) H$_2$ gas, heated by a UV radiation field of intensity comparable to that of the solar neighborhood. This is in agreement with *GALEX UV* observations that show that the intensity of the radiation field in the shock is $G_{UV} = 1.4 \pm 0.2$ [Habing units]. Our model calculations show that far-IR *Herschel Space Observatory* observations will help constraining the structure of the molecular gas. The 12/24 μm flux ratio in the shock is remarkably close to that of the diffuse Galactic interstellar medium, leading to a Galactic PAH/VSG abundance ratio. On the other hand, the properties of the PAH emission spectrum in the shock differ from that of the Galaxy, which may suggest an enhanced fraction of large and neutrals PAHs.
Conclusions. The presence of PAHs and dust grains in the high-speed (~ 1000 km s^{-1}) galaxy collision suggests that dust survives because it may have been protected in dense clouds. Our model assumes a Galactic dust-to-gas mass ratio and size distribution, and present data do not allow to identify significant deviations of the abundances and size distribution of dust grains from that of the Galaxy. *Herschel* data will allow us to study the degeneracy between the structure of the molecular gas and the dust size distribution, and search for signatures of dust processing in the SQ shock.

Key words. ISM: general – ISM: dust, extinction – ISM: molecules – ISM: structure – Atomic processes – Molecular processes – Shock waves – Infrared: ISM – Galaxies: clusters: individual: Stephan's Quintet – Galaxies: evolution – Galaxies: interactions

1. Introduction

Stephan's Quintet (Hickson Compact Group HCG92, Arp 319, hereafter SQ) is an extensively studied compact group of four interacting galaxies that have a complex dynamical history (e.g. Allen & Sullivan, 1980; Moles et al., 1997). A remarkable feature of SQ is that a giant ($\approx 15 \times 35$ kpc) shock is created by an intruding galaxy, NGC 7318b (Sbc pec), colliding into NGC 7319's tidal tail, at a relative velocity of $\sim 1\,000$ km s^{-1}. Evidence for a group-wide shock comes from observations of X-rays from the hot postshock gas in the ridge (Pietsch et al., 1997; Trinchieri et al., 2003, 2005; O'Sullivan et al., 2009), strong radio synchrotron emission from the radio emitting plasma (Allen & Hartsuiker, 1972; Sulentic et al., 2001; Williams et al.,

2002; Xu et al., 2003) and shocked-gas excitation diagnostics from optical emission lines (Xu et al., 2003). This extended region is denoted *"ridge"* or simply *"shock"* in this paper.

Observations with the infrared spectrograph (*IRS*, Houck et al., 2004) onboard the *Spitzer Space Telescope* have revealed a powerful mid-infrared (mid-IR) H$_2$ rotational line emission from warm ($\sim 10^2 - 10^3$ K) molecular gas in the SQ shock (Appleton et al., 2006; Cluver et al., 2009). The H$_2$ emission is extended over the whole ridge, as well as towards the Seyfert 2 galaxy NGC 7319 (Sbc pec) and the so-called SQ-A intergalactic starburst (Xu et al., 1999), beyond the northern tip of the ridge, where CO emission was detected (Gao & Xu, 2000; Smith & Struck, 2001; Lisenfeld et al., 2002). To explain the H$_2$ emission from the SQ ridge, Guillard et al. (2009) considered the collision of two flows of multiphase dusty gas and proposed a model that quantifies the gas cooling, dust destruction, H$_2$ formation and excitation in the postshock medium. H$_2$ gas can

form out of gas that is shocked to velocities sufficiently low ($V_s < 300$ km s^{-1}) for dust to survive. Because H$_2$ molecules form on dust grains (e.g. Cazaux & Tielens, 2004), dust is a key element in this scenario.

Xu et al. (1999, 2003) reported detection of diffuse far-infrared (hereafter FIR) emission from the intergalactic medium (hereafter IGM) with the *Infrared Space Observatory (ISO)*, and proposed that this emission would arise from dust grains that efficiently cool the X-ray emitting plasma via collisions with hot electrons. The FIR emission would then trace the structure of the shock, as suggested by Popescu et al. (2000) for the case of shocks driven into dusty gas that is accreting onto clusters of galaxies. However, the poor spatial resolution of these observations makes it difficult to separate the dust emission associated with star formation (in the neighborhood galaxies, or SQ-A) from that really associated with the shock. In addition, Smith et al. (1996); Guillard et al. (2009) show that the dust cooling efficiency of the hot ($\sim 5 \times 10^6$ K) plasma is expected to be low, because of efficient thermal sputtering of the grains. Although a significant mass of dust may remain in the hot X-ray emitting plasma, most of the grains smaller than 0.1 μm in radius must have been destroyed if we assume that the age of the galaxy collision is $\sim 5 \times 10^6$ yrs (Guillard et al., 2009).

The discovery of bright H$_2$ emission in the ridge set new perspectives on the origin of the dust emission in the SQ ridge. In the context of our model for the H$_2$ formation in the SQ shock, we expect some dust emission from the molecular gas. We use *Spitzer* observations and a model of the dust emission to test this expectation. Recent *Spitzer* observations show that the bright Polycyclic Aromatic Hydrocarbons (henceforth PAHs) and mid-IR continuum emitting regions are spatially correlated with UV emission and associated with star-forming regions in the SQ halo (Cluver et al., 2009). These IR-bright regions do not correlate with the radio, X-ray, or H$_2$ line emission, which trace the shock structure. In this paper we focus on the fainter dust emission from the the SQ ridge itself, outside these star-forming regions. We use the spatial distribution of the mid-IR emission to isolate the dust emission from the shock. UV, near-IR photometry, and optical line spectroscopy are used to constrain the spectral energy distribution (hereafter SED) of the radiation field that is used as an input to the dust model. We consider two limiting cases for the structure of the molecular gas, either diffuse, or fragmented into clouds that are optically thick to UV light. We use an updated version of the Désert et al. (1990) model to compute the dust emission from molecular gas in these two cases, and fit the model results to the observed IR SED in the SQ shock. The galactic dust size distribution is used as a reference.

This paper is organized as follows. Section 2 presents the new IR *Spitzer* observations of SQ, and the UV and near-IR ancillary data we use in this paper. The method used to perform photometry within the SQ shock region and the results are described in sect. 3. Section 4 reports the *Spitzer* observational results (imaging and spectroscopy) about the dust emission in the shock structure, emphasizing the PAH properties in the shock. The physical framework and inputs of the dust modeling is outlined in sect. 5, and the results are discussed and compared to the mid-IR *Spitzer* observations in section 6. In sect. 7 we discuss the dust processing in the shock. Then, we present our conclusions in sect. 8 and we propose new observations to constrain the physical structure of the molecular gas in the shock.

In this paper we assume the distance to the SQ group to be 94 Mpc (with a Hubble constant of 70 km s^{-1} Mpc^{-2}) and a systemic velocity for the group as a whole of 6 600 km s^{-1}. At this distance, 10 arcsec = 4.56 kpc.

2. Observations of the Stephan's Quintet shock

In the following paragraphs we present the new mid-IR (sect. 2.1) observations of SQ, and the ancillary UV (sect. 2.2.1) and near-IR (sect. 2.2.2) data, respectively.

2.1. Spitzer IR imaging and spectroscopy

Stephan's Quintet has been imaged with the *InfraRed Array Camera* (*IRAC*, Fazio et al., 2004) at 3.6, 4.5, 5.8, 8 μm, with the *IRS* blue peak-up imager (PUI) at 16 μm, and with the *Multiband Imaging Photometer for Spitzer* (*MIPS*, Rieke et al., 2004) at 24 and 70 μm. The 70 μm image has been reported in Xu et al. (2008). The pixel sizes are 1.8", 2.45" and 5" at 16, 24 and 70 μm, respectively. Except for the 70 μm image, we direct the reader to Cluver et al. (2009) for a description of the observational details and data reduction. The upper right panel of Fig. 1 show the 16 μm data from the *IRS* blue *PUI*. The bottom left and right panels show the *MIPS* 24 and 70 μm images.

The SQ shock region was also mapped with the *IRS* spectrograph (Cluver et al., 2009). The Short-Low (SL) and Long-Low (LL) modules of the spectrograph have been used, covering the wavelength ranges $5.3 - 14.0$ and $14 - 38$ μm, with spectral resolution of $\lambda/\delta\lambda = 60 - 127$ and $57 - 126$, respectively.

2.2. Ancillary data

The UV and near-IR ancillary data are used to constrain the radiation field that is used as input for dust modeling (sect. 5.2).

2.2.1. GALEX UV imaging

The upper left corner of Fig. 1 shows the near-UV (NUV) image from the *Galaxy Evolution Explorer* mission (*GALEX,* Martin et al., 2005). These observations have been reported by Xu et al. (2005). The pixel size is 1.5" , the wavelength is $\lambda = 2\,267$ Å and the bandwith is $\Delta\lambda = 732$ Å. The far-UV (FUV) image ($\lambda = 1\,516$ Å, $\Delta\lambda = 268$ Å) is also used but is not shown here.

If one excludes the foreground galaxy NGC 7320 (Sd), most of the UV emission is associated with the two spiral members of the group, NGC 7319 and NGC 7318b, and the intragroup medium starburst SQ-A. The galaxy-wide shock structure, which shows up in Hα, radio and X-ray observations, is barely visible on the UV images. Based on the comparison between *ISO* and *GALEX* data, Xu et al. (2005) concluded that most of the UV emission in the ridge is not associated with the large-scale shock itself, but with H regions of the spiral arms of the intruder NGC 7318b.

We use the flux calibration described in the *GALEX* observer's guide[1] and in Morrissey et al. (2007). The unit DN (1 count per second, cps) is equivalent to 108 and 36 μJy for FUV and NUV, or, equivalently, 1.4×10^{-15} and 2.06×10^{-16} erg s^{-1} cm^{-2} Å^{-1}, respectively. We do not apply any aperture correction for the extended source UV photometry on *GALEX* images since the PSF full width half maxima (FWHM) are 4.9" and 4.2" for the NUV and FUV, respectively.

2.2.2. Near-IR WIRC imaging

We use near-IR (NIR) data from recent deep observations with the Wide field IR Camera (*WIRC*) on the Palomar 200-inch tele-

---

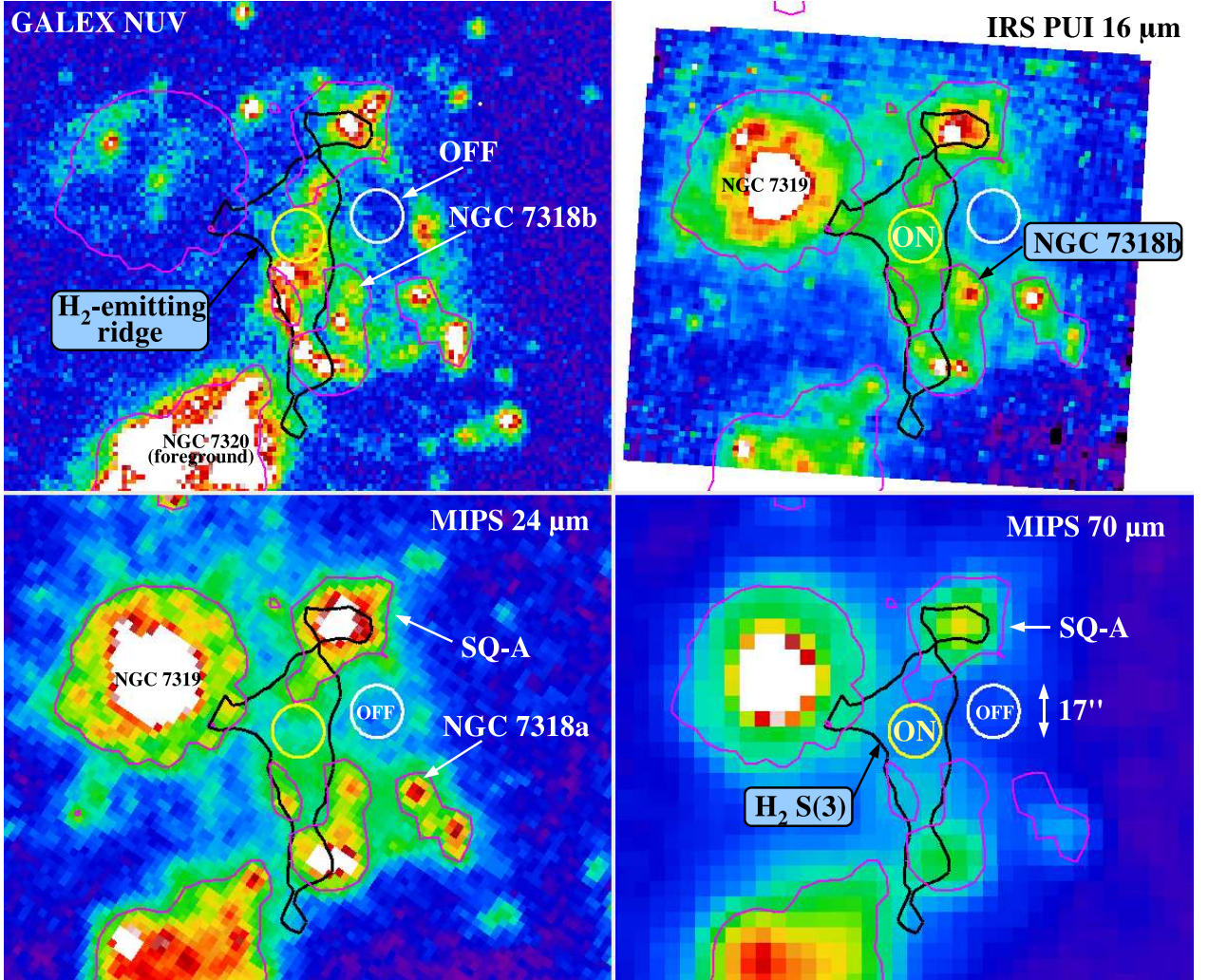[1] http://galexgi.gsfc.nasa.gov/docs/galex/

Fig. 1. UV and mid-IR observations of Stephan's Quintet. *From top left to bottom right:* Near-UV (2 267 Å) *GALEX* image from Xu et al. (2005), *Spitzer IRS* 16 μm peak-up image, 24 μm and 70 μm *Spitzer MIPS* images of the SQ group. For all images, the *black* contours shows the 4σ (0.3 MJy sr^{-1}) 0-0 S(3) H$_2$ line emission detected over the SQ ridge, from *Spitzer IRS* mapping by Cluver et al. (2009). The *magenta* contours show the 24 μm emission at a 0.25 MJy sr^{-1} level. They are used to identify star forming regions that overlap the H$_2$ contours in the ridge. Photometry is performed within the H$_2$ contours, excluding or not these star-forming regions. The circles indicate 17" beams where aperture photometry is also performed. The yellow circle shows the "ON" position in the SQ shock, centered on $\alpha = 22\text{h}35'59.8''$, $\delta = +33°58'16.7''$. The white circle show the "OFF" position we use to subtract the background signal, centered on $\alpha = 22\text{h}35'57.7''$, $\delta = +33°58'23''$.

scope (V. Charmandaris, private communication). The *WIRC* images were taken in July, 2009, and processed with the *Swarp* software[2]. They are $5 - 6$ magnitudes deeper than the corresponding *2MASS* images. The zero-point magnitudes are 24.50, 22.73 and 23.05, so we use flux calibrations of 0.252, 0.830, and 0.402 μJy DN^{-1} for J, H, and K$_\text{s}$, respectively. The corresponding central wavelengths are 1.250, 1.635 and 2.150 μm. The images show that most of the NIR emission in the SQ ridge is associated with the spiral arm of the intruder, NGC 7318b. NIR emission associated with the SQ-A northern starburst is also detected. Central wavelengths of 1.235 ± 0.006, 1.662 ± 0.009, 2.159 ± 0.011 μm are used.

---

[2] http://astromatic.iap.fr/software/swarp

3. Photometry on IR and UV images

We describe the method used to perform the photometry on *Spitzer* mid-IR images for the dust emission and on near-IR and UV images to estimate the radiation field at the position of the SQ shock.

3.1. Method

3.1.1. Dust emission

The SQ field of view is a crowded region (see sect. 4.1 for a description of the spatial distribution of the dust emission). In order to isolate the dust emission from the shock itself, we sum the signal within regions that are not contaminated by IR-emitting,

star-forming regions. Since the shock is surrounded by bright sources, we do not apply any aperture correction. For comparison, three different area are used to perform photometric measurements.

1. The signal is summed over a circular aperture of 17" in diameter that is centered on the SQ ridge, in the middle of the X-ray emitting shock front. This 17" aperture corresponds to the FWHM of the MIPS beam at $\lambda = 70\,\mu$m. It is marked with the yellow circle on Fig. 1 ("ON" position).
2. The signal is integrated over the SQ ridge within the H$_2$ contours (black line on Fig. 1) that define the shock structure. Except SQ-A, the star-forming regions that overlap the H$_2$ region are included. They are defined by the 24 μm iso-flux ($F_{24\,\mu m} > 0.25$ MJy sr^{-1}) contours (magenta line in Fig. 1).
3. The signal is summed over the SQ ridge within the H$_2$ contours by excluding the star forming regions. We subtract the signal that lies within the magenta 24 μm contours that overlap the H$_2$ contours.

To remove the contamination from the halo of the group, we choose to estimate the background level in a region close to the H$_2$-emitting shock. This "OFF" region is marked with the white circle on Fig. 1. For the 70 μm image, we cannot exclude that the flux within the "ON" position is contaminated by the brighter sources around it. Thus, we consider our 70 μm flux as an upper limit.

3.1.2. Radiation field

The radiation field is the integral of the flux over all directions. In the UV domain, due to scattering of light, we can assume that the radiation field is isotropic and estimate its strength from UV photometry at the position of shock. Thus we measure the UV fluxes within the same apertures than for the *Spitzer* images, using the same "OFF" position.

The UV fluxes are corrected for both foreground galactic and SQ internal extinctions. Assuming the galactic extinction curve from Weingartner & Draine (2001a) ($A_V^{(MW)} = 0.24$ for the Milky Way), the FUV and NUV galactic extinctions at *GALEX* wavelengths are respectively $A_{FUV}^{(MW)} = 0.62$ and $A_{NUV}^{(MW)} = 0.72$. We use the Xu et al. (2005) values for the internal SQ extinction, i.e. $A_{FUV}^{(SQ)} = 0.76$ and $A_{NUV}^{(SQ)} = 0.88$.

The near-IR images show that the shock is surrounded by bright sources, in particular NGC 7318b and nearby star-forming regions. Since there is little scattering at these wavelengths, the photometry restricted to the shock area is likely to underestimate the near IR intensity of the radiation field. Thus we choose to integrate the near-IR flux over the whole shock area, after removal of Galactic stars. The choice of the aperture is rather arbitrary and only provide a rough approximation of the near-IR radiation field.

Based on an average optical extinction of $A_V = 0.6$ (Guillard et al., 2009) for the center position in the ridge, and a Galactic extinction curve, we apply the following extinction corrections: $A_J = 0.17$, $A_H = 0.11$, and $A_{K_s} = 0.07$ for J, H, and K$_s$ bands, respectively. We use the values of zero-point fluxes from Cohen et al. (2003), i.e. 1594 ± 28, 1024 ± 20, 666.7 ± 12.6 Jy for J, H, and K$_s$ bands.

3.2. Results

The quantitative results about the photometry performed on IR *Spitzer* images are gathered in table 1. The surface brightnesses

are given for the three area described above. We estimate from the *IRS* spectrum that the 17 μm S(1) and 8 μm S(4) H$_2$ line emission represent respectively 68 % and 62 % of the *IRS* Peak-Up Imager 16 μm and the *IRAC* 8 μm in-band flux within the 17" ON aperture, and we correct for this contamination. The last row of table 1 indicates the fluxes we adopt throughout this paper. The error bars are estimated by using two different background subtractions close to the "OFF" position (8-arcsec shifts in the East-West direction). In addition, we include calibration uncertainties (of the order of 5%).

The results of the UV *GALEX* photometry are gathered in Table 2. The surface brightnesses are given for the three apertures defined in sect. 3.1.1. The UV fluxes measured over the SQ ridge aperture that includes the 24 μm-bright (> 0.25 MJy sr^{-1}) regions are $10 - 25$ % higher than the fluxes where these regions have been removed from the aperture ("SQ ridge (partial)" row). This shows that the UV contamination from these regions is not negligible and thus we subtract this emission to obtain the UV flux associated with the shock only. The brightnesses are background-subtracted and corrected for foreground galactic extinction and SQ internal extinction. From the UV surface brightness values we derive the intensity of the standard interstellar radiation field in Habing units.

The results show that the UV flux in the shock, outside star-forming regions, corresponds to an interstellar radiation field of average intensity $G_{UV} = 1.4 \pm 0.2$ in Habing units[3] (see sect. 5.2.1 for details). The error bar on the G_{UV} factor takes into account two background subtractions obtained by shifting the OFF position by 8" in the East-West direction. **This uncertainty does not take into account the uncertainty on the optical extinction, which may be important because of large spatial variations (up to 2 mag) of the A_V value in the shock.** The value of G_{UV} is used to characterize the intensity of the non-ionizing radiation field in the shock (sect. 5.2).

The extinction-corrected surface brightnesses measured on *Palomar WIRC* images (Fig. 1) are gathered in Table 3.

4. Dust emission from Stephan's Quintet: observational results

This section reports the observational results about the dust emission detected in the SQ ridge. We compare the mid-IR SED and the relative intensities of the PAH bands in the SQ shock to that of the Galactic diffuse interstellar medium (ISM).

4.1. Spatial distribution of the dust emission from the SQ group

Dust is lying outside the galactic disks, in the halo of the group. However, the mid-IR emission does not correlate with the H$_2$, X-ray and radio emissions. The images in Fig. 1 show that the bright mid-IR emitting regions are associated with the NGC 7319 galaxy and with UV-luminous, star-forming regions (Cluver et al., 2009). **Interestingly, these star-forming regions are outside the galactic disks of NGC 7318a and b, suggesting that a significant amount of gas has been displaced from these galaxies by tidal interactions.** If we exclude the foreground galaxy NGC 7320, the bright mid-IR emission comes from the NGC 7319 galaxy, the SQ-A starburst region, and an arc-like feature to the east of the intruding galaxy NGC 7318b. This arc structure is clearly seen on the UV, *IRAC*, and 16 μm

---

[3] The flux of the Habing field ($G_{UV} = 1$) equals 2.3×10^{-3} erg s^{-1} cm^{-2} at $\lambda = 1\,530$ Å (Habing, 1968; Mathis et al., 1983).

Table 1. Summary of the mid-IR photometric measurements[a] performed on the *Spitzer IRAC*, *IRS PUI* 16 μm, and *MIPS* 24, and 70 μm images (Fig. 1). The background-subtracted surface brightnesses are indicated for three different apertures. The last row (17" circular aperture) shows the values we adopt throughout this paper, and in particular for the SED presented in Fig. 2.

Target region	3.6 μm	4.5 μm	5.8 μm	8 μm [e]	16 μm [f]	24 μm	70 μm
SQ ridge [b]	23.7 ± 0.9	11.9 ± 0.2	7.3 ± 0.2	4.2 ± 0.1	1.25 ± 0.05	2.25 ± 0.12	< 6.43
SQ ridge (partial) [c]	19.4 ± 1.7	9.9 ± 1.8	6.0 ± 0.1	3.35 ± 0.11	1.00 ± 0.06	0.89 ± 0.15	< 5.04
17" beam [d]	17.6 ± 0.9	9.15 ± 0.12	5.29 ± 0.15	3.07 ± 0.11	0.88 ± 0.03	0.79 ± 0.15	< 3.91

[a] Fluxes are in units of $\times 10^{-8}$ W m^{-2} sr^{-1}.

[b] Mid-IR signal integrated over the shock structure, defined by the 4σ S(3) H$_2$ rotational line contours (black line on Fig. 1). We exclude the SQ-A star-forming region.

[c] Mid-IR signal integrated over the S(3) H$_2$ rotational line contours by excluding overlaps with the ($\mathcal{F}_{24\,\mu m} > 0.25$ MJy sr^{-1}) 24 μm magenta contours (see Fig. 1). This allows us to partially remove the contribution from star-forming regions to the dust emission.

[d] Mid-IR signal integrated over the 17" beam in the center of the SQ shock structure (yellow circle on Fig. 1)

[e] The contribution of the 8 μm S(4) H$_2$ line emission to the 8 μm in-band flux is subtracted.

[f] The contribution of the 17 μm S(1) H$_2$ line emission to the 16 μm in-band flux is subtracted.

Table 2. Summary of the UV photometric measurements performed on *GALEX* FUV and NUV images (see Fig. 1). The flux columns indicate surface brightnesses that are corrected for the sky background.

Target position	FUV ($\lambda = 1\,516$ Å)		NUV ($\lambda = 2\,267$ Å)	
	Flux $\times 10^{-7}$ [W m^{-2} sr^{-1}]	Radiation Field G [Habing units]	Flux $\times 10^{-7}$ [W m^{-2} sr^{-1}]	Radiation Field G [Habing units]
SQ ridge [a]	2.82 ± 0.34	1.54 ± 0.19	2.74 ± 0.39	1.98 ± 0.29
SQ ridge (partial) [b]	2.29 ± 0.35	1.25 ± 0.19	2.25 ± 0.37	1.63 ± 0.29
17" ON beam [c]	2.49 ± 0.35	1.36 ± 0.19	2.42 ± 0.39	1.75 ± 0.29

[a] UV signal integrated over the shock structure, defined by the 4σ S(3) H$_2$ rotational line contours (black line on Fig. 1). We exclude the SQ-A star-forming region.

[b] UV signal integrated over the S(3) H$_2$ rotational line contours by excluding overlaps with the ($\mathcal{F}_{24\,\mu m} > 0.25$ MJy sr^{-1}) 24 μm magenta contours (see Fig. 1). This allows us to partially remove the contribution from star-forming regions to the dust emission.

[c] UV signal integrated over the 17" beam in the center of the SQ ridge (yellow circle on Fig. 1)

Table 3. Near-infrared *WIRC* surface brightnesses[a] in the J, H and K$_s$ bands for the SQ ridge.

Band		J	H	K$_s$	J:H:K$_s$
WIRC	Flux	8.45 ± 0.64	8.54 ± 0.65	8.07 ± 0.61	1.048: 1.058 : 1
	Unred	9.93 ± 0.77	9.44 ± 0.77	8.60 ± 0.75	1.154 : 1.096 : 1

[a] The fluxes are given in units of 10^{-7} W m^{-2} sr^{-1}. "Unred" indicates the extinction corrected brightness, and the "J:H:K$_s$" column shows flux ratios between the bands.

images. The 24 and 70 μm images show a bright and extended emission at the southern tip of the ridge which may be associated with enhanced star formation in the arc feature. In the following, we focus on the faint emission observed within the SQ ridge, outside star-forming regions. Note that on the 16 μm *IRS Blue Peak-Up* image, the emission in the ridge correlates well with the H$_2$ emission, which is due to the contamination of the H$_2$ 17 μm S(3) line to the in-band flux (sect. 3.2).

Using a combination of the Hα and 24 μm luminosities, or the 7.7 μm PAH emission, Cluver et al. (2009) find an upper limit of $\lesssim 0.08$ M$_\odot$ yr^{-1} on the star formation rate in the shock (as compared with ~ 0.2 M$_\odot$ yr^{-1} in SINGS star forming galaxies), suggesting that the star formation is being quenched in this region.

4.2. Dust emission from the SQ shock, outside star-forming regions

The images and photometric measurements show that thermal dust emission is detected in the SQ shock structure, outside star-forming regions. The SED of the IR emission from the center of the shock is shown on Fig. 2. Among the SEDs listed in table 1, the figure displays that of the last row (17" beam, see sect. 3).

For comparison with Galactic data, the figure also include a 12 μm flux computed by integrating the *IRS* spectrum over the IRAS 12 μm filter bandpass after subtraction of the gas lines. The 12/24 μm flux density ratio in the SQ shock is $\mathcal{F}_\nu^{(SQ)}(12\,\mu m)/\mathcal{F}_\nu^{(SQ)}(24\,\mu m) = 0.97 \pm 0.15$, which is remarkably close to the value for the Galactic diffuse ISM: $\mathcal{F}_\nu^{(MW)}(12\,\mu m)/\mathcal{F}_\nu^{(MW)}(24\,\mu m) = 0.95 \pm 0.07$. The Galactic SED is that measured towards the line-of-sight centered on the
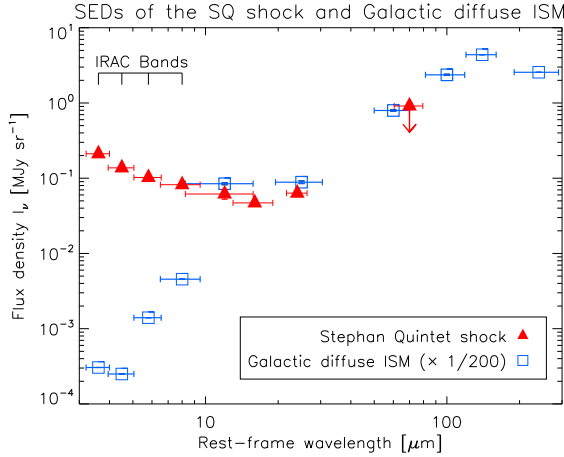
Fig. 2. The SED of the dust emission from the SQ shock seen by *Spitzer* (table 1), compared with that of the Galactic diffuse emission observed with *Spitzer IRAC*, *IRAS* and *DIRBE* towards the line-of-sight centered on the Galactic coordinates (28.6, +0.8). The contribution of the gas lines is subtracted. The Galactic SED is scaled down by a factor 200. Between $3-8\,\mu$m, the SQ flux is much brighter because of the stellar continuum component. Horizontal bars indicate the filters bandwiths.

Galactic coordinates (28.6, +0.8), observed with the ISOCAM-CVF[4] and *Spitzer IRAC* (Flagey et al., 2006). Fig. 2 also shows the *IRAS* 12, 25, 60 and 100 μm fluxes for the Galactic diffuse ISM emission. The *IRAS* SED is extended to 140 and 240 μm using *DIRBE* color ratios at the position of the line of sight. The total column density for this line of sight is estimated to be $N_{\rm H} = 2 \times 10^{22}$ cm^{-2}, and the mean radiation field a few Habing units ($G_{\rm UV} \sim 3$). In the figure, the Galactic SED is scaled down by a factor 200.

We propose that the faint dust emission we have isolated in the center of the SQ shock is diffuse emission associated with the shocked molecular gas present in the ridge. An alternative interpretation is that this dust emission is produced by unresolved star-forming regions in the shock. In that case, the faint emission would be the beam-diluted signal from bright compact sources. We favor the first interpretation for two reasons:

- First, *HST* observations show that there are very few star clusters within the shock. Most of them are associated with NGC 7319, the tidal debris of NGC 7318a/b, and the SQ-A intragroup starburst region (Gallagher et al., 2001). We find only one star cluster ($M_{\rm V} = -10.01$) within our 17″ aperture in the center of the shock.
- Although the SQ SED is poorly constrained in the FIR, the 12/24 μm flux ratio is remarkably similar to that of the Galactic diffuse ISM. The average column density of warm molecular gas in the SQ shock derived from H$_2$ observations is $N_{\rm H} = 2 \times 10^{20}$ cm^{-2}, a factor 100 smaller than that of the Galactic line of sight, in agreement with the scaling factor used to match the fluxes in Fig. 2.

---

[4] Camera equiped with a Circular Variable Filter (CVF) on-board the *Infrared Space Observatory* (ISO)

4.3. Mid-IR spectroscopy: characterization of the dust emission from the SQ shock

4.3.1. *Spitzer IRS* spectrum in the center of the shock

The top panel of Fig. 3 presents a low-resolution *Spitzer IRS* spectrum extracted from a central position of the SQ ridge. This spectrum was obtained by Cluver et al. (2009), averaging all the spectra observed within a 274.2 arcsec^2 (~ 18" $\times$ 15") rectangular aperture around the center of the ON position. These new data has much higher sensitivity and better flux calibration than the first observations reported by Appleton et al. (2006). This spectrum confirms the first results discussed in Appleton et al. (2006). It shows bright S(0) to S(5) H$_2$ rotational lines and forbidden atomic lines, with a remarkable 34.8 μm [Si] feature. Here we focus on the dust emission.

The *IRS* spectrum shows that PAH and thermal dust emission is detected from the center of the SQ ridge, outside star-forming regions. A weak thermal continuum is also visible from 20 to 38 μm. The ratio between the fluxes of the 17 μm S(1) H$_2$ line and the 7.7 μm PAH feature is 1.2 ± 0.2 in the shock, which is about two orders of magnitude higher than the value observed in star-forming galaxies (Roussel et al., 2007).

4.3.2. PAH emission from the SQ shock

The 7.7, 11.3 and 17 μm Aromatic Infrared Bands (AIBs), attributed to PAHs, are detected in the center of the SQ shock. We use the PAHFit IDL tool[5] (Smith et al., 2007) for decomposing the full $5-38\,\mu$m *IRS* spectrum into contributions from PAH features, thermal dust continuum, starlight and gas lines. We do not include any extinction in the fit. The result of the fit on the full $5-38\,\mu$m spectrum is shown in Appendix A, Fig. A.1. This spectral decomposition allows us to remove the gas lines and extract a "pure" dust spectrum, shown on the bottom panel of Fig. 3. PAHFit is run one more time on this spectrum, which allows us to measure accurately the fluxes of the AIBs. The line strengths of the PAH emission features and their ratios are gathered in Tables 4 and 5, respectively.

In Fig. 4 we compare the PAH spectrum from the SQ shock with the *ISOCAM-CVF* spectrum of the diffuse Galactic emission from Flagey et al. (2006), between 5 and 20 μm. The main differences between the two spectra are the following. First, the ratio between the flux in the band at 7.7 μm and the band at 11.3 μm (henceforth $R_{7.7/11.3}$) is a factor ~ 2 lower for SQ ($R_{7.7/11.3}^{(SQ)} = 1.36 \pm 0.07$, see table 5) than for the diffuse Galactic light ($R_{7.7/11.3}^{(MW)} = 2.93 \pm 0.08$). The $R_{7.7/11.3}$ value for the SQ shock is comparable to that measured for AGN of the *SINGs*[6] sample (Smith et al., 2007). Second, the 6.2 μm AIB is absent in the SQ spectrum. Note that the rise of the SQ spectrum at $\lambda < 6\,\mu$m is due to the stellar component. The 17 μm complex is prominent but the 16.4 μm feature is not seen on top of it. This may not be significant because, to our knowledge, this feature is only prominent in the NGC 7023 Galactic PDR[7] (Sellgren et al., 2007). This feature is also observed in the star-forming galaxy NGC 7331 (Smith et al., 2004), but with a higher signal to noise spectrum than the one we have for SQ.

The enhancement of the 11.3 μm AIB compared to the 6.2, 7.7 and 8.6 μm features has been observed on galactic scales in elliptical galaxies (e.g. Kaneda et al., 2005), and in active galac-

---

[5] available on http://tir.astro.utoledo.edu/jdsmith/pahfit.php
[6] Spitzer Infrared Nearby Galaxies Survey, http://sings.stsci.edu/.
[7] Photo-Dissociation Region
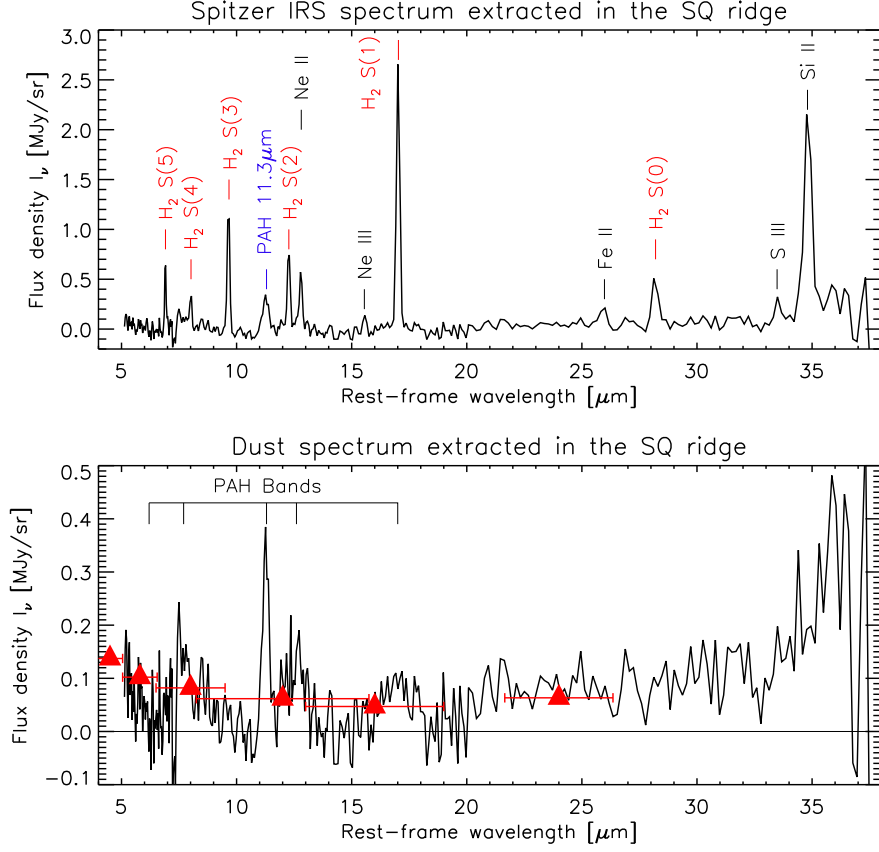
Fig. 3. *Spitzer IRS* mid-IR spectra extracted over a ∼ 18" × 15" area in the center of the SQ shock structure (RA 22:35:59.9, DEC +33:58:16.8). This aperture corresponds approximately to the "ON" beam shown in Fig. 1. *Top:* full spectrum. *Bottom:* gas lines are removed to highlight PAH dust features and thermal dust continuum. Photometric measurements (red triangles) performed on mid-IR images (same as in Table 1 and Fig. 2) are overplotted. Horizontal bars indicate the filters bandwiths.
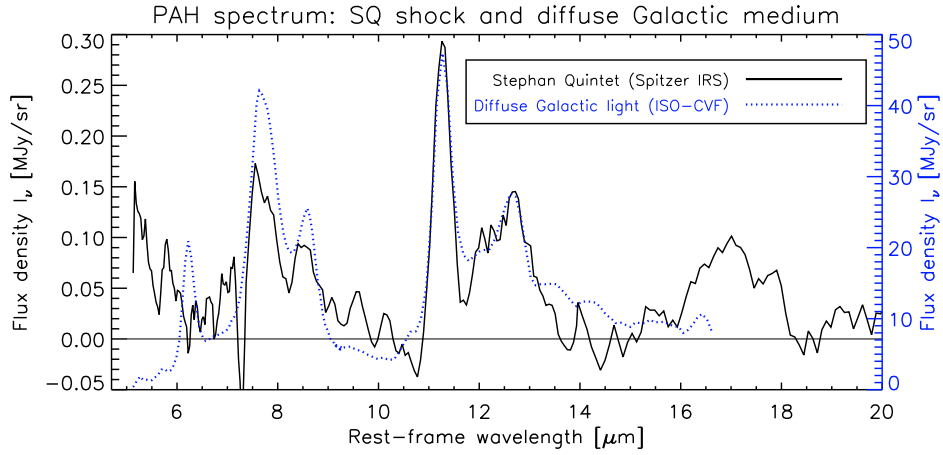
Fig. 4. *Spitzer IRS* PAH emission spectrum extracted in the center of the SQ ridge (black solid line), compared with the *ISOCAM-CVF* spectrum of the diffuse galactic medium (blue dashed line, with flux density labeled on the right). The *IRS* spectrum is smoothed to a resolution $\mathcal{R} = \lambda/\delta\lambda = 24 \to 51$, comparable with the *ISO-CVF* resolution ($\mathcal{R} = 35 \to 45$). Gas lines are removed in both spectra. Note that the flux scales are different for each spectrum (labels on the left for SQ, and on the left for the Galaxy).

Table 4. Fluxes of the PAH bands measured with the PAHFit IDL tool on the *Spitzer IRS* spectrum of the center of the SQ ridge and the *ISO-CVF* spectrum of the Galactic light.

PAH band	Integrated fluxes (see notes for units)				
	$6.2\,\mu$m	$7.7\,\mu$m [c]	$11.3\,\mu$m [c]	$12.6\,\mu$m [c]	$17\,\mu$m [c]
SQ ridge *(IRS)* [a]	< 0.75	3.8 ± 0.1	2.8 ± 0.1	1.2 ± 0.2	0.93 ± 0.04
Galactic *(CVF)* [b]	5.19 ± 0.09	19.05 ± 0.03	6.49 ± 0.17	2.90 ± 0.05	No data

[a] Fluxes are in units of $\times 10^{-9}$ [W m^{-2} sr^{-1}]

[b] Fluxes are in units of $\times 10^{-7}$ [W m^{-2} sr^{-1}]

[c] In the case of PAH blended complexes, we sum the fluxes of the different lorentzian components that contribute to the feature.

Table 5. Flux ratios between the PAH bands for the *Spitzer IRS* spectrum of the center of the SQ ridge and the *ISO-CVF* spectrum of the diffuse Galactic light.

	Flux ratios			
	$R_{6.2/7.7}$	$R_{7.7/11.3}$	$R_{11.3/12.6}$	$R_{11.3/17}$
SQ ridge *(IRS)*	< 0.2	1.36 ± 0.07	1.5 ± 0.2	3.01 ± 0.16
Galactic *(CVF)*	0.272 ± 0.005	2.93 ± 0.08	2.24 ± 0.07	No data

tic nuclei (e.g. Smith et al., 2007). This enhancement has also been discussed in the Galactic diffuse medium (e.g. Flagey et al., 2006) or at small scales, in PDR interfaces (e.g. Rapacioli et al., 2005; Compiègne et al., 2007).

The PAHs emission spectrum depends on their size distribution, hydrogenation and ionization states. The $R_{7.7/11.3}$ PAH band ratio depends mainly on the PAH ionization state. Theoretical (Langhoff, 1996; Bakes et al., 2001a,b; Draine & Li, 2001; Bauschlicher, 2002) and experimental (e.g. Szczepanski & Vala, 1993) studies show that neutral PAHs have lower $R_{7.7/11.3\mu m}$ than charged ones (both anions and cations). The charge state of PAHs is mainly determined by the ionization parameter $G_{UV}\sqrt{T}/n_e$ where G_{UV} is the integrated far ultraviolet (6 − 13.6 eV) radiation field expressed in units of the Habing radiation field, T is the electron temperature and n_e is the electronic density. This parameter translates the balance between photoionisation and recombination rates of electrons (Bakes & Tielens, 1994; Weingartner & Draine, 2001c). Flagey et al. (2006) quantified $R_{7.7/11.3\mu m}$ as a function of the ionization parameter $G_{UV}\sqrt{T}/n_e$ and the PAH mean size. We use their calculations to discuss the ionization state of the PAHs in the SQ shock. Our PAHFit decomposition yields $R_{7.7/11.3\mu m} = 1.4 \pm 0.2$, which translates into $G_{UV}\sqrt{T}/n_e \lesssim 30$ K$^{1/2}$ cm^3. Assuming a warm molecular gas temperature of ~ 150 K and $G_{UV} = 1$, we find that $n_e \gtrsim 0.4$ cm^{-3}. This lower limit is one order of magnitude higher than the electronic densities inferred from observations and modeling of the ionization of cold neutral gas in the Solar neighbourhood (Weingartner & Draine, 2001b). If this interpretation and diagnostic applies, a higher ionization flux from cosmic-rays or X-rays is required to maintain this high electron density.

The $R_{6.2/7.7}$ PAH flux ratio depends on the size of the emitting PAHs (Draine & Li, 2001). The non-detection of the $6.2\,\mu$m band sets a low upper limit of $R_{6.2/7.7} < 0.2$ on the PAH strength ratio, that suggests preferentially large PAHs. Although the method used by Draine & Li (2001) to measure the PAH line strengths is different from ours, we find that both $R_{7.7/11.3}$ and $R_{6.2/7.7}$ flux ratios in SQ can be explained by large (with a number of carbon atoms $N_c \gtrsim 300$) and neutral PAHs in CNM con-

ditions, excited with a $G_{UV} \simeq 1$ interstellar radiation field (see Fig. 17 of Draine & Li, 2001).

5. Modeling dust emission

We present the physical framework and inputs of our modeling of the emission from dust associated with the postshock warm molecular gas. Section 5.1 presents the codes we use to calculate the dust emission. The spectral energy distributions (SEDs) of the radiation field we use for our calculation of the dust emission is described in sect. 5.2.

5.1. The DUSTEM (Dust Emission) code

We use an updated version of the Désert et al. (1990) model, the so-called *DUSTEM* code, to compute the dust emission. The modifications[8] implemented to the Desert et al. model are described in Compiègne et al. (2008). The dust properties, the dust-to-gas mass ratio, and the incident radiation field being given, the code calculates the dust SED νS_ν in units of erg s^{-1} H^{-1}, the distribution of dust temperatures, as well as the UV to IR absorption and scattering cross-sections in units of cm^2 g^{-1}, for each dust grain species, as a function of the wavelength.

We assume the size distributions of each dust components to be a power-law, $n(a) \propto a^{-3.5}$, like in the dust model of Mathis et al. (1977), with minimum and maximum radii listed in the items below. We use the diffuse Galactic ISM size distribution and dust-to-gas mass ratio infered from the fitting of the SED and extinction curve of the diffuse ISM (Compiègne et al., 2008). The *DUSTEM* model includes a mixture of three populations of dust grains with increasing sizes:

– Polycyclic Aromatic Hydrocarbons (PAHs) of radius $a = 0.4 − 1.2$ nm, responsible for the Aromatic Infrared Bands (AIBs) and the FUV non-linear rise in the extinction curve.

[8] In particular, the absorption cross sections of the PAHs (with addition of new Aromatic Infrared Bands, AIBs) and the Big Grains (BGs), as well as the heat capacities (graphite, PAH C-H, silicate and amorphous carbon) have been updated.

– Very Small Grains (VSGs, $a = 1-4$ nm), which are carbonaceous (graphitic) nanoparticles producing the mid-IR continuum emission and the extinction bump at 2175 Å.

– Big Grains (BGs, $a = 4 - 110$ nm) of silicates with carbonaceous mantles or inclusions, which account for the far IR emission and the $1/\lambda$ rise at visible and near-IR wavelengths.

5.2. Radiation fields

In this section we model the radiation field used to compute the dust emission. Stellar radiation is coming from the surrounding galaxies and/or stars in the ridge (Gallagher et al., 2001). The presence of ionizing radiation in the SQ ridge is also indicated by the lack of H gas in the H$_2$-bright shock structure (Sulentic et al., 2001), and by emission from ionized gas lines. Optical line emission diagnostics suggest that shocks are responsible for hydrogen ionization in the ridge (Xu et al., 2003).

Therefore, we consider that the SED of the input radiation field consists of two components: a stellar component (sect. 5.2.1), and photo-ionizing radiation from gas shocked at high-velocities (sect. 5.2.2).

5.2.1. The interstellar radiation field (ISRF)

The photometry performed on NUV and FUV *GALEX* images shows that UV flux in the shock, outside star-forming regions, corresponds to an interstellar radiation field of intensity $G_{UV} = 1.4 \pm 0.2$ (see Table 2). What is the origin to this UV radiation in the shock? We estimate the UV emission in the ridge that comes from H regions associated with star formation in the surrounding sources, i.e. NGC 7318a/b, the star-forming region SQ-A at the northern tip of the shock structure, and NGC 7319. The extinction-corrected FUV luminosities of these main sources that surround the ridge are L_{FUV}(NGC 7318ab) = 8.1×10^9 L$_\odot$, L_{FUV}(SQ-A) = 6.9×10^9 L$_\odot$, and L_{FUV}(NGC 7319) = 6.9×10^9 L$_\odot$ (Xu et al., 2005). Assuming that their distances to the center of the ridge are 10, 20 and 25 kpc, respectively, we find that the total UV flux in the ridge is 3.5×10^{-3} erg s^{-1} cm^{-2}, i.e. $G_{UV} \simeq 1.5$ in Habing units. Most of the UV flux comes from NGC 7318a/b. Although this simple calculation does not take into account the extinction between the UV sources and the ridge, it shows that this estimate of the UV field is roughly consistent with our estimate from UV observations. The very small number (of the order of unity) of star clusters that lie within the center of the SQ shock (Gallagher et al., 2001) shows that their contribution to the UV field is small.

The SED of the ISRF component of the radiation field is shown on Fig. 5 (green dashed line). We use the Mathis et al. (1983) ISRF, scaled by a factor 1.4 to fit the FUV and NUV *GALEX* photometry. The *WIRC* near-IR photometric measurements (see sect. 2.2.2 for observational details) are overlaid on Fig. 5 (see Table 3). The colors of the J, H and K$_s$ fluxes do not exactly match that of the (Mathis et al., 1983) radiation field, but we remind that these measurements are uncertain (see sect. 3.1.2). This effect does not affect significantly our dust modeling since the near-IR part of the radiation field has a small impact on the dust emission.

5.2.2. Photo-ionizing radiation field: shock and precursor components

In the shock sub-region, the [O]6300 Å and [N]6584 Å to Hα line ratios are $\sim$ 0.7 and $\sim$ 0.3, respectively, which is evidence of shock ionization (Xu et al., 2003). Therefore we model the SED of the ionizing field using emission from a radiative shock. In the following we constrain the shock parameters we use to model the emission from the ionized gas. The mid-IR *IRS* spectrum extracted in the core of the shock (Fig. 3) shows fine-structure line emission from [Ne]λ 12.81 μm, [Ne]λ 15.56 μm, [Fe]λ 25.99 μm, [S]λ 33.48 μm, and [Si]λ 34.82 μm. The spatial distribution of this emission and mid-IR line diagnostics of the excitation mechanisms are discussed in Cluver et al. (2009). We summarize here the main results that are relevant to constrain the shock parameters.

The comparison between the high value of $\mathcal{F}_{[NeII]12.8}/\mathcal{F}_{[NeIII]15.6} \sim 3.55$ and shock models (Hartigan et al., 1987; Allen et al., 2008) allows to firmly constrain the range of shock velocities to $\sim 80 - 200$ km s^{-1} (Cluver et al., 2009). In the case of clumpy gas, if we consider the line emission from the shock only (no precursor), the constrain on shock velocities becomes looser. In addition, comparison of the [S]λ 33.5 μm/[S]λ 18.7 μm line ratios with these shock models constrains the pre-shock gas density to be $n_H \lesssim 10$ cm^{-3}. Therefore, we adopt in the following a shock velocity of $V_s = 100$ km s^{-1} and a pre-shock density of $n_H = 1$ cm^{-3}. The photo-ionizing emission spectrum from shocked gas is taken from the library of the Mappings III shock code[9] (Allen et al., 2008). We normalize the shock spectrum to the observed Hα flux[10]. After this normalization, the SED of the ionizing shock emission is weakly sensitive to the two main shock parameters, the shock velocity and the gas density.

Fig. 5 shows the SED of the radiation field we use as input for the *DUSTEM* code to compute the outcoming dust emission from the molecular and ionized gas. The black solid line is the sum of the two contributions (stellar + shock) to the radiation field. The shock spectrum itself is mostly composed of thermal bremsstrahlung (free-free) continuum and resonance lines arising from many different elements and ionic stages. It also shows a prominent low-temperature bound-free continuum of hydrogen, produced in the cool, partially-ionized zone of the recombination region of the shock, and the strong hydrogen two-photon continuum produced mostly by the down-conversion of Lyα photons trapped in this same region of the shock structure. Also present, though to a much weaker scale, is the bound-free continuum arising from the heavier elements, with the helium continuum the most obvious.

In the case of fast shocks ($V_s > 100$ km s^{-1}), the shocked medium emits UV radiation that ionizes the pre-shock medium before it is shocked. A so-called *radiative precursor* propagates ahead of the shock, with an ionization front velocity that exceeds that of the shock. The contribution of the precursor itself is indicated on Fig. 5 by the red dotted line. At 100 km s^{-1}, the total radiative flux of the precursor is one order of magnitude smaller than that of the shock. The green dashed line shows the contribution of the $G_{UV} = 1.4$ ISRF. The UV *GALEX*, Hα line, and near-IR *WIRC* fluxes in the center of the shock are indicated.

The contribution of the precursor to the total H column density and radiative flux depends on the clumpiness of the pre-

---

[9] http://cdsweb.u-strasbg.fr/~allen/mappings_page1.html
[10] $\mathcal{F}_{H\alpha} = 4.1 \times 10^{-9}$ W m^{-2} sr^{-1} from Xu et al. (2003).
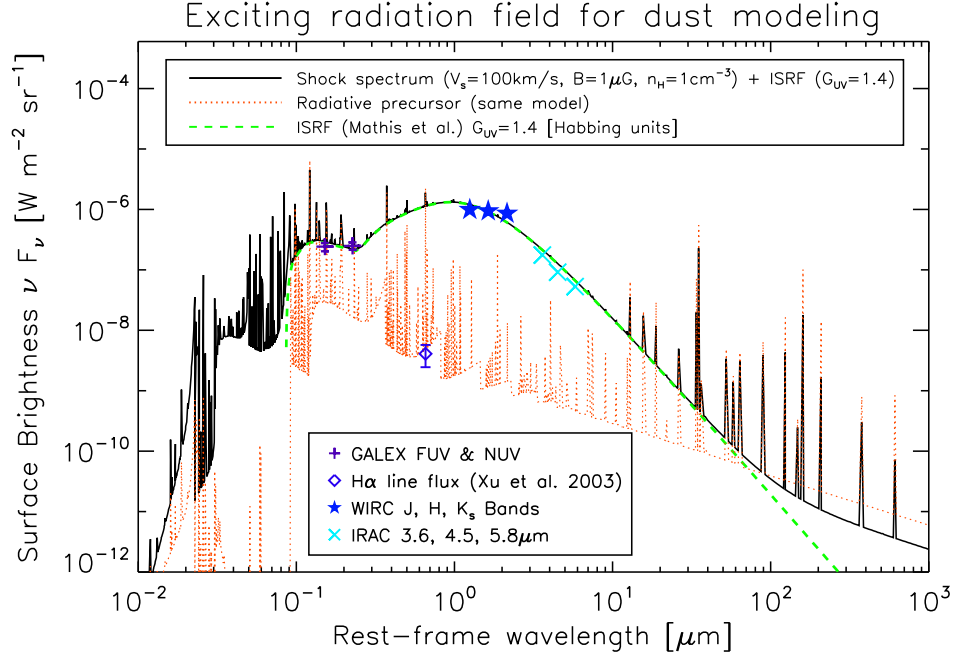
Fig. 5. The 2-component SED of the radiation field (stellar + shock) used as input for dust models to calculate the dust emission from molecular gas. The radiation field is the sum of an ISRF of intensity $G_{UV} = 1.4$, scaled to match the observed UV flux in the shock, and the photo-ionizing spectrum of a $V_s = 100$ km s^{-1} shock, scaled to match the Hα emission in the SQ ridge. The preshock gas density is $n_H = 1$ cm^{-3} and the preshock magnetic field strength is $B_0 = 1\,\mu$G.

shock medium. This contribution is negligible if the molecular gas is clumpy, i.e. fragmented into dense ($n_H > 10^3$ cm^{-3}) clouds that have a small volume filling factor, because most of the ionizing photons do not interact with H$_2$ gas but with volume-filling, ionized plasma optically thin to ionizing radiation. However, diffuse H$_2$ gas is expected to have a much higher volume filling factor. Our modeling of the dust emission from the ionized gas takes into account the precursor contribution, weighted by the volume filling factor of the clumpy molecular gas.

6. On the structure of the molecular gas

The dust emission depends on the optical thickness of the molecular gas to UV radiation. Is the molecular gas diffuse or fragmented in optically thick clumps? In section 6.1 we describe the assumptions we make regarding the structure of the molecular gas. Then we present the results of our modeling of the SED of the dust emission in the SQ shock. We discuss the dust emission for the two physical structures of the H$_2$ gas presented in sect. 6.1: diffuse (sect. 6.2) and clumpy molecular gas (sect. 6.3). Both models includes the contribution of the ionized gas (H) to the dust emission (this calculation is detailed in sect. 6.4). This detailed modeling is used to investigate the influence of the structure of the molecular gas on the shape of the SED, and our results are fitted to mid-IR observations.

6.1. Two limiting cases for the structure of the molecular gas

The spectral energy distribution of the dust emission depends also on the structure of the molecular gas, and in particular on the optical depth of the clouds. The physical structure of the molec-
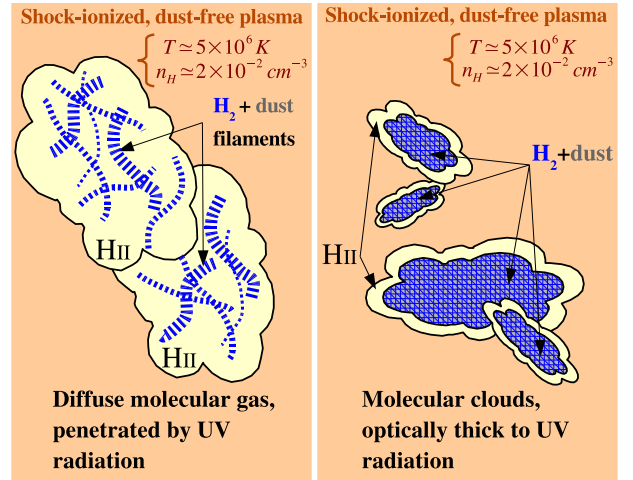
Fig. 6. Sketch of the two limiting physical states of the multiphase molecular gas we are considering in the framework of our modeling of dust emission. *(Left)* Dust is associated with *diffuse* molecular gas that is broken into fragments, filaments or sheets, penetrated by UV radiation. *(Right)* The dusty molecular gas is in clouds that are *optically thick* to UV light.

ular gas in the SQ shock is an open question. In the following we explore these two cases.

1. The molecular gas is *diffuse* as the gas observed in the solar neighborhood through UV spectroscopy

(e.g. Rachford et al., 2002) or in the diffuse Galactic medium through observations of mid-IR H_2 line emission (Falgarone et al., 2005). We assume that the dusty molecular fragments are small enough to be penetrated by UV radiation.

2. The molecular gas is within *molecular clouds* that are *optically thick* to UV photons, as observed in star-forming regions.

Fig. 6 illustrates, in a simplistic manner, the two physical states (diffuse or clumpy) of the molecular gas we are considering. In both cases, the molecular gas is embedded within H gas and shock-heated, X-ray emiting plasma.

In order to compute the dust emission from optically thick (to UV photons) clouds (Fig. 6, right panel), we use the *Meudon PDR* (Photon Dominated Region) code (Le Petit et al., 2006) to compute the radiative transfer through the cloud. This 1-dimensional, steady-state model considers a stationary plane-parallel slab of gas and dust, illuminated by UV radiation. The radiation field output I_ν of the Meudon PDR code is used as input to the *DUSTEM* program to compute the spectral energy distribution (SED) of the dust as a function of the optical depth into the cloud. This 2-step process is iterated to take into account dust heating by the dust IR emission. Usually $4-5$ iterations are needed so that the radiation field converges.

6.2. Dust emission from diffuse molecular gas

The *DUSTEM* code is used to model the dust emission from diffuse molecular gas (sect. 5.1), penetrated by UV photons. The cloud is illuminated by a composite field, made up of a stellar component (ISRF of intensity $G_{UV} = 1.4$ Habing units) and the ionizing radiation from the shocked gas (see sect. 5.2 and Fig. 5). The dust properties are those of sect. 5.1. The dust emission from the ionized gas is included in the model SED. It is calculated separately with the *DUSTEM* code and added to the contribution of the cloud (see sect. 6.4).

The top panel of Fig. 7 shows the full $0.1 - 300\,\mu m$ SED resulting from the model (black solid line), so that both the UV radiation field and IR dust emission can be seen. The dashed line shows the dust emission from the H gas. The three other broken curves show the contributions of the different populations of dust grains, i.e. PAHs, VSGs and BGs, respectively. The *GALEX*, *WIRC* and *Spitzer* fluxes are indicated for comparison (see sect. 3, Tables 1, 2 and 3). Except for the $11.3\,\mu m$ PAH band and the $16\,\mu m$ peak values derived from the *IRS* spectrum (sect. 4.3), the fluxes are mean values of the measurements performed in the center of the SQ ridge (over an aperture of $17''$ in diameter).

The 11.3, 16 and $24\,\mu m$ points are used to fit the model SED. As it may be a lower limit, the $70\,\mu m$ point has not been included in the fit. The gas column density is the only free parameter to fit the data. The abundances and size distribution of the dust grains are Galactic. The model SED is obtained by multiplying the emissivity output of the *DUSTEM* code by the column density of warm molecular gas that is determined from fitting the SED to the mid-IR data. We find that the H_2 column density that best fits the data is $N_H = 1.8 \pm 0.5 \times 10^{20}$ cm^{-2} for a Galactic dust-to-gas mass ratio. This column density obtained from the model is close to the column density derived from the H_2 line fluxes ($N_H \simeq 2.2 \times 10^{20}$ cm^{-2}) within this aperture. This column density is obtained by fitting the rotational H_2 line fluxes with C-shocks models as described in Guillard et al. (2009). This suggests that the column density of cold ($T \lesssim 50$ K) molecular gas

is much smaller than that of the warm H_2. However, this may not be the case because the dust-to-gas mass ratio is possibly lower than the Galactic value we have assumed here.

6.3. Dust emission from clumpy molecular gas

We model the dust emission associated with molecular gas fragmented into clumps that are optically thick to UV radiation. Here the *DUSTEM* and *Meudon PDR* codes (see sect. 5.1) are combined to calculate the emission from a molecular cloud of total $A_V = 3$. The column density of the cloud is thus $N_H^{(c)} = 6.9 \times 10^{21}$ cm^{-2}. The choice of the A_V value is arbitrary. We check that the model SED in the mid-IR domain does not depend much on the total A_V because the mid-IR emission comes mainly from the surface of the cloud. The cloud is illuminated by a composite field (stellar + shock), made up of the ISRF of intensity $G_{UV} = 1.4$ (Habing units) and the ionizing radiation from the shocked gas (see sect. 5.2 and Fig. 5).

Fig. 7 shows the sum of the outcoming radiation (cloud + ionized gas) emission spectrum, plus the incoming radiation, from the UV to the FIR ($0.1 - 300\,\mu m$). The dashed line shows the emission from the ionized gas. The UV, and IR photometric measurements are overlaid for comparison between data and models.

From UV to FIR, the total SED (solid black line) consists of the ISRF, plus the free-free, free-bound and resonance line emission from the shocked gas, the AIBs, the emission from the VSGs and the grey body of the BGs at long wavelengths. The spectrum also shows some fine-structure IR lines, indicated on the spectrum, e.g. $18.7\,\mu m$ [S], $34.8\,\mu m$ [Si], and $157.7\,\mu m$ [C]. To fit the data, the model IR emission from the cloud is scaled by a factor of $f = 0.03$, which represents an effective surface filling factor for the molecular gas. **The low value of f is consistent with the low value of the average optical extinction in the shock region.** For clumps of $A_V = 3$, the average column density of the cloud phase is thus $\langle N_H \rangle = f \times N_H^{(c)} \simeq 2.1 \times 10^{20}$ cm^{-2}. Our specific choice of $A_V = 3$ leads to a value of $\langle N_H \rangle$ that is consistent with the column density of the warm H_2 gas seen by *Spitzer*. For larger values of A_V, the total column density of molecular gas will be larger than the column density of warm H_2 inferred from rotational lines.

6.4. Dust emission from shock- and precursor-ionized gas

We detail how we calculate the emission from dust associated with the ionized gas. We use the input radiation field of Fig. 5, including the ionizing part of the spectrum ($\lambda < 912$ Å), to compute the dust emissivity with the *DUSTEM* code. The column density of ionized gas has been constrained by the integrated flux of the $12.8\,\mu m$ [Ne] fine-structure line, $\mathcal{F}_{[Ne II]}$, measured on the *IRS* spectrum. The $\mathcal{F}_{[Ne III]}/\mathcal{F}_{[Ne II]}$ line flux ratio is low[11], which implies that Ne is the main ionization state of Ne in the shock. Therefore, the column density of ionized gas can be expressed as:

$$N_H^{(ion.gas)} = 2.3 \times 10^{19} \frac{\mathcal{F}_{[Ne II]} \,[\text{W m}^{-2}\,\text{sr}^{-1}]}{1.17 \times 10^{-9}} \frac{10\,\text{cm}^{-3}}{n_e\,(10^4\,\text{K})}\ \text{cm}^{-2} \,. (1)$$

We use the relation between the [Ne] line intensity and the emission measure given in Ho & Keto (2007) and we assume that the electronic density of the 10^4 K gas is $n_e = 10$ cm^{-3}.

---

[11] $\mathcal{F}_{[Ne III]}/\mathcal{F}_{[Ne II]} = 0.14 \pm 0.04$ in the center of the SQ ridge, see Table 3 in Cluver et al. (2009).
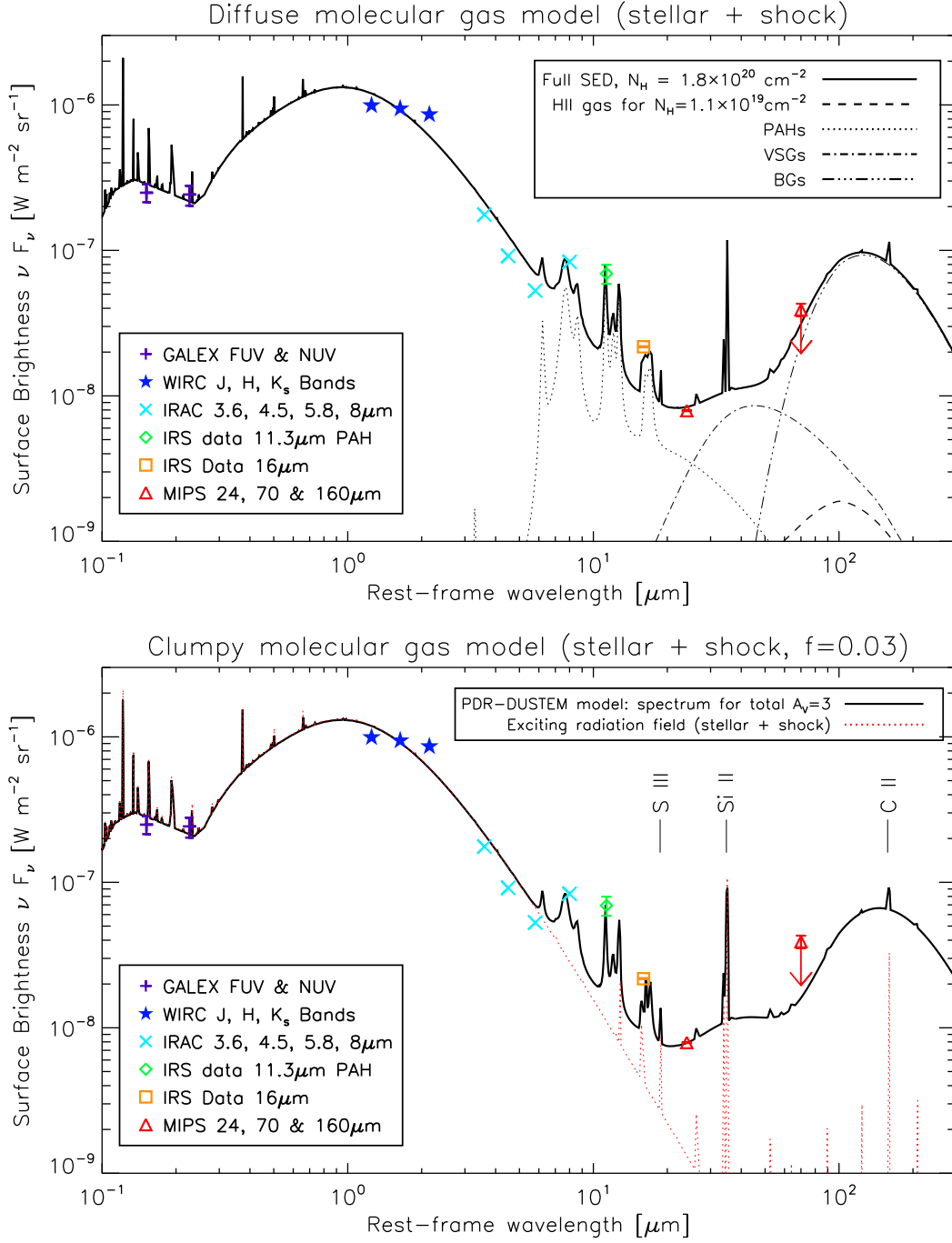
Fig. 7. SED of the dust emission associated with diffuse *(top)* or clumpy *(bottom)* molecular gas. The cloud is exposed to a radiation field consisting of a mixture (stellar + shock) of the Mathis et al. (1977) ISRF (scaled by a factor $G_{UV} = 1.4$) and the ionizing emission spectrum of shock-heated gas for a shock velocity of 100 km s^{-1}. The dashed line shows the contribution of the ionized gas (see text for details). *(top)* The other broken lines show the different contributions of the three populations of grains (PAHs, VSGs, and BGs). Assuming a Galactic dust-to-gas mass ratio, a column density of $N_H = 1.8 \pm 0.5 \times 10^{20}$ cm^{-2} is needed to fit the *Spitzer* data. *(bottom)* The black solid line is the sum of the incoming and outcoming emission from a slab of gas of total $A_V = 3$, calculated with the *Meudon PDR* and *DUSTEM* codes. To fit the *Spitzer* data, the model IR emission is scaled by a factor $f = 0.03$, which represents the effective surface filling factor of the molecular gas.

This value is consistent with the SQ postshock pressure ($\sim 2 \times 10^5$ K cm^{-3}). The column density derived from Eq. 1 is comparable to the H column density derived from the shock model ($N_H(H) = 1.2 \times 10^{19}$ cm^{-2} for a shock + precursor model at a shock velocity of 100 km s^{-1} and a preshock density $n_H = 1$ cm^{-3}).

The dust emission associated with this amount of ionized gas is the black dashed line on the top plot of Fig. 7. The column density of the ionized gas being one order of magnitude smaller than that of the warm H$_2$, the contribution of the ionized gas to the IR dust emission is negligible. Compared to the emission of the cloud itself, the FIR peak of the dusty ionized gas is shifted towards shorter wavelengths ($100\,\mu$m vs. $120\,\mu$m) because of the ionizing part of the radiation field which makes the dust hotter (~ 25 K vs. 30 K).

6.5. Comparison between models and degeneracies

Fig. 8 shows the comparison between the result of the two models presented above. We focus on the dust emission, so the gas lines and the stellar continuum from the ISRF are removed from the spectra. The FIR SEDs are different between the two models. The FIR peak brightness of the SED of the diffuse molecular gas is brighter (by a factor of 1.7) and shifted towards shorter wavelengths compared with the clumpy model. This difference can be easily explained. When the molecular gas is clumpy, the dust grains see, on average, an attenuated radiation field, and are thus colder than in the diffuse model. For a given column density of matter, the FIR brightness is also fainter.

Present observations do not allow us to decide whether the gas is diffuse or fragmented into optically thick clumps. The spatial resolution of *Spitzer* at long wavelengths ($\lambda \gtrsim 70\,\mu$m) is not high enough to obtain accurate photometric measurements. FIR observations with the *Herschel Space Telescope* will provide the sensitivity and angular resolution needed to test our models. However, it may not be so straightforward to conclude on the structure of the molecular gas. In this study we assume a Galactic dust-to-gas mass ratio and size distribution. The IR SED also depends on the relative abundance between VSGs and BGs.

We defer the discussion about future observations needed to disentangle the cloud structure and the dust size distribution to sect. 8.

7. Dust processing in the Stephan's Quintet shock?

The Stephan's Quintet galaxy-wide collision is an extreme environment where observing and modeling dust emission may provide insight into dust processing in shocks. The galaxy collision must have triggered shocks across the whole ISM. As discussed in Guillard et al. (2009), the shock velocity depends on the preshock gas density. Gas at preshock densities $n_H > 0.2$ cm^{-3} has been shocked at velocities small enough ($V_s < 100 - 300$ km s^{-1}) to cool, to keep most of its dust, and to become molecular within a few million years. To account for the H$_2$ emission, the molecular gas must be processed by low-velocity ($5 - 20$ km s^{-1}) MHD shocks, repeatedly. Therefore, the origin and dynamical state of the SQ molecular gas is very different from that of the diffuse Galactic ISM.

In the previous section, we assume that the dust properties in the SQ ridge are identical to those of the Galaxy, which obviously is a simplifying assumption that may be far from reality. In the shock region, we expect dust grains to be intensively processed by various processes (e.g. thermal sputtering

of grains in the hot gas or destruction in shocks due to gas-grain and grain-grain interactions, see Jones, 2004, and references therein) that can affect both the dust-to-gas mass ratio and the dust size distribution. So far, observational evidences of dust processing comes mainly from observations of depletions (Sembach & Savage, 1996). It is much harder to find direct observational evidence for changes in the dust size distribution that can be unambiguously associated with shock-processing. Stephan's Quintet is an outstanding target to look for such evidence on galactic scales.

Dust destruction processes depend on the type of shocks. Guillard et al. (2009) show that within the timescale of the galaxy collision ($\sim 5 \times 10^6$ yr), the destruction of grains smaller than $\sim 0.1\,\mu$m is complete in the hot, teneous gas (corresponding to pre-shock densities $n_H \lesssim \times 10^{-2}$ cm^{-3}) that is shocked at high velocities ($V_s > 300$ km s^{-1}). For intermediate preshock densities ($n_H \sim 0.2 - 0.01$ cm^{-3}, $V_s = 100 - 300$ km s^{-1}), models predict significant dust destruction ($10 - 50\,\%$ in mass) and possibly the production of an excess of small grains by shattering (e.g. Jones & Tielens, 1994). Within the dense ($n_H > 10^3$ cm^{-3}) molecular gas, low-velocity MHD shocks ($5 - 20$ km s^1), may only have little effect on dust (Guillet et al., 2007; Gusdorf et al., 2008).

The present SQ data provide some constrains on the dust size distribution. The detection of PAH emission from such a violent and extreme environment as the SQ shock may be seen as a surprise. PAHs are predicted to be completely destroyed for $V_s \gtrsim 125$ km s^{-1} ($n_H = 0.25$ cm^{-3}) and their structure would be deeply affected for $50 \lesssim V_s \lesssim 100$ km s^{-1} (Micelotta et al., 2009). Therefore, the PAH detection provides interesting constraints on the density structure of the preshock gas. Since it is unlikely that PAHs reform efficiently from carbon atoms in the postshock gas, we conclude that *(i)* they were protected from high-velocity shocks in high preshock density regions ($n_H \gtrsim 0.3$ cm^{-3}), or/and *(ii)* they are the product of the shattering of VSGs in the shock.

We note that the $6.2\,\mu$m AIB is absent and that the $17\,\mu$m complex is prominent. This suggest that large PAHs, which emit more efficiently at larger wavelengths (e.g. Draine & Li, 2007), would be predominant in the shock. This may result from PAH processing in shocks, larger molecules being less fragile than smaller ones (Micelotta et al., 2009). This interpretation is supported by *Spitzer* observations by Tappe et al. (2006) that show a prominent $17\,\mu$m emission from the supernova remnant N132D in the Large Magellanic Cloud.

The $12/24\,\mu$m flux ratio is sensitive to the relative mass abundances between PAHs and VSGs. Fig. 9 shows the predicted $12/24\,\mu$m flux ratio as a function of the PAH / VSG dust mass ratio. For each PAH/VSG ratio, the dust emission spectrum is calculated for an ISRF of $G_{UV} = 1.4$ with the *DUSTEM* code. We derive the 12 and $24\,\mu$m fluxes by integrating the model spectrum over the $12\,\mu$m *IRAS* and $24\,\mu$m *MIPS* filter bandpasses. The PAH/VSG mass ratio in the SQ shock is remarkably close to the value for the Galactic diffuse ISM. A deviation would be expected if the dust had been processed by high-speed (> 100 km s^{-1}) shocks (Jones et al., 1996). Like for PAHs, this may suggest that the postshock dust was lying in the denser regions of the preshock gas, and thus was protected from the effect of fast shocks, as proposed by Guillard et al. (2009). However, as discussed in sect. 4.3.2, the PAH spectrum in the shock is significantly different from that observed in the diffuse Galactic ISM. The fact that the long wavelength bands (11.3 and $17\,\mu$m) are brighter than the 6.2 and $7.7\,\mu$m features imply that a higher fraction of the PAH emission is emitted within the $12\,\mu$m IRAS
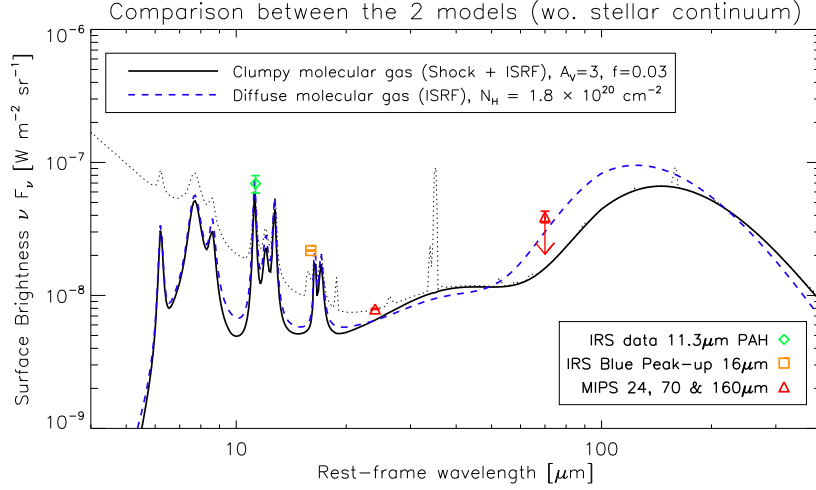
Fig. 8. Comparison between the two models presented in this paper: diffuse (dashed blue line, same model as Fig. 7) and clumpy (black line, same model as Fig. 7) molecular gas. The overlaid points indicate the *Spitzer* fluxes extracted within the shock region (see bottom right inset). The gas lines are removed from these spectra, as well as the IR component of the incident ISRF (G_{UV} = 1.4). For comparison, the clumpy model with stellar continuum is shown on the thin black dotted (same model as Fig. 7).
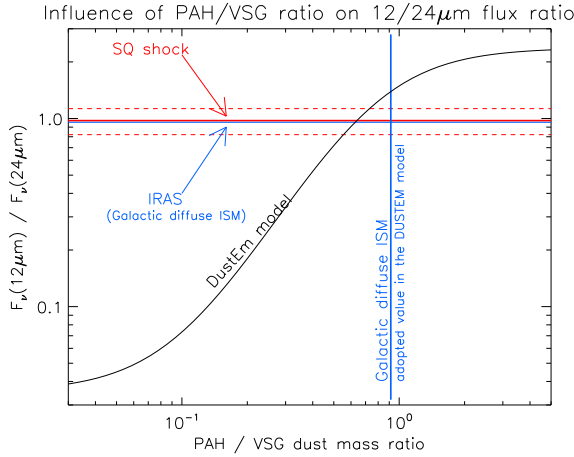
Fig. 9. Predicted 12/24 μm flux ratio from the *DUSTEM* model as a function of the PAH / VSG mass ratio. The horizontal red and blue lines shows the observed 12/24 μm flux ratios for the SQ shock, and the Galactic diffuse ISM (*IRAS* observations). The vertical blue line is the Galactic PAH/VSG ratio adopted in the model (0.915). This value is chosen to fit both the 12/24 μm ratio and the extinction curve.

band. If true, this correction would imply a lower PAH/VSGs abundance than in the Galactic diffuse ISM.

Once FIR *Herschel* data will be available, observations and modeling of the full IR spectral energy distribution would provide diagnostics for measuring the abundances of the different grain populations, and therefore the amount of dust destruction.

In our modeling (sect. 6), we did not consider any thermal emission from collisionally heated dust in the hot plasma. This emission may arise after a fast shock wave has gone through teneous, dusty gas, but it will last a very short period of time ($\sim 10^6$ yr), producing a "flash" of FIR emission, because the

dust cooling efficiency drops as the grain sputtering occurs in the hot (> 10^6 K) gas (Smith et al., 1996; Guillard et al., 2009). However, there are two reasons why this may not be a valid assumption. First, if there is a significant dust mass in grains larger than about 0.3 μm, this dust may survive for $\gtrsim 5 \times 10^6$ yr. These grains may contribute to the FIR emission, as proposed by Xu et al. (2003). Second, we cannot exclude that some dust may be injected into the hot phase by the ablation of clouds, due to their dynamical interaction with the background plasma (Guillard et al., 2009). A continuous supply of dust from the warm to hot phase could balance destruction by sputtering. This possibility needs to be quantified, which is beyond the scope of this paper.

8. Summary and concluding remarks

In this paper, we present *Spitzer* new imaging and spectroscopic observations that reveal PAH and VSGs emission from the galaxy-wide shock in Stephan's Quintet. Here are our main observational results:

- Faint dust emission is detected in the center of the H$_2$-bright SQ shock structure, outside star-forming regions lying in the SQ halo. The 12/24 μm flux density ratio in the SQ ridge is remarkably similar to that of the diffuse Galactic ISM. This suggests that the PAH to VSGs abundance ratio is similar to that of the diffuse ISM of the Galaxy.
- The global mid-IR SED is consistent with the expected dust emission from the amount of warm H$_2$ detected by *Spitzer* ($N_H \simeq 2 \times 10^{20}$ cm^{-2}) for a UV radiation field intensity of $G_{UV} \sim 1$, which is consistent with UV observations of the shock.
- The PAH emission spectrum in the SQ shock is significantly different from that of the diffuse Galactic ISM. The 7.7, 11.3 and 17 μm aromatic bands are detected, but the 6.2 μm band is absent. The 17 μm complex is prominent, but the 16.4 μm is not detected. Interestingly, the 7.7/11.3 μm flux ratio in the SQ shock is a factor $\sim$ 2 lower than that of the dif-

fuse Galactic PAHs. These characteristics may suggest an enhanced fraction of neutral and large PAHs.

Spitzer imaging and spectroscopy reveal powerful H_2 emission in the Stephan's Quintet X-ray giant shock that extends over the full area ($\approx 35' \times 15$ kpc^2) of the ridge (Cluver et al., 2009). We expect some dust emission to come from molecular gas because H_2 forms on dust grains. In this paper we test this interpretation by modeling the IR emission from dust associated with the H_2 gas present in the SQ shock structure, and by comparing the model calculations with *Spitzer* observations.

– We model the emission from dust associated with diffuse or clumpy molecular gas, embedded within H gas and X-ray emitting plasma. The model SED is consistent with mid-IR *Spitzer* observations for both cases, for a Galactic dust-to-gas mass ratio and a Galactic dust size distribution. For diffuse gas, the best-fit column density is $N_H = 1.8\pm0.5\times10^{20}$ cm^{-2}, which is close to the value derived from warm H_2 observations. For clumpy molecular clouds that are optically thick to UV radiation, we find that the H_2 surface filling factor is $f \sim 0.03$. So far, the present data and the degeneracy between the dust size distribution and the cloud structure do not allow to decide whether the molecular gas is diffuse or fragmented into clouds that are optically thick to UV photons.

– The presence of dust in such a high-speed (~ 1000 km s^{-1}) galaxy collision, coexisting with a hot ($T \approx 6 \times 10^6$ K) plasma, shows that dust is able to survive in such a violent environment, perhaps because it is protected from destruction in denser regions (Guillard et al., 2009). The present data do not allow us to identify any deviation of the VSGs/BGs abundance ratio from the diffuse Galactic ISM value. On the other hand, the peculiar properties of the PAH emission in the SQ ridge (summarized above) may be the result of PAH processing in shocks.

Future observations are needed to constrain both the structure of the H_2 gas and the dust properties in the SQ shock:

Far-IR observations. The flux in the FIR is different for the two models (diffuse or clumpy). The spatial resolution of the PACS[12] [$60-210\,\mu$m] instrument on-board the *Herschel Space Observatory* at $70\,\mu$m is comparable to that of *Spitzer* at $24\,\mu$m. It will thus possible to extract the FIR emission from the shock with much more accuracy than with *Spitzer*. This is needed to possibly break some degeneracies of the model and better constrain the space of the key-parameters (e.g. dust-to-gas mass ratio, dust size distribution).

CO observations. The amount of CO gas would be a key-data to characterize the structure of the molecular gas. In July 2009 we performed observations with the with the new broad-band receiver EMIR at the 30m telescope (Pico Veleta, Spain) in order to determine whether a cold ($T < 50$ K) molecular gas reservoir is associated to the warm H_2. These observations, which set a new light on the physical structure and dynamics of the molecular gas in the ridge, will be reported in a forthcoming paper (Guillard et al., in preparation).

The Stephan's Quintet galaxy-collision is a unique environment to study dust survival in shocks, on galactic scales. The presence of dust in the SQ shock stresses the need to revisit the standard calculations of dust survival timescales in the ISM, by taking into account its multiphase structure.

[12] Photodetector Array Camera & Spectrometer

References

Allen, M. G., Groves, B. A., Dopita, M. A., Sutherland, R. S., & Kewley, L. J. 2008, ApJS, 178, 20
Allen, R. J. & Hartsuiker, J. W. 1972, Nature, 239, 324
Allen, R. J. & Sullivan, III, W. T. 1980, A&A, 84, 181
Appleton, P. N., Xu, K. C., Reach, W., et al. 2006, ApJ, 639, L51
Bakes, E. L. O. & Tielens, A. G. G. M. 1994, ApJ, 427, 822
Bakes, E. L. O., Tielens, A. G. G. M., & Bauschlicher, C. W. 2001a, ApJ, 556, 501
Bakes, E. L. O., Tielens, A. G. G. M., jr Bauschlicher, C. W., Hudgins, D. M., & Allamandola, L. J. 2001b, ApJ, 560, 261
Bauschlicher, Jr., C. W. 2002, ApJ, 564, 782
Cazaux, S. & Tielens, A. G. G. M. 2004, ApJ, 604, 222
Cluver, M. E., Appleton, P. N., Boulanger, F., et al. 2009, ApJ, accepted
Cohen, M., Wheaton, W. A., & Megeath, S. T. 2003, AJ, 126, 1090
Compiègne, M., Abergel, A., Verstraete, L., & Habart, E. 2008, A&A, 491, 797
Compiègne, M., Abergel, A., Verstraete, L., et al. 2007, A&A, 471, 205
Désert, F.-X., Boulanger, F., & Puget, J. L. 1990, A&A, 237, 215
Draine, B. T. & Li, A. 2001, ApJ, 551, 807
Draine, B. T. & Li, A. 2007, ApJ, 657, 810
Falgarone, E., Verstraete, L., Pineau Des Forêts, G., & Hily-Blant, P. 2005, A&A, 433, 997
Fazio, G. G., Hora, J. L., Allen, L. E., et al. 2004, ApJS, 154, 10
Flagey, N., Boulanger, F., Verstraete, L., et al. 2006, A&A, 453, 969
Gallagher, S. C., Charlton, J. C., Hunsberger, S. D., Zaritsky, D., & Whitmore, B. C. 2001, AJ, 122, 163
Gao, Y. & Xu, C. 2000, ApJ, 542, L83
Guillard, P., Boulanger, F., Pineau Des Forêts, G., & Appleton, P. N. 2009, A&A, 502, 515
Guillet, V., Pineau Des Forêts, G., & Jones, A. P. 2007, A&A, 476, 263
Gusdorf, A., Cabrit, S., Flower, D. R., & Pineau Des Forêts, G. 2008, A&A, 482, 809
Habing, H. J. 1968, Bull. Astron. Inst. Netherlands, 19, 421
Hartigan, P., Raymond, J., & Hartmann, L. 1987, ApJ, 316, 323
Ho, L. C. & Keto, E. 2007, ApJ, 658, 314
Houck, J. R., Roellig, T. L., van Cleve, J., et al. 2004, ApJS, 154, 18
Jones, A. & Tielens, A. 1994, The Cold Universe, XIIIth Moriond Astrophysics Meeting, ed. T. Montmerle, C. Lada, I. Mirabel, & J. Thanh Van (Gif-sur Yvette: Éditions Frontières)
Jones, A. P. 2004, in Astronomical Society of the Pacific Conference Series, Vol. 309, Astrophysics of Dust, ed. A. N. Witt, G. C. Clayton, & B. T. Draine, 347–+
Jones, A. P., Tielens, A. G. G. M., & Hollenbach, D. J. 1996, ApJ, 469, 740
Kaneda, H., Onaka, T., & Sakon, I. 2005, ApJ, 632, L83
Langhoff, S. 1996, J. Phys. Chem., 100, 2819
Le Petit, F., Nehmé, C., Le Bourlot, J., & Roueff, E. 2006, ApJS, 164, 506
Lisenfeld, U., Braine, J., Duc, P.-A., et al. 2002, A&A, 394, 823
Martin, D. C., Fanson, J., Schiminovich, D., et al. 2005, ApJ, 619, L1
Mathis, J. S., Mezger, P. G., & Panagia, N. 1983, A&A, 128, 212
Mathis, J. S., Rumpl, W., & Nordsieck, K. H. 1977, ApJ, 217, 425
Micelotta, E. R., Jones, A. P., & Tielens, A. G. G. M. 2009, A&A, in press
Moles, M., Sulentic, J. W., & Marquez, I. 1997, ApJ, 485, L69+
Morrissey, P., Conrow, T., Barlow, T. A., et al. 2007, ApJS, 173, 682
O'Sullivan, E., Giacintucci, S., Vrtilek, J. M., Raychaudhury, S., & David, L. P. 2009, ApJ, 701, 1560

Pietsch, W., Trinchieri, G., Arp, H., & Sulentic, J. W. 1997, A&A, 322, 89
Popescu, C. C., Tuffs, R. J., Fischera, J., & Völk, H. 2000, A&A, 354, 480
Rachford, B. L., Snow, T. P., Tumlinson, J., et al. 2002, ApJ, 577, 221
Rapacioli, M., Joblin, C., & Boissel, P. 2005, A&A, 429, 193
Rieke, G. H., Young, E. T., Engelbracht, C. W., et al. 2004, ApJS, 154, 25
Roussel, H., Helou, G., Hollenbach, D. J., et al. 2007, ApJ, 669, 959
Sellgren, K., Uchida, K. I., & Werner, M. W. 2007, ApJ, 659, 1338
Sembach, K. R. & Savage, B. D. 1996, ApJ, 457, 211
Smith, B. J. & Struck, C. 2001, AJ, 121, 710
Smith, J. D. T., Dale, D. A., Armus, L., et al. 2004, ApJS, 154, 199
Smith, J. D. T., Draine, B. T., Dale, D. A., et al. 2007, ApJ, 656, 770
Smith, R. K., Krzewina, L. G., Cox, D. P., Edgar, R. J., & Miller, W. W. I. 1996,
     ApJ, 473, 864
Sulentic, J. W., Rosado, M., Dultzin-Hacyan, D., et al. 2001, AJ, 122, 2993
Szczepanski, J. & Vala, M. 1993, ApJ, 414, 646
Tappe, A., Rho, J., & Reach, W. T. 2006, ApJ, 653, 267
Trinchieri, G., Sulentic, J., Breitschwerdt, D., & Pietsch, W. 2003, A&A, 401,
     173
Trinchieri, G., Sulentic, J., Pietsch, W., & Breitschwerdt, D. 2005, A&A, 444,
     697
Weingartner, J. C. & Draine, B. T. 2001a, ApJ, 548, 296
Weingartner, J. C. & Draine, B. T. 2001b, ApJ, 563, 842
Weingartner, J. C. & Draine, B. T. 2001c, ApJS, 134, 263
Williams, B. A., Yun, M. S., & Verdes-Montenegro, L. 2002, AJ, 123, 2417
Xu, C., Sulentic, J. W., & Tuffs, R. 1999, ApJ, 512, 178
Xu, C. K., Appleton, P. N., Dopita, M., et al. 2008, in Astronomical Society
     of the Pacific Conference Series, Vol. 381, Infrared Diagnostics of Galaxy
     Evolution, ed. R.-R. Chary, H. I. Teplitz, & K. Sheth, 88–+
Xu, C. K., Iglesias-Páramo, J., Burgarella, D., et al. 2005, ApJ, 619, L95
Xu, C. K., Lu, N., Condon, J. J., Dopita, M., & Tuffs, R. J. 2003, ApJ, 595, 665

Online Material

Appendix A: Fitting PAH features

The results of the PAHFit decompositions of the *Spitzer IRS* spectrum of the center of SQ ridge and, for comparison, of the *ISO-CVF* spectrum of the diffuse Galactic medium, are presented in Fig. A.1, A.2 and A.3. No extinction parameter is introduced in the fit.

List of Objects

PAHFit: IRS Spectrum of SQ Shock
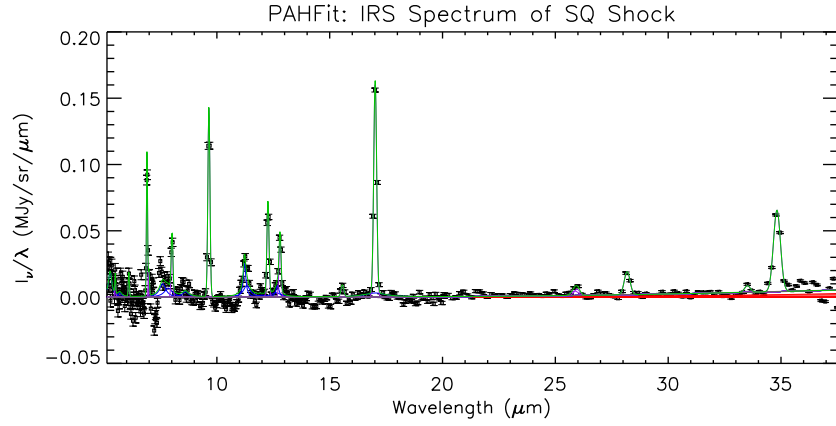
Fig. A.1. Result of a PAHFit run on the full $5 - 38\,\mu$m *Spitzer IRS* spectrum extracted over a ∼ 18" × 15" area centered on the position in the center of the ridge (ON beam on Fig. 1). The gaussian profiles of the gas lines are used to remove their contributions and extract a "pure dust spectrum" (see Fig. A.2).

PAHFit: PAH Spectrum of SQ Shock (no gas lines)
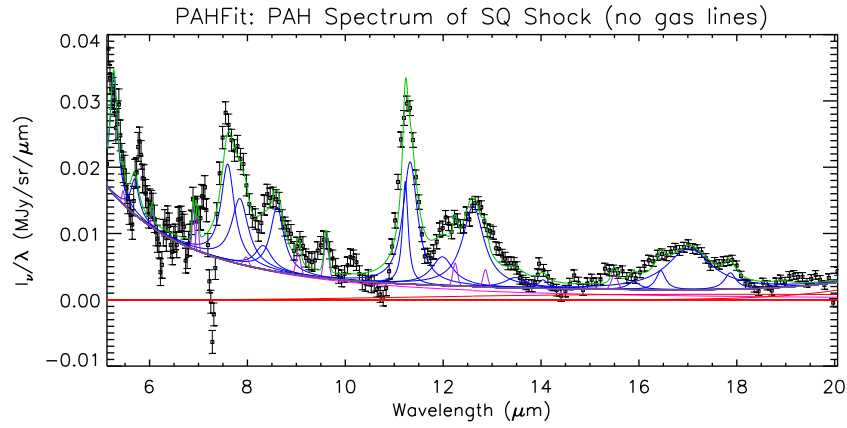
Fig. A.2. PAHFit decomposition of the *Spitzer IRS* dust spectrum (smoothed over 5 resolution elements, and from which gas lines have been removed) extracted in the center of the SQ ridge. Blue solid lines shows the lorentzian components of the PAH decomposition, and the thick gray line is the total (dust + starlight) continuum. The result of the fit is the green solid line.

PAHFit: ISO−CVF Spectrum of diffuse galactic medium
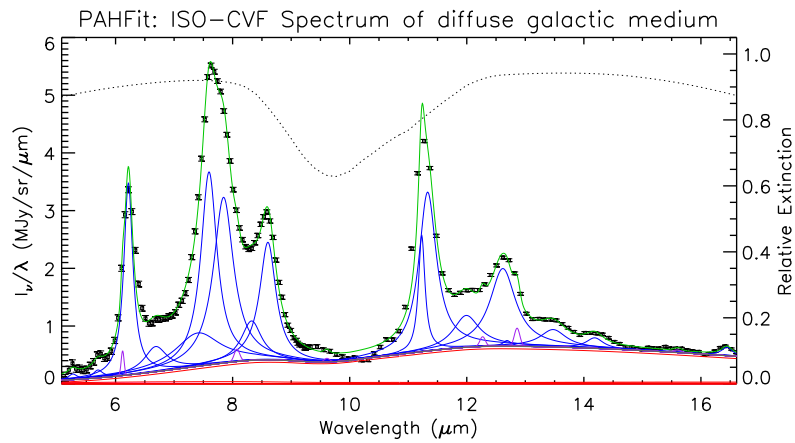
Fig. A.3. PAHFit decomposition of the *ISO-CVF* spectrum of the diffuse Galactic light (Flagey et al., 2006), centered on the Galactic coordinates (26.8, +0.8). The gas lines have been removed from the spectrum. The lorentzian components of the decomposition of the PAH features are shown in blue. All components are diminished by the extinction, indicated by the dotted black line, with axis at right. The solid green line is the full fitted model, plotted on the observed flux intensities and uncertainties.

8.4 Perspectives on revisiting dust survival timescales: impact of the multiphase ISM structure

Observations of dust, from PAHs to BGs, in the violent SQ galaxy collision is certainly a challenge for dust evolution models, and has potentially important consequences for the estimate of dust survival in the ISM.

So far, dust survival timescales are estimated by assuming that the shocked medium is homogeneous. Within the context of the SQ shock, the temperature of the hot plasma in constrains the shock velocity in the tenuous gas to be ≈ 700 km s^{-1}. If we assume that the shocked medium is homogeneous, all the dusty gas is shocked at these very high velocities, and thus the dust destruction timescale would be much shorter than the dust re-formation time.

This issue is also true in the galactic ISM. Let us give a rough estimate of the dust survival timescale in an homogeneous medium, following Jones (2004). Once a dust grain finds itself in the ISM, it is subject to destruction by supernova shock waves. We calculate the the timescale for SN shock waves to destroy all the dust in the ISM, t_{SNR}. If $\epsilon(v_s)$ is the efficiency of grain destruction by a shock of velocity v_s, $M_s(v_s)$ is the mass of gas shocked to a velocity of at least v_s, τ_{SN} the interval between supernovae, and M_{ISM} the total mass of the galactic ISM, then the timescale for grain destruction is given by:

$$\frac{M_{ISM}}{t_{SNR}} = \frac{1}{\tau_{SN}} \int \epsilon(v_s) \mathrm{d}M_s(v_s) \approx \frac{\bar{\epsilon} M_s(100\,\mathrm{km\,s}^{-1})}{\tau_{SN}} \; , \tag{8.1}$$

where $\bar{\epsilon}$ is the mean grain destruction parameter, and $M_s(100\,\mathrm{km\,s}^{-1})$ corresponds to a typical SN shock that affects a sufficient volume of the ISM. Now, to determine the mass shocked to a velocity of at least v_s, we exploit the conservation of the energy E released by the explosion of the SN and write (McKee 1989, McKee (1989)):

$$M_s(v_s) = \frac{E}{\sigma\, v_s^2} \; , \quad \text{and then} \quad t_{SNR} = \sigma \frac{M_{ISM}\, \tau_{SN}}{\bar{\epsilon}\, E} v_s^2 \approx 4 \times 10^8 \; \mathrm{yr} \; , \tag{8.2}$$

where $\sigma = 0.736$ (Ostriker & McKee 1988), and $E = 10^{44}$ J. I use $\bar{\epsilon} = 0.5$, , $M_{ISM} = 5\,10^9$ M$_\odot$ and $\tau_{SN} = 30$ yr. On the other hand, Jones (2004) estimate the dust formation timescale to be $t_f \approx 3 \times 10^9$ yr. Clearly, by comparing t_f and t_{SNR}, dust destruction is faster than stardust formation. This timescale discrepancy is clearly at odds with the observations of dust in the ISM! The conclusion that is generally given is that dust must be (re)formed *in situ* in the ISM. This may be true, but the exact way dust is re-accreted and re-coagulated is still poorly known .

Stephan's Quintet observations may suggest an alternative solution to the issue of dust survival in the ISM. As discussed in paper I, the density inhomogeneities in the preshock medium allow the dust to survive, provided that the density contrast is high enough to reduce the transmitted shock velocity. The multiphase nature of the ISM may increase significantly the overall dust survival timescale.

Chapter 9

H$_2$ in galaxy evolution

There are 10^{11} stars in the galaxy. That used to be a huge number.
But it's only a hundred billion. It's less than the national deficit!
We used to call them astronomical numbers. Now we should call
them economical numbers.

Richard Feynman

Abstract

Molecular gas is the reservoir for star formation, and thus plays a key role in galaxy evolution.
However, so far, the molecular gas has been largely ignored in the description of galaxy evolu-
tion in a cosmological context. In particular, the response of the molecular gas to gas accretion
onto galactic disks, galaxy merging, feedback, and its impact on the energetics of these major
evolutionary phases have so far not been addressed in detail. H$_2$-luminous galaxies open a new
perspective for the study of molecular gas in active phases of galaxy evolution. Our interpretation
of the H$_2$ emission from the Stephan's Quintet galaxy collision set a theoretical framework that
may apply to other astrophysical situations. The H$_2$-luminous radio-galaxy 3C326 is one exam-
ple, where H$_2$ observations allow for the first time to peer at the impact of the AGN-driven jet
onto the molecular gas of the host galaxy. Does the AGN feedback regulate or even suppress star
formation (negative feedback), or does it trigger star formation (positive)? This is a key question
in galaxy evolution.

Contents

9.1 Introduction

Understanding how galaxies formed and evolved is one of the major goals of modern extragalactic astronomy. This dissertation is a first step to address the role of molecular gas within this context. The emerging population of H$_2$-luminous galaxies (with enhanced mid-IR H$_2$ line emission and relatively weak star formation), includes galaxies in several key phases of their evolution, dominated by

gas accretion, galaxy interactions, or galactic winds driven by star formation and AGN. The analysis presented in this manuscript suggests that the warm H$_2$ contributes significantly to the overall energy budget of these galaxies, and may potentially play a central role for galaxy evolution.

This chapter introduces the role of the molecular gas for the energetics of star formation and galaxy mass build-up (sect. 9.2). I point out some major astrophysical questions in this context, with an emphasis on AGN feedback (sect. 9.2.2). Then I present the case of 3C326, a spectacular example of an H$_2$-luminous radio-galaxy for which I have applied the same analytical and numerical approach as for Stephan's Quintet to model the H$_2$ emission and derive gas masses in the system. These results, together with a detailed analysis of the energetics of the system, are gathered in Nesvadba et al. (2009) (hereafter paper IV), submitted to A&A. The observational context of 3C326 is given in sect. 9.3.1 and the paper is reproduced in sect. 9.3.3. This chapter ends with a presentation of some observational (sect. 13.1) and theoretical perspectives (sect. 13.2).

9.2   H$_2$ and feedback in galaxy evolution

Thanks to ever-improving cosmological simulations, we now have a sound comprehension of structure formation on the largest scales. Spectacular progress is made in describing the structure of dark matter, and the history of star formation through cosmic time. However, describing galaxy evolution within this picture is still a challenge.

The reason is that the build-up of baryonic mass in galaxies is regulated by a complex interplay between gravitational collapse and feedback related to AGN and star formation. The dynamical interactions between the ISM phases and their thermal properties play a key role in this regulation. Fig. 9.1 illustrates schematically the mass and energy exchange between the ISM of a galaxy and its halo's environment. In the context of galaxy baryonic mass build-up, two processes compete. On one hand, the activity of the black hole, and the bursts of star formation, create "galactic winds", or "superwinds" on galactic scales (e.g. Heckman et al., 1990) that push the hot/warm gas, and possibly also molecular gas, into the galactic corona, or even further out to the intergalactic space (*outflow*). The relative importance between the impact of black holes or stars depends on the mass of the galaxy, more massive ones being dominated by the AGN activity (e.g. Dekel and Silk, 1986). On the other hand, part of this matter does not escape the gravitational potential well of the galaxy, and falls back onto the galactic disk. In addition, matter from the intergalactic medium, or from a companion galaxy, is accreted onto the disk. These processes are particularly important during the early phases of galaxy evolution at high redshift, when most of the stars in the universe were formed.

In this picture of galaxy formation and evolution, a lot of astrophysical questions remains. We still do not know how gas that falls within dark matter haloes is accreting onto the galactic disk, and how it comes to form stars. On the other hand, it is not clear what is the impact and efficiency of feedback processes from stars or black holes on the molecular gas, and thus on star formation. These questions are related to the regulation of mass build-up in galaxies described above. I will only focus on the second aspect, which is closely related to the theoretical framework developed in my PhD work: *What is the impact of feedback on galaxy evolution?*

Since H$_2$ formation is a natural outcome of gas cooling, and since molecular gas represents the reservoir for star formation, H$_2$ gas must play an important role in all the processes listed above.
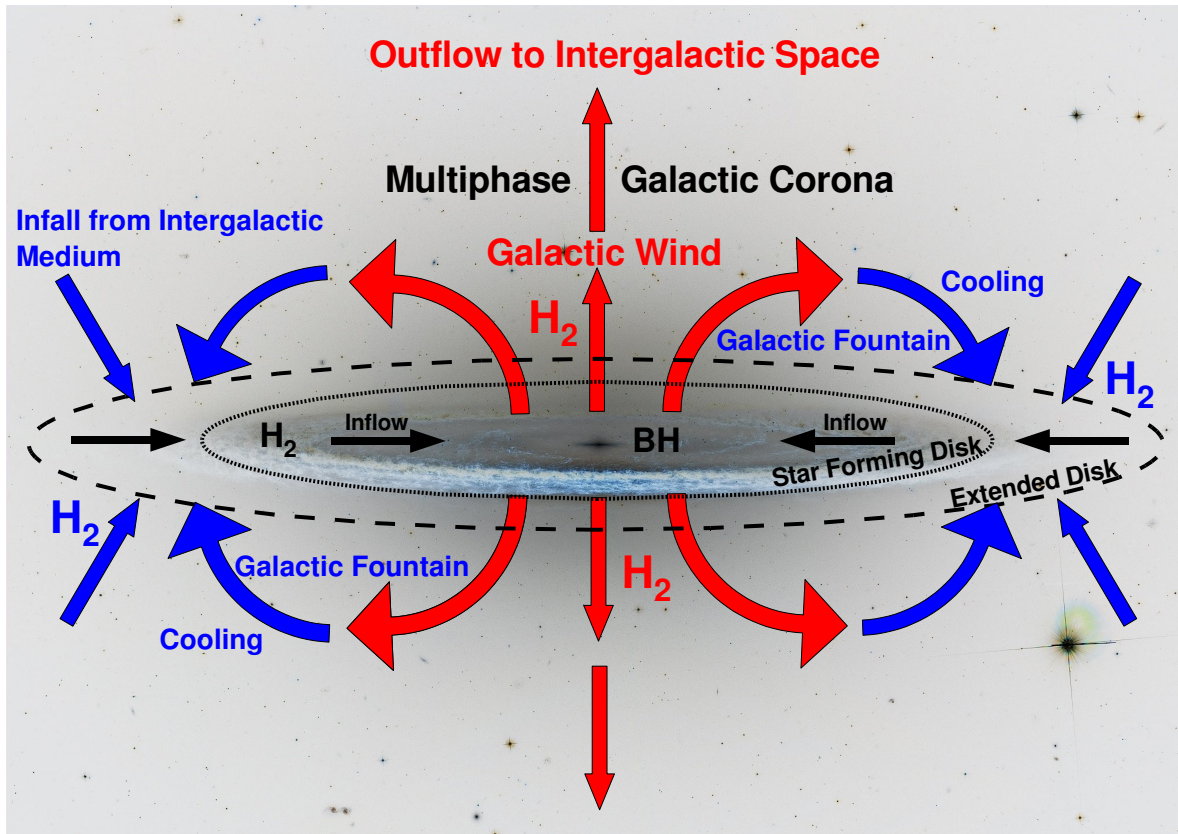
Figure 9.1: Sketch of the complex circulation of the multiphase interstellar matter during galaxy mass build-up. The gas disk of the galaxy is fed by infall from intergalactic space and by gas raining down from the halo. This gas flows inwards and fuel star formation as well as the activity of the central black hole. The blue and red arrows schematically outline these inflows and outflows, and the gas cooling and heating. Observations show that H_2 is a key actor in all stages. Adapted from Boulanger et al. (2009).

Therefore, understanding the role that cold interstellar matter plays in the evolution of galaxies is a key to elucidate the above questions. However, very little is known about its *impact* on the energetics of feedback, and its *response* to it. In a sense, the *Spitzer Space Telescope* has opened a new observational window into the "molecular Universe" through mid-infrared observations of warm H_2. In the following I will emphasize what can we learn from H_2 observations that may help in answering these questions. I distinguish two types of feedback, depending on the powering sources: either star formation or black hole.

9.2.1   Feedback from star formation: H_2 in "superwinds"

Star formation is known from optical to X-ray observations of warm and hot gas to drive galactic winds (Heckman et al., 1990, 2000). Superwinds are generated when the kinetic energy from stellar winds and supernovae is thermalized, generating a region of very hot ($T \approx 10^7 - 10^8$ K) high-pressure plasma in the ISM of a starburst galaxy (Chevalier and Clegg, 1985). As the bubble breaks out of the

disk of the galaxy, the plasma expands producing a weakly-collimated bipolar outflow into the galaxy halo. The outflowing plasma sweeps up and shocks ambient material, creating a superwind.

To understand the impact of these winds on star formation, and thereby on galaxy evolution in general, it is crucial to constrain their impact on the multiphase interstellar medium of galaxies. *Spitzer* mid-IR imaging and spectroscopy have revealed that winds are loaded with molecular gas and dust (see the illustration for the wind of M82 in Fig. 1.3). However, the origin of this molecular gas is still unclear. Is it material lifted up from the galactic disk, or is the molecular gas formed *in situ*, by compression of dusty atomic gas that is advected in the flow? We do not favor the first interpretation because the hot wind is too tenuous to lift up dense molecular clouds from the disk. If one considers a molecular cloud of radius 10 pc and density 10^4 cm^{-3}, entrained in a 500 km s^{-1} superwind at density 10^{-2} cm^{-3}, the acceleration timescale of the cloud would be (Eq. 4.30) $\sim 3 \times 10^{10}$ yr, which is much larger than the dynamical timescale of the outflow ($\sim 10^7$ yr). Following our scenario of H$_2$ formation in the Stephan's Quintet shock (chapter 5), we favor the second interpretation, in which the H$_2$ gas is formed outside galactic disks as the result of the dynamical interaction of the wind with gas in the halo.

The molecular component has previously been ignored in galactic winds studies. Is the molecular gas a dominant mass component of galactic winds? Does it share the outward flow motion of the lighter and warmer gas? Does it fall back on the disk? Is the emission from molecular gas the main dissipative channel that sets the energetic efficiency of galactic winds? The answers to these questions about molecular gas are essential to determine the impact of feedback from star formation on the evolution of galaxies.

9.2.2   H$_2$ and AGN feedback

An even more powerful source for feedback is the central engine of AGN, the supermassive black hole in the center of the host galaxy. A small fraction of the energy released by the growth of the black hole, if absorbed by interstellar matter in the host galaxy, could regulate or even quench star formation by heating and ejecting ambient gas from the disk of the host galaxy under the action of an AGN-driven outflow. This is the so-called *negative AGN feedback*. On the other hand, the impact of the AGN could in principle be also *positive*, by triggering star formation through the interaction of the AGN-driven jet with the ISM of the host galaxy.

Monsters needed to break the hierarchy!

This negative AGN feedback has been often invoked to explain the decline of star formation in massive, early-type galaxies (e.g. Silk and Rees, 1998; Springel et al., 2005; Croton et al., 2006; Hopkins et al., 2006). The large majority of these galaxies appears to have formed most of their stars at high redshift[1], so that they are now "old, red, and dead". These observations are in apparent contradiction with a gradual, "bottom-up", mass assembly. Under the assumption of hierarchical galaxy evolution, one would naïvely think that the gas cools and is accreted gradually onto massive halos. So we should

---

[1]This is indicated by the redshift evolution of luminosity and mass functions of galaxies, and by the characterization of stellar populations, chemical abundances, and structural properties of giant ellipticals in the local universe. Even a small fraction of the gas returned by dying-stars gas should result in star formation rates much larger than observational estimates.

find many more massive, blue, star-forming galaxies, particularly at the centers of groups and clusters. This is called the *hierarchical problem*. AGN "monsters" are then called to break the hierarchical scenario!

It is worth mentioning that an other alternative mechanism, called *morphological quenching*, has been recently proposed by Martig et al. (2009) to account for "red" early-type galaxies. Based on cosmological simulations, they propose that star formation is quenched when the galaxy experiences a morphological transition from a rotating stellar disk to a pressure-dominated stellar spheroid, which induces a steeper potential well and reduces the disk selfgravity. In their simulations, this transition results from the growth of a stellar spheroid, for instance by galaxy merging. The gas in the disk of the galaxy becomes stable against fragmentation, thus reducing star formation efficiency. Though interesting, this process may not be directly related to H_2-luminous objects since it appears that a powerful source of mechanical energy is needed to explain the H_2 emission.

H₂-luminous galaxies as a tool to study AGN feedback

Despite its potential importance, *dixit* Matthew D. Lehnert, "AGN feedback has remained in the realm of theoretical *deus ex machina*". We still do not understand how the transfer of energy from the AGN to the surrounding gas occurs. In particular, a major question is to determine the impact of the AGN-driven jet to the molecular gas settled in the disk of the host galaxy. Is the ISM of the host galaxy blown up in the outflow, thus supressing star formation (*negative feedback*)? Or does the jet trigger shock-compression of clouds, thus enhancing star formation (*positive feedback*)? Or is it both?

Evidences for AGN feedback are now growing. Observations suggest that AGN feedback may be associated mostly with radio-loud AGN. Perhaps the most striking examples are nearby clusters of galaxies, in which the central black hole(s) inject a huge amount of energy (typically $\approx 10^{60}$ erg for the most massive ones) over a rather short timescale ($\approx 10^7$ yr), which seems enough to prevent the cooling of the gas through X-ray emission. This may be an explanation to solve for the "cooling flow problem", in which the amount of hot gas that cools radiatively (inferred from soft X-ray observations) is much less than expected from the harder X-ray luminosity (see McNamara and Nulsen, 2007, and references therein for a review). A number of observations show that cool-core clusters contain large amounts of molecular gas at their center. H_2 was first detected through its near-IR ro-vibrational lines. Warm H_2 has since also been observed through its mid-IR rotational lines with Spitzer (see chapter 1, sect. 1.2.2, Fig. 1.5 and e.g. Egami et al., 2006). Numerous CO detections have also been reported but the spatial distribution and kinematics of the cold molecular gas has only been imaged in a few clusters. For instance CO observations reveal a large amount ($\approx 10^{11}$ $M_\odot$) of cold molecular gas extending in the halo to several tens of kpc from the central elliptical galaxy NGC 1275 (Salomé et al., 2006) in the Perseus A galaxy cluster. This molecular gas is observed to be surprisingly inefficient at forming stars.

Radio galaxies are interesting targets to elucidate the physical mechanisms whereby the AGN can regulate the star formation in its host galaxy. Indeed, radio-galaxies have an AGN and an obvious source of mechanical energy which reaches large scales. They also show signs of outflows (Nesvadba et al., 2006, 2008b, 2009; Holt et al., 2008), strong turbulence, and dissipation of mechanical energy (Ogle et al., 2007, 2009). For the first time, observations of warm molecular gas in radio-galaxies allow to peer at the impact of the radio jet on the energetics of the dense molecular gas, and thus on

star formation. Ogle et al. (2009) find that about 30% of nearby powerful radio galaxies may fall into the class of H$_2$-luminous galaxies presented in chapter 1, which have significant amounts of relatively dense, warm, and surprisingly turbulent molecular gas, but very little star formation.

In the following I shall focus on the example of the 3C326 radio-galaxy, which has been studied in detail by applying the methods developed during my PhD work.

9.3   Are we witnessing negative AGN feedback in the radio galaxy 3C326?

The radio galaxy 3C326 is an outstanding source to study the impact of the radio jets on its molecular gas, and paper IV presents such a study. We report new CO observations of that source that complement the mass and energy budget of the molecular gas in 3C326. We interpret line emission from the ionized and molecular gas within the framework I have developed for the Stephan's Quintet.

The paper IV is reproduced at the end of this chapter. I only give here a brief summary of the main points, as well as additional figures and results from my modeling of H$_2$ excitation in that source. We find that the ISM of this galaxy has very unusual properties: the molecular gas budget is dominated by warm gas at temperatures $T > 100$ K, while diagnostic line ratios suggest that the ionized and molecular gas is mostly excited through shocks.

We also identify a significant outflow of neutral gas which cannot be explained by star formation. We explain these observations through a common physical framework where a fraction of the mechanical energy of the radio jet is being dissipated on small scales within the molecular gas, which powers the observed H$_2$ emission. This is an extension of the classical "cocoon" model, in which the AGN-driven jet inflates a "cocoon" of hot gas that accelerates the warm medium. We now explicitly take into account the multiphase character of the ISM and find that only a small fraction ($\sim 10\%$) of the jet mechanical energy is need to power the H$_2$ emission. The timescale of dissipation of the jet mechanical energy ($10^7 - 10^8$ yr) suggests that the jet could heat the molecular on timescales comparable, or even longer, than the jet lifetime, thus limiting star formation over a long-lasting period of time. Studies of repeated jet activity in radio galaxies suggest that the phse of "quiessence" between two activity cycles could be of similar duration. Thus, the physical gas conditions in AGN host galaxies may play an important role in regulating this cyclical jet activity.

To introduce the paper IV that presents a detailed analysis of the energetics of the molecular gas in 3C326, I briefly present the observational status of 3C326.

9.3.1   Observational context

Two companions...

3C326 is one of the largest radio sources known (Willis and Strom, 1978), with an angular size of 19.5" (1.9 Mpc). It is a system of two companions, 3C326 N (N being for North) and 3C326 S (South), at a redshift of $z = 0.089 \pm 0.001$. Fig. 9.2 shows a radio *(left)* and a mid-IR *(right)* image of the pair. It is not clear which of the two galaxies hosts the AGN that produced the Mpc-scale radio lobes (see Rawlings et al., 1990).

The galaxy 3C326 N has been classified as a LINER from optical spectroscopy (Rawlings et al., 1990). It has strong [O II], Hα, [S II], and weak [O III] lines, whereas 3C 326 S has no detected
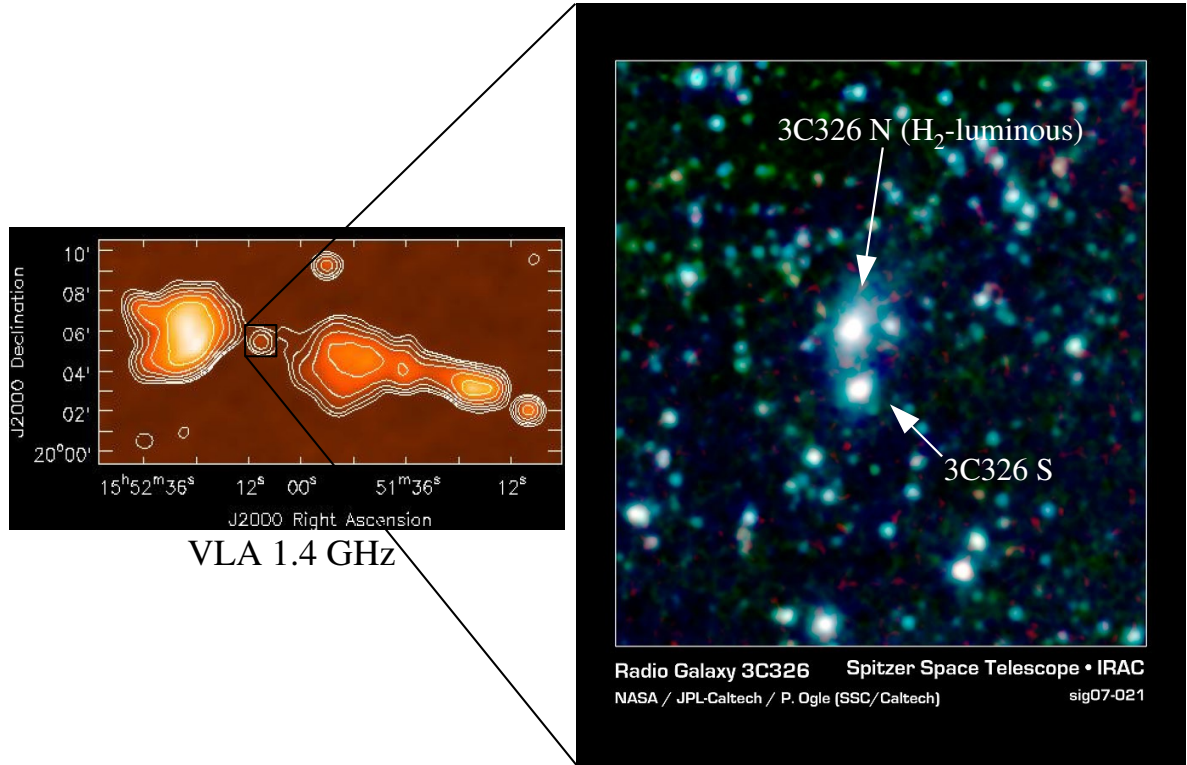
Figure 9.2: Radio VLA (1.4 GHz) (Klein et al., 1994b; Mack et al., 1997) and Spitzer images (Ogle et al., 2007) of the 3C326 radio-galaxy. The system comprises of two galaxies (3C326 North and South). The projected separation between the two is 24.9" (41 kpc). It is not clear which one creates the jet, materialized by the Mpc-scale radio lobes seen on the VLA image.

emission lines (Rawlings et al., 1990; Simpson et al., 1996). Rawlings et al. (1990) suggest that 3C 326N is more typical of FR II radio galaxy hosts than its South companion.

. . . but one H$_2$-luminous source

Based on this observational context, Ogle et al. (2007) targeted the northern companion, 3C326 N, with the *Spitzer IRS*, and found extraordinary powerful H$_2$ rotational line emission. The total emission-line luminosity of 3C326 N is $\mathcal{L}(H_2) = 8.0 \pm 0.4 \times 10^{34}$ W (integrated over the lines S(1) to S(7)). The ratio of the H$_2$ luminosity of the $8 - 70\,\mu$m integrated infrared luminosity is 0.17 ± 0.02, which is $1 - 2$ orders of magnitude higher than normal star-forming galaxies (see discussion in chapter 1).

The optical and mid-IR spectra of 3C326 N (see Fig. 1.2, Fig. 1.4 and Ogle et al., 2007, 2009) suggest a very weak star forming rate (~ 0.07 M$_\odot$ yr^{-1}) although the galaxy holds a large mass of H$_2$ gas ($\approx 10^9$ M$_\odot$).

9.3.2   H$_2$ excitation in 3C326

Like in Stephan's Quintet, the H$_2$ emission in 3C326 is associated with the dissipation of mechanical energy. I have used the grid of MHD shocks presented in chapter 4 to quantify the range of preshock

density and shock velocities that fits the oberved H_2 line fluxes.

The results of the modeling of the H_2 excitation are gathered in Tables 6 and 7 of paper IV. To complement these tables, Fig. 9.3 shows the observed and modeled H_2 excitation diagram for 3C326. As discussed in chapter 6, these fits are not unique. I show here the results for two preshock densities, $n_H = 10^3$ and 10^4 cm^{-3}. The lowest preshock density (10^3 cm^{-3}) is need to fit the 0-0S(0) line, where higher excitation lines S(6) and S(7) require higher densities or higher velocity shocks. Please see paper IV for a discussion of the results, in particular the mass and energy budgets of the molecular gas in this galaxy.

9.3.3   Publication: paper IV

Energetics of the molecular gas in the H_2-luminous radio galaxy 3C326: Evidence for negative AGN feedback [*]

N. P. H. Nesvadba,[1,2] F. Boulanger,[1] P. Salomé,[3] P. Guillard,[1] M. D. Lehnert,[4] G. Pineau des Forets,[1,5] P. Ogle[6] and P. Appleton[7]

[1] Institut d'Astrophysique Spatiale, Campus Universitaire d'Orsay, Bat. 120-121, 91405 Orsay, France
[2] email: nicole.nesvadba@ias.u-psud.fr
[3] Institut de Radioastronomie Millimetrique (IRAM), St. Martin d'Heres, France
[4] GEPI, Observatoire de Paris, CNRS, Université Denis Diderot, Meudon, France
[5] LERMA, Observatoire de Paris, 61, Avenue de l'Observatoire, 75014 Paris, France
[6] Spitzer Science Center, California Institute of Technology, Pasadena, USA
[7] NASA Herschel Science Center, California Institute of Technology, Pasadena, USA

Received / Accepted

ABSTRACT

We present a detailed analysis of the gas conditions in the prototypical H_2-luminous radio galaxy 3C326 N at z∼0.1, in which star formation is strongly suppressed (SFR∼0.07 $M_\odot$ yr^{-1}) in spite of a gas surface density similar to starburst galaxies. Combining new IRAM CO emission-line interferometry with existing Spitzer mid-infrared and SDSS optical spectroscopy, we find that most of the molecular gas is at temperatures ≥150 K, unlike in star-forming galaxies where only 1-10% of the molecular gas is warm, but similar to the gas near the Galactic center. Na D absorption lines indicate an outflow with a terminal velocity of ∼1800 km s^{-1} and mass outflow rates of 30-40 $M_\odot$ yr^{-1}, which cannot be explained by star formation. We propose that the outflow and gas heating are due to the deposition and dissipation of a small fraction of the mechanical energy of the radio jet in the interstellar medium of the host galaxy. Dissipation times are of order 10^{7-8} yrs, similar or greater than the typical jet lifetime, so that gas cooling may be suppressed even between active phases. For 8 more H_2-luminous radio galaxies CO and PAH surface brightnesses suggest that a similar form of AGN feedback could also be suppressing star formation in these galaxies. If radio-activity is a common, and episodic phase of most massive early-type galaxies, then the global energy release of radio-loud AGN in the local universe seems sufficient to counteract secular gas cooling in all massive early-type galaxies of $\geq 10^{11}$ $M_\odot$ through 'maintenance-phase' AGN feedback.

Key words. Galaxies – ... – ...

1. Introduction

Molecular gas plays a critical role for our growing understanding of galaxy evolution. It often dominates the mass budget of the interstellar medium in galaxies, and is most closely related to the intensity at which galaxies form stars (e.g., Kennicutt 1998). Being strongly dissipative, it is also particularly susceptible to the astrophysical processes that drive galaxy evolution – interactions, or feedback from starbursts and AGN – and therefore plays a key role for our understanding of how these processes regulate star formation and galaxy assembly.

It has only recently been recognized that powerful AGN may play a significant role in regulating galaxy growth over cosmological timescales by suppressing gas accretion and star formation (e.g., Silk & Rees 1998; Friaca & Terlevich 1998; Springel et al. 2005; Croton et al. 2006; Ciotti & Ostriker 2007; Scannapieco & Oh 2004). Such AGN 'feedback' would help resolve some of the remaining discrepancies between hierarchical models of galaxy evolution – implying a rather gradual assembly of massive galaxies – and observations, which suggest that massive galaxies formed most of their stars at high redshift, whereas star formation at later epochs was strongly suppressed. Observationally, a picture is emerging where radio jets may play

a large role in transforming the energy ejected by the AGN into kinetic and thermal energy of the interstellar medium of the host galaxy. Observations of radio-loud AGN (e.g., Heckman et al. 1991b,a; Morganti et al. 2005; Emonts et al. 2005; Best et al. 2005, 2006; Nesvadba et al. 2006, 2007; McNamara & Nulsen 2007; Nesvadba et al. 2008; Holt et al. 2008; Baldi & Capetti 2008; Fu & Stockton 2009; Humphrey et al. 2009) and a large number of hydrodynamical simulations (e.g., Krause 2005; Saxton et al. 2005; Heinz et al. 2006; Sutherland & Bicknell 2007; Merloni & Heinz 2007; Antonuccio-Delogu & Silk 2008) suggest that radio-loud AGN inject a few percent of their mechanical energy into the ambient gas, parts of which produce significant outflows of warm gas (Morganti et al. 2003, 2005; Emonts et al. 2005; Nesvadba et al. 2006, 2007; Holt et al. 2008; Nesvadba et al. 2008; Fu & Stockton 2009). However, most previous studies focused on the warm and hot gas at temperatures $\geq 10^4$K, and did not address the impact on the molecular phase, which is a serious limitation if we want to understand how the radio-loud AGN may regulate star formation in the host galaxy.

Observations with the Spitzer IRS spectrograph recently revealed a significant number of "H_2-luminous" galaxies, where the molecular gas does not appear associated with star formation (Haas et al. 2005; Appleton et al. 2006; Egami et al. 2006; Ogle et al. 2007, 2008, 2009; de Messières et al. 2009). The mid-infrared spectra of H_2-luminous galaxies are domi-

---

[*] Based on observations carried out with the IRAM Plateau de Bure Interferometer

nated by bright, pure rotation emission lines of warm molecular hydrogen, ($\mathscr{L}(H_2) = 10^{40} - 10^{43}\,\mathrm{erg\,s^{-1}}$), while classical star-formation indicators like a bright infrared continuum or strong PAH bands are weak or absent. Interestingly, Ogle et al. (2009) find that 30% of their radio-loud AGN taken from the 3CR are H_2 luminous, suggesting this may be a common phenomenon which could be related to interactions with the radio source. They also find a relationship between radio power and H_2 luminosity which may suggest the two are physically related.

To better understand the physical mechanisms causing this relationship, and to evaluate possible consequences for the gas properties and star formation in the host galaxy, we have started CO emission-line observations of H_2 luminous radio galaxies with the IRAM Plateau de Bure Interferometer. Our goal is to constrain the physical properties and masses of the multiphase warm and cold gas in these galaxies, and to measure the gas kinematics. Here we present a detailed analysis of the multiphase gas content, energetics, and dissipation times of the most extreme H_2-luminous radio galaxy 3C326 N at z=0.09 (Ogle et al. 2007, 2008, 2009), based on our new CO(1-0) observations, as well as existing mid-infrared Spitzer and SDSS optical spectroscopy. Specifically we address three questions: What powers the H_2 emission in this galaxy? What is the physical state of the molecular gas, and perhaps most importantly, why is 3C326 N not forming stars?

We find that the interstellar medium of 3C326 N has very unusual physical properties, where the warm molecular gas may dominate the overall molecular gas budget (§4) and where the emission-line diagnostics suggest that the molecular as well as the ionized gas may be mainly excited by shocks (§3) giving rise to luminous line emission at UV to mid-infrared wavelengths. We also identify a significant outflow of neutral gas from Na D absorption profiles, which cannot be explained by star formation (§4.5). We propose a physical framework in which these observations can be understood as a natural consequence of the energy and momentum coupling between the gas phases, which is driven by the mechanical energy injection of the radio jet (§5). This scenario is an extension of the classical 'cocoon' model (e.g., Scheuer 1974; Begelman & Cioffi 1989) explicitly taking into account the multiphase character of the gas, with an emphasis on the molecular gas. We use our observational results to quantify some of the parameters of this scenario, including, perhaps most importantly, the dissipation time of the turbulent kinetic energy of the gas, and find that it is self-consistent and in agreement with the general characteristics of radio-loud AGN.

3C326 N shows evidence for a low star-formation efficiency, which is similar to other H_2 luminous radio galaxies with CO observations in the literature, as would be expected if 3C326 N was a particularly clear-cut example of a common, underlying physical mechanism that is throttling star formation (§6). Long dissipation times suggest that the gas may remain turbulent over timescales of 10^{7-8} years, of order of the lifetime of the radio source, or perhaps even longer (§5.3), while the energy supplied by the radio source may be sufficient to keep much of the gas warm for a Hubble time (§7) as required during the maintenance phase of AGN feedback.

Throughout the paper we adopt n $H_0 = 70\,\mathrm{km\,s^{-1}}$, $\Omega_M = 0.3$, $\Omega_\Lambda = 0.7$ cosmology. In this cosmology, the luminosity distance to 3C326 N is $D_L^{326N} = 411.5$ Mpc. One arcsecond corresponds to a projected distance of 1.6 kpc.

2. Observations

2.1. The H_2 luminous radio galaxy 3C326 N

We present an analysis of the powerful H_2 luminous radio galaxy 3C326 N at z=0.089 (Ogle et al. 2007, 2009). Pure rotation, mid-infrared H_2 lines in 3C326N have an extraordinary luminosity and equivalent width (Ogle et al. 2007). The total emission-line luminosity of 3C326N is L(H2) = $8.0 \pm 0.4 \times 10^{41}\,\mathrm{erg\,s^{-1}}$ (integrated over the lines S(1) to S(7)), corresponding to $17 \pm 2\%$ of the infrared luminosity integrated from 8-70μm. This is the most extreme ratio found with Spitzer so far. The H_2 line emission is not spatially or spectrally resolved, implying a size $<4''$ ($\sim$6 kpc at the distance of the source), and a line width FWHM$\leq$2500 km s^{-1}.

3C326 N is remarkable in that it does not show evidence for strong star formation, in spite of a significant molecular gas mass of $\sim 10^9\,M_\odot$ (Ogle et al. 2007, 2009). This mass corresponds to a mean surface density of warm H_2 within the slit of the short-wavelength spectrograph of Spitzer of $30\,M_\odot\,\mathrm{pc^{-2}}$, a few times larger than the total molecular gas surface density of the molecular ring of the Milky Way (Bronfman et al. 1988). Generally, galaxies with similarly large molecular gas masses show vigorous starburst or AGN activity. However, in 3C326 N the luminosity of the PAH bands and 24 μm dust continuum suggest a star-formation rate of only $\sim 0.07\,M_\odot\,\mathrm{yr^{-1}}$, about 2% of that in the Milky Way. Given this large amount of molecular gas and the high mass surface density, the bolometric AGN luminosity of 3C326 N is also remarkably low.

2.2. CO millimeter interferometry

CO(1–0) emission-line observations of 3C326 were carried out with the IRAM Plateau de Bure Interferometer (PdBI) in two runs in January and July/August 2008 with different configurations. In January, we used the narrow-band and dual-polarisation mode, corresponding to a band width of 950 MHz, or 2740 km s^{-1}, with a channel spacing of 2.5 MHz. The 6 antennae of the PdBI were in the BC configuration at a central frequency of 105.85 GHz, corresponding to the observed wavelength of the CO(1–0) line at a redshift of z=0.089. The final on-source integration time for this run was 6.7 hrs (discarding scans with atmospheric phase instabilities). The FWHP of the synthesized beam in the restored map is $2.5'' \times 2.1''$ with a position angle of $23°$. Only data from this run were used for the CO emission-line measurements.

The presence of a 3mm non-thermal continuum from the radio source and relatively narrow receiver bandwidth made it difficult to rule out a possible contribution of a very broad CO(1–0) line (FWHM$>$1000 km s^{-1}) from the January 2008 data alone. We therefore re-observed 3C326 N in July and August 2008 with the goal of carefully estimating the continuum level, taking advantage of the 1.75 GHz bandwidth in the wide-band single-polarisation mode, corresponding to 4956 km s^{-1}. For these observations we used 5 antennae in the compact D-configuration. The final on-source integration time for this run was 5.2 hours (again, discarding scans with strong atmospheric phase instabilities). We detected the millimeter continuum at a level of S$_{3mm}$=0.99 mJy at the centimeter position of the radio source measured by Rawlings et al. (1990).

Data reduction and analysis relied on GILDAS (Pety 2005). The flux was calibrated against MWC349 and against reference quasars whose flux is monitored with the PdBI. We removed the continuum by assuming a point source at the position of

3C326 N with a flat spectrum of 1 mJy in the uv-plane. The data were then averaged in 71 km s^{-1}-wide velocity channels.

2.3. CO line emission

We show the continuum-free CO(1–0) emission-line map of 3C326 N in the left panel of Figure 1, integrated over 637 km s^{-1} around the line centroid. The central position is slightly offset from the millimeter continuum position (by 0.37$''$×0.80$''$ in right ascension and declination, respectively), corresponding to 1/3 to 1/6 of the beam size, respectively. Given the relatively low signal-to-noise ratio, this offset is not significant.

We measured the CO(1–0) line flux in different apertures to investigate whether the line emission may be spatially extended, finding a larger flux for elliptical Gaussian models than for a point source. This may suggest that the source is marginally spatially extended with a size comparable to our 2.5$''$×2.1$''$ beam. Results for the spectrum integrated over different apertures are summarized in Tables 1 and 2.

In Figure 2 we show our CO(1–0) spectrum of 3C326 N integrated over a 2.5$''$ aperture. The blue line shows the Gaussian line fit which gives a FWHM=350±40 km s^{-1} and an integrated emission-line flux of I$_{CO}$=1.0±0.2 Jy km s^{-1} (over a 5$''$ aperture, corresponding to the slit width of the IRS spectrum). The observed frequency corresponds to a redshift of z=0.0901±0.0001 and is similar to the observed redshift of the optical absorption lines within the uncertainties.

2.4. Optical spectroscopy

We complement these new millimeter observations of the cold molecular gas with publicly available optical spectroscopy from the Sloan Digital Sky Survey (York et al. 2000). This spectrum traces the warm ionized gas and the stellar continuum. It has signal-to-noise ratios of ∼20-30 in the continuum (measured at wavelengths around 5000-6000 Å). 3C326 N is significantly larger than the 3$''$ diameter of the SDSS fibers, hence these are near-nuclear spectra including light from the central 5 kpc. This is well matched to the 2.5$''$×2.1$''$ beam size of our IRAM millimeter observations, and to the 5$''$ slit width of the Spitzer-IRS spectra. The data cover the spectral range between [OII]$\lambda\lambda$3726,3729 and [SII]$\lambda\lambda$6716,6731 emission lines and the Ca H+K, Mg b, Na D absorption lines. All lines are relatively broad and spectrally well resolved at the spectral resolving power of the SDSS of R∼1800 (York et al. 2000). All measured line properties are summarized in Table 3. While the low resolution makes it difficult to resolve certain line doublets, it does allow us to measure velocity dispersions and to analyze the line profiles.

We used the publicly available *Starlight* package (Cid Fernandes et al. 2005) to fit the stellar continuum of 3C326 N, and to correct our emission-line measurements for the underlying continuum emission and stellar absorption lines. *Starlight* allows to fit the optical stellar continuum of a galaxy with a linear combination of simple stellar populations (SSPs) of different ages and metallicities. We used SSPs from the stellar population synthesis models of Bruzual & Charlot (2003) for a wide range of ages (from ∼ 10^7 yrs to several 10^{10} yrs) and metallicities (Z=0.0002-0.05). Wavelengths near strong emission lines are excluded from the fit. Unless stated otherwise, we will in the following only refer to the continuum-subtracted emission lines.

2.5. Emission-line kinematics

After subtracting the underlying continuum emission, we fitted the emission lines with Gaussian distributions, where line widths, fluxes, and redshifts are free parameters, except for the [OII]$\lambda\lambda$3726,3729; [OIII]$\lambda\lambda$4959,5007, [NII]$\lambda\lambda$6548,6583, and [SII]$\lambda\lambda$6716,6731 doublets, where we required the redshifts and line widths in the two lines of each doublet to be identical. For [OIII]$\lambda\lambda$4959,5007, [NII]$\lambda\lambda$6548,6583 we also required a flux ratio of 1/3 between the fainter and the brighter component. Results for individual lines are given in Table 3.

All lines are relatively broad with FWHM∼600 km s^{-1}. Redshifts and line widths are similar within the scatter of ∼ 10 km s^{-1} for all lines. Redshifts are consistent with the systemic redshift of z=0.0900±0.0001 which we obtained from the stellar absorption lines.

Careful inspection of the profiles of the relatively luminous, and spectrally well isolated [OIII]$\lambda\lambda$4959,5007 and [OI]$\lambda\lambda$6300,6363 lines reveals the presence of broad components with widths of FWHM=1635 km s^{-1} (Fig. 3).

To compensate for the difficulty of fitting broad components at relatively low signal-to-noise ratios with more narrow, superimposed components, we required that all four lines have the same redshift and line width, which yields reasonably good residuals. For the broad lines, we do not find a significant blueshift or redshift relative to the narrow components.

Due to the large line widths, several lines are blended, which makes a detailed fit more difficult (namely, these are [OII]λ3726,3729, Hα and [NII]$\lambda\lambda$6548,6583, and [SII]$\lambda\lambda$6716,6731). We did not attempt to fit multiple components to these lines.

2.6. Charcteristics of the Na D Lines

Fig. 4 shows the strong and broad Na D absorption feature that we detect in our SDSS spectrum of 3C326 N. We used the stellar population synthesis models described in §2.4 to estimate and remove the stellar component of the Na D line which can be significant in stellar populations. We also show Mg b in Fig. 4, which is purely stellar and illustrates the accuracy of the population synthesis fit.

Fig. 4 shows that the Na D lines in 3C326 N are very broad, so that we cannot directly measure the equivalent width of each component of the Na D doublet. We therefore modeled the lines using the atomic data complied in Morton (1991), allowing for changes in the turbulent velocity, velocity offsets, and covering fraction. Since we do not resolve individually the lines of the doublet, covering fraction and optical depth are degenerate unless the line shapes are accurately known. The lines are heavily blended and of insufficient S/N to have confidence in the line shapes.

We find that the Na D lines are heavily saturated so that we can only give lower limits on the NaI column densities. Values in the range $4-10 \times 10^{14}$ cm^{-2} (for C$_f$=1 and 0.5 respectively) are most likely. The Doppler parameter of the doublet is ∼800 km s^{-1} with a most probable velocity offset of about -350 km s^{-1} relative to the systemic redshift. For the highest column densities, corresponding to a covering fraction C$_f$ <0.5, the line profile begins to show a "flat core", which is not favored by the data. Therefore, it appears that the best fitting models favor a relatively high covering factor. We note that the best fit Doppler parameter and velocity offset are not very sensitive to the range of columns and covering fractions explored.

3. Spectral diagnostics

The characteristics of the interstellar emission lines can be powered and driven by a number of different astrophysical processes, in particular, energetic photons from starbursts and AGN, or shocks from the mechanical energy injected into the ISM by stars, AGN, or various dynamical processes. Line ratios and equivalent widths can therefore yield valuable insight into the underlying processes in galaxies, a fact that has been used at optical wavelengths since nearly three decades (e.g. Baldwin et al. 1981; Veilleux & Osterbrock 1987). Somewhat in analogy with these optical diagnostics, we will now develop a diagnostic diagram based on CO(1-0), purely rotational H$_2$, and PAH emission, in order to investigate the physical mechanism that is giving rise to the luminous H$_2$ line emission in 3C326 N, before analyzing the optical line ratios to infer the shock properties from the ionized gas, using the radiative hydrodynamic shock models of MAPPINGs III (Allen et al. 2008), an extension of the models of Dopita & Sutherland (1995, 1996).

3.1. H$_2$ line emission as shock diagnostics

The first rotational lines of H$_2$ are the dominant cooling lines for molecular gas over a wide temperature range of $\sim 10^{2-3}$ K. Since critical densities for the S(0) to S(3) lines are moderate (10 to 10^4 cm^{-3} in molecular gas at 500 K Le Bourlot et al. 1999), the lowest rotational states of H$_2$ will be populated by collisions rather than fluorescence. H$_2$ emission lines may originate from a number of processes. H$_2$ is often being associated either with the UV radiation from young stars, or with X-ray heating in photon or X-ray dominated regions. For the cooling flow of Perseus A, Ferland et al. (2008) proposed cosmic-ray heating as the dominant mechanism, whereas Guillard et al. (2009) find that dissipation of mechanical energy is the most plausible process to explain the luminous H$_2$ line emission along the galaxy-wide shock in the nearby interacting group Stephan's Quintet.

The CO(1-0) emisson-line luminosity is associated with the cold molecular phase, to the extent where it is commonly used to estimate the cold molecular gas mass (e.g., Solomon et al. 1997). In star-forming regions, PAH emission is found along the surfaces of molecular clouds heated by UV photons, but not within HII regions, where PAHs are be destroyed (e.g. Cesarsky et al. 1996; Tacconi-Garman et al. 2005). In addition, on galactic scales, a significant fraction of the PAH emission may be related to the diffuse interstellar medium rather than star-forming regions, as argued by Draine & Li (2007) based on the modelling of the dust emission of SINGS galaxies. In both cases, the PAH emission are be powered by UV photons.

Based on these arguments, we propose to use the ratio of H$_2$ to CO(1-0) line emission as a measure of the total heating of the molecular gas per unit molecular gas mass. The ratio of PAH to H$_2$ emission yields the contribution of UV photons to the total H$_2$ heating. In Fig. 5 we combine both line ratios into one diagnostic diagram. Black lines show the line ratios derived for PDR models to illustrate in which parts of the diagram the H$_2$ heating is dominated by UV photons. We estimate the H$_2$ line emission in PDRs based on the calculations of Kaufman et al. (2006). For the PAH emission, we have used the results of Draine & Li (2007) for a PAH-to-dust mass fraction $q_{PAH} = 3.55\%$, the median value for galaxies with Galactic metallicity in the SINGs sample (Draine & Li 2007).

Star-forming galaxies from the SINGS survey fall into the portion of the diagram spanned by the PDR models. Their positions suggest a ratio between the intensity of the UV field and the gas density of about 0.1 to 1 cm^{-3}, and the UV intensity several times that in the solar neighbourhood. Galaxies that have higher H$_2$/PAH emission-line ratios than those expected for PDRs require another heating mechanism other than UV photons. For the SINGS AGN host galaxies, Roussel et al. (2007) argue that X-ray emission from the AGN is unlikely. For their H$_2$-luminous radio galaxies, including 3C326 N, Ogle et al. (2009) rule out X-ray and disfavor cosmic ray heating. By analogy with the shock in Stephan's Quintet (Guillard et al. 2009) they propose that the H$_2$ emission may be powered by mechanical heating of the gas, perhaps due to interactions with neighbouring galaxies or – having a sample of galaxies taken from the 3CR – with the powerful radio-loud AGN. Our detailed analysis of 3C326 N provides a physical framework for how the radio source and the H$_2$ line emission may be related.

3.2. Optical emission-line diagnostics

In the previous section we presented a new, 'molecular' diagnositics to argue that the luminous H$_2$ emission in 3C326 N (as well as other H$_2$ radio galaxies) may be powered by the dissipation of mechanical energy in the interstellar medium of the host galaxy. It may be illustrative to use our SDSS spectra to compare this result with the optical diagnostics.

Table 3 lists the fluxes measured for various optical emission lines in 3C326 N. Comparison with the classical BPT-diagrams (Baldwin et al. 1981; Veilleux & Osterbrock 1987; Kewley et al. 2006) shows that 3C326 N falls within the LINER (Heckman 1980) part of the diagrams, similar to all H$_2$ luminous radio galaxies of Ogle et al. (2009) and also the galaxy-wide shock in Stephan's Quintet (Xu et al. 2003).

The excitation mechanism of the atomic lines in LINERs is a long-standing issue in the literature where some studies favor photo-ionization by the AGN (e.g., Veilleux & Osterbrock 1987) while other studies propose shock excitation (e.g., Clark et al. 1998; Dopita et al. 1997; Monreal-Ibero et al. 2006). Dopita & Sutherland (1995, 1996) show that the spectral characteristics of LINERS can be modeled with excitation from fast, radiative shocks if one ignores the emission from the radiative precursor of the shock, i.e., the ionization of the interstellar gas ahead of the shock by the UV radiation of the shock itself.

The radiative precursor of a fast shock moving into low-density gas adds an emission component which has the spectral characteristics of photoionized gas with a high ionization parameter. However, the line ratios in 3C326 N, in particular the ratio between the [NeII]/[NeIII] lines in the mid-infrared, suggest a low ionization parameter. This apparent contradiction can be resolved if the interstellar medium of 3C326 N is clumpy, which would enhance the escape fraction of hard ionizing photons simply for geometrical reasons. As in the shock of Stephan's Quintet, most of the gas in 3C326 N is in H$_2$ at densities $n_H > 10^3$ cm^{-3} much higher than the density of the ionized gas (Guillard et al. 2009), in good agreement with this scenario.

Quantitatively, using the models of Allen et al. (2008) for 3C326 N, we find that the ratios between the main optical lines in Table 3 are close to those of a 250 km s^{-1} shock moving into ionized gas with a 1 cm^{-3} preshock density and a low magnetic parameter, $B/\sqrt{n} < 1$ μG cm$^{-3/2}$. Observed and modelled line ratios are compared in Table 4. A detailed analysis of the alternative models (and model parameters, as done in Dopita et al. 1997) for the interaction between radio jet and interstellar medium in M87 is beyond the scope of this paper. The results

will guide us in approximating the likely values of the most important shock parameters: velocity and pre-shock gas density.

We also determine the bolometric luminosity of the ionized gas from the observed Hβ luminosity. We used Equations 3.3 and 3.4 of Dopita & Sutherland (1996) to estimate the ratio of Hβ luminosity, $\mathscr{L}_{H\beta}$, to the total luminosity produced by the shock, $\mathscr{L}_s$ scales as $\mathscr{L}_s / \mathscr{L}_{H\beta} = 300 \times V_{s,100}^{0.59}$, where V$_{s,100}$ is the shock velocity in multiples of 100 km s^{-1}. The large correction factor is due to the much larger brightness of the UV emission lines relative to the optical line emission, which we did not observe. With the measured Hβ flux and using this model at face value, we find $\mathscr{L}_s \sim 2 \times 10^{43}$ ergs s^{-1}, a factor $\sim$20 more than the total H$_2$ line luminosity in the S(0)-S(7) rotational lines (Ogle et al. 2009), and corresponding to the isobaric cooling of gas at temperatures of $\sim 10^6$ K for a mass flow of order 1000 M$_\odot$ yr^{-1} through the shock. This mass flow is very large, and we will discuss in §5.3 how this result can be interpreted as a repeated mass cycling of gas phases driven by interactions between the radio jet and the multiphase interstellar medium of the host galaxy. Obviously, due to the uncertainties in the measurement and modeling all of these values have uncertainties of factors of a few.

It is well possible that not all of the optical line emission is excited mechanically. The dynamical interaction between gas phases must include turbulent mixing between the cold and hot gas, which produces extreme UV radiation along the surfaces of cold clouds. This radiation is an additional, and maybe significant, source of ionization powered by the thermal, not the kinetic, energy of the cocoon. Crawford & Fabian (1992) show that this mechanism could account for parts of the line emission in ionized gas in cooling flows, consistent with observed line ratios. In this case, the bolometric correction with respect to Hβ would be a factor about 100, or a factor ~ 3 lower than for shocks (Crawford & Fabian 1992). However, if this was to account for all of the observed line emission from ionized gas, it would imply mass cooling rates of few$\times$100 M$_\odot$ yr^{-1}, which is unrealistic for 3C326 N because it exceeds observational constraints for the central galaxies of cooling-flow clusters (Bregman et al. 2006, show this from OVI absorption line measurements.).

With this caveat in mind, we will in the following adopt a fiducial value of 1×10^{43} erg s^{-1}.

3.3. Photoionization by stars and the AGN

In the above estimates we assumed that all of the optical line emission is due to shocks, and that other processes like photoionization from star formation or the AGN can be neglected. With the low star-formation rate and faint AGN X-ray emission from 3C326 N this galaxy is ideally suited to set stringent limits on the contribution of these processes to the observed line emission. For example, the observed star-formation rate of ≤ 0.07 M$_\odot$ yr^{-1} would imply an Hα luminosity $\mathscr{L}(H\alpha) \sim 1 \times 10^{40}$ erg s^{-1} (corresponding to a Hβ luminosity of few $\times 10^{39}\mathscr{L}_\odot$) for a continuous star-formation history and using the models of Bruzual & Charlot (2003). This corresponds to $\sim 5\%$ of the measured Hα luminosity of 3C326 N.

We can also rule out a dominant role of the AGN in photoionizing the gas, for the simple reason that the [OIII]λ5007 luminosity alone exceeds the luminosity emitted in the X-ray. Ogle et al. (2009) find an X-ray luminosity of 4×10^{40} erg s^{-1} for 3C326 N, whereas our [OIII]λ5007 measurements indicate an [OIII]λ5007 luminosity of log$\mathscr{L}_{[OIII]} = 7 \times 10^{40}$ erg s^{-1} (including the extinction correction of a factor 2).

This simple comparison confirms our previous statement that most of the optical line emission in 3C326 N is produced by the shocked interstellar medium, in agreement with the emission-line diagnostics. We also note that the X-ray emission is too weak to power the observed infrared emission from warm dust, $(0.8 - 2.2 \times 10^{43}$ erg s^{-1} Ogle et al. 2006), but could be explained by heating of the dust associated with the molecular gas through the evolved stellar population.

4. Mass and energy budgets

The relative mass budgets of warm and cold molecular gas and the warm ionized gas provide important constraints on the physical and astrophysical conditions of a galaxy. Typically, in gas-rich, actively star-forming galaxies the amount of cold molecular gas exceeds the masses of warm molecular and ionized gas by factors $10-100$ (see Roussel et al. 2007; Higdon et al. 2006, for samples of nearby galaxies and ULIRGs, respectively). We will now show that this is not the case for H$_2$ luminous radio galaxies, before giving the energy estimates and the outflow properties implied by the observation of the broad, interstellar Na D absorption line. All masses, luminosities, and kinetic energies are summarized in Table 5.

4.1. Molecular gas mass

4.1.1. Direct estimate of the luminosity and mass of warm molecular gas

The mass of warm molecular gas in 3C326 has been estimated by Ogle et al. (2007, 2009) by fitting the H$_2$ S(0) to S(7) rotational line fluxes with 2 or 3 components at different temperatures where H$_2$ excitation and ortho-to-para ratios are assumed to be thermalized. This yields a mass of 1.0×10^9 M$_\odot$.

In the present analysis, we associate the H$_2$ emission with the dissipation of kinetic energy by the molecular gas. Therefore we follow a different approach to estimate the mass and luminosity of warm molecular gas. As in Guillard et al. (2009), we model the dissipation process with magnetic shocks in molecular gas, which maximizes the H$_2$ luminosity per total emitted power. In this sense, our results represent a lower limit to the dissipated energy required to account for the observed H$_2$ luminosity.

Each shock model includes a range of gas temperatures which depend on the shock velocity, pre-shock gas density and intensity of the magnetic field. We use the grid of models presented by Guillard et al. (2009) for proton densities of n$_H = 10^3$ cm^{-3} and 10^4 cm^{-3}, an initial ortho-to-para ratio of 3 and a magnetic parameter, B$/\sqrt{n_H} = 1\mu$G cm$^{-3/2}$.

The shock velocity is the only parameter that we allow to vary. A combination of three shocks is required to match the emission in all 8 H$_2$ lines, S(0) to S(7). These fits provide a scaling factor for each of the three shocks which represents a mass flow, the amount of gas traversing the shocks per unit time. As discussed in Guillard et al. (2009), this fit is not unique but the proposed solution may be used to quantify the relevant range of shock velocities, and to estimate the warm gas masses by multiplying the mass flows per gas cooling time, and the shock luminosities by integrating over all cooling lines.

The corresponding H$_2$ line fluxes are listed in Table 6 for models with two different gas densities, 10^3 and 10^4 cm^{-3}, respectively. They are smaller than the kinetic energy fluxes one may compute from the mass flow and shock velocity because some of the energy is transferred to the magnetic field. The luminosities of the mid-infrared H$_2$ lines are close to the bolometric

values obtained by integrating the emission in all lines because the H$_2$ rotational lines are the main cooling lines of magnetic shocks. Summing over the three shocks we estimate a total luminosity of 10^{42}erg s^{-1} for the molecular Hydrogen.

Table 7 lists the gas cooling times and H$_2$ masses down to temperatures of T=150 K for each of these models. The total mass we obtain for gas at temperatures larger than T=150 K, $1.3 - 2.7 \times 10^9 M_\odot$, is slightly larger than that derived by Ogle et al. (2009), and we will in the following assume a fiducial molecular gas mass of 2×10^9 M$_\odot$. The small difference between the estimates of Ogle et al. (2009) and our results is due to different ortho-to-para ratios and moreover, in our approach we include gas at lower densities, where the S(0) and S(1) lines are not thermalized.

4.1.2. CO(1–0) luminosity and total molecular gas mass

The CO emission-line luminosity is often used as an empirical measure of the mass of cold molecular gas, in spite of the caveat that CO is a trace molecule and therefore cannot be a reliable measure of the total gas mass without a good knowledge of the physical environment. In §2.3 we estimated an integrated CO(1-0) emission-line flux of I_{CO}=1.0±0.2 Jy km s^{-1} from our millimeter spectroscopy at the IRAM Plateau de Bure Interferometer, extracted from a 5″ aperture. Using Equation 3 of Solomon et al. (1997) we translate this value into a CO(1–0) emission-line luminosity of $L_{CO'}$=3.8×10^8 K km s^{-1} pc^2 at a redshift of z=0.090. Applying the usual H$_2$-to-CO conversion factor of 4 $M_\odot$/(K km s^{-1}pc^2) as determined for gas in the molecular ring of the Milky Way (Solomon et al. 1992), this would correspond to a mass of cold molecular gas of M$_{cold}^{326\,N}$ = 1.5×10^9 M$_\odot$.

Comparison with §4.1.1 shows that the amount of warm molecular gas measured directly from the mid-infrared lines is similar to the H$_2$ molecular mass inferred from the CO(1–0) flux estimated from our PdBI observations. This is a highly unusual finding compared to star-forming galaxies where the ratio of warm to cold molecular gas mass is of order 10^{-1} to 10^{-2} (Roussel et al. 2007; Higdon et al. 2006) for the same CO-to-H$_2$ conversion factor. However, it is not very different from the ratio of ∼ 0.3 found in molecular clouds near the Galactic center (Rodríguez-Fernández et al. 2001). In the Galactic center, unlike in ULIRGs, cold dust temperatures indicate that the gas cannot be heated by UV photons (Lis et al. 2001), but possibly by shocks or cosmic rays (Rodríguez-Fernández et al. 2001; Yusef-Zadeh et al. 2007).

In this context it is interesting that the molecular gas in the Galactic center is closely associated with X-ray emitting gas (Amo-Baladrón et al. 2009). All of these observational similarities suggest that the clouds in the Galactic center may serve as a nearby analog for the properties of the molecular gas in 3C326 N. From detailed studies of several molecular species in the Galactic center, Lis et al. (2001); Huettemeister et al. (1998) conclude that all of the molecular gas in this environment may be warm at temperatures above T=50 K. By analogy we caution that the usual distinction between cold and warm gas measured through CO line emission and infrared H$_2$ lines, respectively may not apply to 3C326 N. Most of the CO line emission in 3C326 N could in fact be associated with the warm gas. Observations of higher-J transitions are necessary to test this hypothesis. We used the RADEX LVG code (van der Tak et al. 2007) to verify that the intensity of the CO(1-0) line is relatively insentive to the gas temperature for a given CO column density.

Obviously, given these considerations, the standard conversion factor may not apply at all. With these caveats in mind, we will in the following assume that the two tracers do not represent the same gas, which would correspond to a total gas mass of at most 3.5×10^9 M$_\odot$.

4.1.3. Warm ionized gas mass

We can also estimate the mass of ionized gas in 3C326 N from our SDSS spectra. Assuming case B recombination and following Osterbrock (1989) we can estimate an ionized gas mass, M$_{HII}$ from the Hα emission-line luminosity, $\mathcal{L}_{H\alpha}$, by setting

$$M_{HII} = \frac{\mathcal{L}_{H\alpha}\, m_p}{h\, \nu_{H\alpha}\, \alpha_{H\alpha}^{eff}\, n_e^{-1}} = 9.73 \times 10^6\; \mathcal{L}_{H\alpha,41}\; n_{e,100}^{-1}\; M_\odot, \quad (1)$$

where m_p is the proton mass, h is Planck's constant, $\alpha_{H\alpha}^{eff}$ and $\nu_{H\alpha}$ are the effective recombination cross section and the frequency of Hα, respectively. $n_{e,100}^{-1}$ is the electron density in units of 100 cm^{-3}. The Hα luminosity, $\mathcal{L}_{H\alpha,41}$, is given in units of 10^{41} erg s^{-1}.

In order to estimate extinction-corrected, intrinsic Hα luminosities, we measure the Hα and Hβ fluxes from our SDSS spectra and compare with the expected Balmer decrement of Hα/Hβ=2.9. We find A$_{H\beta}^{326\,N}$=0.8 mag. This implies an extinction-corrected Hα luminosity of $\mathcal{L}(H\alpha)_{ext}^{326} = 2.8 \times 10^{41}$ erg s^{-1}.

We also need to constrain the electron densities in the optical emission-line gas, which we estimate from the line ratios of the density-sensitive [SII]$\lambda\lambda$6716,6731 emission line doublet. Fitting each line of the doublet with Gaussian profiles, we find a line ratio of R^{326N} = 1.3. This is near the low-density limit, and assuming an electron temperature of 10^4 K, these line ratios correspond to electron densities n$_e^{326}$=130 cm^{-3}. With these extinction-corrected Hα luminosities and electron densities, and using Equation 1, we estimate ionized gas masses of M$_{HII}^{326}$ = 2×10^7 M$_\odot$.

4.2. Kinetic energy provided by the radio source

3C326 has a powerful, large radio source of Mpc size and resides in a relatively low-density environment compared to powerful radio galaxies generally (Stocke et al. 1979; Willis & Strom 1978). There is some confusion in the literature regarding which galaxy, 3C326 N or the nearby 3C326 S is associated with the radio lobes. Both candidates have detected radio cores. Rawlings et al. (1990) argue that 3C326 N is the more plausible candidate, having the brighter stellar continuum (and greater stellar mass, Ogle et al. 2007). Only 3C326 N has luminous [OIII]λ5007 line emission consistent with the overall relationship between [OIII]λ5007 luminosity and radio power (Rawlings et al. 1990). 3C326 N appears unresolved at 8.5 GHz with a 2″ beam (Rawlings et al. 1990).

Estimating the intrinsic properties of radio jets, in particular their kinetic power and lifetimes, remains a challenge. The synchrotron emissivity of the radio jet depends on the intrinsic jet power and the ambient conditions, and the jet kinetic power is therefore not easily derived. Estimates based on theoretical arguments suggest factors of ∼10−1000 between radio luminosity and kinetic power (e.g. De Young 1993; Bicknell et al. 1997).

Given these uncertainties, it may be best to use empirical estimates of the jet kinetic power. Bîrzan et al. (2004, 2008) es-

timated the kinetic power of radio sources by comparing the necessary energy to inflate X-ray cavities in galaxy clusters with the luminosities of the radio sources that are inflating them. They find a factor ~ 100 between kinetic and bolometric radio luminosity, with a large upward scatter of up to factors of a few 1000, perhaps suggesting that the correlation is in fact a lower envelope. Using their scaling with the radio luminosity measured at 327 MHz, and measured radio flux, we find kinetic luminosities of $\mathscr{P}^{326}_{k,jet,327} = 4 \times 10^{44}$ erg s^{-1}. For fluxes measured at 1.4 GHz, we find $\mathscr{P}^{326}_{k,jet,1400} = 1.3 \times 10^{45}$ erg s^{-1}. Willis & Strom (1978) suggest a total energy content of 6×10^{59} erg in the radio lobes, which would correspond to a kinetic luminosity of 1.7×10^{45} erg s^{-1} for a fiducial lifetime of 10^7 yrs, in good agreement with our estimate based on the Bîrzan et al. relationship. Using the estimate of Merloni & Heinz (2007) instead, which relies on the 5-GHz core radio power, we find 2×10^{44} erg s^{-1}. The estimates derived with each method change, reflecting the uncertainties of each approach, but the overall result of this section holds, namely, that the kinetic luminosity is of order few$\times 10^{44-45}$ erg s^{-1}.

A closely related quantity is the lifetime of the radio source. Jet lifetimes may either be estimated based on radio spectral indices or estimates of the velocity with which the jet expands, the former typically giving significantly smaller values. For 3C326 specifically, Willis & Strom (1978) carefully investigated the multi-wavelength radio properties finding spectral ages of $1 - 2 \times 10^7$ yrs. Using their estimate of the Alfven speed and size estimate with our cosmology would yield a kinetic age of 6×10^7 yrs for most parts of the radio source, although a region that is somewhat spatially offset and has a different polarization angle, may be as old as $\sim 2 \times 10^8$ yrs. It is unclear whether this is due to an extended activity period, several activity outbreaks, or the second galaxy of the system, 3C326 S, which also has a (fainter) radio core.

4.3. Kinetic energy of the gas

We will now give rough estimates of the related kinetic energies in each phase i. The total kinetic energy in random motion is given by $E_{r,tot} = 3/2 \Sigma m_i \sigma_i^2$. m_i is the gas mass in each phase, and σ_i is the velocity dispersion for the ensemble of clouds derived from the widths of the emission lines (and given in Tables 1 and 3 for CO and the optical lines, respectively), where we set σ = FWHM/2.355.

From the optical and millimeter spectroscopy we have direct measurements of the line width, which is FWHM~ 600 km s^{-1} for the optical lines, and FWHM~ 350 km s^{-1} for the CO lines. Fig. 2 illustrates that due to the relatively low signal-to-noise ratio per bin in the CO spectrum, we may underestimate the line width, which could plausibly be as high as that of the Hβ line. The rotational H$_2$ lines are not spectrally resolved with IRS, yielding an upper limit of $\le$ FWHM$\sim 2500 km s^{-1}$, which is not very constraining. Therefore we do not have a direct constraint for the velocity dispersion of the warm molecular gas. The line widths of CO and the optical lines, which trace gas that is colder, and gas that is warmer than the warm H$_2$, respectively, are not very different (Figure 2), and in fact, the CO emission may be associated with the warm gas (§4.1.2). We therefore expect that the line widths of warm H$_2$ will be in the same range. Relatively similar velocity dispersions in all phases are expected if the observed line widths are primarily due to the velocity dispersion of the ensemble of multi-phase clouds.

Since these spectra are integrated, the line widths will be affected by large-scale motion within the potential of the galaxy. From the spatially-resolved velocity curves for 16 nearby powerful radio galaxies of Holt et al. (2008), we estimate that large-scale velocity gradients at radii of 3-5 kpc (corresponding to our aperture) will not greatly exceed 100 km s^{-1}. For a measured line width of FWHM$\sim 500 - 600$ km s^{-1} a velocity gradient of ≤ 100 km s^{-1} subtracted in quadrature will lead to a negligible correction of ~ 10 km s^{-1} (15 km s^{-1} for the measured CO line width of FWHM=350 km s^{-1}). Therefore we do not believe that the gravitational motion will have a large impact on our measurements. With the velocity and mass estimates given above and in §4, respectively, we obtain a total kinetic energy of $E^{326}_{rd,H2} = 5 \times 10^{57}$ erg for the cold and warm molecular gas. The ionized gas has a much smaller mass and a negligible kinetic energy of $\le 4 \times 10^{55}$ erg. Kinetic energies are summarized in Table 5.

4.4. Mass and energy loss rate of the neutral wind

In attempting to estimate the characteristics of the multiphase medium, absorption lines can play an important role. In §2.6 we described the detection of a significant interstellar component to the Na D absorption line in 3C326 N with a systematic velocity offset to the blue and a pronounced blue wing. This is very similar to what is frequently found in starburst galaxies (Heckman et al. 2000; Martin 2005, 2006), where blueshifted Na D absorption is commonly interpreted as strong evidence that galaxies with intense star formation are driving energetic outflows.

Similarly for radio loud-AGN, Morganti et al. (2005) give compelling evidence for outflows of neutral material in radio galaxies based on studies of HI absorption line profiles at 1.4 GHz. They identify pronounced blueshifted components with velocities of up to ~ 2000 km s^{-1} in a number of galaxies, and a clear excess of blueshifted relative to redshifted material. They emphasize that they find blueshifted material in *all* radio galaxies with sufficiently deep HI spectroscopy, suggesting that outflows of neutral gas may be common amongst powerful radio-loud AGN. Of the two galaxies of Ogle et al. (2009) which have been observed in HI by Morganti et al. (2005), only one is detected with IRS. Interestingly, this is the galaxy with the more pronounced HI absorption, as expected if outflows and H$_2$ line emission are physically related. Therefore, overall, the Na D lines and the HI absorption are likely to be associated and share the same overall kinematics of the warm molecular gas. The relative velocity of the blue wing of the Na D line suggests a terminal velocity of ~ -1800 km s^{-1} for 3C326 N, within the range found by Morganti et al. (2005).

The association between the diagnostics of the warm neutral and molecular media suggests that we can directly estimate the mass and energy outflow rates in 3C326 using the properties of the Na D lines. However, to estimate the energy and mass loss rates of the outflow, we need to constrain the associated column density of neutral – and likely molecular – gas. The relationship between the column density of Hydrogen, N$_H$, and that of Sodium, N$_{Na}$, is determined by the abundance of Na relative to H and the ionization correction for Na (NaI and NaII). If we assume a solar abundance ratio, a depletion factor of 10 (Morton 1975), an ionization correction of a factor of 10, and a NaI column density of 10^{14} cm^{-2}, we find a total H column density of N$_H \sim 10^{21.7}$ cm^{-2}. As a fiducial value we adopt N$_H \sim 10^{21}$ cm^{-2}, but note that the depletion correction could be much higher (Phillips et al. 1984), in particular if the NaI is as-

sociated with the molecular gas. This opens the possibility that 3C326 N may have a significant component of warm neutral gas, but given the absence of HI spectroscopy, the exact amount of this gas is difficult to quantify, in particular, since parts of the Na I could be associated with outflowing molecular gas.

To directly associate the kinematics of the gas with an outflow rate of mass and energy, we assume a simple model of a mass conserving flow with a constant velocity, which extends from some minimal radius to infinity. This gives mass outflow rates of:

$$\dot{M}_{N_H} \sim 50 \, C_f \, \frac{\Omega}{4\pi} \, \frac{r}{1 \mathrm{kpc}} \, \frac{N_H}{10^{21} \, \mathrm{cm}^{-2}} \, \frac{v}{350 \, \mathrm{km \, s}^{-1}} \, M_\odot \, \mathrm{yr}^{-1}, \quad (2)$$

and energy loss rates of

$$\dot{E}_{N_H} \sim 10^{42.5} \, C_f \, \frac{\Omega}{4\pi} \, \frac{r}{1 \mathrm{kpc}} \, \frac{N_H}{10^{21} \, \mathrm{cm}^{-2}} \, \left(\frac{v}{350 \, \mathrm{km \, s}^{-1}}\right)^3 \, \mathrm{erg \, s}^{-1} \, (3)$$

respectively, where C_f is the covering fraction, $\frac{\Omega}{4\pi}$ is the opening angle, v is the outflow velocity. Covering fraction and opening angle are degenerate. The quantities in this estimate are not well constrained but useful for making an order of magnitude estimate. Covering fraction and column density are linearly related in both equations, and therefore our outflow estimates do not depend on the interplay between the two parameters. We have argued that the Na D lines are likely associated ay be a significant (but difficult to quantify without direct HI observations) reservoir of warm atomic gas associated with the molecular gas, or with the molecular gas itself. If either case, the size of the (marginally) resolved CO emission ($2.5'' \times 2.1''$) is likely similar to the size of the Na D absorbing region. If we take the geometrical mean of the half beam width as the entrainment radius, $\sim$1.8 kpc, allowing for a covering fraction of 0.5 to 1, and corresponding column densities of $10^{21.3-21.7}$ cm^{-2}, an opening angle of the outflow of π, and an outflow velocity of 350 km s^{-1} corresponding to the offset velocity (and ignoring the Doppler parameter which suggest higher velocities), we find a mass outflow rate of about 30-40 M$_\odot$ yr^{-1} and an energy loss rate of $\sim 10^{42-43}$ ergs^{-1}.

In starburst galaxies, the energy loss rates estimated with the same method and assumptions correspond only to a few percent of the injected mechanical power (e.g. Heckman et al. 2000; Martin 2005). Most of the outflow energy is likely to be carried by the hot plasma. If the same factor approximately apply for 3C326 N, we would expect a mechanical power of a few $\times 10^{43}$ erg s^{-1} (§4.2).

4.5. Outflow Energtics: A Wind Without A Starburst

The outflow properties of 3C326 N are very reminiscent of what is observed in local starburst galaxies (e.g. Heckman et al. 2000; Martin 2005), which have column densities of $\sim$few$\times 10^{21}$ cm^{-2}, mass and energy outflow rates of a few to a few 10s M$_\odot$ yr^{-1} and 10^{43} erg s^{-1}, respectively, and reach maximal blueshifts of $\sim 400-600$ km s^{-1}. AGN and starburst activity often coincide making it difficult to uniquely identify the energy source that is driving the wind. For 3C326 N this is not the case. Ogle et al. (2007) estimated an upper limit of SFR$\leq$0.07 M$_\odot$ yr^{-1} for the total star formation rate. Assuming that all of this star formation occurs within regions covered by the $3''$ SDSS fibre, this would correspond to a star-formation intensity of SFI$\leq$ 0.004 M$_\odot$ yr^{-1} kpc^{-2}. This is more than an order of

magnitude lower than the SFI$\sim$ 0.1 M$_\odot$ yr^{-1} kpc^{-2} threshold found by Heckman (2003) for starbursts that drive winds. We come to a similar conclusion when comparing with the supernovae rate expected for constant star formation with SFR= 0.07 M$_\odot$ yr^{-1}. Using Bruzual & Charlot (2003) we find a supernova rate of 3.5×10^{-4} yr^{-1}. Assuming that all of the "canonical" energy release of a supernova, 10^{51} erg, will thermalize, we find an energy injection rate of 10^{40} erg s^{-1}, about three orders of magnitude lower than the measured kinetic energy in 3C326 N or the line emission of the warm ionized and molecular gas. For more realistic thermalization efficiencies of few tens of percent, the energy injection from supernovae will be even lower by factors of a few.

In addition, the terminal velocity that we measure is $\sim$3-4$\times$ greater than terminal velocities typically found in starburst-driven winds (which are of order few 100 km s^{-1} Heckman et al. 2000; Martin 2005, 2006) and similar to some of the most powerful starbursts (which have star-formation rates orders of magnitude higher than 3C326). Both arguments indicate that the outflow in 3C326 N is *not* related to star formation. This velocity is also significantly larger than what we may expect from velocities due to a possible interaction with the nearby galaxy 3C326 S (see the discussion in Ogle et al. 2007). The only plausible candidate driving this outflow is a radio-loud AGN.

5. Energy and momentum exchange in the multiphase cocoon

We will now use our observational results to construct a scenario for the interaction between jet and interstellar medium of the host galaxy, which explicitly includes the molecular gas. We will argue that the kinematics and emission-line luminosities of 3C326 N are most likely related to the energy injected by the radio jet, which is being dissipated by the multiphase interstellar medium of the host galaxy. We describe and quantify the energy flow and associated timescales.

5.1. Energy, mass and momentum flow

Much theoretical effort has been dedicated to describing the interactions of radio jets with the ambient medium (for early studies see, e.g., Scheuer 1974; Begelman & Cioffi 1989). Observational evidence that jets may have a profound influence on the interstellar medium of their host galaxies has been known for at least two decades (e.g., van Breugel et al. 1985; Pedlar et al. 1985; Tadhunter 1991; Eales & Rawlings 1993). The 'cocoon model' which describes interactions between radio jet and ambient gas in form of a 'waste energy basket' (Scheuer 1974) of hot, low-density, but high-pressure material that surrounds the thin relativistic jet. This 'cocoon' will expand into the ambient gas and may entrain matter ablated from denser clouds of colder material (e.g., Begelman & Cioffi 1989), drastically enhancing the efficiency with which the jet interacts with the gas of the galaxy compared to simple interactions along the jet working surface ('dentist's drill', Scheuer 1982). We will now extend this scenario by explicitly taking into account the energy, mass, and momentum exchange between different gas phases which result from the injection of mechanical energy by the radio source. This scenario represents the synthesis of our observational results discussed in §§3 to 4.5.

Fig. 7 illustrates our basic scenario of the energy flow in the cocoon. Part of the mechanical energy injected by the radio jet is ultimately transformed into thermal energy of the warm

atomic and molecular gas, giving rise to the observed line emission. A part of the jet kinetic power is also translated into thermal and bulk kinetic energy of the hot cocoon plasma (first box in Fig. 7). This plasma is strongly overpressurized and expands on a timescale shorter than its cooling time, thus driving a net outflow of multiphase gas with outflow rates of a few $\times 10$ $M_\odot$ yr^{-1} (§4.5). In addition, the ablation of cloud material by the hot medium may replenish the hot medium of the cocoon, which would help maintaining a high pressure as the cocoon expands, and enhance the lifetime of the cocoon. Dynamical interactions between the different gas phases drive fragmentation of the molecular clouds and turbulent motions between and within individual fragments (second box in Fig. 7). This may lead to entrainment of parts of the warm and cold medium in the hot wind as described for starburst-driven winds (Heckman et al. 2000).

This interaction between the molecular gas and the outflowing plasma creates a physical environment not very different from that produced by the galaxy-wide shock in Stephan's Quintet (Guillard et al. 2009; Appleton et al. 2006). Similar to the analysis of Guillard et al. (2009), we postulate that turbulent motion in the cocoon drives shocks with velocities that depend on the gas density. In a multiphase medium, differences in gas densities between the cold and hot gas are up to factors of 10^6. For a given ram pressure, this translates into a factor 10^3 in shock velocity. The shocks maintain the amounts of warm molecular and ionized gas that are necessary to explain the observed luminous line emission of the molecular and ionized gas (third box in Fig. 7). Due to the high density, shocks driven into magnetized molecular gas will be slow, with velocities of a few 10s of km s^{-1}, so that H_2 will not be destroyed, but becomes a main gas coolant. This is in agreement with our molecular diagnostic diagram in Fig. 5 and with the pure rotation H_2 line ratios, which are consistent with excitation through slow shocks (§3.1).

The gas cooling times for these shocks listed in Table 7 are very short, of order 10^4 yrs. In order to maintain the gas at the observed temperatures, the cocoon must inject energy over similar timescales. This is important, since these timescales are significantly shorter than the free-fall times of self-gravitating molecular clouds. This is evidence that the gas cannot form gravitationally bound structures and stars, simply because it is continually being stirred up by mechanical interactions with the radio source. We will discuss in §5.3 that the AGN may maintain such conditions over significant timescales (10^{7-8} yrs).

5.2. Efficiency of the energy transfer

Our scenario for powering the line emission and the outflow through mechanical interactions is only realistic if the efficiency of the power transfer in each step is ≤ 1. We have estimates for the jet kinetic power ($\geq$few $\times 10^{44}$ erg s^{-1}, §4.2) and the emission-line luminosity of H_2 and HII ($\sim 10^{43}$). The mechanical power necessary to drive the outflow is similar at an order-of-magnitude level (§4.5). Taken at face value, these estimates indicate that $\sim$10% of the jet kinetic luminosity are deposited within the cocoon, which shows that if our scenario of jet-powered line emission is indeed energetically plausible. The efficiency of the radio jet in driving an outflow – the ratio between the mechanical power carried by the outflow to the power deposited in the cocoon – is about 1. This value is comparable to that derived from observations of starburst-driven outflows (e.g. M82 Strickland & Heckman 2009).

5.3. Dissipation time and length of the H_2-luminous phase

If the radiation of luminous optical and infrared line emission is due to the dissipation of the kinetic energy of the warm and cold interstellar medium, then we can roughly estimate the dissipation time of the kinetic energy of the gas, simply by relating the measured kinetic energy and the emission-line luminosity. In §3.2 we found that the ionized gas, although negligible in the mass budget, dominates the radiative energy budget of the warm and cold interstellar medium with a bolometric luminosity of $\sim 1 \times 10^{43}$ erg s^{-1}, whereas the molecular gas emits a lower luminosity of 1×10^{42} erg s^{-1}. In §4.3 we estimated that the kinetic energy of the molecular gas is most likely $\sim 5 \times 10^{57}$ erg, about two orders of magnitude more than that of the warm ionized gas. (See also Table 5.)

We will now constrain the range of plausible dissipation times, assuming that the UV-optical emission of the ionized gas is powered by the turbulent kinetic energy, and fully participates in the dissipation process. In this case,

$$\tau_{diss} = \frac{3/2 \left(M_{ion}\sigma_{ion}^2 + M_{mol}\sigma_{mol}^2 \right)}{\mathscr{L}_{ion} + \mathscr{L}_{mol}} \sim 1.3 \times 10^7 \text{yr} \qquad (4)$$

But the dissipation time could be significantly larger if the UV-optical lines are not entirely powered by the turbulent energy. The molecular gas could be in a region where the hot plasma has already been accelerated, so that the kinetic energy of the hot wind could be powering the line emission. The direct interaction between the molecular gas and the sourrounding warm and hot gas could be powering the emission of the warm ionized gas. In this case, the kinetic energy of the wind would be the source powering the line emission, not the turbulence of the molecular gas. The kinetic power of the outflow estimated in §4.5 of 10^{43} erg s^{-1} exceed the emission-line luminosity of the ionized gas by about a factor 10. In the extreme case that this accounts for all of the optical line emission, we find for the dissipation time of the turbulent kinetic energy

$$\tau_{diss} = \frac{3/2 \left(M_{mol}\sigma_{mol}^2 \right)}{\mathscr{L}_{mol}} = 1.3 \times 10^8 \text{yr} \qquad (5)$$

These findings have two interesting consequences. First, the dissipation time is much longer than the cooling time predicted by our shock models for the molecular gas (§4.1.1), which is of order 10^4 yrs. This may imply that the turbulent environment of the cocoon feeds a mass and energy cycle similar to that described by Guillard et al. (2009) for Stephan's Quintet, where the gas undergoes many episodes of heating and cooling on "microscopic" scales, effectively maintaining an equilibrium between different gas phases on macroscopic scales. The large mass flow of order 1000 $M_\odot$ yr^{-1} (which we estimated in §3.2 from the H_β luminosity) is a natural outcome of this mass cycle. It is too large to be accounted for by the large-scale bow shock as the jet expands through the galaxy, but may plausibly be produced by shocks that are locally generated, as the dense molecular clouds move relative to the low-density, hot medium. Such a cycling between warm and cold gas phases may also be important for the exchange of momentum between the hot plasma and the warm/cold cloud gas and thereby for the entrainment of cloud gas into the flow.

Second, a dissipation time of $\sim 10^{7-8}$ yrs is significant compared to the lifetime of the radio jet (of order 10^7 yrs, §4.2), or even the duty cycle of jet activity or order 10^8 yrs estimated from

observations of 'rejuvenated' radio sources (e.g., Schoenmakers et al. 2000). If the dissipation time is similar to the lifetime of the radio source, then the energy content of the gas will reflect the *total energy injected by the radio source*, including the early stages of radio activity when the jet was confined within the inner regions of the galaxy, and when the interaction was likely to be particularly efficient. If it is even longer, then it may influence the interstellar medium and star-formation properties of the massive host galaxies of radio-loud AGN even on timescales beyond their 'active' phase. We will come back to this point in §7.3.

6. Molecular gas and star formation

(Cold) molecular gas and star formation are closely related, an observational fact which is now known since about 50 years: Gas surface densities and star formation intensities (star-formation rate surface densities) show a close relationship over several orders of magnitude ('Schmidt-Kennicutt relation' Schmidt 1959; Kennicutt 1998). Does the same relationship apply to H_2 luminous galaxies, where we suspect AGN feedback to be effective?

In Fig. 8 we show a diagram which is very similar to the classical Schmidt-Kennicutt relationship, namely the surface brightness of the $7.7\mu m$ PAH emission as a function of the mass surface density estimated from CO observations. We use the $7.7\mu m$ PAH feature rather than the infrared continuum luminosity as a tracer of star formation, because the continuum may suffer a non-negligible contribution from dust heating due to the AGN. Tadhunter et al. (2007) find that the $24\mu m$ and $70\mu m$ flux of powerful radio galaxies correlate with the [OIII]$\lambda5007$ emission-line luminosity which is considered a measure of the AGN power (e.g. Heckman et al. 2004). They interpret this correlation as evidence for dust heating through the AGN. Apart from the more generic remarks on using PAH emission as a tracer of star formation (§3.1), our approach is also justified by the empirical correlations between PAH emission and star formation found for starbursts (Calzetti et al. 2007; Pope et al. 2008).

Compared to the sequence spanned by galaxies taken from the SINGs survey (Roussel et al. 2007), we find that 3C326 N is offset from the best-fit correlation for the SINGs sources. This seems to be a general trend for H_2-luminous galaxies: We collected galaxies from the sample of Ogle et al. (2009) with CO(1-0) observations in the literature. Including 3C326 N, 4 galaxies have spatially-resolved CO observations in the literature (3C31, NGC5128 – Cen A, and 3C293 have been discussed by Okuda et al. 2005, Israel et al. 1990 and Evans et al. 1999, respectively). 6 more galaxies have CO(1-0) detections or sufficiently tight upper limits, which place them below the relationship marked by the SINGs galaxies. Thus, 9 of the 17 H_2-luminous galaxies of the Ogle et al. (2009) sample have integrated CO detections or sufficiently tight upper limits which place them below the relationship marked by the SINGs galaxies. Obviously, the offset would increase if instead we used the total molecular gas mass (including warm and cold gas). Note that for galaxies for which we only had integrated CO emission-line observations, we used a fiducial radius of 5 kpc. Compared to sources with spatially resolved CO observations, including 3C326 N, this is likely an upper limit, in which case the offset would be even larger. Since the PAH surface brightness is related to the star-formation intensity, the offset to lower PAH luminosities for a given molecular gas mass may imply lower star formation intensities for a given gas surface density than in the reference SINGs galaxies.

Interesting, all H_2 luminous radio galaxies have a roughly similar offset from the SINGs correlation as 3C326 N. This may be surprising, because 3C326 N is the most clear-cut case, and certainly not representative for the full sample. Some H_2-luminous radio galaxies have luminous CO line emission suggesting a molecular gas mass of up to a few $\times10^{10}$ $M_\odot$ (Evans et al. 1999; Papadopoulos et al. 2008), if the standard conversion factors roughly apply (§4.1.2). Ogle et al. (2009) list warm and cold molecular gas masses for a subset of their sample with CO emission-line observations. The ratio of warm to cold molecular gas in some of these galaxies is 10^{-1} to 10^{-2}, not very different from that in star-forming galaxies. Nonetheless, their offset from the sequence of star-forming galaxies suggest that the same process, that is turning cold gas into warm gas in 3C326 N may also be suppressing star formation in these galaxies (or else, change their CO luminosity).

We are not the first to note that star formation in radio galaxies with CO detections appears suppressed relative to radio-quiet galaxies. Okuda et al. (2005) and Papadopoulos et al. (2007) found the same effect for 3C31 and 3C293, respectively. Okuda et al. (2005) pointed out that the molecular disk in 3C31 may simply not be forming stars because it is Toomre-stable, being stabilized by the deep potential well of the massive galaxy. However, Koda et al. (2005) observe star-forming clumps within otherwise Toomre-stable disks, and conclude that another mechanism must be at work, perhaps cloud-cloud collisions, that will additionally heat the molecular disk and keep it stable against collapse.

In light of our previous discussion, heating through the radio source appears to be an attractive non-gravitational mechanism at least in galaxies that host radio-loud AGN, which may enhance the turbulence and heating in a molecular disk, preventing or suppressing gravitational fragmentation and gas collapse and ultimately star formation. For example Neumayer et al. (2007) find that the ro-vibrational H_2 emission lines in Cen A (NGC 5128) are broader than expected from the stellar velocity dispersion, although they have an overall similar velocity field. This would certainly agree with a scenario where a small fraction of the energy injected by the AGN into the multiphase interstellar medium of the host galaxy will finally contribute to increasing the turbulence in the cold gas disk, thus suppressing star formation in an observationally very subtle way. Detailed follow-up observations of a larger sample of H_2-luminous galaxies are certainly necessary to substantiate this speculation. We also note that we have not found any evidence for positive feedback as proposed by, e.g., van Breugel et al. (1985); Begelman & Cioffi (1989); Silk & Norman (2009). If positive feedback dominated in our galaxies, we would expect an offset to higher star-formation rates for a given gas mass in Fig. 8.

7. Implications of this scenario for galaxy evolution

The energy injected by powerful AGN into the interstellar medium and halo of galaxies may play an important role in determining the characteristics of galaxies in the local Universe. For example, the high metallicities, luminosity-weighted stellar ages, and relative abundances of α elements relative to iron suggest rapid, and truncated star formation in the early Universe followed by a long phase of (mostly) passive evolution (e.g., Pipino & Matteucci 2004) for massive galaxies. These observations are consistent with a phase of powerful AGN driven outflows in the early Universe. In fact, studies of powerful radio galaxies at z~ 2 with rest-frame optical integral-field spec-

troscopy reveal energetic outflows which have the potential of removing a significant fraction of the interstellar medium of a massive, gas-rich galaxy within the short timescales necessary to explain the super-solar [α/Fe] ratios and old luminosity weighted ages observed in massive ellipticals (Nesvadba et al. 2006, 2007, 2008). This "quenching" of star-formation by powerful radio jets is in broad agreement with theoretical models explaining the characteristics of massive galaxies. However, in addition to this quenching phase, the radio-loud AGN may also assist in maintaining low observed gas fractions afterwards by inhibiting star formation over cosmological timescales – "maintenance phase". This last phase is important since, even in the absence of mergers, subsequent gas infall and return from the evolving stellar population will replenish the reservoir of cold gas which must be prevented (at least partially) from forming stars.

We have presented a physically motivated picture where the ISM is regulated by the mechanical energy output of the AGN through the radio jet. In this picture, about half of the energy is being dissipated through turbulence in the molecular gas, and half is powering an outflow of warm neutral and ionized gas (HI, optical emission lines, and very likely gas at X-ray temperatures). The high turbulence in the molecular gas both heats it and leads to high velocity dispersions which inhibits efficient star formation. Most importantly, this leads to a natural feedback cycle where the relatively high velocity warm neutral and ionized gas is ejected into the halo and perhaps into the IGM, whereas the high energy dissipation in the molecular gas disrupts the clouds pushing them away from the nuclear region. Over time, these clouds will cool and "rain back down" into the deepest part of the gravitational potential, in analogy to molecular filaments in cool-core clusters (Revaz et al. 2008; Salomé et al. 2008). Morganti et al. (2009) detected a neutral Hydrogen cloud in the radio-loud early-type galaxy NGC315 seen in absorption and emission, which is redshifted relative to the systemic velocity of the galaxy and at a relative distance of a few kpc. This could perhaps be an example of such a filament of gas raining back. In addition, the stellar population will continue to feed the ISM with material which will also cool and descend into the potential well, if the material will not be ablated previously. This may once again fuel an AGN, leading to a self-regulating AGN fueling cycle.

But is this scenario limited to the peculiar gas conditions in H$_2$ luminous radio galaxies? We have so far focused our discussion on 3C326 N which is the most extreme H$_2$ luminous radio galaxy known and therefore well suited to study the physical mechanism responsible for the H$_2$ line emission. However, galaxies are complex astrophysical objects, where a wide spectrum of physical and astrophysical phenomena may act in parallel. In order to illustrate how different formation histories may lead to different observational signatures within a common physical framework, we will in the following contrast 3C326 N with 3C293 at z=0.045. We have chosen 3C293 because it has particularly luminous CO line emission (Evans et al. 1999, and unlike 3C326) and with CO line ratios suggesting the molecular gas is highly excited (Papadopoulos et al. 2008). It also has a significant outflow of neutral gas (Morganti et al. 2003, 2005; Emonts et al. 2005). Its H$_2$ emission-line luminosity, warm molecular gas mass and optical line ratios are very similar to those of 3C326 N (Ogle et al. 2009), which suggests that 3C293 may be a 'gas-rich analog' and thus a foil of 3C326 N.

7.1. Differing Star-formation Histories: Clues to the importance of molecular gas content?

3C326 N and 3C293 have very different star-formation histories. The spectrum of 3C326 N is consistent with an old stellar population with an age of $> 10^{10}$ yrs and a low overall extinction of A$_V$ $\sim$0.17 mag. At most a small fraction of the total stellar mass, $\leq 5\%$, formed recently ($\sim 1 - 2 \times 10^9$ yrs; Fig. 6). Within the 3$''$ aperture of the SDSS fiber, this would correspond to $3 \times 10^9 M_\odot$ of stars formed during the last 1-2 Gyrs, implying a star-formation rate of about $1 M_\odot$ yr^{-1} for a constant star-formation history. We note that this is more than a factor 10 greater than the upper limit on the current star-formation rate of ≤ 0.07 M$_\odot$ yr^{-1} estimated from the infrared emission.

For 3C293 we find a significantly more complex star-formation history (see also Tadhunter et al. 2005). Namely $\sim$ 80% of the stellar mass of 3C293 was formed at high redshift, $\sim$ 20% were formed in a more recent star-formation episode about $1 - 2 \times 10^9$ yrs ago (Tadhunter et al. 2005, found similar results). In addition, the equivalent widths and ratio of the Ca H+K absorption lines require a very young population with an age of $\sim 10^7$ yrs, consistent with the starburst implied by far-infrared luminosity (Papadopoulos et al. 2008). The current burst contributes <1% to the total mass of 3C293, and the star-formation rate of SFR$^{293}_{popsyn}$ $\sim$4 M$_\odot$ yr^{-1} is broadly consistent with the current SFR$^{293}_{IR}$= 7 M$_\odot$ yr^{-1} estimated from the infrared luminosity of 3C293 (Papadopoulos et al. 2008). To evaluate whether this fit is unique, we tested alternative star-formation histories with only one or two of the three populations. Fig. 6 illustrates that the three-component fit indeed is a significantly better representation of the data. The population synthesis fits also yield stellar mass estimates, but we need to correct for the 3$''$ fibre size of the SDSS, which is much smaller than the size of the galaxies. Doing this, we find stellar masses of M$^{326N}_{stellar} = 3 \times 10^{11}$ M$_\odot$ and M$^{293}_{stellar} = 7 \times 10^{11}$ M$_\odot$ for 3C326 N and 3C293, respectively.

7.2. Origin of the gas

3C293 has a $\sim 10\times$ larger reservoir of gas traced through CO line emission than 3C326 N. What is the likely origin of the gas in these galaxies? Both galaxies have nearby galaxies with which they are perhaps interacting. For the pair 3C326 N/S, we find a very low gas mass and red optical colors for both galaxies, suggesting this is a gas-poor system. Indeed our estimate of the stellar and gas mass suggests a gas fraction of only $\sim 1\%$. The star-formation history of 3C326 N appears quiescent and does not indicate that the galaxy was undergoing a starburst due to the interaction. Nonetheless, we may expect the accumulation of a significant amount of cold gas due to mass from its stellar population ($\sim$1 M$_\odot$ yr^{-1}) as well as perhaps accretion from the surrounding halo. How much gas will this likely be?

We use the analysis of Kennicutt et al. (1994) to estimate the amount of gas returned by a single-age stellar population into the interstellar medium over 10 Gyr of passive evolution. Kennicutt et al. (1994) find that depending on the details of the star-formation history and initial mass function, as much as 30-50% of the stellar mass formed in the burst may be returned into the ISM during 10 Gyr. From their Fig. 8 we estimate that the gas return after the first 0.5-1 Gyrs will be of order a few percent of the stellar mass. For the stellar mass of 3C326 N, and ignoring any other mechanism like subsequent star formation or feedback, this would correspond to a total gas mass of several 10^9 M$_\odot$ up to$\sim 1 \times 10^{10}$ M$_\odot$, factors of a few more than the

amount of cold and warm gas we observe in 3C326 N. In addition, with an infall rate of ~ 0.1-1 M$_\odot$ yr^{-1} of gas accreted from the halo (which appears plausible for early and late-type galaxies; Sancisi et al. 2008) over 10^{10} yrs, this gas mass may roughly double. An infall rate of $\sim 0.1 M_\odot$ yr^{-1} of neutral gas has also been estimated by Morganti et al. (2009) from the observation of a narrow, redshifted HI cloud seen in absorption and emission in the nearby, radio-loud early-type galaxy NGC315.

Hence, each of these processes alone could easily explain the observed gas mass of 3C326 N However, they yield gas masses that are significantly lower than the amount of gas necessary for forming the $\sim 10^{11}$ M$_\odot$ of stellar mass in 3C293 during the last Gyr, which is certainly consistent with the assumption of a merger-triggered starburst for this galaxy. So the difference could be in the "mass accumulation histories" of these two AGN.

7.3. Maintaining the low fraction of recent star-formtion

Despite these plausibly different accretion histories, both of the galaxies apparently have low star-formation efficiencies. We estimated that a total of $1 - 2 \times 10^{10}$ M$_\odot$ of warm/cold gas would accumulate in a massive early-type galaxy such as 3C326 N over a Hubble time while 3C293 acquired its gas during an interaction/merger. Is it plausible that the gas in both sources will be heated and substantial fractions removed by the mechanical energy of the jets?

Best et al. (2005) find that the number of radio sources is a strong function of radio power and stellar mass of the host galaxy for a sample of 2000 early-type galaxies with FIRST and NVSS observations taken from the SDSS. For example, for galaxies with stellar mass of $\sim 3 \times 10^{11}$ M$_\odot$ they estimate that $\sim 10\%$ of all galaxies have radio powers $\geq 10^{24}$ W Hz^{-1}, and propose that this may represent a duty cycle, where any given galaxy of this stellar mass will host a similarly powerful radio source for 10% of the time.

Statistically speaking, over 10 Gyrs, a given AGN in a few $\times 10^{11}$ M$_\odot$ galaxy would be active for a total of $\sim 10^9$ yrs (this total 'activity period' which may consist of many radio-loud phases with intermediate, quiescent phases). With the same reasoning as in §4.2 we estimate that a power $\geq 10^{24}$ W Hz^{-1} measured at 1.4 GHz will correspond to a kinetic power of order 10^{43} erg s^{-1}, or a total energy of a few $\times 10^{59}$ erg for a total activity time of 10^9 yrs (about 10% of a Hubble time). A few $\times 10^{58}$ erg of energy are necessary to unbind 10^{10} M$_\odot$ in gas from the potential of a galaxy with few $\times 10^{11}$ M$_\odot$ in stellar mass (Morganti et al. 2005; Nesvadba et al. 2006, 2008). Based on these simple energy considerations, it appears overall plausible that AGN in massive galaxies may regulate gas cooling through the energy injected by their radio sources over a Hubble time as expected for the "maintenance".

However, in addition to the energy requirement, we also have a timescale requirement, since gas cooling must be inhibited in-between phases of radio-loud AGN activity, if AGN are to shape the properties of the ensemble of (massive) galaxies. Several arguments may suggest that this could indeed be possible. First, the dissipation timescales we found in §5.3 of order 10^{7-8} yrs imply that significant fractions of the molecular gas will remain warm during all of the lifetime of the radio jet, and possibly (if the upper limit is more appropriate), also for a significant time afterwards. Interestingly, studies of 'rejuvenated' jet activity suggest timescales of about 10^8 years between activity episodes (Schoenmakers et al. 2000). Second, the mechanical energy injected by radio-loud AGN is sufficient to accelerate and perhaps remove significant amounts of gas. Even if parts

of the entrained material will not reach escape velocity, its density will decrease due to the larger volume. The mean free path of particles between collisions will be greatly enhanced, making the dissipation timescales accordingly longer and delaying the time until this gas will cool and rain back onto the galaxy. Third, the expelled gas may be reheated by the hot halo gas. Forth, the molecular gas we observe may only be transitory, where the molecules are formed by the ram pressure of diffuse gas (Glover et al. 2009) as a result of the dissipation of the turbulent energy. This process does not necessarily lead to the formation of gravitationally bound clouds, in which case the molecular gas will photodissociate and become diffuse when the turbulent pressure and the thermal pressure in the cocoon will drop.

8. Summary

We presented a detailed analysis of the physical gas conditions in the nearby powerful, H$_2$-luminous radio galaxy 3C326 N, which does not show the signatures of active star formation in spite of few $\times 10^9$ M$_\odot$ in molecular gas. With a remarkably large luminosity of $\sim 10^{42}$ erg s^{-1} of the mid-infrared H$_2$ emission lines (corresponding to purely rotational transitions of molecular hydrogen with temperatures > 100 K), 3C326 N is the most "extreme" H$_2$-luminous radio galaxy currently known (Ogle et al. 2007, 2009) A key ingredient of our analysis is the deep CO(1-0) millimeter spectroscopy of 3C326 N which we obtained with the IRAM Plateau de Bure Interferometer, another one is the discovery of a broad, blueshifted Na D absorption line, suggesting a significant outflow. We combine these data with the mid-infrared spectroscopy of Ogle et al. (2007) and optical spectroscopy taken from the SDSS to analyze the energy and gas budget in the cold and warm molecular, and warm neutral and ionized gas for 3C326 N. Our main conclusions are as follows:

(1) We estimate a warm molecular gas mass of $\sim 2 \times 10^9$ M$_\odot$, which is very similar to that derived from our CO(1-0) emission-line observations (1.5×10^9 M$_\odot$), assuming that the CO traces the cold molecular gas and that the "standard" conversion factor approximately applies. A ratio of unity of warm to cold gas mass is about 2 orders of magnitude larger than that found in star-forming galaxies. This indicates a distinct physical state of the molecular gas which may account for the low star-formation efficiency.

(2) Most of the line emission from molecular and ionized gas in 3C326 N is probably powered by the dissipation of mechanical energy through shocks. In analogy to the 'classical' optical emission-line diagnostics we propose a new diagnostic diagram based on the mid-infrared H$_2$, CO and PAH emission, in which 3C326 N and other H$_2$-luminous galaxies clearly fall outside the region where UV photons from the starburst may plausibly dominate the line emission.

(3) Interstellar Na D absorption in the SDSS spectrum of 3C326 N mark an outflow of neutral gas with outflow velocities of up ~ -1800 km s^{-1}, and most likely mass and energy loss rates of $30-40$ M$_\odot$ yr^{-1} and $\sim 10^{43}$ erg s^{-1}, respectively. These values are similar to those found in starburst-driven winds, but the star-formation intensity is orders of magnitude below what is necessary to drive a starburst-driven wind and doesnot provide sufficient energy. We propose that this is the sign of an AGN-driven wind.

(4) Based on these observations we propose a scenario where the outflow and H$_2$ line emission are intricately related and which represents an extension of the well-explored 'cocoon'-model of interactions between radio jets and the ambient gas, which includes for the physics of the molecular gas. In this scenario,the

H$_2$ line emission is powered by turbulence induced within dense clouds that are embedded in the expanding cocoon, with a dissipation time of $\sim 10^{7-8}$ yrs. Thus the kinetic energy of the gas may have been deposited during the early phases of radio-loud AGN activity, when the interaction efficiency between radio source and ISM was probably greatest. Dissipation times of 10^8 yrs are in rough agreement with the duty cycle of jet activity estimated from rejuvenated radio sources.

(5) Comparing PAH and CO surface brightness (in analogy to the "Schmidt-Kennicutt" diagram), we find a significant offset between 3C326 N and other H$_2$-luminous radio galaxies and star-forming galaxies. This suggests that 3C326 N and other H$_2$ luminouos radio galaxies have abnormally low star-formation efficiencies.

(6) Generalizing our results for 3C326 N we find that similar radio-loud episodes in massive galxies may balance the secular supply in cold gas through accretion and the mass return from evolved stars over a Hubble time. If radio-activity is a common, but episodic property of most massive early-type galaxies as suggested by Best et al. (2006), then the long dissipation times of up to $\sim 10^8$ yrs may have consequences for the population of massive galaxies as a whole.

We emphasize that this analysis can only be the first step towards an understanding of how radio-loud AGN regulate the physical conditions of the molecular gas and ultimately star formation in massive galaxies. Many fundamental questions remain, of which we can only list a few. In particular, dissipation times need to be better constrained, in order to infer whether the radio source has a lasting effect beyond the phase of radio activity. This should be addressed through detailed numerical modelling. Other questions can be answered observationally, for example, how is the mass redistributed? What fraction of the material escapes from the gravitational potential of the host galaxy and what fraction will ultimately rain back? What is the role of the AGN in gas-rich galaxies that are the likely outcome of a merger? Our analysis illustrates the importance of following a multi-wavelength approach if we seek to relate the physics and astrophysics of AGN feedback with the physical conditions of the interstellar medium including molecular gas in the host galaxy and the regulation of star formation.

References

Allen, M. G., Groves, B. A., Dopita, M. A., Sutherland, R. S., & Kewley, L. J. 2008, ApJS, 178, 20
Amo-Baladrón, M. A., Martín-Pintado, J., Morris, M. R., Muno, M. P., & Rodríguez-Fernández, N. J. 2009, ApJ, 694, 943
Antonuccio-Delogu, V. & Silk, J. 2008, MNRAS, 389, 1750
Appleton, P. N., Xu, K. C., Reach, W., et al. 2006, ApJ, 639, L51
Baldi, R. D. & Capetti, A. 2008, A&A, 489, 989
Baldwin, J. A., Phillips, M. M., & Terlevich, R. 1981, PASP, 93, 5
Begelman, M. C. & Cioffi, D. F. 1989, ApJ, 345, L21
Best, P. N., Kaiser, C. R., Heckman, T. M., & Kauffmann, G. 2006, MNRAS, 368, L67
Best, P. N., Kauffmann, G., Heckman, T. M., et al. 2005, MNRAS, 362, 25
Bicknell, G. V., Dopita, M. A., & O'Dea, C. P. O. 1997, ApJ, 485, 112
Bîrzan, L., McNamara, B. R., Nulsen, P. E. J., Carilli, C. L., & Wise, M. W. 2008, ApJ, 686, 859
Bîrzan, L., Rafferty, D. A., McNamara, B. R., Wise, M. W., & Nulsen, P. E. J. 2004, ApJ, 607, 800
Bregman, J. N., Fabian, A. C., Miller, E. D., & Irwin, J. A. 2006, ApJ, 642, 746
Bronfman, L., Cohen, R. S., Alvarez, H., May, J., & Thaddeus, P. 1988, ApJ, 324, 248
Bruzual, G. & Charlot, S. 2003, MNRAS, 344, 1000
Calzetti, D., Kennicutt, R. C., Engelbracht, C. W., et al. 2007, ApJ, 666, 870
Cesarsky, D., Lequeux, J., Abergel, A., et al. 1996, A&A, 315, L309
Cid Fernandes, R., Mateus, A., Sodré, L., Stasińska, G., & Gomes, J. M. 2005, MNRAS, 358, 363
Ciotti, L. & Ostriker, J. P. 2007, ApJ, 665, 1038
Clark, N. E., Axon, D. J., Tadhunter, C. N., Robinson, A., & O'Brien, P. 1998, ApJ, 494, 546
Crawford, C. S. & Fabian, A. C. 1992, MNRAS, 259, 265
Croton, D. J., Springel, V., White, S. D. M., et al. 2006, MNRAS, 365, 11
de Messières, G. E., O'Connell, R. W., McNamara, B. R., et al. 2009, ArXiv e-prints
De Young, D. S. 1993, ApJ, 405, L13
Dopita, M. A., Koratkar, A. P., Allen, M. G., et al. 1997, ApJ, 490, 202
Dopita, M. A. & Sutherland, R. S. 1995, ApJ, 455, 468
Dopita, M. A. & Sutherland, R. S. 1996, ApJS, 102, 161
Draine, B. T. & Li, A. 2007, ApJ, 657, 810
Eales, S. A. & Rawlings, S. 1993, ApJ, 411, 67
Egami, E., Rieke, G. H., Fadda, D., & Hines, D. C. 2006, ApJ, 652, L21
Emonts, B. H. C., Morganti, R., Tadhunter, C. N., et al. 2005, MNRAS, 362, 931
Evans, A. S., Sanders, D. B., Surace, J. A., & Mazzarella, J. M. 1999, ApJ, 511, 730
Ferland, G. J., Fabian, A. C., Hatch, N. A., et al. 2008, MNRAS, 386, L72
Friaca, A. C. S. & Terlevich, R. J. 1998, MNRAS, 298, 399
Fu, H. & Stockton, A. 2009, ApJ, 696, 1693
Glover, S. C. O., Federrath, C., Mac Low, M. ., & Klessen, R. S. 2009, ArXiv e-prints
Guillard, P., Boulanger, F., Pineau de Forets, G., & Appleton, P. 2009, A&A accepted
Haas, M., Chini, R., & Klaas, U. 2005, A&A, 433, L17
Heckman, T. M. 1980, A&A, 87, 152
Heckman, T. M. 2003, in Revista Mexicana de Astronomia y Astrofisica, vol. 27, Vol. 17, Revista Mexicana de Astronomia y Astrofisica Conference Series, ed. V. Avila-Reese, C. Firmani, C. S. Frenk, & C. Allen, 47–55
Heckman, T. M., Kauffmann, G., Brinchmann, J., et al. 2004, ApJ, 613, 109
Heckman, T. M., Lehnert, M. D., Miley, G. K., & van Breugel, W. 1991a, ApJ, 381, 373
Heckman, T. M., Lehnert, M. D., Strickland, D. K., & Armus, L. 2000, ApJS, 129, 493
Heckman, T. M., Miley, G. K., Lehnert, M. D., & van Breugel, W. 1991b, ApJ, 370, 78
Heinz, S., Brüggen, M., Young, A., & Levesque, E. 2006, MNRAS, 373, L65
Higdon, S. J. U., Armus, L., Higdon, J. L., Soifer, B. T., & Spoon, H. W. W. 2006, ApJ, 648, 323
Holt, J., Tadhunter, C. N., & Morganti, R. 2008, MNRAS, 387, 639
Huettemeister, S., Dahmen, G., Mauersberger, R., et al. 1998, A&A, 334, 646
Humphrey, A., Iwamuro, F., Villar-Martin, M., Binette, L., & Sung, E. C. 2009, ArXiv e-prints
Israel, F. P., van Dishoeck, E. F., Baas, F., et al. 1990, A&A, 227, 342
Kaufman, M. J., Wolfire, M. G., & Hollenbach, D. J. 2006, ApJ, 644, 283
Kennicutt, Jr., R. C. 1998, ApJ, 498, 541
Kennicutt, Jr., R. C., Tamblyn, P., & Congdon, C. E. 1994, ApJ, 435, 22
Kewley, L. J., Groves, B., Kauffmann, G., & Heckman, T. 2006, MNRAS, 372, 961
Koda, J., Okuda, T., Nakanishi, K., et al. 2005, A&A, 431, 887
Krause, M. 2005, A&A, 436, 845
Le Bourlot, J., Pineau des Forêts, G., & Flower, D. R. 1999, MNRAS, 305, 802
Lis, D. C., Serabyn, E., Zylka, R., & Li, Y. 2001, ApJ, 550, 761
Martin, C. L. 2005, ApJ, 621, 227
Martin, C. L. 2006, ApJ, 647, 222
McNamara, B. R. & Nulsen, P. E. J. 2007, ARA&A, 45, 117
Merloni, A. & Heinz, S. 2007, MNRAS, 381, 589
Monreal-Ibero, A., Arribas, S., & Colina, L. 2006, ApJ, 637, 138
Morganti, R., Oosterloo, T. A., Emonts, B. H. C., van der Hulst, J. M., & Tadhunter, C. N. 2003, ApJ, 593, L69
Morganti, R., Peck, A. B., Oosterloo, T. A., et al. 2009, ArXiv e-prints
Morganti, R., Tadhunter, C. N., & Oosterloo, T. A. 2005, A&A, 444, L9
Morton, D. C. 1975, ApJ, 197, 85
Morton, D. C. 1991, ApJS, 77, 119
Nesvadba, N. P. H., Lehnert, M. D., De Breuck, C., Gilbert, A., & van Breugel, W. 2007, A&A, 475, 145
Nesvadba, N. P. H., Lehnert, M. D., De Breuck, C., Gilbert, A. M., & van Breugel, W. 2008, A&A, 491, 407
Nesvadba, N. P. H., Lehnert, M. D., Eisenhauer, F., et al. 2006, ApJ, 650, 693
Neumayer, N., Cappellari, M., Reunanen, J., et al. 2007, ApJ, 671, 1329
Ogle, P., Antonucci, R., Appleton, P. N., & Whysong, D. 2007, ApJ, 668, 699
Ogle, P., Antonucci, R., Leipski, C., Appleton, P., & Whysong, D. 2008, in Astronomical Society of the Pacific Conference Series, Vol. 386,

Extragalactic Jets: Theory and Observation from Radio to Gamma Ray, ed. T. A. Rector & D. S. De Young, 15–+

Ogle, P., Whysong, D., & Antonucci, R. 2006, ApJ, 647, 161

Ogle, P. et al. 2009, A&A submitted

Okuda, T., Kohno, K., Iguchi, S., & Nakanishi, K. 2005, ApJ, 620, 673

Osterbrock, D. E. 1989, Astrophysics of gaseous nebulae and active galactic nuclei

Papadopoulos, P. P., Isaak, K. G., & van der Werf, P. P. 2007, ApJ, 668, 815

Papadopoulos, P. P., Kovacs, A., Evans, A. S., & Barthel, P. 2008, A&A, 491, 483

Pedlar, A., Unger, S. W., & Dyson, J. E. 1985, MNRAS, 214, 463

Pety, J. 2005, in SF2A-2005: Semaine de l'Astrophysique Francaise, ed. F. Casoli, T. Contini, J. M. Hameury, & L. Pagani, 721–+

Phillips, A. P., Pettini, M., & Gondhalekar, P. M. 1984, MNRAS, 206, 337

Pipino, A. & Matteucci, F. 2004, MNRAS, 347, 968

Pope, A., Chary, R.-R., Alexander, D. M., et al. 2008, ApJ, 675, 1171

Rawlings, S., Saunders, R., Miller, P., Jones, M. E., & Eales, S. A. 1990, MNRAS, 246, 21P

Revaz, Y., Combes, F., & Salomé, P. 2008, A&A, 477, L33

Rodríguez-Fernández, N. J., Martín-Pintado, J., Fuente, A., et al. 2001, A&A, 365, 174

Roussel, H., Helou, G., Hollenbach, D. J., et al. 2007, ApJ, 669, 959

Salomé, P., Revaz, Y., Combes, F., et al. 2008, A&A, 483, 793

Sancisi, R., Fraternali, F., Oosterloo, T., & van der Hulst, T. 2008, A&A Rev., 15, 189

Saxton, C. J., Bicknell, G. V., Sutherland, R. S., & Midgley, S. 2005, MNRAS, 359, 781

Scannapieco, E. & Oh, S. P. 2004, ApJ, 608, 62

Scheuer, P. A. G. 1974, MNRAS, 166, 513

Scheuer, P. A. G. 1982, in IAU Symposium, Vol. 97, Extragalactic Radio Sources, ed. D. S. Heeschen & C. M. Wade, 163–165

Schmidt, M. 1959, ApJ, 129, 243

Schoenmakers, A. P., de Bruyn, A. G., Röttgering, H. J. A., van der Laan, H., & Kaiser, C. R. 2000, MNRAS, 315, 371

Silk, J. & Norman, C. 2009, ApJ, 700, 262

Silk, J. & Rees, M. J. 1998, A&A, 331, L1

Solomon, P. M., Downes, D., & Radford, S. J. E. 1992, ApJ, 387, L55

Solomon, P. M., Downes, D., Radford, S. J. E., & Barrett, J. W. 1997, ApJ, 478, 144

Springel, V., Di Matteo, T., & Hernquist, L. 2005, MNRAS, 361, 776

Stocke, J. T., Adams, M. T., & Jensen, E. B. 1979, in Bulletin of the American Astronomical Society, Vol. 11, Bulletin of the American Astronomical Society, 716–+

Strickland, D. K. & Heckman, T. M. 2009, ApJ, 697, 2030

Sutherland, R. S. & Bicknell, G. V. 2007, ApJS, 173, 37

Tacconi-Garman, L. E., Sturm, E., Lehnert, M., et al. 2005, A&A, 432, 91

Tadhunter, C., Dicken, D., Holt, J., et al. 2007, ApJ, 661, L13

Tadhunter, C., Robinson, T. G., González Delgado, R. M., Wills, K., & Morganti, R. 2005, MNRAS, 356, 480

Tadhunter, C. N. 1991, MNRAS, 251, 46P

van Breugel, W., Miley, G., Heckman, T., Butcher, H., & Bridle, A. 1985, ApJ, 290, 496

van der Tak, F. F. S., Black, J. H., Schöier, F. L., Jansen, D. J., & van Dishoeck, E. F. 2007, A&A, 468, 627

Veilleux, S. & Osterbrock, D. E. 1987, ApJS, 63, 295

Willis, A. G. & Strom, R. G. 1978, A&A, 62, 375

Xu, C. K., Lu, N., Condon, J. J., Dopita, M., & Tuffs, R. J. 2003, ApJ, 595, 665

York, D. G., Adelman, J., Anderson, Jr., J. E., et al. 2000, AJ, 120, 1579

Yusef-Zadeh, F., Wardle, M., & Roy, S. 2007, ApJ, 665, L123
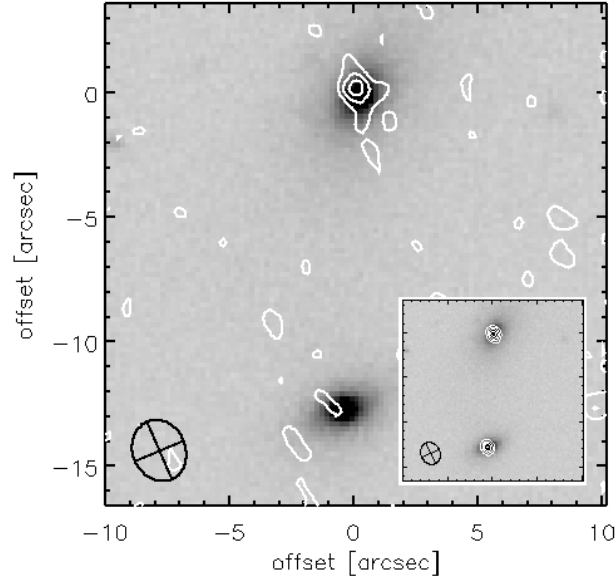
Fig. 1. Continuum-free CO(1-0) emission-line morphology of 3C326 N (white contours) superimposed on the SDSS R-band image of 3C326 N and 3C326 S. Contours are given for 3,4,and 5σ. The inset shows the same SDSS R-band with the line-free 3mm continuum morphology superimposed as white contours. We used the continuum morphologies to align the millimeter and optical data, assuming that the AGN reside in the nuclei of the galaxies. With this alignment, we find an offset of 0.7$''$ between the CO line emission and continuum (millimeter and optical) which, given the faintness of the line emission and much greater beam size, is not signicant. The ellipse in the lower left corner shows the beam size and position angle in both images.
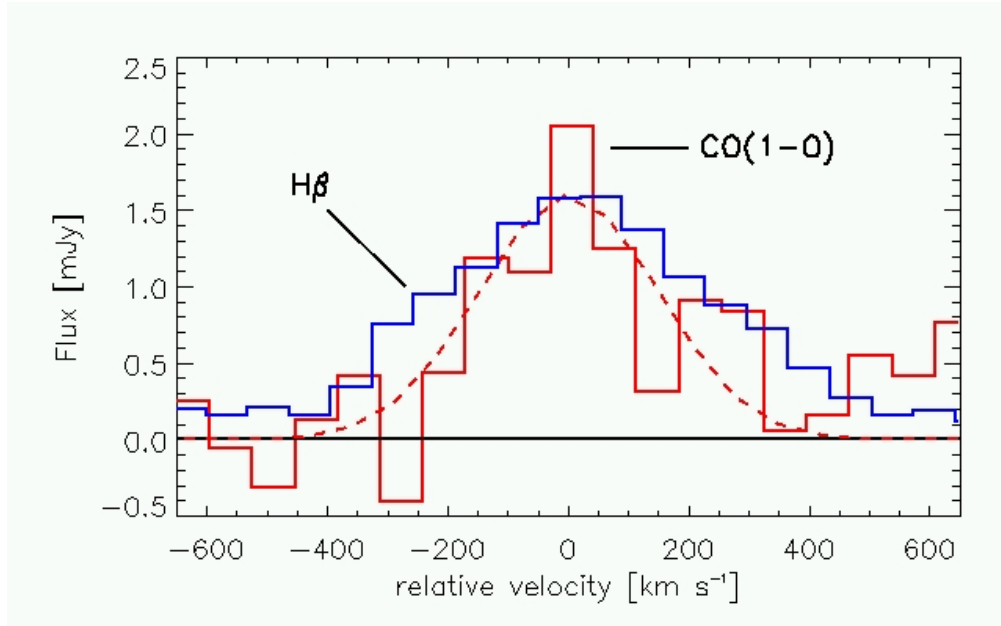
Fig. 2. CO(1-0) millimeter spectrum of 3C326N (red solid line), and Hβ line profile (blue solid line). The red hatched line shows our best fit to the CO(1-0) line profile.
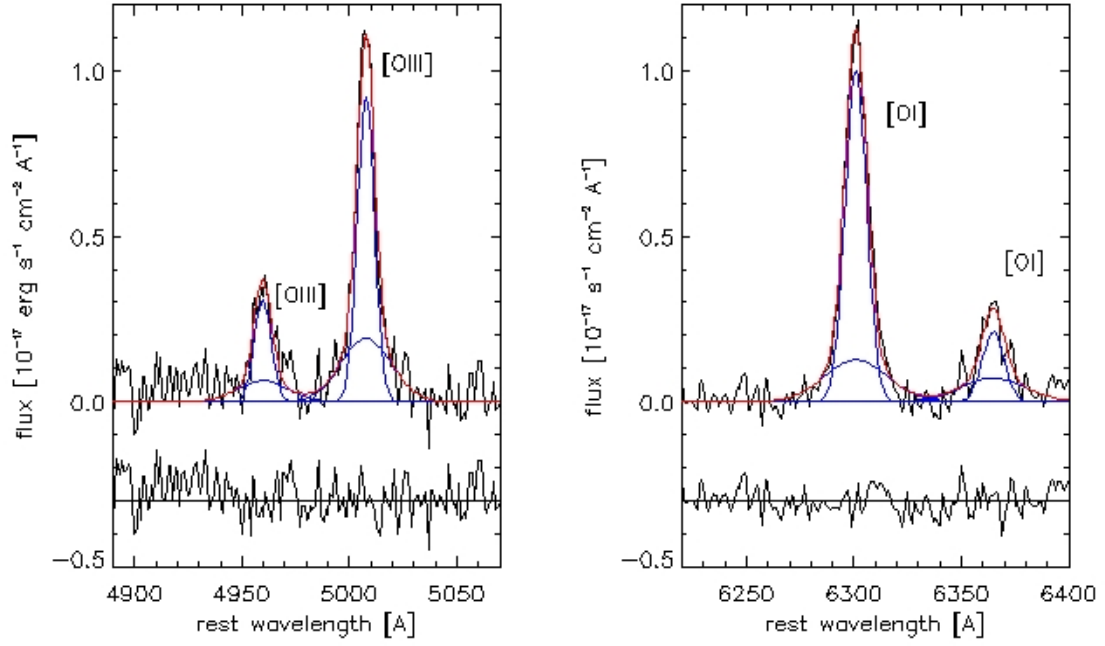
Fig. 3. Multiple-component fits to the [OIII]$\lambda\lambda$4959,5007 and [OI]$\lambda\lambda$6300,6363 line emission in 3C326 N. The broad component is best seen in the [OIII]λ5007 emission line. We assumed the same redshifts and line widths for all lines.
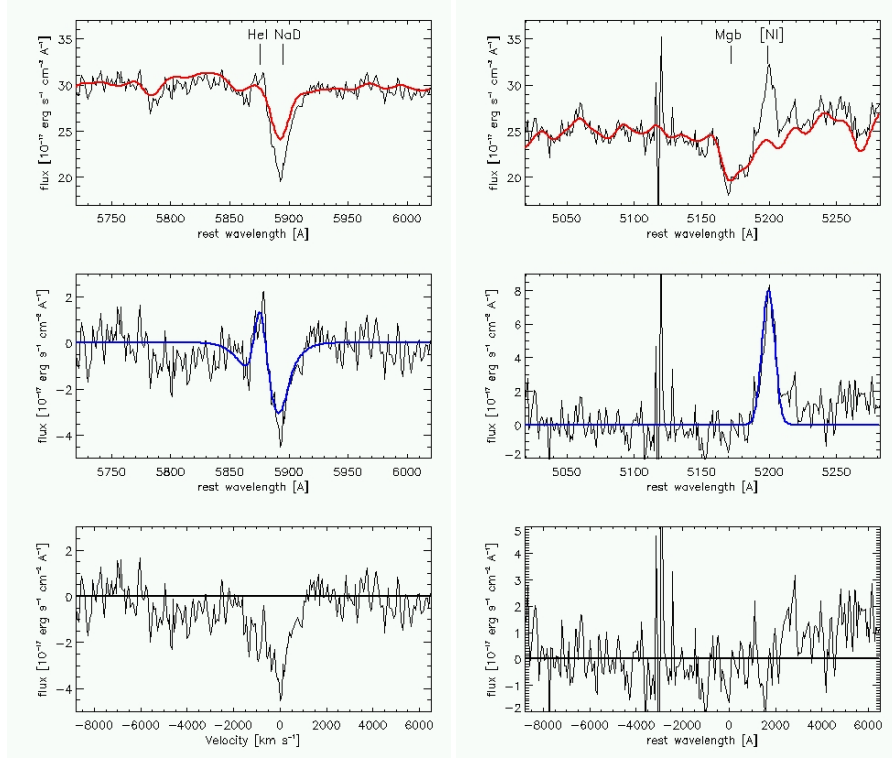
Fig. 4. *left:* NaD absorption line in 3C326 N. In the upper panel, the spectrum is shown in black, and the red line shows the stellar continuum for our best stellar population fit. The two NaD components are not resolved at R=1800. In the mid panel, we show the spectrum with the best-fit stellar continuum subtracted. The blue line in the mid panel marks our absorption line fit with HeIλ5876, and two NaD components (see text). In the lower panel, we show the spectrum with the stellar continuum and the HeI emission-line subtracted. The abscissa gives the velocity offsets relative to a systemic redshift of z=0.090. The Na D profile shows evidence for absorption with blueshifts of up to ~ -1800 km s^{-1}, and potentially, at lower signal-to-noise levels, of up to -6000 km s^{-1}. *right* The same for Mgb, a line which does not have a strong interstellar component. The residual (lower panel) is consistent with noise after subtraction of the stellar component and the NIλ5199 line.
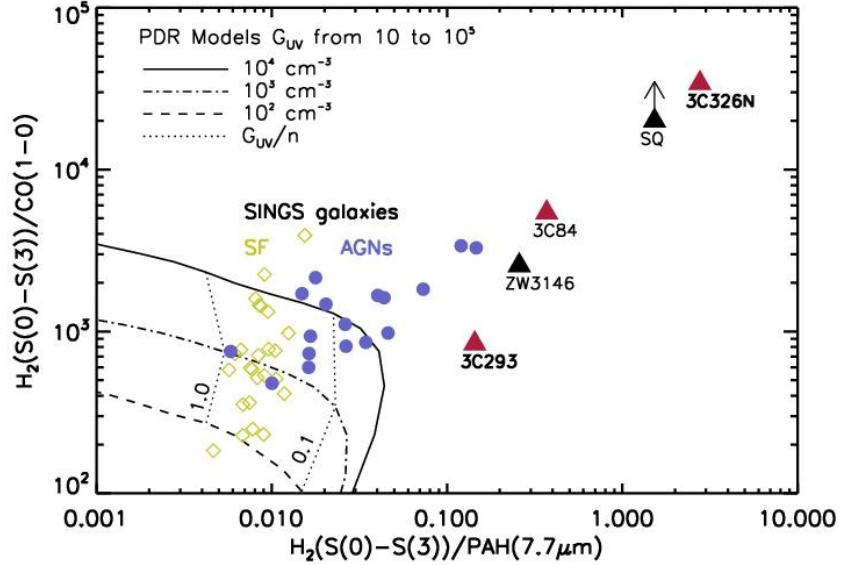
Fig. 5. Molecular diagnostic diagram to distinguish between AGN and star formation based on PAH bands, CO(1-0) and mid-infrared H$_2$ line emission. Lines mark PAH models with different assumptions on the UV radiation fields. See text for details.
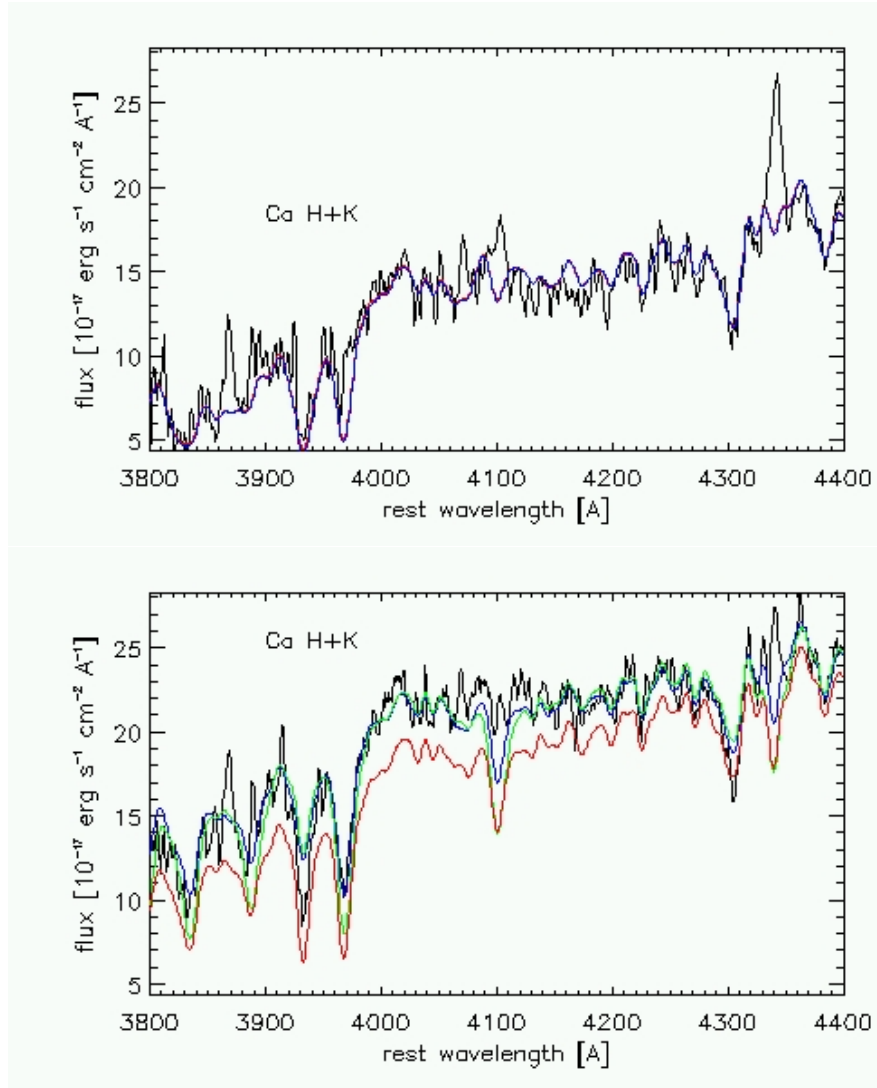
Fig. 6. Wavelengths near the 4000 Å break are most sensitive to the star-formation history of 3C326 N *(upper panel)* and 3C293 *(lower panel)*. The black line marks the SDSS spectum in each panel. Red, blue, and green lines mark the *Starlight* spectral fits for different star-formation histories, see §7.1 for details. *Upper Panel:* Red – Stellar population older than 10^{10} yr. Blue – Old and intermediate-age (few 10^9 yrs) stellar population. Both scenarios fit the data equally well. *Lower Panel:* Red – Stellar population older than 10^{10} yr. Green – Old and intermediate-age (few 10^{8-9} yr) population. Blue – Old , intermediate-age , and young (10^7 yr) stellar population. A single star-formation episode 10^{10} yrs ago does not appear as a good fit to the data; adding a young stellar population (consistent with the observed starburst) improves the fit to the Ca H+K lines, although significant differences remain, especially for the blue component.
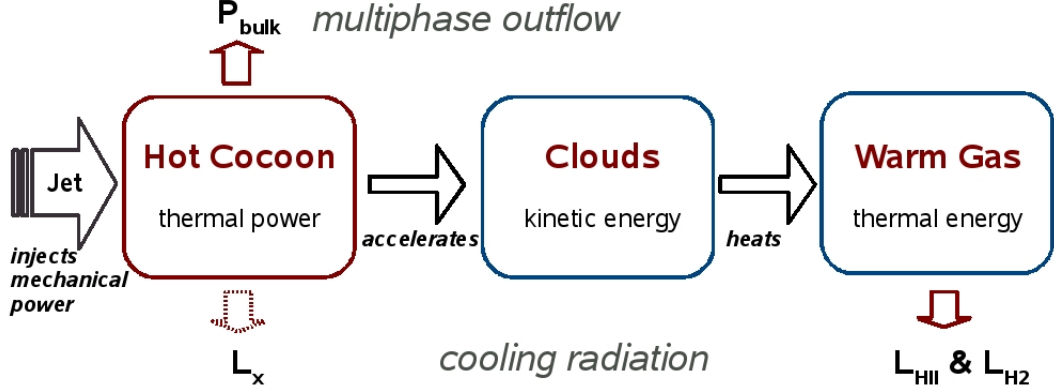
Fig. 7. This diagram outlines the energy flow within the hot "cocoon" that we propose to account for the HII and H$_2$ line emission and the outflow. The flow is powered by the interaction of the jet with the multiphase interstellar medium of the host galaxy (arrow to the left). It involves three energy reservoirs: *(boxes from left to right:)* the thermal energy of the hot plasma surrounding the relativistic radio source, the turbulent kinetic energy of the clouds embedded in the plasma and the thermal energy of the warm HII and H$_2$ gas. The arrows at the bottom represent the "cocoon" energy loss by radiative cooling, that to the top the transformation of thermal energy into bulk kinetic energy of the outflowing gas. The dissipation of the turbulent kinetic energy powers the H$_2$ and HII line emission. The high pressure plasma expands on a time scale shorter than its cooling time through X-ray emission driving a multiphase outflow. Our observational results suggest that the kinetic power of the outflow and the power radiated by the HII and H$_2$ gas are both $\sim 2 \times 10^{43}$ erg s^{-1}. The power input represents $\sim 10\%$ of the mechanical power of the jet.
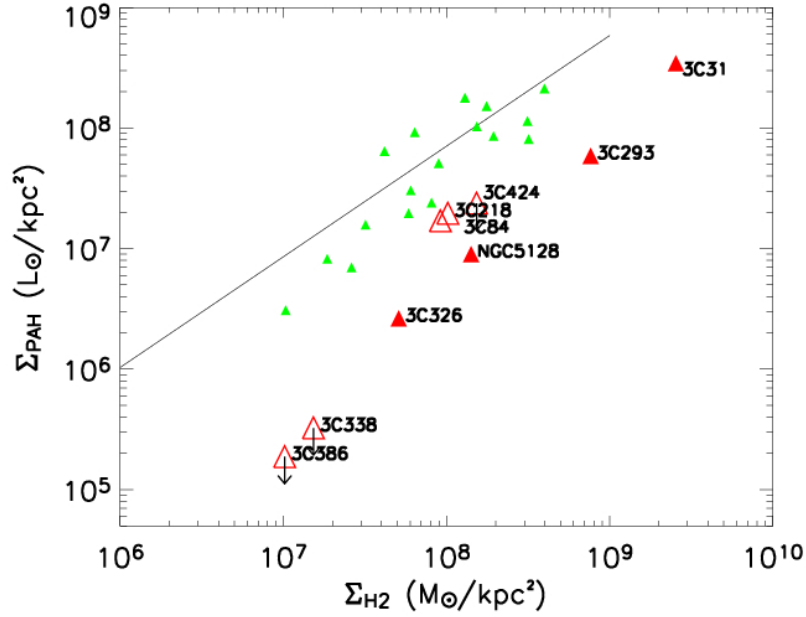
Fig. 8. Star-formation intensity (approximated by the intensity of PAH emission) as a function of CO(1-0) intensity, which approximates the mass of cold molecular Hydrogen. We assume a conversion factor appropriate for the Milky Way for all galaxies. Small filled green triangles mark the SINGs galaxies. The black line marks the best linear fit to this sample. Large red triangles mark H$_2$ luminous radio galaxies from the sample of Ogle et al. (2009), which have CO detections in the literature. Filled triangles mark galaxies with spatially resolved CO observations, whereas empty triangles mark galaxies with integrated measurements. Arrows mark galaxies with sensitive upper limits.

Aperture	v_{obs} [GHz]	Peak [mJy]	Width [km/s]
central pixel	105.744	1.0±0.1	349±87
2.5″×2.1″	105.744	1.1±0.2	351±98
5″×5″	105.744	1.5±0.3	351±98

Table 1. Observational results: CO(1–0) line-fit parameters of (1) the central pixel, (2) a spectrum integrated over a region of 2.5″ by 2.1″ (Dashed line in Fig. 2) and (3), a spectrum integrated over a 5″×5″ aperture corresponding to the slit width of the IRS spectrum.

Aperture	redshift	I$_{line}$ [Jy km s^{-1}]	L′ [K km s^{-1} pc^2]	F$_{cont}$ [mJy]
central pixel	0.0901	0.4±0.1	1.5±0.7×10^8	0.99
2.5″×2.1″	0.0901	0.5±0.1	2±1×10^8	0.99
5″×5″	0.0901	1.0±0.2	3.8±1×10^8	0.99

Table 2. Observational results: Intensity of the CO(1–0) emission line after subtraction of a point-like continumm source with a fixed value of 0.99 mJy at the position of the cm radio-source (Rawlings et al. 1990). L$'_{CO}$ was computed with the formula of Solomon et al. (1997). Results are given for (1) a spectrum integrated over a region of 2.5″ by 2.1″ (Dashed line in Fig. 2) and (2) a spectrum extracted from the the brigthest pixel of the CO(1–0) emission map.

line (1)	λ_{rest} (2)	redshift (3)	FWHM (4)	flux (5)
[OII]	3727.00	0.09019	623.006	9.62
Hβ	4861.30	0.09017	609.581	2.44
[OIII]	4959.90	0.08991	609.468	0.58
[OIII]	5006.90	0.09011	609.468	1.77
[OI]	6300.30	0.09013	612.329	2.22
[OI]	6363.80	0.09013	612.329	0.53
[NII]	6548.10	0.09014	601.356	2.38
Hα	6563.30	0.09007	596.118	9.30
[NII]	6584.10	0.09003	601.356	7.17
[SII]	6716.40	0.09019	605.053	4.86
[SII]	6730.80	0.09019	606.020	3.68

Table 3. Emission-line fluxes in 3C326 N. Column (1) – Line ID. Column (2) – Rest-frame wavelength in Å. Column (3) – Observed wavelength in Å. (3) – Redshift. (4) – Full width at half maximum in km s^{-1}, corrected for an instrumental resolution of 167 km s^{-1}, corresponding to a spectral resolving power of R=1800. (5) – Integrated line flux in units of 10^{-15} erg s^{-1} cm^{-2}. All values are derived after subtracting the best-fit stellar continuum (see text for details). For [OII]$\lambda\lambda$3727, additional uncertainties are due to the unknown line ratio between the two components of the doublets. These are insignificant for the FWHM and flux estimate, and amount to $\sim$ 70 km s^{-1} for the redshift, which however is not one of the important quantities for our analysis.

Line ratio (1)	observed (2)	shock (3)	shock & precursor (4)
Hβ/Hα	0.26	0.33	0.33
[OIII]/Hβ	0.72	0.82	1.48
[OI]/Hα	0.24	0.22	0.13
[NII]λ6584/Hα	0.77	0.68	0.47
[SII]/Hα	0.61	0.52	0.32
[SII]$\lambda\lambda$6716,6731	1.32	1.23	1.24
[NeII](12.81μm)/Hα	0.46	0.45	0.28
[NeII](12.81μm)/[NeIII](15.6μm)	>1.8	2.2	0.73

Table 4. Measured emission-line ratios in 3C326 N and expected ratios for a pure-shock model and a model assuming a shock and precursor (Allen et al. 2008). Column (1) – Line ID. Column (2) – Observed line ratio. Column (3) – Pure shock model. Column (4) – Shock and precursor. The [NeII] flux is taken from Ogle et al. (2009).

	Molecular Gas (1)	Ionized Gas (2)	Radio source (3)	AGN X-ray (4)
obs. luminosity	41.9	41.5	44.6	40.6
bol. luminosity	42.0	43		
Kinetic energy	57.7	55.6	59.8	
Mass	9.3	7.3		
τ_{diss}	8.2	7.2		

Table 5. Overview of the luminosities (in erg s^{-1}), kinetic energies (in erg s^{-1}), masses (in M$_\odot$), and dissipation times. We give the logarithms for all values. Column (1) – Molecular gas measured with IRAM and Spitzer. The dissipation time is given under the assumption that all of the kinetic energy is dissipation through molecular line emission. Column (2) – Warm ionized gas (the observed luminosity is that of Hα). The dissipation time is given under the assumption that all of the UV/optical line emission is due to the dissipation of kinetic energy. Column (3) – Radio luminosity measured at 327 MHz. The kinetic energy was derived by Willis & Strom (1978). Column (4) – X-ray luminosity of the nuclear point source given by Ogle et al. (2009).

Table 6. MHD shock model parameters and predicted H$_2$ line fluxes[a] for 3C326.

n_H [b] [cm^{-3}]	V_s [c] [km s^{-1}]	\multicolumn{8}{c}{H$_2$ LINE FLUXES [10^{-18} W m^{-2}]}	$\mathscr{F}_{H_2}$ [d]	$\mathscr{F}_{bol}$ [e]
		S(0)	S(1)	S(2)	S(3)	S(4)	S(5)	S(6)	S(7)		
10^4	4	0.74	4.51	0.18	6.1×10^{-3}	3×10^{-4}	8.6×10^{-4}	2.9×10^{-4}	7.5×10^{-4}	5.43	13.02
	15	0.09	3.22	3.19	10.36	1.35	0.68	0.02	2.2×10^{-3}	18.92	20.55
	34	4.2×10^{-3}	0.19	0.29	2.32	1.38	5.33	1.58	2.99	14.09	16.35
	Sum	0.84	7.92	3.66	12.69	2.73	6.01	1.60	2.99	38.44	49.92
10^3	4	1.61	3.74	0.018	1.3×10^{-3}	4.3×10^{-4}	1.2×10^{-3}	4×10^{-4}	10^{-3}	5.37	10.6
	24	0.08	3.01	2.44	5.09	0.46	0.17	7×10^{-3}	6.6×10^{-3}	11.3	11.6
	40	0.02	1.01	1.32	7.57	2.73	5.24	0.68	0.56	19.13	20.07
	Sum	1.71	7.75	3.78	12.66	3.2	5.42	0.68	0.56	35.77	
Spitzer Obs.		2.0±0.3	7.5±0.5	4.1±0.4	12.6±0.4	3.1±0.6	5.0±2.5	2.5±1.0	2.9±1.0	39.7±2.3	

[a] This table lists the shock model velocities, the predicted H$_2$ rotational line fluxes, and bolometric luminosities associated with each shock velocity components.
[b] Preshock hydrogen density.
[c] MHD Shock velocity.
[d] Sum of the H$_2$ S(0) to S(7) rotational lines in 10^{-18} W m^{-2}
[e] Sum over all the lines (bolometric luminosity of the shock)

n_H (1)	V_s (2)	Mass flow (3)	t_{cool} (4)	M_{gas} (5)
10^4	4	70100	19050	1.3×10^9
10^4	15	5950	3320	2.0×10^7
10^4	34	730	1000	7.3×10^5
10^3	4	41050	65000	2.7×10^9
10^3	24	1100	11500	1.3×10^7
10^3	40	630	5400	3.4×10^6

Table 7. MHD shock model parameters, mass flows and cooling times. Column (1) – Preshock density in cm^{-3}. Column (2) – Shock velocity in km s^{-1}. Column (3) – Mass flow in M$_\odot$ yr^{-1}. Column (4) – Cooling time in yrs. Column (5) – Gas mass in M$_\odot$.
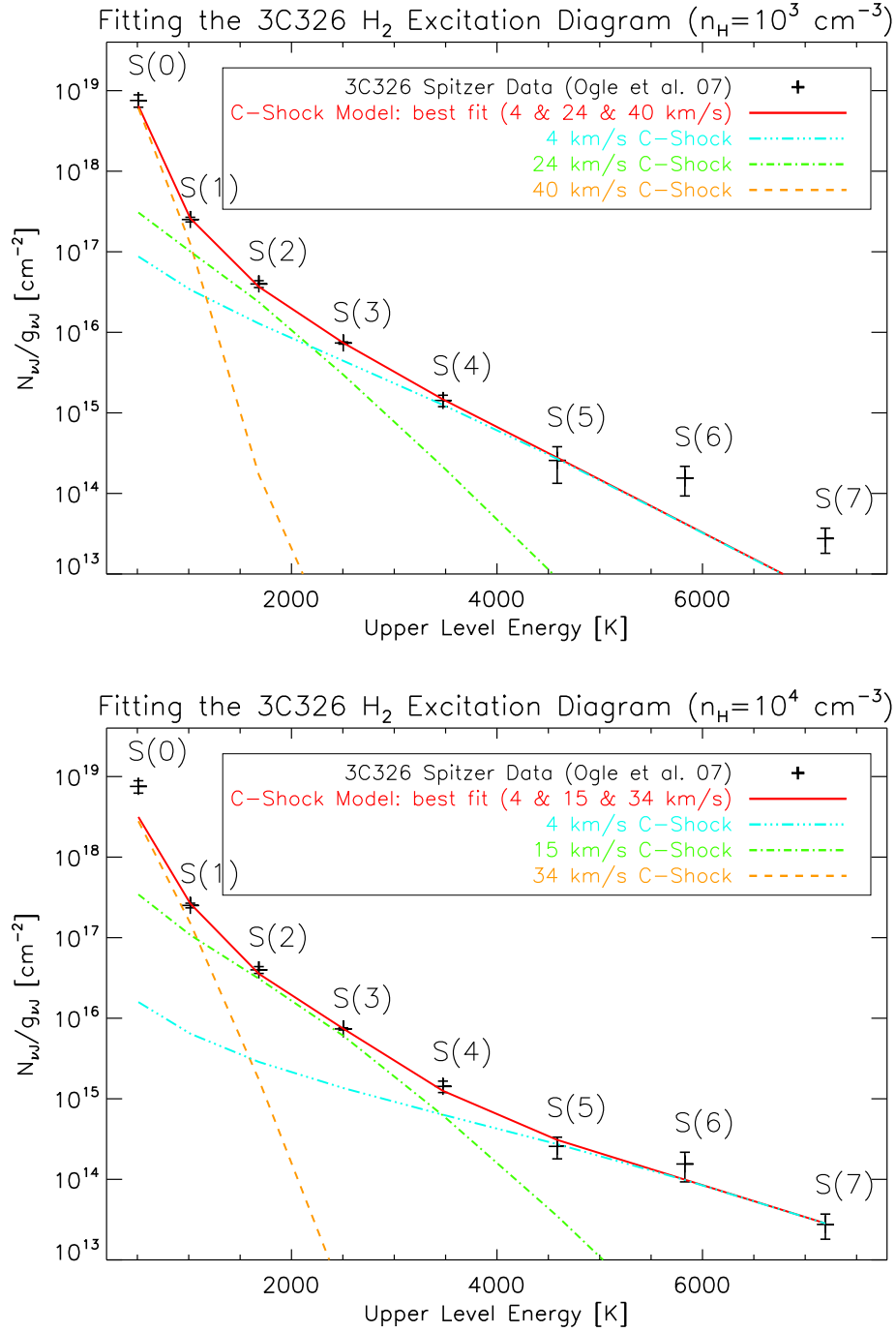
Figure 9.3: Fit of the 3C326 H_2 excitation diagram with 3 shocks MHD for a preshock density $n_H = 10^3$ cm^{-3} *(above)* and $n_H = 10^4$ cm^{-3} *(bottom)*. The shock model used is described in chapter 4. The 3 shock velocities components account for comparable fractions of the total H_2 luminosity but the less energetic component accounts for most of the warm H_2 mass (Table 7 of paper IV).

Part III

The next-generation tool to study (among a few other things...) H_2 in space: the JWST

Chapter 10

The JWST observatory and its Mid-Infrared Instrument (MIRI)

The thing's hollow - it goes on forever - and - oh my God! - it's full of stars!

Arthur C. Clarke (2001: A Space Odyssey)

Abstract

Shortly after the beginning of my PhD, I got involved in the european consortium of the Mid-InfraRed Instrument (MIRI), part of the scientific payload of the James Webb Telescope (JWST). I participated to the cryogenic tests of the instrument and to the preparation of a science proposal related to the physics of H_2 emission in distant galaxies. This chapter present the necessary background needed for the next chapters that discuss my contribution to the testing of MIRI (chap. 11) and to its science applications (chap. 12). The JWST is a large ($6.5\,m$ in diameter) near- and mid-infrared space telescope that will succeed to the Hubble and Spitzer space telescopes. We present an overview of the JWST and its science instruments, with emphasis on MIRI. MIRI provides imaging, coronagraphy and spectroscopy over the $5-28\,\mu m$ band. Its characteristics (data acquisition, observing modes, etc.) and performance (sensitivity) are described.

Contents

10.1 Introduction

The *James Webb Telescope* (hereafter JWST), giant successor to the *Hubble* and *Spitzer* space telescopes, is in preparation since 20 years. We are now in the phase where the flight model instruments have been built and are being tested. The french community, led by the CEA Saclay, IAS

Orsay, Meudon and Marseille institutes, took the responsibility of the mid-infrared ($5 - 29\,\mu$m) camera, a sub-component of the Mid-InfraRed Instrument (MIRI), which is one of the four instruments onboard the JWST.

Six months after the beginning of my PhD, Alain Abergel, who had worked in collaboration with CEA to the definition of the optical performance tests of the instrument, offered me to be part of the MIRI test team, in order to participate in the optical test of the MIRI camera taking place at the CEA, Saclay. Needless to say that I accepted without hesitating! I was interested in opening my skills to instrumentation, but also in gaining knowledge of the MIRI instrument, that will be a milestone of future mid-IR astronomy, and an ideal tool to study the H_2-luminous objects we have been speaking about in the previous chapters. In a sense, this project integrates very well in the science topic of this thesis manuscript.

I soon realized that I was a a tiny grain of sand in an enormous project! In order to have my own and little contribution to the project, I decided to focus on the tests of the Point Spread Function of the instrument, one of the tests designed to check the optical quality of the instrument. I participated in the tests and took the lead of the data analysis of the PSF measurements. This work is described in the next chapter (chap. 11).

In this chapter we provide the necessary background to the next two chapters that present my contributions to the MIRI testing and to the preparation of scientific projects related to the physics of the H_2 emission in active phases of galaxy evolution (chap. 12). I first give a brief overview of the JWST mission, with emphasis on its science instruments. Then I describe in more detail the MIRI instrument I have been working on (sect. 10.3). Imaging and spectroscopic observation modes and sensitivities are discussed. This chapter can also be viewed as an up-to-date working document useful to prepare observations.

10.2 JWST mission overview

10.2.1 Impressive numbers!

The *James Webb Space Telescope* (*JWST*) is a large IR ($0.6 - 28\,\mu$m) telescope with a 6.5 m primary mirror (see Gardner et al., 2006, for a review of the JWST implementation). The Fig. 10.1 shows the main components of the JWST observatory. The launch is planned in 2014, on an Ariane 5 rocket. The JWST will be put in a Lissajous orbit around the Earth-Sun L2 point. Here are a few more figures just to say that it's an enormous project! The total mass of the observatory is $\sim 6\,200$ kg. JWST is an international collaboration between NASA, the European Space Agency (ESA), and the Canadian Space Agency (CSA). The NASA Goddard Space Flight Center is managing the development effort and the prime contractor is Northrop Grumman. The Space Telescope Science Institute (STScI) will operate JWST after launch. The life-cycle cost of the project is estimated at about US\$4.5 billion, for a lifetime of 5 years minimum.

The JWST project started in 1989 (already 20 years ago!), when STScI decided to think about a follow-up to the *Hubble Space Telescope* (HST). Prior to September 10, 2002, the JWST was known as the Next Generation Space Telescope (NGST). JWST was renamed to honor the NASA's second administrator, James Webb (1906-1992), who supervised the Gemini program, pathfinder to the preparation of the Apollo moon program.
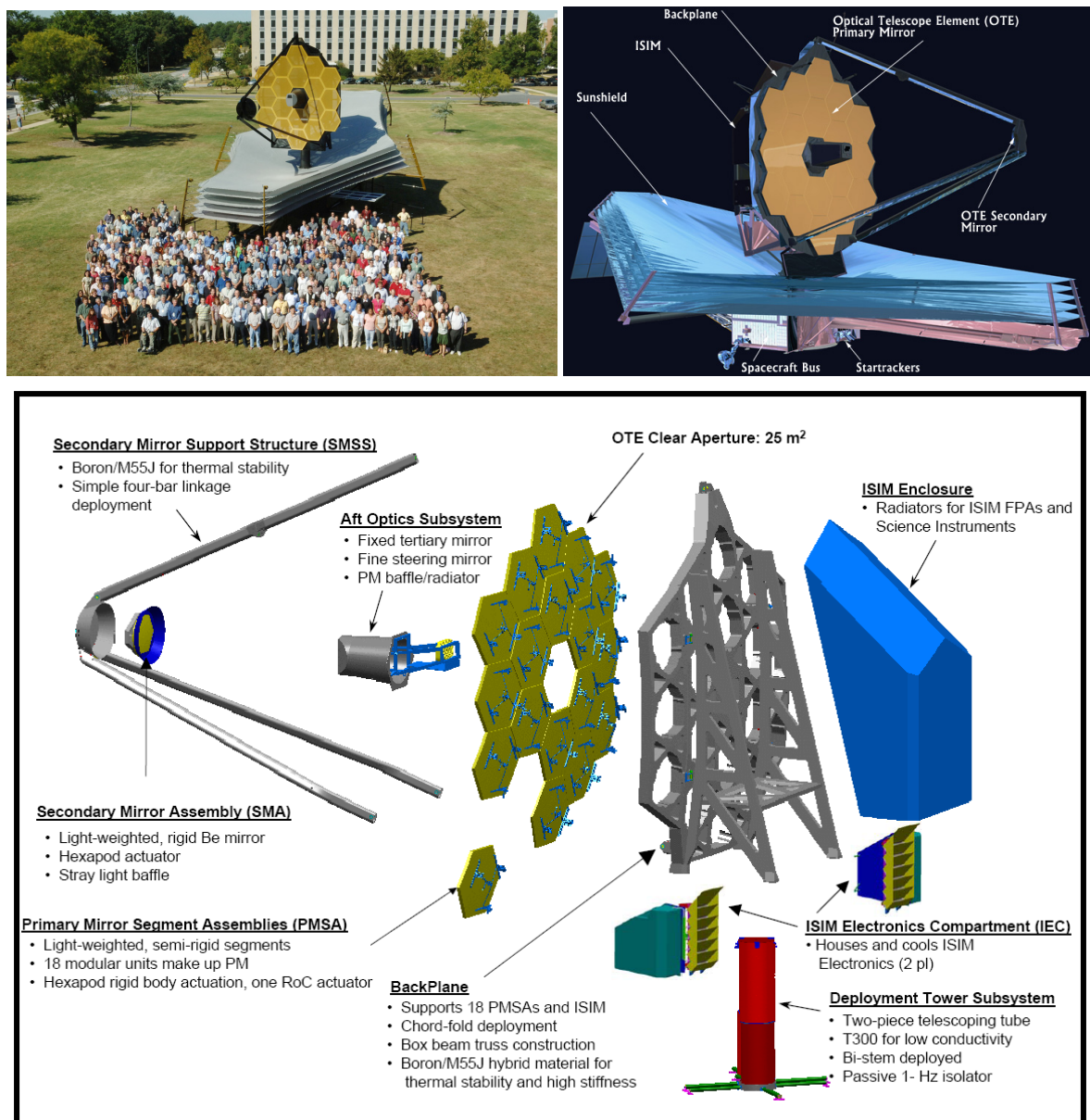
Figure 10.1: The JWST observatory and its optical telescope

The JWST observatory is comprised of the following elements: the spacecraft, the optical telescope element (OTE), and the integrated science instrument module (ISIM).

10.2.2 The spacecraft

The JWST spacecraft is comprised of two elements, the spacecraft bus and the sunshield (see the top right panel of Fig. 10.1):

1. The sunshield subsystem separates the observatory into a warm sun-facing side (spacecraft bus)

and a cold anti-sun side (OTE and ISIM). It enables passive cooling of telescope and instruments (the operating temperature has to be kept under 50 K). The sunshield consists of five layers of thin membranes made from a polymer-based film (Kapton with aluminum and doped-silicon coatings) and supporting equipment such as spreader bars, booms, cabling, and containment shells. When fully deployed, the sunshield that will be about the size of a tennis court!

2. The spacecraft bus provides the support functions for the operation of the JWST Observatory. The bus houses the six major subsystems needed to operate the spacecraft: the Electrical Power Subsystem, the Attitude Control Subsystem, the Communication Subsystem, the Command and Data Handling Subsystem, the Propulsion Subsystem, and the Thermal Control Subsystem.

The JWST architecture, its expected performance and the plans for integration and testing are described in more detail in Nella et al. (2004). Even though many details in the design have changed since the article was written, many of the design choices and procedures are still valid.

10.2.3 The eye of the JWST

The Fig. 10.2 shows some views at the JWST mirror. The JWST telescope has a three-mirror anastigmatic design, with a $25\,\mathrm{m}^2$ collecting area (equivalent to a $\sim 6\,\mathrm{m}$ circular primary), which is ~ 7 times the collecting area of the *HST*. The effective focal ratio is $f/16.67$, and the effective focal length is $131.4\,\mathrm{m}$. The primary mirror consists of 18 hexagonal segments ($\sim 1.3\,\mathrm{m}$ flat-to-flat side), in two rings around the center, resulting in a 6.5 m flat-to-flat diameter. Each segment is made of Beryllium, and has the correct off-axis surface at the nominal cryogenic 40 K temperature of the primary. The mirrors are gold coated, providing a broad spectral bandpass, from 0.6 to $29\,\mu$m.

The wavefront sensing and control subsystem is used to align the segments so that their wavefronts match properly, creating a diffraction-limited image. Each segment will have six actuators to change its focal length. The secondary mirror has 6-degrees of adjustment for collimation and overall focus. Once aligned (about $2-3$ months after launch), the telescope is designed to be diffraction limited at $2\,\mu$m (Strehl ratio of 0.80) and have an encircled energy of 75% within a 0.15 arcsecond radius at $1\,\mu$m (dominated by sub-segment errors). It is estimated that the backplane will be sufficiently stable during slews that the wavefront control adjustments will be needed less than once every two weeks.

10.2.4 Deployment and commissioning

A 6 m telescope does not fit into any launch rocket! The JWST is thus a deployable satellite (Fig. 10.3). During transfer to L2 the different elements of JWST will be deployed and commissioning will start. The observatory has five deployment stages[1] involving the following elements: 1) spacecraft appendages (solar arrays, high gain antenna), 2) sunshield, 3) extend tower, 4) secondary mirror, and 5) primary mirror. All critical deployment points have heaters and can be unlatched and re-latched to relieve any residual long term stress in the structure, even in the cold of outer space.

Deployment of the observatory will start fairly soon after launch, with the sunshade unfolding after 2 days and the secondary and primary mirror deploying after approximately 4 days. First light will occur at about 28 days after launch, initiating wavefront sensing and control activities to align the

---

[1]http://www.jwst.nasa.gov/videos_deploy.html
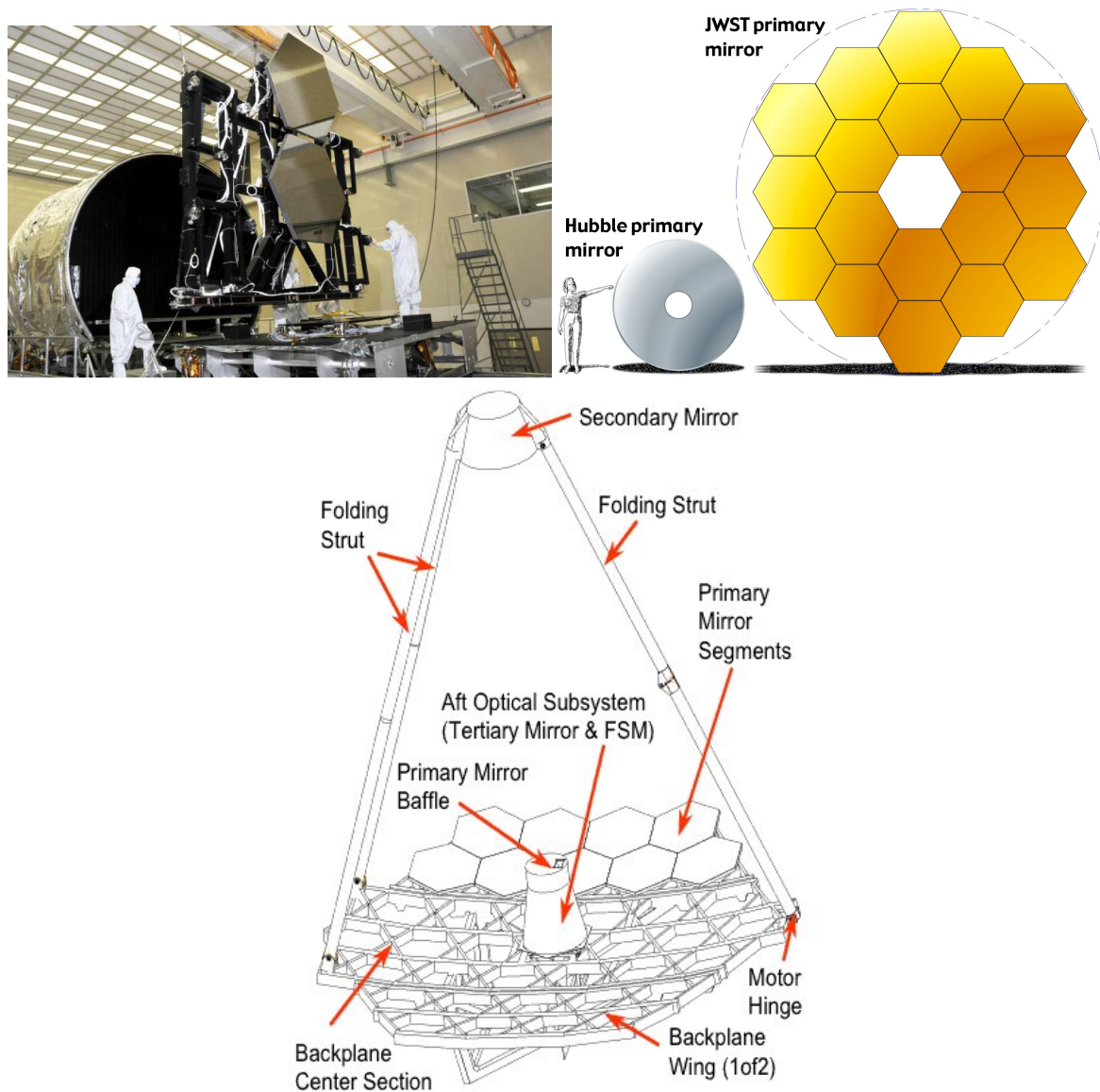
Figure 10.2: The "eye" of the JWST: a 6.5 m segmented mirror. *top left:* cryogenic tests of the Flight Model mirrors (April 2009). *top right:* comparison between *HST* and *JWST* mirrors (2.4 vs. 6.5 m). *bottom:* scheme of the JWST optical telescope element. Two primary mirror "wings" and a tripod structure supporting the secondary mirror are deployed during orbit insertion. A Fine Steering Mirror (FSM) provides accurate pointing, image stabilization (< 7.3 milliarcsec) and dithering.

mirror segments. Instrument checkout will start 37 days after launch, well before the final L2 orbit insertion is obtained after 106 days. Hereafter the full commissioning starts and the observatory will be ready for normal science operations approximately 6 months after launch.
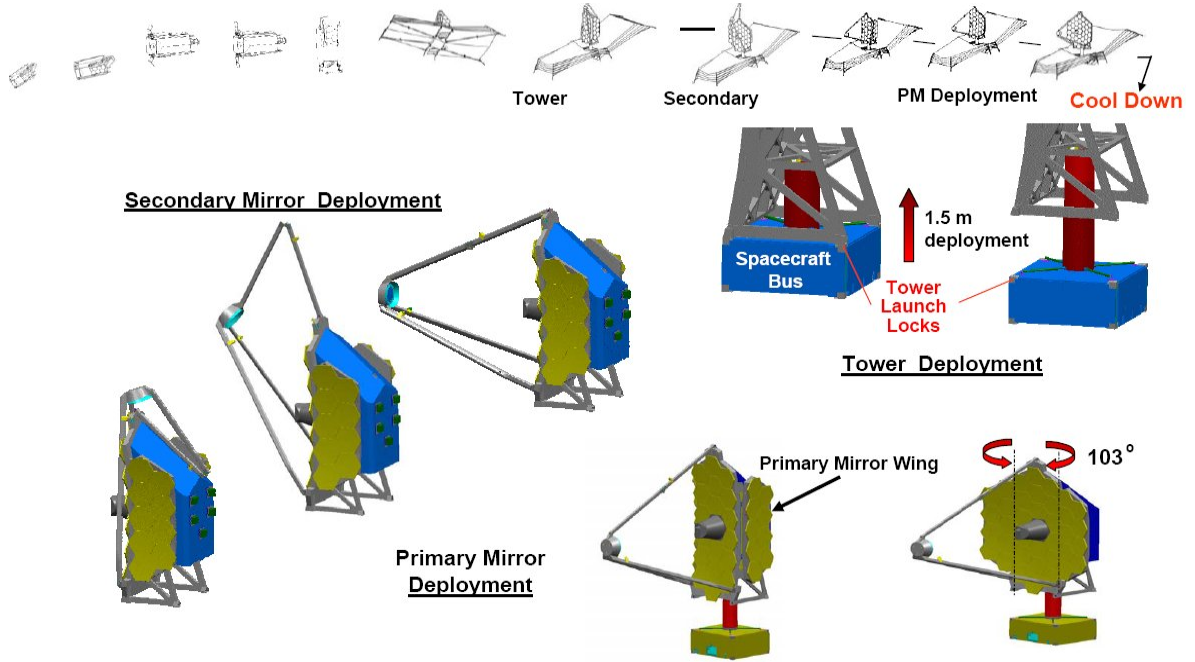
Figure 10.3: The "joints" of the JWST: deploying the sunshield and the optical telescope.

10.2.5   Science instruments on-board JWST

Fig. 10.4 shows the four science instruments gathered into the integrated science instrument module (*ISIM*):

NIRCam: A Near-Infrared Camera ($0.6 - 5\,\mu$m), provided by the University of Arizona. It consists of two broad- and intermediate-band imaging modules, each with a 2.16×2.16 arcmin field of view. The modules have a short and a long wavelength channel, taking images simultaneously with light split by a dichroic at about $2.35\,\mu$m. The short wavelength channel ($0.6 - 2.3\,\mu$m) is sampled at 4096×4096 pixels (0.0317 arcsec/pixel), the long wavelength channels by 2048×2048 pixels (0.0648 arcsec/pixel). The short and long wavelength arms are Nyquist sampled at 2 and $4\,\mu$m respectively. *NIRCam* has ten mercury-cadmium-telluride (HgCdTe) detector arrays, analogous to CCDs found in ordinary digital cameras. Coronagraphs are available in both modules. At the same time it serves as a wavefront sensor for the observatory, measuring the alignment of the 18 mirror pieces of the 6.5m primary mirror.

NIRSpec: A Near-Infrared Spectrograph ($0.6 - 5\,\mu$m), mainly provided by the European Space Agency, under an industrial contract with Astrium. *NIRSpec* provides 3 observing modes: a low resolution $\mathcal{R} \sim 100$ prism mode, an $\mathcal{R} \sim 1000$ multi-object mode and an $\mathcal{R} \sim 3000$ integral field unit or long-slit spectroscopy mode.

In the $\mathcal{R} \sim 100$ and $\mathcal{R} \sim 1000$ modes, *NIRSpec* uses a micro-electromechanical system (MEMS) to provide dynamic aperture shutter masks ("microshutter array"). These masks allow to obtain simultaneous spectra of more than 100 objects in a > 9 arcmin^2 field of view
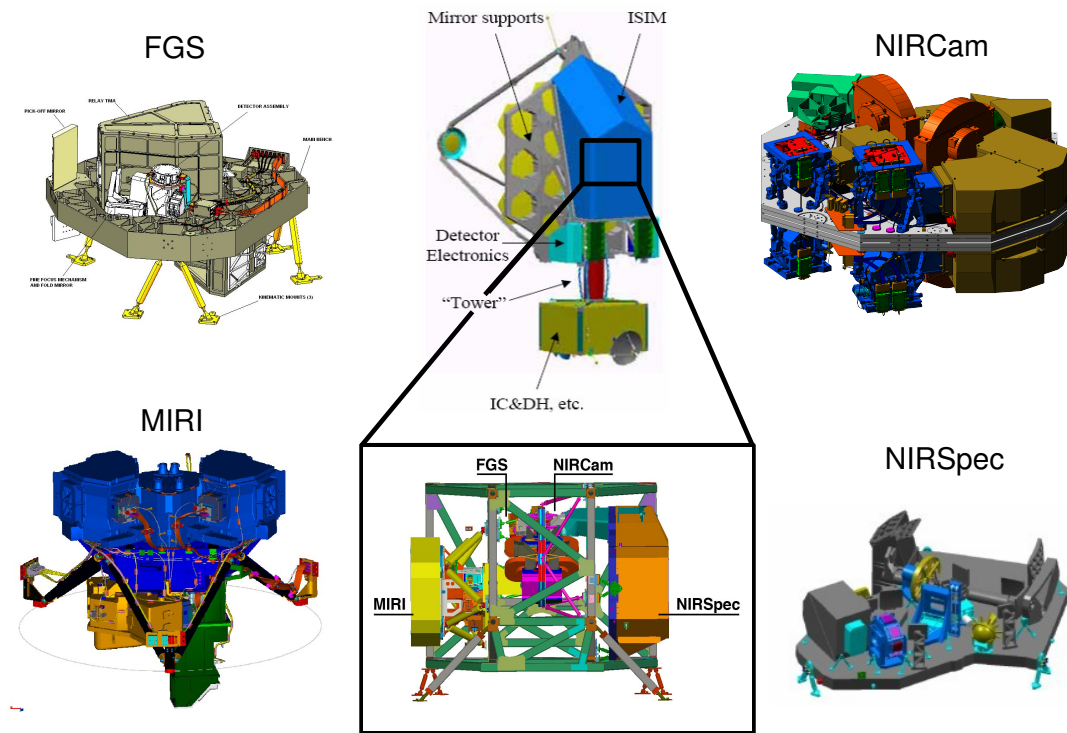
Figure 10.4: The "heart" of the JWST: its four science instruments. *From top left, clockwise:* The Fine Guidance Sensor and Tunable Filter Imager (*FGS-TFI*), the Near-Infrared Camera (*NIRCam*), The Near-Infrared Spectrograph (*NIRSpec*) and the Mid-Infrared Instrument (*MIRI*). The four instruments are integrated into the *ISIM* (Integrated Science Instrument Module), the "chassis" that is supporting the instruments (blue cover behind the telescope, and zoom inset).

($\sim 3.4 \times 3.4$ arcmin^2 at 1 μm). At $\mathcal{R} \sim 100$ one prism spectrum covers the full $0.6 - 5\,\mu$m wavelength range. At $\mathcal{R} \sim 1000$, three gratings cover $1 - 5\,\mu$m. *NIRSpec* detectors are two HgCdTe arrays.

MIRI: A Mid-InfraRed Instrument, developed by a European consortium of more than 20 scientific institutes, nationally funded, with IR detectors and the active cooling system provided by NASA/JPL. MIRI provides imaging and spectroscopy over the $5 - 27\,\mu$m wavelength range. Its design consists of two main modules, an imager and an Integral Field Unit (IFU) medium resolution spectrograph (MRS). Section 10.3 describes the instrument in more details.

FGS-TFI: The Fine Guidance Sensor, provided by the Canadian Space Agency, contains a dedicated Guider and a Tunable Filter Camera. The guider is a sensitive camera that provides support for the observatory's attitude control system (ACS). It is used for both "guide star" acquisition and fine pointing. The sensor operates over a wavelength range of 1 to 5 μm and has two HgCdTe detector arrays. The camera can image two adjacent fields of view, each approximately 2.4×2.4
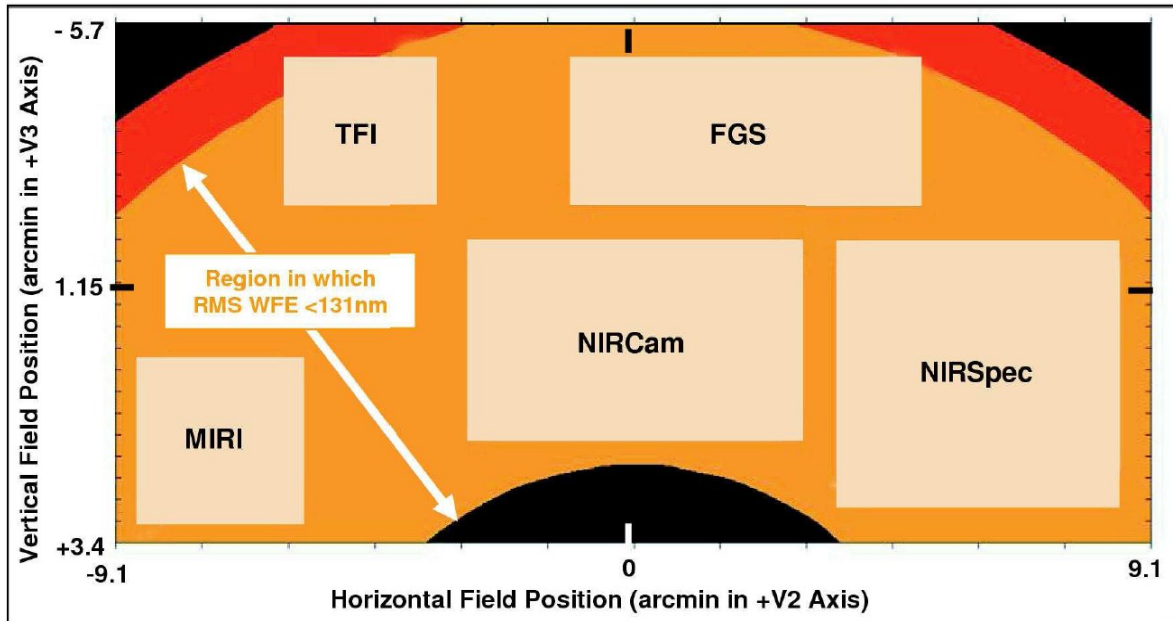
Figure 10.5: The JWST focal plane. The placement of the science instruments in the telescope field of view (FOV) is shown. Instruments share a $\sim 166\,\mathrm{arcmin}^2$ FOV. The orange area shows where the wavefront error (WFE), that results from residuals in the optical design, is smaller than 131 nm rms. This is required for the NIRCam field, to be diffraction-limited at $2\,\mu$m. The outer black area in the figure represents portions of the field of view that have some amount of vignetting.

arcmin^2 in size.

A science instrument known as the FGS Tunable Filter Imager (FGS-TFI) is packaged with the guide camera, but is functionally independent. The FGS-TFI will be used solely for science observations. It has a selectable band of resolution $\mathcal{R} \sim 100$ across its 2.2×2.2 arcmin^2 field between $1.5 - 5\,\mu$m, with a gap between 2.6 and 3.1 micrometers. Tunable Fabry-Perot etalons illuminate the detector array with a single order of interference at a user-selected wavelength. The camera has a single HgCdTe detector array.

10.3   The Mid-Infrared Instrument (MIRI)

10.3.1   Overview of MIRI

Fig. 10.7 shows the whole field of view (FOV) of the Mid-Infrared Instrument (MIRI) focal plane. MIRI is comprised of an imager (henceforth MIRIM) and an IFU spectrograph (MRS, § 10.3.4) that cover the wavelength range $\sim 5 - 28\,\mu$m. MIRIM features three observing modes plus an alignment check mode:

Imaging mode: the camera is equiped with a filter wheel, where broad-band filters are mounted (§ 10.3.2).

ISIM Fast Facts

Key Instrument Characteristics (as of Mar 06)

Instrument	Channel/Mode	Wavelength (microns)	Typical Spectral Resolution (λ/Δλ)	FOV	Angular Resolution (arc sec)	Mega Pixels	Number of Sensor Chip Arrays	Detector Type / Format NIR=18 um pixels MIR=25 um pixels	Detector Temp (K)
NIRCam	Shortwave	0.6 - 2.3	4,10,100	2.2 x 2.2 each of 2 modules	0.032 / pixel	34	8	HgCdTe / 2048 x 2048	40
NIRCam	Longwave	2.4 - 5.0	4,10,100	2.2 x 2.2 each of 2 modules	0.065 / pixel	8	2	HgCdTe / 2048 x 2048	40
NIRSpec	Multi-Object Spec	1.0 - 5.0	1000	203 x 463 mas clear shutter aperture; 26 / x 528 mas pitch, 4 x 171 x 365 shutter array format, 9.7 sq arcmin multi-object targetable solid angle	see FOV	8	2	HgCdTe / 2048 x 2048	37
NIRSpec	Multi-Object Spec	0.6 - 5.0	100	200 x3500 mas x 3, 400 x4000 mas,					
	Long Slits (5)	1.0 - 5.0	100, 1000, 2700	100 x 2000 mas					
	IFU	0.7 - 5.0	2700	3 x 3 arc-sec	0.10 slice width				
MIRI	Imager	5 - 27	4-6	1.9 x 1.4	0.11 / pixel	1	1	SiAs / 1024 x 1024	7
	Low Res Slit	5 - 11	100	5" x 0.6"	see FOV	1	1	SiAs / 1024 x 1024	7
	Med Res IFU	4.87 - 7.76	3000	3.7" x 3.7"	0.18 slice width				
		7.45 - 11.87	3000	4.7" x 4.5"	0.28 slice width	1	1	SiAs / 1024 x 1024	7
		11.47 - 18.24	3000	6.2" x 6.1"	0.39 slice width				
		17.54 - 28.82	2250	7.1" x 7.7"	0.65 slice width				
FGS-TF		1.6 - 2.5, 3.2 - 4.9	100	2.2" x 2.2"	0.065 / pixel	4	1	HgCdTe / 2048 x 2048	40
FGS-Guider		0.8 - 5.0	0.7	2.3 x 2.3 each of 2 modules	0.068 / pixel	8	2	HgCdTe / 2048 x 2048	40
						Total ISIM 66			

JWST Sensitivity (JWST-RQMT-000634 Rev-M Baseline)

Wavelength (microns)	Instrument/Mode	Bandwidth (λ/Δλ)	SNR	Maximum Wall Clock Time (s)	Continuum Flux Density (nJy)	Continuum Flux Density (10^{-33} W m^{-2} Hz^{-1})	Unresolved Line Flux (10^{-21} W m^{-2})
2	NIRCam	4	10	10,000	11.40	0.11	NA
3.5	FGS-TF	100	10	10,000	126.00	1.26	NA
3	NIRSpec/Low Res	100	10	10,000	132.00	1.32	NA
2	NIRSpec/ Med Res	NA	10	100,000	NA	NA	0.57
10	MIRI/ Broadband	5	10	10,000	700.00	7.00	NA
21	MIRI/Broadband	4.2	10	10,000	8700.00	87.00	NA
9.2	MIRI/Spectrometer	2400	10	10,000	NA	NA	10
22.5	MIRI/Spectrometer	1200	10	10,000	NA	NA	56.00

Resource Allocations (as of May 07)

Instrument	Mass: Region 1/2 (kg)	Volume R1 (m³)	Observation Power Region 2 (W)	Uncompressed Data Volume (Gbits / day)
NIRCam	161 / 46	~0.3	52	334
NIRSpec	220 / 44	~3.5	40	232
MIRI	102 / 33	~2.5	37	96
FGS	92 / 21	~0.6	51	68
Total SI	575 / 144		180	max ISIM = 45% (NIRCam prime, NIRSpec parallel cal 24% utilization
Total ISIM	1065 / 340		200	
SI/ISIM	0.54 / 0.42		0.90	NA

Schedule (ISIM Rev-G)

Flight Item	PDR	CDR	Flt Delivery
NIRCam	Oct-04	May-06	Sep-10
NIRSpec	Dec-05	Oct-08	Jul-10
MIRI OBA	Mar-05	Dec-06	Jun-10
MIRI Cryo-Cooler	Feb-08	Dec-08	Sep-10
FGS-Guider	May-05	Mar-07	Jun-10
FGS-TF	May-05	Mar-08	Jun-10
ISIM	Oct-06	Mar-09	Oct-11

Greenhouse: Update: January 09

Figure 10.6: Summary of the main characteristics and sensitivities of the JWST instruments.
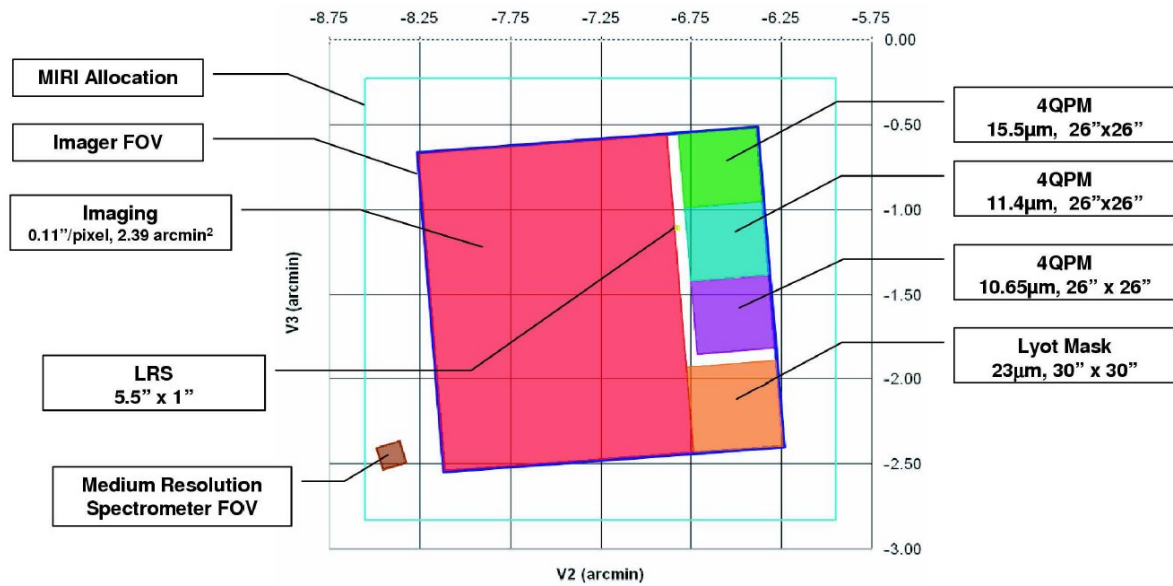
Figure 10.7: Schematic view of the MIRI's focal plane. The biggest 1.9×1.9 arcmin^2 square is the imager field of view. One quarter of the field of view is devoted to coronagraphy (with three 4-Quadrant Phase Mask and one Lyot Mask coronographs), a 5 arcsec wide strip is used for low-resolution spectroscopy (*LRS*), and the remaining 1.4×1.9 arcmin^2 is available for broad-band imaging. The smallest square on the bottom left is the field of view of the medium resolution spectrometer. (From Gardner et al., 2006).

Coronagraphic mode: one Lyot mask (23 μm) and three 4-Quadrant Phase-Masks (4QPM at 10.65, 11.4, 15.5 μm) are fixed in a sub-area of the focal plane. The 4 corresponding pupil diaphragms are located in the filter wheel. The Lyot mask is a classical coronograph with an occulting disk that blocks the direct starlight. The 4QPM coronagraph is based the peculiar design of binary phase mask $(0, \pi)$ dividing the full field of view at the focal plane in four quadrants. The mutual destructive interferences of the coherent light of a source, perfectly centered on the mask, produce a total nulling within the pupil image (see e.g. Rouan et al., 2000, for details). The coronographic mode of MIRI will not be further discussed here.

Low-Resolution Spectrometer: The slit is fixed in the focal plane and the dispersive element (a double prism) in the filter wheel (*LRS*, § 10.3.3).

Alignment check mode: a tool to check the alignment of MIRIM with respect to the telescope. It includes a fused silica lens in the filter wheel to defocus the image of an on-axis point source on the detector.

Fig. 10.8 shows the whole Mid-Infrared Instrument (MIRI) and its structural design. The MIRI structure design uses a six-strut (hexapod) mount that provide the degrees of freedom for kinematic mounting to the ISIM. With the exception of the struts and some filters and prisms, the instrument is made entirely from 6061 aluminium alloy. The nominal operating temperature for the MIRI is 7K. This level of cooling cannot be attained using the passive cooling. Instead, a cryocooler is used. First, a
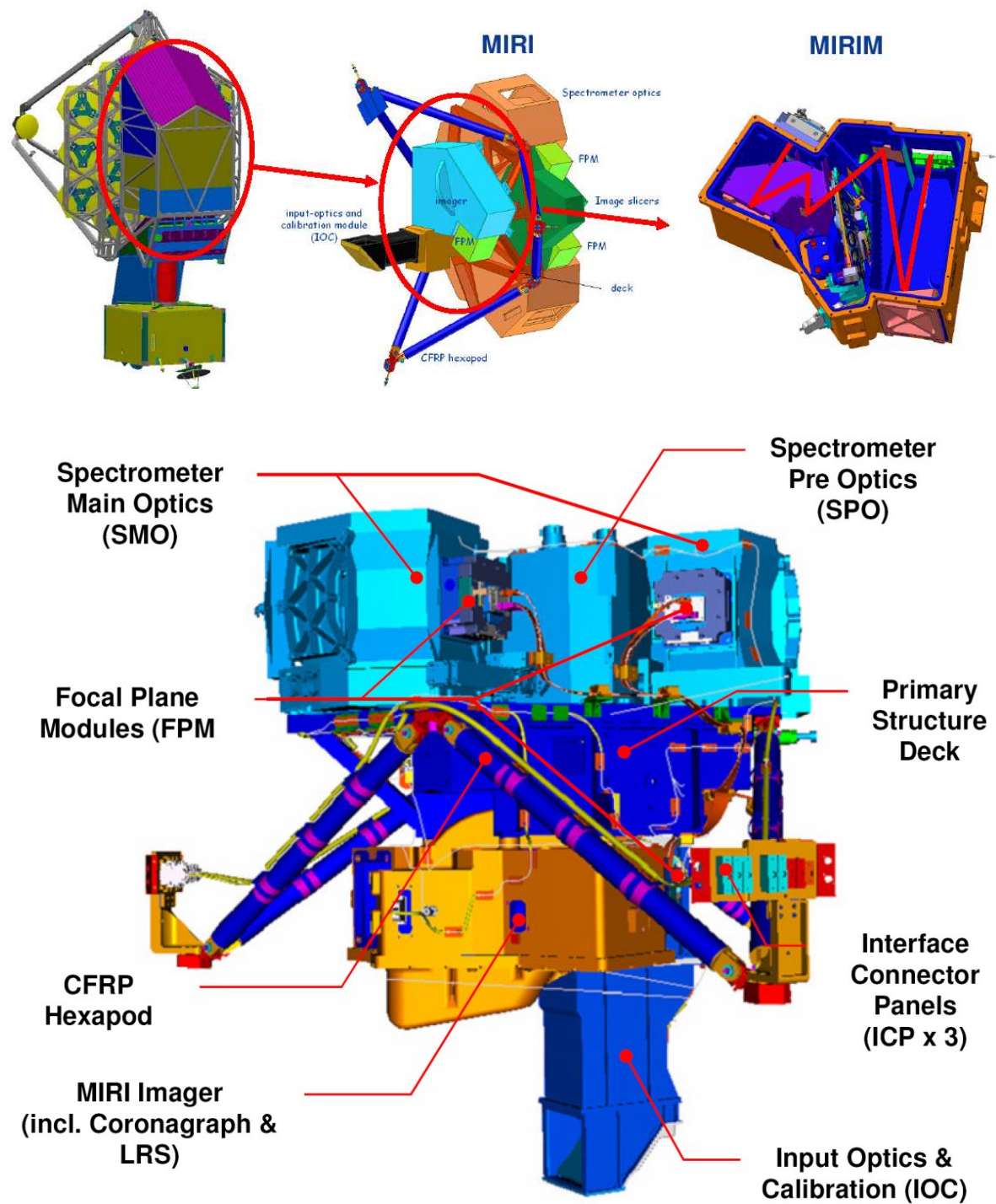
Figure 10.8: *Top panel, from left to right:* The Mid Infra Red Instrument (MIRI) as part of the scientific payload of the JWST, the MIRI Optical Bench Assembly (MIRI-OBA), with the imager in blue, and the MIRIM (Mid Infra Red IMager) mechanical layout, with the filter wheel assembly (FWA). *Bottom:* MIRI's structural concept. The total weigth of MIRI is ≈ 95 kg and its dimensions $\approx 0.9 \times 1 \times 0.8$ m.

Figure 10.9: *Left:* the MIRIM open box. *Middle:* the focal plane, with the four coronograph masks (one Lyot and three 4QPMs). *Right:* the filter wheel, providing the broad-band filters for imaging, the coronograph filters, the double prisms for the LRS, and the alignment lens.

pulse tube precooler gets the instrument down to 18K, and then a Joule-Thomson loop heat exchanger cools it down to 7K. The cryocooler compressor assembly and control electronics are housed in the Spacecraft Bus (see Fig. 10.1).

10.3.2   MIRIM: broad-band imaging and coronography

Optical layout   We briefly describe the optical layout of the camera, shown in Fig. 10.10. The footprints of the beams for 3 different off-axis fields are overlaid on the mechanical layout. The JWST input beam enters MIRIM's focal plane via the Input Optics and Calibration unit (IOC, see Fig. 10.8). The cold MIRIM FOV is $72.76 \, \text{mm} \times 72.76 \text{mm}$ at focal plane, where the coronograph masks are fixed. M1 is a collimating mirror (focal length = 352 mm), and M2 is a flat folding mirror that directs the beam to the cold stop and the filter wheel. The cold stop is a diaphragm required at the OTE pupil image location to reduce the amount of stray light. Because the shape of the diaphragms used for imaging or coronography are different, the use of a single cold stop for all the modes is not possible. Thus, a "pseudo cold stop" is located 10 mm along the optical axis before the OTE pupil image. The diaphragms (mean diameter value around 19 mm), adapted for each mode and attached to the filter wheel, are located exactly at the OTE pupil image position. The M3, M4 and M5 mirrors form a Three-Mirror Anastigmatic (TMA) objective that reflects the light on the detector array.

Imager and coronographic filters   The useful area for the imaging mode is $47.79 \times 71.76 \, \text{mm}^2$, corresponding to $1.25 \times 1.88 = 2.35 \, \text{arcmin}^2$ on the sky (see Fig. 10.10, bottom). The imager will have a pixel scale of 0.11 arcsec/pixel. As the coronagraphic masks are transparent, the area used for the coronagraphic mode could be marginally used in the imaging mode. The only moving part of the imager is an 18-position filter wheel. Filter positions are allocated as follows: 12 filters for imaging, 4 filter and diaphragm combinations for coronagraphy, 1 ZnS-Ge double prism for the low-resolution spectroscopic mode, and 1 dark position. The list and properties of the MIRIM filters are given in
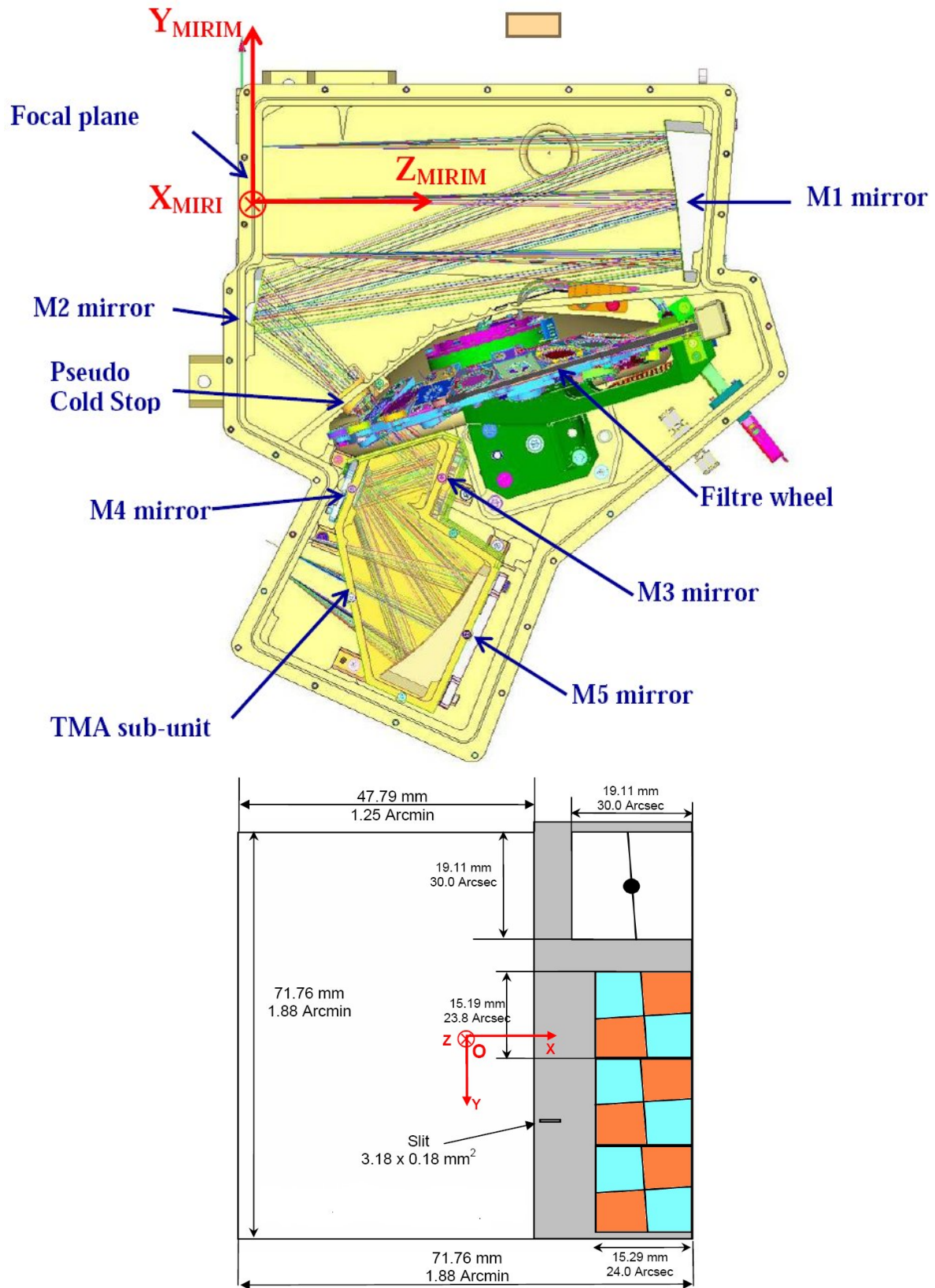
Figure 10.10: *top:* MIRI's mechanical and optical layout with its reference frame. *Bottom:* schematic view of the MIRIM (imager) focal plane, showing the position of the imaging field, the LRS slit, and the coronograph masks (Lyot and the three 4QPM masks).

Table 10.1: MIRIM filters[a] and components of the filter wheel

Filter	λ_0 [μm]	$\Delta\lambda$ [μm]	FoV [arcsec^2]	Material	Comment
F560W	5.6	1.2		CaF$_2$	Broad band
F770W	7.7	2.2		CaF$_2$	PAH, broad band
F1000W	10.0	2.0		ZnSe	Silicate, broad band
F1130W	11.3	0.7		ZnSe	PAH, broad band
F1280W	12.8	2.4	84×113	ZnSe	Broad band
F1500W	15.0	3.0		ZnSe	Broad band
F1800W	18.0	3.0		CdTe	Silicate, broad band
F2100W	21.0	5.0		CdTe	Broad band
F2550W	25.5	4.0		CdTe	Broad band
F2550WR	25.5	4.0		CdTe	Redundant filter [b]
F1065C	10.65	0.53	24×24	ZnSe	4QPM Coronagraph
F1140C	11.4	0.57	24×24	ZnSe	4QPM Coronagraph
F1550C	15.5	0.78	24×24	ZnSe	4QPM Coronagraph
F2300C	23.0	4.6	30×30	CdTe	Lyot Coronagraph
DPA	$5-11$		5×0.28	Ge, ZnS	Double Prism (LRS)
FLENS				Fused silica	Alignment lens
OPAQUE					Closed position (dark)
FND					Neutral density

[a]The filter name, central wavelength, bandwidth, Field of View are presented.

[b]Additional $25.5\,\mu$m spare filter to mitigate risks associated with the technological challenge of manufacturing this element.

table 10.1. The transmission curves of the imager filters are plotted in Fig. 10.11. The coronographic mode will not be detailed here, and we direct the reader to Boccaletti et al. (2005) for details.

Calibration   A calibration facility is dispatched over the IOC and MIRIM. The calibration is achieved through a dedicated optical path, by imaging a point source at the internal edge of the OTE pupil image. The light is reflected through the TMA to illuminate uniformly the detector.

10.3.3   MIRIM: the Low-Resolution Spectrometer (LRS)

The low resolution spectroscopic mode is achieved by a couple of Ge and ZnS prisms, attached to the filter wheel. The first Ge prism cancels the deviation due to the ZnS dispersive prism. The slit is located at the edge of the coronagraphic mask mounting (see Fig. 10.10, bottom). The spectrum ($5-10\,\mu$m) is spread over ~ 3.5 mm over the detector array, so ~ 140 pixels. The nominal resolving power at $7.5\,\mu$m is $\mathcal{R} = 98.5 \pm 6.0$.
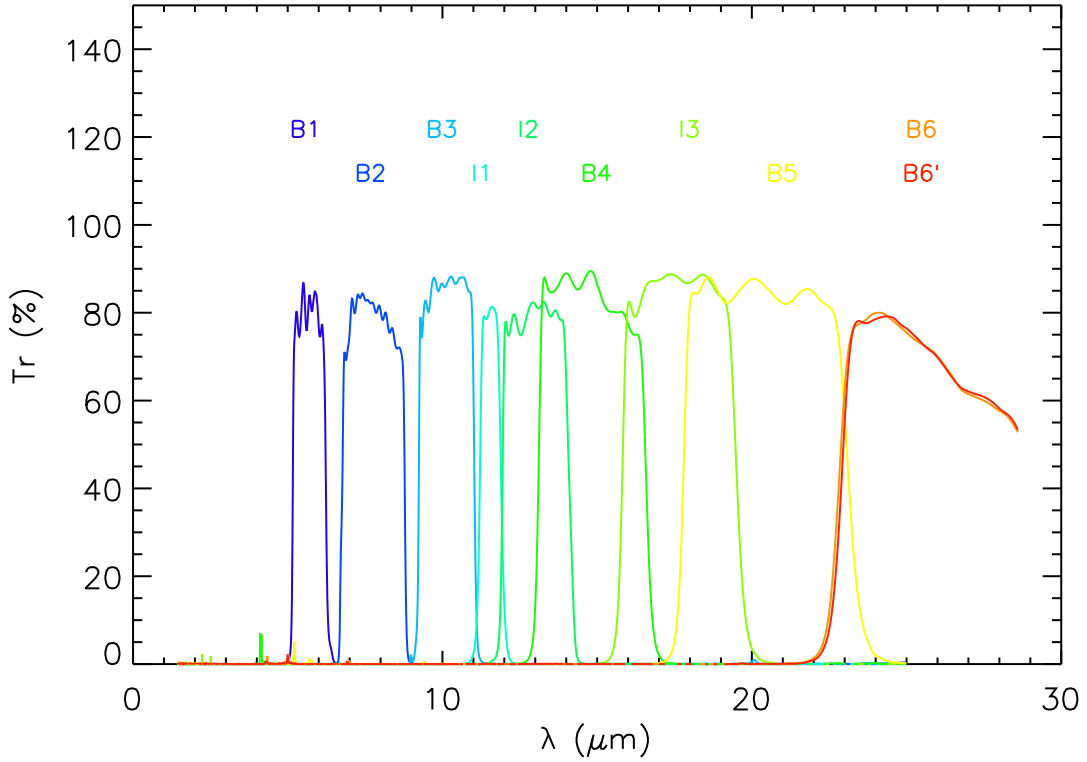
Figure 10.11: Spectral response of the MIRI broad-band filters, measured by K. Justtanont, Onsala Observatory.

10.3.4 The Medium-Resolution Spectrometer (*MRS*)

The Medium Resolution Spectrometer (MRS) is an Integral Field Unit (IFU) that allows spectroscopy to be carried out on a 2-dimensional area of sky in a single observation. Fig. 10.12 illustrates its working principle and Fig. 10.13 shows the optical and mechanical layout of the MRS. The rectangular field of view is divided into narrow slices by mean of a image-slicer mirror. The image slices are arranged along the entrance slit mask (bottom panel of Fig. 10.13) of a first-order diffraction grating, which carries out the dispersion, and imaged onto two 1024×1024 pixels Si:As chips.

The band ($5 - 29\,\mu$m) is divided into 4 IFU channels (Fig. 10.13), which are observed simultaneously. Each channel is equipped with an IFU image slicer designed to match the width of each slice to the diffraction-limited point-spread function of the telescope, at the wavelength of each channel. The spectral band of each IFU channel is subdivided into 3 sub-bands (A, B and C) by means of dichroic filters. Thus, an observation over the entire spectral band is carried out in a set of three exposures.

The table 10.2 gathers the main functional parameters of the MRS. The spectral resolution is $\mathcal{R} \sim 3000$ over the $5 - 29\,\mu$m wavelength range. The field of view ranges from 3.7×3.7 arcsec to 7.7×7.7 arcsec^2 with increasing wavelength, with pixel sizes from 0.2 to 0.65 arcsec. Within this overall field of view, the region of sky corresponding to a spatial sample is set by the slice width in

Channel 1: 4.9-7.8 μm
Channel 2: 7.5-11.9 μm
Channel 3: 11.5-18.2 μm
Channel 4: 17.5-28.8 μm
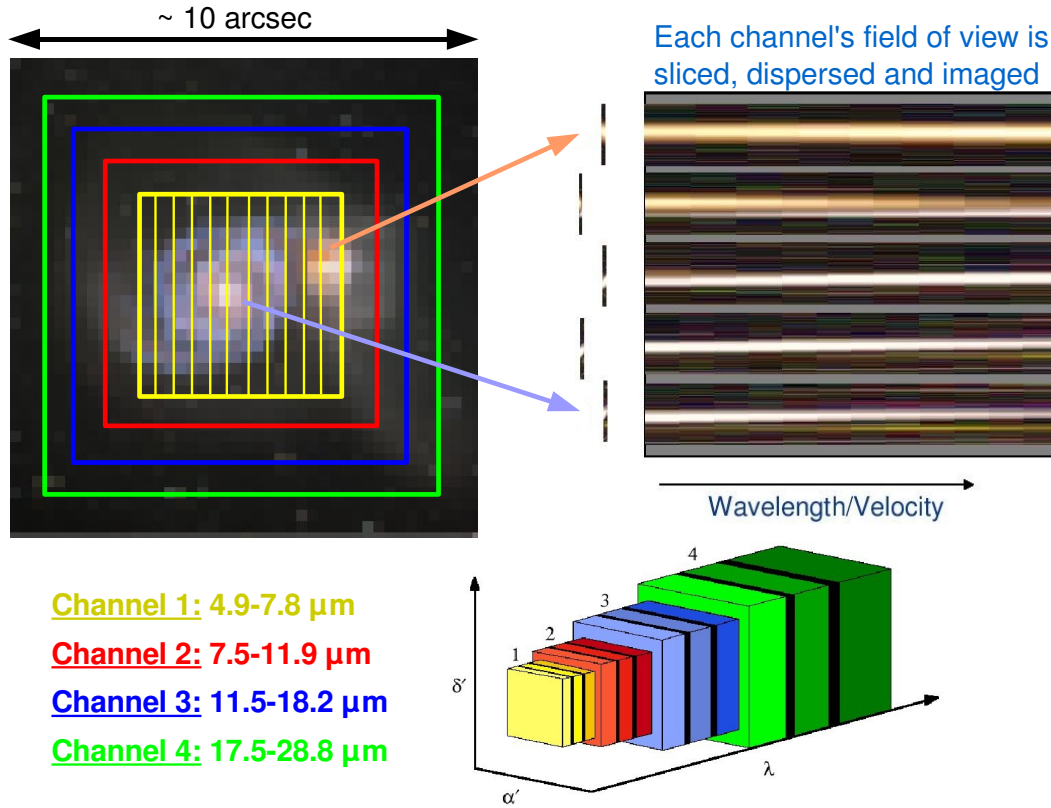
Figure 10.12: *Top:* Sketch of the working principle of the MRS. *Bottom right inset:* The field-of-view and bandwidth coverage (to scale) of MIRI-MRS channels 1 to 4 (from Lorente et al., 2006). The gradation of colour from light to dark in each channel denotes the three exposures A, B and C. The black bands between channels are those spectral regions where the wavelength coverage of adjacent exposures overlap.

the perpendicular to the slice direction (across), and by the pixel field of view in the slice direction (along). The slice widths have been chosen to have odd integer multiples of their half widths matched. The result is that a single telescope offset (of 0.97 arcseconds in the across slice direction and a multiple of 0.10 arcseconds in the along-slice direction) will provide full spatial sampling in all channels simultaneously.

10.3.5 MIRI's detectors, chip readout and sub-arrays

MIRI has three 1024×1024 pixels Arsenic-doped Silicon (Si:As) sensor chip arrays (SCA), two for the MRS, one for the imager (Fig. 10.14, *top left*). With $25\,\mu\text{m} \times 25\mu\text{m}$ pixels, the detecting area in approximately 1 inch $\times$ 1 inch. The previous generation's similar IR detectors at these wavelengths ($5 - 28\,\mu\text{m}$) were the 256×256 pixels, $30\,\mu$m-pitch, Si:As devices built for the IRAC instrument on-board *Spitzer*. The main characteristics of the MIRI detector are gathered in table 10.3. We direct the reader to Love et al. (2005, 2006) for more details.

Key
1 input baffle tube
2 Dichroic wheel A
3 Dichroic wheel B
4 Fold mirror
5 APO
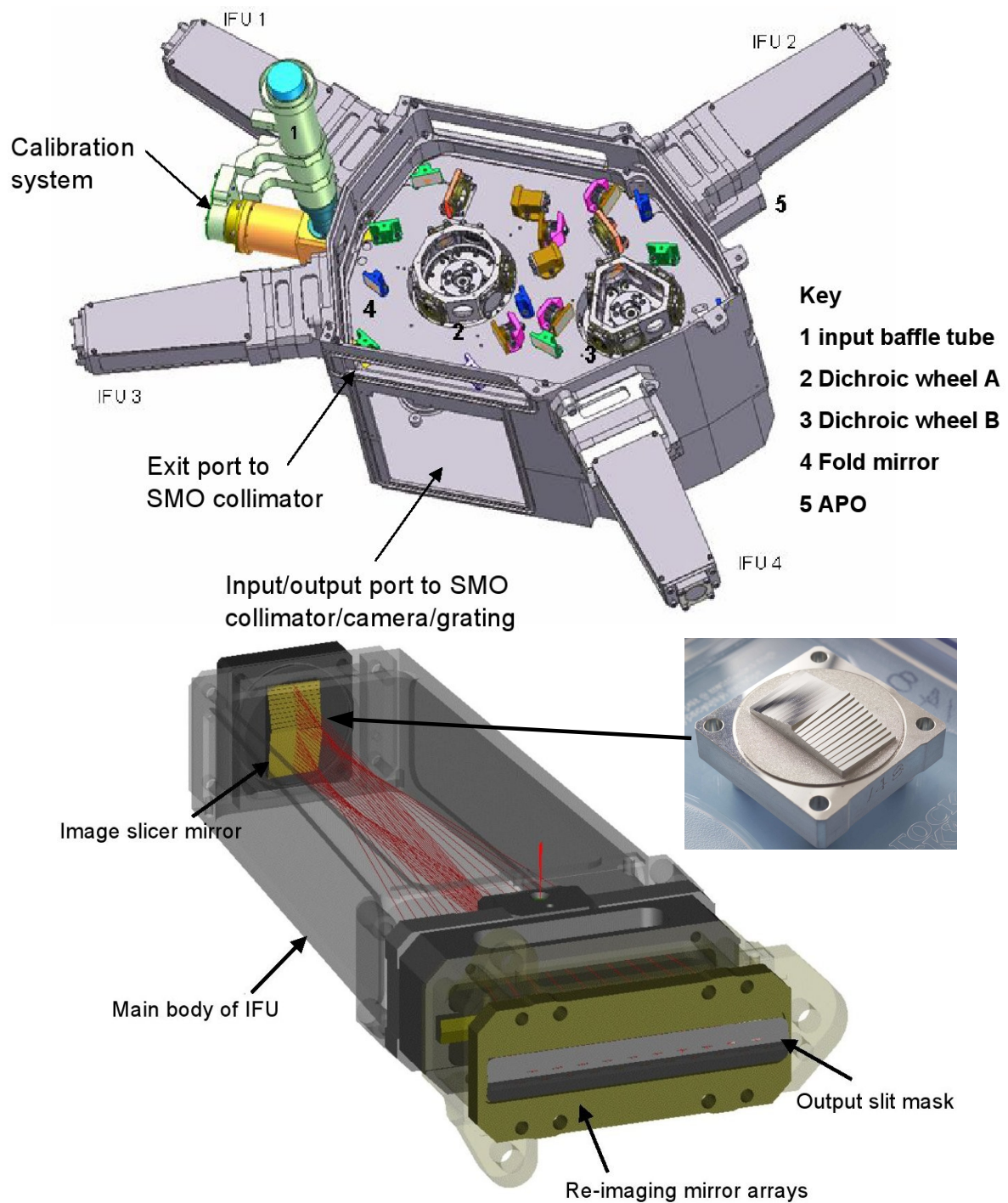
Figure 10.13: *Top:* the opto-mechanical layout of the Medium Resolution Spectrometer (MRS) Pre-Optics. The main beam (1) is separated into the 4 IFU channels. The dichroics sub-divide each channel into 3 sub-bands. *Bottom:* the Integral Field Unit (IFU) and its image slicer mirror.

Table 10.2: Summary of the MIRI-MRS parameters

Channel	FoV in a single integration across × along [arcsec^2]	Spatial sample dimensions across × along slice width / pixel [arcsec^2]	Slices	λ [μm]	$\mathcal{R}_{\text{spectral}}$	Exposure
1	3.70×3.70	0.18×0.20	21	$4.87 - 5.82$	$2450 - 3710$	A
				$5.62 - 6.73$	$2450 - 3710$	B
				$6.49 - 7.76$	$2450 - 3710$	C
2	4.51×4.70	0.28×0.20	17	$7.45 - 8.90$	$2480 - 3690$	A
				$8.61 - 10.28$	$2480 - 3690$	B
				$9.94 - 11.87$	$2480 - 3690$	C
3	6.13×6.20	0.39×0.25	16	$11.47 - 13.67$	$2510 - 3730$	A
				$13.25 - 15.80$	$2510 - 3730$	B
				$15.30 - 18.24$	$2510 - 3730$	C
4	7.93×7.74	0.64×0.27	12	$17.54 - 21.10$	$2070 - 2490$	A
				$20.44 - 24.72$	$2070 - 2490$	B
				$23.84 - 28.82$	$2070 - 2490$	C

Table 10.3: MIRI detector parameters [a]

Parameter	Measured value
Format	1024×1024 pixels
Material	Si:As Inpurity Band Conduction
Pixel size	$25 \, \mu$m
Well capacity	$1 - 2 \times 10^5$ e$^-$
Read-out noise	$10 - 20$ e$^-$ @ 7.1 K
Dark current	< 0.1 e$^-$ s^{-1} @ 7.1 K
RQE [b] $5 - 6 \, \mu$m	$\sim 50\%$ [c]
$6 - 12 \, \mu$m	$\sim 60\%$ [c]
$12 - 24 \, \mu$m	$\sim 70\%$ [c]
$24 - 26 \, \mu$m	$\sim 30\%$ [c]
$26 - 28.2 \, \mu$m	$\sim 5\%$ [c]

[a]These figures are from Love et al. (2006) and should be close to the characteristics of the flight model detectors that were selected in 2008.

[b]Response Quantum Efficiency

[c]The efficiency of the detector is smaller than the intrisic quantum efficiency of the material because of the reflection of light on the Si layer. An anti-reflection coating is used to limit this loss.

The right panel of Fig. 10.14 shows the MIRI detector readout pattern, i.e. the signal on a MIRI pixel evolving with time. The fundamental unit of time is the pixel rate clock; all other times can be
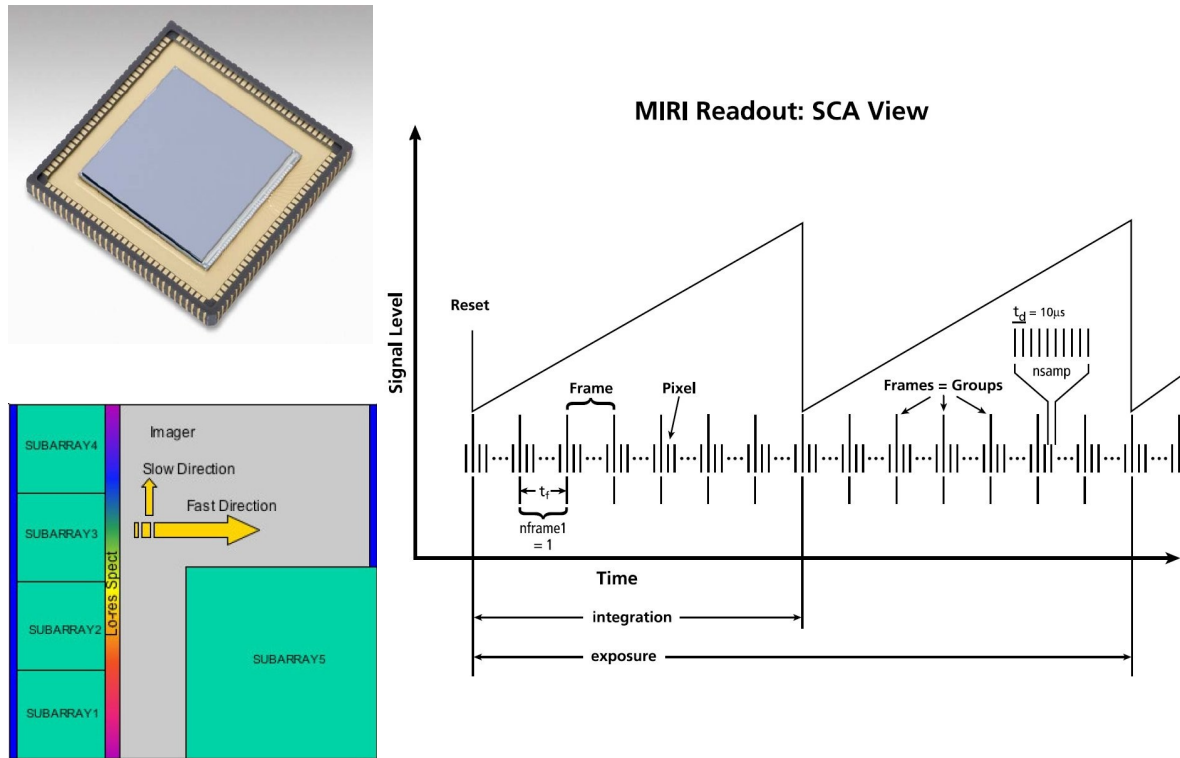
Figure 10.14: *Top left:* MIRI's detector: a SB305 1024×1024 pixels Si:As Sensor Chip Array (SCA), delivered by JPL / Raytheon Vision Systems. *Bottom left:* Pre-defined sub-arrays locations. *Right:* the readout scheme of the MIRI SCA.

calculated from that time base. This time between pixel samples, $t_{\rm d} = 10\,\mu$s, is set by the Focal Plane Electronics master 100 kHz clock. A "frame", the next unit of time, is the number of clock cycles needed to scan through the array, which represents

$$t_{\rm frame} = (256 \text{ pixels} + 8 \text{ for references} + 5 \text{ for reset}) \times (1024 \text{ rows}) \times 10\,\mu\text{s} = 2.755 \text{ s} \quad (10.1)$$

A "group" is a number of frames that are read and coadded together. MIRI does not generally use this feature, so that there is only one frame per group. An "integration" is the length of time the detector is allowed to collect light before resetting to zero, and is defined to be an integer number of frame times in length. Single integrations may range from 3 seconds (2.755 to be precise) up to $4\,000$ seconds. An "exposure" is the length of time MIRI is allowed to collect light before some intervention is needed, e.g. dithering the telescope, changing filters, etc. An exposure is the level at which MIRI is commanded: a command is sent with the number of frames, groups, and integrations that sets up MIRI, and a "GO" command is received to begin the actual exposure.

Two readout modes are implemented, the "Fast" and "Slow" modes. They apply to different kinds of astrophysical observations:

Fast Mode For MIRI observations of bright objects and long wavelength imaging, short source- or background-limited exposures will be used. Observations of the following types will utilize the Fast Mode:

- Broadband imaging at longer wavelengths ($\lambda > 12\,\mu$m)
- Bright object imaging at all wavelengths
- Bright objects with MRS spectroscopy

Some examples of bright objects include nearby star forming regions, the Galactic center, and more generally targets that lie in the Galactic plane. The Fast Mode is simply reading out the array at the fastest possible speed. Each pixel is addressed during the $10\,\mu$s window, sampled once after an appropriate amount of settling time, and the digitised data is sent out to the ISIM. Frame times in fast mode are ~ 3 seconds.

Slow Mode For many MIRI observations involving faint objects, deep imaging and MRS spectroscopy, long background-limited exposures will be required to achieve the needed sensitivity. Observations using SLOWMode will include the following:

- Broadband imaging at short wavelengths ($\lambda < 12\,\mu$m)
- $\mathcal{R} \sim 100$ LRS spectroscopy
- MRS spectroscopy

The Slow Mode increases the overall integration time with the SCAs in the following way. The FPE dwells on a pixel for 10 sample periods (or $100\,\mu$s) resulting in a frame time that is ~ 30 seconds long. The last eight samples are coadded and bit-shifted to a 16-bit value within the FPE before being sent along to the ISIM; the first two samples are discarded. This mode allows the potential of reducing the power dissipation of the detectors quite a bit if it is found to be necessary for stability concerns.

MIRI's arrays have the ability to read out partial frames, or subarrays, through the manipulation of the clocking patterns. This facilitates target acquisition imaging and selective use of the four coronagraph masks, and allows a reduction in the frame time and integration times of < 3 seconds. Subarray modes are only useful for the MIRI Imager. The subarrays are shown in the bottom left panel of Fig. 10.14. Four 256×256 subarrays are defined The four subarrays that match the coronagraphic locations are defined by the MIRI Imager optics and are approximately 256×256 in size. The 512×512 quadrant subarray's position is determined by the user. Subarrays can be defined in any part of the imaging area, with a minimum size of 64×64 pixels. In order to ensure consistent calibration of subarray modes, only a few subarrays will be allowed and the user will select from these predefined sets.

10.3.6   Observation modes: operating MIRI

The basic principles underlying the operation of the MIRI focal plane system (FPS) are as follows:

- the FPS enables four principal types of scientific observation: imaging, coronagraphic imaging, low-resolution slit spectroscopy, and medium resolution integral field spectroscopy.

- all MIRI data are sent to the ISIM Focal Plane Array Processor cards for further processing. There is no processing within the FPS, and on-orbit processing of the data is limited to frame coaddition in some high data rate circumstances.
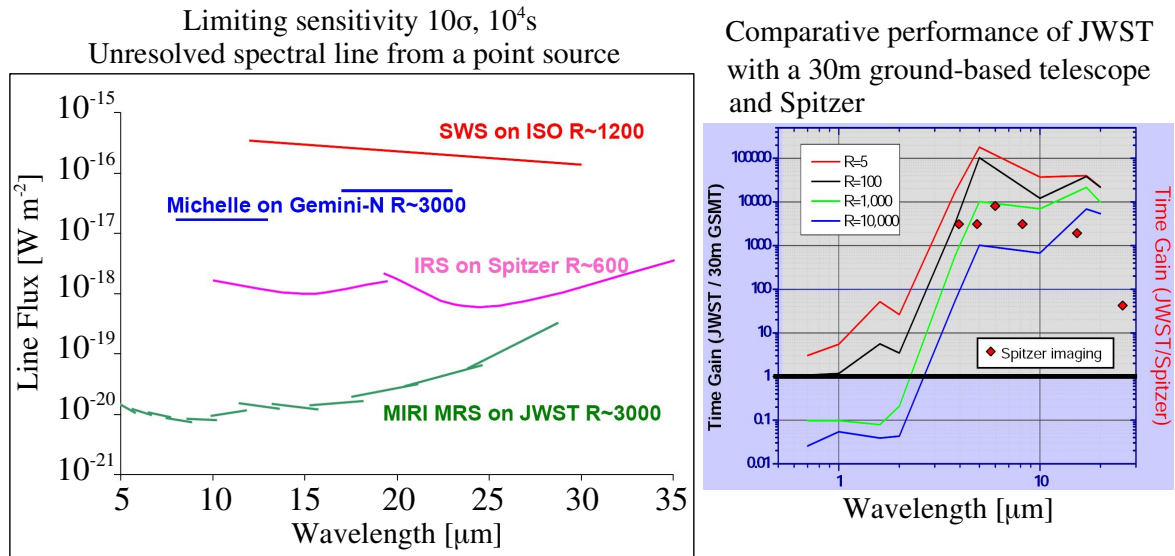
Figure 10.15: *Left:* Comparison of the spectral sensitivities between MIRI/MRS and other facilities. *Right:* Relative time gain of JWST compared to a 30 m Giant Segmented Mirror Telescope (GSMT) and *Spitzer*. The vertical axis is in relative units, where 1.0 means an observation with both JWST and GSMT (and *Spitzer*) will take the same time to reach the same S/N on a point source; a larger number means JWST is faster. Both Y-axis are the same.

- For bright object imaging and for imaging at the longest wavelengths (i.e. largest background emission from telescope), the array is read out at the fastest rate possible and subarrays may be used.

- the MIRI imager and spectrograph may be run in parallel for calibration purposes or target acquisitions.

- Data are taken in a redundant fashion. Sources will be dithered on the focal plane with the Fine Steering Mirror so that each point on the sky is sampled by many different areas of the sensor chip assembly (SCA). For the medium resolution Spectrometer (MRS), this accomplishes spectral as well as spatial dithering.

- Calibration of MIRI will be done periodically to monitor its stability and performance, as well as diagnostic tests and maintenance.

10.3.7 MIRI's sensitivity

All the sensitivities of the broad-band imager, the low-resolution spectrometer, and the medium-resolution IFU spectrometer are gathered in tables 10.4, 10.5, and 10.6, respectively. These figures are particularly helpful to prepare observation proposals (see chapter 12). The results are from modeling (Swinyard et al., 2004) that takes into account the different factors affecting the sensitivity: the background flux from the telescope and surrounding structure, from the instrument optics and structure, and from the zodiacal light, the cosmic ray hitting rate, the detector characteristics, the optical

Table 10.4: Sensitivity of the broad-band MIRI imager (MIRIM) [a]

| Filter | Wavelength | Bandwidth | Sensitivity S/N = 10 in 10 000 s on-chip integration | | Saturation limit |
			point source	extended source	point source
	[μm]	[μm]	[μJy]	[μJy arcsec^{-2}]	mJy
F560W	5.6	1.2	0.15	0.80	14
F770W	7.7	2.2	0.23	0.66	8
F1000W	10.0	2.0	0.50	0.85	11
F1130W	11.3	0.7	1.24	1.63	37
F1280W	12.8	2.4	0.87	0.85	12
F1500W	15.0	3.0	1.21	0.91	11
F1800W	18.0	3.0	3.0	1.6	14
F2100W	21.0	5.0	7.0	2.7	16
F2550W	25.5	4.0	20.0	5.2	22

[a] These figures do not include overheads due to target acquisition and calibration. The sensitivities quoted in this table are updated values of Swinyard et al. (2004).
[b] Saturation based on 10% of flux falling within the brightest pixel at 8 microns and a full frame exposure of 3 seconds integration time.

Table 10.5: Sensitivity of the Low-Resolution Spectrometer (LRS)

| Wavelength | Image FWHM | Spectral Resolving Power $\mathcal{R} = \lambda/\delta\lambda$ | $10\,\sigma$ 10 000 sec sensitivity at EOL (Point source) | |
			Predicted [μJy]	Requirement [μJy]
[μm]	[arcsec]			
7.5	0.24	100	2.8	2.9

efficiency of the instrument, etc. The imaging channel of the instrument is limited by the zodiacal background at wavelengths below $\sim 12\,\mu$m and by the emission from the telescope and sunshields at longer wavelengths. In the case of the MRS spectrometer, the instrument is almost entirely detector noise limited, except in the longest wavelength channel where the background is highest.

In the left panel of Fig. 10.15 we compare the sensitivity of the MIRI Medium Resolution Spectrometer to other facilities. In particular, up to $\sim 20\,\mu$m, the MRS will be about two orders of magnitude more sensitive than was the *IRS* spectrometer on-board *Spitzer*, with a spectral resolution ~ 5 times higher. The right panel of Fig. 10.15 summarizes the relative time gain between JWST instruments and *Spitzer*, or an hypothetical 30 m ground-based telescope. Such a gain in sensitivity will certainly lead to unexpexted discoveries. . .

Table 10.6: Sensitivity of the Medium-Resolution Spectrometer (MRS) [a]

Sub-band	Wavelength Coverage [μm]	Spectral Resolving Power $\mathcal{R} = \lambda/\delta\lambda$	Pixels per Resolution element Spectral	Spatial	Sensitivity S/N = 10 in 10000 second onchip integration Point source + narrow spectral line $[\times 10^{-20}\,\mathrm{W\,m^{-2}}]$	Extended source + narrow spectral line $[\times 10^{-20}\,\mathrm{W\,m^{-2}}$ $\mathrm{arcsec^{-2}}]$	Point source + continuum [mJy]	Saturation Limit Point source [Jy]
1A	4.9 – 5.8		0.9 – 1.1	1.1 – 1.7	2.8 – 2.2	9.7 – 5.6	0.11 – 0.15	
1B	5.6 – 6.7	2400 – 3700	0.9 – 1.2	1.2 – 1.6	2.2 – 2.0	6.2 – 3.9	0.10 – 0.16	5
1C	6.5 – 7.7		0.9 – 1.3	1.2 – 1.6	1.8 – 1.8	4.1 – 2.7	0.10 – 0.18	
2A	7.5 – 8.8		1.1 – 3.1	1.2 – 1.7	1.1 – 0.95	1.7 – 1.1	0.07 – 0.10	
2B	8.6 – 10.2	2400 – 3600	1.1 – 3.7	1.3 – 1.9	0.93 – 1.0	1.1 – 0.86	0.07 – 0.162	3
2C	10.0 – 11.8		1.2 – 4.1	1.6 – 2.2	1.0 – 1.1	0.92 – 0.70	0.08 – 0.16	
3A	11.5 – 13.6		1.0 – 2.1	1.6 – 2.0	1.1 – 1.2	0.73 – 0.58	0.10 – 0.19	
3B	13.3 – 15.7	2400 – 3600	1.1 – 2.2	1.9 – 2.3	1.1 – 1.0	0.54 – 0.36	0.12 – 0.19	2
3C	15.3 – 18.1		1.2 – 2.5	2.2 – 2.6	0.92 – 1.3	0.36 – 0.36	0.12 – 0.29	
4A	17.6 – 21.0		1.7 – 2.1	2.2 – 2.7	1.6 – 3.3	0.44 – 0.66	0.18 – 0.56	
4B	20.5 – 24.5	2000 – 2400	1.9 – 2.4	2.6 – 4.0	2.8 – 7.4	0.59 – 1.1	0.4 – 1.4	2 – 10 [b]
4C	23.9 – 28.6		2.2 – 2.7	3.1 – 3.7	5.7 – 30.0 [b]	0.88 – 3.1 [b]	0.9 – 6.5 [b]	

[a] The sensitivities quoted in this table are updated values of Swinyard et al. (2004).
[b] The quoted sensitivity is for $\lambda = 28.3\ \mu m$.

Chapter 11

First results from JWST/MIRI testing

Pour explorer le champ des possibles, le bricolage est la méthode la plus efficace. "It was like magic. The fact that a few calculations and a bit of do-it-yourself could make the invisible visible..."

Hubert Reeves

Abstract

This chapter presents my contribution to the testing of the Mid Infra Red Instrument (MIRI), part of the scientific payload that will be integrated onto the James Webb Space Telescope (JWST). The first tests at cryogenic temperatures and infrared wavelengths were performed on the Flight Model (FM) of the Mid-InfraRed IMager (MIRIM), from December 2008 to April 2009 at CEA, France. My work is focused on the "microscanning" test, which allows us to characterize the MIRIM optical quality with an unprecedent accuracy. I describe the instrumental test setup and discuss the results of the microscanning analysis that allows to obtain a "high-resolution" Point Spreag Function of the instrument. This analysis is of particular importance, not only for the optical quality check and the MIRI calibration, but also for potential scientific applications.

Contents

11.1   Introduction

Ground tests are essential to ensure the functionality and the optical performance of the instrument. They often lead to design changes from the first models built to the final flight model (FM). The characterization of the instrument (stray light, point spread function, flat field, etc.) has to be as accurate as possible during ground test campaigns since these tests are extremely limited in space.

In this chapter I present my contribution to the extensive test campaign of the MIRI imager (MIRIM, see chap. 10 for a description of the instrument). The first MIRIM optical performance tests in the infrared, at cryogenic temperatures, were performed at CEA, Saclay, during the December 2008 − April 2009 test campaign. I had the chance to participate in these tests, and I took the responsability of the analysis of one of these tests, so-called *microscanning*, which allows to characterize the Point Spread Function[1] (hereafter PSF) of the instrument very accurately. This was a great experience, and I had the opportunity to interact with engineers, and to attend meetings of the European Consortium, in which I had several opportunities to present my work.

It would be impossible to review all the tests and results that were performed on MIRIM. I will rather focus on the PSF analysis. After introducing some generalities about the PSF of the JWST and the context of MIRI testing, I describe in sect. 11.2 the instrumental setup used to simulate the JWST beam and to perform the cold tests. Section 11.3 presents a very brief overview of the tests performed on MIRIM at CEA, Saclay. In sect 11.4, we discuss the response curve of the detector and how we correct the images for the non-linearity of the detector. Then, Sect. 11.5 describes the microscanning test and the method used to reconstruct the high-resolution PSF of MIRIM. Sect. 11.6 discusses the PSF characteristics determined by the microscan analysis. Sect. 11.7 summarizes our results and in sect. 11.8 I briefly give the next steps of MIRI/JWST testing.

Introduction to the PSF of the JWST

From a basic point of of view, the PSF of an imaging system is determined by two things: the pupil shape and the WaveFront Errors (henceforth WFE). Often, the shape of the pupil is well known and relatively simple. For instance, in the case of a circular or annular aperture, the PSF is an Airy disk (the square of a Bessel function). However, for more sophisticated and larger systems, like the JWST or the Keck telescope, pupils are intrinsically a lot more complex. In Fig. 11.1, we illustrate how the pupil shape affects the PSF, building from an open circular pupil of diameter 6.5 m *(left)*, a hexagonal pupil of diameter 6.5 m *(center)*, and a realistic representation of the JWST pupil *(right)*. These PSF have been computed with the JWPSF software described in Cox and Spaans (2006).

Why is it important to characterize the PSF with precision?

The PSF translates the optical quality of the system. A careful measurement of the PSF characteristics is first needed to check the optical performance of the instrument, in order to verify that the instrument is nominally built. This is the main goal of the tests described in this chapter. A precise knowledge of

---

[1]The Point Spread Function is the image of a point source through the instrument. The PSF characterizes the imaging system's spatial response, i.e. its spatial resolution. In technical words, this is the impulse-response of the optical system.
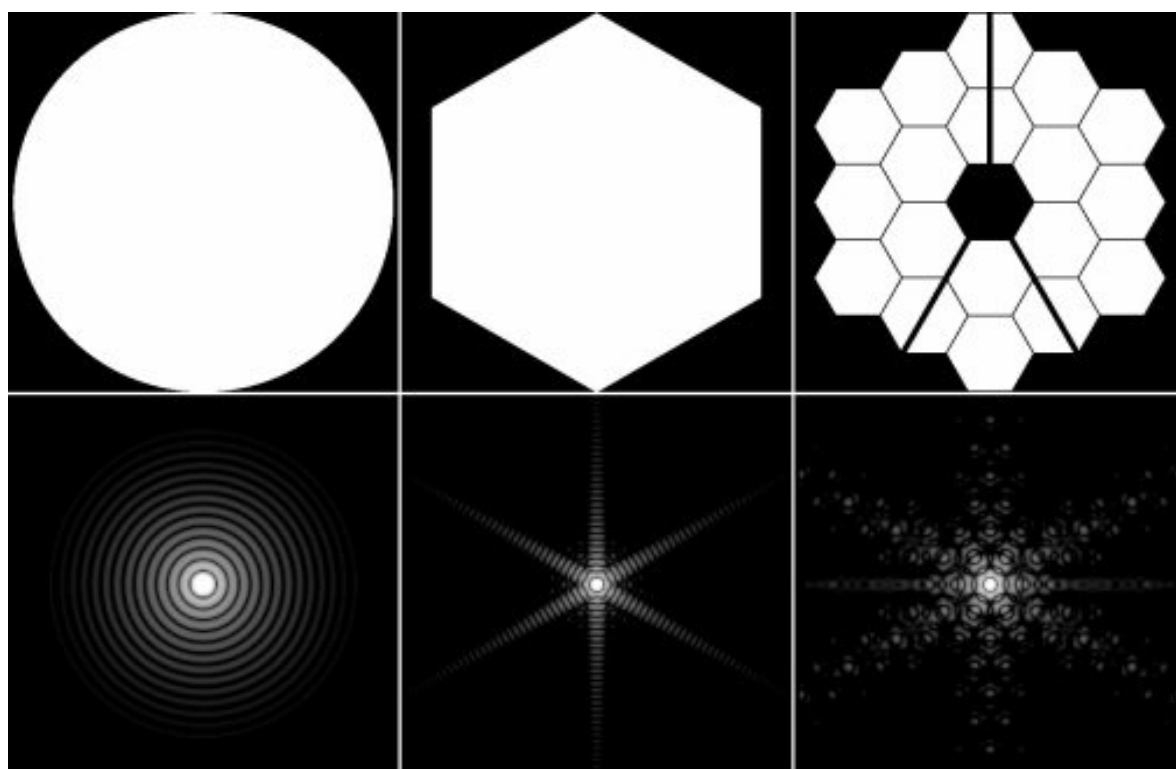
Figure 11.1: The PSF corresponding to each aperture is displayed on a logarithmic grayscale from 10^{-7} to 10^{-3} counts. The total number of counts in each of these simulated PSFs is 1. These PSF have been modeled with the JWPSF software[a].

---

[a]http://www.stsci.edu/jwst/software/jwpsf

the PSF is also crucial for the photometric calibration of the instrument and for scientific applications (photometry, source extraction, etc.).

Before determining if the PSF of the instrument is nominal or not, an important step is to study the impact of aberrations on the PSF. Errors in the wavefront can arise from a variety of sources, including imperfections in the system's optics or atmospheric variations in the case for ground-based observations. These WFE can be extremely difficult to determine. The Fig. 11.2 illustrates the impact of variations of the WFE on the PSF at $2\,\mu$m with the NirCam instrument (see sect. 10.2.5 for a description of the instrument). Two realizations of the WFE and corresponding JWST PSFs are shown. These PSFs differ in the specific distribution of the wavefront error across the pupil. As long as the error budget is satisfied, comparing these PSFs provides an estimate of the PSF differences that could be encountered in the normal course of observations.

A long path to the FM, and a European adventure!

To design and build an instrument like MIRI is a hard and long route! The development and qualification of the optical bench of the MIRI imager (MIRIM) started in 2004, and the first tests of the MIRIM flight model (henceforth FM) started in December 2008. Some hardware parts of the MIRI FM are still being, and will be, manufactured and tested in 2009-2010. MIRI is expected to be delivered to
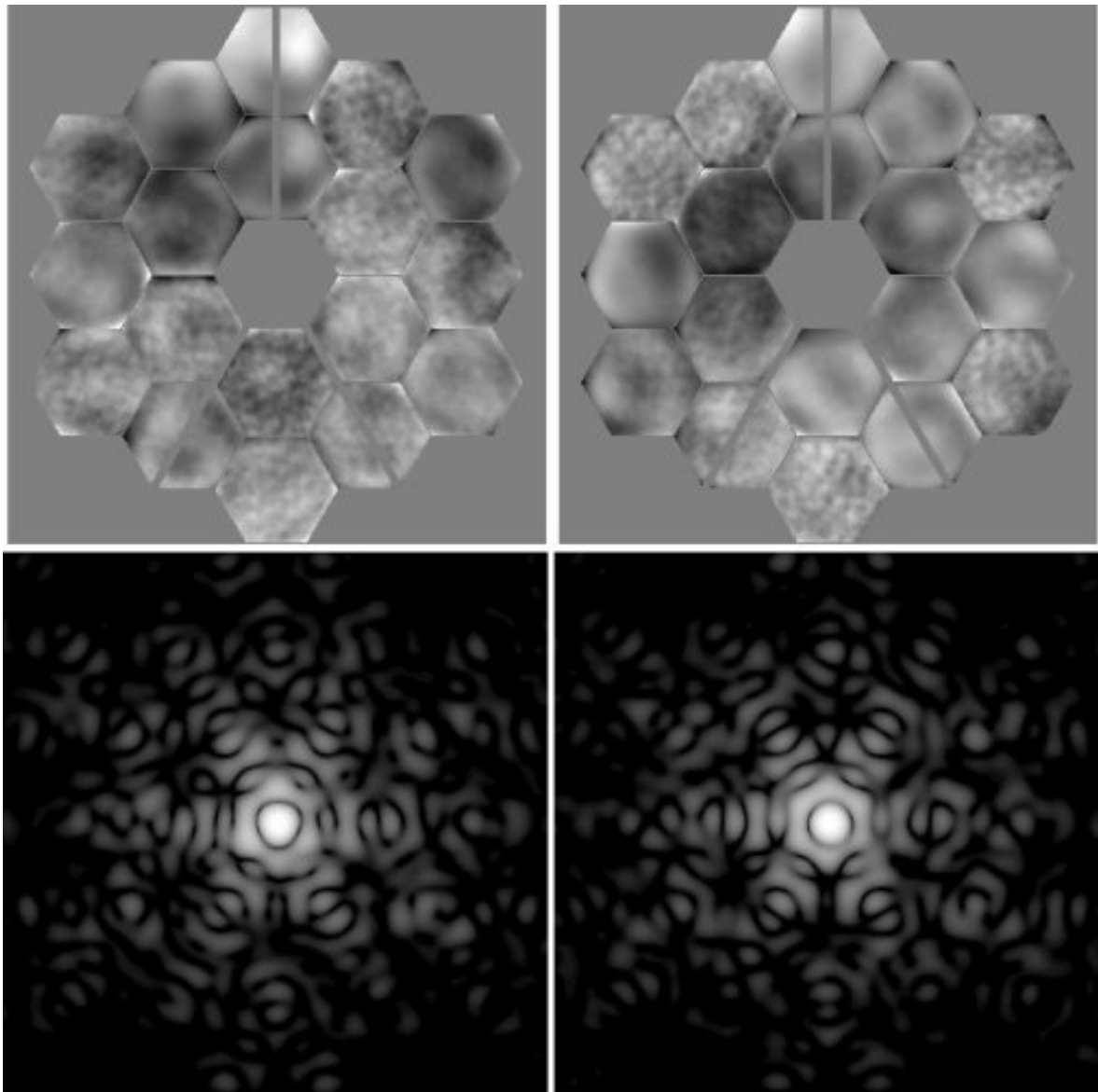
Figure 11.2: Comparison of two JWST error budget Optical Path Difference (OPD) files *(top)* and their associated PSFs *(bottom)* for a wavelength of $2\,\mu$m. OPDs are displayed on a linear grayscale from -400 to 400 nm, while PSFs are displayed on a logarithmic grayscale from 10^{-6} to 10^{-3}. The OPDs include wavefront error (WFE) contributions from the JWST Optical Telescope Element (OTE), the Integrated Science Instrument Module (ISIM), and the Near-Infrared Camera (NIRCam). The RMS WFE of both OPDs is ≈ 110 nm. While the differences in total RMS WFE are small, the impact of these differences on the resultant PSFs is measurable. These PSF have been modeled with the JWPSF software.

NASA at the end of 2010. Then MIRI will be integrated into the Instrument Science Module, at the back of the JWST primary mirror (see chapter 10), and basic testing (alignment, focus, etc.) will be performed in the giant cryogenic chamber at Johnson Space Center, Houston, USA (see 11.8).

Helium bottle   Cryostat   Hexapod cryostat   Cryostat window   IR source

Test bench as built   Telescope Simulator

PM1   Hexapod Source
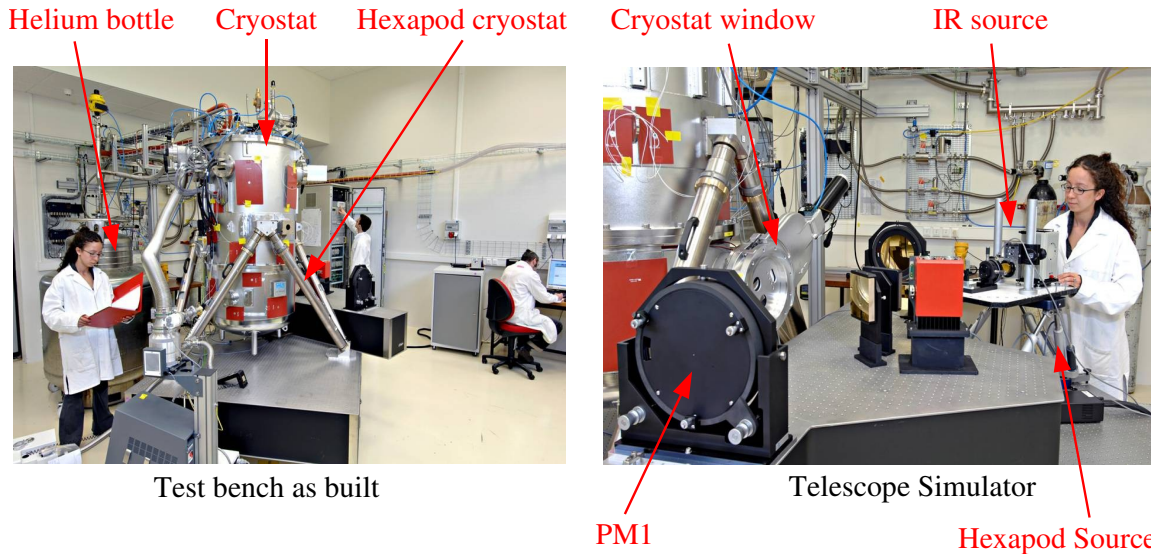
Figure 11.3: Photos of the test bench for testing of MIRIM at CEA, Saclay. The telescope simulator (TS) is lying next to the cryostat where MIRIM is installed. The IR blackbody source is mounted on an hexapod that allows fine motion scanning in the object plane of the TS.

Before the FM, several models of MIRI were built. A first mechanical model (the Structure and Thermal Model, STM) was to test thermal balance, integration and vibration at MIRI level. The first optical model was the Verification model (VM), and it was used to test the integration procedures and the optical performance. Then, the Engineering and Test Model (ETM) was an optically fully representative model, used to verify the optical performance and thermal behaviour of the instrument at cryogenic temperatures at CEA. The different steps leading to the FM integration of the Mid-Infra Red IMager Optical Bench (MIRIM-OB), and the principal results associated with the two test models, the STM and the ETM, were presented in Amiaux et al. (2008). In this chapter, I will focus on the FM.

The different parts of the MIRIM-OB system are built within the different institutes of the European Consortium, then gathered together and integrated at CEA-Saclay. The filters are under the responsibility of University of Sweden. The Double Prism Assembly for the Low-Resolution Spectrometer (LRS, see § 10.3.3) is a Belgium (CSL) and a Germany (University of Köln) collaboration. The coronographic masks are manufactured at Observatoire de Meudon (LESIA) in France. Optical elements are then integrated onto the Filter Wheel Disk under CEA responsibility (see § 10.3.2 for a description of the filter wheel and its filters). The Filter Wheel Disk is delivered to MPIA in Germany for integration on the Filter Wheel cryo-mechanism. Filter Wheel Assembly is then returned to CEA-Saclay for further integration into MIRIM Optical Bench.
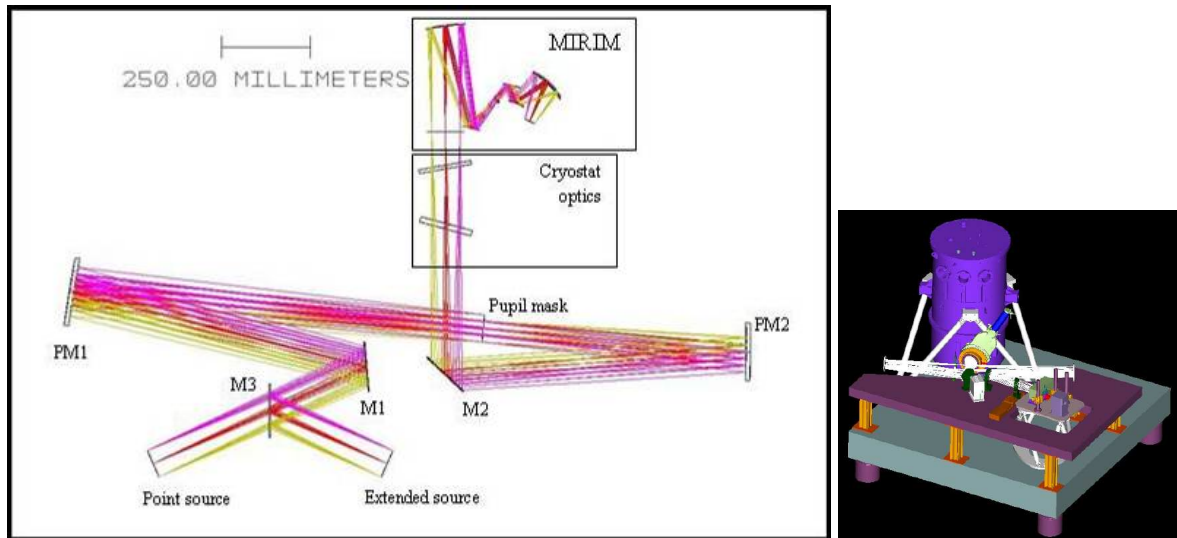
Figure 11.4: The MIRIM test bench. The left panel shows the optical scheme of the Telescope Simulator (TS). The warm TS is installed outside the cryostat (in blue on the right panel) that contains MIRIM. The TS simulates the JWST beam and pupil. It allows the use of a point or extended source, in order to characterize MIRIM in image or coronographic mode.

11.2 Instrumental setup: the MIRIM test bench at CEA

The tests of the MIRIM optical quality have been performed with an ambient temperature Telescope Simulator (hereafter TS), installed outside an helium-cooled cryostat that contains MIRIM-OB (Fig. 11.3). The TS simulates the optical beam delivered by the JWST. The optical conception of the TS is based on two off-axis parabolic mirrors (PM1 and PM2) and a pupil mask in between (Fig. 11.4). The pupil mask is the pupil of the telescope simulator (so-called the "STOP") and it reproduces the pupil of JWST. It is mounted on motorised translation and rotation stages (4 axis: 3 translations and one rotation). This allows fine adjustment to co-align the telescope simulator and MIRIM pupils. These degrees of freedom are also used to simulate pupil shear, which occurs when the pupil stop is mis-aligned with the telescope pupil image.

The telescope simulator was mainly designed by Yuying Longval at IAS, and installed at CEA, Saclay. The field of view of the TS is $80\,\mathrm{mm} \times 80\,\mathrm{mm}$ for a MIRIM field of view of $72\,\mathrm{mm} \times 72\,\mathrm{mm}$. An analysis of the image quality[2] shows that the distortion amounts to 0.33% for the useful field. The aperture is $F/20$ in the image plane. The exit pupil location is 3017.5 mm from the image plane for a diameter of 151.6 mm. The pupil is 75.4 mm in diameter. To implement the MIRIM cryostat in a minimum space, folding mirrors are used.

An IR point source with a shutter is mounted on a remotely controlled hexapod, that can be moved in 3 directions (X, Y and Z). The minimum diameter of the point source is 30 μm, and the temperature of the source is 1150 K for the imaging mode, or 2000 K for the coronographic mode. An extended black body source (400 K) can also be used. The 10K screen in the cryostat is fitted with a neutral

---

[2]The design and optical quality analysis are reported in a document by Y. Longval & A. Abergel (not reproduced here).

Table 11.1: MIRIM images type[a]

Name	Description
DIT	single image from one detector integration time
HCYC1	addition of all the DIT images taken during the first half-cycle of the shutter (open)
HCYC2	addition of all the DIT images taken during the 2nd half-cycle of the shutter (closed)
INTERM	intermediate integrated image from one full cycle of the chopper (HCYC1−HCYC2)
INT	integrated image (addition of all the INTERM images)

[a]We list the different types of images generated with the chopper. The type of images to produce depends also on the test being performed.

density (ND) that reduces the flux due to the 295K background. All the tests were performed when the instrument is cold. During each of the tests, the temperature of the instrument must be between 5 and 7K and stable at ± 250 mK. The detector temperature is 6.7K and is stable at ± 10 mK. For a more detailed description of the test bench, see Amiaux et al. (2008).

At the time of the FM test campaign, the filter wheel assembly was not available because of vibration testing, and only one filter (5.6 μm) was available. The filter wheel was replaced by a "mono-filter wheel" (often called a "cyclop tool"). Since there was no dark position available, a chopper has been used. The different types of images produced are listed in Table 11.1. A measurement cycle consists in two sub-cycles (shutter closed, shutter open). The exposition time, or the total duration of a measurement, T_{exp}, (i.e. total time to get one INT image) is calculated as follows:

$$T_{\mathrm{exp}} = N_{\mathrm{cycles}} \times T_{\mathrm{cycle}} \, , \tag{11.1}$$

where T_{cycle} is the duration of a cycle. We have $N_{\mathrm{cycles}} = N/N_{\mathrm{DIT}}$, where N is the total number of DIT images (see Table 11.1 for definition) required to achieve a given signal ratio and N_{DIT} is the number of DIT images per half cycle. The duration of a cycle is given by

$$T_{\mathrm{cycle}} = 2 \times (N_{\mathrm{DITSKIP}} + N_{\mathrm{DIT}}) \times DIT = 1/f_{\mathrm{CHOP}} \, , \tag{11.2}$$

where N_{DITSKIP} is the number of images to skip at the beginning of the cycle (delay for the shutter to close), DIT the detector integration time, and f_{CHOP} the chopping frequency. The factor of 2 is because there are two half-cycles per cycle: shutter close and shutter open.

11.3 Overview of the MIRIM optical performance tests

The first tests in the infrared, at cryogenic temperatures, were performed on the ETM at CEA, between February and April 2008. An overview of the optical performance tests is presented in the flowchart of Fig. 11.5. The ETM model is fully representative in terms of optical path, but not in terms of alignment of the optical path. Indeed, the ETM FWA is a proto-type without requirements on alignment. Below is a brief description of these tests. Similar tests have been performed on the Flight Model (Dec. 2008−April 2009).
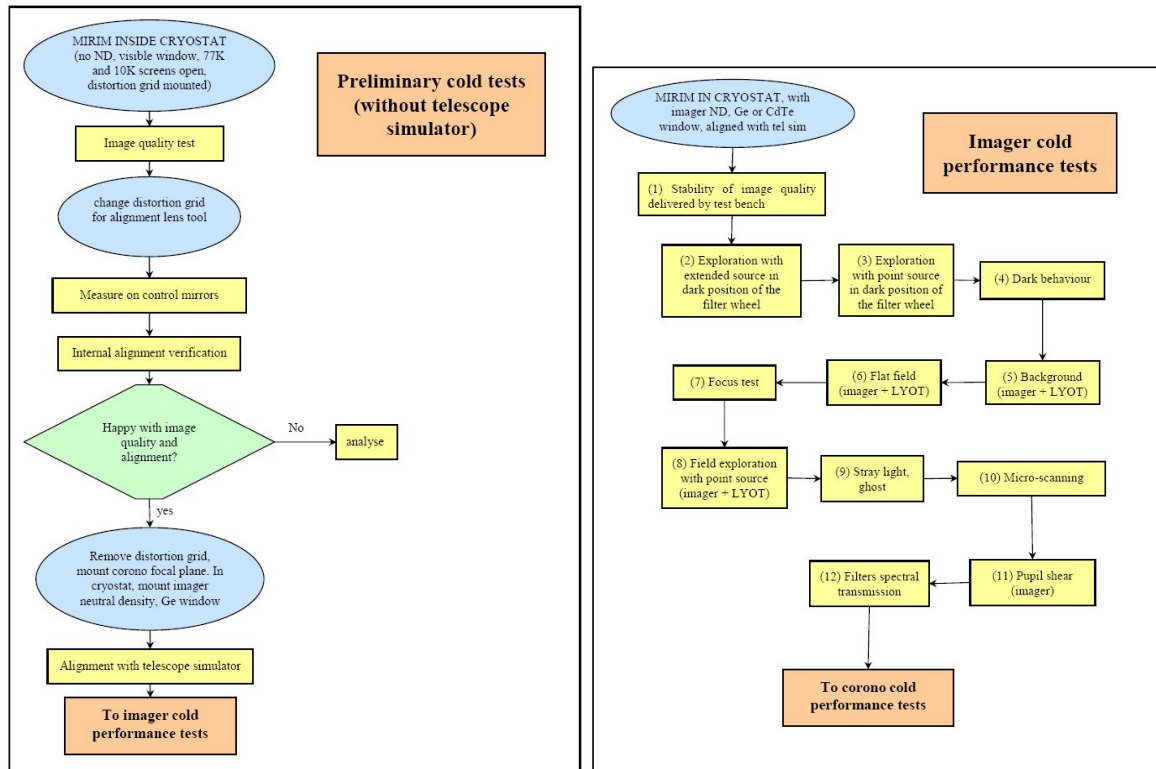
Figure 11.5: Flowchart of the tests performed on the MIRIM Engineering Test Model (ETM) and the Flight Model (FM).

Distortion grid at ambient and cold temperatures: a grid of 87×87 pinholes ($5\,\mu$m in diameter), with a regular pitch, is mounted at the entrance focal plane, illuminated by an optical LED, and imaged with a 2048×2048 CCD chip. This setup allows to measure the magnification and the distorsion over the whole field of view in one image, at ambient temperature (~ 300 K). Shims[3] are used to simulate a possible telescope defocus. The CCD camera tool is equipped with a micrometric translation stage along the optical axis, which allows to explore and to search the best focus position. This test is also performed at cryogenic temperatures and with infrared light, which allows to assess image quality and perform flat field measurements.

Alignment check at ambient and cold: The alignment consists in pointing the coronagraphic diaphragms with an alignment telescope that is coaligned with MIRIM optical axis. A correction is applied by shimming the M1 in order to minimize the shift between the optical axis and the centre of the diaphragms. This test has been performed at ambient and croygenic temperatures.

Image quality with telescope simulator:

---

[3]a shim is a thin and often tapered or wedged piece of material, used to fill spaces between the mirror and its supporting structure. Shims are used in order to adjust the positions of the mirrors.

- Field of View exploration with a point source: a point source ($30\,\mu$m in diameter) is scanned in the FoV to measure its extent, its vignetting, straylight, and search for ghost images.
- Stray light: a very bright point source ($150\,\mu$m pinhole) is scanned out of the field of view (on the mechanical aperture of the focal plane and across its edges).
- Pixel micro-scanning: for accurate measurement of the PSF (see sect. 11.5).

Coronagraphy performance:

- Peak-up: validation of the peak-up mode (accurate positioning of a source at the centre of a coronographic mask)
- Rejection factor: measurement of the attenuation of the coronagraphs.

11.4 Data reduction

11.4.1 Basic reduction steps

For the microscanning, the shutter is used in chopping mode (see sect. 11.2). A total of 8 DIT frames is taken for each cycle (open−close shutter). A 72×64 sub-array is read out, with a detector integration time $DIT = 0.827$ s. Thus, according to Eq. 11.2, the duration of a cycle is $T_{\text{cycle}} = 13.23$ s. For each cycle that is beginning, the first frame is skipped because during this frame the shutter is closing. Then, the following 3 DIT frames are skipped because of latency effects on the detector since the point source is very bright. Therefore, we use the last 4 frames of the cycle. Each exposure comprises 10 cycles, so the exposure time is $T_{\text{exp}} = 132.3$ s. A median image is created from these 10 cycles.

11.4.2 Linearity correction for the response of the detector

JPL and CEA performed tests of the response of the detector and it appears that the detector is non linear over a wide range of ADU values. To quantify the impact of the non-linear response curve on the PSF measurements, S. Ronayette and myself provide two sets of test data: one that is not corrected for the detector response, and the other which is corrected for the non-linearity. I have performed the PSF analysis on the two data sets to compare the results.

The MIRIM detector is a 1024×1024 pixels SiAs array. JPL has delivered a Raytheon SB305 detector to CEA. The detector configuration will be a Sensor Chip Assembly (SCA), i.e. an ultra-light mechanical & electrical housing. CEA has developed an appropriate housing (similar to the MIRI focal plane) to mount the IR detector onto the imager for the cold tests. Thus, qualitative analysis of the optical properties, including stray light performances, are possible.

Fig. 11.6 presents the detector response. Measurements have been done by V. Moreau at CEA on the SB305 detector at 5 K, with an extended blackbody source in front of the detector. The source is at constant temperature (30 K) and the integration time is the only parameter that changes. The longer the integration time, the higher the signal in units of ADU. The 30 K blackbody source does not allow us to explore the linear part of the response curve, at low ADU values, since with the smallest integration time (2.7 s, see chapter 10, sect. 10.3.5), we reach a signal of 26 360 ADU (see Fig. 11.6).
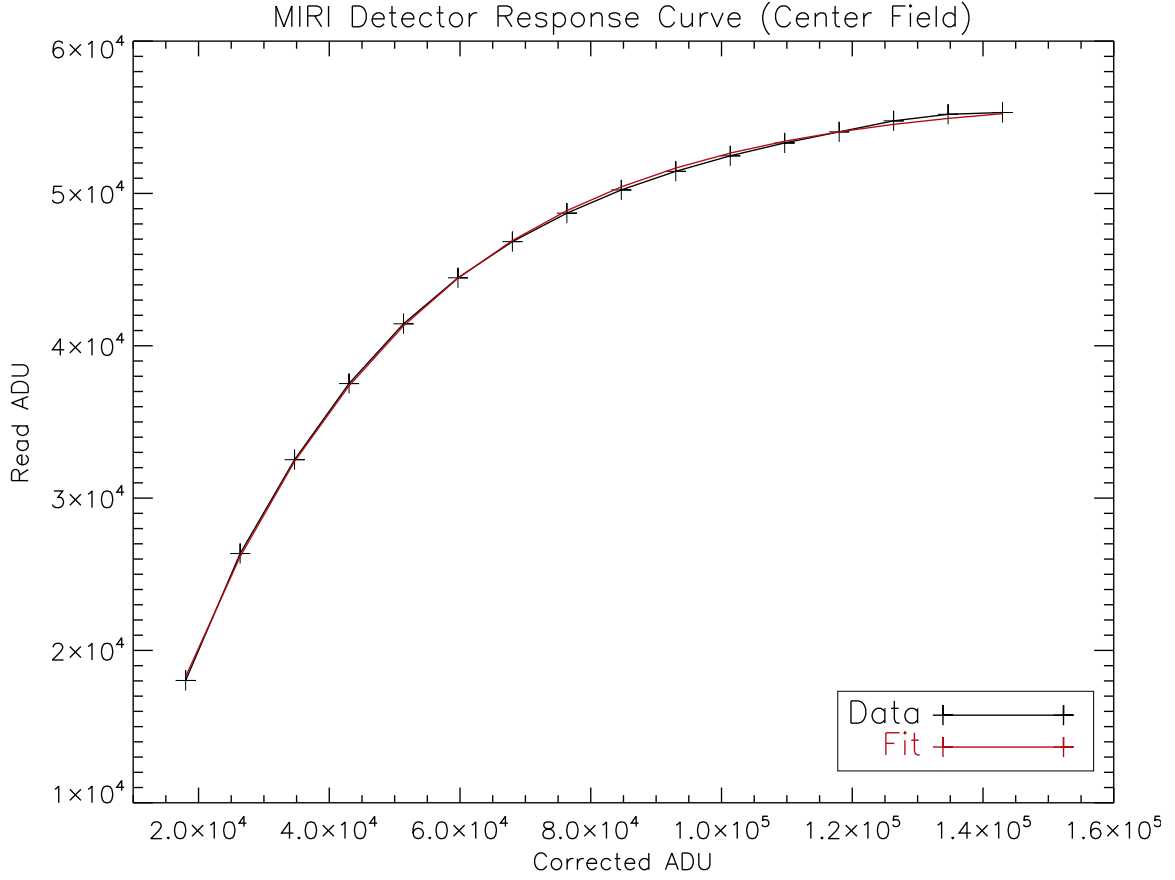
Figure 11.6: The response curve of the MIRI SB305 detector obtained at CEA. Measurements have been done at 5 K. The back curve show the average read ADU values of the pixels in the center of the field as a function of the corrected values (see text for details). The red curve indicates an exponential fit (see § 11.4.2, Eq. 11.4).

Fine measurements a low integrated fluxes were performed with colder black body sources (not shown here). An accurate sampling of the response curve at low ADU values shows that the response is linear for ADU values lower than $\approx 16\,000$ (V. Moreau, private communication) and follows the law:

$$S_{\text{lin}} = \alpha \times t_{\text{int}} + \beta \ , \tag{11.3}$$

where S_{lin} is the signal in ADU in the linear part of the response, $\alpha = 3067$ ADU s^{-1} is the slope of the linear response and $\beta = 18030$ ADU the offset.

The low background signal ($18\,030$ ADU on Fig. 11.6) is measured more accurately with colder black body sources. It allows to do a fine sampling of the beginning of the response curve, at low levels, where the response is approximately linear. Fig. 11.6 shows the read value as a function of the corrected value. To estimate the corrected value, the difference between the linear response (linear fit done at low signal given by Eq. 11.3) and the read value is calculated. To perform the linearity
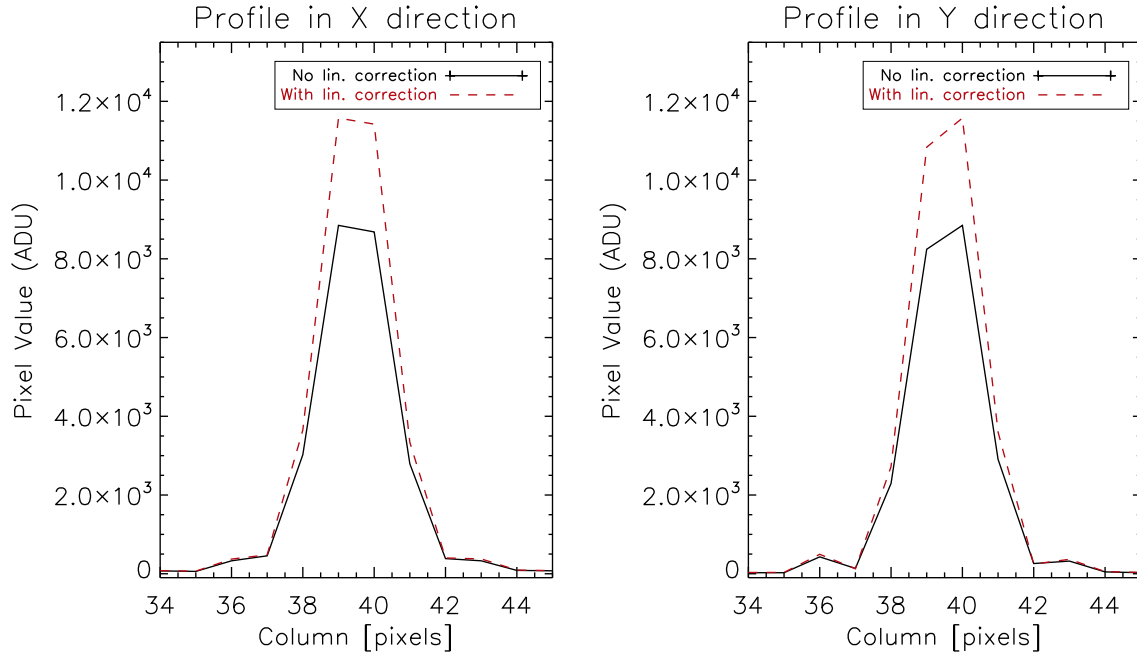
Figure 11.7: The impact of the linearity correction on the low-resolution PSFs. The plots show MIRIM PSFs profiles at $5.6\,\mu$m in two perpendicular directions. The pixel size is $25\,\mu$m. The black line represents data that have not been corrected for the detector response. The red dashed line shows the same PSF profile when the linearity correction is applied.

correction, I have fitted the response curve by an exponential function:

$$S_{\text{read}} = A - B\,e^{-S_{\text{cor}}/C} \; , \tag{11.4}$$

where S_{read} is the read signal in ADU and S_{cor} the corrected one. I found $A = 56\,418.5$, $B = 62\,939.1$ and $C = 35\,990.5$ ADU. The red line on Fig. 11.6 shows the result of the fit.

To apply the linearity correction, we derive S_{cor} from S_{read} and correct all the individual images. Fig. 11.7 compares the PSF profiles when the linearity correction is applied or not. The correction enhances the highest values of the signal, so it improves the sharpness of the PSFs.

11.5 The micro-scanning test

In this section we first describe the goals, principle and experimental method to perform the microscanning. Then, results are discussed. This test, together with field of view measurements, led to the discovery of a defect in the instrument after the first FM1 test campaign. This defect was a tilt of the M4 mirror (see Fig. 10.10 for the position of this mirror in the optical layout of the instrument). This anomaly was corrected and a second test campaign was performed (FM2). We show the differences in the optical quality of the instrument, before and after correction for the two FM test campaigns (FM1 and FM2).
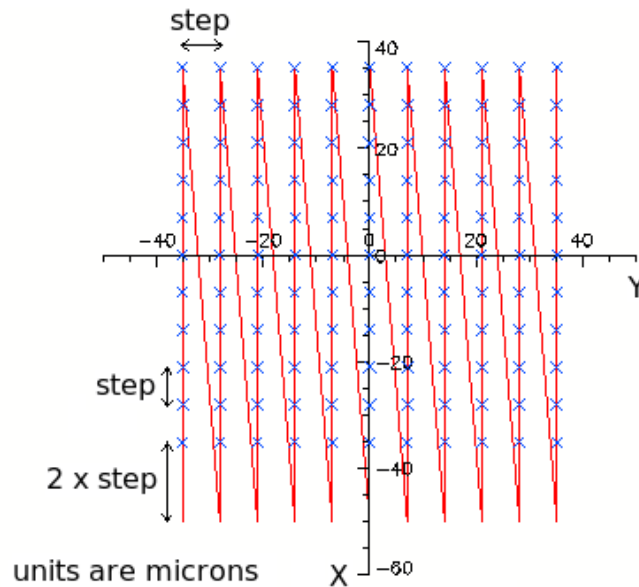
Figure 11.8: *Pattern of the microscan. A* 11×11 *points scanning grid has been performed, corresponding to a total scanning area of 1 pixel on the detector plane. The source has been moved by steps of 7 μm on the hexapod mount of the telescope simulator. This corresponds to individual displacements of 2.5 μm on the detector plane.*

11.5.1   Aims and experimental method

Since the physical size[4] of the pixels is 25 μm, the Point Spread Function (PSF) of the instrument is not Nyquist-sampled at a wavelength of 5.6 μm (the theoretical FWHM of the PSF at 5.6 μm is 0.185", i.e. is less than 2 pixels), which is the shortest wavelength for MIRI, and the most critical for the assessment of the optical quality. Therefore, it is difficult to check the optical quality of the instrument at this wavelength with a single point source image.

The goal of the microscanning test is to obtain a *"high-resolution"* (HR) image of the PSF from multiple "low-resolution" (LR) raw images. In other words, the microscanning aims at providing a highly-sampled image of the PSF. Such a resolution enhancement approach has been an active research area, in particular in image or video processing, and it is sometimes called *over-resolution* image reconstruction, or simply resolution enhancement. Here, the HR PSFs are used to perform an accurate measurement of the MIRIM image quality.

The basis of the inversion method used to analyse the microscanning data has been developed to perform high spectral and spatial resolution spectroscopy with *Spitzer* telescope InfraRed Spectrometer (IRS) data (Rodet et al., 2009). This work relies on a fruitful collaboration between the LSS[5] and the IAS institutes in Orsay. With the help of T. Rodet (LSS), I have applied Matlab algorithms of data inversion to process the microscanning data, and analyse the results with standard tools (IRAF, IDL).

---

[4]The angular size for one pixel is 0.11"

[5]The LSS is the "Laboratoire des Signaux et Systèmes", an institute specialized in signal processing, see http://www.lss.supelec.fr/.
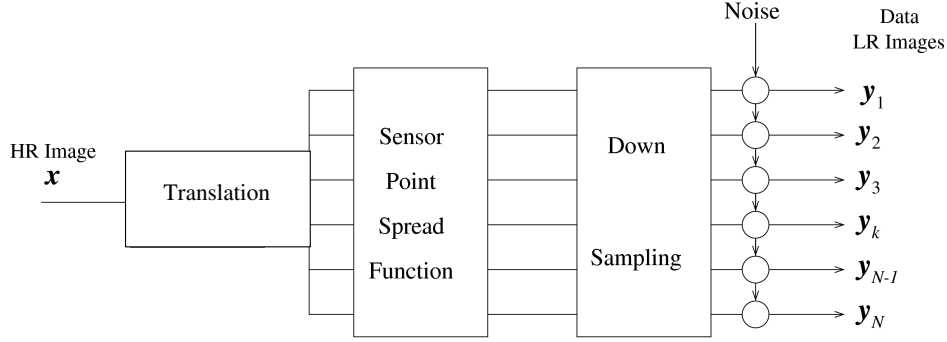
Figure 11.9: Sketch of the direct problem of generation of images. This figure links the high-resolution optical PSF x to the low-resolution ones y_k that we observe.

The microscanning test is performed at cryogenic temperatures and at a wavelength of 5.6 μm. No other filter was available at that time because the filter wheel was not delivered to CEA. The method consists in scanning a point source in a fine spatial resolution. The microscan pattern is given in Fig. 11.8. A 11×11 points grid has been done, corresponding to a total scanning area of 1 MIRIM pixel on the detector plane, i.e. an area of 10^2 pixels^2. The source has been moved by steps of 7 μm on the hexapod mount. This corresponds to individual displacements of 2.5 μm on the detector plane. In the following sub-sections the method we apply to reconstruct the high-resolution images is detailed.

11.5.2   Direct and inverse problem

The total point spread function PSF_{tot} of an imaging system consists of several components. Firstly, the light is diffracted within the optics. This part will be denoted PSF_{opt}. For instance, PSF_{opt} is an Airy disk in case of a circular aperture. Once the light has passed through the optical elements (mirrors, filters, gratings, etc.), the signal is integrated on the sensor (array) composed of squared detectors (pixels). Because the area of a pixel is not infinitely small, this causes blurring (PSF_{det}) which can be modeled by a uniform square function if the spatial response of a pixel is flat over its entire area. The total PSF can be computed by convolution of its different parts[6]:

$$PSF_{\mathrm{tot}} = PSF_{\mathrm{opt}} \star PSF_{\mathrm{det}} \tag{11.5}$$

The process of generation of the images is schematically shown on Fig. 11.9. We denote x the high-resolution (HR) optical PSF. The aim of the deconvolution method is to deduce x from multiple low-resolution images y_k (the observed data).

Let us describe the *direct* problem by assuming that we start from the high-resolution image x. The high-resolution optical PSF x that we want to estimate is first translated because of the motions of the source. Then, the observed and translated images y_k are the result of the convolution by the PSF of the detector, PSF_{det}. In the schematic Fig. 11.9, we separate the integration of the detector in two

---

[6]There are additional parts that contribute to the final PSF that we do not consider here. For instance, motion of the sensor platform causes blurring. In addition the electronic components cause smoothing by applying a low-pass filter to reduce noise.
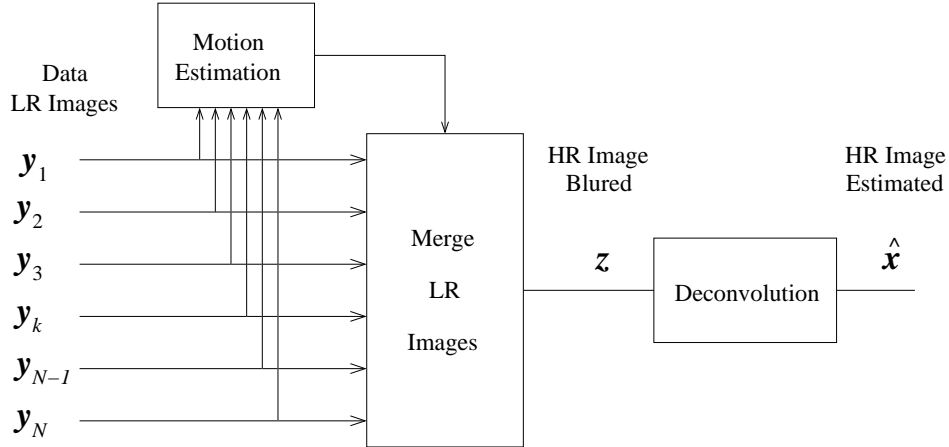
Figure 11.10: Sketch of the different steps to reconstruct the high-resolution image (inverse problem).

steps: *(1)* a convolution by the PSF of an over-sampled (fine grid) detector (a detector that would have smaller pixels than the real detector of the instrument), and *(2)* a down-sampling operation needed to degrade the resolution of the fine detector to the real, low-resolution of the obervations. The ratio between the pixel size on the fine grid and the physical size on the real detector is named *over-sampling factor*, f, which represents the gain in resolution.

We formalize these operations by matrix multiplications. We define three matrices, T_k, R et S, which are associated with the operations of translation, convolution by the impulse-response of a pixel, and down-sampling, respectively. Thus, the direct problem can be summarized as

$$y_k = SRT_k x + n_k \tag{11.6}$$

with $k \in \{1, \ldots, N\}$. N is the total number of images taken at different positions on the detector. n is the noise, whose level is assumed to be commesurate for all the images. Note that in Eq. 11.6, the only operation that is different from an image to another is the translation T_k.

To obtain high values of the over-sampling factor (gain in resolution), one needs to know very precisely the translations between images. Unfortunately, this is not the case for our experimental setup. Although the hexapod (where the point source is mounted) is designed to allow fine motions of the source, we note significant mismatches between the expected position and the effective observed location of the source. Therefore we decided to estimate the relative positions between images by a technique which is independant of the mechanical control of the hexapod. We perform cross-correlation calculations between a reference images and the other translated images in order to estimate the shifts between images. This is the first step of our inversion problem.

Fig. 11.10 shows a sketch of the inverse problem. To reconstruct a high-resolution image from N low-resolution ones, we proceed in three steps:

1. we first estimate the translation between the low-resolution (LR) images by cross correlation (see sect. 11.5.3 for details).
2. then, we co-add the LR images on a fine grid, assuming that there is no convolution by the PSF of the detector.

3. finally, we solve the deconvolution problem.

This algorithm is a simplified version of a more complex algorithm developped by Rodet et al. (2009).

11.5.3 Estimate of the translations between images and co-addition

Although the translation between the point source images is mechanically controlled, we note that the effective position of the source is slightly different from the expected position. Therefore, we compute the shifts between a reference image and the current translated image, and we compare the result to the expected position that the hexapod should have given.

We estimate the relative motions between the images with a cross-correlation technique. To determine sub-pixel translations between images, we perform a bilinear interpolation on an HR grid at a resolution equal to three times the over-sampling factor ($3 \times f$). We define the first image as the the reference image $\boldsymbol{I}_{\mathrm{ref}}$ and we search, in an exhaustive manner, the displacement that maximizes the cross-correlation factor, Cor, between the reference image and the current translated one, $\boldsymbol{I}$. The cross-correlation is computed as:

$$\mathrm{Cor}(\boldsymbol{I}, \boldsymbol{I}_{\mathrm{ref}}) = \frac{1}{\sigma_{\boldsymbol{I}_{\mathrm{ref}}} \, \sigma_{\boldsymbol{I}}} \sum_{\mathrm{i_r, j_r}} \sum_{\mathrm{i, j}} \left(\boldsymbol{I}_{\mathrm{i, j}} - \langle \boldsymbol{I} \rangle\right) \left(\boldsymbol{I}_{\mathrm{ref, i, j}} - \langle \boldsymbol{I}_{\mathrm{ref}} \rangle\right) \tag{11.7}$$

In Eq. 11.7, $\sigma_{\boldsymbol{I}_{\mathrm{ref}}}$ and $\sigma_{\boldsymbol{I}}$ are the standard deviations of the matrices $\boldsymbol{I}_{\mathrm{ref}}$ and $\boldsymbol{I}$, respectively. $\langle \boldsymbol{I}_{\mathrm{ref}} \rangle$ and $\langle \boldsymbol{I} \rangle$ are the averages of $\boldsymbol{I}_{\mathrm{ref}}$ and $\boldsymbol{I}$, respectively.

Then, these motions are compared with the expected values measured with the hexapod. A sub-pixel precision is obtained. Fig. 11.11 shows an example of the comparison between the read position of the hexapod (expected position in blue) and the position estimated by cross-correlation (in red). The agreement between expected and estimated positions for the displacement in the X-direction is very good. However, a slight discrepancy is seen for the Y-direction. The hexapod did not move at the expected positions in this direction. This issue is likely to be due to the control system of the hexapod support, which is not optimally designed to perform translations along the X and Y axis.

The mismatch between estimated and expected relative motions between images introduces errors in the reconstruction method if one uses the expected positions. Therefore, the estimated motions are used to reconstruct the high resolution image. We also compare the results if one uses the expected motions.

Assuming that the translations $\boldsymbol{T}_k$ are known, we co-add low-resolution images $\boldsymbol{y}_k$ onto an over-resolved image (fine grid). We choose the over-sampling factor f such that $7 \leqslant f \leqslant 10$. Thus, a HR image $\boldsymbol{z}$ is created but it is still blurred because of the response of the detector. The slight discrepancy between expected and estimated positions $\boldsymbol{T}_k$ represents a lack of information, in particular in the Y-direction. Some pixels of the HR image $\boldsymbol{z}$ are not present in the data $\boldsymbol{y}_k$.

11.5.4 Deconvolution

We denote $\boldsymbol{z}$ the LR image that have been over-sampled on a fine grid. This image is still "blurred", but its number of pixels is a factor f^2 higher than the observed LR image. $\boldsymbol{z}$ is the convolution of the HR image $\boldsymbol{x}$ that we want to calculate by the impulse-response (PSF) of the detector:

$$\boldsymbol{z} = \boldsymbol{R}\boldsymbol{x} + \boldsymbol{n} \tag{11.8}$$
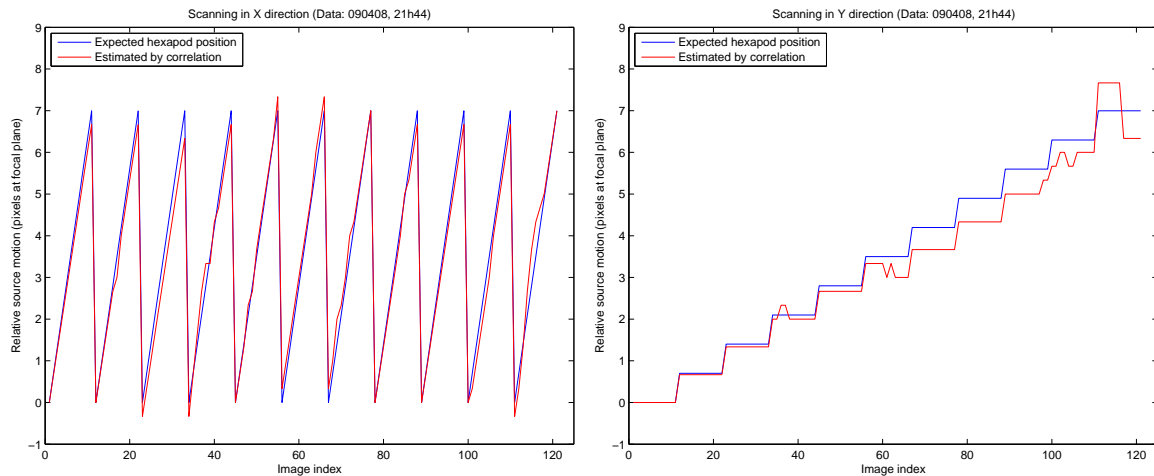
Figure 11.11: Expected vs. Estimated displacements of the source in the X and Y directions during the microscanning. A slight discrepancy is seen between the estimated moves on the image and the expected position of the source for the Y-direction because, in practice, to control the absolute position of the hexapod is difficult. For the X-direction, the agreement is excellent.
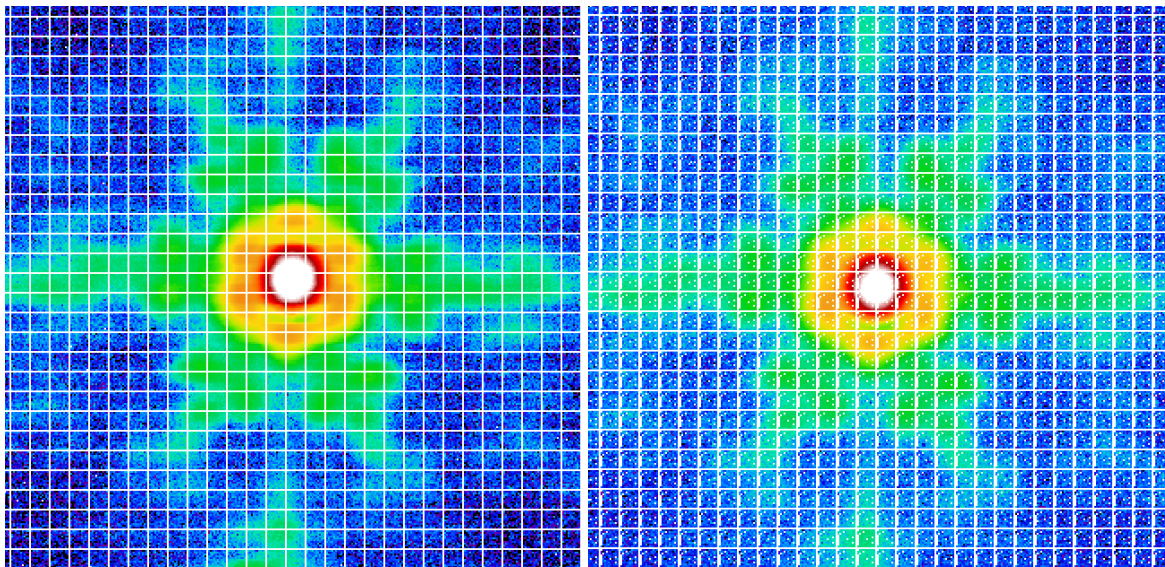
Figure 11.12: PSF data co-added on a fine grid for an over-sampling factor of 11. The white pixels show the truncation of the data (lack of information). The *left* panel shows the co-added image when the expected shifts between images are used. Since the microscan comprises 10 shifts, the truncation of the data is a cross-hatching with 11 pixels between each white line. On the *right* panel, the effective shifts estimated by cross-correlation are used. Additional truncation can be seen, due to the mismatch of the expected and effective translations between images (see text for details).

One cannot apply the classical methods of deconvolution because part of the data is not observed (due to uncertainties on the translations, see sect. 11.5.3). Indeed, there are missing parts, "holes", in the

data because the source is not exactly at its expected position on the fine grid image. The Fig. 11.12 shows the PSF data co-added onto a fine grid with an over-sampling factor of 11. We illustrate the truncation of the data by comparing the results of the co-addition when using the expected positions of the source, to the results when using the shifts estimated by cross-correlation. The additional truncation for the effective translations comes from the mismatch between expected and real position of the source.

We take into account the truncation of the data by introducing a matrix T in Eq. B.1:

$$z = TRx + n = Hx + n \tag{11.9}$$

T is a mask with pixels value of 1 where the data exists, and 0 otherwise. The operator $H = TR$ returns the measurements z from the HR image x.

To solve the deconvolution problem, a Bayesian formalism is used. In practice, the deconvolution consists of minimizing a least-square criterion. The formalism and the method used to solve the deconvolution problem and estimate x is detailed in Appendix B.

11.6 Results

We first describe the results of the first test campaign of the Flight Model (FM1), and show that the PSF characteristics of the intrument were out of specifications. After correction of the defect exhibited with these tests, we compare the results between the FM1 and FM2 test campaigns.

11.6.1 Analysis of the MIRIM PSF

The analysis of the 5.6 μm images taken during the microscanning test was done with IDL routines. The results have been compared and complemented with the use of the IRAF software. Different measurements of the FWHM of the PSFs have been performed (Gauss, Bessel and moffat fits, radial profiles, etc). I have written a technical document for the MIRI European Consortium (EC) about the focus and FOV exploration with a point source tests was written (document MIRI-TN-00743-IAS). In this document (not reproduced here), the techniques used to measure the FWHM of the PSF are detailed. Here we rather focus on the main results of the microscanning test. These results are gathered in an other EC document (see Appendix C, sect. C.3 for a list of these documents) and I have written a SPIE paper that will be submitted for the next SPIE conference "Observational Frontiers of Astronomy for the New Decade" in June 2010.

Fig. 11.14 shows an example of reconstructed HR PSF. The linearity correction is applied and the over-sampling factor is set to 7, i.e. the size of a pixel is 3.6 μm instead of 25 μm for a standard MIRI image. The secondary Airy diffraction ring, which is barely visible on low-resolution images, is exhibited on the HR images, as well as the shape of the lobes. The radial profile of the HR PSF is shown on the right of Fig. 11.14.

Different high-resolution PSF images and all the quantitative results for the FM1 tests are gathered in Table 11.2. The results are shown for images that have been corrected for the detector response (linearity correction). These images correspond to over-sampling factors equal to 7, 10 and 11. The first value corresponds to a reasonable compromise between the gain in resolution and the introduction
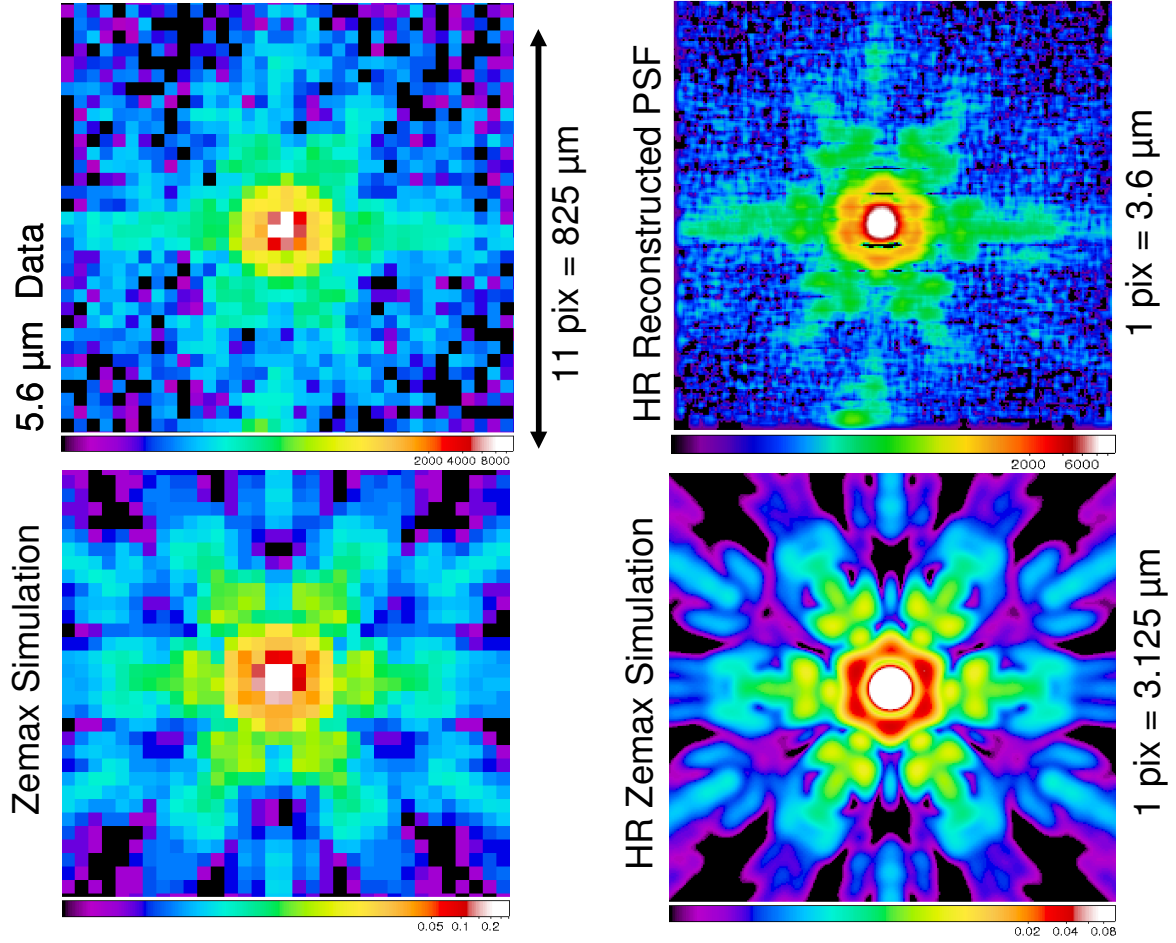
Figure 11.13: Comparison between Low- and High-Resolution images (data in the upper panel, simulations at the bottom). The upper right image is the high-resolution image reconstructed from the data, with an over-sampling factor of 7. The bottom right image show a HR PSF image simulated with Zemax. Note that the shape of the secondary lobes agrees very well between the data and the simulation.

of artefacts in the reconstructed images. The last one (11) is chosen to show the limits of the method. In this case, the pixel size (2.3 μm) is smaller than the microscanning step (2.5 μm). For an over-sampling factor of 7 (resp. 11), one original MIRIM pixel equals to 7^2 (resp. 11^2) pixels in the super-resolution image. The pixel sizes in the HR images are $\sim 3.6\ \mu$m and $\sim 2.3\ \mu$m, respectively.

Table 11.2 also shows the results of the simulations of MIRIM PSFs with Zemax. These simulations are done at two resolutions, the standard one (25 μm / pixel) and a fine, re-sampled one (3.125 μm / pixel) which allows the comparison with the HR reconstructed PSFs.

The correction for the response of the detector decreases the width of the computed MIRIM PSFs. The reason is that the deviation to the linearity is greater at high fluxes than that at low values (see Fig. 11.6 and 11.7). The FWHM of the corrected PSFs are $\sim 5\,\%$ lower than the raw ones. The X, Y, or radial profiles of the SR PSFs are well fitted by an Airy disk (Fig. 11.14). The measured FWHM
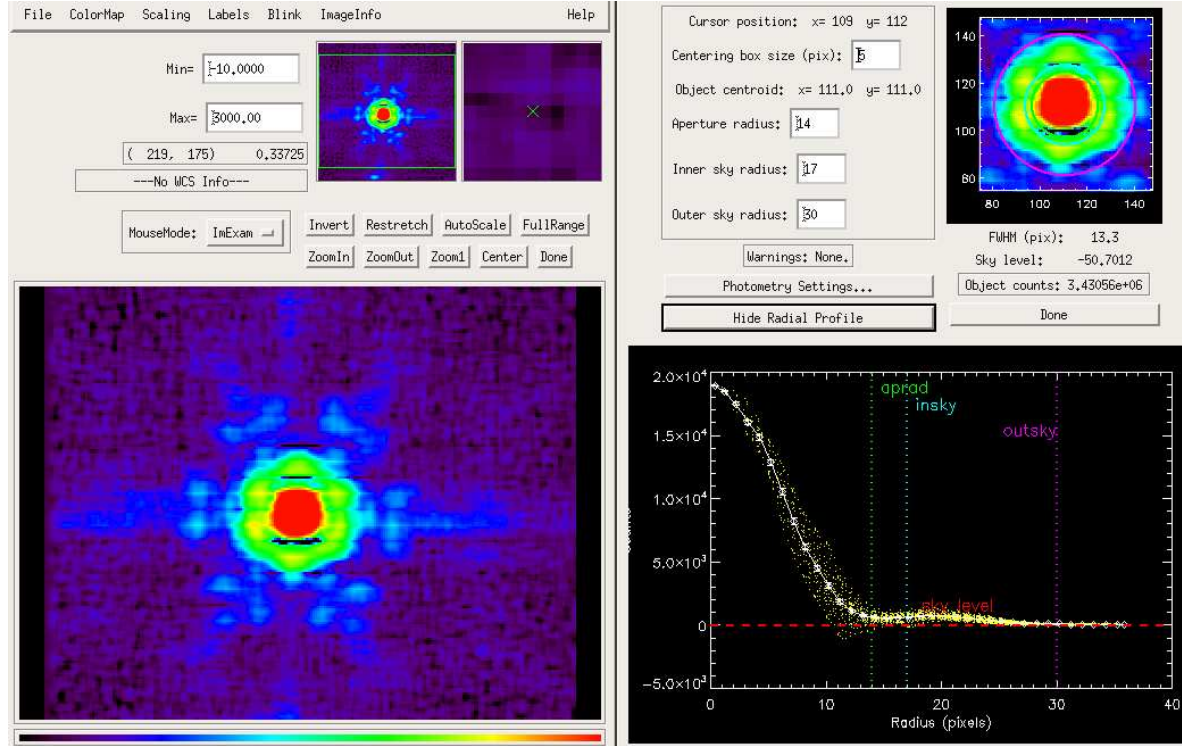
Figure 11.14: Image of the HR PSF and its radial 1D profile. The oversampling factor is 7 and the linearity correction has been applied. The pixel size equals to 3.6 μm. The radial profile has been fitted with an Airy disk function. It gives a FWHM of 47.16 μm.

with Airy fits on the HR PSF are of the order of $46 - 50$ μm for both X- and Y- directions. Gaussian fits to the core of the PSF give slightly lower values ($\sim 44 - 47$ μm).

HR PSF profiles in the X- and Y- directions are shown on Fig. 11.15, 11.16 and 11.17. For comparison, the PSF profiles of one low-resolution image (one single position MIRIM image) is plotted for the corresponding number of pixels. Airy and Gaussian fits have been performed in the X- and Y- directions. We show on Fig. 11.15 and 11.16 the results of the Airy fits on the data and the Zemax simulations. The better sampling of the PSF helps in reconstructing more accurately the main peak of the PSF. The secondary diffraction lobes are also resolved. We note that the positions and amplitudes of the secondary lobes do not match exactly with the Airy fits.

For an over-sampling factor of 11, we reach the limit of the method, and one can see artefacts on the reconstructed image (in both X- and Y- directions, see Table 11.2). They may be due to errors in the motions estimations, signal-to-noise limitations, and simplifications made in the model of the detector and of the pixels (uniform response, etc.). For an over-sampling factor of 7, most of the artefacts are removed in the X- directions. The remaining artefacts in the Y-direction are due to the errors in the motion estimation (see Fig. 11.11). The Y- direction profile exhibit a slight distorsion of the shape of the main peak (Fig. 11.17).
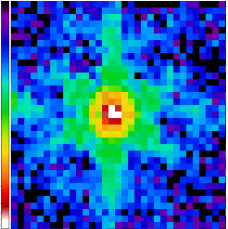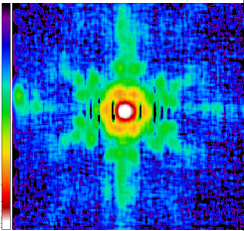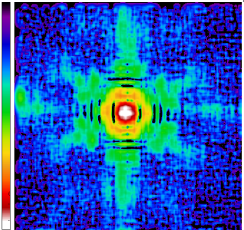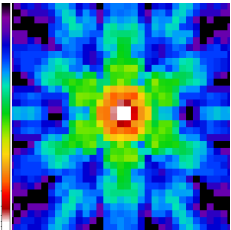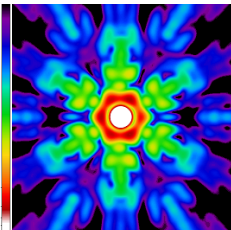
Method		Data						Simulations			
		Low-Resolution		Oversampling 7		Oversampling 11		Zemax Low-R		Zemax High-R	
FWHM		X	Y	X	Y	X	Y	X	Y	X	Y
Gauss		51.54	51.27	47.47	48.51	47.40	48.42	46.33	46.20	40.15	40.07
Airy		56.84	55.61	50.57	49.91	50.69	49.78	51.08	52.10	42.37	42.38
Radial		53.75		51.43		47.64		49.75		43.60	
Direct		50.50		50.03		49.71		47.75		41.88	

Table 11.2: *Summary of the results for the FM1 campaign. The linearity correction is applied. FWHM measurements (in μm) on the low-, super-, resolution (resulting image from the microscanning test), and the simulated PSF. For the super-resolved image, the sampling is increased by a factor of 7 or 11 with respect to a single MIRIM image, i.e. one original MIRIM pixel equals to 7^2 or 11^2 pixels in the super-resolution image. The images shows a 825 μm wide area. Pixels sizes are respectively 25 μm, 3.6 μm, 2.3 μm, 25 μm, and 3.125 μm. The display scale is logarithmic. The results of the PSF FWHM are indicated for 4 different measurements: a 2D gaussian elliptical fit (longest FWHM and perpendicular), a 2D Airy disk fit (X and Y directions), a gaussian fit of the radial profile of the source, and a direct measurement of the FWHM, without assuming a profile shape. The 1 σ uncertainty on the FWHM values are of the order of 0.03 μm. The Zemax simulations were performed on a case where mechanical tolerances were applied in the Monte-Carlos.*

Figure 11.15: Low (2 upper plots) and super-resolution (2 bottom plots) PSF profiles in the X and Y directions. The low-resolution PSF correspond to one single position MIRIM image. For the super-resolution PSF, the sampling is increased by a factor of 7. Red dashed lines are the results of the Airy fits.

Conclusion of the FM1 tests: a defect in the instrument

From the results gathered in Table 11.2, we note that the FWHM of the HR PSFs are systematically larger than the measured FWHM on the HR simulated Zemax PSF. The discrepancy is about $+8$ μm after correction for the non-linearity of the detector. This mismatch is out of the specifications of the instrument. This out-of-specification issue was also revealed independently by an another test. The measurement of the MIRIM field of view shows a vignetting issue, which seems to confirm that a defect is present in the instrument. The left panel of Fig. 11.18 shows the field of view of the imager during the FM1 test campaign. Note that the bottom of the FoV is lost.

Motivated by these tests, a new metrology analysis of the instrument was done by engineers from the CEA, Saclay and IAS, Orsay. The engineers from the IAS provided a "Faro arm", a special tool to perfom the metrology. It was first thought that the root cause of the out-of-specification optical quality of the instrument was due to a misalignment of the detector. It turned out that this was not the case. In-depth investigations concluded to a slight interference between the structure of the Three-Mirror-Anastigmatic (TMA) objective and the M4 mirror (see Fig. 10.10 and sect. 10.3.2 for a description of the optical layout of MIRIM). This design problem caused a tilt of the M4 mirror with respect to its nominal positioning. The M4 mirror has been found damaged, with some bending of its mounting flexible pad. This tilt results in a degradation of the nominal PSF properties and the FoV area.
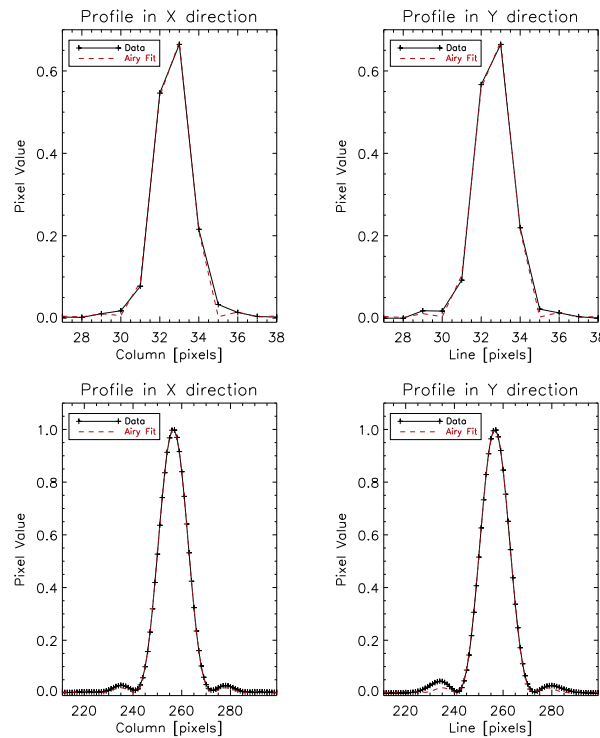
Figure 11.16: Simulated (Zemax, with tolerances) PSF profiles in the X and Y directions at a low-resolution of 25 μm / pixel (2 first plots) and a high-resolution of 3.125 μm / pixel (2 last plots). Red dashed lines are the results of the Airy fits.

The cause of the interference between the TMA structure and the M4 mirror has been removed manually. The damaged M4 mirror was replaced by the Flight Spare model. A second test campaign (FM2) was launched, and we performed the same microscanning analysis to check the optical quality of the PSF. This story illustrates well the need to perform accurate tests on the ground! Indeed, the discrepancy on the PSF characteristics could not have been exhibited without the deconvolution of high-resolution images from the microscanning data.

11.6.2   Results of the FM2 tests after correction of the M4 tilt

Comparison between FM1 and FM2 tests

The results of the microscanning analysis and PSF measurements for the FM2 test campaign are gathered in Table 11.3. Gaussian fits to the PSFs show that the FWHM are of the order of 44 μm (0.19 arcsec) at 5.6 μm, which brings this value inside the specification range[7]. The effect of the correction of the tilt of the M4 mirror is clearly visible on the HR reconstructed PSFs. Note that this effect is not measurable of the raw (LR) images, which emphasizes the importance of this microscanning test and analysis.

---

[7]The specification on the PSF is not expressed in terms of FWHM, but in terms of wavefront errors (WFE). A zemax calculation, performed by S. Ronayette (CEA), was used to translate the WFE into FWHL tolerances.
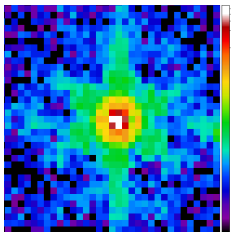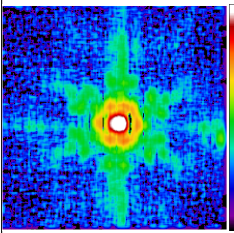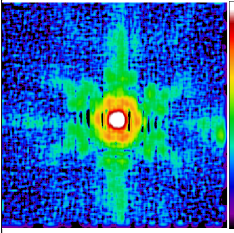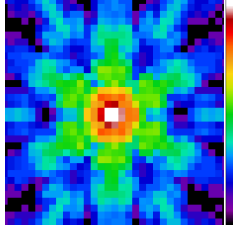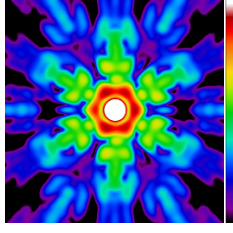
Method		Data						Simulations			
		Low-Resolution		Oversampling 7		Oversampling 10		Zemax Low-R		Zemax High-R	
FWHM		X	Y	X	Y	X	Y	X	Y	X	Y
Gauss		51.54	51.27	44.88	45.70	44.87	45.70	46.33	46.20	40.15	40.07
Airy		56.84	55.61	46.93	47.29	46.63	47.14	51.08	52.10	42.37	42.38
Radial		53.75		47.10		46.15		49.75		43.60	
Direct		50.50		48.67		48.77		47.75		41.88	

Table 11.3: *Summary of the results for the FM2 test campaign. The linearity correction is applied. FWHM measurements (in µm) on the low-, high-resolution (resulting image from the microscanning test), and the simulated PSF. For the HR image, the sampling is increased by a factor of 7 or 11 with respect to a single MIRIM image, i.e. one original MIRIM pixel equals to 7^2 or 11^2 pixels in the super-resolution image. The images shows a 825 µm wide area. Pixels sizes are respectively 25 µm, 3.6 µm, 2.3 µm, 25 µm, and 3.125 µm. The display scale is logarithmic. The results of the PSF FWHM are indicated for 4 different measurements: a 2D gaussian elliptical fit (longest FWHM and perpendicular), a 2D Airy disk fit (X and Y directions), a gaussian fit of the radial profile of the source, and a direct measurement of the FWHM, without assuming a profile shape. The 1σ uncertainty on the FWHM values are of the order of 0.03 µm. The Zemax simulations were performed on a case where mechanical tolerances were applied in the Monte-Carlos.*

Figure 11.17: Comparison between the high-resolution reconstructed data (3.6 μm / pixel, black line) and the simulated (Zemax, with tolerances, 3.125 μm / pixel) PSF profiles (red dashed lines) in the X and Y directions. On the two first plots on the left, we do not correct for the response of the detector. On the two last plots on the right, linearity correction is applied.

Encircled energy of a point source image

The encircled energy is another way of estimating the optical quality of the PSF. The requirements for MIRI are the following. The MIRI imager data shall include more than $56\,\%$ of the encircled energy of the image of a point source at wavelengths longward of $5.6\,\mu$m within the angular diameter of the first dark Airy ring. Note that in the MIRI requirement document, the encircled energy is defined relative to the energy within a radius of 5 arcsec equivalent projected onto the sky.

The encircled energy $E(r)$ of a radially symmetric point spread function $\phi(r)$ can be defined as the integral

$$E(r) = 2\pi \int_0^r \phi(r')dr' \tag{11.10}$$

For the purpose of comparison to the requirement document, we wish to normalise $E(r)$ to 1 at $r = 5$ arcseconds. However, our microscanning data acquisition was done for a sub-array of $\approx 2'' \times 2''$, so we have normalized the encircled energy to a 2 arcsec radius. Therefore it is difficult to relate our results to the specification requirements at 5 arcsec.

Fig. 11.19 shows the encircled energy of a high-resolution PSF in the center of the field of view of the imager, as a function of radius in arcsec (1 pixel = 0.11"). The dashed line shows the encircled energy of a high-resolution MIRIM PSF simulated with the Zemax software. The agreement between

FOV measurements: FM1   **FOV measurements: FM2**
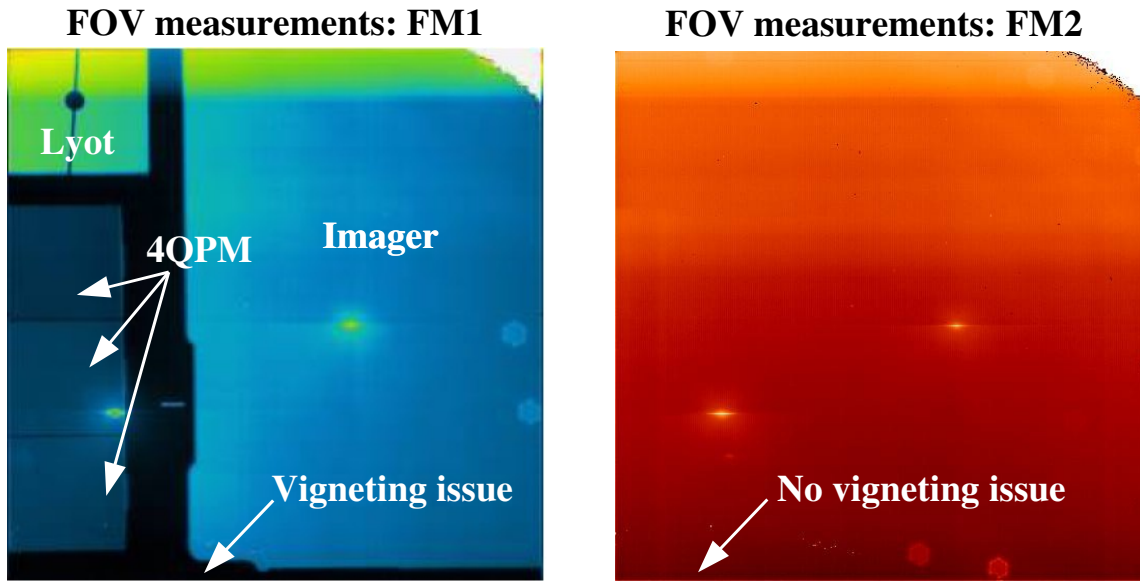
Figure 11.18: Comparison of the Field of View measurement between the two Flight model test campaigns, FM1 and FM2. On the left plot (FM1), the complete MIRIM focal plane is mounted, with the coronograph masks and the LRS slit (see Fig. 10.10 for the pattern of the focal plane). The vignetting issue is clearly seen at the bottom of the image. The black stripe at the bottom shows that a significant fraction of the field of view is lost. On the right plot (FM2), the vignetting issue has been corrected (no black stripe anymore). Note that for the FM2 tests, the coronograph masks are not mounted.
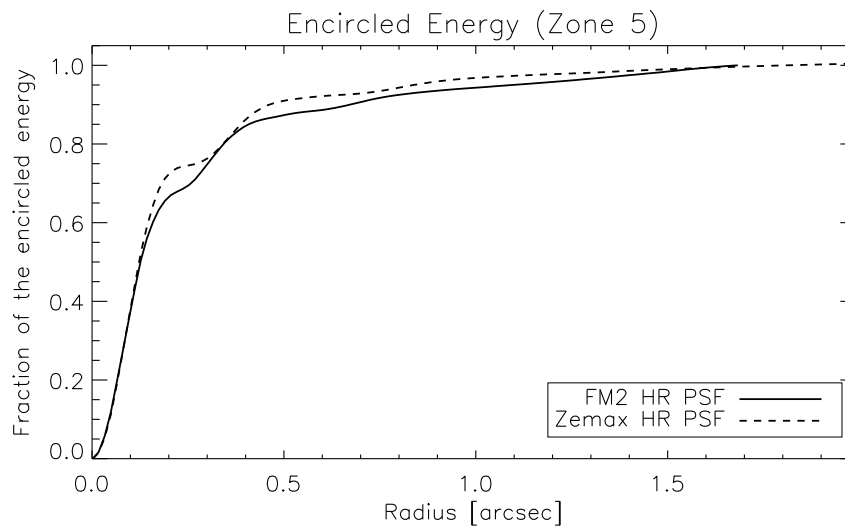
Figure 11.19: Encircled energy of the MIRI high-resolution (HR) PSF as a function of radius in arcsec (1 pixel = 0.11"). The solid line is the result of our deconvolution algorithm to reconstruct a HR image from the data. The dashed line shows a PSF simulated with the Zemax software. The results are shown for a position close to the center of the field fo view of the imager. The inflection point corresponds to the first dark ring of the Airy disk of the PSF.

the two curse is very good, suggesting that the instrument is close to its nominal behaviour. The diameter of the first dark ring can be interpreted as the first point of inflection in $E(r)$, i.e the value of r for which $d^2 E/dr^2 = 0$. We find an encircled energy of 73 % inside the central lobe.

Note that the measured variation of encircled energy with radial distance from a point image is very sensitive to the flux levels at large radial distances. One must ensure that $dE/dr \geqslant 0$ for all values of r for the measurement to make sense. Here, this condition is satisfied because we work at high background values. The telescope simulator is at ambient temperatures, thus producing a high thermal background.

11.7   Summary and conclusions

This chapter reports the first detailed analysis of the characteristics of the Point Spread Function (PSF) of the Flight Model of the JWST Mid-InfraRed IMager (MIRIM). The data are taken at 5.6 μm, the only filter available at that time. We discuss the results of the *"microscanning"* test that has been performed at cryogenic temperatures in December 2008 - March 2009 at CEA, Saclay. This *high-resolution* (HR) technique is used to characterize the MIRIM optical quality. The microscanning consists in a fine, sub-pixel scanning of a point source on the focal plane. A deconvolution algorithm is used to reconstruct HR PSFs. The main results are the following.

1. The microscanning test provides a significant improvement for the analysis of the PSF characteristics. This test allows to resolve the diffraction pattern of MIRIM and to measure accurately the width of the PSF for the FM. We confirm the global shape of the PSF secondary lobes that is seen on HR Zemax simulations.

2. The FWHM of the high-resolution, reconstructed images are $\sim 48 - 50 \, \mu$m, i.e. $0.21 - 0.22$ " for the first test campaign. We note a discrepancy of $\sim +8 \, \mu$m between the data and the high-resolution Zemax simulations. The microscanning test, together with field of view measurements, showed that a defect was present in the instrument. The main cause for the mismatch between simulations and MIRIM data has been identified. Metrology measurements of the MIRIM mechanical and optical layout have shown a out-of-specification tilt of the M4 mirror. This tilt was due to an interference between the MIRIM structure and the mirror. This manufacturing fault has been corrected, and a second test campaign began in February 2009. The results show that the FWHM of the HR PSFs are $44 - 46 \, \mu$m, i.e. $0.19'' - 0.20''$, which is within the specifications. The FWHM are only $\sim +4 \, \mu$m compared to high-resolution simulations.

3. Slight differences between the simulated PSF patterns and the MIRIM HR reconstructed data are exhibited. We discuss the limits of the method due to errors in the relative positions of the images and the lack of information (signal-to-noise limitations, assumptions made on the characteristics of the detector, etc.).

4. The MIRI detector shows a non-linear response curve. This result is confirmed by independant measurements by the Jet Propulsion Laboratory (JPL), responsible for the detector array. We show that the correction for the response of the detector improves the quality of the MIRIM PSFs. The FWHM of the corrected PSFs are ~ 5 % lower than the raw ones.

ISIM Cryo Test Facility, Goddard   OTE Cryo Test Facility, JSC
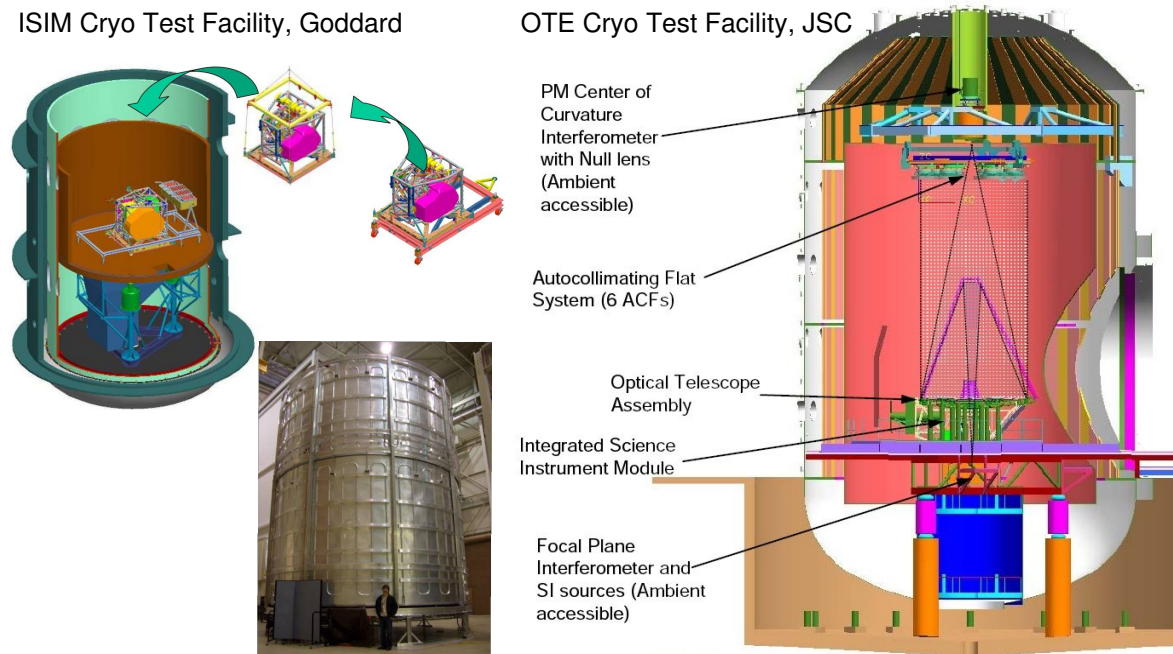
Figure 11.20: *Left:* The cryogenic test chamber at NASA Goddard is being built to perform cryo tests of the Integrated Science Instrument Module (ISIM) containing the 4 JWST instruments. *Right:* The giant cryo test facility at the Johnson Space Center (JSC). The whole JWST Optical Telescope Element (OTE) and the ISIM will be tested at cryogenic temperatures. Optical alignment of the instrument, as well as functional tests and basic optical performance checks will be performed.

11.8 What's next?

MIRI testing is not finished! Today (end of august), the instrument is still at CEA and will be tested with the filter wheel. MIRIM will be delivered to RAL[8] for additional testing (functional and optical performance tests with a cold telescope simulator, as opposed to the warm simulator used at CEA).

After testing of the Optical System at RAL, the Optical Bench Assembly (OBA, see sect. 10.3) will be delivered to NASA Goddard, where the MIRI OBA will be integrated into the Integrated Science Instrument Module (see sect. 10.3) for testing at cryogenic temperatures (see Fig. 11.20). Then, the ISIM is mounted onto the whole telescope (Optical Telescope Element, OTE), and the 6m telescope is tested in the giant cryo test facility at the Johnson Space Center (JSC), in Houston (see Fig. 11.20). Finally, the OTE will be delivered to Kourou for final integration and launch. Let's hope I'll be there!

---

[8]Rutherford Appleton Laboratory, http://www.sstd.rl.ac.uk/

Chapter 12

Science with the JWST and MIRI

They spend their time mostly looking forward to the past.

John Osborne, Look Back in Anger

Abstract

In addition to my participation to the tests of the Mid-InfraRed instrument (MIRI) onboard the JWST, I am involved in the scientific preparation of MIRI, as a member of the European Science Team. The MIRI instrument will be next future of mid-IR infrared observations, and a ideal tool to look at H_2 in active phases of galaxy evolution. This chapter presents a specific proposal ("white paper") I have submitted to the working group "Galaxy evolution between $z = 0.6 - 6$", in preparation of the guaranteed time observations. This proposal is based on our on-going program addressing the multiphase gas physics during highly dissipative phases of galaxy evolution at low and high redshift, which was introduced in chapter 9.

Contents

12.1   Overview of the JWST scientific goals

The science of the JWST is definitively oriented towards high-redshift astrophysics. If one looks at NASA's website, the JWST science drivers are divided into four main topics:

1. First Light (after the big bang); To find and study the first luminous objects; proto-galaxies, supernova, black holes

2. Assembly of Galaxies; To study the merging of proto-galaxies, effects of black holes, history of star formations

3. Birth of Stars and Planetary Systems; JWST will study how stars form in dust clouds, and how chemical elements are produced and re-circulated.

4. Planetary Systems and Origin of Life; To study the formation of planets and obtain direct observations of other planetary systems, as well as study of outer solar system.

Based on these themes, several science working groups were created in January 2009, to start working on precise proposals of observations with MIRI, in preparation of the guaranteed time projects. I "signed up" into two of them: the working group "Galaxy evolution between $z = 0.6 - 6$", led by P. Van Der Werf and the working group "Interstellar medium" led by Alain Abergel.

   With F. Boulanger and N. Nesvadba we started to work on a proposal to observe H_2 luminous objects with MIRI. The next section reproduces the proposal I have written and submitted to the "Galaxy Evolution" group. I also participated to a proposal written by Alain Abergel on the observations of nearby PDRs to probe the gas and dust physics at the cloud/inter-cloud interface.

12.2   Tracing the kinetic energy dissipation associated with galaxy merging and AGN feedback at z $\sim 1.5 - 3.5$ with MIRI

Here is the proposal I have written with F. Boulanger and N. Nesvadba and submitted to the "Galaxy Evolution" working group.

12.2.1   Background

The build-up of baryonic mass in galaxies is regulated by a complex interplay between gravitational collapse, galaxy merging and feedback related to AGN and star formation (Fig. 9.1). These processes may inject sufficient mechanical energy into the interstellar medium (ISM) to potentially have a major impact on star formation and galaxy assembly. This will be particularly important during the early phases of galaxy evolution at high redshift, when galaxies were gas-rich and most of the stars in the universe were formed.

   The molecular gas plays a critical role in this context since it represents an important, if not dominant, cooling agent in the energetics of galaxy merging and feedback. Recent observations by the InfraRed Spectrograph (IRS) onboard the *Spitzer Space Telescope* have discovered a significant and diverse population of low-z objects where the mid-infrared rotational line emission of H_2 is strongly enhanced ($L_{H_2} \sim 10^{40} - 10^{43}$ erg s^{-1}), while star formation is suppressed (Fig. 1.2). This suggest

that shocks are the primary cause of the H$_2$ emission (Ogle et al., 2007; Guillard et al., 2009c). This sample of *H$_2$-luminous sources* includes galaxies in several key phases of their evolution, dominated by gas accretion (Egami et al., 2006), galaxy interactions (Appleton et al., 2006), or galactic winds driven by star formation (e.g. M82 Engelbracht et al., 2006) and AGN (Ogle et al., 2009).

Constraining the impact of merging and AGN feedback on the formation and evolution of massive galaxies can only be addressed through direct observations at $z \sim 2$, near the cosmologically most active period of star formation, galaxy interactions and AGN activity. By analogy to our models on local H$_2$-luminous objects (Guillard et al., 2009c), we expect the mid-IR lines to be the dominant cooling lines for warm, 10^{2-3} K, gas in the strongly shocked, highly turbulent, colliding flows in galaxy interactions (e.g. the galaxy-wide shock in Stephan's Quintet), but also, e.g., in AGN-driven outflows. High gas velocity dispersions measured in $z \sim 2$ actively star-forming galaxies show that the gas kinematics in these systems was strongly disturbed compared to galaxies today (e.g. Lehnert et al., 2009). We expect the molecular gas to be highly turbulent and therefore the warm H$_2$ emission to be more frequent and more powerful than at low-z.

12.2.2 The proposal

The MIRI Medium Resolution Spectrometer (MRS) will be the first IFU instrument to provide the sensitivity and resolving power to spatially and spectrally resolve H$_2$ and forbidden ionized gas lines at rest-frame near-IR and mid-IR wavelengths, out to $z = 1.5 - 3.5$. For the first time, this will allow us to directly investigate the physical state and the kinematics of the ionized gas and the warm (> 150 K) molecular gas that is dynamically heated by the dissipation of mechanical energy associated with galaxy merging and AGN feedback. We propose MIRI/MRS observations of selected sources to address the following questions:

- Are AGN driving massive multiphase outflows carrying away the bulk of the ISM of the galaxy and therefore quenching star formation in the host galaxy? If this is the case, we should observe broad, luminous H$_2$ emission lines, with widths of 1000 km/s or more, by analogy to the large velocity shears and dispersions that have been revealed by near-infrared integral field spectroscopy of the rest-frame optical emission lines in HzRGs (Nesvadba et al., 2006, 2008a). The propose MIRI observations will allow to quantify the energy radiated and carried away by molecular outflows.

- Does the H$_2$ emission trace "pre-starburst" phases of interacting galaxies? *Spitzer* observations of the Stephan's Quintet revealed that H$_2$ line emission represents a major fraction of the bolometric luminosity of the galaxy-wide shock (Appleton et al., 2006). This is a nearby example of an H$_2$-bright, early phase of a galaxy interaction, and we expect these systems to be more frequent and more active at high-z. The proposed MIRI spectroscopy will explore galaxy evolution beyond the active starburst and obscured/unobscured AGN phases, highlighted by luminous dust emission, and test whether H$_2$ emission is scaled-up at high-z or not.

Which lines will we look at? To establish the energy budget of the warm molecular gas and shock diagnostics, we will use, in most cases, the full MIRI spectral range. In particular:

- we will concentrate on the near-IR ro-vibrational lines, e.g. the H_2 1-0 S(1) $2.12\,\mu$m line, and the mid-IR pure rotational H_2 0-0 S(3) $9.7\,\mu$m and S(5) $6.9\,\mu$m lines. These lines will be redshifted in the MRS spectral range ($4.9 - 28.6\,\mu$m) for $z = 1.5 - 3.5$.
- the forbidden ionized gas lines (e.g. [Ne II], [Ne III]) will be used to compare the kinematics of the molecular gas with that of the ionized gas.
- the synergy with NIRSPEC will be helpful to observe the CO bandheads and Ca II triplet to estimate the stellar kinematics. This will allow to estimate the ratio between the bulk galaxy rotation and the gas velocity dispersion in these high-z objects, and provide an absolute rest-frame in which to interpret the gas motions as blueshift or redshift.

12.2.3 The sample

We propose to observe a representative sample of order 20-30 strongly star forming and AGN host galaxies at $z \sim 1.5 - 3.5$, using the MIRI medium-resolution ($R \sim 2200$) spectrometer (MRS, IFU mode). Our sample will include powerful radio galaxies, as well as radio-loud and radio-quiet obscured and unobscured AGN. We will also include powerful, dusty starburst galaxies like sub-millimeter galaxies and infrared-selected galaxies, many of which will be mergers. Suitable parent samples already exist, e.g. Nesvadba et al. 2009, in preparation for HzRGs with deep rest-optical IFU observations; Greve et al. (2005) for SMGs with CO observations; Yan et al. (2005) for powerful infrared galaxies at $z \sim 2$; Farrah et al. (2008) for $24\,\mu$m selected starbursts with PAH detections, etc), and will be extended with the upcoming *Herschel* mission. The development of our models will also help in selecting high-z, non IR-luminous, interacting systems that may be "pre-starbursts".

12.2.4 Observing mode and integration times

Galaxies at high-z are gas-rich and large gas velocity dispersions show that the gas is not fully settled in a rotating disk. This surplus in mechanical energy must be dissipated. Therefore, we expect H_2 emission to be more powerful at high-z than for local sources.

We base the required sensitivity on the H_2 luminosity of the most luminous low-redshift sources at low redshift (a few 10^{43} erg s^{-1}). With the resolving power of the MRS, ($R \sim 2200$), corresponding to a resolution of FWHM ~ 140 km s^{-1}, and typical observed line widths of FWHM ~ 800 km s^{-1}, the lines will be resolved by a factor ~ 6. Typical sizes of the outflows are ~ 5", for an IFU field of view of ~ 8" $\times 8$" for $\lambda > 17\,\mu$m. Given that the spatial sampling is 0.64" across the slice and 0.27" along the slice, we will be able to resolve the molecular gas emission spatially and spectrally and perform the first spectral mappings of molecular AGN outflows at high-redshift. Using the MIRI performance estimation, and assuming a narrow line plus extended source, we can reach an RMS of 10^{-20} W m^{-2} in 1 hour of on-source observing time for a ~ 3" $\times 3$" field. At $z \sim 2.5$ this will correspond to a $10\,\sigma$ detection limit for an H_2 luminosity of 3×10^{43} erg s^{-1}, for the integrated spectrum. The typical observing time will be ~ 1 hr on-source per exposure, i.e. 3 hrs to cover the full wavelength range (A, B and C exposures). The total observing time for this project, excluding overheads, would be of the order of 60 hrs for ~ 20 sources.

Chapter 13

Perspectives

That is the essence of science: Ask an impertinent question, and you are on the way to a pertinent answer.

Jacob Bronowski (Ascent of man)

Abstract

Observations of H_2 luminous galaxies set molecular gas in a new context where one has to account for the presence of H_2 outside galactic disks, characterize its physical state and describe its relation to star formation. These observations and the theoretical framework presented in this manuscript motivate new observations and theoretical studies that are discussed here. In particular, as for Stephan's Quintet, in many of the H_2-luminous galaxies the molecular gas has been detected through the mid-IR H_2 rotational lines prior to any CO observation. Thus we propose to complement our knowledge of the mass and kinematics of the molecular gas in these sources by CO observations. Then I present the theoretical perspectives, with emphasis on new numerical studies that are needed to understand how the bulk kinetic energy released in the multiphase ISM during violent phases of galaxy interactions is transferred into the warm molecular gas.

Contents

13.1 Observational perspectives

This thesis work has rich observational perspectives. The flow of the discovery of H_2-luminous galaxies, and the observational and theoretical work presented in this manuscript, has inspired a large number of follow-up observations. Here are a few examples that will complement our view of molecular gas in galaxy evolution.

13.1.1 The search for molecular gas in active phases of galaxy evolution

A series of upcoming observations are proposed to search for warm H_2 or associated CO gas in...

compact groups of galaxies: a *Spitzer* proposal (P.I.: P.N. Appleton) was prepared during my PhD to search for H_2 in HCGs[1]. This project has been motivated by the discovery of powerful H_2 emission from the Stephan's Quintet group. It has been observed and the data is being reduced. I will participate to the interpretation of this data during my postdoc.

radio-galaxies: we propose to look for CO emission in a sample of radio-galaxies with the IRAM 30-m telescope (P.I.: M. Lehnert). The proposal has been submitted in September 2009. These observations will determine the amount of kinetic energy carried by the cold molecular gas in these radio-galaxies.

Observations at high spatial resolution of two specific radio galaxies, 3C293 and 3C433, with the IRAM Plateau de Bure Interferometer (PdBI) have been proposed (P.I.: N. Nesvadba). These two sources, where powerful H_2 is detected, are more complex than 3C326 because they exhibit star formation.

In addition, a proposal has been submitted (P.I.: N. Nesvadba) to look at the "Minkowski's object", a nearby and young starburst that might be triggered by the jet of a nearby radio galaxy. This is our best candidate for "positive" feedback. The proposal aims at determining the mass and kinematics of the cold molecular gas, in order to check whether these objects verifies the Schmidt law. We plan to complement these observations with VIMOS[2] observations.

the M82 starburst driven wind: We have submitted (P.I.: F. Boulanger) a proposal in September 2009 to look for CO emission in the M82 superwind. We obtained deep *Spitzer IRS* observations of the warm molecular gas in the wind (P.I: L. Armus) but the spectral resolution is not high enough to measure outflow velocities or line widths. The CO data will allow to derive the kinematics of the cold gas in the wind, which will help in elucidating some of the questions raised above.

13.1.2 Observing H_2-luminous galaxies with the JWST

During my PhD work, I have been working on the tests and the scientific preparation of the Mid-Infrared Instrument (MIRI) that will be part of the scientific payload of the James Webb Space Telescope (see chapter 11 and 12).

H_2 in active phases of galaxy evolution at high-z

In particular, I have proposed a specific project to look at high-z H_2-luminous objects with MIRI to the MIRI European Consortium. The proposal is reproduced in chapter 12. It is specific to the MIRI instrument and relies on the background presented in chapter 10. For the first time, MIRI will allow us the study the kinematics and excitation of the warm H_2 gas in high-z objects. To collect a sample of high-z objects, we will use the analogy between the characteristics of VLT/SINFONI[3]

---

[1]Hickson Compact Groups

[2]VIMOS, the VIsible MultiObject Spectrograph, is an optical Integral Field Unit spectrometer mounted on the Very Large Telescope, see http://www.eso.org/sci/facilities/paranal/instruments/vimos/ for details.

[3]Spectrograph for INtegral Field Observations in the Near Infrared, http://www.eso.org/sci/facilities/paranal/instruments/sinfoni/.
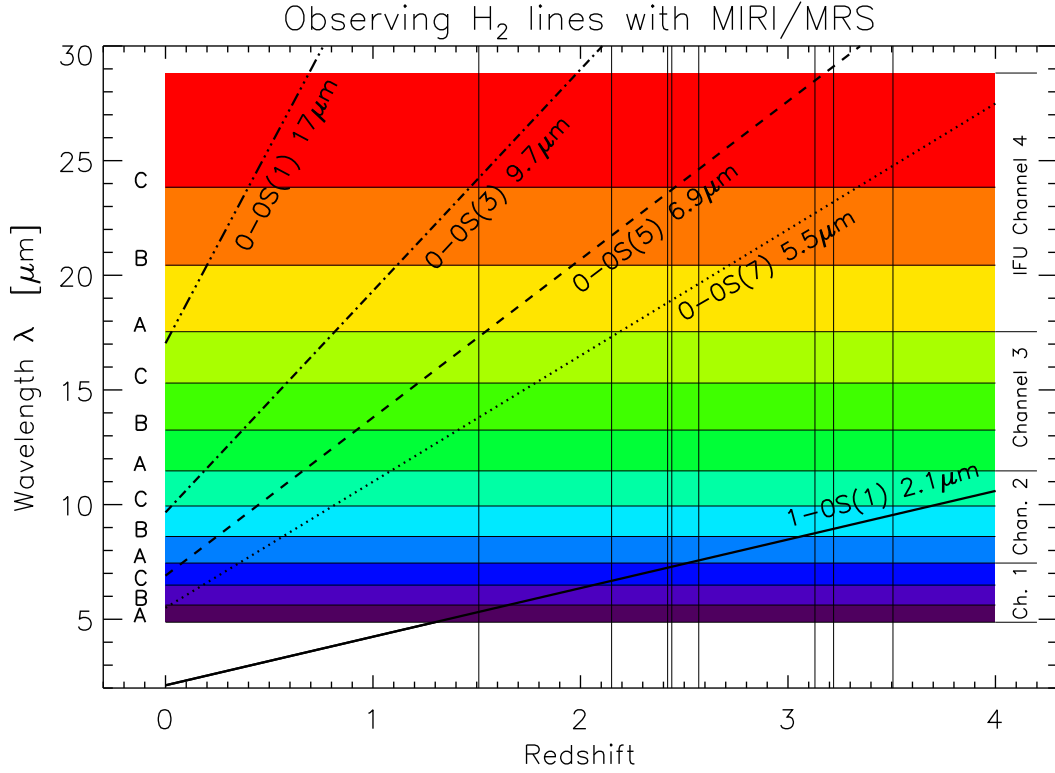
Figure 13.1: Observing H_2 lines at high-redshift with JWST/MIRI. The observed wavelengths of some H_2 lines are shown as a function of the redshift. The colored bars indicate the channels and bands of the Medium Resolution Spectrometer (MRS) of the MIRI instrument. One observation corresponds to four sub-bands, like 1A, 2A, 3A, 4A for instance (see sect. 10.3.4 for technical details about how the MRS is working). The vertical lines indicate the redshifts of some high-z radio-galaxies that might be interesting to look at with MIRI.

and JWST/MIRI. I will use high-z radio-galaxies SINFONI and *Spitzer* data (PI: N. Nesvadba, co-I: P. Guillard) as a starting point to define the observing strategy. MIRI will allow integral field spectroscopy of redshifted optical or H_2 lines (Fig. 13.1), at high spatial (1-2 kpc/pix) and spectral ($\lambda/\Delta\lambda \sim 3\,000$) resolution. This spectral resolution is crucial to measure the kinematics of the

The Fig. 13.1 shows the visibility of the some H_2 lines as a function of redshift. I also indicate, as a function of redshift, in which sub-band of the Medium Resolution Spectrometer (MRS) these lines are falling. This allows to configure the instrument for observations and estimate the integration time. Fig. 13.1 is thus useful to prepare observation proposals.

An infrared high-resolution look at Stephan's Quintet with JWST

In addition, in the near future, I will propose an observational program to investigate Stephan's Quintet with NirCam/NirSpec and MIRI, the near-IR and Mid-IR instruments onboard JWST (see chapter 10 for an introduction to these instruments). The NirCam and MIRI imagers will provide an unprecedented spatial resolution (comparable to the HST at 7 μm) to study small scales structures in the shock.

MIRI will allow us to clearly separate the dust emission associated with star-forming regions from that associated with the shock itself. Multi-band imaging with NirCam and MIRI will allow to build a full map of spectral energy distributions from 0.6 to 28 μm. This may be used to search for variations of the dust properties across the shock. These variations may be interpreted in terms of dust processing in shocks, and possibly related to velocity gradients in the warm molecular gas.

The spectral resolution of NirSpec (see sect. 10.2.5 for technical details) and MIRI's Medium Resolution Spectrometer (sect. 10.3.4) will provide for the first time the kinematics of the warm H_2 gas across the shock. This will allow us to map the relative velocities and dispersion velocities over the SQ ridge, which we will compare with the kinematics of the CO gas presented in chapter 7. This comparison will be particularly useful to estimate the efficiency of the dynamical coupling between the warm and cold molecular gas.

13.2   Theoretical perspectives

The detection of powerful H_2 emission in a diverse set of extragalactic sources with little or no star formation highlights the need to understand the role of H_2 formation and cooling for the dissipation of mechanical energy in a multiphase ISM. The previous sections have shown that these observations provide insights in the physics of galaxy interactions or of the regulation of star forming activity in radio galaxies. An efficient transfer of the bulk kinetic energy to molecular gas is required to make H_2 an important coolant and thus explain these observations. The dissipation of mechanical energy within cold molecular gas, H_2 formation and its collisional excitation, play a key-role in the physics of turbulent mixing of gas phases.

13.2.1   A novel numerical study of the dynamical interactions between gas phases

In my thesis work, I reached a qualitative understanding on how the energy transfer may occur. The fragmented, multiphase structure of the ISM is likely to be a main aspect. The dynamical interactions between gas phases drive a mass cycle which contributes to the energy transfer in two ways: (1) Gas cooling transfers the turbulent energy of the warm H II and H I to the H_2 gas. (2) The thermal instability induced by the gas cooling transfers a significant fraction of the thermal energy of the gas to turbulent energy. The turbulent velocities of the motions generated by the thermal instability are expected to be commensurate with the sound speed in the warmer gas and thus are supersonic for the colder gas. These non-linear aspects of the dynamical interaction between gas phases can only be investigated quantatively with numerical simulations.

Numerical simulations (e.g. Audit and Hennebelle, 2005) show that the thermal instability prevents energy from being radiated by the warmer gas to feed turbulence in the cooler gas. I have started a collaboration with P. Lesaffre and E. Audit which I will pursue and extend during my post-doc. We will use the RAMSES magnetohydrodynamical (MHD) adaptive Mesh Refinement (AMR) 3-D code. It is essential to resolve thermal instability to quantify energy and mass exchanges. This can only be achieved by including chemical evolution and its impact on the cooling efficiencies, and we are currently writing a routine to introduce time-dependent chemistry and thermal diffusion in the code. The main coolants are C^+, O, H_2, and CO. This code will be used to model mass cycling and mechanical energy dissipation in a mutiphase ISM. This will be the first simulation of the physical

and chemical evolution of a thermally unstable multiphase gas including a self-consistent treatment of the H_2, HI, HII and hot phases of the ISM. Including all phases requires a large dynamic range and is beyond the capabilities of state-of-the-art computing. We will hence describe the processes sequentially, starting at the large scales. As we proceed to smaller scales we will include a more detailed description of the thermal budget and chemistry of the gas.

We will first study the effects of a large scale shock on a set of HI clouds embedded in a hot plasma. Then we will study the fate of one of these clouds in greater details as it is being fragmented. We will pay special attention to the energy transfer between these phases. Thanks to our AMR approach and with a careful treatment of the thermal and chemical diffusion accross the boundaries between these various phases, this will be possible.

We will also explore the momentum and energy transfer from a hot stream of gas into an initially static molecular cloud. In both stellar and AGN feedback, it is of crucial importance to determine whether the dynamical coupling between the tenuous outflow and the cloud is efficient, and whether it can power the amount of H_2 emission seen in these H_2-luminous sources.

Due to their proximity, starburst-driven winds or galactic supernova remnants provide a unique opportunity to confront the model with data in great detail. Our interpretation will be based on the physical conditions inferred from these numerical models. They will serve as input for detailed calculations of gas cooling and chemistry in shock models. This method relates the observational approach (sect. 13.1) with our numerical and analytical models, and will also be applied to extragalactic sources.

13.2.2 Towards a phenomenological prescription of the impact of H_2 on the energetics of galaxy evolution

Though H_2 emission is related to small scale processes, its formation and cooling power play a major role in the overall energetics of violent phases of galaxy evolution. Numerical studies of galaxy formation cannot properly account for these processes. Small scale simulations with sufficient resolution to include the detailed *multiphase* gas physics do not include the overall context of feedback processes. Inversely, large-scale simulations can only include gas physics through phenomenological recipes.

From the results obtained from the observational (sect. 13.1.2) and numerical (sect 13.2.1) approach of feedback, an ultimate goal would be to distill reasonably simple, but robust phenomenological equations, which would approximate the physics of energy dissipation, and allow to predict H_2 emission as a function of the physical parameters of a galaxy. These equations will represent a crucial input to cosmological simulations of galaxy formation and the growth of structure. Ultimately, this will allow to determine the role of the gas for the build-up of galaxies, and the importance of starburst and AGN driven winds on the growth and properties of the ensemble of galaxies across cosmic time.

Since most of the galaxy mass build-up occurred at redshifts between 1 and 2, this prescription will need to be tested with direct observations of sources in this redshift range. This will become possible with JWST/MIRI (see sect. 13.1.2).

The last word...

A thesis! What a shock!

In fact, if you think about it, a thesis *is* a shock. To be a PhD student is to be shocked. You are in the shock front, between what you believe to know, the postshock medium, and the unknown, the preshock medium. In this shock front, you are heated to high temperatures, highly excited by your research. Sometimes you feel like going in the postshock, stay there to cool down a little bit, have a fresh shower, to come back to the known. Of course, what you did in the shock front greatly affected the postshock, but also, what you're doing in the shock front affects the future science, but you don't have access to this information[4].

The Physicists' Bill of Rights

Author Unknown

We hold these postulates to be intuitively obvious, that all physicists are born equal, to a first approximation, and are endowed by their creator with certain discrete privileges, among them a mean rest life, n degrees of freedom, and the following rights, which are invariant under all linear transformations:

I. To approximate all problems to ideal cases.

II. To use order of magnitude calculations whenever deemed necessary (i.e., whenever one can get away with it).

III. To use the rigorous method of "squinting" for solving problems more complex than the additions of positive real integers.

IV. To dismiss all functions which diverge as "nasty" and "unphysical".

V. To invoke the uncertainty principle whenever confronted by confused mathematicians, chemists, engineers, psychologists, dramatists, and andere schweinhund.

VI. To the extensive use of "bastard notations" where conventional mathematics will not work.

VII. To justify shaky reasoning on the basis that it gives the right answer.

VIII. To cleverly choose convenient initial conditions, using the principle of general triviality.

IX. To use plausible arguments in place of proofs, and thenceforth refer to those arguments as proofs.

X. To take on faith any principle which seems right but cannot be proved.

Obviously, *la vie n'est pas un long fleuve tranquille*, the preshock medium is inhomogeneous, multiphased, full of surprises. Sometimes you propagate fast, smoothly, in a teneous medium, whereas sometimes you hit a denser problem, and your speed is reduced, you need to think harder! Your physical state in the shock depends on your progression speed. Be careful of not going too fast, be careful of the J-type discontinuity, be careful not to be ionized... otherwise you'll lose something...

---
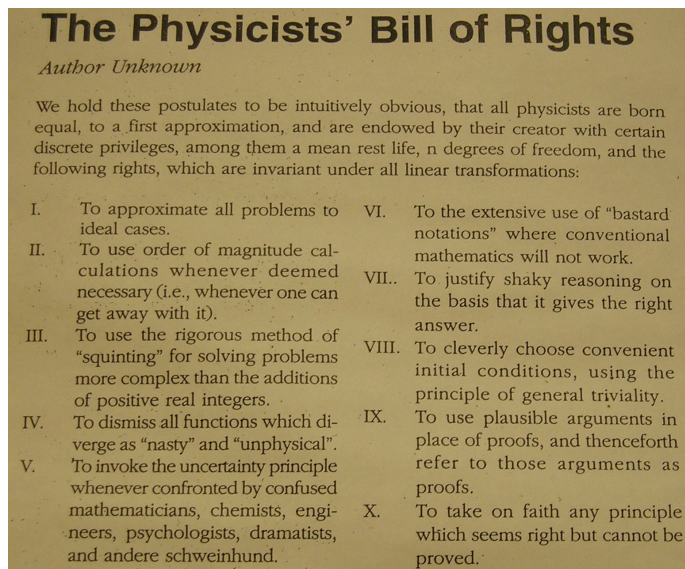
[4] ...unless you can travel at the speed of light... Obviously, you've understood that I'm talking about the radiative precursor here!

Part IV

Appendices

Appendix A

Modeling dust emission: the DUSTEM code

Abstract

This appendix briefly presents the code that I have used to model the dust emission from the Stephan's Quintet galaxy collision. This code, so-called DUSTEM, is an update of the Désert et al. (1990) model, which computes, from an input radiation field, the emission, temperature distribution, absorption and scattering cross-sections, as a function of the wavelength, for a size distribution of grains including stochastically heated PAHs and very small grains. In the case of optically thick (to UV radiation) molecular clouds, the DUSTEM code is coupled to a radiation transfer code to take into account in a self-consistent way both the extinction and the heating of dust grains by their own IR emission.

A.1 Introduction

Since the 1970's, a lot of models were built to reproduce the observations of interstellar dust. The Désert et al. (1990) model is one example among others. Since this first publications, a lot of modifications have been done. The most recent ones are reported in Compiègne et al. (2008). In the following, I briefly give the main features of the *DUSTEM* model, and its key parameters. The interested reader may consult the PhD thesis by Compiègne, M. (2007), Flagey, N. (2007) and Gonzalez Garcia, M. (2009) for a description of the updates included in the code.

A.2 Dust models: populations and size distributions of grains

The *DUSTEM* model includes a mixture of three populations of dust grains with increasing sizes; which is the minimum number of components needed to account for interstellar extinction and IR dust emission. These components are the following.

- Polycyclic Aromatic Hydrocarbons (PAHs) of radius $a = 0.4 - 1.2$ nm, responsible for the Aromatic Infrared Bands (AIBs) and the FUV non-linear rise in the extinction curve. Much of the PAH emission is concentrated in features at 3.3, 6.2, 7.7, 8.6, 11.3 and 17 μm. Duley and Williams (1981), followed by Léger and Puget (1984), identified these features as the optically active vibrational modes of PAH molecules.

- Very Small Grains (VSGs, $a = 1 - 4$ nm), which are carbonaceous nanoparticles producing the mid-IR continuum emission and the extinction bump at 2175 Å.

- Big Grains (BGs, $a = 4 - 110$ nm) of silicates with carbonaceous mantles or inclusions, which account for the far IR emission and the $1/\lambda$ rise at visible and near-IR wavelengths.

Table A.1: Parameters of the DUSTEM code[a].

Component[b]	Abundance	α	$a_{\min}$ [nm]	$a_{\max}$ [nm]	ρ	β
PAHs	4.3×10^{-4}	3.5	0.4	1.2	2.4×10^{-7} [g cm^{-2}]	0
VSGs	4.7×10^{-4}	3.5	1.2	4.0 g cm^{-3}	2.3	0
BGs	6.4×10^{-3}	3.5	4.0	110 g cm^{-3}	3.0	0.61

[a]We list the mass abundance relative to Hydrogen, the parameters of the size distribution $n(a)$ for the three components of the DUSTEM model (it is assumed that $n(a) \propto a^{-\alpha}$ with a between $a_{\min}$ and $a_{\max}$), the mass density ρ of the grains, and their maximum albedo β.

[b]The grain populations are: Polycyclic Aromatic Hydrocarbons (PAHs), Very Small Grains (VSGs), and Big Grains (BGs).

The version of the *DUSTEM* code I have used assumes the size distributions of all the dust populations to be a power-law, $n(a) \propto a^{-3.5}$ (Mathis et al., 1977), with minimum and maximum radii listed in the items above. The parameters of the grains used in the version of the code I use are gathered in Table. A.1.

A.3 Updates and calculations

The model is designed to fit both the interstellar extinction curve (see chapter. 2, sect. 2.3.2, Fig. 2.4) and the infrared dust emission, in particular that of the diffuse interstellar medium. The dust properties, the dust-to-gas mass ratio, and the exciting radiation field are provided by the user. The code then calculates the dust SED νS_ν in units of erg s^{-1} H^{-1}, the distribution of dust temperatures, as well as the UV to IR absorption and scattering cross-sections in units of cm^2 g^{-1}, for each dust grain species, as a function of the wavelength.

Since the original version of Désert et al. (1990), the absorption cross sections of the PAHs (with addition of new Aromatic Infrared Bands, AIBs) and those of the VSGs and BGs, as well as the heat capacities (graphite, PAH C-H, silicate and amorphous carbon) have been updated (Compiègne et al., 2008).

In the diffuse interstellar medium, small grains (PAHs and VSGs) undergo temperature fluctuations triggered by the discrete absorption of stellar photons (see e.g. Draine, 2003, for a review). They cool by emission in the near and mid-IR range. The code computes the probability distribution of temperatures resulting from the stochastic heating of these grains. Conversely, BGs, which have a longer cooling time and a shorter timescale between absorption of two photons because of their size, stay at constant temperature. The code computes their emission as a grey body.

A.4 Inputs of the DUSTEM code

The inputs of the code are the following:

Grain properties: a file, named `grain.dat` list the types of grains and their density in [g cm^{-3}] for all types except the PAHs which are in g cm^{-2}. The types of grains may be chosen from

the following list: 1 = graphite grain (Mie theory for spherical grains in the $1/3 - 2/3$ approximation, see Draine and Lee, 1984). 2 = PAH, 3 = BG (Désert et al., 1990), 4 = VSGs (Désert et al., 1990), 5 = astro-silicates (Mie theory for spherical grains)

The file `propmass.dat` sets the mass abundance of the grains relative to H, `calor.dat` lists the heat capacities for the different available grain species, and `taille.dat` defines the size distribution for each grain population.

Incident radiation field: the file `isrf.dat` contains the flux of the input radiation field in units of erg s^{-1} cm^{-2} Hz^{-1}, and `lambda.dat` is the associated wavelength grid in μm.

Absorption and scattering coefficients are listed in the `QABS_*.dat`, one file for each type of grains.

A.5   Outputs of the DUSTEM code

The code provides the following outputs:

Dust emissivity: the file `dustem.res` gives the dust emissivity in units of erg s^{-1} per Hydrogen atom, as a function of the wavelength, for each population of grains.

Absorption and scattering cross-sections are listed, in units of [cm^2 g^{-1}], as a function of the wavelength in `secteffir.res` for the infrared domain, and in `secteffuv.res` for the UV domain.

A.6   When DUSTEM cooperates with the Meudon PDR[1] code...

The spectral energy distribution of the IR dust emission does not only depend on the radiation field and the grain properties. It also depends on the physical structure of the molecular gas, and in particular on its optical thickness to UV radiation. If a molecular cloud illuminated by a UV radiation field is optically thick to UV photons, the radiation field is attenuated as it penetrates into the cloud, thus reducing the dust heating. In addition, dust emission has a *positive feedback* on its own IR emission. The local IR dust emission contributes to the IR radiation field, and becomes a significant heat source within dark clouds where UV light is attenuated. I briefly describe how these two effects are taken into account in our modeling of dust emission from the Stephan's Quintet galaxy collision presented in chapter 8.

Modeling dust emission from optically thick (to UV) molecular clouds

To model the dust emission from a molecular cloud that is optically thick to UV radiation (see chapter 8 and paper III), I have used the *Meudon PDR* (Photon Dominated Region) code[2] to compute

---

[1]Photon-Dominated Region

[2]This code, fully described in Le Petit et al. (2006), is available on the web on http://aristote.obspm.fr/MIS and will be incorporated in the Virtual Observatory.

the radiative transfer through the cloud. This 1-dimensional, steady-state model considers a stationary plane-parallel slab of gas and dust, illuminated by UV radiation. The radiation field output I_ν of the Meudon PDR code is used as input to the *DUSTEM* program to compute the spectral energy distribution (SED) of the dust as a function of the optical depth into the cloud.

This 2-step process is iterated to take into account dust heating by the dust IR emission. The interface between the *DUSTEM* code and the *Meudon PDR* code represents a significant update, described in the PhD thesis by Gonzalez Garcia, M. (2009). In the present version, so-called *PDR-DUSTEM*, the thermal balance of the grains resulting from the IR continuum emission of the dust is now solved. A first run is done with the *Meudon PDR* code to solve for the radiative transfer and compute the radiation field I_ν through the slab of gas. Then, the *DUSTEM* program is called to compute the dust temperature distribution and the dust contribution to I_ν. This 2-step process is iterated until the calculation of the dust emission has converged (usually $4 - 5$ iterations).

Appendix B

Deconvolution of high-resolution PSF: bayesian formalism

Abstract

In this appendix I give a brief description of the formalism used to devonvolve a high-resolution image from several low-resolution ones. I have applied this algorithm to reconstruct a high resolution PSF image from the data provided by the microscanning test (see chapter 11). This algorithm was developed by T. Rodet at LSS, Orsay.

B.1   The inverse problem

The aim of the deconvolution is to reconstruct a high-resolution image, denoted by $\boldsymbol{x}$, from multiple low-resolution images. These low-resolution images are co-added on a fine grid. We denote $\boldsymbol{z}$ the LR image that have been over-sampled on a fine grid. This image is still "blurred", but its number of pixels is a factor f^2 higher than the observed LR image. $\boldsymbol{z}$ is the convolution of the HR image $\boldsymbol{x}$ that we want to calculate by the impulse-response (PSF) of the detector:

$$\boldsymbol{z} = \boldsymbol{R}\boldsymbol{x} + \boldsymbol{n} \tag{B.1}$$

One cannot apply the classical methods of deconvolution because part of the data is not observed (due to uncertainties on the translations, see sect. 11.5.3). Indeed, there are missing parts, "holes", in the data because the source is not exactly at its expected position on the fine grid image. The Fig. 11.12 shows the PSF data co-added onto a fine grid with an over-sampling factor of 11. We illustrate the truncation of the data by comparing the results of the co-addition when using the expected positions of the source, to the results when using the shifts estimated by cross-correlation. The additional truncation for the effective translations comes from the mismatch between expected and real position of the source.

We recall that, because of truncation of the data (we miss some part of the data on the highly-sampled grid), a truncation matrix $\boldsymbol{T}$ is introduced in Eq. B.1:

$$\boldsymbol{z} = \boldsymbol{T}\boldsymbol{R}\boldsymbol{x} + \boldsymbol{n} = \boldsymbol{H}\boldsymbol{x} + \boldsymbol{n} \tag{B.2}$$

$\boldsymbol{T}$ is a mask with pixels value of 1 where the data exists, and 0 otherwise. The operator $\boldsymbol{H} = \boldsymbol{T}\boldsymbol{R}$ returns the measurements $\boldsymbol{z}$ from the HR image $\boldsymbol{x}$. To solve the deconvolution problem, a bayesian formalism is used. In the following, I briefly give the basis of the formalism we use to estimate $\boldsymbol{x}$, the HR image.

B.2   Bayesian inference

Solving inverse problems involves statistical methods that have been used since many decades to perform signal processing. In practice, these methods rely on the minimization of a quadratic criterion, that we will express below. The estimator used to minimize this criterion can be interpreted in a Bayesian framework. The Bayesian inference process, in which observations are used to infer the probability that an hypothesis is true, is based on the Bayes' theorem. We denote $\boldsymbol{z}$ the measured data and $\boldsymbol{C}$ a variable that gathers the model of data acquisition and the parameters *a priori*. The Bayes' law is expressed as:

$$f(x|z,\,C) = \frac{f(z|x,\,C)\,f(x|C)}{f(z|C)}\;. \tag{B.3}$$

The terms of the Bayes' theorem are the following. $f(z|x,\,C)$ is the *likelihood*, i.e. the probability distribution of the data if we know the physical quantity x. This probability gathers all the information about our knowledge on the data acquisition system, and can be determined by solving the *direct* problem (sect. 11.5.2). In Eq. B.3, $f(x|C)$ is the *prior* probability of x, i.e. the knowledge about x before doing the measurements. It is the *prior* in the sense that it does not take into account any infomation about z. The Bayes' formula gives $f(x|z,\,C)$, the conditional probability of x, given z. it represents all the information we have on the problem. It is also called the *posterior probability* because it is derived from the specified value of z. $f(z|C)$ is the prior probability of z, and acts as a normalizing constant. This constant is chosen as to make the integral of the function $f(x|z,\,C)$ equal to 1, so that it is indeed a probability density function. Intuitively, the Bayes' theorem in this form describes the way in which one's knowledge about observing the HR data ($\boldsymbol{x}$) is updated by having observed the LR data ($\boldsymbol{z}$).

B.3   Least-square criterion and minimization technique

The estimate of the value $\hat{\boldsymbol{x}}$ is given by the argument of the maximum of the *posterior* probability function, often called *posterior* maximum likelihood:

$$\hat{x}_{\mathrm{ML}} = \arg\max(f(x|y,\,C)) \tag{B.4}$$

The noise $\boldsymbol{n}$ is assumed to be Gaussian, independent and uniform over the whole image. Therefore we use a gaussian likelihood:

$$f(z|x,\,C) = K\,e^{-\frac{(z-Hx)^2}{2\,\sigma^2}} \tag{B.5}$$

Therefore we obtain the least-squares estimator:

$$
\begin{aligned}
\hat{x}_{\mathrm{ML}} \;&=\; \arg\max(f(z|x,\,C)) & \text{(B.6)}\\[4pt]
&=\; \arg\max\left(e^{-\frac{(z-Hx)^2}{2\,\sigma^2}}\right) & \text{(B.7)}\\[4pt]
&=\; \arg\max\left(-\frac{(z-Hx)^2}{2\,\sigma^2}\right) & \text{(B.8)}\\[4pt]
&=\; \arg\min((z-Hx)^2) & \text{(B.9)}\\[4pt]
&=\; \arg\min(\|z-\boldsymbol{TRx}\|^2 + \mu\|\boldsymbol{Dx}\|^2) & \text{(B.10)}
\end{aligned}
$$

μ is the regularization parameter. The last equation defines the regularized least-square estimator, where $\boldsymbol{D}$ is the finite differences operator (Laplacian). $\boldsymbol{D}$ has a size $(N-1) \times N$ and can be written as:

$$
\boldsymbol{D} = \begin{bmatrix}
1 & -1 & 0 & 0 & \dots & \dots & 0 \\
0 & 1 & -1 & 0 & \dots & \dots & 0 \\
\vdots & & \ddots & \ddots & & & \vdots \\
\vdots & & & \ddots & \ddots & & \vdots \\
0 & \cdots & \cdots & 0 & 1 & -1 & 0 \\
0 & \cdots & \cdots & 0 & 0 & 1 & -1
\end{bmatrix}
\tag{B.11}
$$

The least-square criterion, Q_{LS}, to minimize in Eq. B.10 is quadratic and can be re-written as:

$$
Q_{\mathrm{LS}}(\boldsymbol{x}) = (\boldsymbol{y} - \boldsymbol{H}\boldsymbol{x})^{\mathrm{t}}(\boldsymbol{y} - \boldsymbol{H}\boldsymbol{x}) + \mu \boldsymbol{x}^{\mathrm{t}} \boldsymbol{D}^{\mathrm{t}} \boldsymbol{D} \boldsymbol{x}
\tag{B.12}
$$

The solution is explicit:

$$
\hat{x}_{\mathrm{ML}} = (\boldsymbol{H}^{\mathrm{t}} \boldsymbol{H} + \mu \boldsymbol{D}^{\mathrm{t}} \boldsymbol{D})^{-1} \boldsymbol{H}^{\mathrm{t}} \boldsymbol{z}
\tag{B.13}
$$

The main issue with this explicit solution is that the size of the matrix $\boldsymbol{H}^{\mathrm{t}}\boldsymbol{H}$ can be large and its inversion can be very time-consuming. Since the criterion to minimize is quadratic, it is convex and has a unique minimizor. We use a method called "gradient descent" or "steepest descent", which consists in starting from whatever value for $\boldsymbol{x}$, and then converge to the solution in the direction of the steepest slope (opposite of the gradient's direction). At each step, this algorithm ensures that, after a sufficient number of iterations, we will approach the required minimum value of the criterion. Thus we calculate the gradient of the criterion to minimize:

$$
g(\boldsymbol{x}) = \frac{\partial Q_{\mathrm{LS}}(x)}{\partial x} = 2\,\boldsymbol{H}^{\mathrm{t}}(\boldsymbol{H}x - z) + 2\mu \boldsymbol{D}^{\mathrm{t}} \boldsymbol{D} x
\tag{B.14}
$$

and we update the solution with the following equation:

$$
x^{k+1} = x^k - \alpha_{\mathrm{opt}}(\boldsymbol{H}^{\mathrm{t}}(\boldsymbol{H}x^k - y) + \mu \boldsymbol{D}^{\mathrm{t}} \boldsymbol{D} x^k)\,,
\tag{B.15}
$$

where α_{opt} is the optimal step to ensure the most efficient descent is the opposite direction of the gradient. This step is calculated by cancelling the gradient with respect to α. In our case, we use a variant of the gradient descent, so-called "conjugate gradient descent", which consists in having orthogonal directions at each descent steps.

Appendix C

Publications

C.1   Refereed Articles

1. **Guillard, P.**, Boulanger, F., Pineau des Forêts, G., Appleton, P.N., H_2 *formation and excitation in the Stephan's Quintet galaxy-wide collision*, 2009, A&A, 502, 515.

2. Boulanger, F., Maillard, J. P., Appleton, P., Falgarone, E., Lagache, G., Schulz, B., Wakker, B. P., Bressan, A., Cernicharo, J., Charmandaris, V., Drissen, L., Helou, G., Henning, T., Lim, T. L., Valentjin, E. A., Abergel, A., Bourlot, J. Le, Bouzit, M., Cabrit, S., Combes, F., Deharveng, J. M., Desmet, P., Dole, H., Dumesnil, C., Dutrey, A., Fourmond, J. J., Gavila, E., Grangé, R., Gry, C., **Guillard, P.** et al. 2008, *The Molecular Hydrogen Explorer*, Experimental Astronomy special issue on Cosmic Vision Proposals.

3. **Guillard, P.**, Boulanger, F., Cluver, M., Appleton, P.N., Pineau des Forêts, G., *Observations and modeling of the dust emission from the H_2-bright galaxy-wide shock in Stephan's Quintet*, 2009, A&A, submitted.

4. **Guillard, P.**; Boulanger, F., Lisenfeld, U., Duc, P.A., Appleton, P.N. & Pineau des Forêts, G., *Complex kinematics of the CO gas in the Stephan's Quintet galaxy collision*, 2009, A&A, in preparation.

5. Nesvadba, N.P.H., Boulanger, F., Salomé, P., **Guillard, P.**, Lehnert, M.D., Pineau des Forêts, G., Ogle, P., Appleton, P.N.,*Energetics of the molecular gas in the H_2-luminous radio galaxy 3C326: Evidence for negative AGN feedback*, 2009, A&A, submitted.

6. M.E. Cluver, P.N. Appleton, **P. Guillard**, F. Boulanger, P. Ogle, P.-A., Duc, N. Lu, J. Rasmussen, W.T. Reach, J.D. Smith, R. Tuffs, K. Xu, M. Yun, *Powerful H_2 line-cooling in Stephan's Quintet: I- Mapping the dominant cooling pathways in group-wide shocks*, 2009, ApJ, accepted for publication.

7. **Guillard, P.**, Jones, A. P., Tielens, A.G.G.M, *Noble gas implantation into SiC stardust: Constrains on dust evolution processes*, 2009, A&A, submitted.

C.2   Proceedings

1. **Guillard, P.** & Boulanger, F. *H_2 Energetics in Galaxy-wide Shocks Insights in Starburst Triggering and Galaxy Formation*, 2008, SF2A-2008: Proceedings of the Annual meeting of the French Society of Astronomy and Astrophysics, p371.

2. J. Amiaux, F. Alouadi, J.L. Augueres, P. Bouchet, M. Bouzat, C. Cavarroc, C. Cloue, P. De Antoni, D. Desforges, A. Donati, D. Dubreuil, D. Eppelle, F. Gougnaud, B. Hervieu, P.O. Lagage, D. Leboeuf, I. Le Mer , Y. Lussignol, P. Mattei, F. Meigner, V. Moreau, E. Pantin, P. Perrin, S. Ronayette, G. Tauzin, S. Poupar, D. Wright, A. Glasse, G. Wright, E. Mazy, J.Y. Plesseria, E. Renotte, T. Ray, A. Abergel, **P. Guillard** et al. *Development approach and first infrared test results of JWST/Mid Infra Red Imager Optical Bench*, 2008, Proc. SPIE, Vol. 7010

3. **Guillard, P.**, Boulanger, F., Pineau des Forêts, G., Appleton, P.N., H$_2$ *formation and excitation in the Stephan's Quintet galaxy-wide shock*, 2007, 4th Spitzer Conference Proceedings, "The Evolving ISM in the Milky Way & Nearby Galaxies".

4. **Guillard, P.**, Jones, A. P., Tielens, A.G.G.M, *The lifecycle of interstellar dust as constrained by noble gas implantation into SiC grains*, 2007, SF2A-2007: Proceedings of the Annual meeting of the French Society of Astronomy and Astrophysics held in Grenoble, France, July 2-6, 2007, Eds.: J. Bouvier, A. Chalabaev, and C. Charbonnel, p.246

5. Theureau, G., **Guillard, P.**, Jegouzo, I., Martin, J.-M., Prugniel, Ph., Serres, B. *HI galaxies and the Nançay Archive*, 2004, SF2A-2004: Semaine de l'Astrophysique Francaise, meeting held in Paris, France, June 14-18, 2004. Edited by F. Combes, D. Barret, T. Contini, F. Meynadier and L. Pagani. Published by EdP-Sciences, Conference Series, 2004, p. 577.

C.3 Technical Reports

1. Ronayette, S., **Guillard, P.**, Pantin, E., Cavarroc, C., Amiaux, J. *JWST/MIRI ETM Optical Results*, 2008, Reference: MIRI-RP-00676-CEA

2. **Guillard, P.** & Augueres, J.L., *Image Quality Analysis of the JWST MIRI Imager: First Cold Tests done at CEA Saclay, Dec. 2007*, 2008, Reference: MIRI-TN-00743-IAS

3. **Guillard, P.**, Rodet, T. & Augueres, J.L., *Image Quality Analysis of the JWST MIRI Imager: High-Resolution PSF Analysis: Microscanning Test*, 2008, Reference: MIRI-TN-00853-IAS

4. **Guillard, P.** & Augueres, J.L., *Image Quality Analysis of the JWST MIRI Imager: Focus and FOV Exploration with a Point Source Tests*, 2008, Reference: MIRI-TN-00867-IAS

Appendix D

Teaching and public outreach

Abstract

During my PhD thesis, I have teached at the University of Paris Sud 11. This teaching validates my "Agrégation" diploma. Here is a short summary of my teaching activities. Besides this, I have participated to public outreach activities at the University of Orsay, such as "Forum faites de la science", "La fête de la science", or "Année Mondiale de l'Astronomie 2009".

2006-2007

- TP de Physique fondamentale (fundamental physics experiments), Master 1. Supervisor: Laurent Verstraete. 45h.
- Coupole d'Astrophysique (CCD astrophysical observations with a 14" telescope), Master 1. Supervisor: Hervé Dole. 15h.
- TD de Mécanique (classical mechanics course), L1 (BSc). Supervisor: Arne Keller.

2007-2008

- TP de Physique fondamentale (fundamental physics experiments), Master 1. Supervisor: Laurent Verstraete. 24h.
- Coupole d'Astrophysique (CCD astrophysical observations with a 14" telescope), Master 1. Supervisor: Hervé Dole. 15h.
- TD de Mécanique (classical mechanics course), L1 (BSc). Supervisor: Arne Keller.
- Astrophysical course in data reduction, Mster 1. Supervisor: Hervé Dole. 16h.
- Astrophysical observation with Master 2 students at the Observatoire de Haute Provence. 3 nights (80 cm, 1.2 m, 2 m telescopes), 30h.

2008-2009

- Coupole d'Astrophysique (CCD astrophysical observations with a 14" telescope), Master 1. Supervisor: Hervé Dole. 20h.
- Astrophysical course in data reduction, Mster 1. Supervisor: Hervé Dole. 16h.
- Astrophysical observation with Master 2 students at the Observatoire de Haute Provence. 6 nights (80 cm, 1.2 m, 2 m telescopes), 60h.

Appendix E

The show must go on!

Abstract

This appendix lists the conferences and schools attended during this PhD thesis. The talks, posters and invited seminars, as well as some associated abstracts, are presented. These contributions are ordered from the most recent to the oldest.

E.1 Conferences

"Hunting for the dark: The Hidden Side of Galaxy Formation", 2009, October 19-23, Qwara, Malta

- **Poster: "Molecular gas and dust in galaxy halos: impact on the energetics of galaxy formation and evolution". P. Guillard, F. Boulanger, N. Nesvadba, P. Ogle, P.N. Appleton, G. Pineau des Forêts.**

  One of the most surprising results obtained with the Spitzer space telescope was the discovery of powerful mid-IR H_2 line emission from a significant number of sources that are in active phases of galaxy evolution. The underlying physics may be a key ingredient to describe the build-up of baryonic mass in galaxies and their evolution. We focus here on the interpretation of observations of interacting/merging systems and AGN host galaxies. They provide insights on the exchange of mass between galaxies and the intergalactic medium and the energetics of galaxy formation. The Stephan's Quintet (SQ), a compact group of interacting galaxies, is a striking example showing that dust survives in a high-speed galaxy collision and that H_2 forms in the halo of the group. This is also true for galactic winds driven by AGN feedback or starbursts. In SQ and in H_2-luminous galaxies in general, we propose that the H_2 emission is powered by the dissipation of the mechanical energy provided by galaxy merging or feedback. Shocks driven into multiphase gas lead to efficient dissipation of this energy at small scales, within molecular gas.

Semaine de l'astrophysique française (SF2A), 2008, June 30 - July 4, Paris, France

- **Talk, PNG Session: "H_2 energetics in Galaxy-wide Shocks: Insights on starburst triggering in galaxy collisions", P. Guillard, F. Boulanger, G. Pineau des Forêts, P.N. Appleton, P. Ogle.**

  How the gas cools and fuels galaxy formation and what processes regulate star formation in galaxies are some major questions of extragalactic astronomy. We focus on galaxy collisions and mergers which are observed to trigger IR-luminous bursts of star formation. Recently,

Spitzer observations show that some interacting systems stand out for having a high H_2 to IR luminosity ratio. We propose that these systems represent an intermediate phase in the evolution of mergers, prior to the starburst. Observations and modeling contribute to define a physical framework of the mechanical energy dissipation in this H_2-luminous stage. The H_2 excitation show that highly-turbulent ($10 - 50$ km/s) molecular gas is formed within hot gas. The cloud turbulence is powered by a slow energy and momentum transfer from the gas bulk motion. We propose that the timescale to dissipate the collision kinetic energy represents the time necessary for the molecular gas to settle in gravitationally bound clouds and therefore to form stars.

- **Poster, PCMI Session: "H_2 Formation and Excitation in the Stephan's Quintet Galaxy-Wide Shock", P. Guillard, F. Boulanger, G. Pineau des Forêts, P.N. Appleton**

  Spitzer has detected an extremely powerful ($L > 10^{41}$ erg s^{-1}), shock-powered, mid-IR H_2 emission towards the Stephan's Quintet (SQ) galaxy group (Appleton et al. 06). This is the first time an almost pure H_2 line spectrum has been seen in an extragalactic object. The luminosity in the H_2 lines exceeds by a factor of ≈ 2 the surface brightness in X-rays. How can we explain such a huge amount of molecular gas ($M_{H_2} \approx 4 \times 10^7$ $M_\odot$) coexisting with a X-ray emitting plasma? How come there is no star formation associated with H_2? We summarize in this poster the main results of a scenario (P. Guillard et al. 08) where the molecular gas is formed in the shock. The pre-shock gas is assumed to be inhomogeneous because the shock has induced formation of both hot (5×10^6 K) plasma and warm (10^{2-3} K) H_2. Our model (P. Guillard et al. 2008) computes the physical and chemical evolution of the shock heated gas, including density inhomogeneities in the pre-shock medium and dust destruction. Schematically, low density preshock gas ($n_H < 0.01 - 0.001$ cm^{-3}) is shocked at high speed (≈ 1000 km/s for SQ) and becomes a dust-free X-ray emitting plasma. Denser gas ($n_H > 0.1$ cm^{-3}) is heated at lower temperatures and dust survives. In the context of the SQ shock, this gas had time to cool and become molecular. Only a fraction of the collision energy is used to heat the hot plasma. Therefore, a large fraction of the gas energy is stored in bulk gas motions. We propose that, in such conditions, the H_2 emission must be powered by a slow transfer of energy from fast bulk gas motions into low velocity (< 40 km/s) supersonic turbulent motions within the molecular gas. We phenomenologically model this turbulent motions by J-type and magnetic C-type shocks into the newly-formed molecular gas. We show that the observed H_2 line fluxes are very well reproduced for densities $n_H = 10^3 - 10^4$ cm^{-3} and shock velocities within the $5 - 35$ km/s range. SQ is a unique object for studying the physics of galaxy-wide shocks and understanding their key-role in the formation and excitation of H_2. This detailed study of the SQ shock defines a physical framework to interpret observations of H_2-bright galaxies in general.

4th Spitzer Conference, The Evolving ISM in the Milky Way and Nearby Galaxies, 2007, December 2-5, Pasadena, USA

- **The Stephan's Quintet: a beautiful case of H_2 formation in shocks**

  Recently, Spitzer IRS (Infra-Red Spectrometer) observations led to the unexpected detection of extremely bright mid-IR ($L > 10^{41}$ erg s^{-1}) H_2 rotational line emission (Appleton et al. 2006) from warm gas towards the group-wide shock in Stephan's Quintet (hereafter SQ). This

first result was quickly followed by the detection of bright H_2 line emission from more distant galaxies (Egami et al. 2006, Ogle et al. 2007) and from the NGC 1275 and NGC 4696 cooling flows (Johnstone et al. 2007).

Because of the absence or relative weakness of star forming signatures (dust features, ionized gas lines) in the mid-infrared Spitzer spectra, the H_2 emission must be powered by large-scale shocks, associated with galaxy interactions but also possibly with gas infall and AGN feedback. But how can we explain such a huge amount of molecular gas coexisting with a hot plasma at 5×10^6 K ? How come there is no (or very few) star formation associated with H_2?

I will focus this talk on SQ, a group of four interacting galaxies. The shock is created by the galaxy NGC 7318b which is colliding with a tidal stream at a relative velocity of $\sim 1\,000$ km/s. SQ is then a unique object where one can study the physics of galactic wide shocks. I will present the results of a model capable of interpreting the observations. Two key-points of our calculations of the physical and chemical evolution of the shock-heated dusty plasma will be emphasized: dust destruction and the inhomogeneity of the galaxy and intragroup gas. Schematically, low density ($n_H < 0.1\,\mathrm{cm}^{-3}$) gas is shocked at high speed. It becomes the X-ray emitting gas where dust is destroyed. Higher density gas ($n_H > 1\,\mathrm{cm}^{-3}$) is heated to lower temperatures and the dust survives. In the context of the SQ shock, this gas had time to cool and become molecular.

In the near future, this model will be extended to more distant objects belonging to this newly discovered and potentially important population of H_2-bright galaxies. In particular, these H_2 mid-IR lines appear to be a powerful diagnostic of unexplored steps in galaxy evolution.

Semaine de l'astrophysique française (SF2A), 2007, July 5-6, Grenoble, France

- **Talk, PCMI Session: "Noble Gas Implantation into SiC Stardust: Constraints on Astrophysical Processes". P. Guillard, A. Jones, A.G.G.M. Tielens**

Primitive meteorites contain presolar grains that originated in stellar outflows and supernovae ejecta prior to the formation of the solar system. We show that the measured elemental abundances of noble gas atoms trapped into meteoritic SiC grains can be understood in terms of ion irradiation and erosion in circumstellar and interstellar media. A simple atom implantation and grain erosion model has been developed that allows us to provide new insights on dust processing and on the physical conditions that reign in these environments.

E.2   Seminars

STScI, John Hopkins University, 2008, October, 14, Baltimore, USA

- **H_2 Formation and Excitation in Galaxy-wide Shocks**

Princeton University, 2008, October, 10, Princeton NJ, USA

- **H_2 Formation and Excitation in Galaxy-wide Shocks**

KIPAC, Stanford University, 2008, October, 8, Stanford, USA

- **H$_2$ Formation and Excitation in Galaxy-wide Shocks**

IPAC, Caltech, 2008; October, 1, Pasadena, USA

- **H$_2$ Formation and Excitation in Galaxy-wide Shocks**

Spitzer space telescope observations led to the surprising detection of a diverse set of extra-galactic sources whose infrared spectra are dominated by line emission of molecular hydrogen. The absence or relative weakness of typical signs of star formation (like dust features or lines of ionized gas) suggest the presence of large quantities of molecular gas with no (or very little) associated star formation. These observations set a new light on the contribution of H$_2$ to the cooling of the interstellar medium, on the relation between molecular gas and star formation, and on the energetics of galaxy formation.

I will focus on the striking example of the galaxy-wide shock in Stephan's Quintet, where a galaxy is colliding with a tidal tail at a relative velocity of 1000 km/s. Observations show that exceptionally turbulent H$_2$ gas is coexisting with a hot, X-ray emitting plasma. The extreme mid-IR H$_2$ emission from the shock exceeds that of the X-rays. I will present the observations and show how they can be interpreted by considering that the shock is moving through an inhomogeneous medium. Observations suggest that most of the shock energy is transferred to bulk kinetic energy of the H$_2$ gas. The turbulent energy of the post-shock gas drives a mass cycle across the different gas phases where H$_2$ is forming out of the hot/warm gas. This interpretation puts the H$_2$ emission into a broader astrophysical context including optical and X-ray observations.

We propose that the turbulence in the clouds is powered by a slow energy and momentum transfer from the bulk motion of the gas, and that the dissipation of this turbulent energy in turn is powering the H$_2$ emission. The timescale to dissipate the kinetic energy from the collision may set the relaxation time for the molecular gas to settle in gravitationally bound clouds and ultimately to form stars.

Our detailed study of Stephan's Quintet represents an important step in defining a physical framework to describe the dissipation of mechanical energy in H$_2$-luminous galaxies. I will discuss the relevance of H$_2$ formation for the energetics of key processes that participate in galaxy formation: galaxy interactions, gas accretion, and AGN feedback.

GEPI, Observatoire de Paris-Meudon, 2008, September, 8

- **H$_2$ emission in galaxy-wide shocks: insights in starburst triggering**

E.3 Schools

"Supercomputing & Numerical Techniques in Astrophysics Fluid Flow Modeling", Evora, Portugal, 2009, February 2-15

A training school devoted to an integrated overview of the numerical and computational techniques that are most adequate to model different astrophysical fluid flow phenomena by means of supercomputing simulations. I have attended theoretical and laboratory courses and made use of the supercomputer facility at the University of Coimbra and the University of Evora.

"Indo-French training school in optical astronomical observations", Pune, India, 2007, February 12-27

During the two weeks of the school, one week was devoted for observations with the IUCAA Girawali Observatory 2-m telescope, followed by data reduction and presentation of scientific results. Rest of the time was used to introduce the basic fundamentals of optical observations. With Amit Patak, we presented two projects: "The IUCAA deep field", and "Spectroscopy of AGN".

"International Max Planck Research School: Physics of the Interstellar Medium", 2006, September 5-13, Heidelberg, Germany

A one-week school with courses and practical exercises on ISM physics. We also visited the MPI.

"École des Houches: interstellar dust", 2006, May 1-5, Les Houches, France

A one week school devoted to the physics and chemistry of interstellar dust.

E.4 JWST/MIRI European Consortium Meetings

EC meeting, 2009, April, 28-30, Leicester, UK

I have presented my work on the PSF microscanning analysis of the MIRI instrument. I also participated in the scientific discussion in the Galaxy Evolution and the ISM working groups. I have presented a project about observations of H_2 galaxies with MIRI within the Galaxy Evolution working group.

EC meeting, 2009, January, 19-23, Leuven, Belgium

I have presented my work on the PSF microscanning analysis of the MIRI instrument. The science working groups were formed during this meeting. I participated to the first scientific discussions in the Galaxy Evolution and ISM working groups.

EC Science team meeting, 2008, May 26-30, Onsala, Sweden

I have presented a talk entitled "Observing H_2-luminous galaxies with MIRI: what can we learn on galaxy evolution?" in the framework on scientific discussions for the preparation of the science of the JWST/MIRI instrument.

EC Test team meeting, 2007, September 4-8, Leiden, Netherlands

It was my first European Consortium meeting about the JWST Instrument. I remember having been completely lost by the technical talks and overwhelmed by an incredibly long list of acronyms!

List of Tables

List of Figures

Bibliography

T. Abel and Z. Haiman. "The Role of H2 Molecules in Cosmological Structure Formation". In F. Combes and G. Pineau Des Forets, eds., *Molecular Hydrogen in Space*, 237–+ (2000). [ADS].

J. M. Ajello, D. Shemansky, T. L. Kwok, and Y. L. Yung. "Studies of extreme-ultraviolet emission from Rydberg series of H2 by electron impact". Phys. Rev. A29 (1984) 636–653. [ADS].

H. Alfven. *Cosmical electrodynamics* (1950). [ADS].

S. Allam, R. Assendorp, G. Longo, M. Braun, and G. Richter. "Far infrared properties of Hickson compact groups of galaxies. I. High resolution IRAS maps and fluxes." A&AS117 (1996) 39–82. [ADS].

M. G. Allen, B. A. Groves, M. A. Dopita, R. S. Sutherland, and L. J. Kewley. "The MAPPINGS III Library of Fast Radiative Shock Models". ApJS 178 (2008) 20–55. 0805.0204, [ADS].

R. J. Allen and J. W. Hartsuiker. "Radio Continuum Emission at 21 cm near Stephan's Quintet". Nature 239 (1972) 324–+. [ADS].

R. J. Allen and W. T. Sullivan, III. "The low and high redshift neutral hydrogen associated with Stephan's Quintet". A&A 84 (1980) 181–190. [ADS].

S. W. Allen, A. C. Fabian, A. C. Edge, M. W. Bautz, A. Furuzawa, and Y. Tawara. "ASCA and ROSAT observations of distant, massive cooling flows." MNRAS283 (1996) 263–281. arXiv:astro-ph/9609201, [ADS].

V. Ambartsumian. "Report on Solvay Conference". In R. Brussels, Stoops, ed., *La Structure et l'Evolution de l'Univers*, 11th Solvay Conference Report, 241 (1958).

L. Amiaud, J. H. Fillion, F. Dulieu, A. Momeni, and J. L. Lemaire. "Probing amorphous solid water by temperature programmed desorption experiments with molecular hydrogen: from compact to porous ices". Molecules in Space and Laboratory (2007). [ADS].

J. Amiaux, F. Alouadi, J. L. Augueres, P. Bouchet, M. Bouzat, C. Cavarroc, C. Cloue, P. De Antoni, et al. "Development approach and first infrared test results of JWST/Mid Infra Red Imager Optical Bench". In *Society of Photo-Optical Instrumentation Engineers (SPIE) Conference Series*, vol. 7010 (2008). [ADS].

K. Aoki, G. Kosugi, A. S. Wilson, and M. Yoshida. "The Radio Emission of the Seyfert Galaxy NGC 7319". ApJ 521 (1999) 565–571. arXiv:astro-ph/9812365, [ADS].

K. Aoki, H. Ohtani, M. Yoshida, and G. Kosugi. "High Velocity Outflow in the Extended Emission-Line Region of the Seyfert Galaxy NGC 7319". AJ 111 (1996) 140. [ADS].

P. N. Appleton, K. C. Xu, W. Reach, M. A. Dopita, Y. Gao, N. Lu, C. C. Popescu, J. W. Sulentic, et al. "Powerful High-Velocity Dispersion Molecular Hydrogen Associated with an Intergalactic Shock Wave in Stephan's Quintet". ApJL 639 (2006) L51–L54. arXiv:astro-ph/0602554, [ADS].

L. Armus, J. Bernard-Salas, H. W. W. Spoon, J. A. Marshall, V. Charmandaris, S. J. U. Higdon, V. Desai, L. Hao, et al. "Detection of the Buried Active Galactic Nucleus in NGC 6240 with the Infrared Spectrograph on the Spitzer Space Telescope". ApJ 640 (2006) 204–210. arXiv:astro-ph/0511381, [ADS].

H. Arp. "Neighborhoods of spiral galaxies. I. Multiple interacting galaxies." ApJ 185 (1973a) 797–808. [ADS].

H. Arp. "Stephan's Quintet of Interacting Galaxies". ApJ 183 (1973b) 411–440. [ADS].

H. Arp and J. Kormendy. "Faint Surface-Brightness Features Between NGC 7331 and Stephant's Quintet". ApJL 178 (1972) L101+. [ADS].

H. Arp and J. Lorre. "Image processing of galaxy photographs". ApJ 210 (1976) 58–64. [ADS].

E. Audit and P. Hennebelle. "Thermal condensation in a turbulent atomic hydrogen flow". A&A 433 (2005) 1–13. arXiv:astro-ph/0410062, [ADS].

N. A. Bahcall, D. E. Harris, and H. J. Rood. "X-ray emission from Stephan's Quintet and other compact groups". ApJL 284 (1984) L29–L33. [ADS].

S. A. Balbus. "Local dynamic thermal instability". ApJL 303 (1986) L79–L82. [ADS].

J. Ballesteros-Paredes, E. Vázquez-Semadeni, and J. Scalo. "Clouds as Turbulent Density Fluctuations: Implications for Pressure Confinement and Spectral Line Data Interpretation". ApJ 515 (1999) 286–303. arXiv:astro-ph/9806059, [ADS].

E. E. Barnard. "On the dark markings of the sky, with a catalogue of 182 such objects." ApJ 49 (1919) 1–24. [ADS].

M. C. Begelman and A. C. Fabian. "Turbulent mixing layers in the interstellar and intracluster medium". MNRAS244 (1990) 26P–29P. [ADS].

J. H. Black and A. Dalgarno. "Molecular Hydrogen in Interstellar Clouds." In *Bulletin of the American Astronomical Society*, vol. 5 of *Bulletin of the American Astronomical Society*, 380–+ (1973). [ADS].

J. H. Black and E. F. van Dishoeck. "Fluorescent excitation of interstellar H2". ApJ 322 (1987) 412–449. [ADS].

A. Boccaletti, P. Baudoz, J. Baudrand, J. M. Reess, and D. Rouan. "Imaging exoplanets with the coronagraph of JWST/MIRI". Advances in Space Research 36 (2005) 1099–1106. [ADS].

K. J. Borkowski and E. Dwek. "The Fragmentation and Vaporization of Dust in Grain-Grain Collisions". ApJ 454 (1995) 254–+. [ADS].

F. Boulanger, J. P. Maillard, P. Appleton, E. Falgarone, G. Lagache, B. Schulz, B. P. Wakker, A. Bressan, et al. "The molecular hydrogen explorer H2EX". Experimental Astronomy 23 (2009) 277–302. 0805.3109, [ADS].

A. Boulares and D. P. Cox. "Galactic hydrostatic equilibrium with magnetic tension and cosmic-ray diffusion". ApJ 365 (1990) 544–558. [ADS].

J. Braine, P.-A. Duc, U. Lisenfeld, V. Charmandaris, O. Vallejo, S. Leon, and E. Brinks. "Abundant molecular gas in tidal dwarf galaxies: On-going galaxy formation". A&A 378 (2001) 51–69. arXiv:astro-ph/0108513, [ADS].

B. R. Brandl, J. Bernard-Salas, H. W. W. Spoon, D. Devost, G. C. Sloan, S. Guilles, Y. Wu, J. R. Houck, et al. "The Mid-Infrared Properties of Starburst Galaxies from Spitzer-IRS Spectroscopy". ApJ 653 (2006) 1129–1144. arXiv:astro-ph/0609024, [ADS].

B. H. Bransden and C. Joachin. *Physics of atoms and molecules* (Longman, 1983).

P. N. Brown, G. D. Byrne, and A. C. Hindmarsh. "VODE: A Variable-Coefficient ODE Solver". SIAM J Sci and Stat Comput 10 (1989) 1038–1051.

E. M. Burbidge and G. R. Burbidge. "A Further Investigation of Stephan's Quintet." ApJ 134 (1961a) 244–+. [ADS].

E. M. Burbidge and G. R. Burbidge. "Recent investigations of groups and clusters of galaxies." AJ 66 (1961b) 541–550. [ADS].

D. Calzetti, R. C. Kennicutt, C. W. Engelbracht, C. Leitherer, B. T. Draine, L. Kewley, J. Moustakas, M. Sosey, et al. "The Calibration of Mid-Infrared Star Formation Rate Indicators". ApJ 666 (2007) 870–895. 0705.3377, [ADS].

J. J. Carroll, A. Frank, E. G. Blackman, A. J. Cunningham, and A. C. Quillen. "Outflow-Driven Turbulence in Molecular Clouds". ApJ 695 (2009) 1376–1381. 0805.4645, [ADS].

G. R. Carruthers. "Rocket Observation of Interstellar Molecular Hydrogen". ApJL 161 (1970) L81+. [ADS].

P. Caselli and P. C. Myers. "The Line Width–Size Relation in Massive Cloud Cores". ApJ 446 (1995) 665–+. [ADS].

J. Cernicharo, A. M. Heras, A. G. G. M. Tielens, J. R. Pardo, F. Herpin, M. Guélin, and L. B. F. M. Waters. "Infrared Space Observatory's Discovery of C4H2, C6H2, and Benzene in CRL 618". ApJL 546 (2001) L123–L126. [ADS].

S. Chandrasekhar. *Hydrodynamic and hydromagnetic stability* (1961). [ADS].

D. F. Chernoff. "Magnetohydrodynamic shocks in molecular clouds". ApJ 312 (1987) 143–169. [ADS].

R. A. Chevalier and A. W. Clegg. "Wind from a starburst galaxy nucleus". Nature 317 (1985) 44–+. [ADS].

M. E. Cluver, P. N. Appleton, F. Boulanger, P. Guillard, P. Ogle, P.-A. Duc, N. Lu, J. Rasmussen, et al. "Powerful H2 line-cooling in Stephan's Quintet : I- Mapping the dominant cooling pathways in group-wide shocks". ApJ , accepted (2009).

F. Combes and D. Pfenniger. "Perspectives for detecting cold H2 in outer galactic disks." A&A 327 (1997) 453–466. arXiv:astro-ph/9707217, [ADS].

M. Compiègne, A. Abergel, L. Verstraete, and E. Habart. "Dust processing in photodissociation regions. Mid-IR emission modelling". A&A 491 (2008) 797–807. 0809.5026, [ADS].

Compiègne, M. *Etude de l'évolution des poussières interstellaires dans les régions dominées par le rayonnement*. Ph.D. thesis, IAS, Université Paris Sud 11 (2007).

C. J. Conselice, J. S. Gallagher, III, and R. F. G. Wyse. "On the Nature of the NGC 1275 System". AJ 122 (2001) 2281–2300. `arXiv:astro-ph/0108019`, [ADS].

L. L. Cowie and C. F. McKee. "The evaporation of spherical clouds in a hot gas. I - Classical and saturated mass loss rates". ApJ 211 (1977) 135–146. [ADS].

N. L. J. Cox and M. Spaans. "The effects of metallicity, radiation field and dust extinction on the charge state of PAHs in diffuse clouds: implications for the DIB carrier". A&A 451 (2006) 973–980. [ADS].

T. E. Cravens, G. A. Victor, and A. Dalgarno. "The absorption of energetic electrons by molecular hydrogen gas". Planet. Space Sci.23 (1975) 1059–1070. [ADS].

D. J. Croton, V. Springel, S. D. M. White, G. De Lucia, C. S. Frenk, L. Gao, A. Jenkins, G. Kauffmann, et al. "The many lives of active galactic nuclei: cooling flows, black holes and the luminosities and colours of galaxies". MNRAS365 (2006) 11–28. `arXiv:astro-ph/0508046`, [ADS].

R. M. Crutcher. "Magnetic Fields in Molecular Clouds: Observations Confront Theory". ApJ 520 (1999) 706–713. [ADS].

I. Dabrowski. "The Lyman and Werner bands of H2". Canadian Journal of Physics 62 (1984) 1639–1664. [ADS].

I. Dabrowski and G. Herzberg. "The Lyman and Werner bands of H_2". Can J Phys 62 (1984) 1639.

A. Dalgarno, J. H. Black, and J. C. Weisheit. "Ortho-Para Transitions in H2 and the Fractionation of HD". Astrophys. Lett.14 (1973) 77–+. [ADS].

A. Dalgarno, M. Yan, and W. Liu. "Electron Energy Deposition in a Gas Mixture of Atomic and Molecular Hydrogen and Helium". ApJS 125 (1999) 237–256. [ADS].

T. M. Dame, D. Hartmann, and P. Thaddeus. "The Milky Way in Molecular Clouds: A New Complete CO Survey". ApJ 547 (2001) 792–813. `arXiv:astro-ph/0009217`, [ADS].

M. A. de Avillez and D. Breitschwerdt. "Global dynamical evolution of the ISM in star forming galaxies. I. High resolution 3D simulations: Effect of the magnetic field". A&A 436 (2005) 585–600. `arXiv:astro-ph/0502327`, [ADS].

G. E. de Messières, R. W. O'Connell, B. R. McNamara, M. Donahue, P. E. J. Nulsen, G. M. Voit, and M. W. Wise. "Spitzer Mid-Infrared Spectra of Cool-Core Galaxy Clusters". ArXiv e-prints (2009). `0908.3445`, [ADS].

A. Dekel and J. Silk. "The origin of dwarf galaxies, cold dark matter, and biased galaxy formation". ApJ 303 (1986) 39–55. [ADS].

F.-X. Désert, F. Boulanger, and J. L. Puget. "Interstellar dust models for extinction and emission". A&A 237 (1990) 215–236. [ADS].

S. Dib, E. Bell, and A. Burkert. "The Supernova Rate-Velocity Dispersion Relation in the Interstellar Medium". ApJ 638 (2006) 797–810. `arXiv:astro-ph/0506339`, [ADS].

S. Dib and A. Burkert. "Thermal Instability in the Interstellar Medium and Structure Formation". In F. Combes and D. Barret, eds., *SF2A-2002: Semaine de l'Astrophysique Francaise*, 25–+ (2002). [ADS].

R. L. Dickman, R. L. Snell, and F. P. Schloerb. "Carbon monoxide as an extragalactic mass tracer". ApJ 309 (1986) 326–330. [ADS].

C. Dominik and A. G. G. M. Tielens. "The Physics of Dust Coagulation and the Structure of Dust Aggregates in Space". ApJ 480 (1997) 647. [ADS].

M. A. Dopita and R. S. Sutherland. "Spectral Signatures of Fast Shocks. II. Optical Diagnostic Diagrams". ApJ 455 (1995) 468–+. [ADS].

M. A. Dopita and R. S. Sutherland. "Spectral Signatures of Fast Shocks. I. Low-Density Model Grid". ApJS 102 (1996) 161–+. [ADS].

M. A. Dopita and R. S. Sutherland. *Astrophysics of the diffuse universe* (Astrophysics of the diffuse universe, Berlin, New York: Springer, 2003. Astronomy and astrophysics library, ISBN 3540433627, 2003). [ADS].

J. E. Dove and M. E. Mandy. "The rate of dissociation of molecular hydrogen by hydrogen atoms at very low densities". ApJL 311 (1986) L93–L96. [ADS].

B. T. Draine. "Interstellar shock waves with magnetic precursors". ApJ 241 (1980) 1021–1038. [ADS].

B. T. Draine. "Interstellar Dust Grains". ARAA 41 (2003) 241–289. astro-ph/0304489, [ADS].

B. T. Draine and H. M. Lee. "Optical properties of interstellar graphite and silicate grains". ApJ 285 (1984) 89–108. [ADS].

B. T. Draine and C. F. McKee. "Theory of interstellar shocks". ARAA 31 (1993) 373–432. [ADS].

B. T. Draine and E. E. Salpeter. "Destruction mechanisms for interstellar dust". ApJ 231 (1979a) 438–455. [ADS].

B. T. Draine and E. E. Salpeter. "On the physics of dust grains in hot gas". ApJ 231 (1979b) 77–94. [ADS].

W. W. Duley and D. A. Williams. "The infrared spectrum of interstellar dust - Surface functional groups on carbon". MNRAS196 (1981) 269–274. [ADS].

W. W. Duley and D. A. Williams. *Interstellar chemistry* (Academic Press, London, 1984). [ADS].

F. Durret. "Nuclear and extranuclear ionized gas in nine Seyfert 2 galaxies". A&AS105 (1994) 57–66. [ADS].

E. Dwek. "The infrared diagnostic of a dusty plasma with applications to supernova remnants". ApJ 322 (1987) 812–821. [ADS].

E. Dwek and R. K. Smith. "Energy Deposition and Photoelectric Emission from the Interaction of 10 eV to 1 MeV Photons with Interstellar Dust Particles". ApJ 459 (1996) 686–+. [ADS].

E. Egami, G. H. Rieke, D. Fadda, and D. C. Hines. "A Large Mass of H2 in the Brightest Cluster Galaxy in Zwicky 3146". ApJL 652 (2006) L21–L24. arXiv:astro-ph/0610164, [ADS].

B. G. Elmegreen and J. Scalo. "Interstellar Turbulence I: Observations and Processes". ARAA 42 (2004) 211–273. arXiv:astro-ph/0404451, [ADS].

C. W. Engelbracht, P. Kundurthy, K. D. Gordon, G. H. Rieke, R. C. Kennicutt, J.-D. T. Smith, M. W. Regan, D. Makovoz, et al. "Extended Mid-Infrared Aromatic Feature Emission in M82". ApJL 642 (2006) L127–L132. arXiv:astro-ph/0603551, [ADS].

E. Falgarone. "Structure of Molecular Clouds". EAS Publications Series 4 (2002) 87–87. [ADS].

D. Farrah, C. J. Lonsdale, D. W. Weedman, H. W. W. Spoon, M. Rowan-Robinson, M. Polletta, S. Oliver, J. R. Houck, et al. "The Nature of Star Formation in Distant Ultraluminous Infrared Galaxies Selected in a Remarkably Narrow Redshift Range". ApJ 677 (2008) 957–969. 0801.1842, [ADS].

G. J. Ferland, A. C. Fabian, N. A. Hatch, R. M. Johnstone, R. L. Porter, P. A. M. van Hoof, and R. J. R. Williams. "The origin of molecular hydrogen emission in cooling-flow filaments". MNRAS386 (2008) L72–L76. arXiv:0802.2535, [ADS].

G. J. Ferland, K. T. Korista, D. A. Verner, J. W. Ferguson, J. B. Kingdon, and E. M. Verner. "CLOUDY 90: Numerical Simulation of Plasmas and Their Spectra". PASP 110 (1998) 761–778. [ADS].

K. M. Ferrière. "The interstellar environment of our galaxy". Reviews of Modern Physics 73 (2001) 1031–1066. arXiv:astro-ph/0106359, [ADS].

R. A. Fiedler and T. C. Mouschovias. "Ambipolar Diffusion and Star Formation: Formation and Contraction of Axisymmetric Cloud Cores. II. Results". ApJ 415 (1993) 680–+. [ADS].

G. B. Field. "Thermal Instability". ApJ 142 (1965) 531–+. [ADS].

G. B. Field, D. W. Goldsmith, and H. J. Habing. "Cosmic-Ray Heating of the Interstellar Gas". ApJL 155 (1969) L149+. [ADS].

E. L. Fitzpatrick and D. Massa. "An analysis of the shapes of ultraviolet extinction curves. III - an atlas of ultraviolet extinction curves". ApJS 72 (1990) 163–189. [ADS].

D. J. Fixsen, C. L. Bennett, and J. C. Mather. "COBE Far Infrared Absolute Spectrophotometer Observations of Galactic Lines". ApJ 526 (1999) 207–214. [ADS].

Flagey, N. *Propriétés et évolution des poussières du milieu interstellaire*. Ph.D. thesis, IAS, Université Paris Sud 11 (2007).

D. R. Flower. "The rotational excitation of H2 by H2". MNRAS297 (1998) 334–336. [ADS].

D. R. Flower. *Molecular collisions in the interstellar medium* (Cambridge University Press, 2007). [ADS].

D. R. Flower, J. Le Bourlot, G. Pineau des Forêts, and S. Cabrit. "The contributions of J-type shocks to the H2 emission from molecular outflow sources". MNRAS341 (2003) 70–80. [ADS].

D. R. Flower and G. Pineau des Forêts. "The influence of grains on the propagation and structure of C-type shock waves in interstellar molecular clouds". MNRAS343 (2003) 390–400. [ADS].

D. R. Flower, G. Pineau des Forets, D. Field, and P. W. May. "The structure of MHD shocks in molecular outflows: grain sputtering and SiO formation". MNRAS280 (1996) 447–457. [ADS].

D. R. Flower, G. Pineau des Forets, and T. W. Hartquist. "Theoretical studies of interstellar molecular shocks. I - General formulation and effects of the ion-molecule chemistry". MNRAS216 (1985) 775–794. [ADS].

D. R. Flower, G. Pineau-Des-Forets, and T. W. Hartquist. "Theoretical studies of interstellar molecular shocks. II - Molecular hydrogen cooling and rotational level populations". MNRAS218 (1986) 729–741. [ADS].

D. R. Flower, G. Pineau Des Forêts, and C. M. Walmsley. "The importance of the ortho:para H2 ratio for the deuteration of molecules during pre-protostellar collapse". A&A 449 (2006) 621–629. arXiv:astro-ph/0601429, [ADS].

D. R. Flower and G. D. Watt. "On the ortho-H2/para-H2 ratio in molecular clouds". MNRAS209 (1984) 25–31. [ADS].

P. C. Fragile, S. D. Murray, P. Anninos, and W. van Breugel. "Radiative Shock-induced Collapse of Intergalactic Clouds". ApJ 604 (2004) 74–87. `arXiv:astro-ph/0311298`, [ADS].

M. Fukugita and P. J. E. Peebles. "The Cosmic Energy Inventory". ApJ 616 (2004) 643–668. `arXiv:astro-ph/0406095`, [ADS].

S. C. Gallagher, J. C. Charlton, S. D. Hunsberger, D. Zaritsky, and B. C. Whitmore. "Hubble Space Telescope Images of Stephan's Quintet: Star Cluster Formation in a Compact Group Environment". AJ 122 (2001) 163–181. `arXiv:astro-ph/0104005`, [ADS].

D. Galli and F. Palla. "The chemistry of the early Universe". A&A 335 (1998) 403–420. `astro-ph/9803315`, [ADS].

Y. Gao and C. Xu. "CO in Stephan's Quintet: First Evidence of Molecular Gas in the Intragroup Starburst". ApJL 542 (2000) L83–L87. `arXiv:astro-ph/0008112`, [ADS].

J. P. Gardner, J. C. Mather, M. Clampin, R. Doyon, M. A. Greenhouse, H. B. Hammel, J. B. Hutchings, P. Jakobsen, et al. "The James Webb Space Telescope". Space Science Reviews 123 (2006) 485–606. `arXiv:astro-ph/0606175`, [ADS].

T. N. Gautier, III, U. Fink, H. P. Larson, and R. R. Treffers. "Detection of molecular hydrogen quadrupole emission in the Orion Nebula". ApJL 207 (1976) L129–L133. [ADS].

D. Gerlich. "Ortho-para transitions in reactive H+ + H2 collisions". J. Chem. Phys.92 (1990) 2377–2388. [ADS].

T. Giannini, C. McCoey, A. Caratti o Garatti, B. Nisini, D. Lorenzetti, and D. R. Flower. "On the excitation of the infrared knots along protostellar jets". A&A 419 (2004) 999–1014. `arXiv:astro-ph/0402395`, [ADS].

T. Giannini, C. McCoey, B. Nisini, S. Cabrit, A. Caratti o Garatti, L. Calzoletti, and D. R. Flower. "Molecular line emission in HH54: a coherent view from near to far infrared". A&A 459 (2006) 821–835. `arXiv:astro-ph/0607375`, [ADS].

O. Gnat and A. Sternberg. "Time-dependent Ionization in Radiatively Cooling Gas". ApJS 168 (2007) 213–230. `astro-ph/0608181`, [ADS].

Gonzalez Garcia, M. *Gas phase and icy H2O in photon-dominates regions*. Ph.D. thesis, Observatoire de Paris-Meudon; IAS, UniversitÃl' Paris Sud 11 (2009).

P. Goudfrooij and T. de Jong. "Interstellar matter in Shapley-Ames elliptical galaxies. IV. A diffusely distributed component of dust and its effect on colour gradients." A&A 298 (1995) 784–+. `arXiv:astro-ph/9504011`, [ADS].

R. J. Gould and E. E. Salpeter. "The Interstellar Abundance of the Hydrogen Molecule. I. Basic Processes." ApJ 138 (1963) 393–+. [ADS].

G. Gregori, F. Miniati, D. Ryu, and T. W. Jones. "Enhanced Cloud Disruption by Magnetic Field Interaction". ApJL 527 (1999) L113–L116. `arXiv:astro-ph/9910357`, [ADS].

T. R. Greve, F. Bertoldi, I. Smail, R. Neri, S. C. Chapman, A. W. Blain, R. J. Ivison, R. Genzel, et al. "An interferometric CO survey of luminous submillimetre galaxies". MNRAS359 (2005) 1165–1183. `arXiv:astro-ph/0503055`, [ADS].

P. Guillard, F. Boulanger, M. E. Cluver, , P. N. Appleton, and G. Pineau des Forets. "Observations and modeling of dust emission from the H2-bright galaxy-wide shock in Stephan's Quintet". A&A , submitted (2009a).

P. Guillard, F. Boulanger, P. A. Duc, U. Lisenfeld, P. N. Appleton, and G. Pineau des Forets. "Energetics of the CO gas in the Stephan's Quintet galaxy-wide shock". A&A in prep (2009b).

P. Guillard, F. Boulanger, G. Pineau Des Forêts, and P. N. Appleton. "H2 formation and excitation in the Stephan's Quintet galaxy-wide collision". A&A 502 (2009c) 515–528. `0904.4239`, [ADS].

V. Guillet, A. P. Jones, and G. Pineau Des Forêts. "Shocks in dense clouds. II. Dust destruction and SiO formation in J shocks". A&A 497 (2009) 145–153. [ADS].

V. Guillet, G. Pineau Des Forêts, and A. P. Jones. "Shocks in dense clouds. I. Dust dynamics". A&A 476 (2007) 263–277. [ADS].

Guillet, V. *Dust evolution in interstellar shocks*. Ph.D. thesis, IAS, Université Paris Sud 11 (2008), [ADS].

A. Gusdorf. *Molecular emission in regions of star formation*. Ph.D. thesis, IAS, UniversitÃľ Paris Sud 11; Physics department, Durham University (2008).

A. Gusdorf, S. Cabrit, D. R. Flower, and G. Pineau Des Forêts. "SiO line emission from C-type shock waves: interstellar jets and outflows". A&A 482 (2008) 809–829. `0803.2791`, [ADS].

C. M. Gutiérrez, M. López-Corredoira, F. Prada, and M. C. Eliche. "New Light and Shadows on Stephan's Quintet". ApJ 579 (2002) 592–599. `arXiv:astro-ph/0202521`, [ADS].

E. Habart. *Couplage entre le gaz et les grains dans le milieu interstellaire*. Ph.D. thesis, IAS, UniversitÃľ Paris Sud 11 (2001).

E. Habart, F. Boulanger, L. Verstraete, G. Pineau des Forêts, E. Falgarone, and A. Abergel. "H2 infrared line emission across the bright side of the rho Ophiuchi main cloud". A&A 397 (2003) 623–634. [ADS].

E. Habart, F. Boulanger, L. Verstraete, C. M. Walmsley, and G. Pineau des Forêts. "Some empirical estimates of the H2 formation rate in photon-dominated regions". A&A 414 (2004) 531–544. `astro-ph/0311040`, [ADS].

P. Hartigan. "Shock Waves in Outflows from Young Stars". Ap&SS287 (2003) 111–122. [ADS].

J. Hartmann. "Investigations on the spectrum and orbit of delta Orionis." ApJ 19 (1904) 268–286. [ADS].

T. G. Hawarden, G. S. Wright, S. K. Ramsay-Howat, M. Y. Takamiya, and S. D. Ryder. "Molecular Hydrogen Emission (MHE) Galaxies: a New (Near Infrared) Spectroscopic Class". In M. Rosada, L. Binette, and L. Arias, eds., *Galaxies: the Third Dimension*, vol. 282 of *Astronomical Society of the Pacific Conference Series*, 246–+ (2002). [ADS].

T. M. Heckman, L. Armus, and G. K. Miley. "On the nature and implications of starburst-driven galactic superwinds". ApJS 74 (1990) 833–868. [ADS].

T. M. Heckman, S. A. Baum, W. J. M. van Breugel, and P. McCarthy. "Dynamical, physical, and chemical properties of emission-line nebulae in cooling flows". ApJ 338 (1989) 48–77. [ADS].

T. M. Heckman, M. D. Lehnert, D. K. Strickland, and L. Armus. "Absorption-Line Probes of Gas and Dust in Galactic Superwinds". ApJS 129 (2000) 493–516. `arXiv:astro-ph/0002526`, [ADS].

C. Heiles and T. H. Troland. "The Millennium Arecibo 21 Centimeter Absorption-Line Survey. IV. Statistics of Magnetic Field, Column Density, and Turbulence". ApJ 624 (2005) 773–793. `arXiv:astro-ph/0501482`, [ADS].

P. Hennebelle, R. Banerjee, E. Vázquez-Semadeni, R. S. Klessen, and E. Audit. "From the warm magnetized atomic medium to molecular clouds". A&A 486 (2008) L43–L46. `0805.1366`, [ADS].

P. Hennebelle and M. Pérault. "Dynamical condensation in a thermally bistable flow. Application to interstellar cirrus". A&A 351 (1999) 309–322. [ADS].

E. Herbst and W. Klemperer. "The Formation and Depletion of Molecules in Dense Interstellar Clouds". ApJ 185 (1973) 505–534. [ADS].

J. W. Hewitt, J. Rho, M. Andersen, and W. T. Reach. "Spitzer Observations of Molecular Hydrogen in Interacting Supernova Remnants". ApJ 694 (2009) 1266–1280. `0901.1622`, [ADS].

P. Hickson. "Systematic properties of compact groups of galaxies". ApJ 255 (1982) 382–391. [ADS].

S. J. U. Higdon, L. Armus, J. L. Higdon, B. T. Soifer, and H. W. W. Spoon. "A Spitzer Space Telescope Infrared Spectrograph Survey of Warm Molecular Hydrogen in Ultraluminous Infrared Galaxies". ApJ 648 (2006) 323–339. `arXiv:astro-ph/0605359`, [ADS].

D. Hollenbach and C. F. McKee. "Molecule formation and infrared emission in fast interstellar shocks. I Physical processes". ApJS 41 (1979) 555–592. [ADS].

D. Hollenbach and C. F. McKee. "Molecule formation and infrared emission in fast interstellar shocks. III - Results for J shocks in molecular clouds". ApJ 342 (1989) 306–336. [ADS].

D. Hollenbach and E. E. Salpeter. "Surface Recombination of Hydrogen Molecules". ApJ 163 (1971) 155–+. [ADS].

D. J. Hollenbach and A. G. G. M. Tielens. "Dense Photodissociation Regions (PDRs)". ARAA 35 (1997) 179–216. [ADS].

J. Holt, C. N. Tadhunter, and R. Morganti. "Fast outflows in compact radio sources: evidence for AGN-induced feedback in the early stages of radio source evolution". MNRAS387 (2008) 639–659. `0802.1444`, [ADS].

P. F. Hopkins, L. Hernquist, T. J. Cox, B. Robertson, and V. Springel. "Determining the Properties and Evolution of Red Galaxies from the Quasar Luminosity Function". ApJS 163 (2006) 50–79. `arXiv:astro-ph/0508167`, [ADS].

L. Hornekær, A. Baurichter, V. V. Petrunin, D. Field, and A. C. Luntz. "Importance of Surface Morphology in Interstellar H2 Formation". Science 302 (2003) 1943–1946. [ADS].

J. P. Huchra, W. F. Wyatt, and M. Davis. "New bright Seyfert Galaxies". AJ 87 (1982) 1628–1633. [ADS].

M. L. Humason, N. U. Mayall, and A. R. Sandage. "Redshifts and magnitudes of extragalactic nebulae." AJ 61 (1956) 97–162. [ADS].

T. A. Jacobs, R. R. Giedt, and N. Cohen. "Kinetics of Hydrogen Halides in Shock Waves. II. A New Measurement of the Hydrogen Dissociation Rate". J. Chem. Phys.47 (1967) 54–57. [ADS].

C. J. Jog and P. M. Solomon. "A triggering mechanism for enhanced star formation in colliding galaxies". ApJ 387 (1992) 152–161. [ADS].

R. M. Johnstone, N. A. Hatch, G. J. Ferland, A. C. Fabian, C. S. Crawford, and R. J. Wilman. "Discovery of atomic and molecular mid-infrared emission lines in off-nuclear regions of NGC 1275 and NGC4696 with the Spitzer Space Telescope". MNRAS382 (2007) 1246–1260. arXiv:astro-ph/0702431, [ADS].

A. Jones and A. Tielens. *The Cold Universe, XIIIth Moriond Astrophysics Meeting* (Gif-sur Yvette: Éditions Frontières, 1994).

A. P. Jones. "Dust Destruction Processes". In A. N. Witt, G. C. Clayton, and B. T. Draine, eds., *Astrophysics of Dust*, vol. 309 of *Astronomical Society of the Pacific Conference Series*, 347–+ (2004). [ADS].

R. D. Joseph, R. Wade, and G. S. Wright. "Detection of molecular hydrogen in two merging galaxies". Nature 311 (1984) 132–+. [ADS].

M. Jura. "Interstellar clouds containing optically thin H2". ApJ 197 (1975) 575–580. [ADS].

H. Kaneda, T. Onaka, I. Sakon, T. Kitayama, Y. Okada, and T. Suzuki. "Properties of Polycyclic Aromatic Hydrocarbons in Local Elliptical Galaxies Revealed by the Infrared Spectrograph on Spitzer". ApJ 684 (2008) 270–281. 0805.3257, [ADS].

S.-H. Kim, P. G. Martin, and P. D. Hendry. "The size distribution of interstellar dust particles as determined from extinction". ApJ 422 (1994) 164–175. [ADS].

R. I. Klein, C. F. McKee, and P. Colella. "On the hydrodynamic interaction of shock waves with interstellar clouds. 1: Nonradiative shocks in small clouds". ApJ 420 (1994a) 213–236. [ADS].

U. Klein, K. H. Mack, R. Strom, R. Wielebinski, and U. Achatz. "A High Frequency Radio Continuum Investigation of Giant Radio Galaxies - Part One - Observations of Six Objects at 2.8-CENTIMETERS Wavelength". A&A 283 (1994b) 729–+. [ADS].

S. Komossa, V. Burwitz, G. Hasinger, P. Predehl, J. S. Kaastra, and Y. Ikebe. "Discovery of a Binary Active Galactic Nucleus in the Ultraluminous Infrared Galaxy NGC 6240 Using Chandra". ApJL 582 (2003) L15–L19. arXiv:astro-ph/0212099, [ADS].

P. Kornreich and J. Scalo. "The Galactic Shock Pump: A Source of Supersonic Internal Motions in the Cool Interstellar Medium". ApJ 531 (2000) 366–383. [ADS].

L. E. Kristensen. *Observational analysis of the physical conditions in galactic and extragalactic active star forming regions*. Ph.D. thesis, LERMA, Observatoire de Paris-Meudon; LAMAP, Université de Cergy-Pontoise (2007), [ADS].

L. E. Kristensen, T. L. Ravkilde, D. Field, J. L. Lemaire, and G. Pineau Des Forêts. "Excitation conditions in the Orion molecular cloud obtained from observations of ortho- and para-lines of H {2}". A&A 469 (2007) 561–574. [ADS].

G. Lagache, J.-L. Puget, and H. Dole. "Dusty Infrared Galaxies: Sources of the Cosmic Infrared Background". ARAA 43 (2005) 727–768. arXiv:astro-ph/0507298, [ADS].

L. D. Landau and E. M. Lifshitz. *Fluid mechanics* (1959). [ADS].

R. B. Larson. "Turbulence and star formation in molecular clouds". MNRAS194 (1981) 809–826. [ADS].

J. Le Bourlot, G. Pineau des Forêts, and D. R. Flower. "The cooling of astrophysical media by H_2". MN-RAS305 (1999) 802–810. [ADS].

J. Le Bourlot, G. Pineau des Forêts, D. R. Flower, and S. Cabrit. "New determinations of the critical velocities of C-type shock waves in dense molecular clouds: application to the outflow source in Orion". MNRAS332 (2002) 985–993. [ADS].

F. Le Petit, C. Nehmé, J. Le Bourlot, and E. Roueff. "A Model for Atomic and Molecular Interstellar Gas: The Meudon PDR Code". ApJS 164 (2006) 506–529. arXiv:astro-ph/0602150, [ADS].

H. M. Lee, H. Kang, and D. Ryu. "Supersonic Collisions between Two Gas Streams". ApJ 464 (1996) 131–+. arXiv:astro-ph/9512101, [ADS].

A. Léger and J. L. Puget. "Identification of the 'unidentified' IR emission features of interstellar dust?" A&A 137 (1984) L5–L8. [ADS].

M. D. Lehnert, N. P. H. Nesvadba, L. L. Tiran, P. D. Matteo, W. van Driel, L. S. Douglas, L. Chemin, and F. Bournaud. "Physical Conditions in the Interstellar Medium of Intensely Star-Forming Galaxies at Redshift~2". ApJ 699 (2009) 1660–1678. 0902.2784, [ADS].

S. Leon, F. Combes, and T. K. Menon. "Molecular gas in galaxies of Hickson compact groups". A&A 330 (1998) 37–56. arXiv:astro-ph/9709121, [ADS].

S. Lepp and R. McCray. "X-ray sources in molecular clouds". ApJ 269 (1983) 560–567. [ADS].

J. Lequeux. *The interstellar medium* (The interstellar medium, Translation from the French language edition of: Le Milieu Interstellaire by James Lequeux, EDP Sciences, 2003 Edited by J. Lequeux. Astronomy and astrophysics library, Berlin: Springer, 2005, 2005). [ADS].

A. Li and B. T. Draine. "On Ultrasmall Silicate Grains in the Diffuse Interstellar Medium". ApJL 550 (2001) L213–L217. arXiv:astro-ph/0012147, [ADS].

D. N. Limber and W. G. Mathews. "The Dynamical Stability of Stephan's Quintet." ApJ 132 (1960) 286–+. [ADS].

U. Lisenfeld, J. Braine, P.-A. Duc, E. Brinks, V. Charmandaris, and S. Leon. "Molecular and ionized gas in the tidal tail in Stephan's Quintet". A&A 426 (2004) 471–479. arXiv:astro-ph/0407473, [ADS].

U. Lisenfeld, J. Braine, P.-A. Duc, S. Leon, V. Charmandaris, and E. Brinks. "Abundant molecular gas in the intergalactic medium of Stephan's Quintet". A&A 394 (2002) 823–833. arXiv:astro-ph/0208494, [ADS].

X. Liu and D. E. Shemansky. "Ionization of Molecular Hydrogen". ApJ 614 (2004) 1132–1142. [ADS].

N. P. F. Lorente, A. C. H. Glasse, G. S. Wright, and M. García-Marín. "Specsim: the MIRI medium resolution spectrometer simulator". In *Society of Photo-Optical Instrumentation Engineers (SPIE) Conference Series*, vol. 6274 (2006). [ADS].

P. J. Love, E. J. Beuville, E. Corrales, J. J. Drab, A. W. Hoffman, R. S. Holcombe, and N. A. Lum. "1024 x 1024 Si as IBC detector arrays for MID-IR astronomy". In *High Energy, Optical, and Infrared Detectors for Astronomy II. Edited by Dorn, David A.; Holland, Andrew D.. Proceedings of the SPIE, Volume 6276, pp. 62761Y (2006).*, vol. 6276 (2006). [ADS].

P. J. Love, A. W. Hoffman, N. A. Lum, K. J. Ando, J. Rosbeck, W. D. Ritchie, N. J. Therrien, R. S. Holcombe, et al. "1024 x 1024 Si:As IBC detector arrays for JWST MIRI". In T. J. Grycewicz and C. J. Marshall, eds., *Focal Plane Arrays for Space Telescopes II. Edited by Grycewicz, Thomas J.; Marshall, Cheryl J. Proceedings of the SPIE, Volume 5902, pp. 58-66 (2005).*, vol. 5902, 58–66 (2005). [ADS].

D. Lutz, E. Sturm, R. Genzel, H. W. W. Spoon, A. F. M. Moorwood, H. Netzer, and A. Sternberg. "ISO spectroscopy of star formation and active nuclei in the luminous infrared galaxy <ASTROBJ>NGC 6240</ASTROBJ>". A&A 409 (2003) 867–878. arXiv:astro-ph/0307552, [ADS].

M.-M. Mac Low, D. S. Balsara, J. Kim, and M. A. de Avillez. "The Distribution of Pressures in a Supernova-driven Interstellar Medium. I. Magnetized Medium". ApJ 626 (2005) 864–876. arXiv:astro-ph/0410734, [ADS].

M.-M. Mac Low, C. F. McKee, R. I. Klein, J. M. Stone, and M. L. Norman. "Shock interactions with magnetized interstellar clouds. 1: Steady shocks hitting nonradiative clouds". ApJ 433 (1994) 757–777. [ADS].

K.-H. Mack, U. Klein, C. P. O'Dea, and A. G. Willis. "Multi-frequency radio continuum mapping of giant radio galaxies". A&AS123 (1997) 423–444. [ADS].

P. R. Maloney, D. J. Hollenbach, and A. G. G. M. Tielens. "X-Ray–irradiated Molecular Gas. I. Physical Processes and General Results". ApJ 466 (1996) 561–+. [ADS].

G. Manicò, G. Ragunì, V. Pirronello, J. E. Roser, and G. Vidali. "Laboratory Measurements of Molecular Hydrogen Formation on Amorphous Water Ice". ApJL 548 (2001) L253–L256. [ADS].

S. Maret, E. A. Bergin, D. A. Neufeld, J. D. Green, D. M. Watson, M. O. Harwit, L. E. Kristensen, G. J. Melnick, et al. "Spitzer Mapping of Molecular Hydrogen Pure Rotational Lines in NGC 1333: A Detailed Study of Feedback in Star Formation". ApJ 698 (2009) 1244–1260. 0904.0603, [ADS].

M. Martig, F. Bournaud, R. Teyssier, and A. Dekel. "Morphological quenching of star formation: making early-type galaxies red". ArXiv e-prints (2009). 0905.4669, [ADS].

N. L. Martín-Hernández, E. Peeters, C. Morisset, A. G. G. M. Tielens, P. Cox, P. R. Roelfsema, J.-P. Baluteau, D. Schaerer, et al. "ISO spectroscopy of compact H II regions in the Galaxy. II. Ionization and elemental abundances". A&A 381 (2002) 606–627. astro-ph/0110653, [ADS].

J. S. Mathis, W. Rumpl, and K. H. Nordsieck. "The size distribution of interstellar grains". ApJ 217 (1977) 425–433. [ADS].

C. D. Matzner. "Protostellar Outflow-driven Turbulence". ApJ 659 (2007) 1394–1403. arXiv:astro-ph/0701022, [ADS].

C. E. Max, G. Canalizo, B. A. Macintosh, L. Raschke, D. Whysong, R. Antonucci, and G. Schneider. "The Core of NGC 6240 from Keck Adaptive Optics and Hubble Space Telescope NICMOS Observations". ApJ 621 (2005) 738–749. arXiv:astro-ph/0411590, [ADS].

P. W. May, G. Pineau des Forêts, D. R. Flower, D. Field, N. L. Allan, and J. A. Purton. "Sputtering of grains in C-type shocks". MNRAS318 (2000) 809–816. [ADS].

J. F. McCarthy, W. J. Forrest, D. A. Briotta, Jr., and J. R. Houck. "The galactic center - 16-30 micron observations and the 18 micron extinction". ApJ 242 (1980) 965–975. [ADS].

C. F. McKee. "Interstellar Dust". In L. Allamandola and A. Tielens, eds., *Interstellar Dust*, 431 (1989).

C. F. McKee and L. L. Cowie. "The interaction between the blast wave of a supernova remnant and interstellar clouds". ApJ 195 (1975) 715–725. [ADS].

C. F. McKee and D. J. Hollenbach. "Interstellar shock waves". ARAA 18 (1980) 219–262. [ADS].

C. F. McKee and J. P. Ostriker. "A theory of the interstellar medium - Three components regulated by supernova explosions in an inhomogeneous substrate". ApJ 218 (1977) 148.

B. R. McNamara and P. E. J. Nulsen. "Heating Hot Atmospheres with Active Galactic Nuclei". ARAA 45 (2007) 117–175. 0709.2152, [ADS].

G. Mellema, J. D. Kurk, and H. J. A. Röttgering. "Evolution of clouds in radio galaxy cocoons". A&A 395 (2002) L13–L16. arXiv:astro-ph/0209601, [ADS].

G. Mie. "BeitrÃd'ge zur Optik trÃijber Medien, speziell kolloidaler MetallÃűsungen". Ann Phys Leipzig 25 (1908) 377âĂŞ445.

M. S. Miesch and E. G. Zweibel. "Shock propagation and the generation of magnetohydrodynamic wave fields in inhomogeneous molecular clouds". ApJ 432 (1994) 622–640. [ADS].

M. Moles, J. W. Sulentic, and I. Marquez. "The Dynamical Status of Stephan's Quintet". ApJL 485 (1997) L69+. arXiv:astro-ph/9707194, [ADS].

D. J. Mullan. *The Structure of Hydromagnetic Shocks in Regions of Very Low Ionization.* Ph.D. thesis, AA(UNIVERSITY OF MARYLAND COLLEGE PARK.) (1969), [ADS].

D. J. Mullan. "The structure of transverse hydromagnetic shocks in regions oflow ionization". MNRAS153 (1971) 145–+. [ADS].

S. D. Murray and D. N. C. Lin. "Energy Dissipation in Multiphase Infalling Clouds in Galaxy Halos". ApJ 615 (2004) 586–594. arXiv:astro-ph/0407411, [ADS].

C. Nehmé, J. Le Bourlot, F. Boulanger, G. Pineau Des Forêts, and C. Gry. "Modeling of diffuse molecular gas applied to HD 102065 observations". A&A 483 (2008) 485–493. 0802.4003, [ADS].

J. Nella, P. D. Atcheson, C. B. Atkinson, D. Au, A. J. Bronowicki, E. Bujanda, A. Cohen, D. Davies, et al. "James Webb Space Telescope (JWST) Observatory architecture and performance". In J. C. Mather, ed., *Society of Photo-Optical Instrumentation Engineers (SPIE) Conference Series*, vol. 5487, 576–587 (2004). [ADS].

N. P. H. Nesvadba, F. Boulanger, P. Salomé, P. Guillard, M. D. Lehnert, G. Pineau des Forets, and P. N. Ogle, P. Appleton. "Energetics of the molecular gas in the H2-luminous radio galaxy 3C326: Evidence for negative AGN feedback". A&A , submitted (2009).

N. P. H. Nesvadba, M. D. Lehnert, R. I. Davies, A. Verma, and F. Eisenhauer. "Integral-field spectroscopy of a Lyman-break galaxy at z = 3.2: evidence for merging". A&A 479 (2008a) 67–73. 0711.1491, [ADS].

N. P. H. Nesvadba, M. D. Lehnert, C. De Breuck, A. M. Gilbert, and W. van Breugel. "Evidence for powerful AGN winds at high redshift: dynamics of galactic outflows in radio galaxies during the "Quasar Era"". A&A 491 (2008b) 407–424. 0809.5171, [ADS].

N. P. H. Nesvadba, M. D. Lehnert, F. Eisenhauer, A. Gilbert, M. Tecza, and R. Abuter. "Extreme Gas Kinematics in the z=2.2 Powerful Radio Galaxy MRC 1138-262: Evidence for Efficient Active Galactic Nucleus Feedback in the Early Universe?" ApJ 650 (2006) 693–705. arXiv:astro-ph/0606530, [ADS].

D. A. Neufeld, S. Lepp, and G. J. Melnick. "Thermal Balance in Dense Molecular Clouds: Radiative Cooling Rates and Emission-Line Luminosities". ApJS 100 (1995) 132–+. [ADS].

D. A. Neufeld, G. J. Melnick, P. Sonnentrucker, E. A. Bergin, J. D. Green, K. H. Kim, D. M. Watson, W. J. Forrest, et al. "Spitzer Observations of HH 54 and HH 7-11: Mapping the H2 Ortho-to-Para Ratio in Shocked Molecular Gas". ApJ 649 (2006) 816–835. `arXiv:astro-ph/0606232`, [ADS].

P. Ogle, R. Antonucci, P. N. Appleton, and D. Whysong. "Shocked Molecular Hydrogen in the 3C 326 Radio Galaxy System". ApJ 668 (2007) 699–707. `arXiv:0707.0896`, [ADS].

P. Ogle, F. Boulanger, R. Antonucci, P. N. Appleton, and D. Whysong. "Radio Jet Feedback in Molecular Hydrogen Emission Galaxies". ApJ , submitted (2009).

Y. Ohyama, S. Nishiura, T. Murayama, and Y. Taniguchi. "Unusual Emission-Line Regions in the Tidal Arm of NGC 7318B in Stephan's Quintet". ApJL 492 (1998) L25+. [ADS].

D. E. Osterbrock. *Astrophysics of gaseous nebulae and active galactic nuclei* (Research supported by the University of California, John Simon Guggenheim Memorial Foundation, University of Minnesota, et al. Mill Valley, CA, University Science Books, 1989). [ADS].

E. O'Sullivan, S. Giacintucci, J. M. Vrtilek, S. Raychaudhury, R. Athreya, T. Venturi, and L. P. David. "A Joint GMRT/X-ray study of galaxy groups". ArXiv e-prints (2009a). `0906.5610`, [ADS].

E. O'Sullivan, S. Giacintucci, J. M. Vrtilek, S. Raychaudhury, and L. P. David. "A Chandra X-ray View of Stephan's Quintet: Shocks and Star Formation". ApJ 701 (2009b) 1560–1568. `0812.0383`, [ADS].

P. Padoan, A. Nordlund, and B. J. T. Jones. "The universality of the stellar initial mass function". MNRAS288 (1997) 145–152. [ADS].

M. Padovani, D. Galli, and A. E. Glassgold. "Cosmic-ray ionization of molecular clouds". A&A 501 (2009) 619–631. `0904.4149`, [ADS].

T. Passot and E. Vázquez-Semadeni. "Density probability distribution in one-dimensional polytropic gas dynamics". Phys. Rev. E58 (1998) 4501–4510. `arXiv:physics/9802019`, [ADS].

G. R. Petitpas and C. L. Taylor. "A High-Resolution Mosaic of Molecular Gas in Stephan's Quintet". ApJ 633 (2005) 138–147. `arXiv:astro-ph/0508117`, [ADS].

D. Pfenniger, F. Combes, and L. Martinet. "Is dark matter in spiral galaxies cold gas? I. Observational constraints and dynamical clues about galaxy evolution". A&A 285 (1994) 79–93. `arXiv:astro-ph/9311043`, [ADS].

W. Pietsch, G. Trinchieri, H. Arp, and J. W. Sulentic. "X-ray emission components from Stephan's Quintet resolved with the ROSAT HRI." A&A 322 (1997) 89–97. [ADS].

G. Pineau des Forets, D. R. Flower, and J.-P. Chieze. "The physical and chemical effects of C-shocks in molecular outflows". In B. Reipurth and C. Bertout, eds., *Herbig-Haro Flows and the Birth of Stars*, vol. 182 of *IAU Symposium*, 199–212 (1997). [ADS].

V. Pirronello, O. Biham, C. Liu, L. Shen, and G. Vidali. "Efficiency of Molecular Hydrogen Formation on Silicates". ApJL 483 (1997) L131+. `arXiv:astro-ph/9704236`, [ADS].

H. Plana, C. Mendes de Oliveira, P. Amram, M. Bolte, C. Balkowski, and J. Boulesteix. "Detection and Velocities of $H\alpha$ Emission Regions in Stephan's Quintet". ApJL 516 (1999) L69–L72. [ADS].

A. Y. Poludnenko, A. Frank, and E. G. Blackman. "Hydrodynamic Interaction of Strong Shocks with Inhomogeneous Media. I. Adiabatic Case". ApJ 576 (2002) 832–848. `arXiv:astro-ph/0109282`, [ADS].

E. C. D. Pope, T. W. Hartquist, and J. M. Pittard. "Cold gas in the intracluster medium: implications for flow dynamics and powering optical nebulae". MNRAS389 (2008) 1259–1265. `0806.3394`, [ADS].

C. C. Popescu, A. Misiriotis, N. D. Kylafis, R. J. Tuffs, and J. Fischera. "Modelling the spectral energy distribution of galaxies. I. Radiation fields and grain heating in the edge-on spiral NGC 891". A&A 362 (2000) 138–150. `arXiv:astro-ph/0008098`, [ADS].

S. Rawlings, R. Saunders, P. Miller, M. E. Jones, and S. A. Eales. "A New Identification for the Giant Radiosource 3C326". MNRAS246 (1990) 21P–+. [ADS].

F. Renaud. *Simulation of high-velocity collisions in Stephan's Quintet.* Master's thesis, ENSPS (2007).

P. Richter, B. P. Wakker, B. D. Savage, and K. R. Sembach. "A Far Ultraviolet Spectroscopic Explorer Survey of Molecular Hydrogen in Intermediate-Velocity Clouds in the Milky Way Halo". ApJ 586 (2003) 230–248. `arXiv:astro-ph/0211356`, [ADS].

D. Rigopoulou, D. Kunze, D. Lutz, R. Genzel, and A. F. M. Moorwood. "An ISO-SWS survey of molecular hydrogen in starburst and Seyfert galaxies". A&A 389 (2002) 374–386. `arXiv:astro-ph/0206135`, [ADS].

W. G. Roberge and B. T. Draine. "A new class of solutions for interstellar magnetohydrodynamic shock waves". ApJ 350 (1990) 700–721. [ADS].

T. Rodet, F. Orieux, J. . Giovannelli, and A. Abergel. "Data inversion for over-resolved spectral imaging in astronomy". ArXiv e-prints (2009). `0902.1936`, [ADS].

D. Rouan, P. Riaud, A. Boccaletti, Y. Clénet, and A. Labeyrie. "The Four-Quadrant Phase-Mask Coronagraph. I. Principle". PASP 112 (2000) 1479–1486. [ADS].

H. Roussel, G. Helou, D. J. Hollenbach, B. T. Draine, J. D. Smith, L. Armus, E. Schinnerer, F. Walter, et al. "Warm Molecular Hydrogen in the Spitzer SINGS Galaxy Sample". ApJ 669 (2007) 959–981. `arXiv:0707.0395`, [ADS].

P. Salomé, F. Combes, A. C. Edge, C. Crawford, M. Erlund, A. C. Fabian, N. A. Hatch, R. M. Johnstone, et al. "Cold molecular gas in the Perseus cluster core. Association with X-ray cavity, Hα filaments and cooling flow". A&A 454 (2006) 437–445. `arXiv:astro-ph/0603350`, [ADS].

J. Scalo and B. G. Elmegreen. "Interstellar Turbulence II: Implications and Effects". ARAA 42 (2004) 275–316. `arXiv:astro-ph/0404452`, [ADS].

J. M. Scalo. "Theoretical approaches to interstellar turbulence". In D. J. Hollenbach and H. A. Thronson, Jr., eds., *Interstellar Processes*, vol. 134 of *Astrophysics and Space Science Library*, 349–392 (1987). [ADS].

M. Schmidt. "The Rate of Star Formation." ApJ 129 (1959) 243–+. [ADS].

K. Schofield. "An evaluation of kinetic rate data for reactions of neutrals of atmospheric interest". Planet. Space Sci.15 (1967) 643–+. [ADS].

G. Shaw, G. J. Ferland, N. P. Abel, P. C. Stancil, and P. A. M. van Hoof. "Molecular Hydrogen in Star-forming Regions: Implementation of its Microphysics in CLOUDY". ApJ 624 (2005) 794–807. `arXiv:astro-ph/0501485`, [ADS].

M.-S. Shin, J. M. Stone, and G. F. Snyder. "The Magnetohydrodynamics of Shock-Cloud Interaction in Three Dimensions". ApJ 680 (2008) 336–348. `arXiv:0802.2708`, [ADS].

G. S. Shostak, R. J. Allen, and W. T. Sullivan, III. "HI synthesis observations of the high-redshift galaxies in Stephan's Quintet". A&A 139 (1984) 15–24. [ADS].

F. Shu. *Physics of Astrophysics, Vol. II: Gas Dynamics* (Published by University Science Books, 648 Broadway, Suite 902, New York, NY 10012, 1991., 1991). [ADS].

J. M. Shull. "Disruption and sputtering of grains in intermediate-velocity interstellar clouds". ApJ 226 (1978) 858–862. [ADS].

J. M. Shull and S. Beckwith. "Interstellar molecular hydrogen". ARAA 20 (1982) 163–190. [ADS].

J. Silk and M. J. Rees. "Quasars and galaxy formation". A&A 331 (1998) L1–L4. `arXiv:astro-ph/9801013`, [ADS].

C. Simpson, M. Ward, D. L. Clements, and S. Rawlings. "Emission-line ratios in a radio-selected sample of active galactic nuclei." MNRAS281 (1996) 509–521. [ADS].

J. D. Slavin, J. M. Shull, and M. C. Begelman. "Turbulent mixing layers in the interstellar medium of galaxies". ApJ 407 (1993) 83–99. [ADS].

B. J. Smith and C. Struck. "New Observations of Extra-Disk Molecular Gas in Interacting Galaxy Systems, Including a Two-Component System in Stephan's Quintet". AJ 121 (2001) 710–726. `arXiv:astro-ph/0011093`, [ADS].

R. K. Smith, L. G. Krzewina, D. P. Cox, R. J. Edgar, and W. W. I. Miller. "Time-dependent Cooling and Grain Destruction in Hot Dusty Plasmas: A Simplified Model and Principal Results". ApJ 473 (1996) 864–+. [ADS].

P. M. Solomon and J. W. Barrett. "The CO - H2 Mass Conversion Factor". Dynamics of Galaxies and Their Molecular Cloud Distributions 146 (1991) 235–+. [ADS].

P. M. Solomon, A. R. Rivolo, J. Barrett, and A. Yahil. "Mass, luminosity, and line width relations of Galactic molecular clouds". ApJ 319 (1987) 730–741. [ADS].

L. Spitzer. *Physics of Fully Ionized Gases* (1962). [ADS].

L. Spitzer, Jr. and E. B. Jenkins. "Ultraviolet studies of the interstellar gas". ARAA 13 (1975) 133–164. [ADS].

L. J. Spitzer. "On a Possible Interstellar Galactic Corona." ApJ 124 (1956) 20–+. [ADS].

V. Springel, T. Di Matteo, and L. Hernquist. "Modelling feedback from stars and black holes in galaxy mergers". MNRAS361 (2005) 776–794. `arXiv:astro-ph/0411108`, [ADS].

P. C. Stancil, S. Lepp, and A. Dalgarno. "The Deuterium Chemistry of the Early Universe". ApJ 509 (1998) 1–10. [ADS].

J. Stebbins. "The Dark Galaxy". The Scientific Monthly 39 (1934) 129–143. [ADS].

J. Stebbins. "Dust between the Stars". The Scientific Monthly 40 (1935) 270–272. [ADS].

T. P. Stecher. "Interstellar Ectinction in the Ultraviolet." ApJ 142 (1965) 1683–+. [ADS].

T. P. Stecher and B. Donn. "On Graphite and Interstellar Extinction". ApJ 142 (1965) 1681–+. [ADS].

M. Stephan. "Nebulae (new) discovered and observed at the observatory of Marseille". CR Acad Sci Paris 84 (1877) 641.

B. Stepnik, A. Abergel, J.-P. Bernard, F. Boulanger, L. Cambrésy, M. Giard, A. P. Jones, G. Lagache, et al. "Evolution of dust properties in an interstellar filament". A&A 398 (2003) 551–563. [ADS].

A. Sternberg. "Ultraviolet fluorescent molecular hydrogen emission". ApJ 347 (1989) 863–874. [ADS].

A. Sternberg, A. Dalgarno, and S. Lepp. "Cosmic-ray-induced photodestruction of interstellar molecules in dense clouds". ApJ 320 (1987) 676–682. [ADS].

J. W. Sulentic, M. Rosado, D. Dultzin-Hacyan, L. Verdes-Montenegro, G. Trinchieri, C. Xu, and W. Pietsch. "A Multiwavelength Study of Stephan's Quintet". AJ 122 (2001) 2993–3016. arXiv:astro-ph/0111155, [ADS].

R. S. Sutherland, G. V. Bicknell, and M. A. Dopita. "The Numerical Simulation of Radiative Shocks. II. Thermal Instabilities in Two-dimensional Models". ApJ 591 (2003) 238–257. [ADS].

R. S. Sutherland and M. A. Dopita. "Cooling functions for low-density astrophysical plasmas". ApJS 88 (1993) 253–327. [ADS].

B. Swinyard, T. Nakagawa, P. Merken, P. Royer, T. Souverijns, B. Vandenbussche, C. Waelkens, P. Davis, et al. "The space infrared telescope for cosmology and astrophysics: SPICA A joint mission between JAXA and ESA". Experimental Astronomy 23 (2009) 193–219. [ADS].

B. M. Swinyard, G. H. Rieke, M. Ressler, A. Glasse, G. S. Wright, M. Ferlet, and M. Wells. "Sensitivity estimates for the mid-infrared instrument (MIRI) on the JWST". SPIE 5487 (2004) 785–793. [ADS].

G. A. Tammann. "Stephan's Quintet or Quartet?" Astrophys. Lett.7 (1970) 111–+. [ADS].

A. G. G. M. Tielens. *The Physics and Chemistry of the Interstellar Medium* (Cambridge University Press, 2005). [ADS].

A. G. G. M. Tielens and L. J. Allamandola. "Composition, structure, and chemistry of interstellar dust". Astrophysics and Space Science Library 134 (1987) 397–469. [ADS].

A. G. G. M. Tielens, C. F. McKee, C. G. Seab, and D. J. Hollenbach. "The physics of grain-grain collisions and gas-grain sputtering in interstellar shocks". ApJ 431 (1994) 321–340. [ADS].

R. Timmermann. "Ortho-H 2/Para-H 2 Ratio in Low-Velocity Shocks". ApJ 498 (1998) 246–+. [ADS].

S. Tine, S. Lepp, R. Gredel, and A. Dalgarno. "Infrared Response of H 2 to X-Rays in Dense Clouds". ApJ 481 (1997) 282–+. [ADS].

S. Tiné, D. A. Williams, D. C. Clary, A. J. Farebrother, A. J. Fisher, A. J. H. M. Meijer, J. M. C. Rawlings, and C. J. Davis. "Observational Indicators of Formation Excitation of H2". Ap&SS288 (2003) 377–389. [ADS].

G. Trinchieri, J. Sulentic, D. Breitschwerdt, and W. Pietsch. "Stephan's Quintet: The X-ray anatomy of a multiple galaxy collision". A&A 401 (2003) 173–183. arXiv:astro-ph/0302590, [ADS].

G. Trinchieri, J. Sulentic, W. Pietsch, and D. Breitschwerdt. "Stephan's Quintet with XMM-Newton". A&A 444 (2005) 697–710. arXiv:astro-ph/0506761, [ADS].

R. J. Trumpler. "Absorption of Light in the Galactic System". PASP 42 (1930) 214–+. [ADS].

J. Turner, K. Kirby-Docken, and A. Dalgarno. "The Quadrupole Vibration-Rotation Transition Probabilities of Molecular Hydrogen". ApJS 35 (1977) 281–+. [ADS].

E. A. Valentijn and P. P. van der Werf. "First Extragalactic Direct Detection of Large-Scale Molecular Hydrogen in the Disk of NGC 891". ApJL 522 (1999) L29–L33. [ADS].

J. M. van der Hulst and A. H. Rots. "VLA observations of the radio continuum emission from Stephan's Quintet". AJ 86 (1981) 1775–1780. [ADS].

P. P. van der Werf, R. Genzel, A. Krabbe, M. Blietz, D. Lutz, S. Drapatz, M. J. Ward, and D. A. Forbes. "Near-infrared line imaging of NGC 6240 - Collision shock and nuclear starburst". ApJ 405 (1993) 522–537. [ADS].

E. Vazquez-Semadeni. "Hierarchical Structure in Nearly Pressureless Flows as a Consequence of Self-similar Statistics". ApJ 423 (1994) 681–+. [ADS].

E. Vázquez-Semadeni, A. Gazol, and J. Scalo. "Is Thermal Instability Significant in Turbulent Galactic Gas?" ApJ 540 (2000) 271–285. arXiv:astro-ph/0001027, [ADS].

S. Veilleux, D. S. N. Rupke, and R. Swaters. "Warm Molecular Hydrogen in the Galactic Wind of M82". ApJL 700 (2009) L149–L153. 0907.1422, [ADS].

L. Verdes-Montenegro, M. S. Yun, J. Perea, A. del Olmo, and P. T. P. Ho. "Effects of Interaction-induced Activities in Hickson Compact Groups: CO and Far-Infrared Study". ApJ 497 (1998) 89–+. arXiv:astro-ph/9711127, [ADS].

W. Vieser and G. Hensler. "Evaporation and condensation of spherical interstellar clouds. Self-consistent models with saturated heat conduction and cooling". A&A 475 (2007a) 251–262. 0709.0623, [ADS].

W. Vieser and G. Hensler. "The evolution of interstellar clouds in a streaming hot plasma including heat conduction". A&A 472 (2007b) 141–153. 0704.3592, [ADS].

J. M. Vilchez and J. Iglesias-Paramo. "Atlas of H alpha Emission of a Sample of Nearby Hickson Compact Groups of Galaxies". ApJS 117 (1998) 1–+. [ADS].

G. M. Voit. "Energy deposition by X-ray photoelectrons into interstellar molecular clouds". ApJ 377 (1991) 158–170. [ADS].

J. C. Weingartner and B. T. Draine. "Dust Grain-Size Distributions and Extinction in the Milky Way, Large Magellanic Cloud, and Small Magellanic Cloud". ApJ 548 (2001) 296–309. astro-ph/0008146, [ADS].

D. Wilgenbus, S. Cabrit, G. Pineau des Forêts, and D. R. Flower. "The ortho:para-H2 ratio in C- and J-type shocks". A&A 356 (2000) 1010–1022. [ADS].

B. A. Williams, M. S. Yun, and L. Verdes-Montenegro. "The VLA H I Observations of Stephan's Quintet (HCG 92)". AJ 123 (2002) 2417–2437. [ADS].

A. G. Willis and R. G. Strom. "Multifrequency observations of very large radio galaxies. I - 3C 326". A&A 62 (1978) 375–392. [ADS].

M. G. Wolfire, D. Hollenbach, C. F. McKee, A. G. G. M. Tielens, and E. L. O. Bakes. "The neutral atomic phases of the interstellar medium". ApJ 443 (1995) 152–168. [ADS].

L. Wolniewicz, I. Simbotin, and A. Dalgarno. "Quadrupole Transition Probabilities for the Excited Rovibrational States of H 2". ApJS 115 (1998) 293–+. [ADS].

J.-H. Woo and C. M. Urry. "Active Galactic Nucleus Black Hole Masses and Bolometric Luminosities". ApJ 579 (2002) 530–544. arXiv:astro-ph/0207249, [ADS].

S. A. Wrathmall and D. R. Flower. "The rovibrational excitation of H2 induced by H". Journal of Physics B Atomic Molecular Physics 40 (2007) 3221–3230. [ADS].

S. A. Wrathmall, A. Gusdorf, and D. R. Flower. "The excitation of molecular hydrogen by atomic hydrogen in astrophysical media". MNRAS382 (2007) 133–138. [ADS].

E. Xanthopoulos, T. W. B. Muxlow, P. Thomasson, and S. T. Garrington. "MERLIN observations of Stephan's Quintet". MNRAS353 (2004) 1117–1125. [ADS].

C. Xu, J. W. Sulentic, and R. Tuffs. "Starburst in the Intragroup Medium of Stephan's Quintet". ApJ 512 (1999) 178–183. arXiv:astro-ph/9808344, [ADS].

C. K. Xu. "Stephan's Quintet: A Multi-galaxy Collision". In *Publication of Purple Mountain Observatory* (2006). arXiv:astro-ph/0601084, [ADS].

C. K. Xu, P. N. Appleton, M. Dopita, Y. Gao, N. Y. Lu, C. Popescu, W. T. Reach, J. Sulentic, et al. "Spitzer Observations of Stephan's Quintet – IGM Dust and Gas in a Multi-galaxy Collision". In R.-R. Chary, H. I. Teplitz, & K. Sheth, ed., *Infrared Diagnostics of Galaxy Evolution*, vol. 381 of *Astronomical Society of the Pacific Conference Series*, 88–+ (2008). [ADS].

C. K. Xu, J. Iglesias-Páramo, D. Burgarella, R. M. Rich, S. G. Neff, S. Lauger, T. A. Barlow, L. Bianchi, et al. "Ultraviolet Emission and Star Formation in Stephan's Quintet". ApJL 619 (2005) L95–L98. arXiv:astro-ph/0411319, [ADS].

C. K. Xu, N. Lu, J. J. Condon, M. Dopita, and R. J. Tuffs. "Physical Conditions and Star Formation Activity in the Intragroup Medium of Stephan's Quintet". ApJ 595 (2003) 665–684. arXiv:astro-ph/0306261, [ADS].

L. Yan, R. Chary, L. Armus, H. Teplitz, G. Helou, D. Frayer, D. Fadda, J. Surace, et al. "Spitzer Detection of Polycyclic Aromatic Hydrocarbon and Silicate Dust Features in the Mid-Infrared Spectra of z ˜ 2 Ultraluminous Infrared Galaxies". ApJ 628 (2005) 604–610. arXiv:astro-ph/0504336, [ADS].

H. W. Yorke, G. Tenorio-Tagle, P. Bodenheimer, and M. Rozyczka. "The combined role of ionization and supernova explosions in the destruction of molecular clouds". A&A 216 (1989) 207–214. [ADS].

M. S. Yun, L. Verdes-Montenegro, A. del Olmo, and J. Perea. "Molecular Gas and Infrared Emission in HCG 31 and HCG 92 (Stephan's Quintet) and Tidal Interactions in Compact Group Environment". ApJL 475 (1997) L21+. [ADS].

F. Yusef-Zadeh, M. Wardle, and S. Roy. "Cosmic-Ray Heating of Molecular Gas in the Nuclear Disk: Low Star Formation Efficiency". ApJL 665 (2007) L123–L126. 0707.0910, [ADS].

Y. B. Zeldovich and Y. P. Raizer. *Elements of gas dynamics and the classical theory of shock waves* (1966). [ADS].

Index